Thermodynamic Modeling and Experimental Study of the Al-Cr-Cu-Fe-Mg-Mn-Si System

Senlin Cui

A thesis submitted to McGill University in partial fulfilment of the requirements of the degree of Doctorate of Philosophy

September 2016
Department of Mining and Materials Engineering
McGill University
Montreal, Canada

Dedication

I would like to dedicate this thesis to my beloved family in China.

Contents

Abstract

Aluminum alloys are extensively used in civil engineering, ship building, automotive, and aerospace industry. The requirement of improving fuel efficiency and weight reduction of vehicle triggers a resurgence of research of aluminum in automobile industry. Al 6xxx series alloys are commonly utilized as extruded materials because of their high strength, formability and ductility, weldability, corrosion resistance, and low cost. The whole chain of Al alloy component manufacturing starts from aluminum melt refining, to casting, homogenization, rolling/extrusion, and finally heat treatment. The microstructure evolution of Al alloys is controlled by both thermodynamics and kinetics. The driving forces for each processing step basically include the chemical driving force or thermodynamic driving force, the interfacial energy, the mechanical driving force, etc. Thermodynamics related to chemical reactions and phase transformations is thus of fundamental importance.

The study of thermochemical properties and phase diagram of Al alloys is helpful for new Al alloy composition design and process optimization. The CALPHAD (CALculation of PHAse Diagram) approach is one of the most efficient ways to study alloy thermodynamics systematically. With a well-developed Al alloy thermodynamic database, the phase equilibria and thermodynamic properties can be calculated for complex alloy systems.

As a cornerstone for the understanding of various phenomena in Al 6xxx alloys, the current work focuses on the development of a thermodynamic database for the Al-Cr-Cu-Fe-Mg-Mn-Si system via a coupled experimental and thermodynamic modeling approach. Isothermal sections in the Al rich corner of the Al-Cr-Mg system were measured at 400, 450, and 500 °C via equilibrated alloys, diffusion couples, and differential thermal analysis (DSC). The thermodynamic optimizations of the binary Al-Cr, Cu-Cr, Cu-Mg, Cr-Si, and Fe-Si systems were newly performed, and the thermodynamic descriptions of the Al-Mn, Cu-Mn, Cr-Fe, Cr-Mg, and Cr-Mn systems were revised. The ternary Al-Cu-Cr, Al-Cu-Mg, Al-Cu-Si, Al-Cr-Mg, Al-Cr-Mn, Al-Cr-Si, Cu-Fe-Cr, Cu-Fe-Mn, Cu-Mg-Si, Cr-Fe-Si, and Fe-Mg-Si systems were thermodynamically modeled, and the Al-Cu-Mn system was revised. Moreover, the quaternary Al-Cu-Mg-Si system was remodeled. The optimization or revision of the thermodynamic descriptions of all the systems were based on

the current experimental results and the critically evaluated literature data including phase diagram, enthalpy of mixing, activity, Gibbs energy of formation, enthalpy of formation, standard entropy, heat capacity, etc. The liquid phase was described using the Modified Quasi-chemical Model (MQM) in pair approximation, and the Compound Energy Formalism (CEF) was utilized for the descriptions of all the solid phases. The order-disorder transitions (bcc_A2/bcc_B2 transition and bcc_B2/bcc_D03 transition) were modeled using the split compound energy formalism. A self-consistent set of thermodynamic description for the Al-Cr-Cu-Fe-Mg-Mn-Si system was obtained by combining the currently assessed thermodynamic parameters with the thermodynamic parameters available in the literature.

The obtained thermodynamic database was applied to investigate the recycling of Al alloys. The effect of each major and impurity alloying element on the types of precipitates and their amounts in both the solidification and equilibrium conditions were also systematically investigated for the Al 6xxx series alloys using the thermodynamic calculations with the present new database.

Résumé

Les alliages d'aluminium sont largement utilisés dans le génie civil, la construction navale, l'automobile et l'industrie aérospatiale. L'exigence d'amélioration de l'efficacité énergétique et de la réduction du poids des véhicules a déclenché une résurgence de la recherche sur l'aluminium dans l'industrie automobile. Les alliages d'Al de la série 6xxx sont couramment utilisés comme matières extrudées en raison de leur résistance élevée, de leur ductilité et formabilité, de leur soudabilité, de leur résistance à la corrosion et de leur faible coût. L'ensemble de la chaîne de fabrication de composants en alliage d'aluminium commence avec le raffinage de l'Al à l'état fondu puis se poursuit avec la coulée, l'homogénéisation, le laminage/extrusion et se termine avec un traitement thermique. L'évolution de la microstructure des alliages d'Al est contrôlée par la thermodynamique et la cinétique. Les forces motrices pour chaque étape de traitement comprennent essentiellement la force motrice chimique ou la force motrice thermodynamique, l'énergie interfaciale, la force motrice mécanique, etc. La thermodynamique liée aux réactions chimiques et aux transformations de phase est donc d'une importance fondamentale.

L'étude des propriétés thermodynamiques et des diagrammes de phase des alliages d'Al est utile pour les nouveaux modèles de composition d'alliage d'Al et d'optimisation des processus. L'approche CALPHAD (CALcul de diagramme de PHAse) est l'un des moyens les plus efficaces pour étudier systématiquement la thermodynamique des alliages. Avec une bonne base de données thermodynamiques d'alliages d'Al, les équilibres de phases et les propriétés thermodynamiques peuvent être calculées pour des systèmes d'alliages complexes.

En tant que pierre angulaire de la compréhension de différents phénomènes dans les alliages d'Al 6xxx, le travail en cours se concentre sur le développement d'une base de données thermodynamiques pour le système Al-Cr-Cu-Fe-Mg-Mn-Si via une approche couplée de modélisation expérimentale et thermodynamique. Des sections isothermes dans le coin riche en Al du système Al-Cr-Mg ont été mesurées à 400, 450 et 500 °C par l'intermédiaire d'alliages équilibrés, de couples de diffusion et d'analyse thermique différentielle (DSC). L'optimisation thermodynamique des systèmes binaires Al-Cr, Cu-Cr, Cu-Mg, Cr-Si, et Fe-Si fut nouvellement

effectuée et les descriptions thermodynamiques des systèmes Al-Mn, Cu-Mn, Cr-Fe, Cr-Mg et Cr-Mn ont été révisés. Les systèmes ternaires Al-Cu-Cr, Al-Cu-Mg, Al-Cu-Si, Al-Cr-Mg, Al-Cr-Mn, Al-Cr-Si, Cu-Fe-Cr, Cu-Fe-Mn, Cu-Mg-Si, Cr-Fe-Si, et Fe-Mg-Si ont été modélisés thermodynamiquement et le système Al-Cu-Mn a été révisé. En outre, le système quaternaire Al-Cu-Mg-Si a été remodelisé. L'optimisation ou la révision des descriptions thermodynamiques de tous les systèmes ont été basé sur nos nouveaux résultats expérimentaux et sur l'évaluation critique de données de la littérature tel que des diagrammes de phases, des enthalpies de mélange, des activités, des énergies de Gibbs de formation, des enthalpies de formation, des entropies standards, des capacités calorifiques, etc. La phase liquide a été décrite à l'aide du modèle quasi-chimique modifié (MQM) approximant les paires et le formalisme d'énergie des composés (CEF) a été utilisé pour la description de toutes les phases solides. Les transitions ordre-désordre (bcc_A2/bcc_B2 et bcc_B2/bcc_D03) ont été modélisées en utilisant le formalisme d'énergie des composés de scission. Un ensemble cohérent de paramètres thermodynamiques pour le système Al-Cr-Cu-Fe-Mg-Mn-Si a été obtenu en combinant les paramètres thermodynamiques actuellement évalués avec les paramètres thermodynamiques disponibles dans la littérature.

La base de données thermodynamiques obtenue a été utilisée pour étudier le recyclage des alliages d'Al. L'effet de chaque élément majeur d'impuretés d'alliage sur les types de précipités et leurs quantités dans des conditions de solidification et d'équilibre a également été systématiquement étudié pour les alliages de la série 6xxx Al en utilisant des calculs thermodynamiques avec notre nouvelle base de données.

Acknowledgements

I would like to acknowledge the McGill Engineering Doctorate Award (MEDA) program from McGill University for financial support.

My thesis was partial financially supported by my supervisor, associate Prof. In-Ho Jung, from the funding of GM Canada and the Natural Sciences and Engineering Research Council of Canada, I would like to thank him also.

Financial supports from the Aluminium Research Centre – REGAL, CALPHAD Inc., and Foundation of Stiftelsen för Tillämpad Termodynamik are acknowledged.

I would like to thank all the members of the High Temperature Thermochemistry Laboratory in Department of Mining and Materials Engineering at McGill University for providing a friendly working environment.

I would like to thank Dr. Pierre Hudon for translating the abstract into French and Mr. Lang Shi at Electron Microprobe Facility at McGill University for analyzing samples.

Preface

Most of the work presented was performed at Department of Mining and Materials Engineering, McGill University, Canada. As the major investigator, Senlin Cui contributed to all the literature survey, literature review, thermodynamic optimizations, experiment design and experiments, experimental data analysis, and manuscripts drafting. In-Ho Jung contributed to the manuscripts drafting. In chapter 4, Jinhua Xin computed the enthalpy of formation of the $Al_{18}Cr_2Mg_3$ phase using first principles calculations, Senlin Cui and Junghwan Kim cooperatively did each other's PhD experiments. Chapters 4, 5, 6, 7, 9, 10, 11, and 12 presented in the present dissertation are planned to publish as papers in peer reviewed journals.

Chapter 1 Introduction

1.1 Background

Al alloys are widely used in civil engineering, automotive, ship building, and aerospace industry due to their high strength, formability, weldability, corrosion resistance, and low density [1]. Demand for Al in final products has increased 30-fold since 1950, and reaches 45 million tonnes per year. It is forecasted that there is a continuous growth and the demand will reach 2-3 times of today's level by 2050 [2].

Al is the most abundant metallic element on earth and has a face centred cubic (fcc) structure. It is known that high purity Al with low strength which cannot cater for the need of different working conditions. Alloying elements, such as Mg, Si, Cu, Mn, and Zn, are commonly added to pure Al to form Al alloys. Al alloys with specialized amounts and types of alloying elements are categorized into different series due to their characterized properties. For instance, Al alloyed with Mg and Si is nominated as 6xxx series which are easy machining, welding, and can be precipitation hardened. Fe and Cr are also common elements in Al alloys. Fe is considered as the major impurity element with detrimental effect in most cases. Cr is added into Al alloys as dispersoid former [3]. Different types of precipitates containing Cr such as $Al_{11}Cr_4$ and Al_7Cr [4] can form during high temperature annealing. These phases are normally used for grain refinement which has strong effect on the recovery, recrystallization, and grain growth processes.

Several processes, such as liquid refining, casting, homogenization, extrusion, and heat treatment, etc., can take place in the whole chain of Al alloy components manufacturing. The microstructure of Al alloys undergoes various kinds of evolutions which are controlled by both the thermodynamics and kinetics behind. For instance, the refining of Al melts is actually based on the thermochemical properties of the constitutional elements. The evolution of microstructure during solidification, homogenization, and final heat treatment processes is mainly governed by thermodynamics, diffusivities of alloying elements, and interfacial energy. Therefore, it will be very helpful if the thermodynamic properties of the alloy system are well studied before new alloy

design and manufacturing process optimization. The time and the cost of new alloy development can be substantially shortened.

The CALPHAD technique initiated by Kaufman et al. [5] is proved to be an efficient way to study the phase diagram of multicomponent Al system [6]. In the CALPHAD type of assessment, all the available thermodynamic and phase equilibrium data in the system are critically evaluated and assessed. From the optimization, a set of self-consistent thermodynamic parameters for the system studied can be obtained to represent the Gibbs energy of each phase in the system. With the aid of thermodynamic software such as Thermocalc [7] and FactSage [8] the thermodynamic properties and phase diagram can be calculated. The database is developed from the low order system to the high order one. Well-established thermodynamic database of the low order systems based on the reliable thermodynamic models has certain rationality in the prediction of the thermodynamic properties and phase relation in multicomponent system.

The current PhD work is a part of the automotive partnership Canada (APC) project. This APC project aimed to develop high strength, high crash efficiency, and extruded aluminum front rails for lightweight bodies. One part of this project is to develop a new Al alloy with high strength and high energy absorption ability based on the properties of the "pilot" alloy AA6063. Accurate Al alloy thermodynamic database for the Al 6xxx series alloy system is the prerequisite for the new alloy composition design and the manufacturing process optimization. The current PhD thesis focuses on the development of a CALPHAD-type thermodynamic database which includes all the major alloy elements in Al 6xxx series alloys covering the Al-Cr-Cu-Fe-Mg-Mn-Si system.

1.2 The CALPHAD method

Phase diagram represents the phase relation of a system at the thermodynamic equilibrium condition. The phase condition of material is determined by the phase composition and temperature, and phase diagram is actually a type of diagram to show the state of material related to temperature and chemistry. At a given temperature and composition, the state which has a minimum Gibbs energy is stable. If the Gibbs energy of each phase at different temperature and

composition is known, the phase diagram can be calculated on the basis of the Gibbs energy minimization or parallel tangent line theory.

Under the equilibrium condition, the total Gibbs energy of a closed system should reach its minimum:

$$G = \sum_{\varphi} n^{\varphi} g^{\varphi} = \min \tag{1.1}$$

where n^{φ} is the number of moles of phase φ, and g^{φ} is the molar Gibbs energy of phase φ.

The chemical potential of element i, μ_i is defined as:

$$\mu_i = g_i = (\partial G / \partial n_i)_{T,P,n_{j \neq i}} \tag{1.2}$$

where G is the Gibbs energy of a solution, n_i is the number of moles of component i, and g_i is the partial molar Gibbs energy of component i. μ_i should be equal in all the phases that are in equilibrium,

$$\mu_i^1 = \mu_i^2 = \cdots = \mu_i^{\varphi} \tag{1.3}$$

The CALPHAD type of computational thermodynamics is one of the most mature and extensively used phase diagram calculation techniques. During thermodynamic modeling, crystal structure, magnetic ordering, and chemical ordering information are considered in the development of thermodynamic model for each phase. The Gibbs energy expression of a solution phase is given based on the thermodynamic model. Thermodynamic parameters can be optimized by a least square method to minimize the difference between the model predicted value and the related experimentally measured ones. Finally, the phase diagram can be calculated from the model with optimized parameters according to the phase equilibrium condition.

The reliability of the developed thermodynamic database highly depends on the experimental data considered in the course of the database development. The measured experimental data, such as phase diagram information, enthalpy of mixing, activity, Gibbs energy, etc., should be strictly evaluated to ensure a high accuracy of the optimized thermodynamic parameters. A standard thermodynamic optimization process is divided into literature survey, critical evaluation of experimental data, model selection, optimization, and database development. In the first step, the literature available experimental and theoretical phase diagram data, thermodynamic quantities (enthalpies, activities, etc.), and crystallographic information (symmetry, site occupations, etc.) are collected. Afterwards, all the collected information is analyzed and assembled. Experimental data should be preliminarily selected by checking the appropriateness of experimental methods, systematic errors, impurities, etc. In the third step, the stable phases and the corresponding thermodynamic model for each phase are selected based on the crystal structure and evaluated phase diagram information. Finally, optimization of the model parameters for the Gibbs energy of each phase should be done via the least square fit to reproduce the evaluated experimental data. The consistency among the selected experimental data should be checked during the optimization. Some inconsistent data may need to be excluded from the optimization. If the thermodynamic model could not give a reasonable description of the phase, alternative model should be considered. Once a set of consistent thermodynamic description of lower order systems is obtained, the extrapolation behavior to higher order systems should be checked. Unreasonable extrapolation indicates that the thermodynamic parameters of lower order systems have consistency problem. The finally obtained thermodynamic description of a system can be used to back calculate the phase diagram and thermodynamic properties of the system.

As the development of various thermodynamic databases, the CALPHAD approach is becoming more and more popular in new material and process design. Until now, several scientific groups [9-11] have contributed to the development of thermodynamic databases. The available commercial thermodynamic softwares are Thermocalc [12], Pandat [13], and FactSage [14]. Thermoclac software was developed by KTH (Royal Institute of Technology) in Sweden. Thermocalc company dedicates to the model and database development for the thermo-physical properties of materials. The Compound Energy Formalism (CEF) [15] developed by Thermocalc community is the most widely used model for the thermodynamic modeling of the solid and liquid

phases. Thermocalc also did pioneering work in the modeling of alloy thermodynamics and diffusion for both metallic and oxide systems. Pandat which was ogringinally developed by University of Wisconsin (Madison, USA) also has developed the alloy thermodynamic database and diffusion database. The FACT group at Ecole Polytechnique in Canada has collaborated with GTT technology in Germany to develop the FactSage software. The FACT group is mainly focused on the modeling of phase diagram and thermo-physical properties of oxides, salts, and metallic system.

1.3 Objective

The current work focuses on the development of a thermodynamic database of the Al-Cr-Cu-Fe-Mg-Mn-Si system using a coupled experiment and thermodynamic modeling approach for the 6xxx series aluminum alloys. This is a fundamental part of the APC project to develop high strength and high crash efficiency extruded aluminum front rails for lightweight bodies. The general structure can be seen in Fig. 1.1. There are five research themes, and the interplay of teams can be seen. The present study will provide fundamental alloy design concept and providing guidences for casting and heat treatment process. This project is financially funded by GM (General Motors) Canada and NSERC (The Natural Sciences and Engineering Research Council of Canada).

Many binary and ternary sub-systems within the Al-Cr-Cu-Fe-Mg-Mn-Si system have been critically evaluated and thermodynamically optimized and stored in the FactSage FTlite database. In this study, the thermodynamic modeling of the binary and ternary systems in particular with Cr are performed. The detailed list of the systems investigated in the present PhD thesis is shown below:

- 10 binary systems include: The Al-Cr system, the Al-Mn system, the Cr-Fe system, the Cr-Mg system, the Cr-Mn system, the Cr-Si system, the Cr-Cu system, the Cu-Mg system, the Cu-Mn system, and the Fe-Si system;
- 12 ternary systems include: The Al-Cr-Si system, the Al-Cr-Mn system, the Al-Cr-Mg system, the Al-Cu-Cr system, the Al-Cu-Mn system, the Al-Cu-Mg system, the

Al-Cu-Si system, the Cu-Fe-Mn system, the Cu-Fe-Cr system, the Fe-Mg-Si system, the Fe-Cr-Si system, and the Cu-Mg-Si system;

- 1 quaternary system includes: The Al-Cu-Mg-Si system.

The optimized thermodynamic database will be utilized for new front rail Al alloy design and extending the FactSage light alloy database.

1.4 Organization

The present PhD thesis includes 13 chapters and it is organized as below:

- **Chapter 1** is the general introduction.
- **Chapter 2** is the general overview of the thermodynamic models related to the present PhD thesis.
- **Chapter 3** briefly introduces the experimental techniques, sample preparation, and characterization techniques for the current phase diagram study.
- **Chapter 4** presents the experimental results of the Al-Cr-Mg system and the thermodynamic modeling results of the Al-Cr, Cr-Mg, and Al-Cr-Mg systems.
- **Chapter 5** shows the thermodynamic modeling results of the Al-Mn, Cr-Mn, and Al-Cr-Mn systems.
- **Chapter 6** is the thermodynamic modeling results about the Cr-Si and Al-Cr-Si systems.
- **Chapter 7** presents the thermodynamic assessment results of the Cu-Cr, Fe-Cr, Cu-Mn, Cu-Fe-Cr, and Cu-Fe-Mn systems.
- **Chapter 8** presents the optimization results about the Al-Cu-Cr and Al-Cu-Mn systems.
- **Chapter 9** is the thermodynamic assessment results of the Cu-Mg, Al-Cu-Mg, Al-Cu-Si, and Al-Cu-Mg-Si systems.
- **Chapter 10** gives the thermodynamic reassessment results of the Fe-Si system with two sets of different thermodynamic descriptions.
- **Chapter 11** presents the thermodynamic modeling results of the Fe-Cr-Si and Fe-Mg-Si systems.

- **Chapter 12** is the application part of this thesis. The thermodynamic database developed in this study are utilized to analyze the recycling of aircraft Al alloys and to study the phase fraction map of 6xxx series Al alloys in both equilibrium state and during solidification.
- **Chapter 13** summarizes the results of the present PhD thesis, and gives some suggestions for the future work.

References

1. Panigrahi, S.K. and R. Jayaganthan, *Development of ultrafine grained Al-Mg-Si alloy with enhanced strength and ductility.* J. Alloys Compd., 2009. **470**(1-2): p. 285-288.
2. Cullen Jonathan, M. and M. Allwood Julian, *Mapping the global flow of aluminum: from liquid aluminum to end-use goods.* Environ Sci Technol, 2013. **47**(7): p. 3057-64.
3. Lodgaard, L. and N. Ryum, *Precipitation of dispersoids containing Mn and/or Cr in Al-Mg-Si alloys.* Mater. Sci. Eng., A, 2000. **A283**(1-2): p. 144-152.
4. Radetic, T., M. Popovic, and E. Romhanji, *Microstructure evolution of a modified AA5083 aluminum alloy during a multistage homogenization treatment.* Mater. Charact., 2012. **65**: p. 16-27.
5. Kaufman, L. and H. Bernstein, *Computer calculation of phase diagrams.* New York：Academic Press, 1970.
6. Du, Y., S. Liu, L. Zhang, H. Xu, D. Zhao, A. Wang, and L. Zhou, *An overview on phase equilibria and thermodynamic modeling in multicomponent Al alloys: Focusing on the Al-Cu-Fe-Mg-Mn-Ni-Si-Zn system.* CALPHAD: Comput. Coupling Phase Diagrams Thermochem., 2012. **35**(3): p. 427-445.
7. Andersson, J.O., T. Helander, L. Hoglund, P. Shi, and B. Sundman, *Thermo-Calc & DICTRA, computational tools for materials science.* CALPHAD Comput. Coupling Phase Diagrams Thermochem., 2002. **26**(2): p. 273-312.
8. Bale, C.W., P. Chartrand, S.A. Degterov, G. Eriksson, K. Hack, R. Ben Mahfoud, J. Melancon, A.D. Pelton, and S. Petersen, *FactSage thermochemical software and databases.* CALPHAD Comput. Coupling Phase Diagrams Thermochem., 2002. **26**(2): p. 189-228.
9. http://www.imdpm.net.
10. http://www.phases.psu.edu.

11. http://www.crct.polymtl.ca.
12. http://www.thermocalc.com.
13. http://www.computherm.com.
14. http://www.factsage.com.
15. Sundman, B. and J. Ågren, *A regular solution model for phases with several components and sublattices, suitable for computer applications.* J. Phys. Chem. Solids, 1981. **42**(4): p. 297-301.

Figure captions

Fig.1.1 APC project overview indicating the high level linkage and participating organizations (UW: University of Waterloo, U Sher: University of Sherbrooke, McGill: McGill University).

Figure

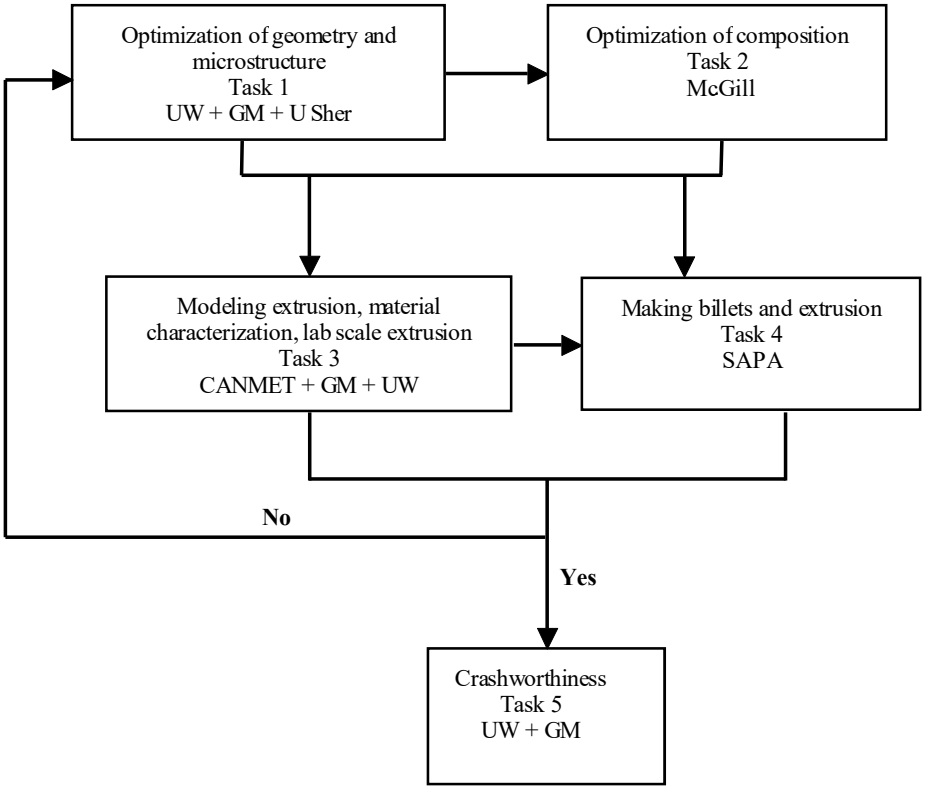

Fig.1.1 APC project overview indicating the high level linkage and participating organizations (UW: University of Waterloo, U Sher: University of Sherbrooke, McGill: McGill University).

Chapter 2 Thermodynamic models

2.1 Pure elements and stoichiometric compounds

The Gibbs free energies of pure elements and stoichiometric compounds by definition can be expressed as:

$$G_T = H_T - S_T T \tag{2.1}$$

where G_T, H_T, and S_T are the Gibbs energy, enthalpy, and entropy at temperature T in Kelvin, respectively. The enthalpy and entropy at a given temperature can be expressed as functions of heat capacity C_p by:

$$H_T = \Delta H^o_{298.15} + \int_{298.15}^{T} C_P dT \tag{2.2}$$

$$S_T = S^o_{298.15} + \int_{298.15}^{T} \frac{C_P}{T} dT \tag{2.3}$$

where $\Delta H^o_{298.15}$ is the enthalpy of formation at 298.15 K and $S^o_{298.15}$ is the entropy at 298.15 K. The Gibbs energies of stoichiometric compounds are thus can be described using C_P, $S^o_{298.15}$, and $\Delta H^o_{298.15}$. Theoretically, the heat capacity expression of each compound can be obtained by numerical fitting of the experimentally measured heat content data or/and heat capacity data. The heat capacity expression can be predicted using the Neumann-Kopp relation in case no reliable experimental heat capacity data available.

In an alternate way, the temperature dependent molar Gibbs energies of the pure elements and stoichiometric compounds are described in the form:

$$G_i(T) - H_i^{SER} = a + bT + cT\ln T + dT^2 + eT^{-1} + fT^3 + gT^7 + hT^{-9}, \quad T_1 < T < T_2 \tag{2.4}$$

where H_i^{SER} is the molar enthalpy of element *i* at 298.15 K and 1 bar in its standard element reference (SER) state. This type of power series can be valid only for a limited temperature region, here delimited as T_1 and T_2. Other quantities are directly related to the molar Gibbs energy by,

$$H_i(T) - H_i^{SER} = a - cT - dT^2 + 2eT^{-1} - 2fT^3 \ldots \tag{2.5}$$

$$S_i = -b - c(1 + \ln(T)) - 2d + eT^{-2} - 3fT^2 \ldots \tag{2.6}$$

$$C_p = -c - 2dT - 2eT^{-2} - 6fT^2 \ldots \tag{2.7}$$

If the elements or compounds have magnetic transition behavior, an additional magnetic contribution term ΔG^{mag} given by the Hillert-Jarl-Inden model [1] should be taken into account as:

$$\Delta G^{mag} = RT\ln(\beta^{\varphi} + 1)g(\tau^{\varphi}) \tag{2.8}$$

where τ is given by T/T^* and T^* is the critical temperature for magnetic transition. That is, the Curie temperature T_C for ferromagnetic materials or Neel temperature T_N for antiferromagnetic materials. β is the average magnetic moment per mole of atom expressed in Bohr magnetons. $g(\tau^{\varphi})$ is a polynomial function derived by Hillert and Jarl [1]:

$$g(\tau^{\varphi}) = 1 - \left[\frac{79\tau^{-1}}{140p} + \frac{474}{497}\left(\frac{1}{p} - 1\right)\left(\frac{\tau^3}{6} + \frac{\tau^9}{135} + \frac{\tau^{15}}{600}\right)\right]/D \qquad \tau \le 1 \tag{2.9}$$

$$g(\tau^{\varphi}) = -\left[\frac{\tau^{-5}}{10} + \frac{\tau^{-15}}{315} + \frac{\tau^{-25}}{1500}\right]/D \qquad \tau > 1 \tag{2.10}$$

where $D = \frac{518}{1125} + \frac{11692}{15975}\left(\frac{1}{p} - 1\right)$. Here p is 0.40 for the bcc_A2 structure and 0.28 for other structures.

The Gibbs energies of all the pure elements used in the current work are taken from the SGTE pure element database complied by Dinsdale [2].

2.2 Liquid solution

In an ideal substitutional solution, there is no interaction between the constituents, and these constituents are randomly distributed. In this special case, the Gibbs energy of the solution is expressed as:

$$G = \sum_{i=1}^{n} x_i G_i^o + RT \sum_{i=1}^{n} x_i \ln(x_i) \tag{2.11}$$

where x_i is the mole fraction of constituent *i*, G_i^o is the molar Gibbs energy of pure *i*. $\sum_{i=1}^{n} x_i G_i^o$ is the reference Gibbs energy, and $RT\sum_{i=1}^{n} x_i \ln(x_i)$ is the contribution to Gibbs energy due to random mixing in the one dimensional Ising approximation.

In an ideal solution the bond energy between two unlike constituents is equal to that between two identical constituents. None ideal behavior of a solution can be simplified by introducing the energy difference for these different bonds:

$$\varepsilon_{ij} = E_{ij} - 0.5(E_{ii} + E_{jj}) \tag{2.12}$$

where E_{ij} are the bond energy between *i* and *j*, and ε_{ij} is the interaction energy. If ε_{ij} is negative it means that different constituents prefer to be together, that means long-range ordering, short-

range ordering, and/or clustering might happen. If ε_{ij} is positive, the mixing of different constituents is unfavorable, and phase separation and formation of miscibility gap might happen.

In a substitutional solution the constituents have the same probability of occupying any site in the lattice (randmon mixing). The Gibbs energy is given using the regular solution (or random mixing) model:

$$G = \sum_{i=1}^{n} x_i G_i^o + RT \sum_{i=1}^{n} x_i \ln(x_i) + G_m^{ex} \tag{2.13}$$

where the excess Gibbs energy $G_m^{ex} = \sum_i \sum_{j>i} x_i x_j L_{ij}$ and $L_{ij} = z/2\, \varepsilon_{ij}$ (z is the number of bonds). L_{ij} can be given in the form of Redlich-Kister (RK) polynomial [3] to mathematically explore the excess energy as a function of composition and temperature,

$$L_{ij} = \sum_{v=0}^{k} (x_i - x_j)^v L_{ij}^v \tag{2.14}$$

when v=0, $G_m^{ex} = x_A x_B L_{AB}^0$, which is called the regular solution model, when v=1, $G_m^{ex} = x_A x_B (L_{AB}^0 + L_{AB}^1 (x_A - x_B))$, which is called the sub-regular solution model, and when v=2, $G_m^{ex} = x_A x_B (L_{AB}^0 + L_{AB}^1 (x_A - x_B) + L_{AB}^2 (x_A - x_B)^2)$, which is called the sub-sub-regular solution model.

However, the substitiutional solution model with the assumption of random mixing of components has limitation when the bonding energy ε_{ij} deviates significantly from ideal solution condition. In a liquid solution with short range ordering (SRO), different atoms are more likely to be together due to the energetic reason. The enthalpy of mixing will have a characterized "V" shape with the variation of composition. One example is the Mg-Sn binary system [4]. The activity can change by several orders of magnitude over a small composition range. This type of feature of liquid is hard to be described using Eq. (2.13). Fictions constituents are normally introduced to

describe SRO. Technically, the associate solution model and quasi-chemical model are developed to model the liquid phase with strong SRO.

In the current PhD thesis, the Modified Quasi-chemical Model (MQM) [5, 6] is accepted to model the liquid phase. The MQM was successfully applied to many ionic liquid solutions [7] exhibiting strong SRO behavior and recently extend to model liquid metallic solution [8]. The recent modification of the MQM expand the excess Gibbs energy in the form of a polynomial in pair fractions [5] instead of component fractions. Also, the coordination numbers of each sub-binary can be independently selected to reproduce the SRO more accurately for individual binary liquid solution. The MQM is described below in details:

Assume the atoms A and B are distributed over the sites of a quasi-lattice in a binary A-B liquid solution. The following pair exchange reaction exists:

$$(A\text{-}A) + (B\text{-}B) = 2(A\text{-}B): \quad \Delta g_{AB} \tag{2.15}$$

where (*A*-*B*) is a first-nearest-neighbor pair of A and B. The Gibbs energy change for the formation of two moles of (*A*-*B*) pairs according to the reaction (2.15) is Δg_{AB}. Then the Gibbs energy of the solution is given by:

$$G = (n_A G_A^o + n_B G_B^o) - T\Delta S^{config} + n_{AB}(\Delta g_{AB}/2) \tag{2.16}$$

where G_A^o and G_B^o are the molar Gibbs energy of the pure components A and B, respectively. n_A and n_B are the numbers of moles of A and B atoms, and n_{AB} is the number of moles of (*A*-*B*) pairs. ΔS^{config} is the entropy of mixing given by a random distribution of the (*A*-*A*), (*B*-*B*), and (*A*-*B*) pairs in the one-dimensional Ising approximation:

$$\Delta S^{config} = -R(n_A \ln x_A + n_B \ln x_B) - R\left[n_{AA}\ln\left(\frac{x_{AA}}{Y_A^2}\right) + n_{BB}\ln\left(\frac{x_{BB}}{Y_B^2}\right) + n_{AB}\ln\left(\frac{x_{AB}}{2Y_A Y_B}\right)\right] \tag{2.17}$$

where x_{ij} is the pair fraction, and Y_i is the coordination equivalent fraction defined as:

$$x_A = n_A/(n_A + n_B) \tag{2.18}$$

$$x_{AB} = n_{AB}/(n_{AA} + n_{BB} + n_{AB}) \tag{2.19}$$

$$Y_A = x_{AA} + \frac{1}{2}(x_{AB}) \tag{2.20}$$

Δg_{AB} is the excess part of Gibbs energy to reproduce the thermodynamic properties of the liquid phase of a binary A-B system, which is expanded in terms of pair fractions:

$$\Delta g_{AB} = \Delta g^0_{AB} + \sum_{i\geq 1} g^{i0}_{AB}(x_{AA})^i + \sum_{j\geq 1} g^{0j}_{AB}(x_{BB})^j \tag{2.21}$$

where Δg^0_{AB}, g^{i0}_{AB}, and g^{0j}_{AB} are the adjustable model parameters which can be functions of temperature.

In MQM, let Z_A be the coordination number of component A, the following relation holds: $Z_A n_A = 2n_{AA} + \sum_{n\neq m} n_{mn}$. The coordination numbers of A and B, Z_A and Z_B, can be varied with composition to reproduce the short-range-ordering as follows:

$$\frac{1}{Z_A} = \frac{1}{Z^A_{AA}}\left(\frac{2n_{AA}}{2n_{AA} + n_{AB}}\right) + \frac{1}{Z^A_{AB}}\left(\frac{n_{AB}}{2n_{AA} + n_{AB}}\right) \tag{2.22}$$

$$\frac{1}{Z_B} = \frac{1}{Z^B_{BB}}\left(\frac{2n_{BB}}{2n_{BB} + n_{AB}}\right) + \frac{1}{Z^B_{BA}}\left(\frac{n_{AB}}{2n_{BB} + n_{AB}}\right) \tag{2.23}$$

where Z^A_{AA} is the value of Z_A when all the nearest neighbors of an A atom are A atoms, and Z^A_{AB} is the value of Z_A when all the nearest neighbors are B atoms.

Similar to other model, the MQM model can be easily extended to multicomponent system. Here takes a ternary system as an example:

The Gibbs energy of the liquid solution is given by:

$$G = \sum_{m=1}^{3} n_m G_m^o - T\Delta S^{config} + \sum_{n>m}^{3}\sum_{m=1}^{3} n_{mn}(\Delta g_{mn}/2) \tag{2.24}$$

and the configurational entropy of mixing ΔS^{config} is given by:

$$\Delta S^{config} = -R\sum_{m=1}^{3} n_m \ln x_m - R\left[\sum_{m=1}^{3} n_{mm} \ln\left(\frac{x_{mm}}{Y_m^2}\right) + \sum_{n>m}^{3}\sum_{m=1}^{3} n_{mn} \ln\left(\frac{x_{mn}}{2Y_m Y_n}\right)\right] \tag{2.25}$$

where n_{mm} is the moles of each type of pairs, x_{mn} is the pair fraction, and Y_m the is coordination equivalent fraction defined as:

$$x_{mn} = n_{mn} \Big/ \left(\sum_{i=1}^{3} n_{ii} + \sum_{\substack{i=1 \\ j>i}}^{3} n_{ij}\right) \tag{2.26}$$

$$x_m = n_m \Big/ \sum_{i=1}^{3} n_i \tag{2.27}$$

$$Y_m = x_{mm} + \frac{1}{2}\sum_{n\neq m} x_{mn} \tag{2.28}$$

For MQM in the ternary or higher order system, the geometric extrapolation technique is used to predict the Gibbs energy of ternary solutions from the sub-binary solution parameters depending on the nature of each ternary liquid solution. Then, if necessary, ternary excess parameters can be added to better reproduce the available data.

There are four types of extrapolation techniques, namely Kohler, Muggianu, Kohler/Toop, and Muggianu/Toop, which are commonly used by FactSage community. Kohler and Muggianu

are symmetric models, while Kohler/Toop and Muggianu/Toop are asymmetric models. Fig. 2.1 presents the four normally used extrapolation models. Figs. 2.1(a) to (d) are the Kohler model, Kohler/Toop model, Muggianu model, and Muggianu/Toop model, respectively.

In the Kohler-type symmetric extrapolation technique, the interaction parameter Δg_{12} is expressed as:

$$\Delta g_{12} = \Delta g_{12}^{0} + \sum_{(i+j)\geq 1} g_{12}^{ij} \left(\frac{x_{11}}{x_{11}+x_{22}+x_{12}} \right)^{i} \left(\frac{x_{22}}{x_{11}+x_{22}+x_{12}} \right)^{j}$$
$$+ \sum_{\substack{i\geq 0 \\ j\geq 0 \\ k\geq 0}} g_{12(3)}^{ijk} \left(\frac{x_{11}}{x_{11}+x_{22}+x_{12}} \right)^{i} \left(\frac{x_{22}}{x_{11}+x_{22}+x_{12}} \right)^{j} Y_3^{k} \tag{2.29}$$

In the Kohler-Toop extrapolation technique, assume component 1 be the asymmetric component in the 1-2-3 system. That is, the energy of forming (1-2) nearest-neighbor pair (and similarly for (1-3) pair) is assumed to be constant as component 2 is replaced by component 3 in the 1-2-3 ternary system. Then, the interaction energy expression goes:

$$\Delta g_{12} = \Delta g_{12}^{0} + \sum_{(i+j)\geq 1} g_{12}^{ij} (x_{11})^{i} (x_{22}+x_{23}+x_{33})^{j}$$
$$+ \sum_{\substack{i\geq 0 \\ j\geq 0 \\ k\geq 0}} g_{12(3)}^{ijk} (x_{11})^{i} (x_{22}+x_{23}+x_{33})^{j} \left(\frac{Y_3}{Y_2+Y_3} \right)^{k} \tag{2.30}$$

, and Δg_{23} is expressed as Eq. (2.29).

The quaterarny and higher order systems can be also calculated similarly using the geometric extrapolation model. The details can be found from Pelton [9].

2.3 Solid solution phases

Here random mixing solid solution phases refer to the substitutional solutions in its disordered states, which include the fcc_A1, bcc_A2, hcp_A3, diamond_A4, cbcc_A12, cub_A13 phases, etc.

The molar Gibbs energies of random ternary solid solution phases are described using the Bragg-Willimas random mixing model in the form of R-K polynomial:

$$ {}^{o}G_m^{\phi} = \sum_{i=1}^{3} x_i \, {}^{o}G_i^{\phi} + RT\sum_{i=1}^{3} x_i \ln x_i + \sum_{i=1}^{3}\sum_{j>i}^{3} x_i x_j L_{ij}^{\phi} + \sum_{i=1}^{3}\sum_{j>i}^{3}\sum_{k>j}^{3} x_i x_j x_k L_{ijk}^{\phi} + \Delta G^{mag} \tag{2.31} $$

where ${}^{o}G_i^{\phi}$ is the molar Gibbs energy of pure element *i* with the ϕ state, *R* is gas constant, *T* is temperature in Kelvin, L_{ij}^{ϕ} is the binary interaction parameter, and L_{ijk}^{ϕ} is the ternary interaction parameter. Further, L_{ij}^{ϕ} is expanded in the form of $\sum_{v=0} L_{ij}^{v}(x_i - x_j)^v$ and L_{ijk}^{ϕ} is written as $x_i L_{ijk}^{i} + x_j L_{ijk}^{j} + x_k L_{ijk}^{k}$. ΔG^{mag} is a term to taken into account the effect of magnetic contribution to the Gibbs energy. ΔG^{mag} is described by Hillert-Jarl-Inden model [1] using Eqs. (2.8-2.10). In fact, the Bragg-Willimas random mixing model is equivalent to the one sublattice Compound Energy Formalism (CEF).

The Gibbs energies of other solid solutions with more than two none vacany sublattices are described using CEF. CEF is extended to an arbitrary number of sub-lattices and constituents on each sub-lattice by Sundman and Ågren [10]. The concept of constituent array was introduced to describe the model. The constituent array specifies one or more constituents on each sub-lattice and is denoted as *I*, while individual constituents are denoted as *i*, sometimes with a superscript *s* denotes the sub-lattice *s*. The constituent arrays can be any orders and zeroth order has just one constituent on each sub-lattice. The Gibbs energy of CEF is expressed as:

$$ G_m = G_m^{srf} + G_m^{config} + G_m^{ex} \tag{2.32} $$

$$G_m^{srf} = \sum_{I0} P_{I0}(Y) G_{I0}^o \tag{2.33}$$

$$G_m^{config} = RT \sum_{s=1}^{n} a_s \sum_{i=1}^{n_s} y_i^s \ln(y_i^s) \tag{2.34}$$

$$G_m^{ex} = \sum_{I0} P_{I1}(Y) L_{I1} + \sum_{I2} P_{I2}(Y) L_{I2} + \ldots \tag{2.35}$$

where I_0 is a constituent array of zeroth order specifying one constituent in each sub-lattice, $P_{I_0}(Y)$ is the product of the constituent fractions specified by I_0. G_{I0}^o is the formation Gibbs energy of the compound I_0. a_s is the number of sites on each sub-lattice and y_i^s is used to denote the constituent fraction of *i* on sub-lattice s or the site fraction of *i* on sub-lattice s. The excess term, G_m^{ex}, includes sums of all the possible interaction parameters defined by component arrays of the first order, second order, etc.

Here takes the γ_H phase in the Al-Cr-Mn ternary system as an example. A sub-lattice model: $(Al, Cr, Mn)_2(Al, Cr, Mn)_3(Cr, Mn)_2(Al)_6$ is utilized. And the Gibbs energy of the γ_H phase is presented as:

$$\begin{aligned}
{}^{o}G_m^{\gamma_H} &= \sum_{i=1}\sum_{j=1}\sum_{k=1} y_i' y_j'' y_k''' y_{Al}'''' \, {}^{o}G_{i:j:k:Al}^{\gamma_H} + 2RT\sum_{i=1} y_i' \ln y_i' + 3RT\sum_{i=1} y_i'' \ln y_i'' \\
&+ 2RT\sum_{i=1} y_i''' \ln y_i''' + \sum_{i=1}\sum_{j>i}\sum_{k=1}\sum_{m=1} y_i' y_j' y_k'' y_m''' \sum_{v=0} (y_i' - y_j')^v L_{ij:k:m:Al}^v \\
&+ \sum_{i=1}\sum_{j>i}\sum_{k=1}\sum_{m=1} y_i'' y_j'' y_k' y_m''' \sum_{v=0} (y_i'' - y_j'')^v L_{k:ij:m:Al}^v \\
&+ \sum_{i=1}\sum_{j>i}\sum_{k=1}\sum_{m=1} y_i''' y_j''' y_k' y_m'' \sum_{v=0} (y_i''' - y_j''')^v L_{k:m:ij:Al}^v + \ldots
\end{aligned} \tag{2.36}$$

where y_i', y_i'', y_i''', and y_i'''' are the site fraction of element *i* in the first, second, third, and fourth sub-lattice, respectively. ${}^{o}G_{i:j:k:Al}^{\gamma\_H}$ is the molar Gibbs energy of the hypothetical compound $i_2j_3k_2Al_6$. $L_{ij:k:m:Al}^v$, $L_{k:ij:m:Al}^v$, and $L_{k:m:ij:Al}^v$ are the interaction parameters.

In CEF, the Gibbs energies of the consitituent compounds are the primary model parameters. The proper assignment of the Gibbs energy is critical for the successful description of complex solid solutions.

2.4 Magnetic ordering

For those systems with magnetic ordering, the Gibbs energy is normally divided into two parts: none magnetic order part (G_m^o) and the magnetic order part (ΔG^{mag}). The Gibbs energy of a solid solution is described using Eq. (2.31). The magnetic order part is described using Hillert and Jarl [1] model using Eqs. (2.8-2.10). The Curie temperature and Bohr magneton can be also described by a liner combination of pure element properties with the excess terms in the form of R-K polynomial.

2.5 Chemical ordering

In perfect crystals, atoms arrange periodically on the crystal lattice in a totally ordered state. This can only happen at 0 K for solid phases. Atoms arrange randomly at high temperature and arrange regularly at low temperature in many alloys and solid solutions. This type of change is called order-disorder phase transition. Order-disorder transition belongs to second order transition. In order to describe this type of phase transition, one formalism is required to describe the Gibbs energy of the order state and disorder state simultaneously. Order-disorder transition is a hazard part of the CALPHAD type of phase diagram calculation. Currently, only the order transitions in the bcc and fcc structures can be well modeled. In fcc structure, there are fcc_A1, fcc_L12, and fcc_L10 three variants. The fcc_A1 structure is normal face centred cubic structure. The fcc_L12 ordering means that the eight corner atoms are different from the atoms on the face center. The ideal stoichiometry of fcc_L12 state is A_3B. It is recommended to model the ordering in fcc structure using a four sub-lattice model. There are bcc_A2, bcc_B2, and bcc_D03 structures in the body centred cubic structure. The bcc_B2 structure with an ideal stoichiometry of AB refers to the centre atom in a unit cell is different from those at the corner. The bcc_D03 structure has a unit

cell which is 8 times of the normal bcc_A2 structure and four diagonal center positions are occupied by one type of element and other positons can be randomly occupied. The ideal stoichiometry of bcc_D03 is A_3B. A two sub-lattice model is needed to describe the A2/B2 transition, and a four sub-lattice model is required for the modeling of the A2/B2 and B2/D03 transitions simultaneously.

The Gibbs energy of a phase with order-disorder transition is described using:

$$G_m = G_m^{dis}(x) + \Delta G_m^{ord}(y) \tag{2.37}$$

where $G_m^{dis}(x)$ is the Gibbs energy of the disordered state which is independent of the ordering. $G_m^{dis}(x)$ is described using Eq. (2.13). $\Delta G_m^{ord}(y)$ is the contribution of long-range ordering and equals to zero when the phase is in disorder state. The ordering contribution is simply given as:

$$\Delta G_m^{ord}(y) = G_m^{ord}(y) - G_m^{ord}(y = x) \tag{2.38}$$

where $G_m^{ord}(y)$ is used to describe the ordering.

Here takes the Fe-Si system as an example. The A2/B2 transisiton can be modeled using a two sublattice model, $(Fe, Si)_{0.5}(Fe, Si)_{0.5}$. Then the Gibbs energy of the bcc phase is expressed as [11]:

$$G_{bcc}^{o} = \sum_i x_i G_i^o + \sum_{i=1}\sum_{j>i} x_i x_j L_{ij}^{\phi} + \sum_{i=1}\sum_{j=1} y_i^{'} y_j^{''} G_{ij}^{ord} + \frac{1}{2}\sum_{i=1}\sum_{j=1} RT y_j^i \ln(y_j^i)$$
$$+ \sum_{i=1}\sum_{j>i}\sum_{k=1} y_i^{'} y_j^{'} y_k^{''} \sum_{v=0} (y_i^{'} - y_j^{'})^v L_{ij:k}^v + \sum_{i=1}\sum_{j>i}\sum_{k=1} y_k^{'} y_i^{''} y_j^{''} \sum_{v=0} (y_i^{''} - y_j^{''})^v L_{k:ij}^v + \Delta G^{Mag} \tag{2.39}$$

In order to keep the internal consistency of this model, it is better to follow the relationships:

$$G_{ij}^{ord} = G_{ji}^{ord} = -L_{ij:*}^0 = -L_{*:ij}^0 = \Delta G_{AB} \tag{2.40}$$

$$G_{ii}^{ord} = G_{jj}^{ord} = 0 \tag{2.41}$$

where ΔG_{AB} is the adjustable parameter.

The D03 ordered contribution can be described using the four sublattice model: (Fe, Si)$_{0.25}$(Fe, Si)$_{0.25}$(Fe, Si)$_{0.25}$(Fe, Si)$_{0.25}$. And the Gibbs energy expression is described as [11]:

$$G_{bcc}^{o} = \sum_{i} x_i G_i^o + \sum_{i=1}\sum_{j>i} x_i x_j L_{ij}^{\phi} + \sum_{i=1}\sum_{j=1}\sum_{k=1}\sum_{m=1} y_i^{'} y_j^{''} y_k^{'''} y_m^{''''} G_{ijkm}^{ord} + \frac{1}{4}\sum_{i=1}\sum_{j=1} RT y_j^i \ln(y_j^i)$$

$$+ \sum_{i=1}\sum_{j>i}\sum_{k=1}\sum_{m=1}\sum_{n=1} y_i^{'} y_j^{'} y_k^{''} y_m^{'''} y_n^{''''} \sum_{v=0} (y_i^{'} - y_j^{'})^v L_{ij:k:m:n}^v + \sum_{i=1}\sum_{j>i}\sum_{k=1}\sum_{m=1}\sum_{n=1} y_i^{''} y_j^{''} y_k^{'} y_m^{'''} y_n^{''''} \sum_{v=0} (y_i^{''} - y_j^{''})^v L_{k:ij:m:n}^v$$

$$+ \sum_{i=1}\sum_{j>i}\sum_{k=1}\sum_{m=1}\sum_{n=1} y_i^{'''} y_j^{'''} y_k^{'} y_m^{''} y_n^{''''} \sum_{v=0} (y_i^{'''} - y_j^{'''})^v L_{k:m:ij:n}^v$$

$$+ \sum_{i=1}\sum_{j>i}\sum_{k=1}\sum_{m=1}\sum_{n=1} y_i^{''''} y_j^{''''} y_k^{'} y_m^{''} y_n^{'''} \sum_{v=0} (y_i^{''''} - y_j^{''''})^v L_{k:m:n:ij}^v + \Delta G^{Mag} \tag{2.42}$$

and similar relations are applied [11]:

$$G_{Fe:Fe:Fe:Fe}^{ord} = G_{Si:Si:Si;Si}^{ord} = 0 \tag{2.43}$$

$$G_{Fe:Fe:Si:Si}^{ord} = G_{Si:Si:Fe:Fe}^{ord} = \Delta G_{FeSi}^{B2} \tag{2.44}$$

$$G_{Fe:Fe:Fe:Si}^{ord} = G_{Fe:Fe:Si:Fe}^{ord} = G_{Fe:Si:Fe:Fe}^{ord} = G_{Si:Fe:Fe:Fe}^{ord} = 1/4\,\Delta G_{FeSi}^{B2} + \Delta G_{Fe3Si}^{D03} \tag{2.45}$$

$$G_{Fe:Si:Si:Si}^{ord} = G_{Si:Fe:Si:Si}^{ord} = G_{Si:Si:Fe:Si}^{ord} = G_{Si:Si:Si:Fe}^{ord} = 1/4\,\Delta G_{FeSi}^{B2} + \Delta G_{FeSi3}^{D03} \tag{2.46}$$

$$G_{Fe:Si:Fe:Si}^{ord} = G_{Fe:Si:Si:Fe}^{ord} = G_{Si:Fe:Fe:Si}^{ord} = G_{Si:Fe:Si:Fe}^{ord} = \Delta G_{Fe2Si2}^{B32} \tag{2.47}$$

$${}^0L_{Fe,Si:Fe:Fe:Fe} = {}^0L_{Fe:Fe,Si:Fe:Fe} = {}^0L_{Fe:Fe:Fe,Si:Fe} = {}^0L_{Fe:Fe:Fe:Fe,Si} =$$

$$= {}^0L_{Fe,Si:Si:Fe:Fe} = {}^0L_{Si:Fe,Si:Fe:Fe} = {}^0L_{Fe:Fe:Fe,Si:Si} = {}^0L_{Fe:Fe:Si:Fe,Si} = -1/4\,\Delta G_{FeSi}^{B2} - \Delta G_{Fe3Si}^{D03} \tag{2.48}$$

$${}^0L_{Fe,Si:Fe:Si:Si} = {}^0L_{Fe:Fe,Si:Si:Si} = {}^0L_{Si:Si:Fe,Si:Fe} = {}^0L_{Si:Si:Fe:Fe,Si} =$$

$$= {}^0L_{Fe,Si:Si:Si:Si} = {}^0L_{Si:Fe,Si:Si:Si} = {}^0L_{Si:Si:Fe,Si:Si} = {}^0L_{Si:Si:Si:Fe,Si} = -1/4\,\Delta G_{FeSi}^{B2} - \Delta G_{FeSi3}^{D03} \tag{2.49}$$

$${}^0L_{Fe,Si:Fe:Fe:Si} = {}^0L_{Fe:Fe,Si:Fe:Si} = {}^0L_{Fe:Si:Fe,Si:Fe} = {}^0L_{Fe:Si:Fe:Fe,Si} =$$

$$={}^{0}L_{Fe,Si:Fe:Si:Fe}={}^{0}L_{Fe:Fe,Si:Si:Fe}={}^{0}L_{Si:Fe:Fe,Si:Fe}={}^{0}L_{Si:Fe:Fe:Fe,Si}$$

$$={}^{0}L_{Fe,Si:Si:Fe:Si}={}^{0}L_{Si:Fe,Si:Fe:Si}={}^{0}L_{Fe:Si:Fe,Si:Si}={}^{0}L_{Fe:Si:Si:Fe,Si}$$

$$={}^{0}L_{Fe,Si:Si:Si:Fe}={}^{0}L_{Si:Fe,Si:Si:Fe}={}^{0}L_{Si:Fe:Fe,Si:Si}={}^{0}L_{Si:Fe:Si:Fe,Si}=-1/4\,\Delta G_{FeSi}^{B2}-1/2\,\Delta G_{Fe2Si2}^{B32} \quad (2.50)$$

where the ΔG_{FeSi}^{B2}, ΔG_{Fe3Si}^{D03}, ΔG_{FeSi3}^{D03}, and ΔG_{Fe2Si2}^{B32} are the adjustable parameters.

References

1. Hillert, M. and M. Jarl, *A model for alloying effects in ferromagnetic metals.* CALPHAD Comput. Coupling Phase Diagrams Thermochem., 1978. **2**(3): p. 227-38.
2. Dinsdale, A.T., *SGTE data for pure elements.* CALPHAD Comput. Coupling Phase Diagrams Thermochem., 1991. **15**(4): p. 317-425.
3. Redlich, O. and A.T. Kister, *Thermodynamics of nonelectrolytic solutions. Algebraic representation of thermodynamic properties and the classification of solutions.* Ind. Eng. Chem., 1948. **40**: p. 84,5-8.
4. Ghosh, P., M. Mezbahul-Islam, and M. Medraj, *Critical assessment and thermodynamic modeling of Mg-Zn, Mg-Sn, Sn-Zn and Mg-Sn-Zn systems.* CALPHAD Comput. Coupling Phase Diagrams Thermochem., 2012. **36**: p. 28-43.
5. Pelton, A.D. and P. Chartrand, *The modified quasi-chemical model: Part II. Multicomponent solutions.* Metall. Mater. Trans. A, 2001. **32A**(6): p. 1355-1360.
6. Pelton, A.D., S.A. Degterov, G. Eriksson, C. Robelin, and Y. Dessureault, *The modified quasichemical model I - binary solutions.* Metall. Mater. Trans. B, 2000. **31B**(4): p. 651-659.
7. Robelin, C., P. Chartrand, and A.D. Pelton, *Thermodynamic evaluation and optimization of the ($NaNO_3$ + KNO_3 + Na_2SO_4 + K_2SO_4) system.* J. Chem. Thermodyn., 2015. **83**: p. 12-26.
8. Cui, S., M. Paliwal, and I.-H. Jung, *Thermodynamic Optimization of Ca-Fe-Si System and Its Applications to Metallurgical Grade Si-Refining Process.* Metall. Mater. Trans. E, 2014. **1**(1): p. 67-79.

9. Pelton, A.D., *A general "geometric" thermodynamic model for multicomponent solutions.* CALPHAD Comput. Coupling Phase Diagrams Thermochem., 2001. **25**(2): p. 319-328.
10. Sundman, B. and J. Ågren, *A regular solution model for phases with several components and sublattices, suitable for computer applications.* J. Phys. Chem. Solids, 1981. **42**(4): p. 297-301.
11. Ohnuma, I., S. Abe, S. Shimenouchi, T. Omori, R. Kainuma, and K. Ishida, *Experimental and thermodynamic studies of the Fe-Si binary system.* ISIJ Int., 2012. **52**(4): p. 540-548.

Figure captions

Fig. 2.1 Four geometric models: symmetric model (a) and (c), and asymmetric model (b) and (d) [9].

Figures

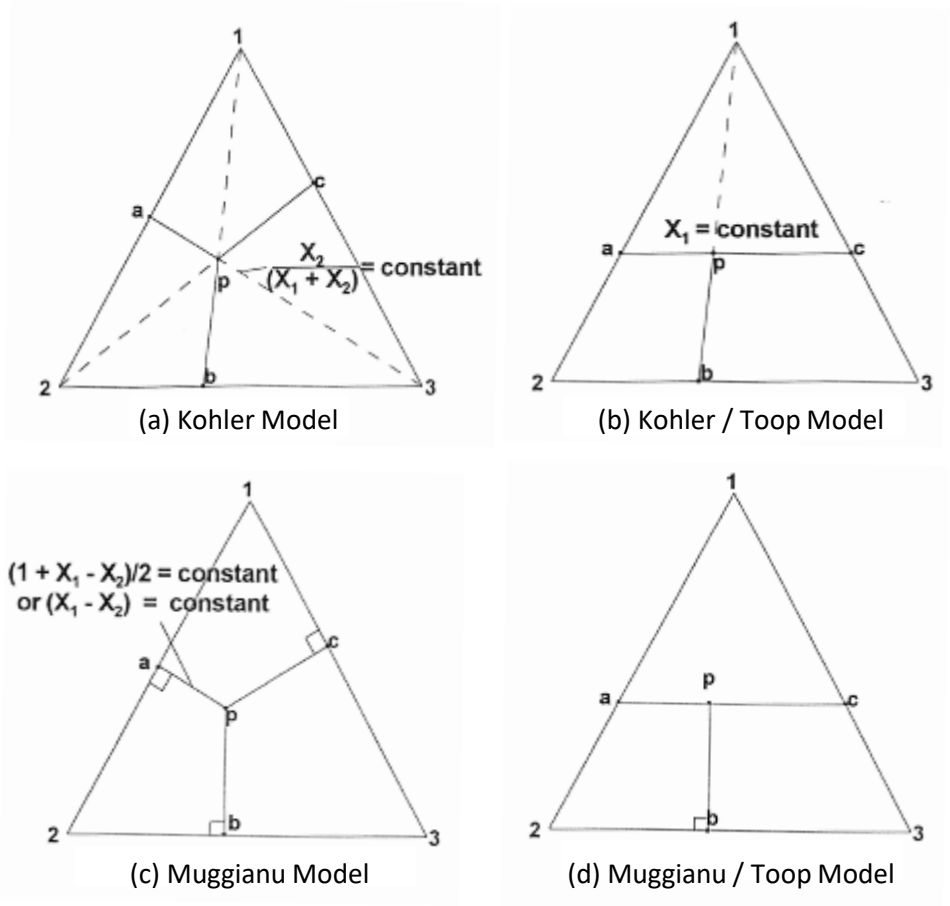

Fig. 2.1 Four geometric models: symmetric model (a) and (c), and asymmetric model (b) and (d) [9].

Chapter 3 Experimental methods

3.1 Phase diagram determination methods

3.1.1 Equilibration/quenching

Equilibration/quenching method (equilibrated alloy) is a traditional way to determine alloy phase diagram. Alloy preparation, homogenization, and characterization are the three major steps for this method. Alloy preparation is the key step for the phase diagram determination in the equilibrated alloy method. Generally speaking, the alloy chemistries should be uniformly distributed in the phase diagram of a completely unknown system. However, the composition of the prepared alloys may be only focused on certain unknown region depending on the purpose of the experiment. The nominal composition of the prepared alloy sample could change due to oxidation or melting loss. High purity metals are normally used as starting materials for the sample preparation to ensure a reliable sample composition and to avoid contamination. Sample preparation methods including high temperature melting of alloys, arc melting, induction melting, and powder metallurgy method can be utilized depending on the accessibility of the experimental facilities and physical properties of the constitutional alloy elements. In this study, induction melting was utilized for sample preparation.

Homogenization heat treatment for sufficient time is necessary to ensure the alloy samples are in their equilibrium state. The prepared samples have a solidification microstructure with micro-segregation of alloying elements. In the homogenization process, the alloy samples are kept in a furnace at a target temperature typically below the solidus temperature of the alloys for a period of time. One of the most important factors for equilibration is diffusion which makes the homogenization of the alloy possible. The annealing time should be properly set depends on the diffusivity of the alloy elements. After the annealing is finished, the samples are quenched from the annealing temperature to room temperature. The equilibrium phases at the homogenization temperature can then be frozen to room temperature.

The quenched samples can be analyzed by x-ray diffraction analysis (XRD), scanning electron microscope (SEM) analysis, and electron microprobe analysis (EPMA) to construct isothermal sections of the phase diagram. On the other hand, the quenched samples can also be used to construct isoplethal section by differential thermal analysis (DTA) and differential scanning calorimetry (DSC) techniques. These thermal analysis techniques can be used to monitor the phase transition temperature in the alloy sample during heating and cooling.

3.1.2 Diffusion couple

According to the assumption that local equilibrium is achieved at the phase interfaces in the diffusion zone, diffusion couple can be used to measure phase diagram. Local equilibrium means that an infinitesimally thick layer adjacent to the interface in such a diffusion zone is effectively in thermodynamic equilibrium with the layers on the other side of the interface. Theoretically, only single phase region can form in a binary diffusion couple, and two phase region can form in a ternary diffusion couple. For example, a diffusion controlled interaction in a multiphase binary system which will result in a diffusion zone with single phase product layer separated by parallel interfaces in a sequence indicated by the related binary phase diagram. The diffusion zone morphology developed is defined by the type, structure, number, shape, and topological arrangement of the newly formed phases. The average composition in the planes parallel to the original interface throughout the diffusion zone is diffusion path.

In the diffusion couple method, the experimental procedure is diffusion couple preparation, homogenization, and characterization. In conventional diffusion couple, the bonding faces of the diffusion couple components are flatly grounded and polished, and clamped together. So that the two components are in intimate contact with each other and produces different interfacial phase layers. During the homogenization process, diffusion happens at the contacted interface which makes the two components bonding together. Diffusion electrolytic and electroless plating techniques, plasma spraying, chemical vapor deposition (CVD), thermal evaporation, electron beam evaporation, and laser evaporation techniques can also be used to prepare diffusion couples.

In the present PhD thesis, the diffusion couple was prepared by liquid/solid coupling. When one component in diffusion couple has much lower melting temperature than the other, one component can be melt first, and then put another solid component into the liquid followed by quenching. In this way, perfect solid/liquid bonding interface can be prepared. In the present study, Al-Mg/Cr diffusion couple is prepared by liquid Al-Mg alloy and solid Cr.

The homogenization heat treatment is basically to ensure the alloy elements have enough time to diffuse and to form different stable phases in the system. During annealing, different atmosphere, like vacuum and inert gas, can be used to protect the diffusion couple from oxidation. After homogenization, the diffusion couples should be quenched and cut perpendicularly to diffusion interface for metallographic analysis. Similar to equilibrated alloys, the phases formed in the diffusion couple can be characterized by EPMA and SEM analysis.

3.1.3 Thermal analysis

Thermal analysis is also an effective way to measure phase diagram. When an alloy is heated and/or cooled, a certain property such as heat flow is monitored continuously to detect the temperature at which a phase transition takes place. This method can be used to quickly explore the limits of phase stability, as is in-situ phase transition measurement, the possible problem of phase transition during quenching process can be avoid. The phase transition involves an enthalpy change. Thus, heat flow can be monitored to detect the phase change. Traditional thermal analysis measures the temperature vs. time curve where a thermal arrest indicates a phase transition. In DTA measurement, the test sample and an inert reference sample are heated and cooled under identical conditions and the temperature difference between the test sample and reference sample are recorded. There will be exothermic or endothermic peaks on the measured curve when phase transition takes place in the sample that involves release or absorption of heat. On the other hand, DSC measures the energy absorbed or emitted by the sample monitored as a function of temperature or time. In the present PhD thesis, DSC is utilized for thermal analysis.

3.2 Sample preparation

3.2.1 Equilibrated alloy sample

For the Al-Cr-Mg ternary system, the equilibration/quenching method was used to investigate the isothermal phase diagrams. Magnesium turnings (Alfa Aesar, 99.98 wt.% purity), aluminum rod (Alfa Aesar, 99.999 wt.% purity), and electrolytic chromium (Alfa Aesar, 99.995 wt.% purity) were used as raw materials for experiments. Al rod was firstly cut into small pieces using diamond saw and carefully sand polished to remove the oxide layer. Similar treatment was carried out for Cr pieces to remove the oxide layer. An Al-8.5 wt.% Cr master alloy of 27 g was first melted in an induction furnace at 950 °C. The Al-Cr alloy was put into a high purity Al_2O_3 crucible internally lined with a thin layer of boron nitride (BN). The BN acted as a diffusion barrier between the charge and crucible. The Al_2O_3 crucible was then put into the graphite crucible for induction melting. During melting process, purified Ar gas was flowed. The argon gas was purified by a Mg turning furnace which was set at 500 °C to remove the residual oxygen in argon gas. The oxygen content in the argon gas was less than 10^{-8} ppm according to the measurement using an oxygen senor. The master alloy was melted 4 times to ensure a homogeneous sample composition.

After the preparation of the master alloy, it was sand polished to remove the outer layer. The master alloy was then cut into 6 pieces. Then the piece of master alloy and proper amount of Mg was used for induction melting as sample. 1 wt.% of extra Mg was added to compensate the weight loss during melting due to Mg vaporization. Like the master alloy, each sample was re-melted for 4 times. The weight loss of the sample was found to be less than 0.3 wt.%. Each quenched sample was cut into 4 pieces as experimental samples.

The experimental samples were tightly wrapped by aluminum foils and then annealed at 400 and 450 °C for 30 and 25 days, respectively, in a tube furnace flowed by argon gas. Two alloys (qA and qB) were annealed at 500 °C for 31 hours. After the designated equilibration, the samples were quickly taken out from the furnace and quenched into ice water. The samples were then cut into small pieces, mounted, and polished for microanalysis.

3.2.1 Diffusion couple sample

In the Al-Cr-Mg system, diffusion couple technique together with conventional quenching and microscopic analysis was used for the measurement of the phase diagram at 400 °C. Al and Mg particles will always fully melt before Cr particles, so it is easy to make diffusion couple using liquid Al-Mg alloy and solid Cr. An induction melting furnace with graphite crucible under controlled atmosphere with continuously flowing argon gas purified by Mg turning furnace at 500 °C was used (as described above). The starting material was carefully pre-treated to remove the outer oxides layer. In the present study, the Al-Mg alloy mixtures with composition of Al-30 at.% Mg, Al-15 at.% Mg, and Al-12.5 at.% Mg were mixed with a piece of Cr and melted in an induction furnace at 850 °C for 10 minutes to form diffusion couples. Then, the power of induction furnace was turned off to rapidly cool down the sample. The diffusion couple prepared in this way has remaining Cr particle covered by Al-Mg alloys (Only small amount of Cr was melted during short melting time). Fig. 3.1 shows the imagine of one diffusion couple composed of Cr and SC3 (Al-30 at.% Mg).

The diffusion couples were tightly wrapped by aluminum foils and then annealed at 400 °C for 30 days in a tube furnace flowed by high purity argon gas. The samples were subsequently taken out from the furnace and rapidly quenched into ice water. The diffusion couple samples were then mounted, and polished for microanalysis.

3.3 Characterization techniques

In chapter 4, alloy samples were characterized by using XRD, SEM with energy dispersive spectrometry (EDS), and EPMA with wavelength-dispersive spectrometry (WDS).

The SEM analysis was carried out using the SU3500 equipped with EDS detector, back scatter electron detector, and secondary electron detector. During the analysis, an accelerating voltage of 20 kV was used for the SEM microanalysis. Due to the low conductivity of Al alloy sample, carbon tape was used to increase the conductivity of samples. All the micrographic images were taken using the BSE detector in the present work. EDS analysis was carried out for all the phase for composition analysis. EDS area map analysis was utilized to get the overall composition

of the samples. There are no standard samples were used during the EDS composition analysis for further calibration in the present PhD work.

The EPMA was carried out with the JEOL-8900L probe using WDS. An accelerating voltage of 15 kV was utilized with a 20 nA beam current and beam size of 2 μm. In order to accurately measure the composition of phases, MgO, Al_2O_3, and Cr metal were used as standards for the ZAF correction in the EPMA. All the phase composition of equilibrated alloys and diffusion couples was confirmed by WDS measurements.

In the phase diagram experiment, XRD analysis was carried out using the Bruker Discover D8 X-ray diffractometer equipped with HiSTAR area detector and Cu Kα radiation. An accelerating voltage of 40 kV and a beam current of 40 mA was used for the analysis. Only bulk XRD was used in the present work to identify the phases.

The DSC was carried out using the Jupiter STA 449 F3 thermal analyzer (NETZSCH Instruments, Germany).

In chapter 12, all the Al alloy samples supported by GM company were characterized by the SU3500. The phase compositions were only measured by EDS analysis.

Figure captions

Fig. 3.1 Overlook of a diffusion couple composed of Cr and alloy SC3 (Al-30 at.% Mg).

Figure

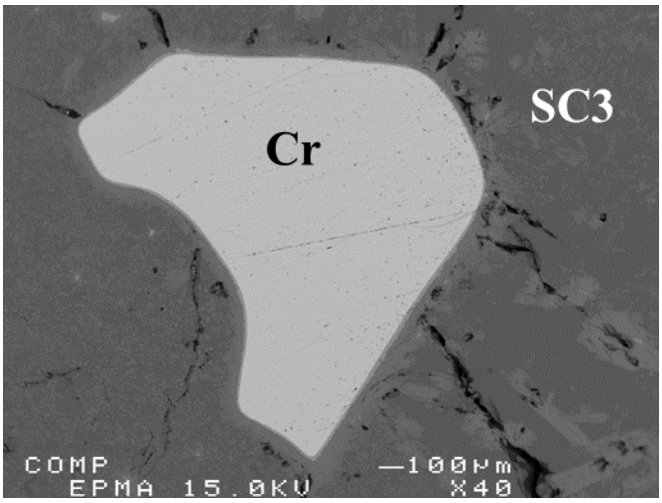

Fig. 3.1 Overlook of a diffusion couple composed of Cr and alloy SC3 (Al-30 at.% Mg).

Chapter 4 A coupled experimental and thermodynamic study of the Al-Cr and Al-Cr-Mg systems

(Submitted to Journal Alloy and Compound)

Senlin Cui [1, 2], In-Ho Jung [1, 2], Junghwan Kim [1], and Jinghua Xin [3]

1 Department of Mining and Materials Engineering, McGill University, 3610 University Street, Montreal, Quebec, H3A 0C5, Canada

2 Aluminium Research Centre-REGAL, McGill University, Montreal, Quebec, H3A 0C5, Canada

3 State Key Laboratory of Powder Metallurgy, Central South University, Changsha, Hunan, 410083, PR China

Abstract

The phase relation in the Al rich corner of the Al-Cr-Mg system was re-investigated at 400, 450, and 500 °C using diffusion couples, quenching experiments, and differential thermal analysis techniques. The homogeneity range of the $Al_{18}Cr_2Mg_3$ phase was determined to be Al-(8.7 ± 0.6) at.% Cr-(13.0 ± 2) at.% Mg. It was also confirmed that there is no ternary compound other than $Al_{18}Cr_2Mg_3$ in the Al-Al_7Mg_3-Cr system. A thermodynamic modeling for the binary Al-Cr and ternary Al-Cr-Mg systems was carried out based on the critically evaluated experimental data and new phase equilibria data from the present study.

Key words:

Al-Cr system; Al-Cr-Mg system; phase diagram; CALPHAD; first principles calculation.

4.1 Introduction

Al 6xxx series alloys have been used as extruded materials for automotive applications due to their high strength, formability and ductility, weld ability, and corrosion resistance. Proper controls of alloying elements and precipitates are the key determinants of the extrusion ability of Al alloys. Cr is a dispersoid former added to Al alloys for grain refinement [1-4]. The addition of Cr promotes the formation of the Al_7Cr and $Al_{18}Cr_2Mg_3$ dispersoid phases which can inhibit the generation and growth of recrystallized grains and thus slow down the kinetics of recrystallization, and improve the super-plasticity [5, 6]. Suitable amount of Cr addition can also enhance the strength of Al alloy and excess will have detrimental effects. The formation of precipitates depends on the thermodynamic properties of the alloy system. Therefore, accurate phase relation in the Al-Cr-Mg ternary system is of importance for Al alloy design containing Cr.

The phase diagram data on the Al-Cr-Mg system is only limited to the Al-Mg rich corner [7] due to the high melting temperature of Cr (1907 °C) and low boiling temperature of Mg (1091 °C). Little et al. [8] claimed that the T phase (an Al-Cr-Mg ternary phase) is a solid solution with variation of Mg content which extends at least from $Mg_3Cr_2Al_{25}$ to $Mg_3Cr_{1.3}Al_{15}$. However, other observations [9-12] considered the T phase as a stoichiometric compound with the composition of $Al_{18}Cr_2Mg_3$. Besides, there is no thermodynamic information available in the literature for this phase. Recently, the liquidus line in the Cr rich side of the Al-Cr binary system was investigated for the first time by Stein et al. [13]. The reaction between liquid, fcc_A1, and Al_7Cr ($Al_{45}Cr_7$) is proved to be a peritectic reaction [14]. None of the previous optimization can address these two new features of the Al-Cr system simultaneously. No ternary optimization of the Al-Cr-Mg system has been performed previously.

In the thermodynamic “optimization” of a system, all the available thermodynamic and phase equilibrium data are evaluated simultaneously in order to obtain a set of model parameters for the Gibbs energies of all the phases as functions of temperature and composition. Thermodynamic property data, such as activity data, can aid the evaluation of phase diagram, and phase diagram measurements can be used to deduce thermodynamic properties. From the Gibbs energy equations, all the thermodynamic properties and phase diagrams can be back-calculated. In

this way, all the data are rendered self-consistent and obey the thermodynamic principles. Discrepancies in the available data can often be resolved, and interpolations and extrapolations can be made in a thermodynamically correct manner. The thermodynamic database resulting from the optimization can be self-consistently built from low order to high order systems and applied to industrial processes and alloy design.

The aims of the present study are to (i) re-investigate the inhomogeneity range of the T phase and phase relation related to the T phase in the Al-Cr-Mg system by phase diagram experiments, (ii) calculate the enthalpy of formation of the T phase based on first principles calculation, and (iii) critically evaluate and optimize the phase diagram and thermodynamic data in the Al-Cr and Al-Cr-Mg systems.

4.2 Literature review

4.2.1 The Al-Cr system

Murray [15] evaluated the Al-Cr phase diagram mainly based on the experimental data from Köster et al. [16]. Phases exist in the system include liquid, fcc_A1, bcc_A2, Al_7Cr, $Al_{11}Cr_2$, Al_4Cr, α-Al_9Cr_4, β-Al_9Cr_4, γ-Al_9Cr_4, α-Al_8Cr_5, β-Al_8Cr_5, $AlCr_2$, and Cr rich phase X. Recently, Okamoto [17] updated the Al-Cr phase diagram. In his evaluation, the decomposition of $Al_{11}Cr_2$ occurred at 785 °C and the phase regions related to α-Al_9Cr_4, β-Al_9Cr_4, γ-Al_9Cr_4, α-Al_8Cr_5, and β-Al_8Cr_5 in the assessment of Murray [15] were modified to α-Al_8Cr_5 and β-Al_8Cr_5 phase regions. Besides, an additional compound $Al_{11}Cr_4$ was implemented.

The Al-Cr system was previously assessed by Saunders and Rivlin [18], Liang et al. [19], Tokunaga et al. [20], and Hu et al. [21]. In the earliest assessment conducted by Saunders and Rivlin [18], all the intermetallic phases were treated as stoichiometric compounds. While in the later assessment work of Liang et al. [19], Tokunaga et al. [20], and Hu et al. [21], the Al_9Cr_4 phase was treated as an extension of the Al_8Cr_5 phase. In particular, Tokunaga et al. [20] considered the α-Al_8Cr_5 and β-Al_8Cr_5 phases as one solid solution, while Liang et al. [19] and Hu et al. [21] treated

them as separated phases. A brief review of the available experimental thermodynamic and phase diagram data is given below.

The formation enthalpies of different compounds were measured by Kubaschewski and Heymer [22], Meschel and Kleppa [23], and Mahdouk and Gachon [24]. Kubaschewski and Heymer [22] reported the heat of formation of the Al-Cr alloys from 35 at.% Al to 88.5 at.% Al at 300-350 °C using the calorimetry technique. Meschel and Kleppa [23] measured the formation enthalpy of the Al_8Cr_5 compound using a direct synthesis calorimeter. Mahdouk and Gachon [24] reported the formation enthalpies of different compounds at 710-1203 °C by a direct reaction calorimeter. In addition, Tokunaga et al. [20] calculated the enthalpy of formation of the Al_2Cr phase using first principles calculations. Although there is a certain scatter, in general, the reported results are consistent with each other.

The enthalpy of mixing in the liquid Al-Cr alloys were measured by Sudavtsova et al. [25], Saltykov et al. [26], and Esin et al. [27] using the calorimetry technique. Sudavtsova et al. [25] measured the partial and integral enthalpy of mixing of liquid from 0 to 30 at.% Cr alloys at 1647 °C. Saltykov et al. [26] measured the partial and integral enthalpy of mixing of liquid up to 40 at.% Cr at 1450 °C. Besides, Esin et al. [27] determined the partial enthalpy of mixing of Cr up to 55 at.% Cr in the melt at 1557 °C. All these experimental results agree with each other.

Johnson et al. [28] measured the activity of Al in the solid Cr-Al alloys at 890-1126 °C and 13-80 at.% Al using an isopiestic calorimeter. Oforka and Argent [29] determined the activity of liquid Al and solid Cr at 1150 °C by means of a Knudsen cell mass spectrometry method. Samokhval and Vecher [30] investigated the the electron motive force (emf) of Al-Cr alloys containing up to 58 at.% Al using the galvanic cell of $|Al(liq.), CaAlF_5, CaF_2|CaF_2|Al_xCr_{(1-x)}(s), CaAlF_5, CaF_2|$ at 660-757 °C. The integral Gibbs free energy, enthalpy, and entropy of formation with respect to liquid Al and solid Cr at 707 °C were reported from the electron motive force (emf) results.

The solubility of Cr in fcc_A1 between 250 and 660 °C was studied by Fink and Freche [31] using microscopic analysis, Hori [32] using thermal analysis and microscopic analysis, Koch

and Winterhager [33] using electric conductivity and expansion measurements and x-ray diffraction analysis (XRD), Raynor and Little [34] using micrographic analysis, and Kuznetsov et al. [35] using electric resistivity, micro-hardness, and crystal lattice measurements. The measured solubilities of Cr in fcc_A1 by different groups are generally in good agreement.

The solubility of Cr in liquid Al was measured by Hori [32] and Goto and Dogane [36] using thermal analysis, Fink and Freche [31] and Zoller [37] using thermal analysis and equilibration, and Eremenko et al. [38] using equilibration. The reported data agree generally with each other except for the data from Hori [32] and Goto and Dogane [39] which show much large solubility of Cr in liquid Al.

There is discrepancy for the reaction type of liquid + Al_7Cr = fcc_A1. According to the above Cr solubility measurements in liquid and fcc_A1, Al_7Cr should melt peritectic ly. However, the differential thermal analysis (DTA) and microanalysis results by Costa Neto et al. [40], the XRD, differential scanning calorimetric (DSC), and electron probe microanalysis (EPMA) results by Du et al. [41], and microanalysis of laser melted Al-Cr alloys by Almeida and Vilar [42] indicated a eutectic reaction of Liquid = fcc_A1 + Al_7Cr. Recently, Kurtuldu et al. [14] re-analyzed this reaction to be a peritectic reaction using planar front solidification experiments in a Bridgman furnace. Considering the solid solubilities of Cr in fcc_A1 and liquid and the solidification results by Kurtuldu et al. [14], the equilibria between the liquid, Al_7Cr, and fcc_A1 phases should be a peritectic type. The invariant equilibrium temperature reported from different sources is consistent and within 654-661.4 °C.

The overall phase diagram studies of the Al-Cr system include Köster et al. [16] using thermal analysis, magnetic susceptibility measurements, and XRD, Mahdouk and Gachon [24] using EPMA, XRD, and DTA, Costa Neto et al. [40] using DTA and microanalysis, Grushko et al. [43] using powder XRD, DTA, scanning electron microscope (SEM) analysis, and transmission electron microscope (TEM) analysis, and Chen [44] using DTA.

The Al_7Cr phase is stable from room temperature and melts incongruently to liquid and $Al_{11}Cr_2$ at 790 °C by Köster et al. [16], 835 °C by Costa Neto et al. [40] and Du et al. [41], 795 °C by Chen [44], and 799 °C by Mahdouk and Gachon [24].

The $Al_{11}Cr_2$ phase forms through a peritectic reaction from the Liquid and Al_4Cr phases. According to Köster et al. [16], the $Al_{11}Cr_2$ phase formed at 940 °C and is stable down to room temperature. However, the study by Costa Neto et al. [40] indicated that the $Al_{11}Cr_2$ phase could be unstable at room temperature. Mahdouk and Gachon [24] claimed that this phase decomposed to Al_7Cr and Al_4Cr at 785 °C from their EPMA, calorimetric, and DTA results. The recent measurements of the Al-Cr-Mn ternary system by Grushko et al. [43] indicated that the $Al_{11}Cr_2$ phase is stable even at low temperature and has a large solubility of Mn. The $Al_{11}Cr_2$ phase was thus treated to be stable down to room temperature in the present study.

Köster et al. [16] reported three polymorphs of Al_9Cr_4, α-Al_9Cr_4, β-Al_9Cr_4, and γ-Al_9Cr_4, with the transition temperature at 1060 °C (β → γ) and 700 °C (α → β), and two polymorphs of the Al_8Cr_5 phase, α-Al_8Cr_5 and β-Al_8Cr_5, with a transition temperature of 1125 °C. These phases are located within the composition range of 30-42.5 at.% Cr. Recently, Grushko et al. [43] revisited the phase relation between 25 and 50 at.% Cr. To the contrary of the previous investigation, only one high temperature phase γ_H and one low temperature phase γ_L were identified in this composition range. The low temperature phase has a rhombohedral distorted γ-brass structure with $\alpha < 90^o$ continuously varying with composition. While the previously reported ε / ε1 (Al_9Cr_4_H / Al_9Cr_4_L) transformation was not detected. The cubic γ_H phase forms via a peritectic transition from the bcc_A2 and liquid phases at 1320 °C which is substantially lower than the 1350 °C measured by Köster et al. [16] and similar to the temperatures measured by Costa Neto et al. [40], Grushko et al. [43], and Chen [44]. The Al_2Cr phase forms at about 910 °C [16] via a congruent transition from the bcc_A2 solid solution. Den Broeder et al. [45] and Van Tendeloo et al. [46] studied the phase relation close to the $AlCr_2$ phase using TEM analysis. A new phase X with two orientation variants was found to accompanied with the bcc_A2 phase. Thus, Den Broeder et al. [45] and Van Tendeloo et al. [46] tentatively modified the X phase in the stable equilibrium phase diagram. As discussed by Murray [15], the X phase might be a metastable phase region of

supersaturated bcc_A2 + $AlCr_2$ two phase region. In this work, the X phase is excluded from the assessment.

The liquidus reported by Köster et al. [16], Costa Neto et al. [40], Grushko et al. [43], Mahdouk and Gachon [47], and Du et al. [41] are in generally good agreement with each other. Recently, Stein et al. [13] measured the phase equilibria from 49.1 at.% Cr to 79.3 at.% Cr using thermal analysis. The solid/liquid equilibrium was measured for the first time in this region. The microstructure analysis indicated that the γ_H phase forms in a peritectic way. Their results are consistent with the measured phase diagram by Köster et al. [16]. This set of experimental data is the only available data for the solid/liquid equilibria in the Cr rich region, so it is very important for the thermodynamic modeling of the liquid phase in the present study.

The measured invariant reactions are summarized in Table 4.1. Six compounds, Al_7Cr ($Al_{45}Cr_7$), $Al_{11}Cr_2$ (Al_5Cr), Al_4Cr, γ_H (Al_8Cr_5_H), γ_L (Al_8Cr_5_L), and Al_2Cr, are stable in the Al-Cr system according to the present evaluation. The crystal structure information of the intermetallic phases in the Al-Cr system is summarized in Table 4.2.

4.2.2 The Al-Cr-Mg system

Experimental information available in the literature for the Al-Cr-Mg system is only limited to the Al-Mg rich side of the system. No thermodynamic assessment has been reported for this ternary system.

The major phase diagram measurements include the studies by Erdmann-Jesnitzer [9], Hofmann and Herzer [48], Little et al. [8], and Ohnishi et al. [11, 12]. Erdmann-Jesnitzer [9] investigated the phase relations in the Al rich corner up to 23 wt.% Cr and 37 wt.% Mg using thermal analysis and optical microanalysis. An isothermal section at 400 °C in the Al rich and Cr poor region was presented. Hofmann and Herzer [48] measured the solubility of Cr in fcc_A1 by electrical resistance measurements with the supplements of XRD and microscopic analysis. Isothermal section of the Al rich region up to 20 wt.% Mg and 10 wt.% Cr at 460 °C was investigated by Little et al. [8] using optical microscopy analysis. Ohnishi et al. [11, 12] measured

the Al rich side of the Al-Mg-Cr phase diagram up to 6 wt.% Cr and 15 wt.% Mg at 400, 500, and 550 °C using XRD and microanalysis. The ternary T phase in the Al rich corner was reported by Erdmann-Jesnitzer [9] to be an ideal stoichiometric compound of $MgCrAl_8$, by Little et al. [8] to be a ternary solution with varying composition from $Mg_3Cr_2Al_{25}$ to $Mg_3Cr_{1.3}Al_{15}$, and then by Ohnishi et al. [11, 12] to be a stoichiometric compound with the composition of $Al_{18}Cr_2Mg_3$. Samson [49, 50] determined the crystal structure of the T phase using single crystal XRD. The ideal composition of the T phase was reported to be $Al_{18}Cr_2Mg_3$ with the space group of Fd-3m and 184 atoms per unit cube. This result was later confirmed by Kerimov et al. [51]. A summary of the crystal structure information for the ternary compound T is given in Table 4.3. No other ternary phase has been reported in this ternary system.

4.3 Phase diagram experiments

High purity magnesium turnings (Alfa Aesar, 99.98 wt.% purity), aluminum rod (Alfa Aesar, 99.999 wt.% purity), and electrolytic chromium (Alfa Aesar, 99.995 wt.% purity) were used as raw materials for the present experiments. Al-8.5 wt.% Cr master alloy was first prepared by melting at 950 °C in an induction furnace for 30 minutes under an argon atmosphere ($O_2 < 10^{-8}$ ppm) purity by magnesium turning furnace which is set at 500 °C. During the melting, high purity Al_2O_3 crucible internally lined with a thin layer of boron nitride (BN) was used. The BN acted as a diffusion barrier between the charge and crucible. The weight loss of the sample is less than 0.3 wt.%. Then, the melted master alloy was sand polished to remove the surface layer and cut into 6 pieces. Suitable amount of Mg was mixed with the master alloy in the subsequent induction melting to prepare 5 ternary alloys. Each alloy was then cut into 4 pieces as experimental samples. The samples were tightly wrapped by aluminum foils and then homogenized at 400 and 450 °C for 30 and 25 days respectively, in a tube furnace flowed by argon gas. Two alloys (qA and qB) were annealed at 500 °C for 31 hours. After the designated equilibration, the samples were quickly taken from the furnace and quenched into ice water.

Due to the high melting temperature feature of Cr, it is practically difficult to prepare master alloys contain high Cr content. Diffusion couple is an alternatively better choice for the phase diagram study of system where one constitutional element has a melting temperature higher

than the boiling temperature of another. In the Al-Cr-Mg system, Al and Mg particles will always fully melt before Cr particles, so it is easy to make diffusion couple using the liquid Al-Mg alloy with solid Cr. In the present study, the Al-Mg alloy mixtures with composition of Al-30 at.% Mg, Al-15 at.% Mg, and Al-12.5 at.% Mg were mixed with a piece of Cr and melted in an induction furnace at 850 °C for 10 minutes to form diffusion couples. Then, the power of induction furnace was turned off to rapidly cool down the sample. The diffusion couple prepared in this way has remaining Cr particle covered by Al-Mg alloys (Only small amount of Cr was melted due to short time). Therefore, the interface oxidization can be avoided during the homogenization process. Three diffusion couple samples were subsequently annealed at 400 °C for 30 days and followed by rapid water quenching.

After metallographic analysis, all the samples were examined by SEM, EPMA, and XRD. The SEM analysis was carried out using the SU3500 equipped with energy dispersive spectrometry (EDS) detector and back scatter electron (BSE) detector. An accelerating voltage of 20 kV was used for the SEM microanalysis. EPMA analysis was carried out with the JEOL-8900L probe using wavelength-dispersive spectrometry (WDS). An accelerating voltage of 15 kV was utilized with a 20 nA beam current and beam size of 2 μm. MgO, Al_2O_3, and Cr metal were used as standards for the ZAF correction. The XRD analysis was carried out using the Bruker Discover D8 X-ray diffractometer equipped with HiSTAR area detector and Cu Kα radiation. An accelerating voltage of 40 kV and a beam current of 40 mA was used for the analysis.

4.4 First principles calculation

The density functional theory (DFT) [52] was utilized by means of the Vienna Ab initio Simulation Package (VASP) [53, 54] to evaluate the enthalpy of formation of the T ($Al_{18}Cr_2Mg_3$) phase. The total energies of the Fd-3m $Al_{18}Cr_2Mg_3$ [51], Fm-3m Al, Im-3m Cr, and $P6_3/mmc$ Mg were calculated within the Generalized Gradient Approximation (GGA) [55] proposed by Perdew, Burke, and Ernzerh (PBE) [56]. Electron wave functions were expanded in a plane wave basis with a cut off energy of 350 eV. An energy convergence criterion of 10^{-7} eV and Hellmann-Feynman force tolerance of 0.01 eV/Å were used. The *k*-points meshes for the integrations over Brillouin zone (BZ) was constructed using Monkhorst-Pack scheme [57] and at least 10000 *k*

points per reciprocal atom were employed. All the structures were firstly relaxed using the Methfessel-Paxton method [58], and the self-consistent static calculation using the tetrahedron method with Blochl corrections [59] was performed afterwards to obtain more precise energies. The effect of spin polarization in Cr leads to a spin-polarized calculation.

The enthalpy of formation of the $Al_{18}Cr_2Mg_3$ compound can be defined as follows:

$$\Delta H_f(Al_{18}Cr_2Mg_3) = E(Al_{18}Cr_2Mg_3) - \frac{3}{23}E(Mg) - \frac{2}{23}E(Cr) - \frac{18}{23}E(Al) \quad (4.1)$$

where E is the static energy (per mole-atoms) at 0 K for compound and pure metals, respectively. Since the influence of pressure on the condensed phases was ignored and the energy was calculated at 0 K without any entropic contribution, the calculated energy of formation was taken to be equivalent to the enthalpy of formation of the compound at 298 K. The calculated results are summarized in Table 4.3.

4.5 Thermodynamic modeling

There are many stoichiometric compounds and solution phases in the Al-Cr-Mg ternary system as listed below.

(i) Liquid solution: ternary solution consists of Al, Cr, and Mg with a large miscibility in the low Al region.

(ii) Solid solutions: ternary solid solutions include fcc_A1, bcc_A2, and hcp_A3. Four Al-Cr binary solid solutions include Al_4Cr, γ_H (Al_8Cr_5_H), γ_L (Al_8Cr_5_L), and $AlCr_2$. Two Al-Mg binary solid solutions are the AlMg_β and AlMg_γ phases.

(iii) Stoichiometric compounds: The Al_7Cr, $Al_{11}Cr_2$, $Al_{30}Mg_{23}$, and T ($Al_{18}Cr_2Mg_3$) phases.

The sub-lattice models used of these phases are presented in Table 4.4.

4.5.1 Pure elements and stoichiometric compounds

The Gibbs energies of pure elements and stoichiometric compounds can be expressed as a function of temperature at constant pressure:

$$G_T = H_T - S_T T \tag{4.2}$$

$$H_T = \Delta H^o_{298.15} + \int_{298.15}^{T} C_p dT \tag{4.3}$$

$$S_T = S^o_{298.15} + \int_{298.15}^{T} C_p / T dT \tag{4.4}$$

where H_T and S_T are enthalpy and entropy at temperature T, respectively. $\Delta H^o_{298.15}$ and $S^o_{298.15}$ are the enthalpy of formation and entropy of formation at 298.15 K, and C_p is the heat capacity. In the present assessment, the Gibbs energy data for the pure elements are taken from the SGTE pure element database compiled by Dinsdale [60]. In the case of stoichiometric compounds, the Neumann-Kopp rule is used for C_p if there is no C_p data are available and then $\Delta H^o_{298.15}$ and $S^o_{298.15}$ are optimized to reproduce the available thermodynamic and phase diagram data.

4.5.2 Liquid

The Gibbs energy of liquid is described using the Modified Quasi-chemical Model (MQM) proposed by Pelton et al. [61, 62]. In MQM, the pair exchange reaction is assumed to describe the Gibbs energy of solution. For example, for a binary A-B system, the following pair exchange reaction can be considered:

$$(A\text{-}A) + (B\text{-}B) = 2(A\text{-}B): \qquad \Delta g_{AB} \tag{4.5}$$

where (*A*-*A*), (*B*-*B*), and (*A*-*B*) are the first-nearest-neighbor atom pairs. Δg_{AB} is the non-configurational Gibbs energy change for the formation of two moles of (*A*-*B*) pairs. The Gibbs energy of a binary solution is then expressed as:

$$G = n_A G_A^o + n_B G_B^o - T\Delta S^{config} + (n_{AB}/2)\Delta g_{AB} \tag{4.6}$$

where n_i is the number of moles of *i* atoms, and n_{AB} is the number of moles of (*A*-*B*) pairs. If the coordination equivalent fraction defined as Y_A and the pair fraction as x_{AB}, then the relation between n_{AB}, Y_A, and x_{AB} is given by:

$$Y_A = x_{AA} + \frac{1}{2}(x_{AB}) \tag{4.7}$$

$$x_{AB} = n_{AB}/(n_{AA} + n_{BB} + n_{AB}) \tag{4.8}$$

$$x_A = n_A/(n_A + n_B) \tag{4.9}$$

The configurational entropy of mixing due to the random distribution of the three types of pairs in the one-dimensional Ising approximation ΔS^{config} is given by:

$$\Delta S^{config} = -R(n_A \ln x_A + n_B \ln x_B) - R\left[n_{AA} \ln\left(\frac{x_{AA}}{Y_A^2}\right) + n_{BB} \ln\left(\frac{x_{BB}}{Y_B^2}\right) + n_{AB} \ln\left(\frac{x_{AB}}{2Y_A Y_B}\right)\right] \tag{4.10}$$

The excess Gibbs energy of the liquid A-B alloys, Δg_{AB} which can be expanded as a polynomial in terms of pair fractions as:

$$\Delta g_{AB} = \Delta g_{AB}^0 + \sum_{i\geq 1} g_{AB}^{i0}(x_{AA})^i + \sum_{j\geq 1} g_{AB}^{0j}(x_{BB})^j \tag{4.11}$$

where Δg_{AB}^0, g_{AB}^{i0}, and g_{AB}^{0j} are the model parameters which can be functions of temperature. The coordination number of component A is defined as Z_A, the following relation holds: $Z_A n_A = 2n_{AA} + \sum_{i\neq j} n_{ij}$ (j>i).

In MQM, the coordination numbers of A and B, Z_A and Z_B, can be varied with composition to reproduce the short-range-ordering as follows:

$$\frac{1}{Z_A} = \frac{1}{Z_{AA}^A}\left(\frac{2n_{AA}}{2n_{AA}+n_{AB}}\right) + \frac{1}{Z_{AB}^A}\left(\frac{n_{AB}}{2n_{AA}+n_{AB}}\right) \tag{4.12}$$

$$\frac{1}{Z_B} = \frac{1}{Z_{BB}^B}\left(\frac{2n_{BB}}{2n_{BB}+n_{AB}}\right) + \frac{1}{Z_{BA}^B}\left(\frac{n_{AB}}{2n_{BB}+n_{AB}}\right) \tag{4.13}$$

where Z_{AA}^A is the value of Z_A when all the nearest neighbors of an A atom are A atoms, and Z_{AB}^A is the value of Z_A when all the nearest neighbors are B atoms. Z_{BB}^B and Z_{BA}^B are defined in an analogous manner. In the present study for the Al-Cr system, Z_{ii}^i and Z_{ij}^i for all the elements are set to be 6, as the minimum enthalpies of the liquid Al-Cr solution were found at almost $x_{Cr} = 0.5$. Once the Gibbs energy descriptions of the three sub-binary liquid solutions are optimized, the Gibbs energy of the ternary liquid solution can be calculated using the geometric extrapolation model [61, 62]. In the present Al-Cr-Mg system, the Toop type of extrapolation technique with Al as an asymmetric component was used because the Gibbs energy of the liquid Al-Cr and Al-Mg solutions deviates negatively from ideal solution while the liquid Cr-Mg solution shows strong positive deviation from ideal solution with the formation of a liquid miscibility gap. Then, the Gibbs energy of an A-B-C ternary solution can be expressed by:

$$G = n_A G_A^o + n_B G_B^o + n_C G_C^o - T\Delta S^{config} + (n_{AB}/2)\Delta g_{AB} + (n_{AC}/2)\Delta g_{AC} + (n_{BC}/2)\Delta g_{BC} \tag{4.14}$$

where each pair formation energy term can be extrapolated as [61, 62]:

$$\Delta g_{AB} = \Delta g_{AB}^0 + \sum_{(i+j)\geq 1} g_{AB}^{ij} x_{AA}^i (x_{BB} + x_{BC} + x_{CC})^j$$

$$+ \sum_{\substack{i\geq 0 \\ j\geq 0 \\ k\geq 1}} g_{AB(C)}^{ijk} x_{AA}^i (x_{BB} + x_{BC} + x_{CC})^j \left(\frac{Y_C}{Y_B + Y_C}\right)^k \tag{4.15}$$

and

$$\Delta g_{BC} = \Delta g^{0}_{BC} + \sum_{(i+j)\geq 1} g^{ij}_{BC} \left(\frac{x_{BB}}{x_{BB} + x_{CC} + x_{BC}} \right)^{i} \left(\frac{x_{CC}}{x_{BB} + x_{CC} + x_{BC}} \right)^{j}$$
$$+ \sum_{\substack{i\geq 0 \\ j\geq 0 \\ k\geq 0}} g^{ijk}_{BC(A)} \left(\frac{x_{BB}}{x_{BB} + x_{CC} + x_{BC}} \right)^{i} \left(\frac{x_{CC}}{x_{BB} + x_{CC} + x_{BC}} \right)^{j} Y_{A}^{k} \quad (4.16)$$

where *A* is Al, asymmetric component in the ternary solution, and *B* and *C* are Cr and Mg, symmetric components respectively. The ternary parameters, $g^{ijk}_{AB(C)}$ and $g^{ijk}_{BC(A)}$, can be also added to make more accurate description of the Gibbs energy of the liquid solution if necessary. In the present study, no ternary parameters were necessary to reproduce the available experimental data. That is, the Gibbs energy of the ternary Al-Cr-Mg liquid solution was predicted from the binary model parameters using MQM with the Toop extrapolation technique.

4.5.3 Solid solutions

The well-known compound energy formulism (CEF) [63] is utilized for the description of the thermodynamic properties of all the solid phases. The substitutional solid solutions, the fcc_A1, bcc_A2, and hcp_A3 phases are described as ternary solutions with a sub-lattice model as (Al, Cr, Mg)$_1$(Va)$_x$ (x = 1 for fcc_A1 and hcp_A3, and x = 3 for bcc_A2.). For the fcc_A1, bcc_A2, and hcp_A3 phases, no ternary parameters are added because the concentrations of solutes in each solution are very small. Similar to the study by Hu et al. [21], the Al_4Cr phase is modeled with a sub-lattice model of $(Cr)_1(Al, Va)_4$. The γ_L, γ_H, and $AlCr_2$ phases are described as $(Al)_{12}(Cr)_5(Al, Cr)_9$, $(Al, Cr)_2(Al, Cr)_3(Al)_2(Cr)_6$, and $(Al, Cr)_1(Al, Cr)_2$, respectively.

For instance, the Gibbs energy of the γ_H phase described by CEF as:

$$
{}^{o}G_{m}^{\gamma\_H} = \sum_{i=1}\sum_{j=1} y_i^{'} y_j^{''}\, {}^{o}G_{i:j:Al:Cr}^{\gamma\_H} + 2RT\sum_{i=1} y_i^{'} \ln y_i^{'} + 3RT\sum_{j=1} y_j^{''} \ln y_j^{''}
$$

$$
+ \sum_{i<j}\sum_{k=1} y_i^{'} y_j^{'} y_k^{''} \sum_{v=0} (y_i^{'} - y_j^{'})^{v} L_{ij:k:Al:Cr}^{v} + \sum_{k=1}\sum_{i<j} y_k^{'} y_i^{''} y_j^{''} \sum_{v=0} (y_i^{''} - y_j^{''})^{v} L_{k:ij:Al:Cr}^{v}
$$

$$
+ \sum_{i<j}\sum_{m<n} y_i^{'} y_j^{'} y_m^{''} y_n^{''} L_{ij:mn:Al:Cr} \qquad (4.17)
$$

where $y_i^{'}$ and $y_j^{''}$ are the site fractions of i and j elements in the first and second sub-lattice respectively. ${}^{o}G_{i:j:Al:Cr}^{\phi}$ is the molar Gibbs energy of the hypothetical compound $i_2j_3Al_2Cr_6$. $L_{ij:k:Al:Cr}^{v}$, $L_{k:ij:Al:Cr}^{v}$, and $L_{ij:mn:Al:Cr}$ are the interaction parameters and reciprocal parameters.

4.6 Results and discussions

The Al-Cr binary system was optimized firstly by utilizing the critically evaluated phase diagram and thermodynamic properties data reviewed in section 4.2.1. Then the Al-Cr-Mg system was optimized using the presently obtained thermodynamic description of the Al-Cr system coupled with the previous description of the Al-Mg and Cr-Mg systems. All the available phase diagram data review in section 4.2.2 and new phase diagram data obtained in this study were simultaneously considered in the optimization. The final optimized thermodynamic parameters are listed in Table 4.4. All the thermodynamic calculations were performed using the FactSage software [64].

4.6.1 Thermodynamic modeling of the binary systems

4.6.1.1 The Al-Mg and Cr-Mg systems

Thermodynamic modeling of the Al-Mg system was done by Chartrand [65]. All the model parameters were taken without any modification in the present study. In case of the Cr-Mg system, there are very few experimental data available. Ansara [66] performed the thermodynamic assessment of the Cr-Mg system using the Bragg-Williams random mixing model for the liquid

phase. In the present study, the description of the solid phases by Ansara [66] were taken without any modification, but the original description of the liquid phase was changed using MQM in order to keep the consistent thermodynamic model for all the binary liquid solutions in the Al-Cr-Mg ternary system. The model parameters of MQM for the Cr-Mg solution was optimized to reproduce the same phase diagram as original modeling by Ansara [66]. The calculated phase diagrams of the Al-Mg and Cr-Mg systems are presented in Fig. 4.1.

4.6.1.2 The Al-Cr system

The Al-Cr phase diagram is shown in Fig. 4.2 along with the experimental data. The solid lines are the calculated phase diagram from the present study and the dotted lines are from the previous thermodynamic assessment by Hu et al. [21]. Although the ideal composition for the Al_7Cr phase is $Al_{45}Cr_7$, the Al_7Cr phase was modeled as the stoichiometry of Al_7Cr for simplification. The non-stoichiometry of the Al_4Cr phase was modeled as $(Al, Va)_4Cr$ in this study, which is the same as the sub-lattice model of Hu et al. [21], because this sub-lattice model can give a better description of the phase boundary of the two phase region of (Al_4Cr + γ_L). The sub-lattice models of γ_L, γ_H, and $AlCr_2$ were well defined in the work of Hu et al. [21] based on their crystal-structure data, and these models were adopted in the present study. The parameters of the liquid and stoichiometric solid phases were roughly optimized first based on the thermodynamic data such as enthalpy and activity of liquid and solids. Then, the phase diagram data were simultaneously considered in the final optimization. In the modeling of the γ_L and γ_H phases, the parameters optimized by Hu et al. [21] were partially adopted.

As can be seen in Fig. 4.2, the largest difference between the present study and the previous assessment by Hu et al. [21] can be found in the Cr rich region. The recent liquidus and solidus by Stein et al. [13] are well reproduced in this study. The solubility limits of the bcc_A2 solid solution and the $AlCr_2$ phase are much well reproduced than the previous study. According to the present optimization, peritectic reaction of Liquid + bcc_A2 = γ_H happens at 1320 °C. This reaction temperature was reported to be 1350 °C by Köster et al. [16], 1315 °C by Costa Neto et al. [40], 1320 °C by Chen [44] and Grushko et al. [43], and 1321 °C by Stein et al. [13]. The calculated peritectoid reaction of bcc_A2 + γ_H = γ_L is at 1140 °C which perfectly agrees with the measured

value from Chen [44], Grushko et al. [43], and Stein et al. [13]. The homogeneity ranges of the γ_L and γ_H phases were more accurately described than the previous assessment study by employing one and two interaction parameters, respectively. The congruent decomposition of $AlCr_2$ to bcc_A2 is calculated at 913 °C which is higher than the value reported by Köster et al. [16] only by 3 degrees. The presently optimized invariant temperature for the bcc_A2 = γ_L + $AlCr_2$ eutectoid rection is 870 °C which is about 13 degrees lower than the values reported by Chen [44], Grushko et al. [43], and Stein et al. [13], but agrees well with the early data from Köster et al. [16] and Costa Neto et al. [40]. Two excess interaction parameters were employed for the $AlCr_2$ phase to reproduce the homogeneity range of $AlCr_2$ more accurately than the previous study by Hu et al. [21].

The optimized liquidus in this study agrees well with the experimental data as can be seen from Fig. 4.2. The calcualted metatectic γ_H = liquid + γ_L reaction is at 1060 °C. The Al_4Cr phase forms via a peritectic reaction from the liquid and γ_L phases at 1030 °C which agrees with the results by Köster et al. [16]. Similarly, the $Al_{11}Cr_2$ and Al_7Cr phases have peritectic reactions calculated at 904 °C and 799 °C, respectively.

Enlarged phase diagram in the Al rich region is shown in Fig. 4.3. The solubility of Cr increases as the temperature increase and reaches a maximum of 0.36 at.% Cr at the peritectic reaction temperature of 662 °C. While the solubility of Cr in solid Al is well reproduced in the present modeling, the optimized solubility of Cr in liquid Al is lower than the experimental data especially in the temperature range between 650 and 750 °C, which is very unusual. Therefore, no high order parameters were introduced in the present optimization.

The optimized mixing enthalpy of the liquid phase is presented in Fig. 4.4 along with the experimental data. The calculated integral enthalpy of mixing of liquid at 1450 °C is shown in Fig. 4.4(a) and it is in excellent agreement with the experimental data from Sudavtsova et al. [25] and Saltykov et al. [26]. The partial enthalpies of mixing of Cr and Al at 1450 °C are shown in Fig. 4.4(b) compared with the experimental data by Esin et al. [27], Salthkov et al. [26], and Sudavtsova et al. [25]. The optimized value from Hu et al. [21] is also appended for comparison. It can be seen that the calculated results from the present optimization is slightly better than the results of Hu et

al. [21]. The optimized enthalpies of formation of the intermetallic compounds at 298.15 K are presented in Fig. 4.5 along with the experimental data from Kubaschewski and Heymer [22], Meschel and Kleppa [23], and Mahdouk and Gachon [24], and the first principles calculations results from Tokunaga et al. [20]. The present assessment is more satisfactory with the measured data in the Al rich side. Both the present results and those from Hu et al. [21] are more negative than the experimental data by Kubaschewski and Heymer [22], but consistent with the data of Tokunaga et al. [20] in the Cr rich side. In general, the experimental data from Kubaschewski and Heymer [22] are more positive than others. So their results may be less accurate and the real enthalpy data would be lower than their experimental results especially in the Cr rich region.

The calculated activities of Al (liquid standard state) and Cr (solid standard state) at 1150 °C are compared with the experimental data from Oforka and Argent [29] in Fig. 4.6(a). Fig. 4.6(b) shows the calculated activity of liquid Al at 1000 °C compared with the experimental data from Johnson et al. [28]. In both cases, the present optimization results are similar to the previous results by Hu et al. [21]. The present calculated results in the Al rich region at both temperatures agree well with the experimental data, but the reproduction of the experimental data in the Cr rich side is less accurate. However, it should be noted that the present calculation results in the Cr rich side are lower than the experimental data at 1150 °C but higher than the data at 1000 °C. This indicates that there is most probably a certain discrepancy between the experimental data and the present calculations should be satisfactory.

4.6.2 Experimental and thermodynamic modeling results of the Al-Cr-Mg system

4.6.2.1 Experimental results

The experimental results for equilibrium quenching and diffusion couple experiments from the present study are summarized in Table 4.5.

The SEM backscatter electron (BSE) microphotographs of the samples equilibrated at 400 °C for 30 days are shown in Fig. 4.7. According to the EDS analysis, the sample S0 is a binary

alloy with the two phase mixtures of fcc_A1 + Al_7Cr. Small amount of the $Al_{11}Cr_2$ phase is still remained in the core of the Al_7Cr phase due to slow kinetics of Cr in solid state, but this is considered as unstable phase which is not influence to the phase equilibria of fcc_A1 + Al_7Cr. Similarly, small amount of the $Al_{11}Cr_2$ phase is remained in the sample S1 where fcc_A1, Al_7Cr, and T are the equilibrium phases. The sample S2 contains fcc_A1 + T equilibrium phases, and the samples S3, S4, and S5 are composed of three phase assemblage of fcc _A1 + T + Al_3Mg_2. The bulk XRD profiles for S2 and S4 are presented in Fig. 4.8 to confirm the equilibrium phases.

Fig. 4.9 shows the SEM BSE images of the diffusion couples SC1, SC3, and SC5 equilibrated at 400 ºC for 30 days. The diffusion paths of the samples are also plotted in Fig. 4.10 along with the calculated phase diagram from the present study. As can be seen in Fig. 4.9(a), three binary intermetallic phases, γ_L, Al_4Cr, and Al_7Cr, and a ternary T phase were observed around Cr particle in the diffusion couple sample SC1. Most probably, the layer of $AlCr_2$ was too thin to be well detected in SEM analysis. The two phases assemblage of T + fcc_A1 was observed outside the T layer where Cr diffusion was very limited (Fig. 4.9(b)). In the diffusion couple SC3 (see Figs. 4.9(c) and (d)), the γ_L, Al_4Cr, and T phases were formed around Cr particle, and the three phases assemblage of Al_3Mg_2 + fcc_A1 + T was observed in Al-Mg rich region. Similarly, $AlCr_2$, γ_L, Al_4Cr, and T layers were formed in the diffusion couple SC5 with the three phases assemblage of Al_3Mg_2 + fcc_A1 + T in the Al-Mg rich region (see Figs. 4.9(e) and (f)).

The SEM BSE images of equilibrium alloys after the homogenization at 450 °C are shown in Fig. 4.11. The sample compositions of T0 and T2 are within three phase region of fcc_A1 + Al_3Mg_2 + T. Fcc_A1 and T are in equilibrium in the sample T3. The sample T4 is a binary Al-Cr alloy containing the fcc_A1 and Al_7Cr phases. The three phase equilibrium of fcc_A1, T, and Al_7Cr is found in the sample T5.

In order to determine the stability of the T ($Al_{18}Cr_2Mg_3$) phase at high temperature, two equilibration experiments were carried out at 500 °C. The SEM BSE images of the two measured samples are shown in Fig. 4.12. The alloy qA (Fig. 4.12(a)) is composed of T and liquid two phases, and the alloy qB is composed of the T, fcc_A1, and liquid phases. The size of T crystal is relatively small because the equilibration time was relatively short. The existence of the liquid phase can be

confirmed also from quenched dendritic microstructure. A small amount of Al_3Mg_2 quenched crystals was also detected by XRD. There is no doubt that the ternary T phase is stable at least up to 500 °C.

One of the main purposes of the present phase diagram study was to determine the homogeneity range of the ternary T phase. The different alloy compositions and diffusion couples were intentionally designed around the T phase region to measure the boundary of homogeneity range of the T phase. According to the present EPMA results for equilibrium samples and diffusion couple samples, the T phase has a small homogeneity range. The compositions of Cr and Mg can vary within ± 0.6 at.% and ± 2 at.%, respectively, from its ideal composition of $Al_{18}Cr_2Mg_3$.

Unfortunately, the melting point of T was not directly determined in the present study. However, one alloy with a nominal composition of Al-9.5 at.% Mg-4.1 at.% Cr which is composed of two phases assemblage of fcc_A1 + T was prepared for DSC analysis using the Jupiter STA 449 F3 thermal analyzer (NETZSCH Instruments, Germany). The measured DSC profile up to 750 °C is presented in Fig. 4.13(a). In the present study, the DSC run was done only one heating cycle because above 750 °C, significant amount of Mg was oxidized according to the simultaneous thermogravimetric measurement so the composition of the original alloy changed which gave inconsistent thermal arrests. Two thermal arrests were recorded: low temperature one at 445. 3 °C has a very small peak which is considered due to the inhomogeneity of the original sample, and the high temperature one at 618.2 °C shows a large endothermic peak, which should relate to the melting of the T phase. According to the present thermodynamic calculations as shown in Fig. 4.13(b), there is partial melting with the invariant reaction at 627 °C involving T, Al_7Cr, fcc_A1, and liquid.

4.6.2.2 Thermodynamic modeling of the Al-Cr-Mg system

According to the present evaluation, the ternary T ($Al_{18}Cr_2Mg_3$) phase allows certain deviation from its stoichiometric composition. As the inhomogeneity range is quite small, it is reasonable to treat this phase as a stoichiometric compound. The calculated enthalpy of formation via first principles calculation in this study was utilized as the initial value of enthalpy of formation

and the Gibbs energy of the T phase was optimized by considering the phase boundary related to the T phase. Since limited thermodynamic and phase diagram information about the liquid phase is available, the Gibbs energy of the liquid phase was simply predicted from the binary model parameters without any ternary interactions.

The calculated Al rich isothermal sections are presented in Fig. 4.14. Fig 4.14(a) is the calculated isothermal section at 400 °C compared with the experimental data from Ohnishi et al. [11, 12] and the present measurement. The solubility of Cr and Mg in the fcc_A1 solution is very low. The calculated phase diagram at 450 and 460 °C are presented in Figs. 4.14(b) and (c) respectively. The measured data from Ohnishi et al. [11, 12], Little et al. [8], and the current measurements are also appended for comparison. It can be seen that as the temperature increase the measured solubility of Cr and Mg increase. The solubility of Cr is more prone to temperature. The phase relationship at 450 and 460 °C are very similar. The only difference is that the liquid phase already becomes stable instead of the Al_3Mg_2 phase. The measured phase equilibria at 500 °C by the present quenching experiment are compared with the currently optimized phase diagram in Fig. 4.14(d). A comparison between the measured and calculated isothermal section at 550 °C is presented in Fig. 4.14(e). In all the isothermal sections, the phase relationships from the previous experiments and the present experiments are well reproduced. In addition, the solid phase compositions determined from the present study by EDS and WDS are well matched with the calculation results.

Based on the evaluated Gibbs energy of the T phase along with all the binary descriptions of the solid and liquid phases, the phase diagrams in the ternary Al-Cr-Mg system are predicted as shown in Fig. 4.15. The isothermal sections from 300 to 700 °C shows that the T phase is stable. The predicted peritectic melting temperature of the T phase ($T \rightarrow L + Al_4Cr + AlCr_2$) in the present study is 816 °C.

The liquidus projection of the Al-Cr-Mg system is predicted in Fig. 4.16. According to the present prediction, a wide range of liquid miscibility gap extended from the Cr-Mg system occupy the ternary system up to 65 at.% of Al. The primary phase regions of the γ_L, γ_H, Al_4Cr, $Al_{11}Cr_2$, Al_7Cr, and T phases are calculated. Because the invariant temperatures of the Al-Cr system are

much higher than those of the Al-Mg system, the primary phase regions of the Al-Mg phases are very small (only existing in the composition less than 1 at.% of Cr). Although the predicted diagrams in the present study can reasonably provide a general feature of the phase relation and primary phase regions in this ternary system, more experiments should be carried out in the future in particular for the low Al region (less than 50 at.%) to confirm the prediction. At least the present thermodynamic modeling can accurately describe the phase diagrams in the Al rich region as shown in Fig. 4.14 according to the comparison with the available experimental data.

4.7 Summary

Equilibrium alloys, diffusion couples, and DSC experiments were utilized to determine the phase relation in the Al-Mg rich side of the Al-Cr-Mg system at 400, 450, and 500 °C. The existence of the ternary $Al_{18}Cr_2Mg_3$ compound and its homogeneity range was confirmed. The diffusion couple samples were prepared by solid/liquid reaction, which can be very effective to measure the phase diagram of the system where one of the components has significantly high melting temperature than others, like the Al-Cr-Mg system. The enthalpy of formation of the $Al_{18}Cr_2Mg_3$ phase was calculated using the first principles calculations method. A thermodynamic optimization was carried out for the Al-Cr and Al-Cr-Mg systems on the basis of the critically evaluated literature information and the present experiment results. New phase diagrams for the ternary Al-Cr-Mg system were predicted from the optimized model parameters.

Acknowledgement

The authors would like to thank the financial support from NSERC-Automotive Partnership Canada program in Canada. Senlin Cui would also like to thank the McGill Engineering Doctorate Award (MEDA) from McGill University for financial support. A part of the research presented in this paper was financed by the Fonds de recherché du Québec -Nature et technologies by the intermediary of the Aluminum Research Centre – REGAL.

References

1. Verma, R., P.A. Friedman, A.K. Ghosh, C. Kim, and S. Kim, *Superplastic forming characteristics of fine-grained 5083 aluminum.* J. Mater. Eng. Perform., 1995. **4**(5): p. 543-50.
2. Kannan, K. and J.P. Hirth, *Mixed mode fracture toughness and low cycle fatigue behavior in an HSLA-80 steel.* Scr. Mater., 1998. **39**(6): p. 743-748.
3. Mikhailovskaya, A.V., I.S. Golovin, A.A. Zaitseva, V.K. Portnoi, P. Droettboom, and J. Cifre, *Effect of Mn and Cr additives on recrystallization kinetics and grain boundary relaxation parameters of Al-4.9 Mg alloy.* Fiz. Met. Metalloved., 2013. **114**(3): p. 268-278.
4. Sharma, M.M., *Microstructural and mechanical characterization of various modified 7XXX series spray formed alloys.* Mater. Charact., 2008. **59**(1): p. 91-99.
5. Watanabe, H., S. Muromachi, and N. Kono, *Superplastic magnesium-aluminum eutectic alloy containing strontium*. 1987, (Japan Metals and Chemicals Co., Ltd., Japan). Application:JP.p. 6 pp.
6. Zhang, X.-m., Z.-l. Zhou, J.-g. Tang, B. Ke, J.-l. Hu, and H. Ouyang, *Effects of Cr on microstructure and properties of Al-Mg-Si-Cu aluminum alloy.* Cailiao Gongcheng, 2013. 58 (12): p. 49-53.
7. Rogl, P., S. Stiltz, and F.H. Hayes, *The Al-Cr-Mg system (aluminum-chromium-magnesium).* J. Phase Equilib., 1992. **13**(3): p. 317-23.
8. Little, K., H.J. Axon, and W. Hume-Rothery, *The constitution of aluminum-magnesium-zinc-chromium alloys at 460 °C.* J. Inst. Met., 1948. **75**(Paper No. 1141): p. 39-50.
9. Erdmann-Jesnitzer, F., *The aluminum corner of the three-component system aluminum-magnesium-chromium.* Aluminium-Arch., 1940. **29**.
10. Hanemann, H. and A. Schrader, *The ternary systems of aluminum. III. Systems aluminum-nickel-silicon, aluminum-magnesium-chromium and aluminum-copper-nickel.* Z. Metallkd., 1941. **33**: p. 20-1.
11. Ohnishi, T., Y. Nakatani, and K. Shimizu, *Phase diagram in the aluminum rich side of the aluminum-magnesium-manganese-chromium quaternary system.* Keikinzoku, 1973. **23**(10): p. 437-43.

12. Ohnishi, T., Y. Nakatani, and K. Shimizu, *Phase diagrams and ternary compounds of aluminum-magnesium-chromium and aluminum-magnesium-manganese systems in the aluminum rich corner.* Keikinzoku, 1973. **23**(5): p. 202-9.
13. Stein, F., C. He, and I. Wossack, *The liquidus surface of the Cr-Al-Nb system and re-investigation of the Cr-Nb and Al-Cr phase diagrams.* J. Alloys Compd., 2014. **598**: p. 253-265.
14. Kurtuldu, G., P. Jessner, and M. Rappaz, *Peritectic reaction on the Al rich side of Al-Cr system.* J. Alloys Compd., 2015. **621**: p. 283-286.
15. Murray, J.L., *The Al-Cr (aluminum-chromium) system.* J. Phase Equilib., 1998. **19**(4): p. 368-375.
16. Köster, W., E. Wachtel, and K. Grube, *Constitution and magnetic properties of aluminum-chromium alloys.* Z. Metallkd., 1963. **54**: p. 393-401.
17. Okamoto, H., *Al-Cr (aluminum-chromium).* J. Phase Equilib. Diffus., 2008. **29**(1): p. 112-113.
18. Saunders, N. and V.G. Rivlin, *A critical review and thermodynamic calculations for the aluminum-rich portion of the aluminum-chromium-iron phase diagram.* Z. Metallkd., 1987. **78**(11): p. 795-801.
19. Liang, Y., C. Guo, C. Li, and Z. Du, *Thermodynamic modeling of the Al-Cr system.* J. Alloys Compd., 2008. **460**(1-2): p. 314-319.
20. Tokunaga, T., H. Ohtani, and M. Hasebe, *Thermodynamic assessment of the Al-Cr system by combining the first-principles and CALPHAD methods.* Mater. Sci. Forum, 2007. **539-543**(Pt. 3, THERMEC 2006): p. 2407-2412.
21. Hu, B., W.-W. Zhang, Y. Peng, Y. Du, S. Liu, and Y. Zhang, *Thermodynamic reassessment of the Al-Cr-Si system with the refined description of the Al-Cr system.* Thermochim. Acta, 2013. **561**: p. 77-90.
22. Kubaschewski, O. and G. Heymer, *Heats of formation of transition-metal aluminides.* Trans. Faraday Soc., 1960. **56**: p. 473-8.
23. Meschel, S.V. and O.J. Kleppa, *The standard enthalpies of formation of some 3d transition metal aluminides by high-temperature direct synthesis calorimetry.* NATO ASI Ser., Ser. E, 1994. **256**(METALLIC ALLOYS): p. 103-12.

24. Mahdouk, K. and J.-C. Gachon, *Thermodynamic investigation of the aluminum-chromium system.* J. Phase Equilib., 2000. **21**(2): p. 157-166.
25. Sudavtsova, V.S., A.V. Shuvalov, and N.O. Sharkina, *Thermochemical properties of liquid binary alloys in the aluminum-(chromium, nickel) system.* Rasplavy, 1990(4): p. 97-9.
26. Saltykov, P., V.T. Witusiewicz, I. Arpshofen, H.J. Seifert, and F. Aldinger, *Enthalpy of mixing of liquid Al-Cr and Cr-Ni alloys.* J. Mater. Sci. Technol. , 2002. **18**(2): p. 167-170.
27. Esin, Y.O., P.V. Gel'd, M.S. Petrushevskii, N.P. Bobrov, G.M. Ryss, V.V. Sokolov, I.P. Pazdnikov, and A.Y. Dubrovskii, *Enthalpies of formation of molten binary aluminum alloys with yttrium, zirconium, vanadium, and chromium.* v sb., Splavy Redk. Met. s Osobymi Fiz.-khim. Svoistvami, 1975: p. 177-80.
28. Johnson, W., K. Komarek, and E. Miller, *Thermodynamic properties of solid chromium-aluminum alloys at 1000 ºC.* Trans. Met. Soc. AIME (Amer. Inst. Mining, Met., Petrol. Eng.), 1968. **242**(8): p. 1685-8.
29. Oforka, N.C. and B.B. Argent, *Thermodynamics of nickel-chromium-aluminum alloys.* J. Less-Common Met., 1985. **114**(1): p. 97-109.
30. Samokhval, V.V. and A.A. Vecher, *Thermodynamic properties of chromium-aluminum alloys.* Izv. Akad. Nauk SSSR, Metal., 1971(6): p. 164-7.
31. Fink, W.L. and H.R. Freche, *Equilibrium relations in aluminum-chromium alloys of high purity.* Trans. Am. Inst. Min., Metall. Pet. Eng., 1933. **104**: p. 325-34.
32. Hori, S., *Study of certain aluminum-chromium alloys.* Research Repts. Sumitomo Met. Inds., 1935. **2**: p. 351-72.
33. Koch, W. and H. Winterhager, *The solubility of chromium in aluminum.* Metallwirtsch., Metallwiss., Metalltech., 1938. **17**: p. 1159-63.
34. Raynor, G.V. and K. Little, *The constitution of the aluminum rich aluminum-chromium alloys.* J. Inst. Met., 1945. **71**(Pt. 9, Paper No. 1002): p. 481-9.
35. Kuznetsov, G.M., A.D. Barsukov, and M.I. Abas, *Study of manganese, chromium, titanium, and zirconium solubility in solid aluminum.* Izv. Vyssh. Uchebn. Zaved., Tsvetn. Metall., 1983(1): p. 96-100.
36. Goto, M. and G. Dogane, *An aluminum and chromium alloy.* Nippon Kogyo Kaishi, 1927. **No. 512**: p. 931-6.

37. Zoller, H., *The action of zinc, magnesium, silicon, copper, iron, manganese, and titanium on the primary crystallization of Al_7Cr.* Schweiz. Arch., 1960. **26**: p. 437-48;478-91.
38. Eremenko, V.N., Y.V. Natanzon, and V.P. Titov, *Kinetics of chromium dissolution in aluminum at 700-900 °C.* Izv. Akad. Nauk SSSR, Met., 1980(6): p. 217-20.
39. Goto, M. and G. Dogane, *An aluminum and chromium alloy.* J. Inst. Met., 1927. **43**: p. 446.
40. Costa Neto, J.G., S. Gama, and C.A. Ribeiro, *Experimental study of the aluminum-chromium equilibrium diagram.* J. Alloys Compd., 1992. **182**(2): p. 271-80.
41. Du, Y., J.C. Schuster, and Y.A. Chang, *Experimental identification of the degenerated equilibrium in extreme Al end of the Al-Cr system.* J. Mater. Sci., 2005. **40**(4): p. 1023-1025.
42. Almeida, A. and R. Vilar, *Al-Al_7Cr eutectic in Al-Cr alloys synthesized by laser alloying.* Scr. Mater., 2010. **63**(8): p. 811-814.
43. Grushko, B., E. Kowalska-Strzeciwilk, B. Przepiorzynski, and M. Surowiec, *Investigation of the Al-Cr γ-range.* J. Alloys Compd., 2005. **402**(1-2): p. 98-104.
44. Chen, H., *PhD thesis, Central South University, Changsha, China.* 2008.
45. Den Broeder, F.J.A., G. Van Tendeloo, S. Amelinckx, J. Hornstra, R. De Ridder, J. Van Landuyt, and H.J. Van Daal, *Microstructure of chromium-aluminum ($Cr_{100-x}Al_x$) alloys (10 at.% ≲ x ≲ 33 at.%) studied by means of transmission electron microscopy and diffraction. II. Discovery of a new phase.* Phys. Status Solidi A, 1981. **67**(1): p. 233-48.
46. Van Tendeloo, G., F.J.A. Den Broeder, S. Amelinckx, R. De Ridder, J. Van Landuyt, and H.J. Van Daal, *Microstructure of chromium-aluminum ($Cr_{100-x}Al_x$) alloys (10 at.% ≲ x ≲ 33 at.%) studied by means of transmission electron microscopy and diffraction. I. Microstructure of the β-phase.* Phys. Status Solidi A, 1981. **67**(1): p. 217-32.
47. Mahdouk, K. and J.-C. Gachon, *New results about the Al-Cr binary phase diagram.* Arch. Metall., 2001. **46**(3): p. 233-238.
48. Hofmann, W. and R.W. Herzer, *The solid solubility of chromium in aluminum with up to two percent magnesium.* Metallwirtsch., Metallwiss., Metalltech., 1940. **19**: p. 141-3.
49. Samson, S., *Crystal structure of the intermetallic compound $Mg_3Cr_2Al_{18}$.* Nature (London, U. K.), 1954. **173**: p. 1185-6.
50. Samson, S., *The crystal structure of the intermetallic compound $Mg_3Cr_2Al_{18}$.* Acta Crystallogr., 1958. **11**: p. 851-7.

51. Kerimov, K.M., S.F. Dunaev, and E.M. Sljusarenko, *Investigation of the structure of ternary phases in aluminum-magnesium-titanium, aluminum-magnesium-vanadium and aluminum-magnesium-chromium systems.* J. Less-Common Met., 1987. **133**(2): p. 297-302.
52. Kohn, W. and C. Majumdar, *Continuity between bound and unbound states in a Fermi gas.* Phys. Rev., 1965. **138**(6A): p. 1617-20.
53. Kresse, G. and J. Furthmuller, *Efficiency of ab-initio total energy calculations for metals and semiconductors using a plane-wave basis set.* Comput. Mater. Sci., 1996. **6**(1): p. 15-50.
54. Kresse, G. and J. Furthmueller, *Efficient iterative schemes for ab initio total-energy calculations using a plane-wave basis set.* Phys. Rev. B Condens. Matter, 1996. **54**(16): p. 11169-11186.
55. Perdew, J.P., J.A. Chevary, S.H. Vosko, K.A. Jackson, M.R. Pederson, D.J. Singh, and C. Fiolhais, *Atoms, molecules, solids, and surfaces: applications of the generalized gradient approximation for exchange and correlation.* Phys. Rev. B Condens. Matter, 1992. **46**(11): p. 6671-87.
56. Perdew, J.P., K. Burke, and M. Ernzerhof, *Generalized gradient approximation made simple.* Phys. Rev. Lett., 1996. **77**(18): p. 3865-3868.
57. Monkhorst, H.J. and J.D. Pack, *Special points for Brillouin-zone integrations.* Phys. Rev. B Condens. Matter, 1976. **13**(12): p. 5188-5192.
58. Methfessel, M. and A.T. Paxton, *High-precision sampling for Brillouin-zone integration in metals.* Phys. Rev. B Condens. Matter, 1989. **40**(6): p. 3616-21.
59. Blochl, P.E., O. Jepsen, and O.K. Andersen, *Improved tetrahedron method for Brillouin-zone integrations.* Phys. Rev. B Condens. Matter, 1994. **49**(23): p. 16223-33.
60. Dinsdale, A.T., *SGTE data for pure elements.* CALPHAD Comput. Coupling Phase Diagrams Thermochem., 1991. **15**(4): p. 317-425.
61. Pelton, A.D. and P. Chartrand, *The modified quasi-chemical model: Part II. Multicomponent solutions.* Metall. Mater. Trans. A, 2001. **32A**(6): p. 1355-1360.
62. Pelton, A.D., S.A. Degterov, G. Eriksson, C. Robelin, and Y. Dessureault, *The modified quasichemical model I - binary solutions.* Metall. Mater. Trans. B, 2000. **31B**(4): p. 651-659.

63. Sundman, B. and J. Ågren, *A regular solution model for phases with several components and sublattices, suitable for computer applications.* J. Phys. Chem. Solids, 1981. **42**(4): p. 297-301.
64. Bale, C.W., P. Chartrand, S.A. Degterov, G. Eriksson, K. Hack, R. Ben Mahfoud, J. Melancon, A.D. Pelton, and S. Petersen, *FactSage thermochemical software and databases.* CALPHAD Comput. Coupling Phase Diagrams Thermochem., 2002. **26**(2): p. 189-228.
65. Chartrand, P., *Thermodynamic assessment of the Al-Mg system.* Unpublished work, 2006.
66. Ansara, I., A. Dinsdale, T, and M. Rand, H, *COST 507.* Thermochemical database for light metal alloys, 1998. **2**.
67. Wu, H., M. Zhang, B. Xu, and G. Ling, *Preparation and characterization of $Al_{11}Cr_4$ phase by diffusion of Al/Cr composite film.* J. Alloys Compd., 2014. **610**: p. 492-497.
68. Cooper, M.J., *The structure of the intermetallic phase θ (Cr-Al).* Acta Crystallogr., 1960. **13**: p. 257-63.
69. Ohnishi, T., Y. Nakatani, and K. Okabayashi, *Crystal sturctures of intermetallic θ, η, and ε phases in the aluminum-chromium system.* Bull. Univ. Osaka Prefect., Ser. A, 1975. **24**(2): p. 183-91.
70. Audier, M., M. Durand-Charre, E. Laclau, and H. Klein, *Phase equilibria in the Al-Cr system.* J. Alloys Compd., 1995. **220**(1-2): p. 225-30.
71. Ellner, M., J. Braun, and B. Predel, *X-ray investigations on the chromium-aluminum phases belonging to the W family.* Z. Metallkd., 1989. **80**(5): p. 374-83.
72. Bradley, A.J. and S.S. Lu, *An x-ray study of the chromium-aluminum equilibrium diagram.* J. Inst. Met., 1937. **60**(Advance copy No. 769): p. 19 pp.

Table captions

Table 4.1 Summary of the invariant reactions in the Al-Cr system.

Table 4.2 Summary of crystal structure information of the stable compounds in the Al-Cr system.

Table 4.3 Summary of crystal structure information and enthalpy of formation for the compound T ($Al_{18}Mg_3Cr_2$) in the Al-Cr-Mg system.

Table 4.4 Summary of optimized model parameters for the Al-Cr-Mg system (J mol^{-1} or J mol^{-1} K^{-1}).

Table 4.5 Summary of the present experimental results for the phase equilibria at 400, 450, and 500 °C.

Figure captions

Fig. 4.1 Calculated phase diagram of (a) the Al-Mg system and (b) the Cr-Mg system.

Fig. 4.2 Calculated phase diagram of the Al-Cr system along with the measured experimental data.

Fig. 4.3 Enlarged phase diagram in the Al rich side of the Al-Cr system.

Fig. 4.4 Calculated enthalpy of the liquid Al-Cr solution. (a) Integral enthalpy of mixing at 1450 ^{o}C, and (b) partial enthalpy of mixing of Al and Cr at 1450 ^{o}C along with the related experimental data.

Fig. 4.5 Calculated enthalpy of formation of the Al-Cr system at 298.15 K along with the experimental data.

Fig. 4.6 (a) Calculated activities of Al with respect to the pure liquid standard state and Cr with respect to the solid bcc_A2 standard state at 1150 °C, and (b) calculated activity of Al at 1000 °C with respect to pure liquid along with the experimental data.

Fig. 4.7 Microstructures of different alloys annealed at 400 °C for 30 days. (a) Alloy sample S0, (b) S1, (c) S2, (d) S3, (e) S4, and (f) S5.

Fig. 4.8 Bulk XRD profiles of (a) alloy sample S2, and (b) S4 after annealing at 400 °C for 30 days.

Fig. 4.9 Microstructures of diffusion couples annealed at 400 °C for 30 days. (a) and (b) SC1, (c) and (d) SC3, and (e) and (f) SC5.

Fig. 4.10 The measured diffusion paths of diffusion couples SC1, SC3, and SC5 at 400 °C along with the calculated phase diagram in the present study.

Fig. 4.11 Microstructures of different alloys annealed at 450 °C for 25 days. (a) Alloy sample T0, (b) T2, (c) T3, (d) T4, and (e) T5.

Fig. 4.12 The quenched microstructures of the alloys (a) qA and (b) qB annealed at 500 °C for 31 hours.

Fig. 4.13 (a) The measured DSC profile of alloy sample with a nominal composition Al-9.5 at.% Mg-4.1 at.% Cr. (b) Calculated isopleth of Al-Cr_3Mg_7 along with the measured experimental data from DSC analysis in (a).

Fig. 4.14 Calculated isothermal sections in the Al rich part of the Al-Cr-Mg system in comparison to the experimental data at (a) 400 °C, (b) 450 °C, (c) 460 °C, (d) 500 °C, and (e) 550 °C.

Fig. 4.15 Predicted isothermal sections from 300 to 1800 ºC in the Al-Cr-Mg system from the present thermodynamic assessment.

Fig. 4.16 Predicted liquidus projection of the Al-Cr-Mg system. (a) Entire composition range, and (b) enlarged diagram in the Al rich region.

Table 4.1 Summary of the invariant reactions in the Al-Cr system.

Reaction type	Reaction (at. % Si)			Temperature °C	Method [a]	Ref.
Eutectic	Liquid = Al_7Cr + fcc_A1					
				654	TA	[39]
				660	TA	[31]
	0.19	0.37	0	661.4	TA	[37]
				661	TA	[16]
				657	DTA	[40]
				656	DTA	[47]
				659.7	DTA, DSC	[41]
				662		This work
Peritectic	Liquid + $Al_{11}Cr_2$ = Al_7Cr					
				725	TA	[39]
				790	TA	[16]
				835	DTA	[40]
				795	DTA	[44]
				799	DTA	[47]
				835	DTA, DSC	[41]
				799		This work
Peritectic	Liquid + Al_4Cr = $Al_{11}Cr_2$					
				1011	TA	[39]
				940	TA	[16]
				906	DTA	[47]
				944	DTA	[41]
				904		TW
Eutectoid	$Al_{11}Cr_2$ = Al_7Cr + Al_4Cr					
				785		[47]
				783		This work
Peritectic	Liquid + γ_L = Al_4Cr					
				1030	TA	[16]

		1035	DTA	[40]
		1037	DTA	[44]
		1037	DTA	[47]
		1040	DTA	[43]
		1030		This work
Metatectic	γ_H = Liquid + γ_L			
		1170	TA	[16]
		1164	DTA	[40]
		1060	DTA	[44]
		1060	DTA	[43]
		1060		This work
Peritectic	Liquid + bcc_A2 = γ_H			
		1350	TA	[16]
		1315	DTA	[40]
		1320	DTA	[43]
		1320	DTA	[44]
		1321±2	DTA	[13]
		1320		This work
Peritictoid	bcc_A2 + γ_H = γ_L			
		1125		[16]
		1115	DTA	[40]
		1140	DTA	[43]
		1140	DTA	[44]
		1138±2	DTA	[13]
		1140		This work
Eutectoid	bcc_A2 = γ_L + $AlCr_2$			
		870	TA	[16]
		872	DTA	[40]
		882	DTA	[43]
		882	DTA	[44]

		876±2	DTA	[13]
		870		This work
Congruent	bcc_A2 = $AlCr_2$			
		910	TA	[16]
		913		This work
Peritectoid	$Al_{11}Cr_4$ = Al_4Cr + γ_L			
		829	DTA	[67]
		829		This work

[a] TA = Thermal Analysis; DTA = Differential Thermal Analysis; DSC = Differential Scanning Calorimetry.

Table 4.2 Summary of crystal structure information of the stable compounds in the Al-Cr system.

Phase	Space group	System	Prototype	Pearson symbol	Lattice parameters (nm)			Comment	Reference
					a	b	c		
Al_7Cr	C2/m	Monoclinic	$Al_{45}Cr_7$	mC104	2.5196	0.7574	1.0949	β=128.71º	[68]
$Al_{11}Cr_2$	P-2	Monoclinic		mP48	1.288	0.7652	1.0639	β=128.41º	[69]
Al_4Cr	$P6_3/mmc$	Hexagonal	μ_Al_4Mn	hP574	1.998		2.467	β=119.33º	[70]
γ_H	I43m	Cubic	Cu_5Zn_8	cI52	0.9065				[71]
γ_L	R3m	Rhombohedral	Al_8Cr_5	hR26	1.2719		0.7936		[72]
$AlCr_2$	I4/mmm	Tetragonal	$MoSi_2$	tI26	0.299984		0.86303		[72]

Table 4.3 Summary of crystal structure information and enthalpy of formation for the compound T ($Al_{18}Mg_3Cr_2$) in the Al-Cr-Mg system.

Space group	System	Lattice parameters (nm)	Formation enthalpy (kJ/mol)	Magnetic moment (μ_B)	Reference
Fd-3m	Cubic	1.45			[12]
Fd-3m	Cubic	1.45			[51]
		1.45 [a]	-238.50 [a]	-0.0001 [a]	This work
			-246.50 [b]		This work

[a] First principles calculation. [b] CALPHAD type of assessment.

Table 4.4 Summary of optimized model parameters for the Al-Cr-Mg system (J mol^{-1} or J mol^{-1} K^{-1}).

Phase	Thermodynamic parameters	Ref.
Liquid (Al, Cr, Mg)	$Z^{Al}_{AlAl} = Z^{Mg}_{MgMg} = Z^{Si}_{SiSi} = Z^{Al}_{AlSi} = Z^{Al}_{AlMg} = Z^{Mg}_{MgAl} = Z^{Mg}_{MgSi} = Z^{Si}_{SiAl} = Z^{Si}_{SiMg} = 6$	
	$\Delta g_{Al,Cr} = -6250.02 - 4.71T + (-4978.96 - 4.73T)x_{AlAl} + (836.80 + 1.88T)x^2_{AlAl}$ $-1602.81x_{CrCr}$	This work
	$\Delta g_{Al,Mg} = -2761.44 + 1.53T + (-418.40 + 0.63T)x_{AlAl}$	[65]
	$\Delta g_{Cr,Mg} = 40526.40 - 3671.76\,x_{CrCr} - 12667.36\,x_{MgMg}$	This work
fcc_A1 $(Al, Cr, Mg)_1(Va)_1$	${}^0L_{Al,Cr:Va} = -57135.57$	This work
	$L_{Al,Mg:Va} = 2803.66 + 0.52T + (-280.75 + 0.54T)(x_{Al} - x_{Mg})$	[65]
	$L_{Cr,Mg:Va} = 80.00T$	[66]
bcc_A2 $(Al, Cr, Mg)_1(Va)_3$	${}^0L_{Al,Cr:Va} = -56356.80 - 6.32T$ ${}^1L_{Al,Cr:Va} = -7654.74$	This work
	$L_{Al,Mg:Va} = 5020.80$	[65]
	$L_{Cr,Mg:Va} = 80.00T$	[66]
hcp_A3 $(Al, Cr, Mg)_1(Va)_1$	$L_{Al,Mg:Va} = 2510.40$	[65]
	${}^0L_{Al,Cr:Va} = -35000.00 + 6.00T$	[66]
	$L_{Cr,Mg:Va} = 80.00T$	[66]

Al_4Cr $(Cr)_1(Al, Va)_4$	${}^oG_{Cr:Va} = 25000.00 + {}^oG_{Cr}^{bcc}$	[21]
	${}^oG_{Cr:Al} = -84930.41 + 3.81T + 4{}^oG_{Al}^{fcc} + {}^oG_{Cr}^{bcc}$	This work
	${}^0L_{Cr:Al,Va} = 28226.27$	
γ_L $(Al)_{12}(Cr)_5(Al, Cr)_9$	${}^oG_{Al:Cr:Al} = -357006.16 + 20.16T + 21{}^oG_{Al}^{fcc} + 5{}^oG_{Cr}^{bcc}$	This work
	${}^oG_{Al:Cr:Cr} = -320932.55 - 109.52T + 12{}^oG_{Al}^{fcc} + 14{}^oG_{Cr}^{bcc}$	
	${}^0L_{Al:Cr:Al,Cr} = -632060.44 + 29.07T$	[21]
γ_H $(Al, Cr)_2(Al,$ $Cr)_3(Cr)_2(Al)_6$	${}^oG_{Al:Al:Cr:Al} = -124435.30 + 11{}^oG_{Al}^{fcc} + 2{}^oG_{Cr}^{bcc}$	[21]
	${}^oG_{Cr:Cr:Cr:Al} = 2357.31 - 103.77T + 6{}^oG_{Al}^{fcc} + 7{}^oG_{Cr}^{bcc}$	
	${}^oG_{Cr:Al:Cr:Al} = 9\cdot{}^oG_{Al}^{fcc} + 4\cdot{}^oG_{Cr}^{bcc}$	
	${}^oG_{Al:Cr:Cr:Al} = -243506.24 - 42.08T + 8{}^oG_{Al}^{fcc} + 5{}^oG_{Cr}^{bcc}$	This work
	${}^0L_{Al,Cr:*:Cr:Al} = -183139.26$	
	${}^0L_{*:Al,Cr:Cr:Al} = -63705.75 - 25.22T$	
$AlCr_2$ $(Al, Cr)_1(Al, Cr)_2$	${}^oG_{Al:Al} = 10000.00 + 3{}^oG_{Al}^{fcc}$	This work
	${}^oG_{Cr:Cr} = 10000.00 + 3{}^oG_{Cr}^{bcc}$	
	${}^oG_{Al:Cr} = -36594.81 - 14.91T + {}^oG_{Al}^{fcc} + 2{}^oG_{Cr}^{bcc}$	
	${}^oG_{Cr:Al} = 52331.31 + 16.84T + 2{}^oG_{Al}^{fcc} + {}^oG_{Cr}^{bcc}$	
	${}^0L_{Al,Cr:*} = -8922.60$	
	${}^0L_{*:Al,Cr} = -38108.20$	

Al_7Cr $(Al)_7(Cr)$	${}^oG_{Al:Cr} = -107000.00 + 14.81T + 7{}^oG_{Al}^{fcc} + {}^oG_{Cr}^{hcp}$	This work
$Al_{11}Cr_2$ $(Al)_{11}(Cr)_2$	${}^oG_{Al:Cr} = -195000.00 + 16.99T + 11{}^oG_{Al}^{fcc} + 2{}^oG_{Cr}^{hcp}$	This work
AlMg_β $Al_{19}(Al, Mg)_2Mg_{12}$	${}^oG_{Al:Al:Mg} = -82111.42 - 13.81T + 12{}^oG_{Mg}^{hcp} + 21{}^oG_{Al}^{fcc}$ ${}^oG_{Al:Mg:Mg} = -72446.38 - 27.61T + 14{}^oG_{Mg}^{hcp} + 19{}^oG_{Al}^{fcc}$	[65]
AlMg_γ $Mg_{10}(Al, Mg)_{24}(Al, Mg)_{24}$	${}^oG_{Mg:Al:Al} = 178762.94 - 203.00T + 10{}^oG_{Mg}^{hcp} + 48{}^oG_{Al}^{fcc}$ ${}^oG_{Mg:Al:Mg} = 359507.52 - 197.67T + 34{}^oG_{Mg}^{hcp} + 24{}^oG_{Al}^{fcc}$ ${}^oG_{Mg:Mg:Al} = -208741.60 + 78.46T + 34{}^oG_{Mg}^{hcp} + 24{}^oG_{Al}^{fcc}$ ${}^oG_{Mg:Mg:Mg} = 359154.56 - 174.64T + 58{}^oG_{Mg}^{hcp}$	[65]
$Al_{30}Mg_{23}$	${}^oG_{Al:Mg} = -116327.71 - 72.99T + 30{}^oG_{Al}^{fcc} + 23{}^oG_{Mg}^{hcp}$	[65]
$Al_{18}Cr_2Mg_3$	${}^oG_{Al:Cr:Mg} = -246497.84 - 11.07T + 18{}^oG_{Al}^{fcc} + 2{}^oG_{Cr}^{hcp} + 3{}^oG_{Mg}^{hcp}$	This work

Table 4.5 Summary of the present experimental results for the phase equilibria at 400, 450, and 500 °C.

No.	Nominal composition (EDS) (mole fraction)			T °C	Homogenization time (day)	Phase identification (XRD)	Phase composition (WDS) (mole fraction)		
	Al	Cr	Mg				Al	Cr	Mg
S0	0.952	0.048	0	400	30	fcc_A1	0.997	0.003	0.000
						Al_7Cr	0.863	0.137	0.000
S1	0.889	0.054	0.057	400	30	fcc_A1	0.981	0.003	0.016
						T	0.782	0.090	0.129
						Al_7Cr	0.859	0.139	0.002
S2	0.840	0.033	0.128	400	30	fcc_A1	0.909	0.001	0.090
						T	0.770	0.089	0.141
S3	0.669	0.022	0.309	400	30	fcc_A1	0.880	0.000	0.120
						Al_3Mg_2	0.619	0.000	0.381
						T	0.769	0.087	0.144
S4	0.747	0.025	0.228	400	30	fcc_A1	0.877	0.000	0.122
						Al_3Mg_2	0.618	0.000	0.382
						T	0.766	0.087	0.147
S5	0.656	0.013	0.331	400	30	fcc_A1	0.881	0.000	0.119
						Al_3Mg_2	0.618	0.000	0.382
						T	0.769	0.087	0.144
T0	0.670	0.005	0.325	450	25	fcc_A1	0.864	0.000	0.136

						Al_3Mg_2	0.617	0.000	0.382
						T	0.768	0.088	0.144
T2	0.717	0.028	0.255	450	25	fcc_A1	0.823	0.000	0.177
						Al_3Mg_2	0.615	0.000	0.385
						T	0.767	0.088	0.144
T3	0.867	0.027	0.106	450	25	fcc_A1	0.919	0.001	0.080
						T	0.773	0.089	0.139
T4	0.956	0.044	0	450	25	fcc_A1	0.996	0.004	0.000
						Al_7Cr	0.861	0.139	0.000
T5	0.904	0.047	0.049	450	25	fcc_A1	0.988	0.002	0.010
						T	0.791	0.089	0.120
						Al_7Cr	0.859	0.138	0.002
qA	0.703	0.060	0.237	500	31h	T	0.773	0.086	0.141
						Liquid	-	-	-
	0.732[a]	0.047[a]	0.221[a]			Al_3Mg_2 [b]	-	-	-
qB	0.745	0.043	0.212	500	31h	T	0.773	0.087	0.140
						fcc_A1	0.863	0.00045	0.136
						Liquid	-	-	-
	0.765[a]	0.035[a]	0.200[a]			Al_3Mg_2 [b]	-	-	-
SC1				400	30	γ_L	0.674	0.326	0.0001
						Al_4Cr	0.784	0.209	0.008
						Al_7Cr	0.855	0.139	0.005

						T	0.778	0.088	0.134
	0.832	0.045	0.123	400	30	T	0.778	0.086	0.136
						fcc_A1	0.905	0.00144	0.093
SC3				400	30	γ_L	0.685	0.314	0.001
						Al_4Cr	0.768	0.211	0.020
						T	0.774	0.088	0.137
	0.704	0.005	0.291	400	30	Al_3Mg_2	0.619	0.0006	0.380
						fcc_A1	0.914	0.0004	0.086
						T	0.777	0.0861	0.137
SC5				400	30	$AlCr_2$	0.381	0.618	0.00049
						γ_L	0.599	0.399	0.00150
						Al_4Cr	0.795	0.205	0.00049
						T	0.778	0.087	0.13493
	0.819	0.033	0.148	400	30	Al_3Mg_2	0.625	0.001	0.374
						fcc_A1	0.892	0.001	0.107
						T	0.775	0.087	0.138

[a] Determined from WDS measurements.

[b] Minor quenched crystal determined from XRD technique.

Figures

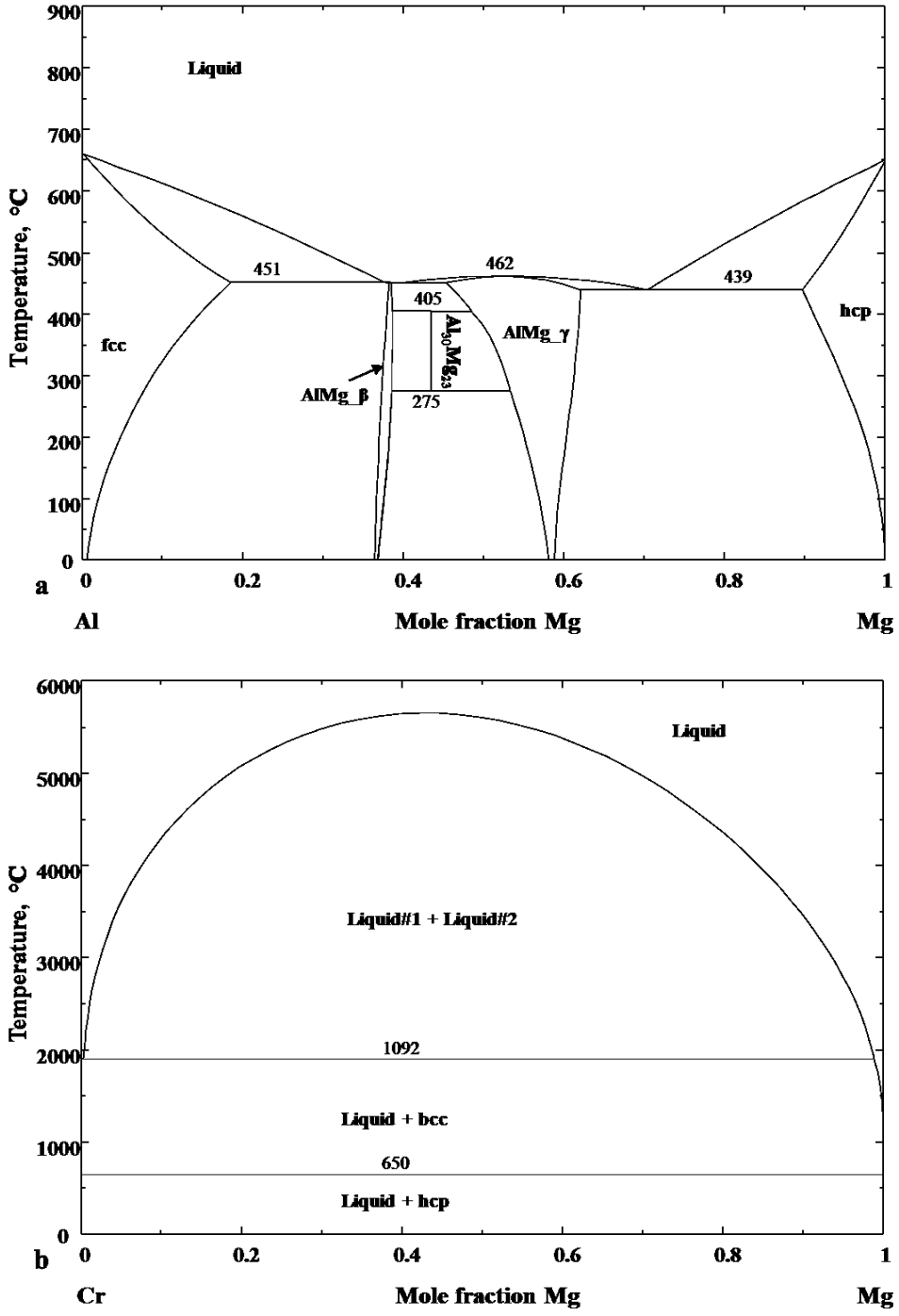

Fig. 4.1 Calculated phase diagram of (a) the Al-Mg system and (b) the Cr-Mg system.

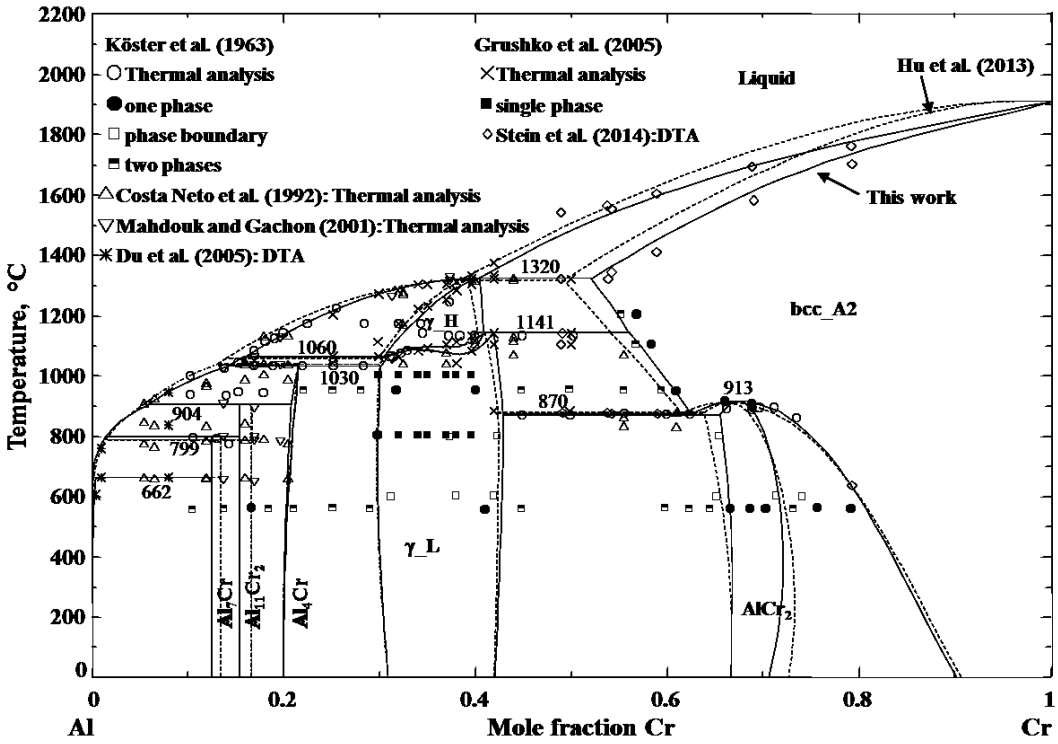

Fig. 4.2 Calculated phase diagram of the Al-Cr system along with the measured experimental data.

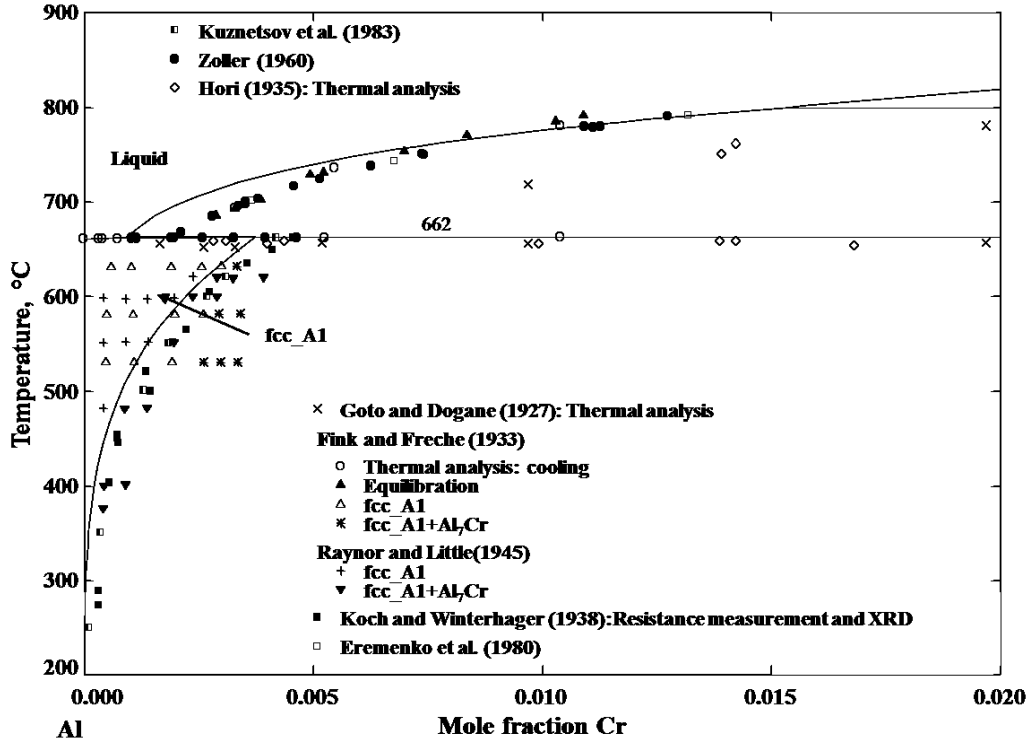

Fig. 4.3 Enlarged phase diagram in the Al rich side of the Al-Cr system.

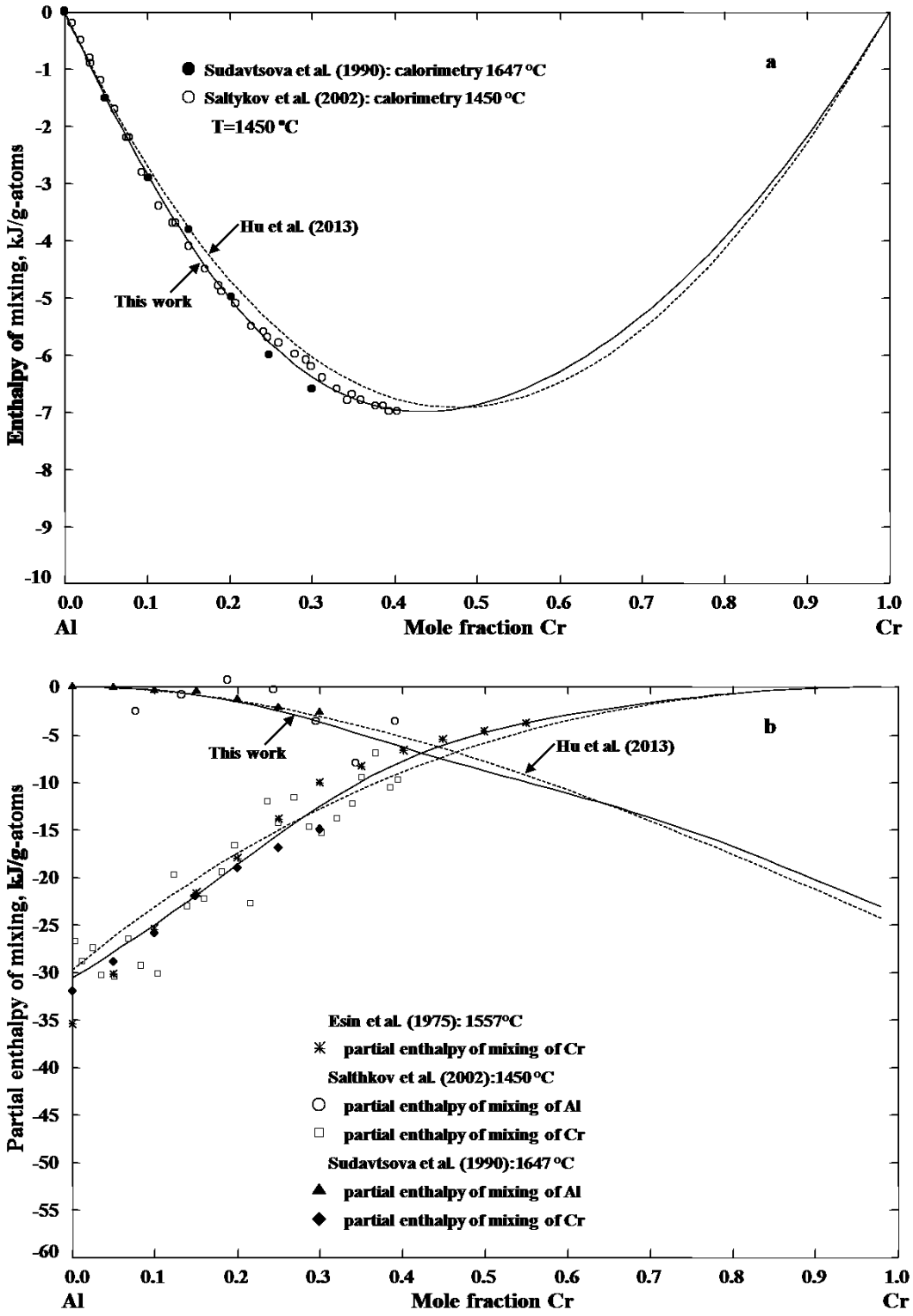

Fig. 4.4 Calculated enthalpy of the liquid Al-Cr solution. (a) Integral enthalpy of mixing at 1450 ^{o}C, and (b) partial enthalpy of mixing of Al and Cr at 1450 ^{o}C along with the related experimental data.

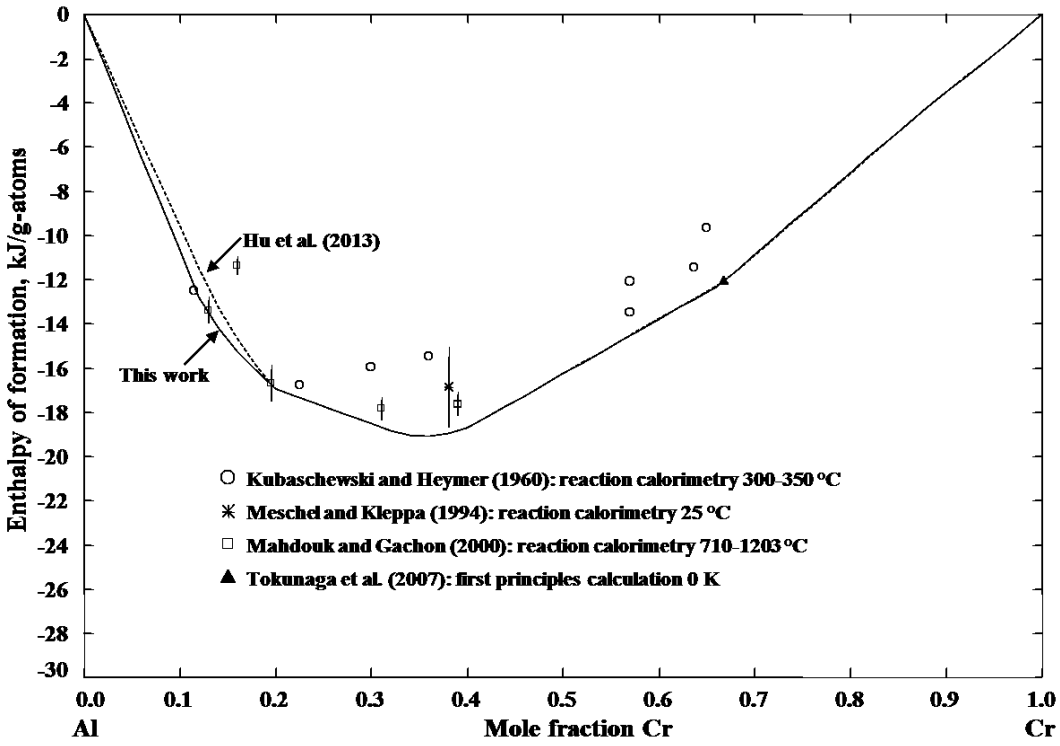

Fig. 4.5 Calculated enthalpy of formation of the Al-Cr system at 298.15 K along with the experimental data.

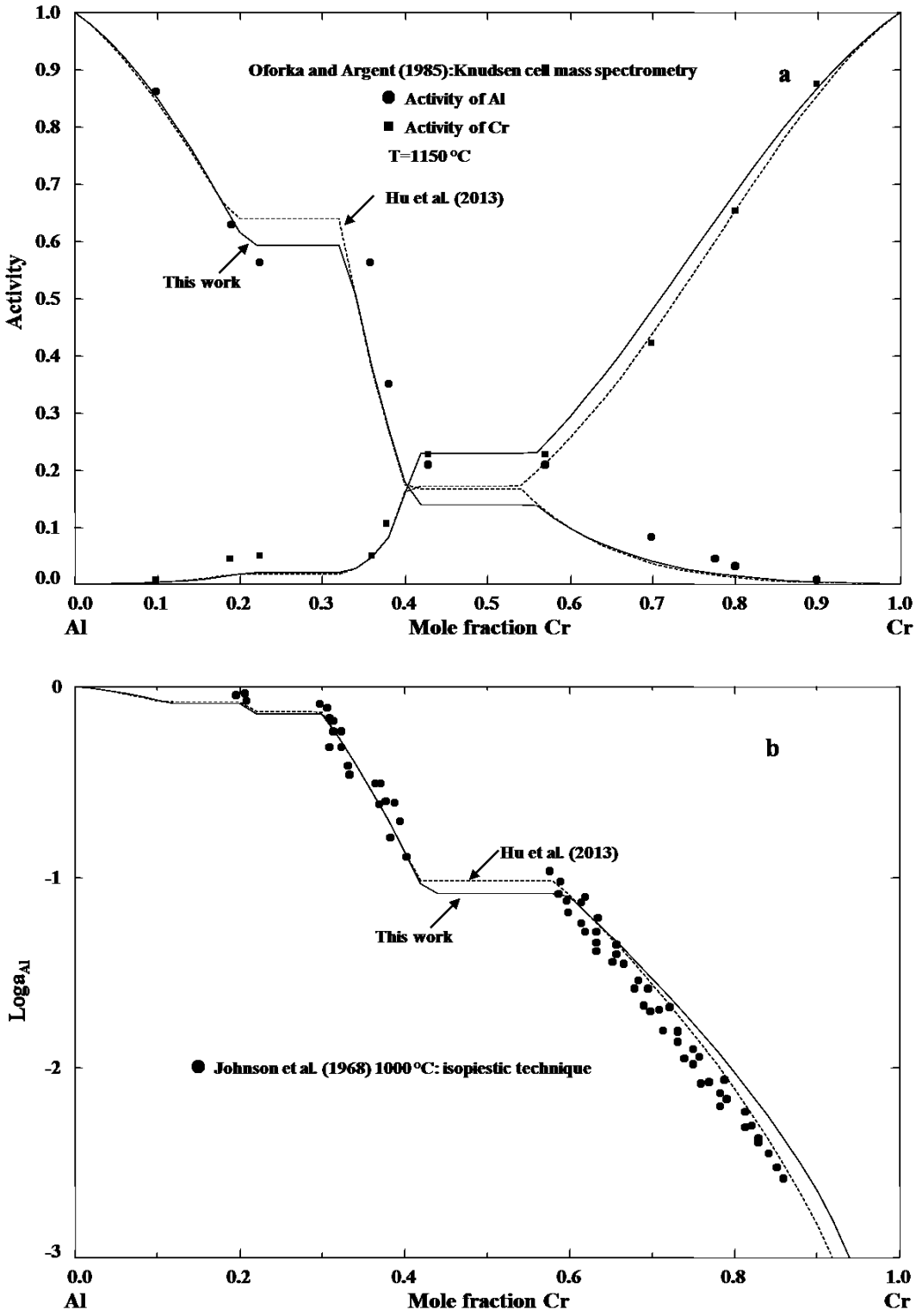

Fig. 4.6 (a) Calculated activities of Al with respect to the pure liquid standard state and Cr with respect to the solid bcc_A2 standard state at 1150 °C, and (b) calculated activity of Al at 1000 °C with respect to pure liquid along with the experimental data.

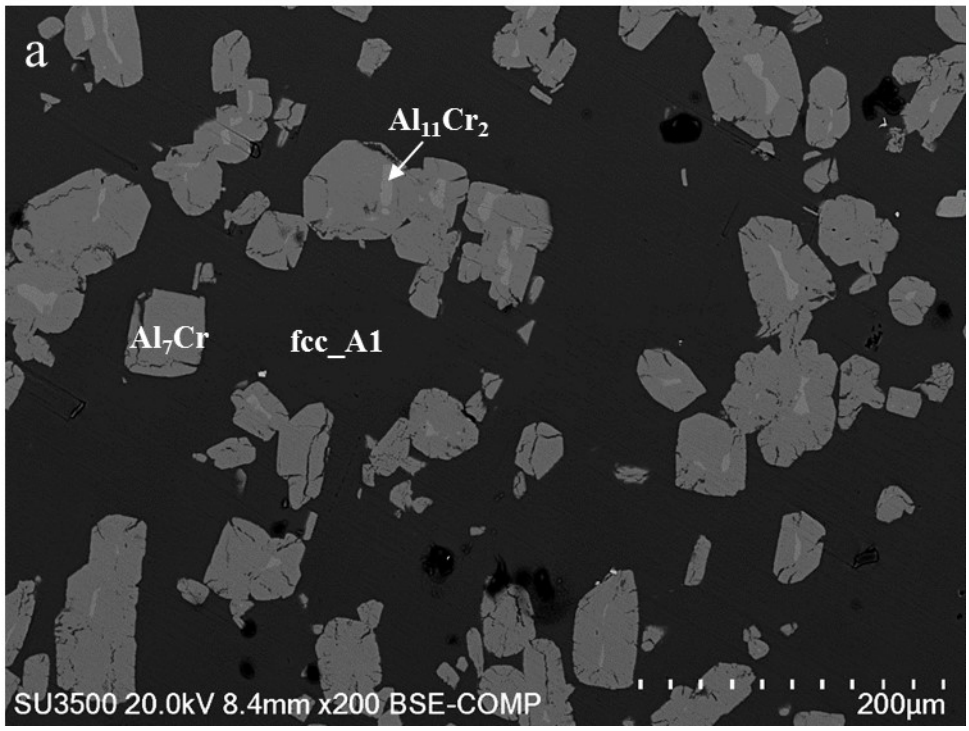
a
$Al_{11}Cr_2$
Al_7Cr
fcc_A1
SU3500 20.0kV 8.4mm x200 BSE-COMP
200μm

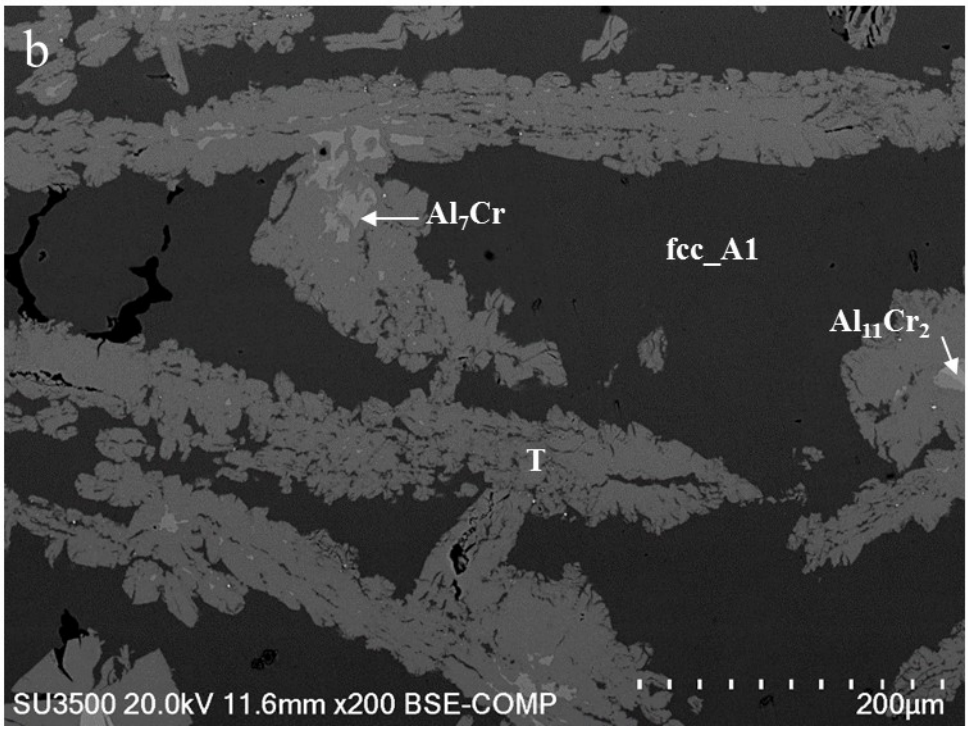
b
Al_7Cr
fcc_A1
$Al_{11}Cr_2$
T
SU3500 20.0kV 11.6mm x200 BSE-COMP
200μm

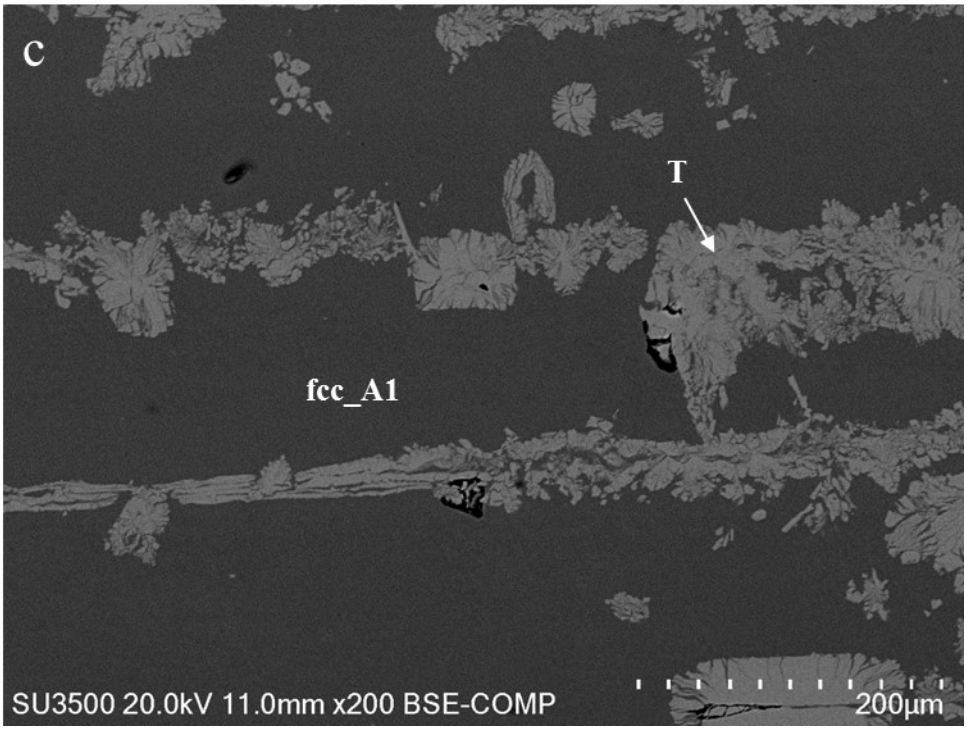
c
T
fcc_A1
SU3500 20.0kV 11.0mm x200 BSE-COMP
200μm

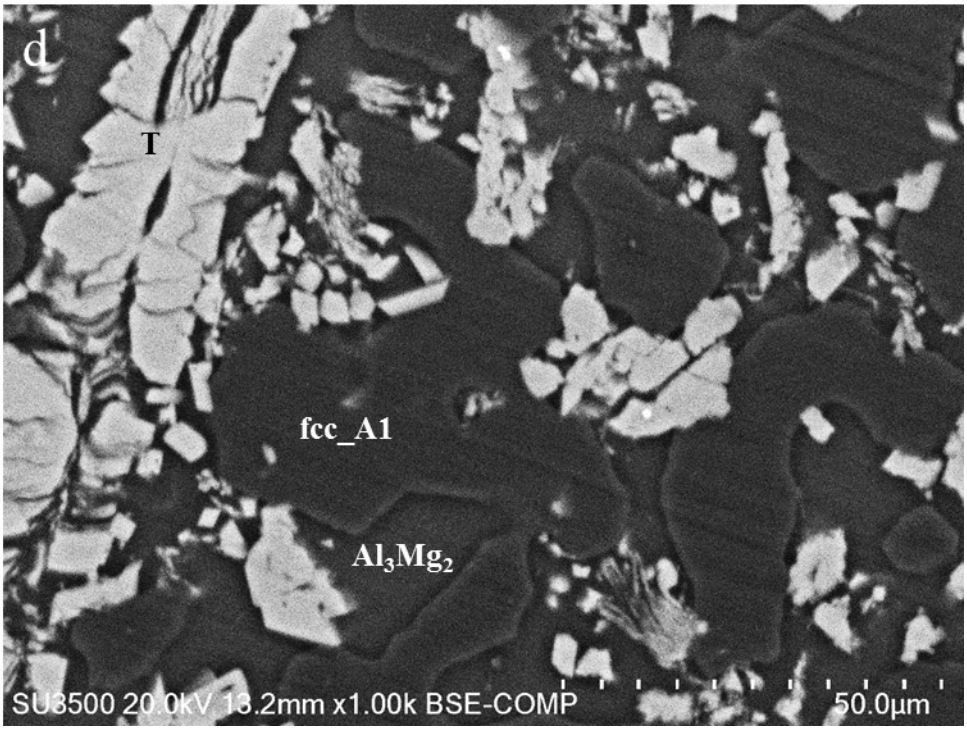
d
T
fcc_A1
Al3Mg2
SU8500 20.0kV 13.2mm x1.00k BSE-COMP
50.0μm

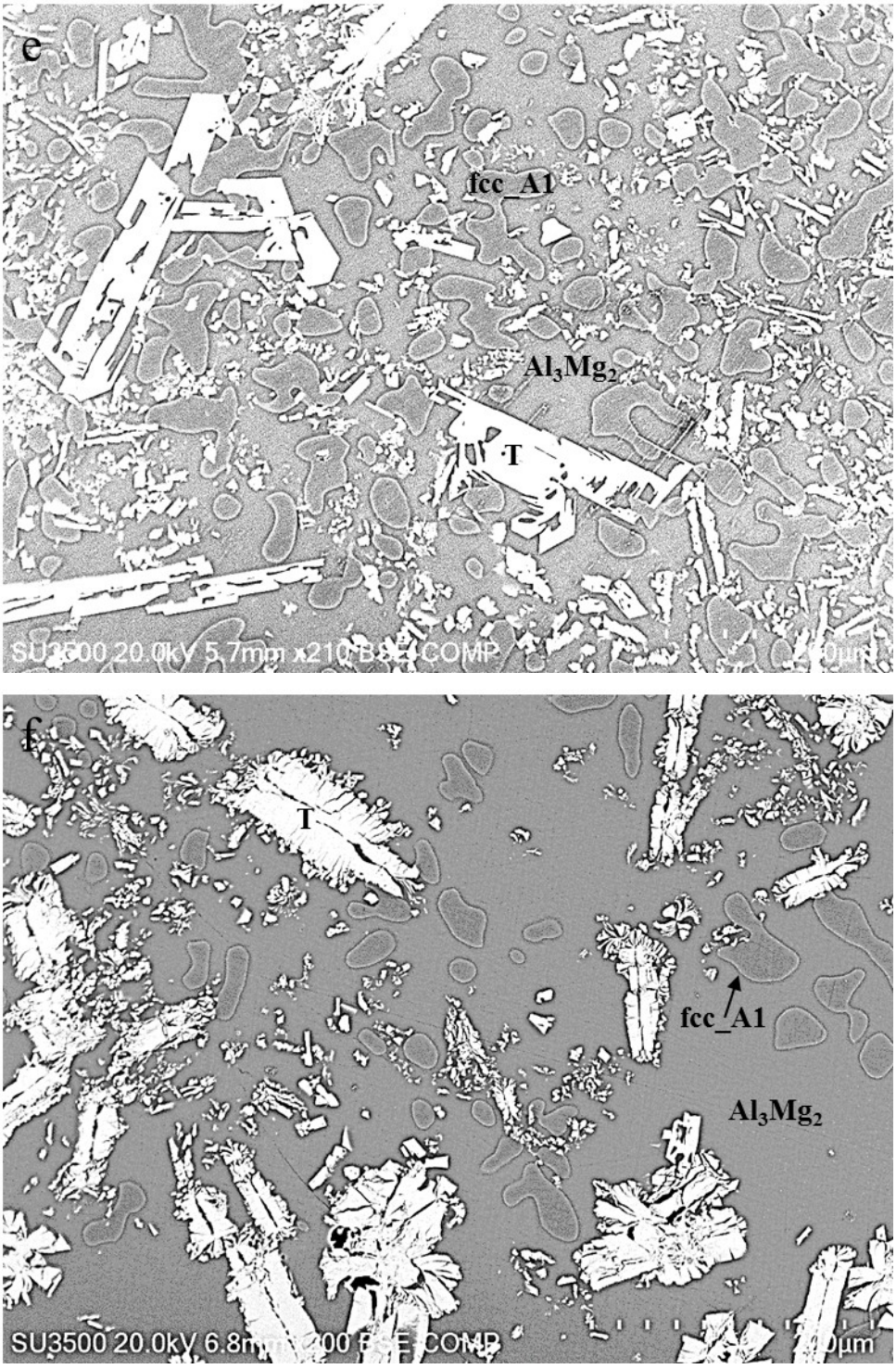

Fig. 4.7 Microstructures of different alloys annealed at 400 °C for 30 days. (a) Alloy sample S0, (b) S1, (c) S2, (d) S3, (e) S4, and (f) S5.

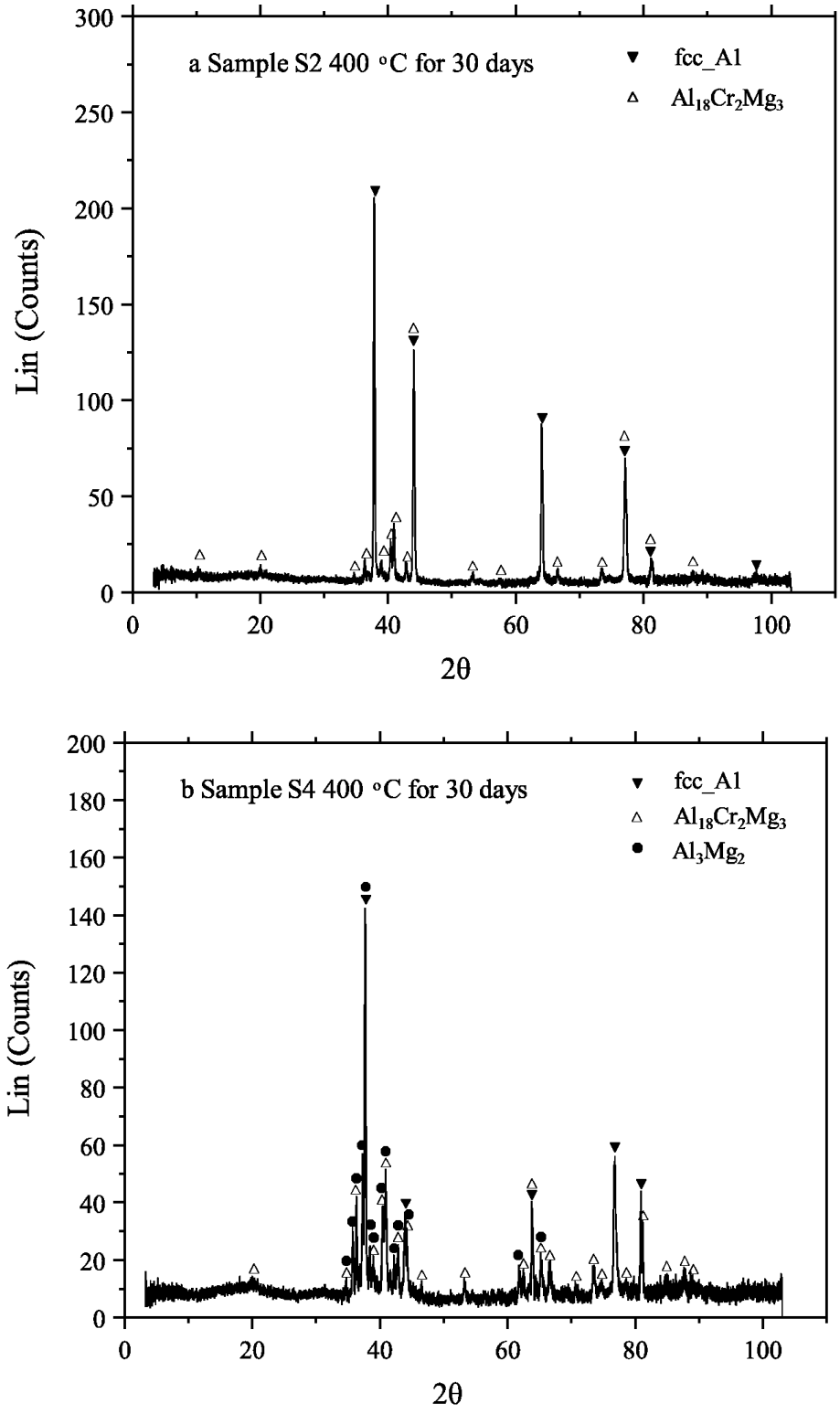

Fig. 4.8 Bulk XRD profiles of (a) alloy sample S2, and (b) S4 after annealing at 400 °C for 30 days.

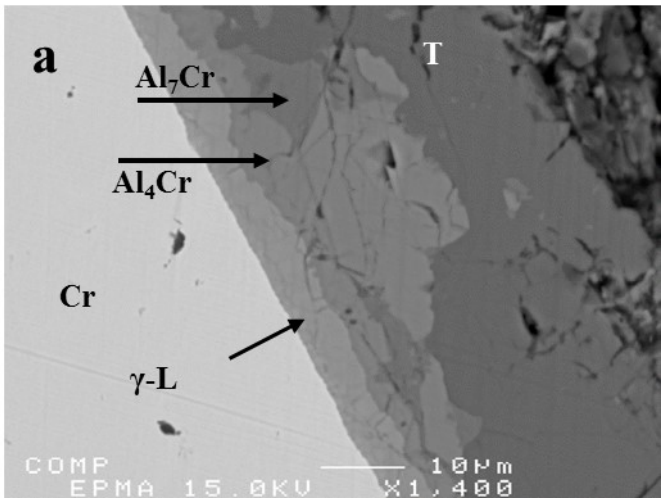
a
T
Al_7Cr
Al_4Cr
Cr
γ-L
COMP
EPMA 15.0KV
10μm
X1,400

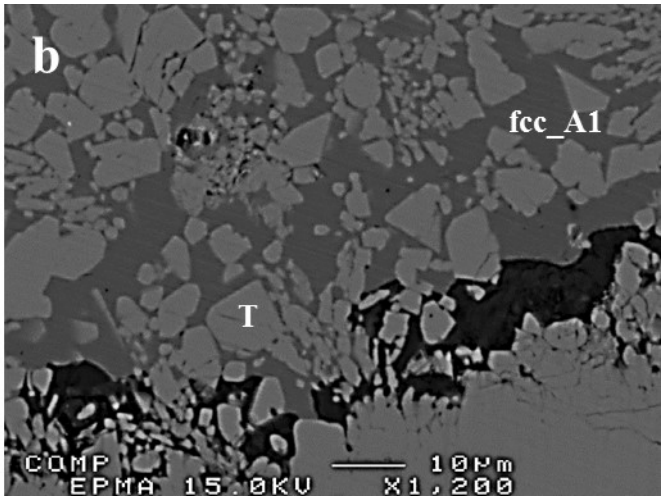
b
fcc_A1
T
COMP
EPMA 15.0KV
10μm
X1,200

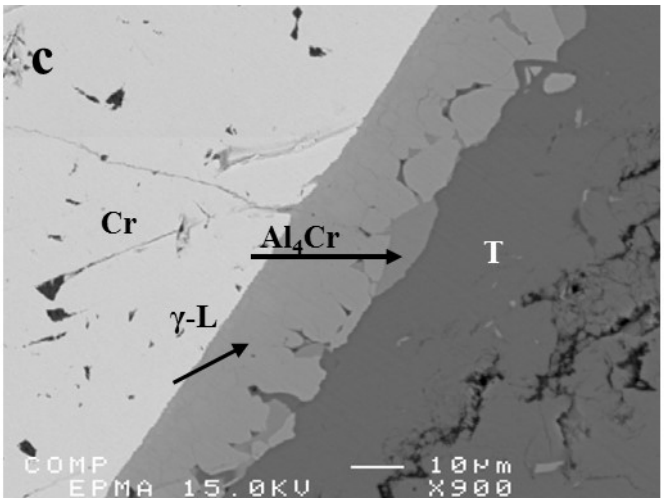
c
Cr
Al_4Cr
T
γ-L
COMP
EPMA 15.0KV
10μm
X900

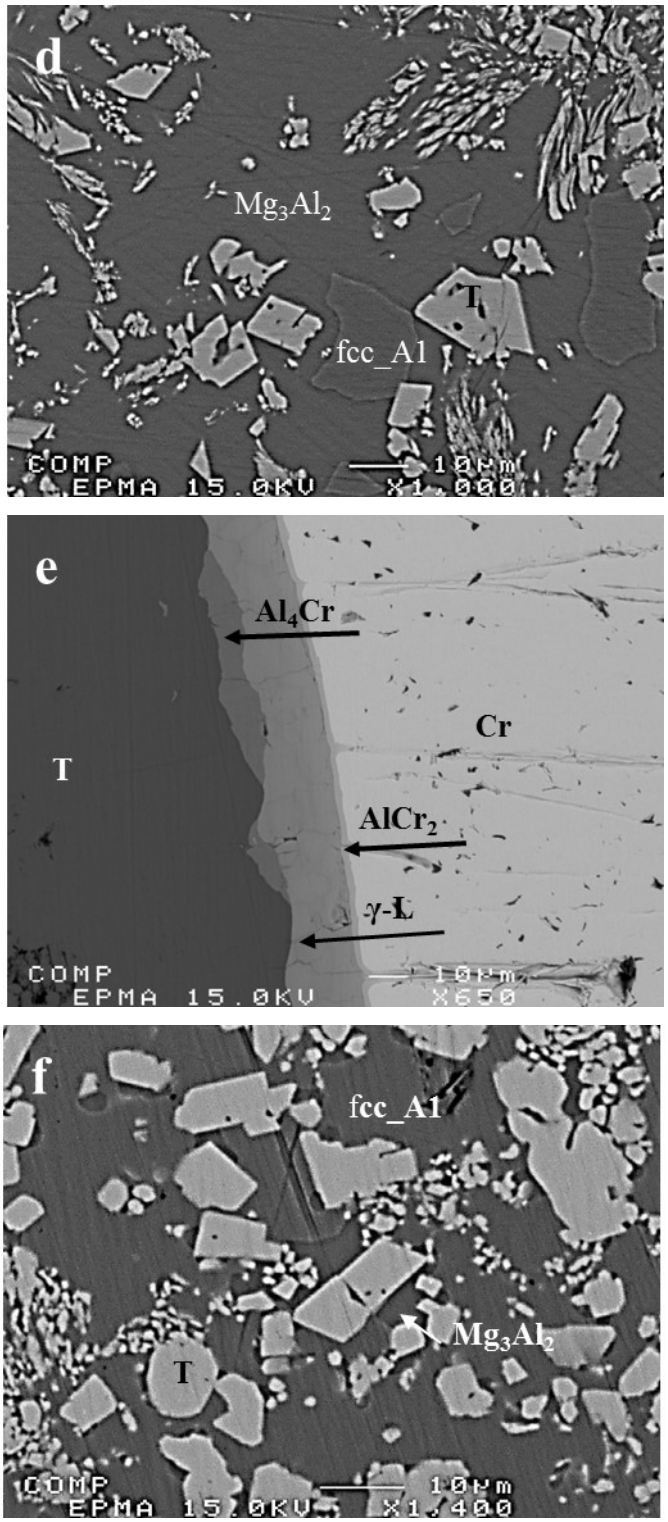

Fig. 4.9 Microstructures of diffusion couples annealed at 400 °C for 30 days. (a) and (b) SC1, (c) and (d) SC3, and (e) and (f) SC5.

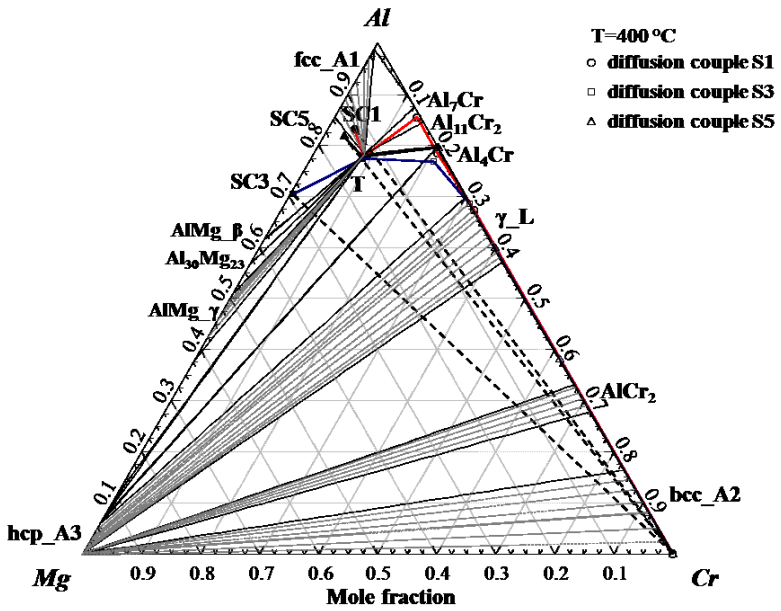

Fig. 4.10 The measured diffusion paths of diffusion couples SC1, SC3, and SC5 at 400 °C along with the calculated phase diagram in the present study.

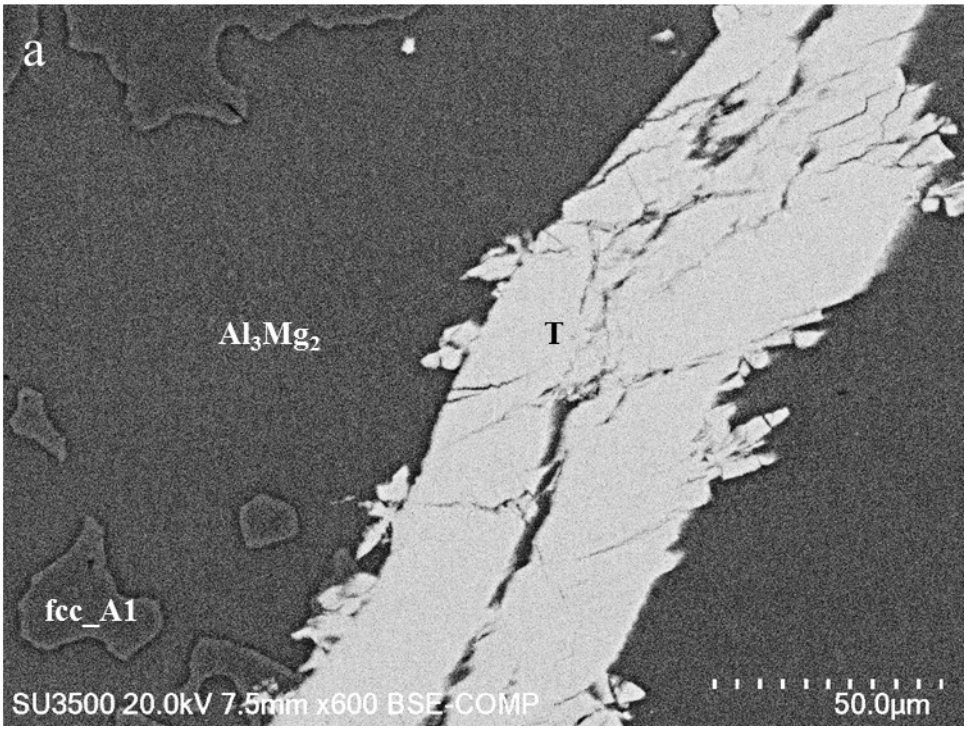
a
Al_3Mg_2
T
fcc_A1
SU3500 20.0kV 7.5mm x600 BSE-COMP
50.0μm

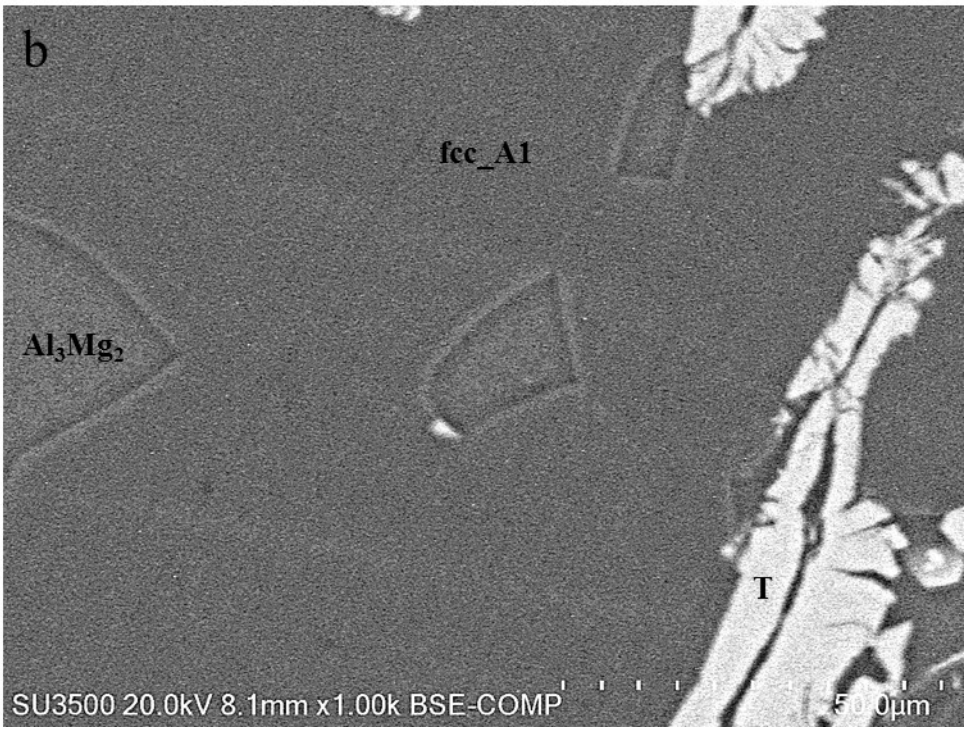
b
fcc_A1
Al_3Mg_2
T
SU3500 20.0kV 8.1mm x1.00k BSE-COMP

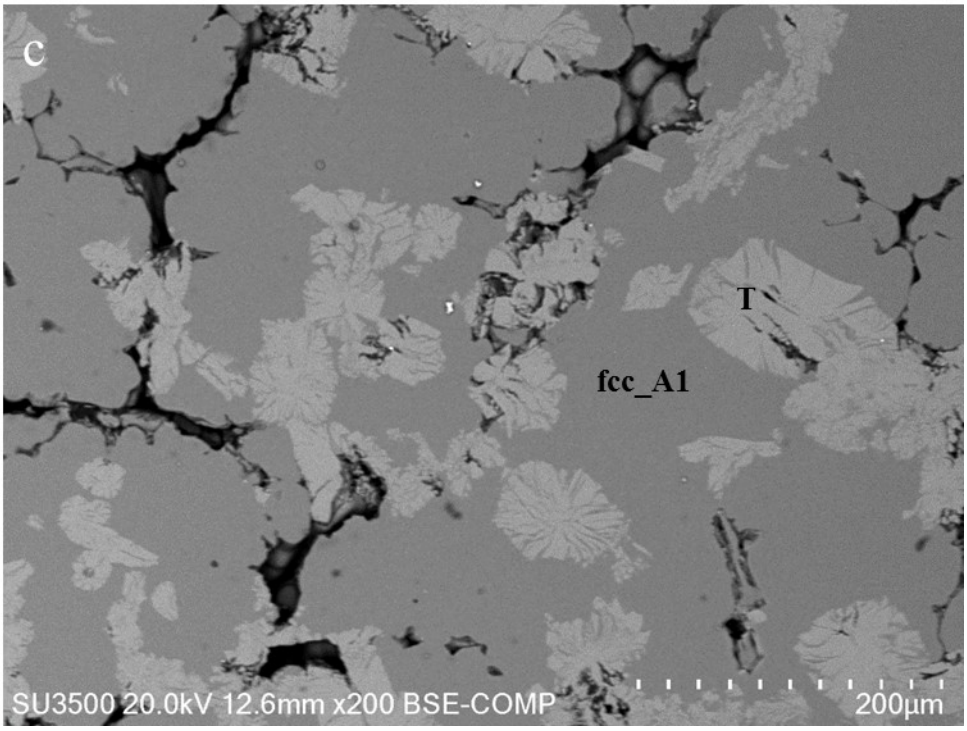
c
T
fcc_A1
SU3500 20.0kV 12.6mm x200 BSE-COMP
200µm

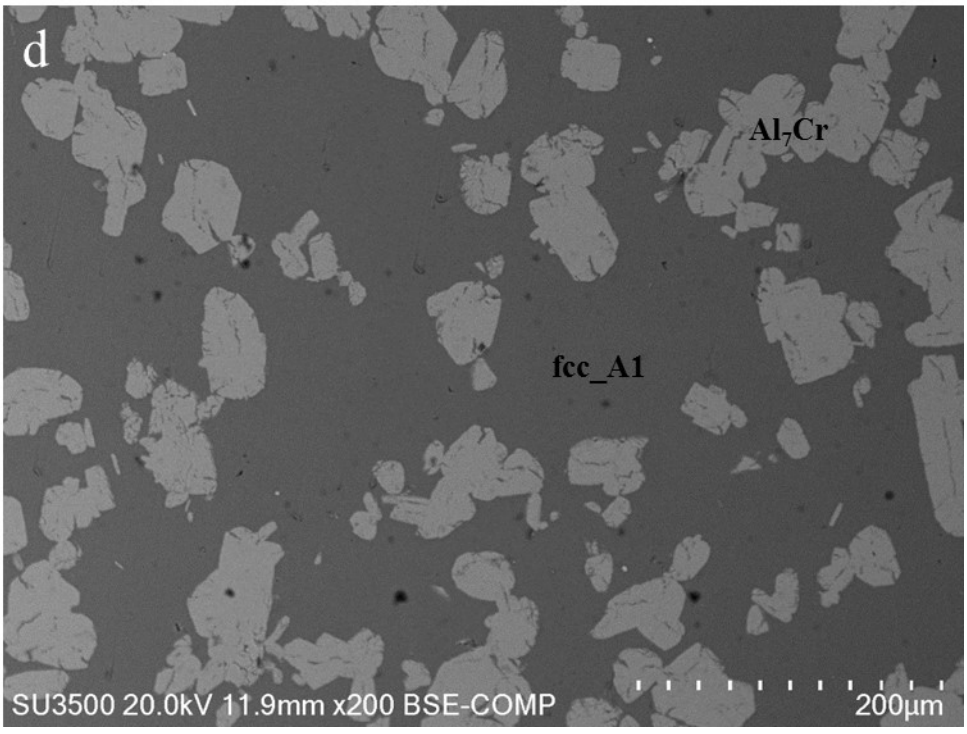
d
Al7Cr
fcc_A1
SU3500 20.0kV 11.9mm x200 BSE-COMP
200µm

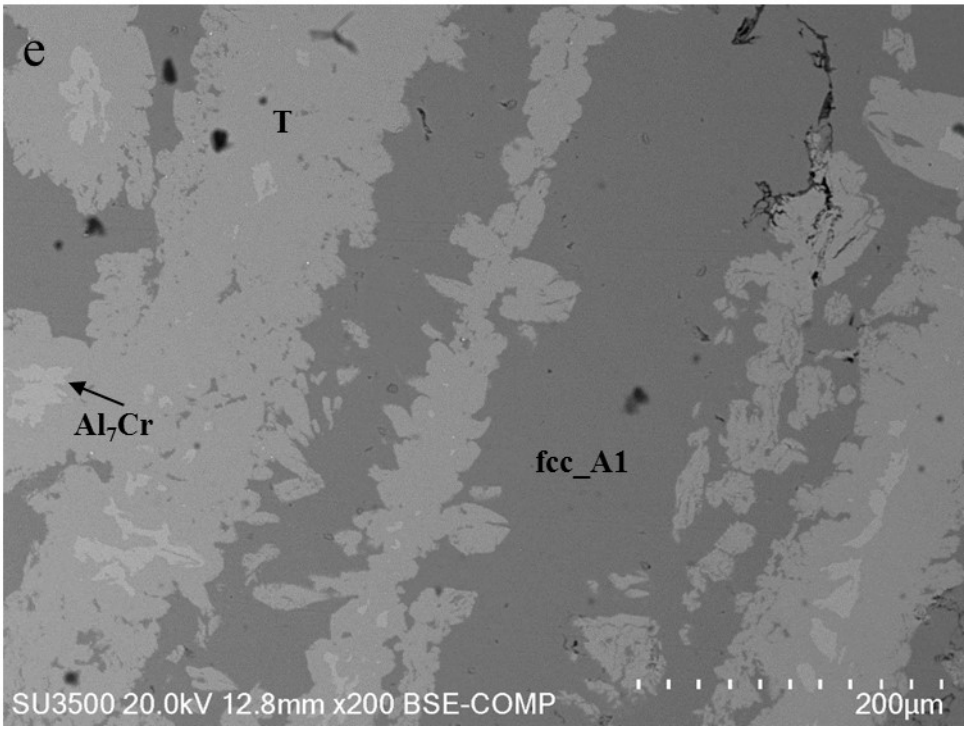

Fig. 4.11 Microstructures of different alloys annealed at 450 °C for 25 days. (a) Alloy sample T0, (b) T2, (c) T3, (d) T4, and (e) T5.

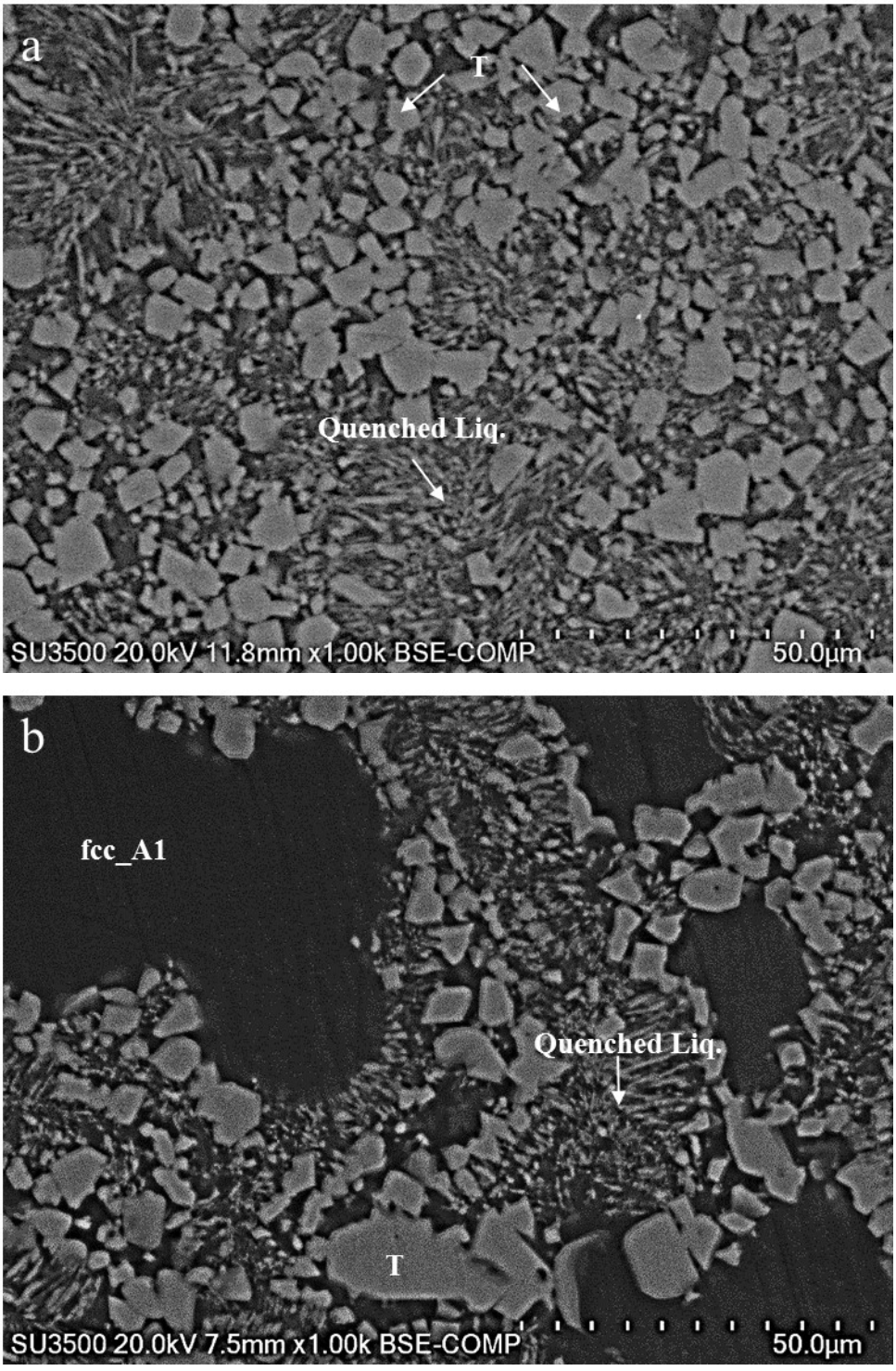

Fig. 4.12 The quenched microstructures of the alloys (a) qA and (b) qB annealed at 500 °C for 31 hours.

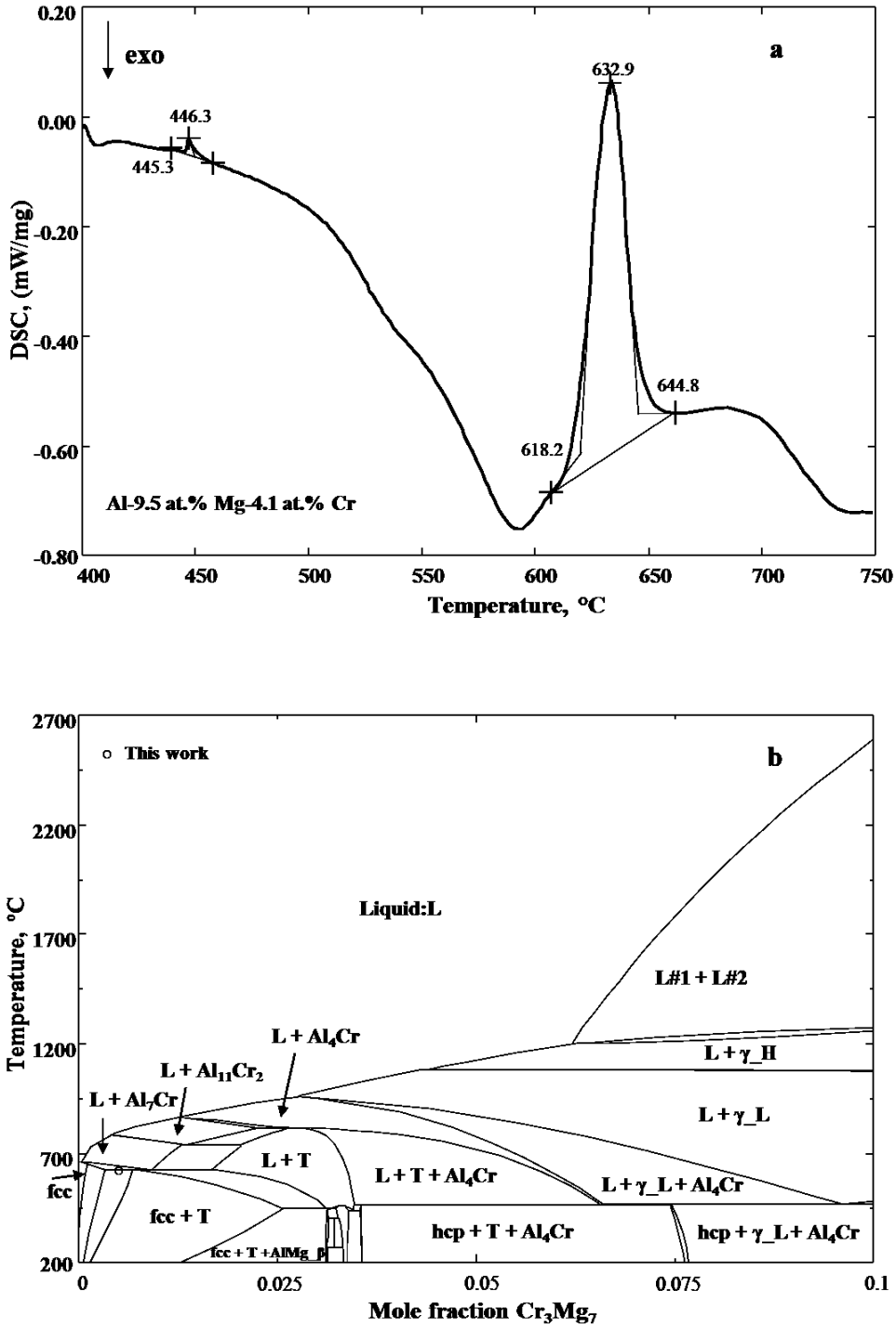

Fig. 4.13 (a) The measured DSC profile of alloy sample with a nominal composition Al-9.5 at.% Mg-4.1 at.% Cr. (b) Calculated isopleth of Al-Cr_3Mg_7 along with the measured experimental data from DSC analysis in (a).

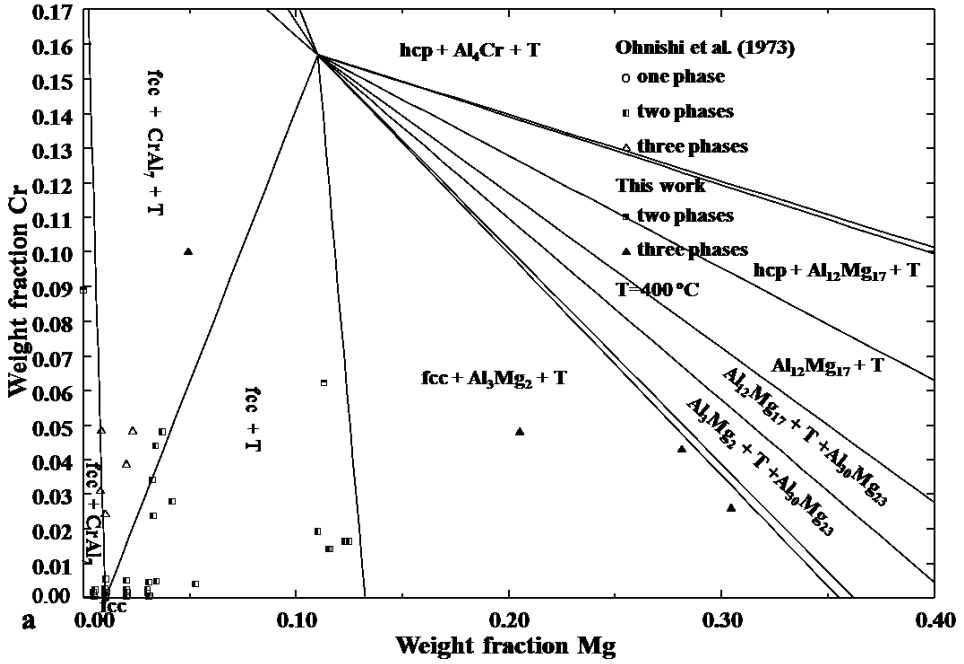
Weight fraction Cr
Weight fraction Mg
a
hcp + Al4Cr + T
Ohnishi et al. (1973)
one phase
two phases
three phases
This work
two phases
three phases
T=400 °C
fcc + CrAl7 + T
fcc + T
fcc + Al3Mg2 + T
hcp + Al12Mg17 + T
Al12Mg17 + T
Al12Mg17 + T +Al30Mg23
Al3Mg2 + T +Al30Mg23
fcc + CrAl7
fcc

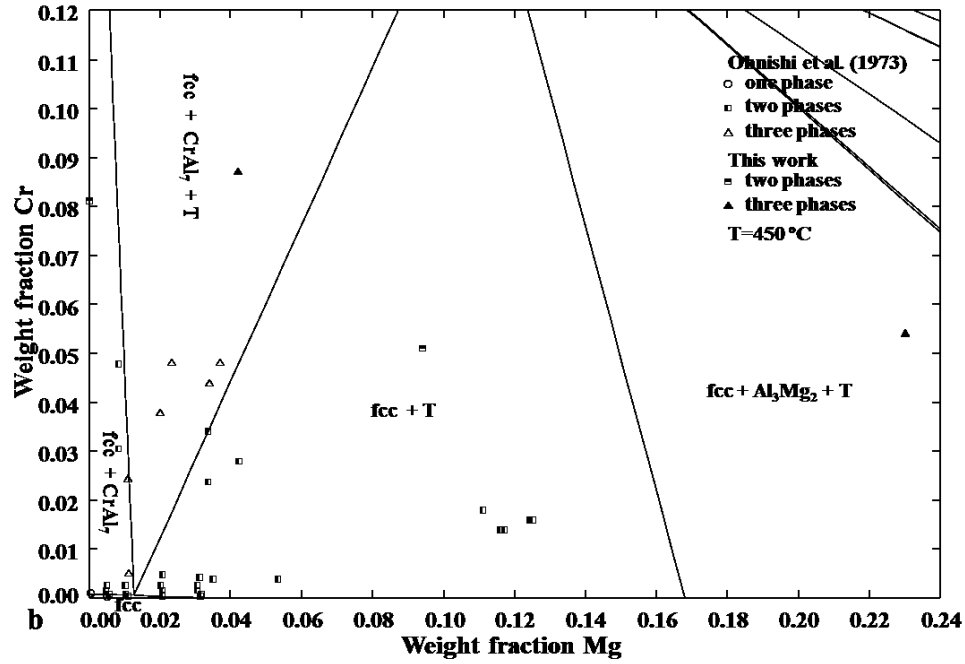
Weight fraction Cr
Weight fraction Mg
b
Ohnishi et al. (1973)
one phase
two phases
three phases
This work
two phases
three phases
T=450 °C
fcc + CrAl7 + T
fcc + T
fcc + Al3Mg2 + T
fcc + CrAl7
fcc

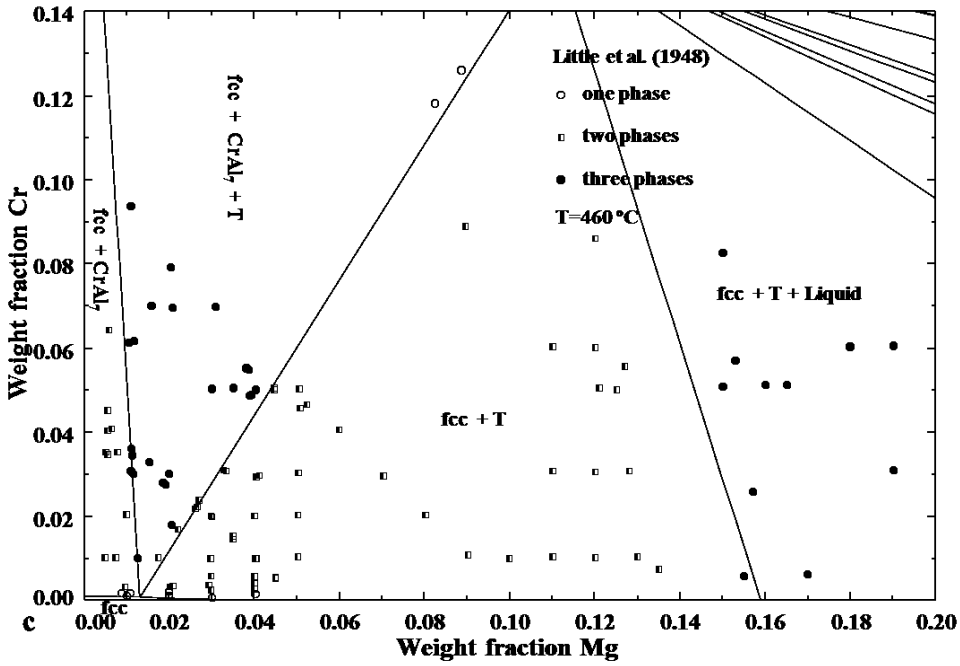
Little et al. (1948)
one phase
two phases
three phases
T=460 °C
fcc + CrAl7 + T
fcc + CrAl7
fcc + T
fcc + T + Liquid
fcc
Weight fraction Cr
Weight fraction Mg
c

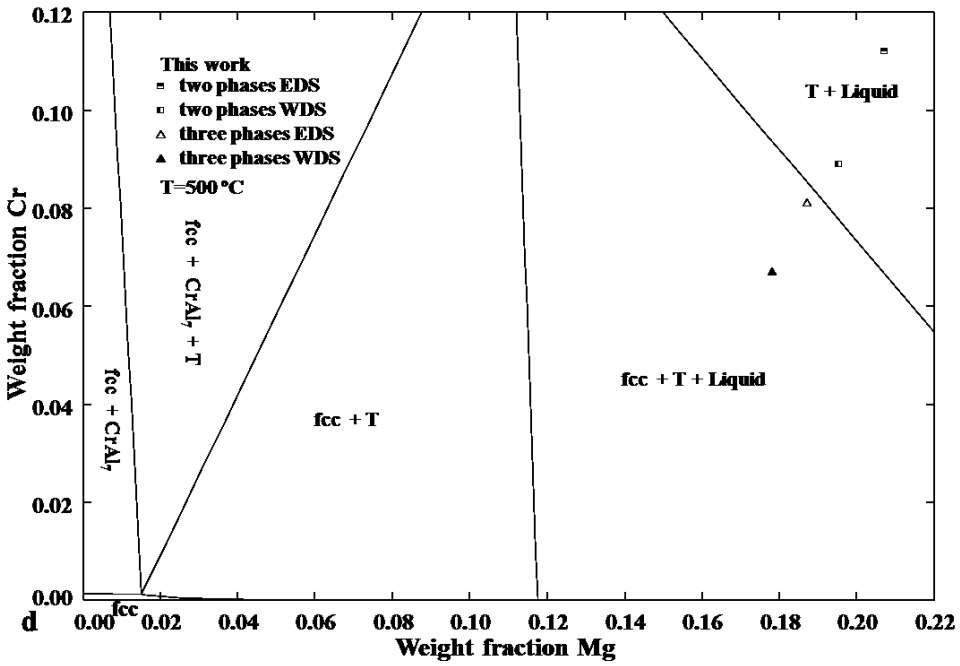
This work
two phases EDS
two phases WDS
three phases EDS
three phases WDS
T=500 °C
fcc + CrAl7 + T
fcc + CrAl7
fcc + T
fcc + T + Liquid
T + Liquid
fcc
Weight fraction Cr
Weight fraction Mg
d

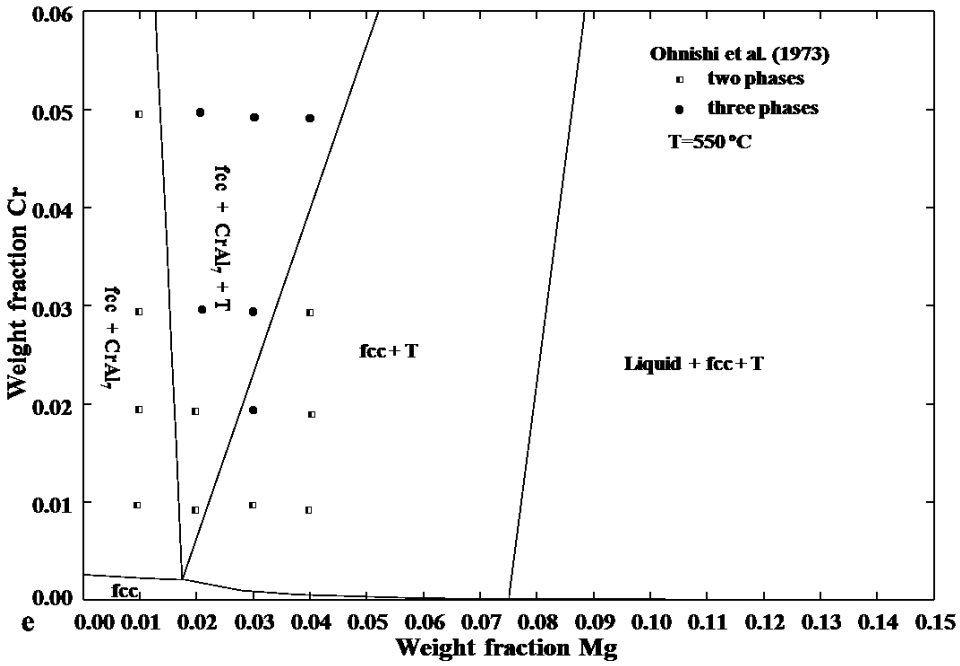

Fig. 4.14 Calculated isothermal sections in the Al rich part of the Al-Cr-Mg system in comparison to the experimental data at (a) 400 °C, (b) 450 °C, (c) 460 °C, (d) 500 °C, and (e) 550 °C.

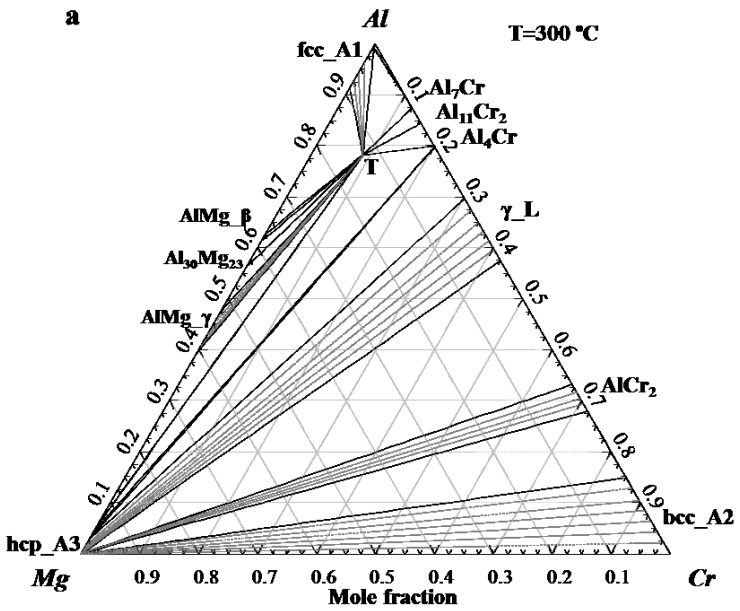
a
Al
T=300 °C
fcc_A1
Al7Cr
Al11Cr2
Al4Cr
T
γ_L
AlMg_β
Al30Mg23
AlMg_γ
AlCr2
bcc_A2
hcp_A3
Mg
Cr
0.9 0.8 0.7 0.6 0.5 0.4 0.3 0.2 0.1
Mole fraction

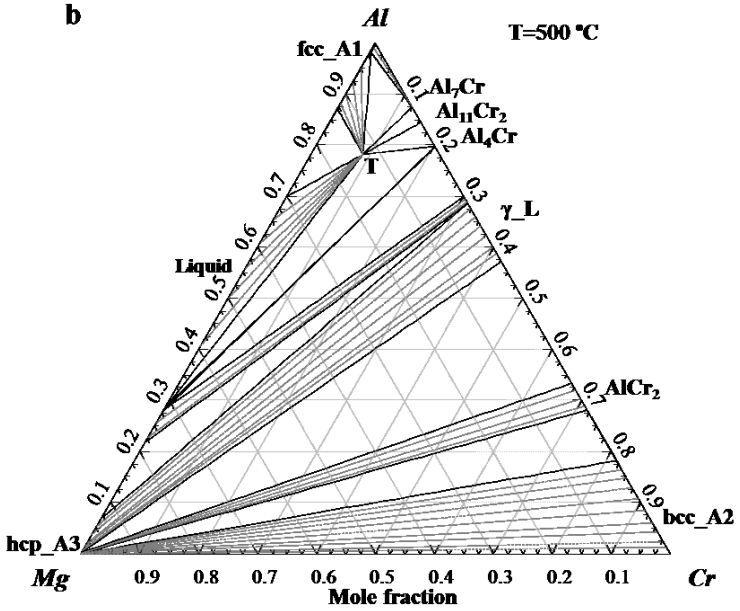
b
Al
T=500 °C
fcc_A1
Al7Cr
Al11Cr2
Al4Cr
T
γ_L
Liquid
AlCr2
bcc_A2
hcp_A3
Mg
Cr
0.9 0.8 0.7 0.6 0.5 0.4 0.3 0.2 0.1
Mole fraction

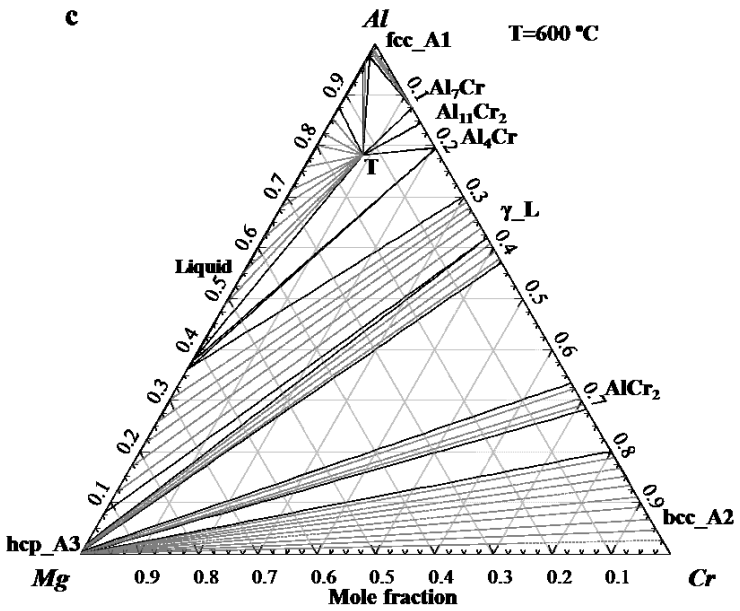
c
Al
fcc_A1
T=600 °C
Al7Cr
Al11Cr2
Al4Cr
T
γ_L
Liquid
AlCr2
bcc_A2
hcp_A3
Mg
Cr
0.9 0.8 0.7 0.6 0.5 0.4 0.3 0.2 0.1
Mole fraction

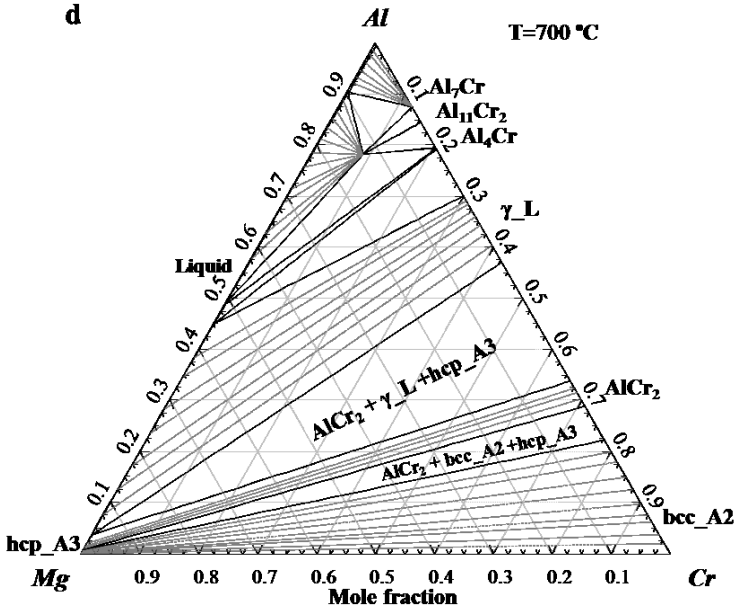
d
Al
T=700 °C
Al7Cr
Al11Cr2
Al4Cr
γ_L
Liquid
AlCr2 + γ_L +hcp_A3
AlCr2 + bcc_A2 +hcp_A3
AlCr2
bcc_A2
hcp_A3
Mg
Cr
0.9 0.8 0.7 0.6 0.5 0.4 0.3 0.2 0.1
Mole fraction

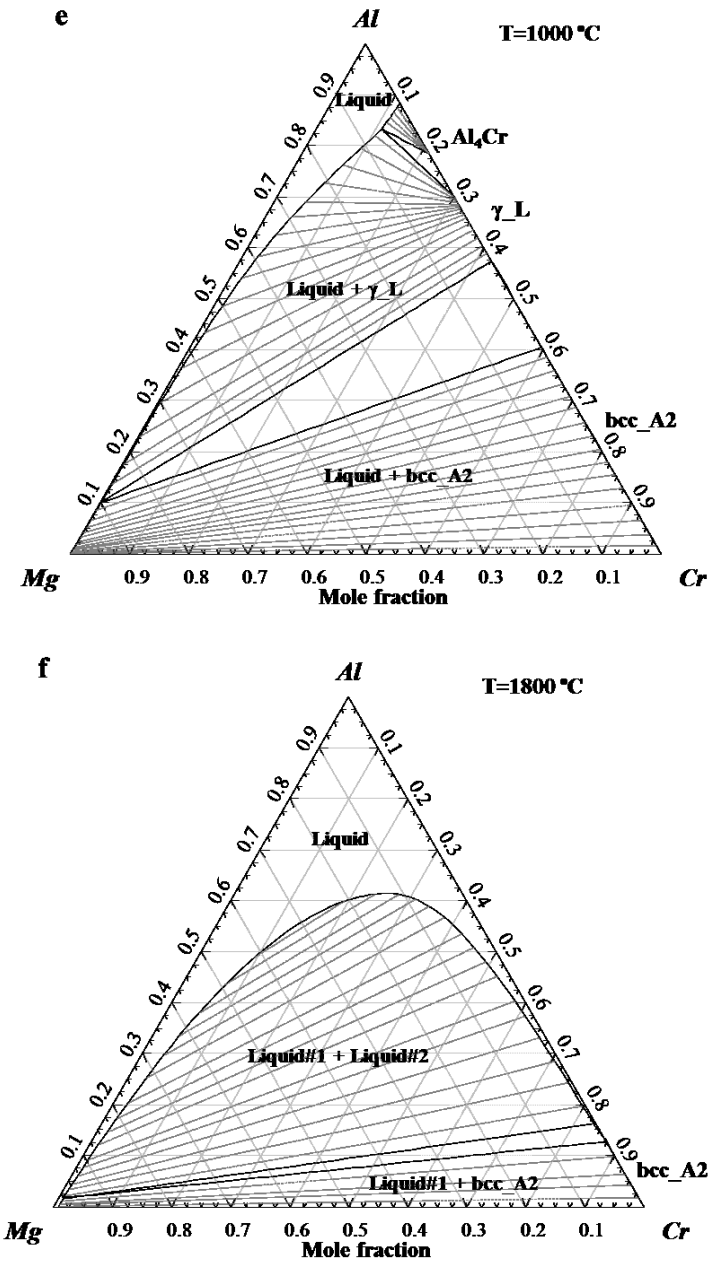

Fig. 4.15 Predicted isothermal sections from 300 to 1800 ºC in the Al-Cr-Mg system from the present thermodynamic assessment.

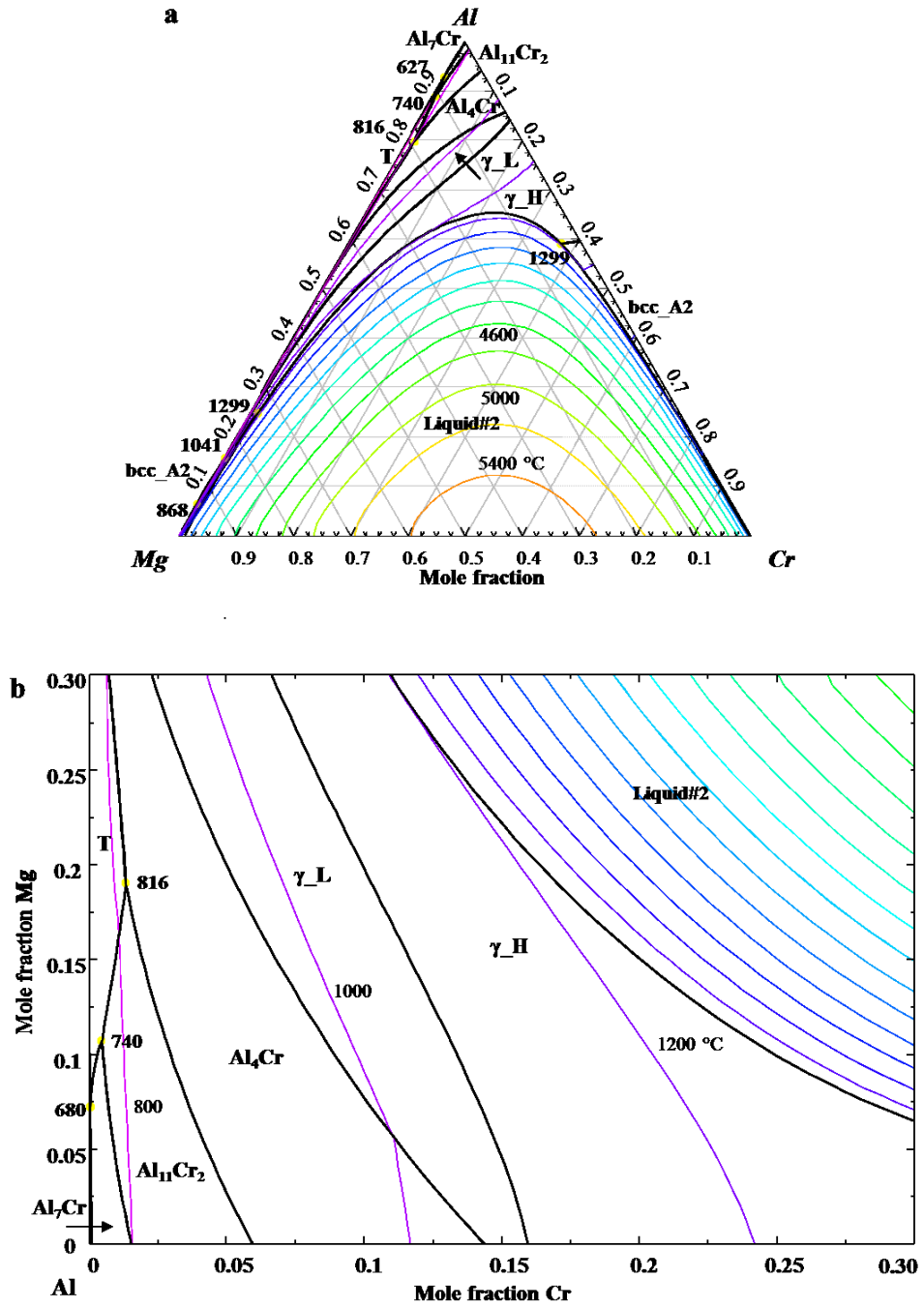

Fig. 4.16 Predicted liquidus projection of the Al-Cr-Mg system. (a) Entire composition range, and (b) enlarged diagram in the Al rich region.

Chapter 5 Thermodynamic modeling of the Al-Cr-Mn ternary system

(Submitted to Metallurgical and Materials Transactions A)

Senlin Cui and In-Ho Jung

Department of Mining and Materials Engineering, McGill University, 3610 University Street, Montreal, Quebec, H3A 0C5, Canada

Abstract

The phase diagram information available in the literature on the Al-Cr-Mn system was comprehensively evaluated and optimized for the first time to obtain a set of Gibbs energies of all the solid and liquid phases in the Al-Cr-Mn system. The Modified Quasi-chemical Model (MQM) was utilized to describe the Gibbs energy of the liquid phase of the Al-Cr-Mn system. The Compound Energy Formalism (CEF) was used to model the solid solution phases. A revision of the Al-Mn system was simultaneously conducted to consider the γ_H (Al_8Mn_5) phase. The liquid Cr-Mn phase was also remodeled using the Modified Quasi-chemical Model (MQM) to obtain a consistent description of the ternary Al-Cr-Mn liquid phase. Accurate description of the phase diagram of the entire Al-Cr-Mn system was obtained from the thermodynamic models with optimized parameters in the present study, and the model parameters were used to predict the thermodynamic properties of the ternary system.

Key words:

Al-Mn system; Cr-Mn system; Al-Cr-Mn system; phase diagram; thermodynamic modeling.

5.1 Introduction

Aluminum alloy is commonly used as extrusion material for structural applications in automotive and aerospace industry. The extrusion behavior of Al alloy is related to its composition and a series of microstructural evolutions throughout the whole chain of material processing from casting, homogenization, to extrusion. The final mechanical properties of Al alloy are also highly dependent on the chemistry and microstructure. Thus, it is necessary to study the relationship between alloy composition, microstructure, extrudability, and mechanical properties. It is known that Mn and/or Cr are added into Al alloys as dispersoid formers [1]. Different types of precipitates containing Mn and/or Cr like $Al_{11}(Mn, Cr)_4$, $Al_6(Mn, Cr)$, $Al_7(Cr, Mn)$ [2] can form during high temperature annealing which have limited direct effect on the mechanical properties. However, these phases have strong influence to the recovery, recrystallization, and grain growth processes, and therefore they are normally used for grain refinement. The formation of different types of Mn and Cr containing dispersoid is governed by the relative thermodynamic stability of each phase and the diffusion kinetics of elements behind. As a fundamental part, it is necessary to study the thermodynamic properties of Al alloys. Therefore, accurate thermodynamic information of alloy is the key fundamental knowledge for alloy design and its process optimization. As a part of a large research program to develop new high strength Al alloy for automotive application. The present authors are developing a comprehensive new Al alloy database especially focusing on the inclusion of Cr in conventional Al alloy chemistry. In the present study, the thermodynamic modeling results of the Al-Cr-Mn system are presented.

There are three sub-binaries in the Al-Cr-Mn system. The thermodynamic descriptions of the three binaries are the requisite for the thermodynamic modeling of the Al-Cr-Mn system. Thermodynamic modeling of the Al-Mn system was previously carried out by Jansson [3], Liu et al. [4], and Du et al. [5] using the Bragg-Williams random mixing model for the liquid phase, by Shukla and Pelton [6] and Asgar-Khan and Medraj [7] using the Modified Quasi-chemical Model (MQM) for the liquid phase. Recently, Kim and Kang [8] revised the thermodynamic description of the Al-Mn binary obtained by Du et al. [5] using MQM for the liquid phase. However, the thermodynamic description of the γ_H (Al_8Mn_5) phase was not included. The crystal structure of the γ_H phase was recently reported by Grushko et al. [9] to be the same as that (Al_8Cr_5) in binary

Al-Cr system and forms a continuous solid solution at high temperature. In order to model this new feature, it is necessary to add the thermodynamic description of the γ_H phase in the Al-Mn binary system on the basis of the previous work by Kim and Kang [8] and Du et al. [5]. On the other hand, the Cr-Mn system was previously reviewed by Venkatraman and Neumann [10] and assessed by Lee [11]. After the thermodynamic modeling conducted by Lee [11], there are no new phase equilibria data or thermodynamic data reported in the literature. The Al-Cr system was recently reassessed by the present authors [12]. The Al rich region of the ternary Al-Cr-Mn system was previously optimized by Jiang et al. [13]. However, the sub-binary systems are different from the Al alloy database developed in the present study. They also considered only the recent experiment data by Grushko et al. [9] in their optimization for only the Al rich region (above 60 at.% of Al). That is, there is no comprehensive thermodynamic modeling of the Al-Cr-Mn system covering the entire composition range. Therefore, more comprehensive evaluation of all the available experimental data and a thermodynamic reassessment for this ternary system is necessary.

In the present thermodynamic modeling, the liquid phase is described using MQM and the solid solution phases are described by the Compound Energy Formalism (CEF). In particular, the present work will focus on (1) the revision of the binary Al-Mn system including the thermodynamic description of the γ_H phase, (2) the revision of the binary Cr-Mn system by modeling the binary liquid phase using MQM, and (3) the thermodynamic modeling of the ternary Al-Cr-Mn system.

5.2 Critical evaluation of literature information

5.2.1 The Al-Mn system

In the present study, the previous optimization of the Al-Mn system by Kim and Kang [8] was revised to take into account the γ_H phase. Thus, only the phase equilibria data related to the γ_L and γ_H phases are reviewed here. Kono [14] investigated the Al-Mn phase diagram in the composition range from 47 to 60 at.% Mn by thermal analysis, X-ray diffraction (XRD), and optical microscopic analysis. Koch et al. [15] measured the phase equilibria in the composition range between 40 wt.% and 100 wt.% Mn by thermal analysis and XRD phase analysis. Köster

and Watchtel [16] measured the phase transformations related to the γ_L and γ_H phases by magnetic analysis and susceptibility measurements. Later, Gödecke and Köster [17] measured the phase relation from 10 at.% Mn to 45 at.% Mn with the aid of differential thermal analysis (DTA) and quenched equilibrium alloys coupled with microstructural analysis. Robinson et al. [18] measured the phase transition temperature at 30 at.% Mn by DTA. All these phase diagram experimental data are used in the present optimization to model the Gibbs energy of the γ_L and γ_H phases.

5.2.2 The Cr-Mn system

Lee [11] previoiusly conducted a thermodynamic assessment of the Cr-Mn system using all the available phase diagram information in the literature, so it is unnecessary to perform completely new optimization. In the present study, all the thermodynamic description of the solid phases from Lee [11] are used without any modification. Only the liquid phase is optimized using MQM in this study. Therefore, only the phase equilibria information related to the liquid phase was reviewed here. Carlile et al. [19] measured the solid/liquid phase equilibria in the entire composition range of the Cr-Mn system using the thermal analysis technique. Greenaway et al. [20] studied the liquidus curve in the Cr-Mn system from 0 to 60 at.% Mn using thermal analysis. Hellawell and Hume-Rothery [21] also measured the solid/liquid phase equilibria in the Cr rich side (from pure Mn up to 15 at.% Cr) using a thermal analysis method. These experimental data were utilized to re-optimize the Gibbs energy of the liquid phase of the binary system.

5.2.3 The Al-Cr-Mn system

The Al-Cr-Mn system was previously evaluated by Villars et al. [22] for the experimental data up to 1972. Later, Raghavan [23] updated the ternary phase diagram by considering the experimental work by Schenk et al. [24]. A recent update by Raghavan [25] also included the new experimental results from Grushko et al. [9] and Balanetskyy et al. [26]. A more detailed review about the Al-Cr-Mn system is given below.

Raynor and Little [27] measured the phase relations from Al to 6 wt.% Mn and 6 wt.% Cr at 400, 500, 550, 580, and 600 °C by microanalysis, XRD, and thermal analysis. The fcc_A1 primary solid solution, Al_6Mn, ternary compound G ($Al_{12}Mn$), and the ternary extension of the Al_7Cr phase were observed. In addition, a vertical section at 95 wt.% Al was also presented. Later, Clare [28] measured the phase equilibrium at 550 °C in the Al rich Al-Cr-Mn system contain 0 to 15 wt.% Cr and 0 to 20 wt.% Mn by equilibrium alloy followed by microanalysis and XRD. The G phase previously reported by Raynor and Little [27] was found to be stable only below 590 °C. Wachtel and Kopp [29] investigated the phase constitution of the Al-Cr-Mn system at 25 to 60 at.% Al by thermal analysis, magnetic measurements, quenched equilibrium alloy followed by metallography, XRD, and micro-hardness phase analysis. Three isothermal sections (1070, 970, and 780 °C) and isopleths (10 at.% Cr and 33.3 at.% Al) were measured. The liquidus projection of the ternary system was proposed. According to their experimental results, there are continuous solid solutions between the bcc_A2, γ_H, and γ_L phases of the Al-Cr and Al-Mn systems. At the meantime, Wachtel and Rein [30] studied the phase diagram of the Mn rich region of the Al-Cr-Mn system using metallography, thermal analysis, magneto-thermal analysis, and XRD. Isothermal sections of the Mn rich region at 840, 950, and 1050 °C and isopleth sections at 2.5 at.% Al and 20 at.% Cr were presented. Later, Ohnishi et al. [31] determined the phase relations of the Al-Mn-Cr system in the Al rich corner at 600, 580, 550, and 500 °C using quenching experiments followed by microanalysis and XRD phase determination. The G phase was determined to be of bcc structure with a composition of Al_{12}(Mn, Cr) and stable below 590 °C. Subsequently, Schenk et al. [24] studied the liquid-solid equilibria in the subsection Al_4Cr-Al_4Mn-Al using DTA and quenching experiments followed by scanning electron microanalysis (SEM) and transmission electron microanalysis (TEM). Recently, Grushko et al. [9] measured the Al-Cr-Mn phase diagram in the composition range of 60 to 100 at.% Al at 560 to 1010 °C. Partial phase diagrams at 1010, 950, 900, 800, 715, 685, 661, 600, and 560 °C were determined using DTA, and quenched equilibrium alloy followed by powder XRD, SEM, and TEM measurements. The G phase was re-confirmed to be a ternary extension of the $Al_{12}Mn$ phase. The wide extensions of Al_7Cr, $Al_{11}Cr_2$, Al_6Mn, Al_4Mn, and Al_3Mn ($Al_{29}Mn_{10}$) to the ternary by the replacement of Cr with Mn were measured. And the $Al_{11}Mn_4$, γ_L, and γ_H phases also form continuous solid solutions. Balanetskyy et al. [26] used the same experimental techniques as Grushko et al. [9] to determine the liquidus and solidus surfaces of the Al-Cr-Mn system at 60 to 100 at.% Al. Seven ternary

reactions involving the liquid phase were detected. Besides, three solid state four-phase equilibria were reported.

The early experimental data of Raynor and Little [27] which are only limited to a very narrow composition range. The experimental data measured by Clare [28], Ohnishi et al. [31], Schenk et al. [24], Grushko et al. [9], and Balanetskyy et al. [26] are considered as reliable data and are utilized in the current optimization since they are all consistent with each other in the Al rich corner. The binary phase diagrams used by Wachtel and Kopp [29] and Wachtel and Rein [30] are different from the generally accepted ones. The reported liquidus projection by Wachtel and Kopp [29] is quite different from that by Balanetskyy et al. [26] in particular in the region related to γ_H. Consequently, the experimental data from Wachtel and Kopp [29] and Wachtel and Rein [30] are only used for the phase relation in the Cr and Mn rich regions.

5.3 Thermodynamic modeling

5.3.1 Liquid phase

The Gibbs energy of liquid Al-Cr-Mn phase is described using MQM in pair approximation, proposed by Pelton et al. [32, 33]. MQM can more successfully describe both liquid ionic solutions [34] or liquid metallic solution [35] especially showing strong short range ordering in the liquid state than Bragg-Williams (BW) random mixing model. Assume the atoms A and B in an A-B binary system occupy a quasi-lattice in the liquid solution, then the pair exchange reaction can be written as:

$$(A\text{-}A) + (B\text{-}B) = 2(A\text{-}B) : \quad \Delta g_{AB} \tag{5.1}$$

where (*A*-*A*), (*B*-*B*), and (*A*-*B*) represent the first-nearest-neighbor atom pairs. Δg_{AB} is the non-configurational Gibbs energy change for the formation of two moles of (*A*-*B*) pairs. The Gibbs energy of a binary solution is then written as:

$$G = n_A G_A^o + n_B G_B^o - T\Delta S^{config} + (n_{AB}/2)\Delta g_{AB} \tag{5.2}$$

where n_i is the number of moles of *i* atoms, and n_{AB} is the number of moles of (*A*-*B*) pairs. ΔS^{config} is the configurational entropy of mixing given by a random distribution of the three types of pairs (*A*-*A*, *B*-*B*, and *A*-*B*) in the one-dimensional Ising approximation:

$$\Delta S^{config} = -R(n_A \ln x_A + n_B \ln x_B) - R\left[n_{AA} \ln\left(\frac{x_{AA}}{Y_A^2}\right) + n_{BB} \ln\left(\frac{x_{BB}}{Y_B^2}\right) + n_{AB} \ln\left(\frac{x_{AB}}{2Y_A Y_B}\right)\right] \tag{5.3}$$

where x_i is the mole fraction of *i* atoms, x_{ij} is the pair fraction, and Y_i is the coordination equivalent fraction. Let Z_i be the coordination number of *i* given by $Z_i n_i = 2n_{ii} + \sum_{A \neq B} n_{AB}$ (*B*>*A*) and which is 6 in the present study. Then, x_i, x_{ij}, and Y_i are given by definition as:

$$x_i = n_i/(n_A + n_B) \tag{5.4}$$

$$x_{ij} = n_{ij}/(n_{AA} + n_{BB} + n_{AB}) \tag{5.5}$$

$$Y_i = x_{ii} + \frac{1}{2}(x_{ij}) \tag{5.6}$$

here the excess Gibbs energy, Δg_{AB}, is expanded as a polynomial in terms of pair fractions and is given as:

$$\Delta g_{AB} = \Delta g_{AB}^0 + \sum_{i \geq 1} g_{AB}^{i0} (x_{AA})^i + \sum_{j \geq 1} g_{AB}^{0j} (x_{BB})^j \tag{5.7}$$

where Δg_{AB}^0, g_{AB}^{i0}, and g_{AB}^{0j} are the model parameters which can be a function of temperature.

Once the Gibbs energy of each binary liquid solution was successfully described, the Gibbs energy of ternary liquid solution can be predicted using the geometric extrapolation technique. If necessary, a few ternary correction term can be further introduced to more accurately describe the

Gibbs energy of the ternary liquid phase. Considering the thermodynamic properties of each sub-binary liquid phase, the Toop type of extrapolation technique [32, 33] is applied to the Al-Cr-Mn system with Al as an asymmetric component. The liquid solutions of Al-Cr and Al-Mn are very negatively deviated from idea solution behavior, while the liquid Cr-Mn is close to an ideal solution. The Gibbs energy of ternary a liquid A-B-C solution can be expressed as follows:

$$G = n_A G_A^o + n_B G_B^o + n_C G_C^o - T\Delta S^{config} + (n_{AB}/2)\Delta g_{AB} + (n_{AC}/2)\Delta g_{AC} + (n_{BC}/2)\Delta g_{BC} \quad (5.8)$$

where each pair formation energy term can be extrapolated as [32, 33]:

$$\Delta g_{AB} = \Delta g_{AB}^0 + \sum_{(i+j)\geq 1} g_{AB}^{ij} x_{AA}^i (x_{BB} + x_{BC} + x_{CC})^j$$

$$+ \sum_{\substack{i\geq 0 \\ j\geq 0 \\ k\geq 1}} g_{AB(C)}^{ijk} x_{AA}^i (x_{BB} + x_{BC} + x_{CC})^j \left(\frac{Y_C}{Y_B + Y_C}\right)^k \quad (5.9)$$

and

$$\Delta g_{BC} = \Delta g_{BC}^0 + \sum_{(i+j)\geq 1} g_{BC}^{ij} \left(\frac{x_{BB}}{x_{BB} + x_{CC} + x_{BC}}\right)^i \left(\frac{x_{CC}}{x_{BB} + x_{CC} + x_{BC}}\right)^j$$

$$+ \sum_{\substack{i\geq 0 \\ j\geq 0 \\ k\geq 0}} g_{BC(A)}^{ijk} \left(\frac{x_{BB}}{x_{BB} + x_{CC} + x_{BC}}\right)^i \left(\frac{x_{CC}}{x_{BB} + x_{CC} + x_{BC}}\right)^j Y_A^k \quad (5.10)$$

where A is Al, asymmetric component in the ternary solution, and B and C are Cr and Mn, symmetric components, respectively. The ternary parameters, $g_{AB(C)}^{ijk}$ and $g_{BC(A)}^{ijk}$, can be also added to make more accurate description of the Gibbs energy of the liquid solution.

5.3.2 Solid solutions

The Gibbs energy of the solid solution phases are described using the well-known Compound Energy Formulism (CEF) [36]. Fcc_A1, bcc_A2, hcp_A3, cub_A13, and cbcc_A12 are considered as one sub-lattice solution of (Al, Cr, Mn). The γ_L phase forms continuous solid solution from the Al-Cr to the Al-Mn system. The sub-lattice structure of $(Al)_{12}(Cr, Mn)_5(Al, Cr, Mn)_9$ is accepted for this phase. Similarly, $(Al, Cr, Mn)_2(Al, Cr, Mn)_3(Cr, Mn)_2(Al)_6$ is used for the γ_H phase. A sub-lattice structure of $(Al, Cr, Mn)(Al, Cr, Mn)_2$ is used to take into account the considerable solubility of Mn in the $AlCr_2$ phase. The Al_4Cr and Al_4Mn phases form a continuous solid solution of $(Al, Va)_4(Cr, Mn)$ named as Al_4Cr. Similarly, the extension of binary $Al_{29}Mn_{10}$, $Al_{11}Cr_2$, $Al_{11}Cr_4$, Al_7Cr, $Al_{99}Mn_{23}$, Al_6Mn, $Al_{12}Mn$, σ_L, and σ_H to the ternary system are modeled by considering the sub-lattice structures of $(Al, Cr, Mn)_{29}(Cr, Mn)_{10}$, $Al_{11}(Mn, Cr)_2$, $Al_{11}(Mn, Cr)_4$, $Al_7(Cr, Mn)$, $Al_{99}(Mn, Cr)_{23}$, $Al_6(Mn, Cr)$, $Al_{12}(Mn, Cr)$, $(Mn)_8(Cr)_4(Al, Mn, Cr)_{18}$, and $(Mn)_8(Cr)_4(Al, Mn, Cr)_{18}$, respectively.

As an example, the molar Gibbs energy of the γ_H phase using CEF expressed as:

$$
\begin{aligned}
{}^{o}G_m^{\gamma\_H} &= \sum_{i=1}\sum_{j=1}\sum_{k=1} y_i^{'} y_j^{''} y_k^{'''} y_{Al}^{''''}\, {}^{o}G_{i:j:k:Al}^{\gamma\_H} + 2RT\sum_{i=1} y_i^{'} \ln y_i^{'} + 3RT\sum_{i=1} y_i^{''} \ln y_i^{''} \\
&+ 2RT\sum_{i=1} y_i^{'''} \ln y_i^{'''} + \sum_{i=1}\sum_{j>i}\sum_{k=1}\sum_{m=1} y_i^{'} y_j^{'} y_k^{''} y_m^{'''} \sum_{v=0} (y_i^{'} - y_j^{'})^v L_{ij:k:m:Al}^v \\
&+ \sum_{i=1}\sum_{j>i}\sum_{k=1}\sum_{m=1} y_i^{''} y_j^{''} y_k^{'} y_m^{'''} \sum_{v=0} (y_i^{''} - y_j^{''})^v L_{k:ij:m:Al}^v \\
&+ \sum_{i=1}\sum_{j>i}\sum_{k=1}\sum_{m=1} y_i^{'''} y_j^{'''} y_k^{'} y_m^{''} \sum_{v=0} (y_i^{'''} - y_j^{'''})^v L_{k:m:ij:Al}^v + \ldots
\end{aligned}
\tag{5.11}
$$

where $y_i^{'}$, $y_i^{''}$, $y_i^{'''}$, and $y_i^{''''}$ are the site fractions of element *i* in the first, second, third, and fourth sub-lattice, respectively. ${}^{o}G_{i:j:k:Al}^{\gamma\_H}$ is the molar Gibbs energy of the hypothetical compound $i_2j_3k_2Al_6$. $L_{ij:k:m:Al}^v$, $L_{k:ij:m:Al}^v$, and $L_{k:m:ij:Al}^v$ are the interaction parameters. The model parameters optimized in the present study are the Gibbs energy of hypothetical compound end member ${}^{o}G_{i:j:k:Al}^{\gamma\_H}$ and the interaction parameters (*L*).

5.3.3 Pure elements and stoichiometric compounds

The Gibbs energies of pure elements and stoichiometric compounds are expressed as a function of temperature using the following expression:

$$G_i^o(T) = \Delta H_{298.15}^o + \int_{298.15}^{T} C_P dT - T(S_{298.15}^o + \int_{298.15}^{T} \frac{C_P}{T} dT) \quad (5.12)$$

where $\Delta H_{298.15}^o$ and $S_{298.15}^o$ are the standard molar enthalpy and entropy of the element *i* at 298.15 K and 1 bar, and C_P is the heat capacity of *i*. G^{mag} is a term to take into account the effect of magnetic contribution to Gibbs energy and is given by the Hillert-Jarl-Inden model [37] as:

$$G^{mag} = RT\ln(\beta^{\varphi} + 1)g(\tau^{\varphi}) \quad (5.13)$$

where the τ is given by T/T^*; and T^* is the Curie temperature T_C for ferromagnetic materials or Neel temperature T_N for antiferromagnetic materials. β is the average magnetic moment per mole of atoms expressed in Bohr magnetons. $g(\tau^{\varphi})$ is a polynomial function derived by Hillert and Jarl [37]. In the present study, the Gibbs energy data for the pure elements are taken from the SGTE pure element database compiled by Dinsdale [38].

5.4 Results and discussions

Recently, the Al-Cr system was re-assessed by the present authors [12]. The calculated phase diagram is presented in Fig. 5.1. The model parameters of the Al-Cr system were used in the present study without any modification. The optimization of the thermodynamic parameters for the Al-Mn, Cr-Mn, and Al-Cr-Mn systems were carried out on the basis of the critically evaluated phase diagram information available in the literature reviewed in section 5.2. All the thermodynamic calculations were carried out using the FactSage software [39].

The γ_L phase in the binary Al-Mn system was firstly revised from the previous assessment by Du et al. [5] and Kim and Kang [8] and the γ_H phase was newly added in the binary description based on the available phase diagram experimental data. Thermodynamic description of all the other phases were taken from the previous studies [5, 8]. The liquid phase of the Cr-Mn system was re-modeled using MQM based on the experimental phase boundary related to the liquid phase. All the solid thermodynamic descriptions were taken from the assessment by Lee [11]. Then, a ternary optimization was conducted by combining the thermodynamic description of each binary system to reproduce the phase diagram data in the ternary system reviewed in section 5.2. The final optimized thermodynamic parameters for the Al-Cr-Mn ternary system are presented in Table 5.1. The optimization procedure and results are discussed below.

5.4.1 The Al-Mn system

The revised binary Al-Mn phase diagram from this study along with the available experiment data is presented in Fig. 5.2. During the present optimization process, the parameters of the γ_L phase were slightly modified to reproduce the invariant temperatures related to the γ_H and γ_L phases. The addition of the γ_H phase does not noticeably change the liquidus line. As can be seen in Fig. 5.2, a good agreement between the measured and the calculated phase diagram is achieved. The optimized peritectic temperature of liquid + bcc_A2 = γ_H is 1049 °C which is close to the evaluated value of 1048 °C by McAlister and Murray [40]. The peritectic temperature of liquid + γ_H = $Al_{29}Mn_{10}$ is 1004 °C which is only 2 degrees higher than the evaluated value [40]. The peritectiod reaction of $Al_{29}Mn_{10}$ + γ_H = γ_L happens at 958 °C instead of the eutectoid reaction of γ_H = γ_L + $Al_{29}Mn_{10}$ at 957 °C [40]. The optimized invariant temperature (991°C) for the bcc_A2 + γ_H = γ_L is the same as the evaluated one [40]. Al_4Mn and Al_4Cr form a continuous solid solution. As Al_4Cr is described with the $(Al, Va)_4Cr$ structure, the stoichiometric Al_4Mn was modified to be expressed as a solution of $(Al, Va)_4Mn$. There was no change of the invariant reactions related to Al_4Mn after the modification.

5.4.2 The Cr-Mn system

The calculated Cr-Mn phase diagram along with the measured experimental data related to the liquidus and solidus of the system is shown in Fig. 5.3. The previously assessed phase diagram (the dotted lines) from Lee [11] is also appended for comparison. It can be seen from Fig. 5.3 that the calculated liquidus and solidus of the Cr-Mn system from this study reproduce more accurately the experimental data from Hellawell and Hume-Rothery [21], Greenaway et al. [20], and Carlile et al. [19] than those assessed by Lee [11]. The calculated peritectic reaction temperature in this study are very close to those assessed by Lee [11]. The enthalpy of mixing of the liquid phase at 1900 °C is also compared with the result by Lee [11] in Fig. 5.4. As expected from the phase diagram, the liquid phase in this system would behave very close to an ideal solution. The present enthalpy of mixing is more close to ideal behavior. In total, five model parameters with two small temperature dependent terms were used for MQM to describe the Gibbs energy of the liquid Cr-Mn system.

5.4.3 The Al-Cr-Mn system

As there is no thermodynamic data available in the literature, all the thermodynamic parameters of the solid and liquid solutions were optimized from the available phase diagram information. A series of isothermal sections from 1070 °C to 500 °C are presented in Fig. 5.5. As can be seen in the isothermal sections, the bcc_A2, and cub_A13 phases have wide single phase regions in the low Al concentration region. The $AlCr_2$ phase has noticeably extension from the Al-Cr side, and the maximum solubility of Mn in $AlCr_2$ reaches about 0.3 mole fraction of Mn. The γ_H and γ_L solutions form complete solid solutions between the Al-Cr and Al-Mn system at high and low temperature, respectively. The Al_4Cr phase also forms a complete solid solution from the Al-Cr to Al-Mn side. Several other solutions such as $Al_{11}Mn_4$, $Al_{99}Mn_{23}$, $Al_{11}Cr_2$, Al_7Cr, and Al_6Mn also form significant solid solutions in this ternary system. The G phase which is an extension of $Al_{12}Mn$ appears below 590 °C. In General, all the phase diagram experimental data are reasonably well reproduced in the present optimization.

The stability regions of the γ_H and γ_L phases at 1070 °C and 970 °C are calculated slightly smaller than the experimental data by Wachtel and Kopp [29]. This discrepancy originated from the well established Al-Mn system. However, the stability of the γ_L phase at 780 °C is well

reproduced. The experimental phase diagram data at the high Al region by Grushko et al. [9] in the temperature range from 600 °C to 1010 °C are all well reproduced. The calculated three phase region of bcc + cub + $AlCr_2$ at 780 °C is slightly off (about 5 at.% Al) towards the Al side compared to the experimental data by Wacthel and Kopp [29]. However, the topology of the phase relation at 780 °C is very well reproduced.

The calculated isothermal sections at 600, 580, 550, and 500 °C are presented in Figs. 5.5(j) to 5(n). The experiment results from Ohnishi et al. [31], Grushko et al. [9], and Clare [28] are also plotted for comparison. The G (Al_{12}(Mn, Cr)) phase is a ternary extension of the binary $Al_{12}Mn$ phase which becomes more stable with decreasing temperature. The Al_7Cr, $Al_{11}Cr_2$, and Al_6Mn phases also form ternary solid solutions. The experimental data at low temperatures are well reproduced as can be seen in Figs. 5.5(j) to (n).

A series of isopleth sections are shown in Fig. 5.6 along with the related experimental data from Wacthel and Kopp [29] and Wacthel and Rein [30]. The experimental data in the isopleth of 2.5 at.% Al are satisfactorily reproduced in the present optimization as shown in Fig. 5.6(a). During the optimization process, solubilities of Al in both the σ_H and σ_L phases were introduced in the ternary system to ensure the correct phase relation in the low Al region. The calculated isopleth section with 33.3 at.% Al is presented in Fig. 5.6(b) with the available experimental data. The calculated solidus and liquidus show a certain deviation from the experimental data from Wacthel and Rein [30] in the Cr rich side although the general trend is consistent with the experimental data. This is due to the difference in the liquidus and solidus in the Al-Cr system. In the present thermodynamic description of the Al-Cr system, the recent experimental data by Stein et al. [41] for the liquidus and solidus of the bcc_A2 phase were taken into account. However, the bcc_A2, $AlCr_2$, and cub_A13 phase regions are well reproduced. The calculated isopleth sections of 10 and 20 at.% Cr are presented in Figs. 5.6(c) and (d). It can be seen from these two diagrams that the agreement between the calculated results and the measured data are quite acceptable.

The calculated primary crystalline phase diagram of the ternary Al-Cr-Mn system is presented in Fig. 5.7(a). The enlarged diagram for the Al rich region is shown in Fig. 5.7(b). The available experimental data are also plotted for comparison. The primary phase region of γ_L is

calculated larger than experimental results by Balanetskyy et al. [26]. The primary phase region of Al_4Cr is calculated smaller than the experimental results. The experimental primary phase region of Al_4Cr in the Al-Cr rich corner is wider than the well-established phase diagram of the binary Al-Mn system, which indicates the possible error in their experiments. In order to reproduce the stability region of the γ_L phase by Wacthel and Rein [30] in the isothermal sections (see in Fig. 5.5), the primary phase region of the γ_L solution is calculated to be wider than the experimental data by Balanetskyy et al. [26]. That is, regarding to the γ_L phase, the experimental data of Wacthel and Rein [30] and Balanetskyy et al. [26] seem to be inconsistent.

The calculated solidus projection is shown in Fig. 5.8. As can be seen from the diagram that the agreement between the calculations and the reported data by Balanetskyy et al. [26] is good except that the Al_4Cr + γ_L + $Al_{29}Cr_{10}$ three phase triangle is shifted to the Al-Mn rich side by about 5 at.% Mn.

The calculated ternary invariant reactions involving the liquid phase are listed in Table 5.2. The available experimental invariant temperatures are also listed for comparison. It can be seen from Table 5.2 that the calculated invariant temperatures are very close to the reported ones by Balanetskyy et al. [26], except that the four phase equilibrium of liquid + γ_L + Al_4Cr + $Al_{29}Mn_{10}$ is about 50 °C lower than the experimentally measured one.

One of the challenges of the present thermodynamic modeling of this ternary system was the accurate description of the complex solid solutions of γ_H and γ_L. As these solid solutions are in the middle of the ternary system, the proper descriptions of these phases are crucial to reproduce the phase relation in the ternary system. Both the γ_H and γ_L phases are stable in binary Al-Cr and Al-Mn systems. However, the range of the composition in each binary system is largely different as shown in Figs. 5.1 and 5.2. Therefore, in order to reproduce the homogeneity range of these phases in two binary systems, the CEF models for these two phases require many pseudo end-members, as shown in Fig. 5.9. In the case of the γ_L solution, two binary end-members are used for the Al-Mn and Al-Cr systems, respectively, and two additional ternary end-members should be fixed to reproduce the phase stability of this phase. In the case of the γ_H phase, the Gibbs energies of four end-members in each binary system and ten ternary end-members,

in total eighteen end-members, should be simultaneously optimized. Because the homogeneity ranges of the γ_H and γ_L phases in two sub-binary Al-Cr and Al-Mn systems are very different, the optimized stabilities of the binary end-members in the Al-Mn system are quite different from those in the binary Al-Cr system. This causes the great difficulty in the modeling of these phases in ternary system. For example, γ_H has six ternary end-members far from the homogeneity region of this phase. So it is very difficult to assign proper Gibbs energies of these end-members from the available phase diagram information. When we first combined binary model parameters with reasonable Gibbs energies of the ternary end-members (if the stability of these ternary end-members is too strong, it can intervene into the stability region of the bcc phase), a large miscibility gap was calculated between the binary systems. The only way to suppress the miscibility gap and make a continuous solid solution between the two binary systems was using interaction parameters. The rest of the ternary solid solutions were also simultaneously optimized to reproduce the entire phase relationship as shown in Figs. 5.5 to 5.6. There are no thermodynamic property measurements for this ternary system. In the future, if thermodynamic data for many ternary solutions are measured, the Gibbs energy descriptions of these solutions can be more accurately determined.

5.5 Summary

A comprehensive evaluation and optimization of all the available phase diagram information in the ternary Al-Cr-Mn system was carried out. Thermodynamic description of the liquid phase in the binary Cr-Mn system was revised using the Modified Quasi-chemical Model. The binary Al-Mn system was revised by the addition of the γ_H phase. The Modified Quasi-chemical Model was applied to describe the thermodynamic properties of the ternary liquid phase. The solid solution phases were described using the Compound Energy Formalism considering the complex sublattice structures. A comparison between the calculated and measured thermodynamic and phase diagram information indicates that the present thermodynamic description can reproduce most of the reliable experimental data in the Al-Cr-Mn system. The optimized model parameters can be used to calculate any phase diagram sections and thermodynamic properties of the ternary Al-Cr-Mn system.

Acknowledgement

The authors would like to thank the financial support from NSERC-Automotive Partnership Canada program in Canada. Senlin Cui would also like to thank the McGill Engineering Doctorate Award (MEDA) from McGill University for financial support.

References

1. Lodgaard, L. and N. Ryum, *Precipitation of dispersoids containing Mn and/or Cr in Al-Mg-Si alloys.* Mater. Sci. Eng., A, 2000. **A283**(1-2): p. 144-152.
2. Radetic, T., M. Popovic, and E. Romhanji, *Microstructure evolution of a modified AA5083 aluminum alloy during a multistage homogenization treatment.* Mater. Charact., 2012. **65**: p. 16-27.
3. Jansson, A., *A thermodynamic evaluation of the aluminum-manganese system.* Metall. Trans. A, 1992. **23A**(11): p. 2953-62.
4. Liu, X.J., I. Ohnuma, R. Kainuma, and K. Ishida, *Thermodynamic assessment of the aluminum-manganese (Al-Mn) binary phase diagram.* J. Phase Equilib., 1999. **20**(1): p. 45-56.
5. Du, Y., J. Wang, J. Zhao, J.C. Schuster, F. Weitzer, R. Schmid-Fetzer, M. Ohno, H. Xu, Z.-k. Liu, S. Shang, and W. Zhang, *Reassessment of the Al-Mn system and a thermodynamic description of the Al-Mg-Mn system.* Int. J. Mater. Res., 2007. **98**(9): p. 855-871.
6. Shukla, A. and A.D. Pelton, *Thermodynamic Assessment of the Al-Mn and Mg-Al-Mn Systems.* J. Phase Equilib. Diffus., 2009. **30**(1): p. 28-39.
7. Asgar-Khan, M. and M. Medraj, *Thermodynamic description of the Mg-Mn, Al-Mn and Mg-Al-Mn systems using the modified quasichemical model for the liquid phases.* Mater. Trans., 2009. **50**(5): p. 1113-1122.
8. Kim, M.-S. and Y.-B. Kang, *Thermodynamic Modeling of the Fe-Mn-C and the Fe-Mn-Al Systems Using the Modified Quasichemical Model for Liquid Phase.* J. Phase Equilib. Diffus., 2015. **36**(5): p. 453-470.

9. Grushko, B., W. Kowalski, D. Pavlyuchkov, S. Balanetskyy, and M. Surowiec, *On the constitution of the Al rich part of the Al-Cr-Mn system.* J. Alloys Compd., 2009. **468**(1-2): p. 87-95.
10. Venkatraman, M. and J.P. Neumann, *The Cr-Mn (chromium-manganese) system.* Bull. Alloy Phase Diagrams, 1986. **7**(5): p. 457-62, 503-4.
11. Lee, B.J., *A thermodynamic evaluation of the chromium-manganese and iron-chromium-manganese systems.* Metall. Trans. A, 1993. **24A**(9): p. 1919-33.
12. Cui, S., I.-H. Jung, J. Kim, and J. Xin, *A coupled experimental and thermodynamic study of the Al-Cr and Al-Cr-Mg systems*, submitted to J. Alloys Compd.
13. Jiang, M., L. Chen, W. Pang, A. Qiu, X. Lu, and C. Li, *Thermodynamic modeling of Al-Cr-Mn system.* Zhongguo Youse Jinshu Xuebao, 2011. **21**(4): p. 856-864.
14. Kono, H., *Ferromagnetic phase in manganese-aluminum system.* J. Phys. Soc. Jpn., 1958. **13**: p. 1444-51.
15. Koch, A.J.J., P. Hokkeling, M.G. van der Steeg, and K.J. de Vos, *New material for permanent magnets on a base of Mn and Al.* J. Appl. Phys., 1960. **31**: p. 75S-77S.
16. Köster, W. and E. Wachtel, *Constitution and magnetic properties of aluminum-manganese alloys with more than 25 at.% Mn.* Z. Metallkd., 1960. **51**: p. 271-80.
17. Gödecke, T. and W. Köster, *Constitution of the aluminum-manganese system.* Z. Metallk., 1971. **62**(10): p. 727-32.
18. Robinson, J.A.J., F.H. Hayes, A. Serneels, F. Weitzer, and P. Rogl, *COST 507-definiation of thermochemical and thermophysical properties to provide a database for the develpoment of new light alloys.* 1998. **1**: p. 230.
19. Carlile, S.J., J.W. Christian, and W. Hume-Rothery, *The equilibrium diagram of the system chromium-manganese.* J. Inst. Met., 1949. **76**: p. 169-94; Paper No 1214.
20. Greenaway, H.T., S.T.M. Johnstone, and M. McQuillan, *High-temperature thermal analysis with the tungsten/molybdenum thermocouple.* J. Inst. Met., 1951. **80**: p. 109-14; Paper No 1330.
21. Hellawell, A. and W. Hume-Rothery, *The constitution of alloys of iron and manganese with transition elements of the first long period.* Phil. Trans. Roy. Soc. London, Ser. A, 1957. **249**: p. 417-59.

22. Villars, P., A. Prince, and H. Okamoto, *Al-Cr-Mn.* Handbook of Ternary Alloy Phase Diagrams, 1995. ASM International, Materials Park, OH**,** (3): p. 3128-3143.
23. Raghavan, V., *Al-Cr-Mn (aluminum-chromium-manganese).* J. Phase Equilib. Diffus., 2008. **29**(2): p. 171-172.
24. Schenk, T., M. Durand-Charre, and M. Audier, *Liquid-solid equilibria in the Al rich corner of the Al-Mn-Cr system.* J. Alloys Compd., 1998. **281**(2): p. 249-263.
25. Raghavan, V., *Al-Cr-Mn (Aluminum-Chromium-Manganese).* J. Phase Equilib. Diffus., 2009. **30**(6): p. 620-623.
26. Balanetskyy, S., W. Kowalski, and B. Grushko, *Liquidus, solidus and reaction scheme of the Al rich part of Al-Cr-Mn.* J. Alloys Compd., 2009. **474**(1-2): p. 147-151.
27. Raynor, G.V. and K. Little, *The constitution of the aluminum-rich alloys of aluminum, chromium, and manganese.* J. Inst. Met., 1945. **71**(Pt. 10, Paper No. 1003): p. 493-524.
28. Clare, J.W.H., *Constitution of aluminum rich alloys of the aluminum-chromium-manganese system.* Trans. Am. Inst. Min., Metall. Pet. Eng., 1959. **215**: p. 429-33.
29. Wachtel, E. and W.U. Kopp, *Constitution and properties of the ternary system aluminum manganese-chromium.* Z. Metallkd., 1965. **56**(2): p. 121-9.
30. Wachtel, E. and U. Rein, *Constitution of the manganese corner of the ternary aluminum-manganese-chromium system.* Z. Metallkd., 1965. **56**(10): p. 690-4.
31. Ohnishi, T., Y. Nakatani, and K. Shimizu, *Constitution in the solid state of aluminum-rich alloys in the aluminum-manganese-chromium ternary system.* Keikinzoku, 1972. **22**(8): p. 504-11.
32. Pelton, A.D. and P. Chartrand, *The modified quasi-chemical model: Part II. Multicomponent solutions.* Metall. Mater. Trans. A, 2001. **32A**(6): p. 1355-1360.
33. Pelton, A.D., S.A. Degterov, G. Eriksson, C. Robelin, and Y. Dessureault, *The modified quasichemical model I - binary solutions.* Metall. Mater. Trans. B, 2000. **31B**(4): p. 651-659.
34. Robelin, C., P. Chartrand, and A.D. Pelton, *Thermodynamic evaluation and optimization of the ($NaNO_3$ + KNO_3 + Na_2SO_4 + K_2SO_4) system.* J. Chem. Thermodyn., 2015. **83**: p. 12-26.

35. Jung, I.-H., D.-H. Kang, W.-J. Park, N.J. Kim, and S. Ahn, *Thermodynamic modeling of the Mg-Si-Sn system.* CALPHAD Comput. Coupling Phase Diagrams Thermochem., 2007. **31**(2): p. 192-200.
36. Hillert, M., *The compound energy formalism.* J. Alloys Compd., 2001. **320**(2): p. 161-176.
37. Hillert, M. and M. Jarl, *A model for alloying effects in ferromagnetic metals.* CALPHAD Comput. Coupling Phase Diagrams Thermochem., 1978. **2**(3): p. 227-38.
38. Dinsdale, A.T., *SGTE data for pure elements.* CALPHAD Comput. Coupling Phase Diagrams Thermochem., 1991. **15**(4): p. 317-425.
39. Bale, C.W., P. Chartrand, S.A. Degterov, G. Eriksson, K. Hack, R. Ben Mahfoud, J. Melancon, A.D. Pelton, and S. Petersen, *FactSage thermochemical software and databases.* CALPHAD Comput. Coupling Phase Diagrams Thermochem., 2002. **26**(2): p. 189-228.
40. McAlister, A.J. and J.L. Murray, *The (Al-Mn) aluminum-manganese system.* Bull. Alloy Phase Diagrams, 1987. **8**(5): p. 438-47.
41. Stein, F., C. He, and I. Wossack, *The liquidus surface of the Cr-Al-Nb system and re-investigation of the Cr-Nb and Al-Cr phase diagrams.* J. Alloys Compd., 2014. **598**: p. 253-265.
42. Ansara, I., A. Dinsdale, and M. Rand, *COST 507*-Thermochemical database for light metal alloys, 1998. **2**: p. 143-144.
43. Hu, B., W.-W. Zhang, Y. Peng, Y. Du, S. Liu, and Y. Zhang, *Thermodynamic reassessment of the Al-Cr-Si system with the refined description of the Al-Cr system.* Thermochim. Acta, 2013. **561**: p. 77-90.

Table captions

Table 5.1 Summary of the optimized model parameters for the Al-Cr-Mn system (J mol^{-1} or J mol^{-1} K^{-1}).

Table 5.2 Summary of the invariant reactions involving the liquid phase in the ternary Al-Cr-Mn system. (The composition of the liquid phase for each invariant reaction is also indicated.)

Figure captions

Fig. 5.1 The calculated Al-Cr phase diagram [12].

Fig. 5.2 The revised Al-Mn phase diagram in this study compared with the experimental data.

Fig. 5.3 The revised Cr-Mn phase diagram in this study compared with the experimental data.

Fig. 5.4 Calculated enthalpy of mixing of the liquid Cr-Mn phase at 1900 °C compared to the calculated one from Lee [11].

Fig. 5.5 Calculated isothermal sections of the Al-Cr-Mn system compared with the experimental data at different temperatures. (a) 1070 °C, (b) 1010 °C, (c) 970 °C, (d) 950 °C, (e) 900 °C, (f) 800 °C, (g)780 °C, (h) 715 °C, (i) 685 °C, (j) 600 °C, (k) 580 °C, (m) 550 °C, and (n) 500 °C.

Fig. 5.6 Calculated isoplethal sections of the Al-Cr-Mn system at (a) 2.5 at.% Al, (b) 33.3 at.% Al, (c) 10 at.% Cr, and (d) 20 at.% Cr.

Fig. 5.7 Calculated liquidus projection of the Al-Cr-Mn system compared with the experiment data. (a) The entire composition range, and (b) the enlarged Al rich region.

Fig. 5.8 Calculated solidus projection of the Al-Cr-Mn system compared with the experimental data by Balanetskyy et al. [26].

Fig. 5.9 Schematic diagrams of the end members for CEF used in this study, and stability ranges of the γ_L and γ_H phases. (a) The γ_L phase, and (b) the γ_H phase.

Table 5.1 Summary of the optimized model parameters for the Al-Cr-Mn system (J mol^{-1} or J mol^{-1} K^{-1}).

Phase	Thermodynamic parameters	Ref.
Liquid (Al, Cr, Mn)	$\Delta g_{Al,Cr} = -6250.02 - 4.707T + (-4978.96 - 4.728T)x_{AlAl} + (836.8 + 1.883T)x_{AlAl}^2$ $-1602.81x_{CrCr}$	[12]
	$\Delta g_{Al,Mn} = -17572.8 + 6.07T + (-4602.40 + 1.26T)x_{AlAl}^2 + (-4184.00 + 1.67T)x_{MnMn}^2$	[8]
	$\Delta g_{Cr,Mn} = -1464.40 + 2.26T + (+376.56 + 0.59T)x_{CrCr} - 414.22x_{MnMn}$	This work
	$g^{001}_{Al,Cr,(Mn)} = -3250.97 - 1.67T$, $g^{001}_{Al,Mn,(Cr)} = -322.17 - 4.18T$, $g^{001}_{Cr,Mn,(Al)} = -836.80 - 5.02T$	This work
fcc_A1 $(Al, Cr, Mn)_1(Va)_1$	${}^0L_{Al,Cr:Va} = -57135.57$	[12]
	${}^0L_{Al,Mn:Va} = -69938.0 + 27.17958T$, ${}^1L_{Al,Mn:Va} = 8248.9$	[5]
	${}^0L_{Cr,Mn:Va} = -19088 + 17.5423T$ $T_{C\,Cr,Mn:Va} = -1109x_{Cr} - 1620x_{Mn}$ $\beta_{Cr,Mn:Va} = -2.46x_{Cr} - 1.86x_{Mn}$	[11]
bcc_A2 $(Al, Cr, Mn)_1(Va)_3$	${}^0L_{Al,Cr:Va} = -56356.8 - 6.32T$ ${}^1L_{Al,Cr:Va} = -7654.74$	[12]
	${}^0L_{Al,Mn:Va} = -111336.2 + 44.48059T$ ${}^1L_{Al,Mn:Va} = -68691.8 + 44.52653T$	[5]

	${}^{0}L_{Cr,Mn:Va} = -20328 + 18.7339T$	[11]
	${}^{1}L_{Cr,Mn:Va} = -9162 + 4.4183T$	
	$T_{C\,Cr,Mn:Va} = -311.5x_{Cr} - 580x_{Mn} + x_{Cr}x_{Mn}[-1325 - 1133(x_{Cr} - x_{Mn})^2 - 10294(x_{Cr} - x_{Mn})^4$ $+ 26706(x_{Cr} - x_{Mn})^6 - 28117(x_{Cr} - x_{Mn})^8]$	
	$\beta_{Cr,Mn:Va} = -0.008x_{Cr} - 0.27x_{Mn}$ $+ x_{Cr}x_{Mn}[+0.48643 - 0.72035(x_{Cr} - x_{Mn})^2 - 1.93265(x_{Cr} - x_{Mn})^4]$	
	${}^{0}L_{Al,Cr,Mn:Va} = 66161.59 - 111.59T$	This work
	${}^{1}L_{Al,Cr,Mn:Va} = -80307.70 - 12.55T$	
	${}^{2}L_{Al,Cr,Mn:Va} = -58296.93 - 8.37T$	
hcp_A3 $(Al, Cr, Mn)_1$	${}^{o}G_{Cr} = 41840 + {}^{o}G_{Cr}^{bcc}$	[12]
	${}^{0}L_{Al,Cr:Va} = -35000.00 + 6.00T$	[42]
	${}^{0}L_{Al,Mn:Va} = -95264.1 + 33.09659T$	[5]
	${}^{1}L_{Al,Mn:Va} = -56880.6 + 43.14119T$	
	${}^{2}L_{Al,Mn:Va} = 14430.2$	
	${}^{0}L_{Cr,Mn:Va} = 60000$	[11]
	${}^{0}L_{Al,Cr,Mn:Va} = -750735.12$	This work

	${}^{1}L_{Al,Cr,Mn:Va} = -643603.80 - 20.92T$	
	${}^{2}L_{Al,Cr,Mn:Va} = -191493.31 - 16.74T$	
cub_A13 (Al, Mn, Cr)(Va)	${}^{o}G_{Cr:Va} = 15899.00 + 0.63T + {}^{o}G_{Cr}^{bcc}$	[11]
	${}^{0}L_{Cr,Mn:Va} = -31260 + 16.49T$	
	${}^{0}L_{Al,Mn:Va} = -118512.30 + 52.74T$	[5]
	${}^{1}L_{Al,Mn:Va} = -3174.9$	
	${}^{0}L_{Al,Cr:Va} = -96232.00$	This work
	${}^{0}L_{Al,Cr,Mn:Va} = -578647.20 + 418.40T$	
	${}^{2}L_{Al,Cr,Mn:Va} = -106867.73 + 22.01T$	
cbcc_A12 (Al, Cr, Mn)(Va)	${}^{o}G_{Cr:Va} = 11087 + 2.7196T + {}^{o}G_{Cr}^{bcc}$	[11]
	${}^{0}L_{Cr,Mn:Va} = -36796 + 20.385T$	
	${}^{0}L_{Al,Mn:Va} = -63000 + 21T$	[5]
Al_4Cr $(Cr, Mn)_1(Al, Va)_4$	${}^{o}G_{Cr:Va} = 25000 + {}^{o}G_{Cr}^{bcc}$	[43]
	${}^{o}G_{Mn:Al} = -109088.5 + 36.67T + 4{}^{o}G_{Al}^{fcc} + {}^{o}G_{Mn}^{cbcc}$	[5]
	${}^{o}G_{Cr:Al} = -84930.410 + 3.81T + 4{}^{o}G_{Al}^{fcc} + {}^{o}G_{Cr}^{bcc}$	[12]
	${}^{o}G_{Mn:Va} = 192464.00 + {}^{o}G_{Mn}^{cbcc}$	This work
	${}^{0}L_{Mn:Al,Va} = 28226.270$	

	${}^{0}L_{Cr,Mn:*} = -34518.00$	
	${}^{1}L_{Cr,Mn:*} = 22723.30 - 30.42T$	
	${}^{0}L_{Cr:Al,Va} = 28226.270$	[12]
γ_L $(Al)_{12}(Cr, Mn)_5(Al, Cr, Mn)_9$	${}^{o}G_{Al:Cr:Al} = -357006.160 + 20.163T + 21{}^{o}G_{Al}^{fcc} + 5{}^{o}G_{Cr}^{bcc}$	[12]
	${}^{o}G_{Al:Cr:Cr} = -320932.548 - 109.516T + 12{}^{o}G_{Al}^{fcc} + 14{}^{o}G_{Cr}^{bcc}$	
	${}^{o}G_{Al:Mn:Al} = -199849.60 - 60.25T + 21{}^{o}G_{Al}^{fcc} + 5{}^{o}G_{Mn}^{cbcc}$	This work
	${}^{o}G_{Al:Mn:Mn} = -791382.68 + 290.39T + 12{}^{o}G_{Al}^{fcc} + 14{}^{o}G_{Mn}^{cbcc}$	
	$\Delta g = {}^{o}G_{Al:Mn:Mn} + {}^{o}G_{Al:Cr:Cr} - {}^{o}G_{Al:Cr:Mn} - {}^{o}G_{Al:Mn:Cr}$	
	$I = {}^{o}G_{Al:Mn:Cr} - {}^{o}G_{Al:Cr:Mn} - 4{}^{o}G_{Cr}^{bcc} + 4{}^{o}G_{Mn}^{cbcc}$	
	$\Delta g = -140313.5 + 226.9T;\ I = 122030.54 + 46.02T$	
	${}^{o}G_{Al:Mn:Cr} == -424985.62 + 12{}^{o}G_{Al}^{fcc} + 9{}^{o}G_{Cr}^{bcc} + 5{}^{o}G_{Mn}^{cbcc}$	
	${}^{o}G_{Al:Cr:Mn} = -547016.16 - 46.024T + 12{}^{o}G_{Al}^{fcc} + 5{}^{o}G_{Cr}^{bcc} + 9{}^{o}G_{Mn}^{cbcc}$	
	${}^{0}L_{Al:Cr,Mn:Al} = -196229.60$	
	${}^{0}L_{Al:Cr,Mn:Cr} = -167360.00$	
	${}^{0}L_{Al:Cr,Mn:Mn} = -209200.00$	
	${}^{0}L_{Al:Mn:Al,Cr} = -543920.00 + 33.25T$	
	${}^{0}L_{Al:Cr:Al,Mn} = -635131.20 + 286.19T$	

	${}^{0}L_{Al:Mn:Al,Mn} = -522188.30 + 244.35T$	
	${}^{1}L_{Al:Mn:Al,Mn} = 38014.60$	
	${}^{0}L_{Al:Cr:Cr,Mn} = {}^{0}L_{Al:Mn:Cr,Mn} = -167360.00$	
	${}^{0}L_{Al:Cr:Al,Cr} = -632060.437 + 29.071T$	[43]
γ_H $(Al, Cr, Mn)_2(Al, Cr, Mn)_3(Cr, Mn)_2(Al)_6$	${}^{o}G_{Al:Al:Cr:Al} = -124435.30 + 11{}^{o}G_{Al}^{fcc} + 2{}^{o}G_{Cr}^{bcc}$	[43]
	${}^{o}G_{Cr:Cr:Cr:Al} = 2357.31 - 103.77T + 6{}^{o}G_{Al}^{fcc} + 7{}^{o}G_{Cr}^{bcc}$	
	${}^{o}G_{Cr:Al:Cr:Al} = 9{}^{o}G_{Al}^{fcc} + 4{}^{o}G_{Cr}^{bcc}$	
	${}^{o}G_{Al:Cr:Cr:Al} = -243506.24 - 42.08T + 8{}^{o}G_{Al}^{fcc} + 5{}^{o}G_{Cr}^{bcc}$	[12]
	${}^{o}G_{Al:Al:Mn:Al} = 11{}^{o}G_{Al}^{fcc} + 2{}^{o}G_{Mn}^{cbcc}$	This work
	${}^{o}G_{Cr:Al:Mn:Al} = -158992.00 + 9{}^{o}G_{Al}^{fcc} + 2{}^{o}G_{Cr}^{bcc} + 2{}^{o}G_{Mn}^{cbcc}$	
	${}^{o}G_{Cr:Cr:Mn:Al} = 195183.60 - 205.02T + 6{}^{o}G_{Al}^{fcc} + 5{}^{o}G_{Cr}^{bcc} + 2{}^{o}G_{Mn}^{cbcc}$	
	${}^{o}G_{Mn:Al:Cr:Al} = 313800.00 + 9{}^{o}G_{Al}^{fcc} + 2{}^{o}G_{Cr}^{bcc} + 2{}^{o}G_{Mn}^{cbcc}$	
	${}^{o}G_{Mn:Al:Mn:Al} = -264550.14 + 42.15T + 9{}^{o}G_{Al}^{fcc} + 4{}^{o}G_{Mn}^{cbcc}$	
	${}^{o}G_{Mn:Cr:Cr:Al} = -117152.00 + 6{}^{o}G_{Al}^{fcc} + 5{}^{o}G_{Cr}^{bcc} + 2{}^{o}G_{Mn}^{cbcc}$	
	${}^{o}G_{Mn:Cr:Mn:Al} = 6{}^{o}G_{Al}^{fcc} + 3{}^{o}G_{Cr}^{bcc} + 4{}^{o}G_{Mn}^{cbcc}$	
	${}^{o}G_{Mn:Mn:Cr:Al} = 150624.00 + 6{}^{o}G_{Al}^{fcc} + 2{}^{o}G_{Cr}^{bcc} + 5{}^{o}G_{Mn}^{cbcc}$	
	${}^{o}G_{Mn:Mn:Mn:Al} = -238387.58 + 12.55T + 6{}^{o}G_{Al}^{fcc} + 7{}^{o}G_{Mn}^{cbcc}$	

$${}^{o}G_{Al:Cr:Mn:Al} = 308151.60 - 205.02\,T + 8{}^{o}G_{Al}^{fcc} + 3{}^{o}G_{Cr}^{bcc} + 2{}^{o}G_{Mn}^{cbcc}$$

$${}^{o}G_{Al:Mn:Mn:Al} = 8{}^{o}G_{Al}^{fcc} + 5{}^{o}G_{Mn}^{cbcc}$$

$${}^{o}G_{Cr:Mn:Cr:Al} = 92048.00 + 6{}^{o}G_{Al}^{fcc} + 4{}^{o}G_{Cr}^{bcc} + 3{}^{o}G_{Mn}^{cbcc}$$

$${}^{o}G_{Cr:Cr:Mn:Al} = 195183.60 - 205.02\,T + 6{}^{o}G_{Al}^{fcc} + 5{}^{o}G_{Cr}^{bcc} + 2{}^{o}G_{Mn}^{cbcc}$$

$${}^{o}G_{Cr:Mn:Mn:Al} = 6{}^{o}G_{Al}^{fcc} + 2{}^{o}G_{Cr}^{bcc} + 5{}^{o}G_{Mn}^{cbcc}$$

$${}^{0}L_{Al,Cr:Al:Mn:Al} = -315473.60 + 16.74\,T$$

$${}^{0}L_{Al,Cr:Cr:Mn:Al} = 15271.60 - 209.20\,T$$

$${}^{0}L_{Cr,Mn:Al:Cr:Al} = -539736.00$$

$${}^{0}L_{Cr,Mn:Cr:Cr:Al} = -539736.00$$

$${}^{0}L_{Cr,Mn:Mn:Cr:Al} = -292880.00$$

$${}^{0}L_{Cr,Mn:Al:Mn:Al} = -161502.40 - 20.92\,T$$

$${}^{0}L_{Cr,Mn:Cr:Mn:Al} = -100416.00 - 149.37\,T$$

$${}^{0}L_{Cr,Mn:Mn:Mn:Al} = -334720.00$$

$${}^{0}L_{Cr,Mn:Cr:Mn:Al} = -100416.00 - 149.37\,T$$

$${}^{0}L_{Al:Al,Cr:Mn:Al} = -364008.00$$

$${}^{0}L_{Cr:Al,Cr:Mn:Al} = 535133.60 - 627.60\,T$$

$${}^{0}L_{Mn:Al,Cr:Mn:Al} = -376560.00$$

$${}^{0}L_{Mn:Al,Mn:Cr:Al} = 251040.00$$

$${}^{0}L_{Al:Al,Mn:Mn:Al} = -215919.50 + 158.99\,T$$

$${}^{0}L_{Cr:Al,Mn:Mn:Al} = -282863.50$$

$${}^{0}L_{Mn:Al,Mn:Mn:Al} = -215919.50 + 158.99\,T$$

$${}^{0}L_{Cr:Cr,Mn:Cr:Al} = 41840.00$$

$${}^{0}L_{Cr:Cr,Mn:Mn:Al} = -332628.00 + 41.84\,T$$

$${}^{0}L_{Mn:Cr,Mn:Mn:Al} = -234304.00$$

$${}^{0}L_{Cr:Al:Cr,Mn:Al} = -460240.00$$

$${}^{0}L_{Mn:Al:Cr,Mn:Al} = -460240.00$$

$${}^{0}L_{Al:Cr:Cr,Mn:Al} = -529359.68 + 167.36\,T$$

$${}^{0}L_{Cr:Cr:Cr,Mn:Al} = -581241.28 + 167.36\,T$$

$${}^{0}L_{Mn:Cr:Cr,Mn:Al} = -251040.00$$

$${}^{0}L_{Cr:Mn:Cr,Mn:Al} = -251040.00$$

$${}^{0}L_{Mn:Mn:Cr,Mn:Al} = -585760.00$$

$${}^{0}L_{Al,Cr:Al:Cr:Al} = -183139.262 \qquad [12]$$

$${}^{0}L_{Al,Cr:Cr:Cr:Al} = -183139.262$$

$${}^{0}L_{Al:Al,Cr:Cr:Al} = -63705.751 - 25.221T$$

	${}^{0}L_{Cr:Al,Cr:Cr:Al} = -63705.751 - 25.221T$	
$AlCr_2$ $(Al, Cr, Mn)_1(Al, Cr, Mn)_2$	${}^{o}G_{Al:Al} = 10000 + 3{}^{o}G_{Al}^{fcc}$	[12]
	${}^{o}G_{Cr:Cr} = 10000 + 3{}^{o}G_{Cr}^{bcc}$	
	${}^{o}G_{Al:Cr} = -36594.81 - 14.91T + {}^{o}G_{Al}^{fcc} + 2{}^{o}G_{Cr}^{bcc}$	
	${}^{o}G_{Cr:Al} = 52331.31 + 16.84T + 2{}^{o}G_{Al}^{fcc} + {}^{o}G_{Cr}^{bcc}$	
	${}^{o}G_{Al:Mn} = -31254.48 + 20.92T + {}^{o}G_{Al}^{fcc} + 2{}^{o}G_{Mn}^{cbcc}$	This work
	${}^{o}G_{Cr:Mn} = 104600.00 + {}^{o}G_{Cr}^{bcc} + 2{}^{o}G_{Mn}^{cbcc}$	
	${}^{o}G_{Mn:Al} = 2{}^{o}G_{Al}^{fcc} + G_{Mn}^{cbcc}$	
	${}^{o}G_{Mn:Cr} = 104600.00 + 2{}^{o}G_{Cr}^{bcc} + {}^{o}G_{Mn}^{cbcc}$	
	${}^{o}G_{Mn:Mn} = 10000.00 + 3{}^{o}G_{Mn}^{cbcc}$	
	${}^{0}L_{*:Cr,Mn} = -204597.60 + 83.68T$	
	${}^{1}L_{*:Cr,Mn} = -882.82 + 8.37T$	
	${}^{0}L_{Al,Cr:*} = -8922.60$	[12]
	${}^{0}L_{*:Al,Cr} = -38108.20$	
Al_7Cr $(Al)_7(Cr, Mn)$	${}^{o}G_{Al:Cr} = -107000 + 14.81T + 7{}^{o}G_{Al}^{fcc} + {}^{o}G_{Cr}^{bcc}$	[12]
	${}^{o}G_{Al:Mn} = -94746.68 + 20.92T + 7{}^{o}G_{Al}^{fcc} + {}^{o}G_{Mn}^{cbcc}$	This work
	${}^{0}L_{Al:Cr,Mn} = -21212.88 - 8.03T$	
	${}^{1}L_{Al:Cr,Mn} = -12552.00$	

$Al_{11}Cr_2$	${}^{o}G_{Al:Cr} = -195000 + 16.99T + 11\,{}^{o}G_{Al}^{fcc} + 2\,{}^{o}G_{Cr}^{bcc}$	[12]
$(Al)_{11}(Cr, Mn)_2$	${}^{o}G_{Al:Mn} = -189518.46 + 50.21T + 11\,{}^{o}G_{Al}^{fcc} + 2\,{}^{o}G_{Mn}^{cbcc}$	This work
	${}^{0}L_{Al:Cr,Mn} = -79491.82$	
	${}^{1}L_{Al:Cr,Mn} = 11924.40$	
$Al_{11}Mn_4$	${}^{o}G_{Al:Mn} = -350550 + 97.89915\,T + 11\,{}^{o}G_{Al}^{fcc} + 4\,{}^{o}G_{Mn}^{cbcc}$	[5]
$(Al)_{11}(Mn, Cr)_4$	${}^{o}G_{Al:Cr} = -180972.64 - 83.68\,T + 11\,{}^{o}G_{Al}^{fcc} + 4\,{}^{o}G_{Cr}^{bcc}$	This work
	${}^{0}L_{Al:Cr,Mn} = -347669.48 + 169.03\,T$	
	${}^{1}L_{Al:Cr,Mn} = -72508.72 + 41.84\,T$	
	${}^{2}L_{Al:Cr,Mn} = -418860.24 + 292.88\,T$	
$Al_{29}Mn_{10}$	${}^{o}G_{Al:Mn} = -744944.46 + 130.36\,T + 29\,{}^{o}G_{Al}^{fcc} + 10\,{}^{o}G_{Mn}^{cbcc}$	[5]
$(Al, Mn, Cr)_{29}(Mn, Cr)_{10}$	${}^{o}G_{Mn:Mn} = 195000.01 + 39\,{}^{o}G_{Mn}^{cbcc}$	
	${}^{o}G_{Al:Cr} = -713560.28 + 63.60\,T + 29\,{}^{o}G_{Al}^{fcc} + 10\,{}^{o}G_{Cr}^{bcc}$	This work
	${}^{o}G_{Mn:Cr} = 29\,{}^{o}G_{Mn}^{cbcc} + 10\,{}^{o}G_{Cr}^{bcc}$	
	${}^{o}G_{Cr:Mn} = 129704.00 + 10\,{}^{o}G_{Mn}^{cbcc} + 29\,{}^{o}G_{Cr}^{bcc}$	
	${}^{o}G_{Cr:Cr} = 195000.01 + 39\,{}^{o}G_{Cr}^{bcc}$	
	${}^{1}L_{Al,Mn:Cr} = -2510400.00$	
	${}^{0}L_{Al:Mn,Cr} = -585760.00 + 146.44\,T$	
	${}^{1}L_{Al:Mn,Cr} = -339740.80 + 209.20\,T$	

	${}^{0}L_{Al,Mn:Mn} = -664034.27$	[5]
$Al_{99}Mn_{23}$ $(Al)_{99}(Mn, Cr)_{23}$	${}^{o}G_{Al:Mn} = -2510049 + 837.903\,T + 99\,{}^{o}G_{Al}^{fcc} + 23\,{}^{o}G_{Mn}^{cbcc}$	[8]
	${}^{o}G_{Al:Cr} = -794960.00 + 99\,{}^{o}G_{Al}^{fcc} + 23\,{}^{o}G_{Cr}^{bcc}$	This work
	${}^{0}L_{Al:Mn,Cr} = -1610840 - 190.1628\,T$	
Al_6Mn $(Al)_6(Mn, Cr)$	${}^{o}G_{Al:Mn} = -109091 + 35.22\,T + 6\,{}^{o}G_{Al}^{fcc} + {}^{o}G_{Mn}^{cbcc}$	[5]
	${}^{o}G_{Al:Cr} = -83680.00 + 6\,{}^{o}G_{Al}^{fcc} + {}^{o}G_{Cr}^{bcc}$	This work
	${}^{0}L_{Al:Mn,Cr} = -60249.60 + 41.84\,T$	
$G\_Al_{12}Mn$ $(Al)_{12}(Mn, Cr)$	${}^{o}G_{Al:Mn} = -110389.5 + 36.80T + 12\,{}^{o}G_{Al}^{fcc} + {}^{o}G_{Mn}^{cbcc}$	[5]
	${}^{o}G_{Al:Cr} = -97336.58 + 83.68\,T + 12\,{}^{o}G_{Al}^{fcc} + {}^{o}G_{Cr}^{bcc}$	This work
	${}^{0}L_{Al:Mn,Cr} = -178137.98 + 37.66\,T$	
	${}^{1}L_{Al:Mn,Cr} = 116993.01 - 52.30\,T$	
σ_L $(Mn)_8(Cr)_4(Al, Mn, Cr)_{18}$	${}^{o}G_{Mn:Cr:Mn} = -172946.06 + 69.02\,T + 4\,{}^{o}G_{Cr}^{bcc} + 18\,{}^{o}G_{Mn}^{bcc} + 8\,{}^{o}G_{Mn}^{fcc}$	[11]
	${}^{o}G_{Mn:Cr:Cr} = -65859.51 + 22\,{}^{o}G_{Cr}^{bcc} + 8\,{}^{o}G_{Mn}^{fcc}$	
	${}^{o}G_{Mn:Cr:Al} = -794960.00 + 209.20\,T + 18\,{}^{o}G_{Al}^{fcc} + 4\,{}^{o}G_{Cr}^{bcc} + 8\,{}^{o}G_{Mn}^{cbcc}$	This work
	${}^{0}L_{Mn:Cr:Al,Cr} = -203844.48 + 167.36\,T$	
	${}^{0}L_{Mn:Cr:Al,Mn} = -878640.00 + 292.88\,T$	
	${}^{1}L_{Mn:Cr:Al,Mn} = -253968.80 + 83.68\,T$	
	${}^{0}L_{Mn:Cr:Cr,Mn} = -1095770.98 + 862.03\,T$	[11]

σ_H $(Mn)_8(Cr)_4(Al, Mn, Cr)_{18}$	${}^{o}G_{Mn:Cr:Mn} = -74263.07 - 10.71T + 4{}^{o}G_{Cr}^{bcc} + 18{}^{o}G_{Mn}^{bcc} + 8{}^{o}G_{Mn}^{fcc}$ ${}^{o}G_{Mn:Cr:Cr} = -192369.02 + 152.47T + 22{}^{o}G_{Cr}^{bcc} + 8{}^{o}G_{Mn}^{fcc}$	[11]
	${}^{o}G_{Mn:Cr:Al} = -391559.64 - 167.36T + 18{}^{o}G_{Al}^{fcc} + 4{}^{o}G_{Cr}^{bcc} + 8{}^{o}G_{Mn}^{cbcc}$ ${}^{0}L_{Mn:Cr:Al,Cr} = -198488.96 - 292.88T$ ${}^{0}L_{Mn:Cr:Al,Mn} = -523000.00 - 8.37T$ ${}^{1}L_{Mn:Cr:Al,Mn} = 148619.86 - 125.52T$	This work
	${}^{0}L_{Mn:Cr:Cr,Mn} = 90000.00$	[11]
Cr_3Mn_5 $(Cr)_3(Mn)_5$	${}^{o}G_{Cr:Mn} = -72550 + 21.1732T + 3{}^{o}G_{Cr}^{bcc} + 5{}^{o}G_{Mn}^{cbcc}$	[11]

Table 5.2 Summary of the invariant reactions involving the liquid phase in the ternary Al-Cr-Mn system. (The composition of the liquid phase for each invariant reaction is also indicated.)

Reaction type	Reaction			Temperature °C	Reference
	at.% Al	at.% Cr	at.% Mn		
Quasi-Peritectic	Liquid + bcc_A2#1 = hcp_A3 + γ_H				
	51.29	8.26	40.45	1213.5	This work
Quasi-Peritectic	Liquid + hcp_A3 = bcc_A2#2 + γ_H				
	57.74	1.31	40.96	1166	This work
Quasi-Peritectic	Liquid + γ_H = γ_L + $Al_{29}Mn_{10}$				
	81.37	1.69	16.94	1005	This work
				1000	[26]
Quasi-Peritectic	Liquid + γ_L = Al_4Cr + $Al_{29}Mn_{10}$				
	86.46	4.64	8.9	951	This work
				998	[26]
Eutectic	Liquid = Al_4Cr + $Al_{11}Mn_4$ + $Al_{29}Mn_{10}$				
	88.77	2.19	9.05	913	This work
Peritectic	Liquid + $Al_{29}Mn_{10}$ + Al_4Cr = $Al_{11}Mn_4$				
	86.57	0.11	13.32	920	This work
Quasi-Peritectic	Liquid + Al_4Cr = $Al_{11}Cr_2$ + Al_6Mn				
	98.7	0.06	1.24	687	This work
Quasi-Peritectic	Liquid + $Al_{99}Mn_{23}$ = Al_6Mn + Al_4Cr				
	97.33	0.11	2.56	688	This work
				705	[26]
Peritectic	Liquid + $Al_{11}Cr_2$ = Al_6Mn + Al_7Cr				
	99.13	0.04	0.83	662	This work
Quasi-Peritectic	Liquid + Al_7Cr = $Al_{11}Cr_2$ + fcc_A1				
	99.38	0.07	0.54	658	This work
				657	[26]

Quasi-Peritectic	Liquid + $Al_{11}Cr_2$ = Al_6Mn + fcc_A1				
	98.37	0.08	1.55	657.8	This work
				658	[26]

Figures

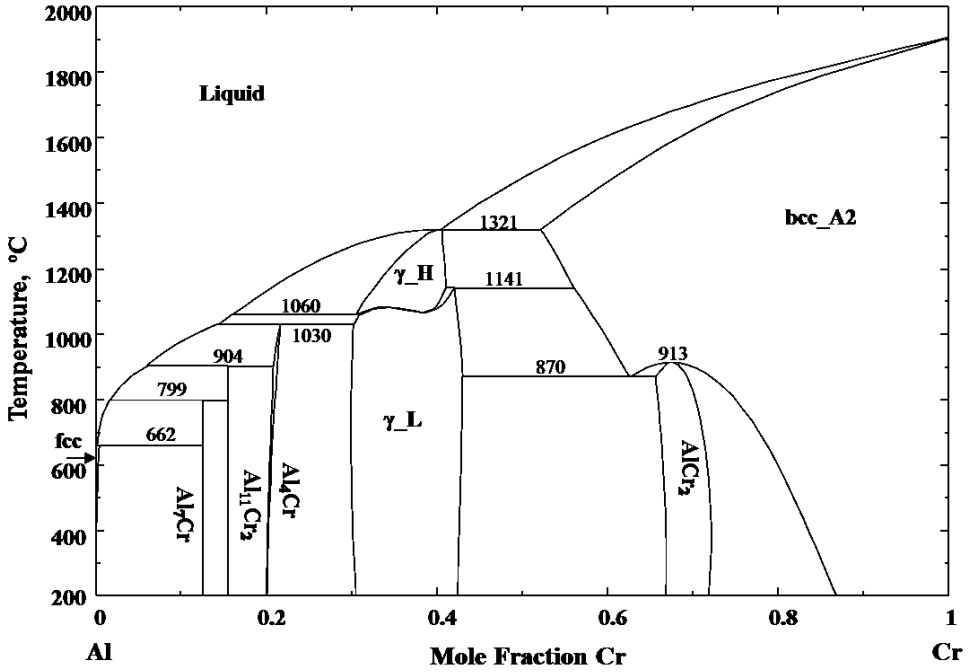

Fig. 5.1 The calculated Al-Cr phase diagram [12].

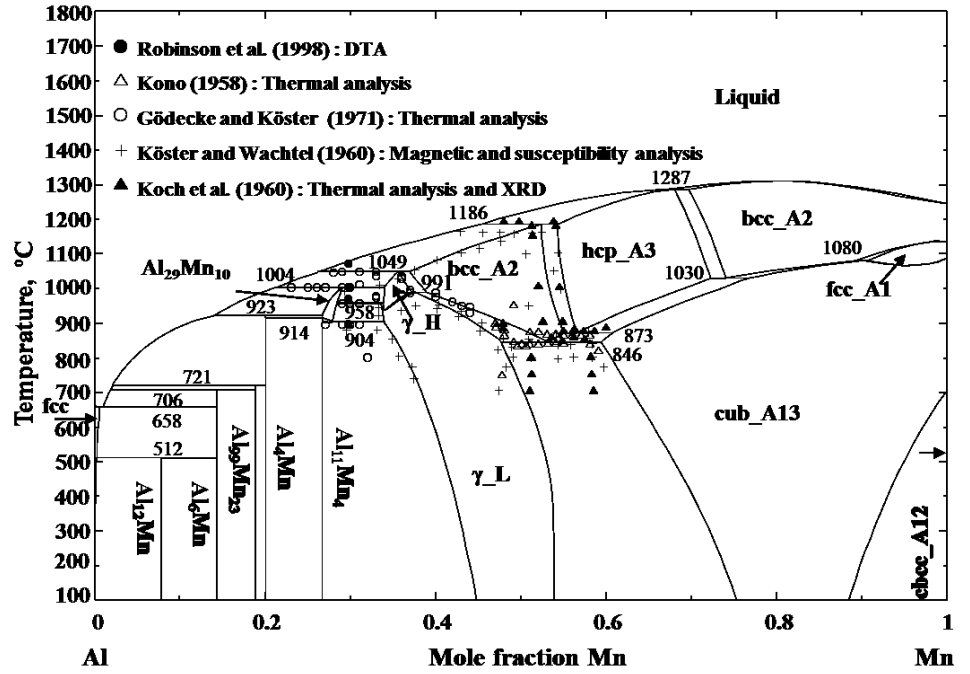

Fig. 5.2 The revised Al-Mn phase diagram in this study compared with the experimental data.

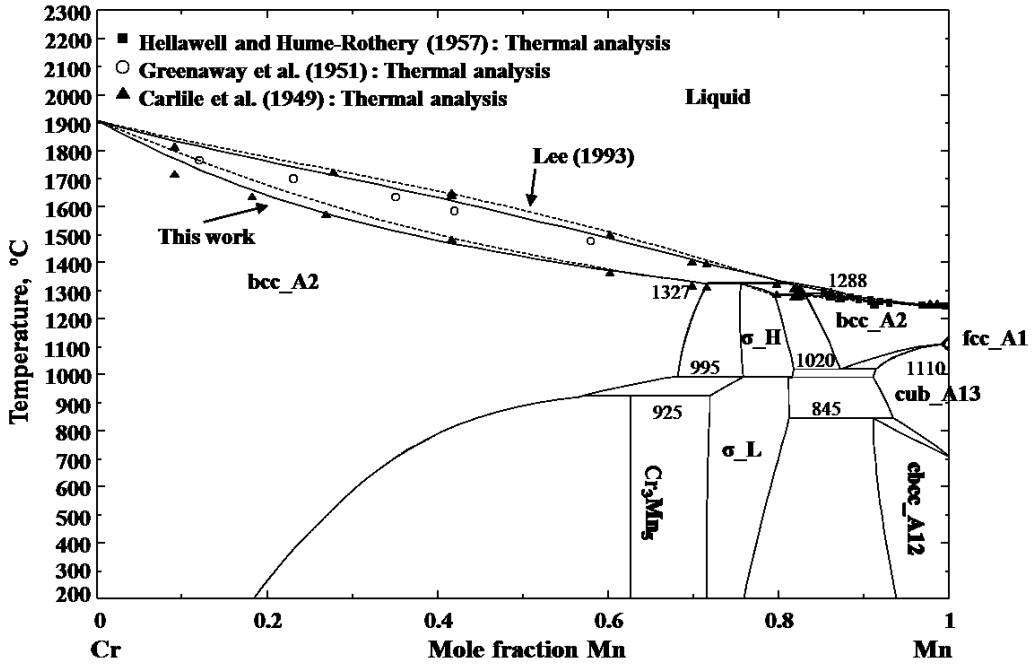

Fig. 5.3 The revised Cr-Mn phase diagram in this study compared with the experimental data.

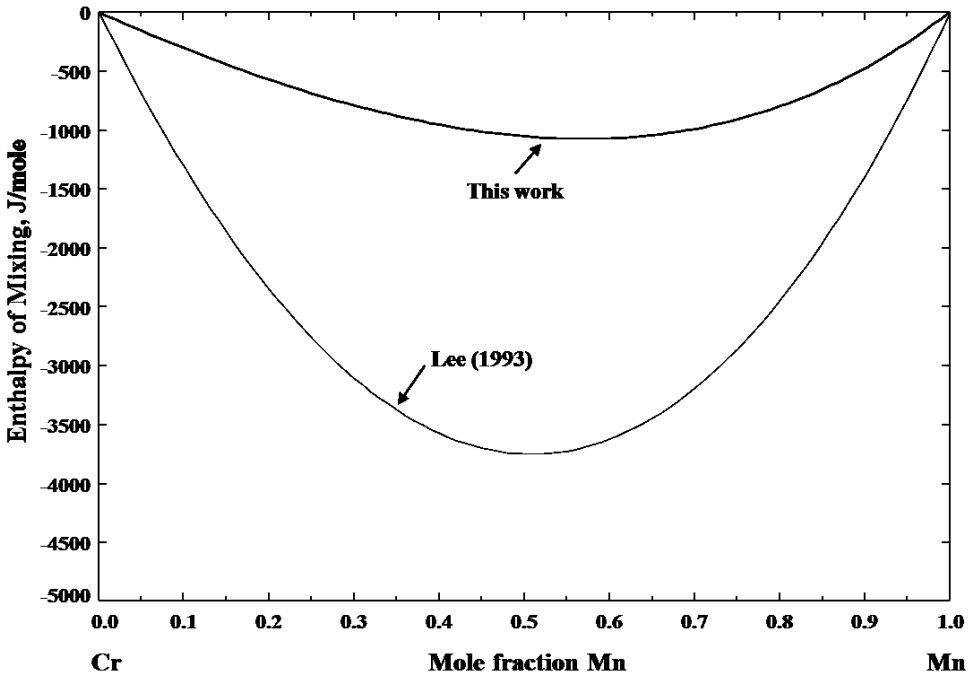

Fig. 5.4 Calculated enthalpy of mixing of the liquid Cr-Mn phase at 1900 °C compared to the calculated one from Lee [11].

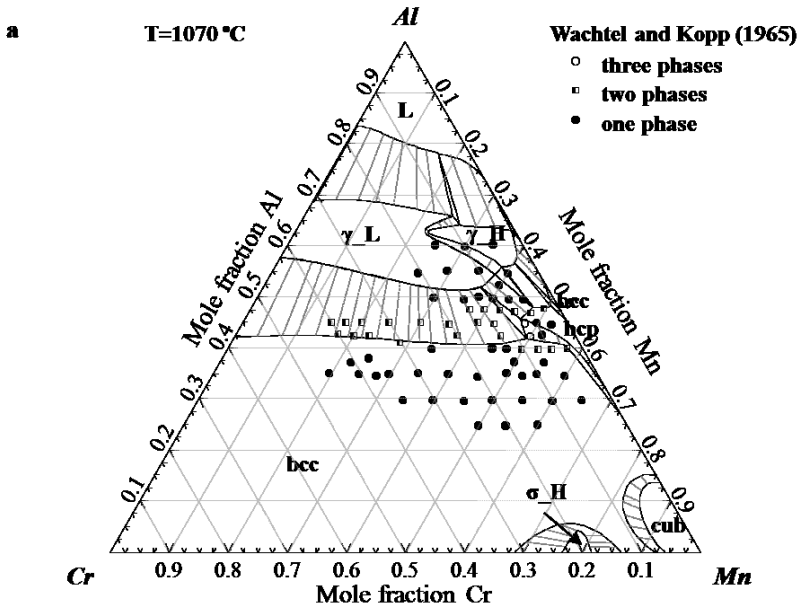
a
T=1070 °C
Al
Wachtel and Kopp (1965)
three phases
two phases
one phase
L
γ_L
γ_H
bcc
hcp
bcc
σ_H
cub
Mole fraction Al
Mole fraction Mn
Mole fraction Cr
Cr
Mn
0.9 0.8 0.7 0.6 0.5 0.4 0.3 0.2 0.1

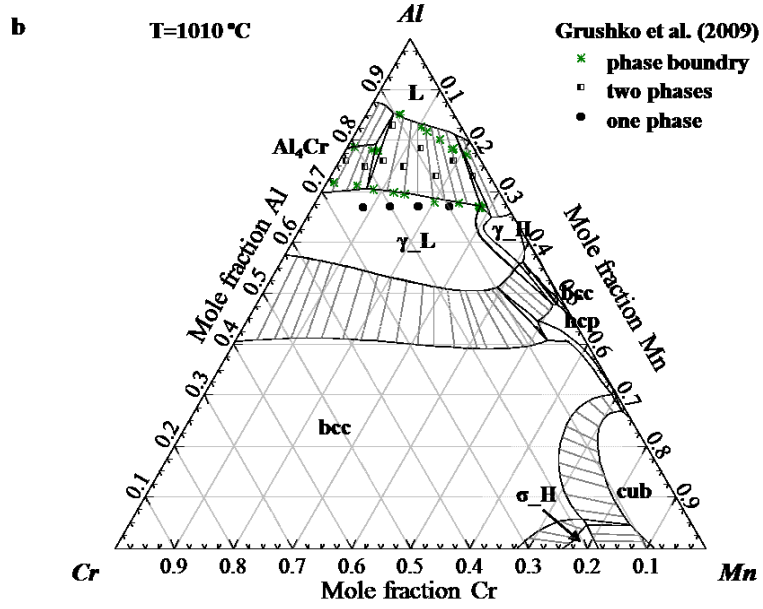
b
T=1010 °C
Al
Grushko et al. (2009)
phase boundry
two phases
one phase
L
Al4Cr
γ_L
γ_H
bcc
hcp
bcc
σ_H
cub
Mole fraction Al
Mole fraction Mn
Mole fraction Cr
Cr
Mn
0.9 0.8 0.7 0.6 0.5 0.4 0.3 0.2 0.1

c

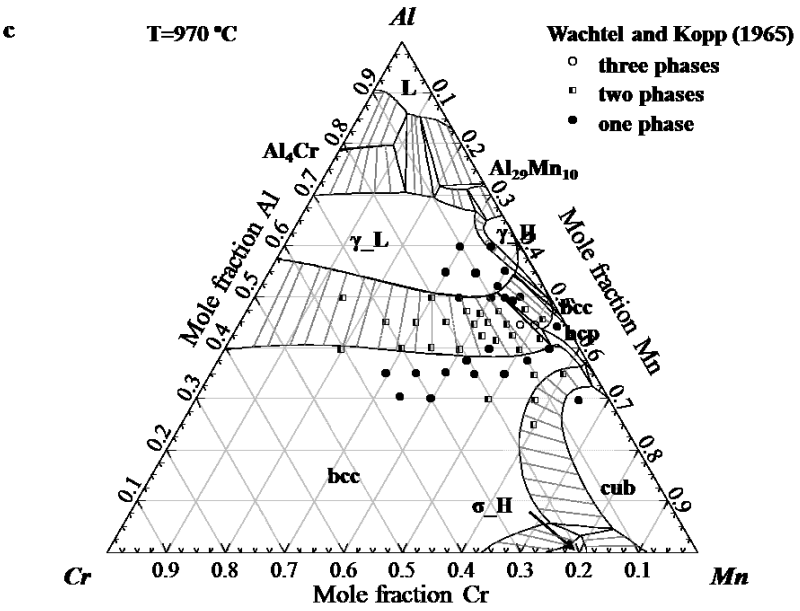
T=970 °C
Al
Wachtel and Kopp (1965)
three phases
two phases
one phase
L
Al4Cr
Al29Mn10
γ_L
γ_H
bcc
hcp
bcc
cub
σ_H
Mole fraction Al
Mole fraction Mn
Mole fraction Cr
Cr
Mn

d

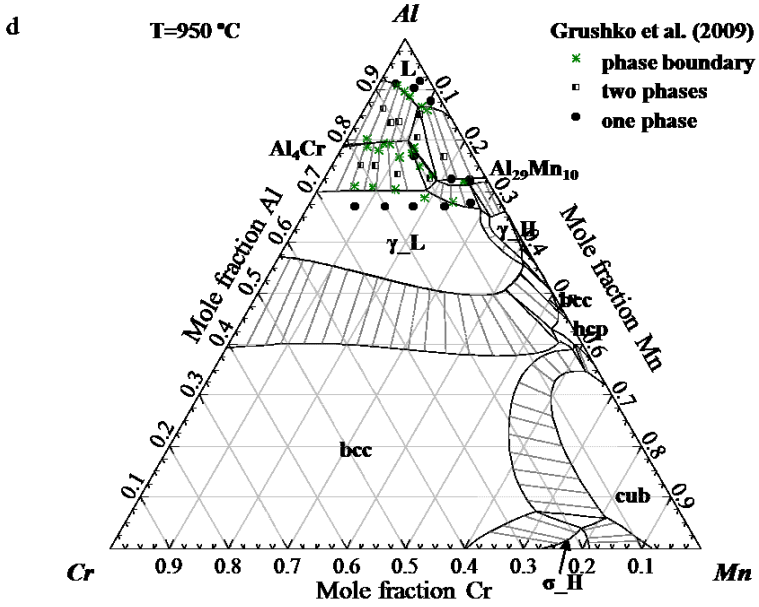
T=950 °C
Al
Grushko et al. (2009)
phase boundary
two phases
one phase
L
Al4Cr
Al29Mn10
γ_L
γ_H
bcc
hcp
bcc
cub
σ_H
Mole fraction Al
Mole fraction Mn
Mole fraction Cr
Cr
Mn

e

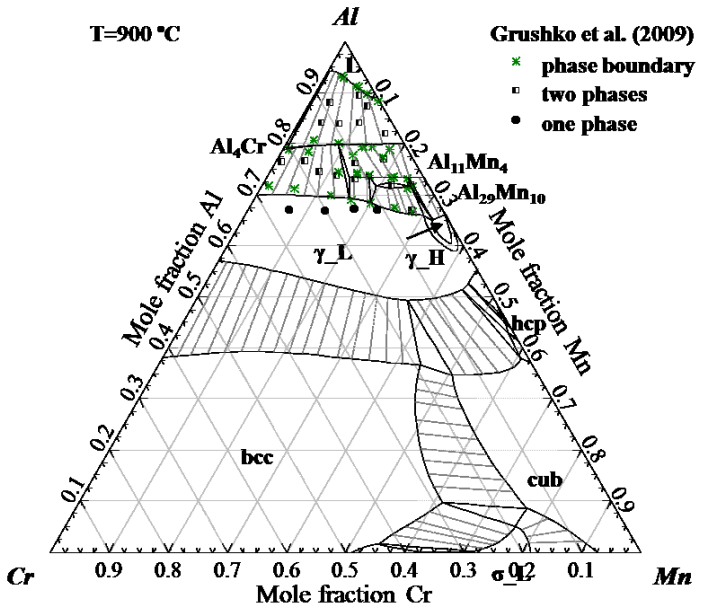
T=900 °C
Al
Cr
Mn
Grushko et al. (2009)
phase boundary
two phases
one phase
L
Al4Cr
Al11Mn4
Al29Mn10
γ_L
γ_H
hcp
bcc
cub
σ_1
Mole fraction Al
Mole fraction Mn
Mole fraction Cr

f

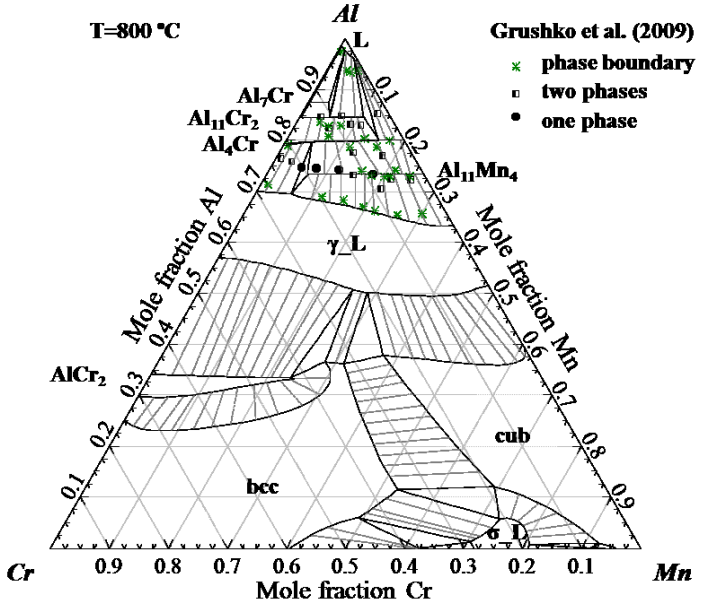
T=800 °C
Al
Cr
Mn
Grushko et al. (2009)
phase boundary
two phases
one phase
L
Al7Cr
Al11Cr2
Al4Cr
Al11Mn4
γ_L
AlCr2
cub
bcc
σ_1
Mole fraction Al
Mole fraction Mn
Mole fraction Cr

g

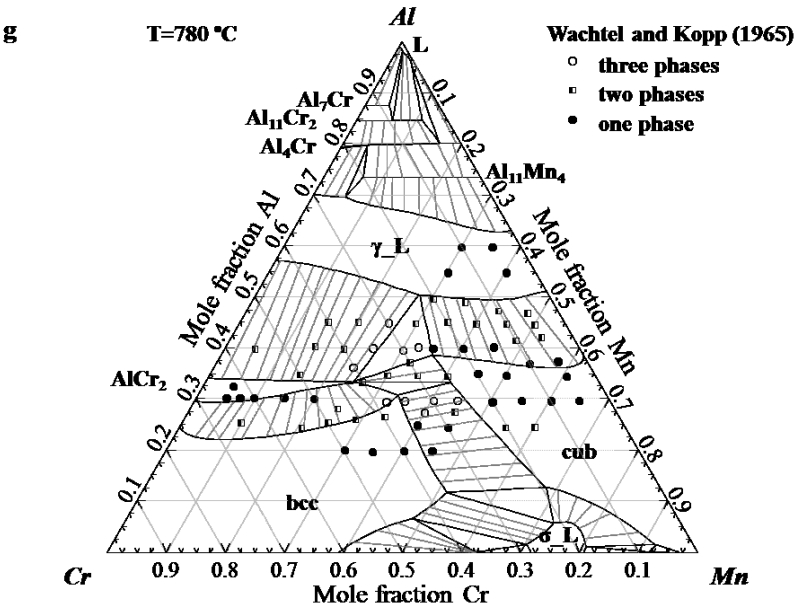
T=780 °C
Wachtel and Kopp (1965)
three phases
two phases
one phase
Al
L
Al7Cr
Al11Cr2
Al4Cr
Al11Mn4
γ_L
AlCr2
cub
bcc
σ_L
Cr
Mn
Mole fraction Al
Mole fraction Cr
Mole fraction Mn

h

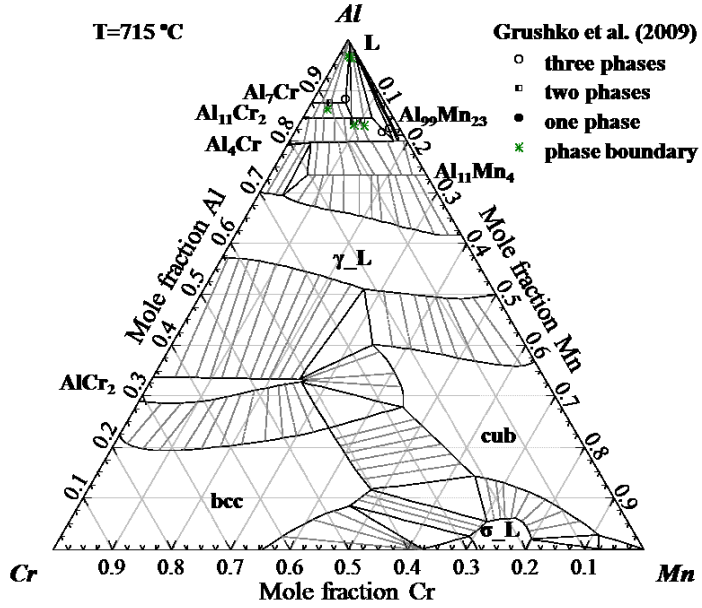
T=715 °C
Grushko et al. (2009)
three phases
two phases
one phase
phase boundary
Al
L
Al7Cr
Al11Cr2
Al4Cr
Al99Mn23
Al11Mn4
γ_L
AlCr2
cub
bcc
σ_L
Cr
Mn
Mole fraction Al
Mole fraction Cr
Mole fraction Mn

i

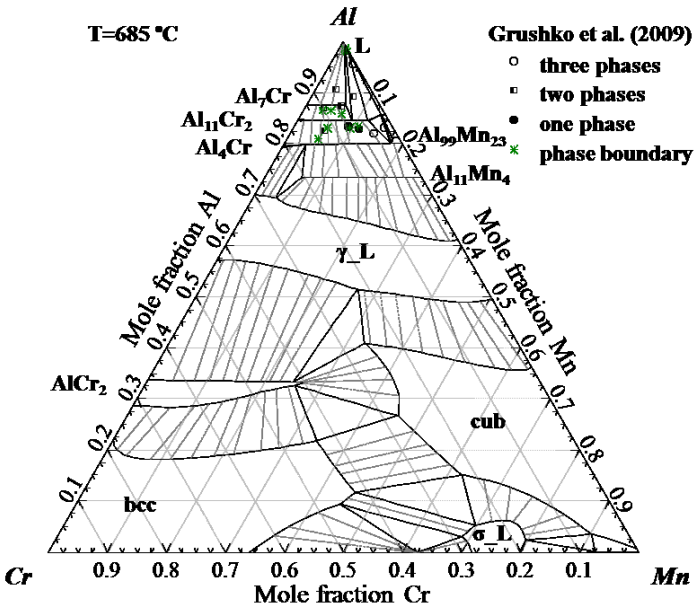
T=685 °C
Al
L
Grushko et al. (2009)
three phases
two phases
one phase
phase boundary
Al7Cr
Al11Cr2
Al4Cr
Al99Mn23
Al11Mn4
γ_L
cub
AlCr2
bcc
σ_L
Mole fraction Al
Mole fraction Mn
Cr
Mn
Mole fraction Cr

j

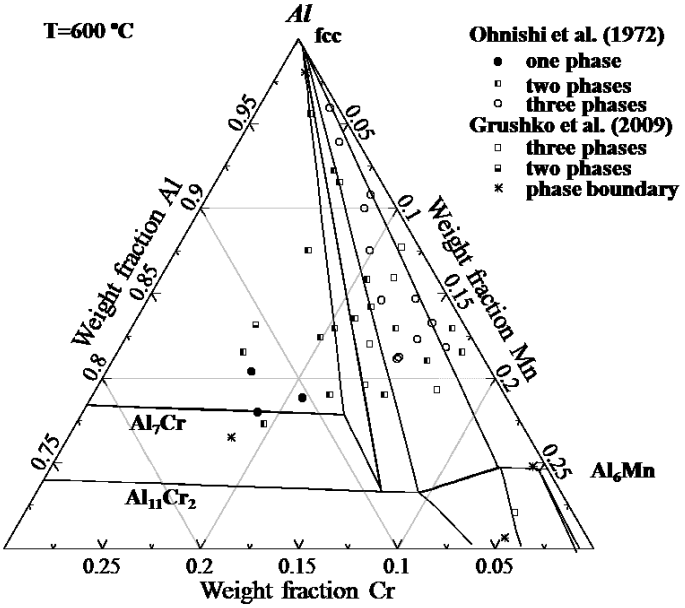
T=600 °C
Al
fcc
Ohnishi et al. (1972)
one phase
two phases
three phases
Grushko et al. (2009)
three phases
two phases
phase boundary
Weight fraction Al
Weight fraction Mn
Al7Cr
Al11Cr2
Al6Mn
Weight fraction Cr

k

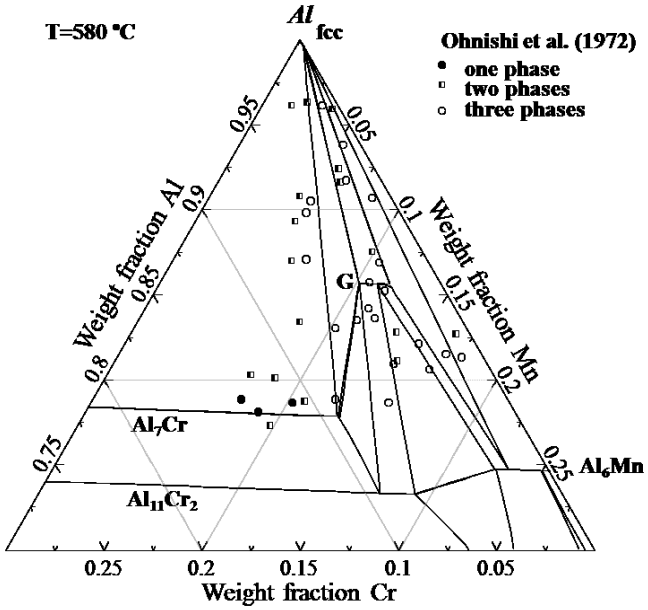
T=580 °C
Al fcc
Ohnishi et al. (1972)
one phase
two phases
three phases
Weight fraction Al
Weight fraction Mn
Weight fraction Cr
G
Al7Cr
Al11Cr2
Al6Mn
0.95
0.9
0.85
0.8
0.75
0.05
0.1
0.15
0.2
0.25

m

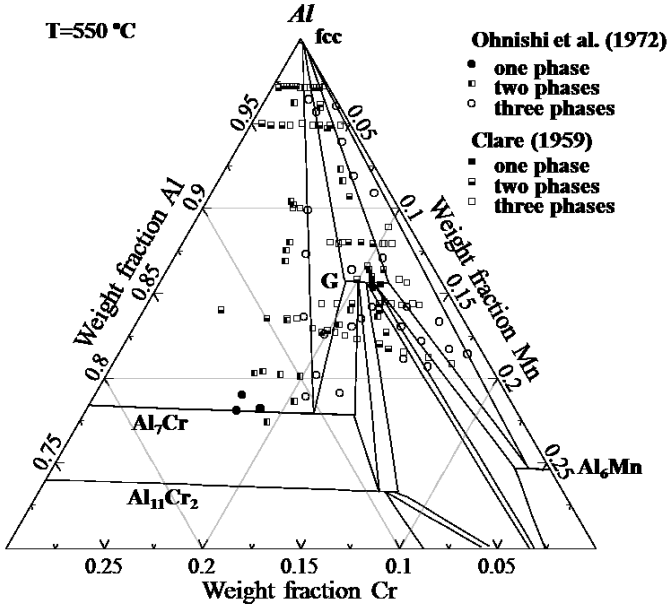
T=550 °C
Al fcc
Ohnishi et al. (1972)
one phase
two phases
three phases
Clare (1959)
one phase
two phases
three phases
Weight fraction Al
Weight fraction Mn
Weight fraction Cr
G
Al7Cr
Al11Cr2
Al6Mn
0.95
0.9
0.85
0.8
0.75
0.05
0.1
0.15
0.2
0.25

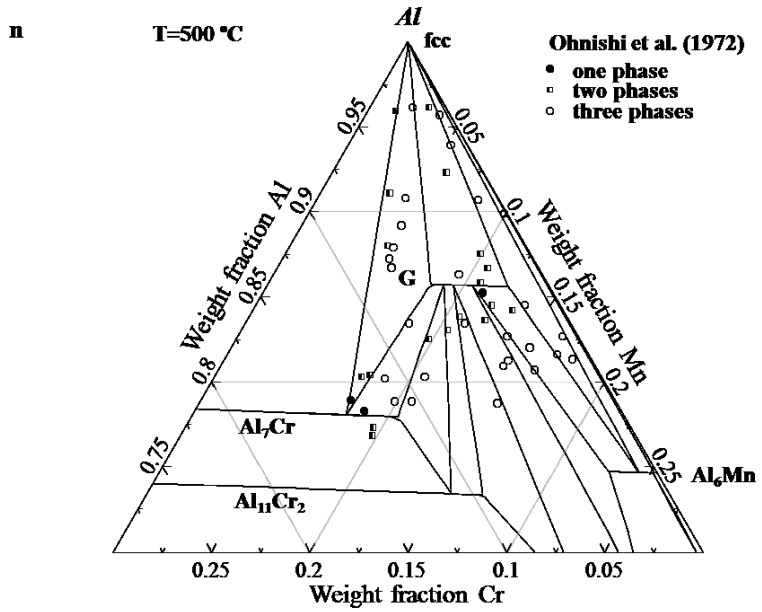

Fig. 5.5 Calculated isothermal sections of the Al-Cr-Mn system compared with the experimental data at different temperatures. (a) 1070 °C, (b) 1010 °C, (c) 970 °C, (d) 950 °C, (e) 900 °C, (f) 800 °C, (g)780 °C, (h) 715 °C, (i) 685 °C, (j) 600 °C, (k) 580 °C, (m) 550 °C, and (n) 500 °C.

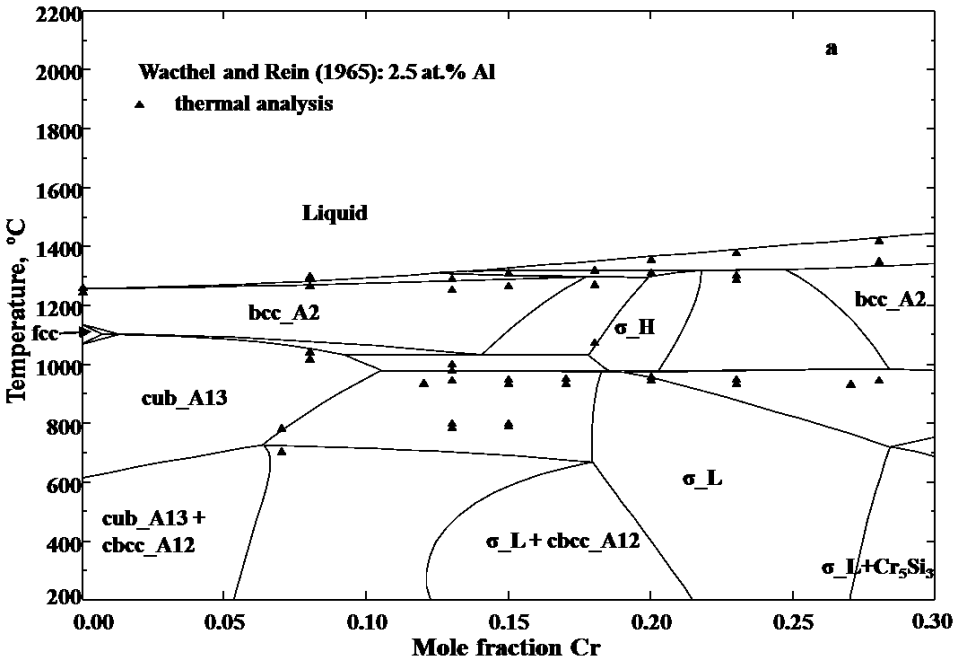
a
Wacthel and Rein (1965): 2.5 at.% Al
thermal analysis
Liquid
bcc_A2
fcc
σ_H
bcc_A2
cub_A13
σ_L
cub_A13 +
cbcc_A12
σ_L + cbcc_A12
σ_L+Cr5Si3
Temperature, °C
Mole fraction Cr

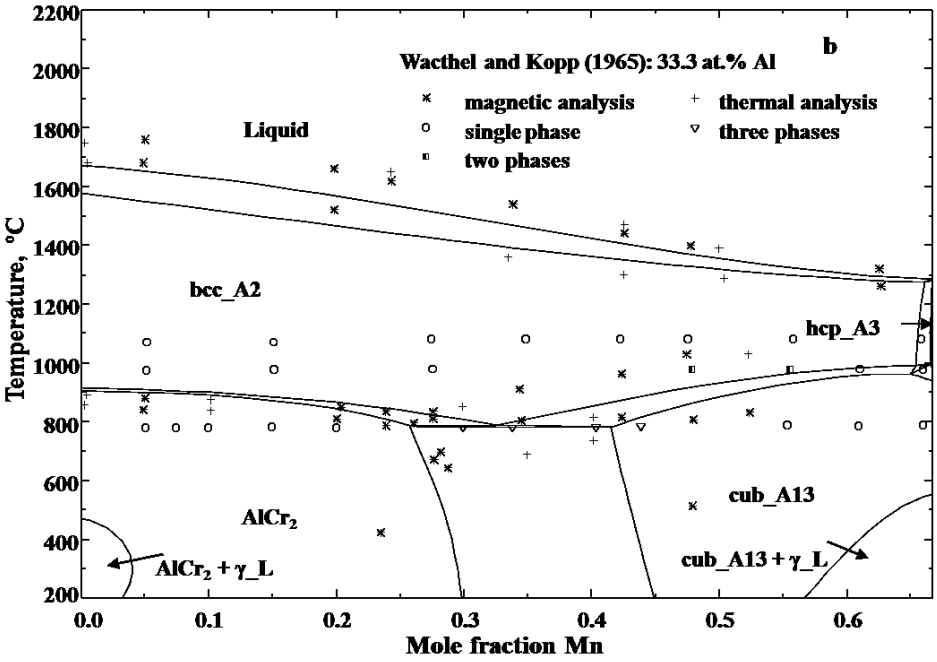
b
Wacthel and Kopp (1965): 33.3 at.% Al
magnetic analysis
thermal analysis
single phase
three phases
two phases
Liquid
bcc_A2
hcp_A3
cub_A13
AlCr2
AlCr2 + γ_L
cub_A13 + γ_L
Temperature, °C
Mole fraction Mn

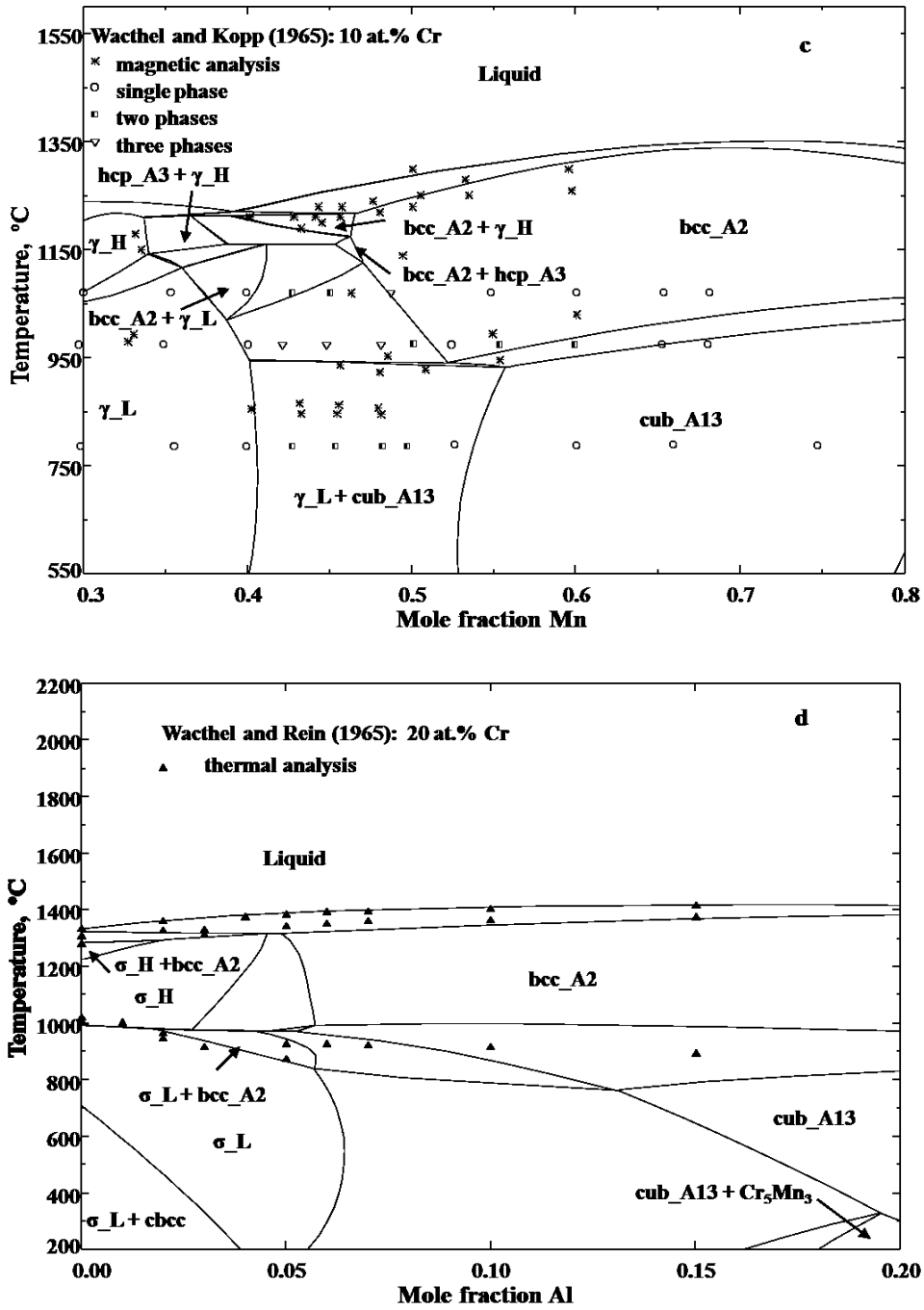

Fig. 5.6 Calculated isoplethal sections of the Al-Cr-Mn system at (a) 2.5 at.% Al, (b) 33.3 at.% Al, (c) 10 at.% Cr, and (d) 20 at.% Cr.

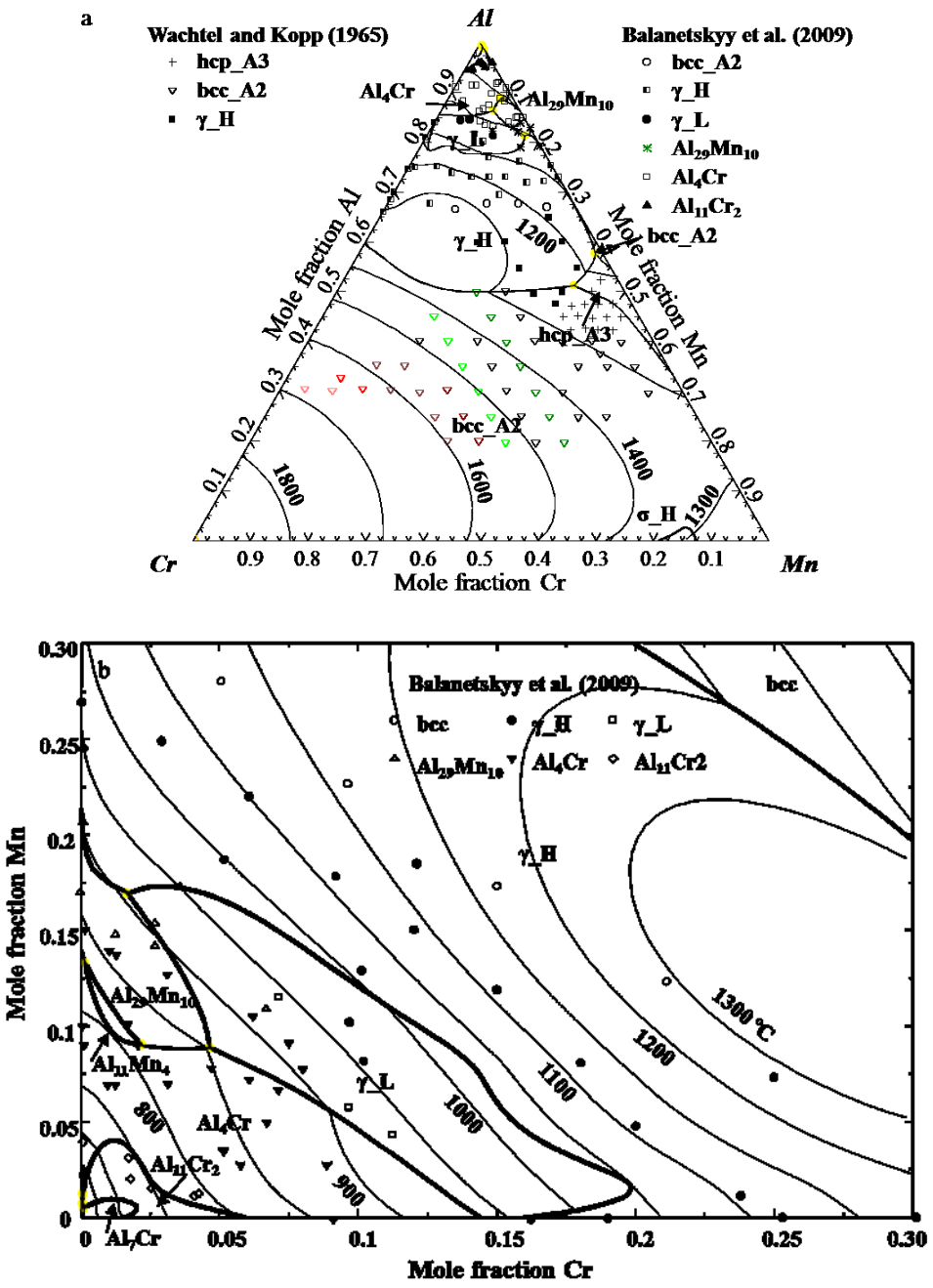

Fig. 5.7 Calculated liquidus projection of the Al-Cr-Mn system compared with the experiment data. (a) The entire composition range, and (b) the enlarged Al rich region.

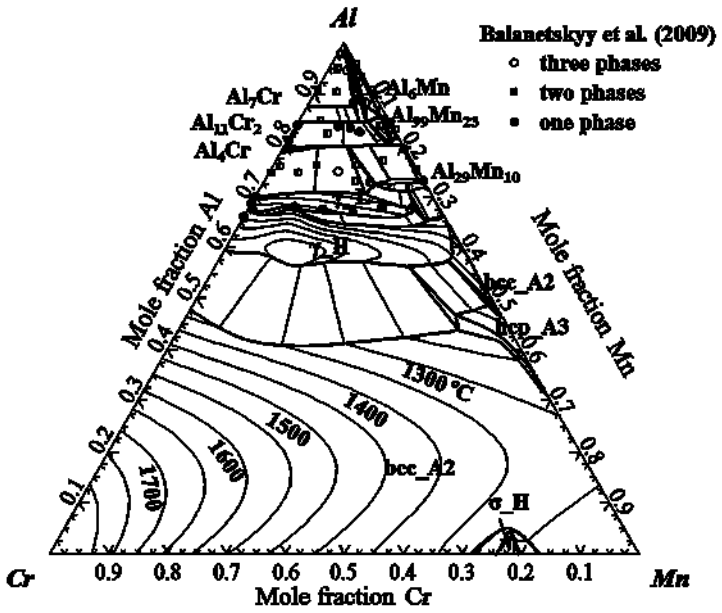

Fig. 5.8 Calculated solidus projection of the Al-Cr-Mn system compared with the experimental data by Balanetskyy et al. [26].

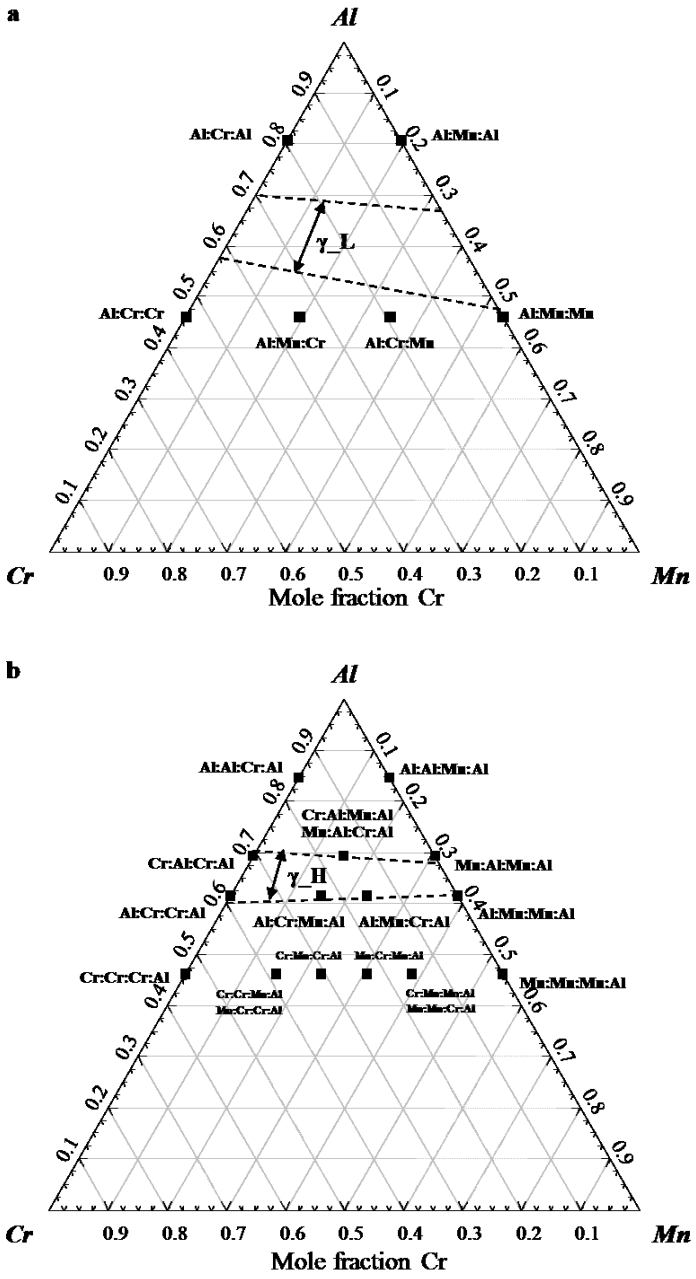

Fig. 5.9 Schematic diagrams of the end members for CEF used in this study, and stability ranges of the γ_L and γ_H phases. (a) The γ_L phase, and (b) the γ_H phase.

Chapter 6 Thermodynamic assessments of the Cr-Si and Al-Cr-Si systems

Senlin Cui and In-Ho Jung

Department of Mining and Materials Engineering, McGill University, 3610 University Street, Montreal, Quebec, H3A 0C5, Canada

Abstract

Thermodynamic assessments for the Cr-Si and Al-Cr-Si systems were conducted on the basis of the critically evaluated thermodynamic and phase diagram data available in the literature. The Modified Quasi-chemical Model (MQM) was utilized to model the Gibbs energy of the liquid phase and the Compound Energy Formalism (CEF) was used to model the solid solution phases. Comprehensive comparison between the model-predicted and the experimentally measured phase diagram and thermodynamic property data indicates that the optimized thermodynamic descriptions for the Cr-Si and Al-Cr-Si systems are reliable. Accurate thermodynamic descriptions obtained in the present work in the form of a set of Gibbs energies of all the solid and liquid phases, and the model parameters can be used to calculate the phase equilibria and thermodynamic properties in the Al-Cr-Si system at any composition and temperature.

Key words:

The Cr-Si system; the Al-Cr-Si system; phase diagram; thermodynamic modeling.

6.1 Introduction

Al-Si alloys have considerable potential applications in automotive industry. For instance, they can be used as piston pins, pistons, and connecting rods in the automotive engines. These alloys are characterized by low thermal expansion coefficient, good wear and corrosion resistance, high fatigue strength, lightness in weight, and ease of welding [1]. The high volume fraction of primary Si phase particulates contributes to these good properties. However, the formation of coarse brittle primary Si phase has detrimental effect on the mechanical behavior of high Si Al-Si alloys. In addition, Fe as a normal impurity in Al alloys can form certain Fe bearing needle-like phases which deteriorate the mechanical properties such as strength and ductility. The addition of some modifiers like Na, Nd, and rare earth elements can refine the primary Si phase during solidification. The addition of small amount of Cr/Mn or Mn and Cr can also strikingly refine the Fe-bearing needle-like phases in Al-Si alloys into short-plate shape or even into granular α-Al(Fe, Mn, Cr)Si phases [2-4].

The mechanical properties of Al alloys are related to its microstructure and structure of components. The microstructural evolution in Al alloys is basically determined by their thermo-chemical properties and diffusivities of alloying elements. To design Al-Si alloys with controlled primary Si and Fe-bearing phases, it is of fundamental importance to understand the phase relation and thermodynamic properties of Al-Si alloys. As Cr is one of the structure modifiers for Al alloys, it is necessary to critically study the thermodynamics of the Al-Cr-Si system.

Knowledge about the three sub-systems is the prerequisite for the accurate description of the Al-Cr-Si system. Well-established thermodynamic descriptions of the Al-Cr [5], Al-Si [6], and Cr-Si [7] systems are already available in the literature. However, the thermodynamic properties of the Cr-Si liquid phase were described by Chen et al. [7] using the Bragg Williams random mixing model. For consistency of the liquid solution, the liquid Cr-Si solution is re-optimized using the Modified Quasi-chemical Model (MQM) in this study and then a new thermodynamic modeling for the entire Al-Cr-Si ternary system is carried out.

6.2 Critical evaluation of literature information

6.2.1 The Cr-Si system

The literature information for the Cr-Si system was firstly reviewed by Gokhale and Abbaschian [8]. Okamoto [9] briefly updated the Cr-Si phase diagram on the basis of the thermodynamic modeling carried out by Coughanowr et al. [10]. Later, the phase diagram of the Cr-Si system was redraw by Okamoto [11] according to the new thermodynamic assessment by Du and Schuster [12]. The first version of the thermodynamic modeling for the Cr-Si system was done by Coughanowr et al. [10]. Four binary phases, Cr_3Si, Cr_5Si_3, CrSi, and $CrSi_2$, form in the Cr-Si system. The Cr_3Si and $CrSi_2$ phases were modeled as solid solution phases, while the CrSi and $CrSi_2$ phases were modeled as stoichiometric compounds. Besides, the polymorphic transition between the α_Cr_5Si_3 and β_Cr_5Si_3 phases was neglected. Later, Du and Schuster [10] re-optimized the Cr-Si system by also including the new thermodynamic data from Meschel and Kleppa [13] and their own experimental results in the CrSi-Si partial system. The β_Cr_5Si_3 phase was also considered in their thermodynamic modeling. Recently, Chen et al. [7] re-examined the melting behavior of the Cr_5Si_3 phase to be form via a peritectic melting reaction. The thermodynamic description of the Cr-Si system by Du and Schuster [12] was updated to meet this new feature. A summary of the crystal structure information of all the stable compounds in the Cr-Si system is listed in Table 6.1.

The available phase diagram measurements include Kurnakov [14], Kieffer et al. [15], Goldschmidt and Brand [16], Dudkin and Kuznetsova [17], Dubrovskaya and Gel'd [18], Sevchnikov et al. [19], Chang [20], Voronov et al. [21], Kocherzhinsky [22], Pyatkova et al. [23], Würker et al. [24], and Du and Schuster [12]. Kurnakov [14] measured the phase equilibria in the Cr-Si system by means of thermal analysis and microstructural analysis. Four phases, Cr_3Si, Cr_2Si, CrSi, and $CrSi_2$, were reported to form congruently and a primitive version of phase diagram was reported. In addition, the solubilities of Si in Cr from 700 to 1400 °C were reported. Later, Kieffer et al. [15] investigated the phase relation in the binary Cr-Si system using thermal analysis, microanalysis, and x-ray diffraction (XRD) analysis. The crystal structures of the Cr_3Si, CrSi, Cr_5Si_3, and $CrSi_2$ phases were reported. Sevchnikov et al. [19] measured the equilibrium phase

diagram of the Cr-Si system in the whole composition range by quenching experiments followed by XRD, and metallographic analysis, and differential thermal analysis (DTA). Chang [20] also measured the entire Cr-Si phase diagram using melting point measurements, DTA, XRD, and metallographic analysis. Recently, Du and Schuster [12] re-analyzed the experimental data by Chang [20] and certain corrections on the proposed Cr-Si phase diagram by Chang [20] were made. Kocherzhinsky [22] measured the melting temperatures of all the compounds in the Cr-Si system using DTA: $CrSi_2$ congruently at 1475 ± 5 °C, Cr_5Si_3 congruently at 1720 ± 5 °C, Cr_3Si congruently at 1770 ± 10 °C, and CrSi incongruently at 1475 ± 5 °C. Besides, the invariant temperatures of four three-phase equilibria were detected. Recently, Du and Schuster [12] measured the partial phase diagram of the CrSi-Si system by means of DTA followed by XRD phase analysis. The melting point of the $CrSi_2$ phase was measured to be 1438 ± 2 °C.

The homogeneity of Cr_3Si were measured by Pyatkova et al. [23] to be 22.5 to 25.5 at.% Si at 1000 °C using XRD and metallographic analysis, Jurisch and Behr [25] to be 23.3 to 24.8 at.% Si at 1000 °C using single crystal XRD analysis, and Sevchnikov et al. [19] at the temperature between 1100 and 1600 °C. The data reported by Pyatkova et al. [23] and Jurisch and Behr [25] are in good agreement but show deviation from the results by Sevchnikov et al. [19]. The measurements by Pyatkova et al. [23] and Jurisch and Behr [25] were considered as more reliable in this study.

The homogeneity range of the $CrSi_2$ phase was measured by Dudkin and Kuznetsova [17] to be 66.44 to 67.00 at.% Si according to the electrical conductivity measurements, Dubrovskaya and Gel'd [18] to be from 65.56 to 67.17-67.61 at.% Si at 1150 °C by means of metallographic analysis, XRD, and densitometric measurements, Voronov et al. [21] between 1100 and 1300 °C using microanalysis. The measured solubilities of $CrSi_2$ from Dudkin and Kuznetsova [17], Dubrovskaya and Gel'd [18], and Voronov et al. [21] are consistent with each other.

Würker et al. [24] measured the solubility of Cr in Si to be less than 6×10^{-6} at.% Cr by means of the radiochemical and electrical methods from 900 to 1280 °C. And the solubility of Cr in Si is so small that can be neglected in the current optimization.

The heat capacities and heat contents were measured by Golutvin and Liang [26], Kalishevich et al. [27], Kalishevich et al. [28], and Surikov et al. [29]. More specifically, Golutvin and Liang [26] measured the heat contents of the Cr_3Si, Cr_5Si_3, CrSi, and $CrSi_2$ phases using bomb calorimetry at 298-873 K. Kalishevich et al. [28] measured the heat capacities of Cr, Si, Cr_3Si, Cr_5Si_3, CrSi, and $CrSi_2$ at 54 to 300 K using an adiabatic calorimeter. Later, Kalishevich et al. [27] measured the heat capacities and the heat contents of Cr_5Si_3 and $CrSi_2$ in the temperature range of 55 to 300 K using an adiabatic calorimeter, and in the temperature range of 400 to 2000 K using an adiabatic mixing calorimeter. Surikov et al. [29] measured the heat capacities of the Cr_3Si phase from 10 to 300 K using an adiabatic calorimeter. Schlesinger [30] recommended the heat contents of the Cr_2Si, CrSi, and Cr_5Si_3 phases based on the critically evaluated literature data.

The heat of formations of the Cr_3Si and Cr_5Si_3 phases at 298 K were measured by Golutvin and Liang [26] using bomb calorimetry and Meschel and Kleppa [13] using high temperature direct synthesis calorimetry. These data were also estimated by Eremenko et al. [31] and Lukashenko et al. [32] from the electron motive force (emf) measurements data, Chart [33] from the Knudsen effusion vapor pressure data. The heat of formation of the CrSi phase was measured by Golutvin and Liang [26] using bomb calorimetry and Meschel and Kleppa [13] using high temperature direct synthesis calorimetry. It was also derived by Eremenko et al. [34], Eremenko et al. [31], and Lukashenko et al. [32] from their emf data, Chart [33] from the Kundsen effusion vapor pressure data, while the formation enthalpy of the $CrSi_2$ phase was investigated by Golutvin and Liang [26] using bomb calorimetry and Topor and Kleppa [35] using a high temperature mixing calorimeter. It was also derived by Eremenko et al. [34], Eremenko et al. [31], and Lukashenko et al. [32] from the emf data, and Chart [33] from the Knudsen effusion vapor pressure data.

The entropy of Cr_3Si at 298 K was derived by Kalishevich et al. [28] and Surikov et al. [29] from the low temperature heat capacity data, Eremenko et al. [31] and Lukashenko et al. [32] from the emf measurements, Chart [33] from the vapor pressure measurement data. The entropy of Cr_5Si_3 at 25 °C was derived by Kalishevich et al. [28] from the low temperature heat capacity data, Eremenko et al. [31] and Lukashenko et al. [32] from the emf measurements, Chart [33] from the vapor pressure measurement data. The entropy of CrSi at 298 K was derived by Kalishevich et al. [28] from the low temperature heat capacity data, Eremenko et al. [34], Eremenko et al. [31], and

Lukashenko et al. [32] from the emf measurements, Chart [33] from the vapor pressure data. And the entropy of $CrSi_2$ at 298 K was determined by Kalishevich et al. [28] from the low temperature heat capacity data, Eremenko et al. [34], Eremenko et al. [31], and Lukashenko et al. [32] from the emf measurements data, and Chart [33] from the vapor pressure data.

Thermodynamic properties such as Gibbs energies of formation for the intermetallic phases, activity, and enthalpy of mixing were investigated by many researchers [31-34, 36-38]. Eremenko et al. [31, 34] measured the Gibbs energies of formation of the $CrSi_2$, CrSi, Cr_5Si_3, and Cr_3Si phases by emf measurements in the temperature range between 700 and 850 °C. Lukashenko et al. [32] measured the Gibbs energies of CrSi, Cr_5Si_3, and Cr_3Si by emf measurements at 680-860 °C, and presented the Gibbs energies of formation of CrSi, Cr_5Si_3, and Cr_3Si at 777 °C. The Gibbs energies of formation of the intermetallic phases in the Cr-Si system were measured at 1377 °C by Chart [33] using the Knudsen effusion vapour pressure technique. The same technique was utilized by Riegert et al. [36] to measure the thermodynamic properties in the liquid Cr-Si alloys at 1627 °C in the composition range from 28.7 to 55.8 at.% Cr and Myers et al. [37] to measure the activities of Cr and Si at 1227 °C. Esin et al. [38] measured the partial and integral enthalpy of mixing of the liquid Cr-Si alloys up to 68 at.% Cr at 1723 °C using a high temperature calorimeter.

6.2.2 The Al-Cr-Si system

Thermodynamic modeling of the Al-Cr-Si system was previously conducted by Liang et al. [39] and Hu et al. [40]. These two sets of thermodynamic assessments can give very good descriptions of most of the reliable experimental data. The phase diagram of this ternary system or/and crystal structures of the ternary compounds were measured by Mondolfo [41], Pratt and Raynor [42, 43], Robinson [44, 45], Brukl et al. [46], Esslinger et al. [47], Gupta [48], Weitzer et al. [49, 50], Chen et al. [51], and Zhou et al. [52].

Mondolfo [41] reported two compounds α (AlCrSi) and β (AlCrSi). The α (AlCrSi) phase is of hexagonal structure with a chemical composition of Al_6CrSi and the β (AlCrSi) is of monoclinic structure with Al_4CrSi_2. A ternary eutectic reaction Liquid = (Al) + (Si) + α (AlCrSi) was detected at 575 °C. Later, Pratt and Raynor [42, 43] studied the phase relation in the Al rich

corner. The primary crystallization behavior of various alloys was measured by examining slowly cooled alloys, and an isothermal section in the Al rich corner at 550 °C was proposed. Two compounds α (AlCrSi) and β (AlCrSi) were found. The α (AlCrSi) phase showed an ideal atomic arrangement of Al_3CrSi. While the β (AlCrSi) phase has an approximate composition of 45 wt.% Cr and 42 wt.% Si. Robinson [44, 45] determined the crystal structure of α (AlCrSi) to be $Al_{13}Si_4Cr_4$ (F-43m) and the hexagonal structure β (AlCrSi) to be $Al_6Cr_3Si_6$ using single crystal powder XRD. Brukl et al. [46] measured the partial isothermal section up to above 30 at.% Cr of the Al-Cr-Si system at 1300 °C. The solubility of Al in $CrSi_2$ was determined to be about 25 at.% Al. Esslinger et al. [47] presented two isoplethal sections at 5 wt.% Cr and 4 wt.% Si based on their DTA measurements.

Recently, Gupta [48] studied the microstructure and composition of the binary and ternary intermetallics in the Al-Cr-Si system using ternary diffusion couples made of Cr and Al-Si eutectic alloys. The $CrSi_2$ phase dissolved up to 20 at.% Al. The ternary isothermal sections at 800, 900, 1000, and 1100 °C were constructed based on the electron probe microanalysis (EPMA) results. A new quasic-peritectic reaction Liquid + $CrAl_4$ = $Al_{13}Cr_4Si_4$ (τ1) + $Al_{11}Cr_2$ was observed between 680 and 710 °C. The peritectic reaction Liquid + $CrSi_2$ + Cr_2Al_{11} = $Al_{13}Cr_4Si_4$ (τ1) was also modified to be Liquid + $CrSi_2$ + $CrAl_4$ = $Al_{13}Cr_4Si_4$ (τ1). According to Gupta [48], no ternary compound appeared above 800 °C. On the contrary, Weitzer et al. [49, 50] reported a ternary τ3 phase exist in the Al-Cr-Si system at 800 °C. The reported composition range of the τ3 phase was from $Al_{61}Cr_{27}Si_{12}$ to $Al_{65}Cr_{27}Si_8$. They also determined the crystal structure of the τ3 phase. Chen et al. [51] presented a detailed investigation of the isothermal section at 800 °C using XRD and SEM analysis for the alloy samples. Four ternary phases were identified: τ1 ($Cr_4Al_{13}Si_4$), τ2 (Cr_3Al_9Si), τ3 ($Cr_4(Al, Si)_{11}$), and τ4 ($Al_{58}Cr_{31.5}Si_{10.5}$). They also reported that the composition of τ3 varies from $Al_{61}Cr_{27}Si_{12}$ to $Al_{65}Cr_{27}Si_8$ and τ4 is stable above 1000 ºC. The solubility of Al in $CrSi_2$ was measured to be up to 25 at.% Al, and the solubility of Si in Cr_5Al_8 and $CrAl_4$ was reported to be about 1.8 at.% Si and 10.4 at.% Si, respectively. They did not observe the binary Al_7Cr phase at 800 ºC. Most recently, Zhou et al. [52] determined the isothermal section at 700 °C in the Al-Cr-Si system by means of SEM and XRD analysis for the equilibrated alloy samples. Similar to Chen et al. [51], the stable τ1, τ2, and τ3 ternary phases was observed at 700 °C. However, the $Al_{11}Cr_2$ phase was not observed. The solubility of Si in $AlCr_2$ was very low specially,

while the solubility of Al in $CrSi_2$, CrSi, and Cr_5Si_3 at 700 °C reached 25.9, 3.5, and 9.0 at.%, respectively.

According to the present evaluation, the measured phase diagram information from Esslinger et al. [47], Chen et al. [51], Zhou et al. [52], and Gupta [48] are applicable for the thermodynamic optimization. However, as discussed above, the isothermal sections presented by Gupta [48] did not show the presence of any ternary compounds, and the Al_8Cr_5 and Al_9Cr_4 phases were treated separately which is inconsistent with other result [5]. Thus, the measured isothermal sections by Gupta [48] were only used to adjust the high temperature phase relation and the stability of the liquid phase. A summary of the crystal structure information of the ternary compounds is presented in Table 6.1.

There is no measurement on the thermodynamic properties in the Al-Cr-Si system. Hu et al. [40] reported the enthalpy of formation of τ1 and τ2 at 0 K to be -17.69 and -18.07 kJ/mole-atoms, respectively, from first principles calculations with the generalized gradient approximation (GGA).

6.3 Thermodynamic modeling

6.3.1 Liquid phase

The Modified Quasi-chemical Model (MQM) proposed by Pelton et al. [53, 54], which considers the short range ordering of nearest neighbour atoms, was applied to describe the Gibbs energy of the liquid phase. MQM was successfully applied to many ionic solutions [55] which exhibiting strong short range ordering behaviour. MQM has been also applied to model the liquid phase of metallic system [5] which exhibits a strong short range ordering behavior. Assume the atoms A and B in the liquid phase occupy a quasi-lattice in the liquid solution, then the following pair exchange reaction can be written:

$$(A\text{-}A) + (B\text{-}B) = 2(A\text{-}B) : \quad \Delta g_{AB} \tag{6.1}$$

where (*A*-*A*), (*B*-*B*), and (*A*-*B*) are the first-nearest-neighbor atom pairs. Δg_{AB} is the non-configurational Gibbs energy change for the formation of two moles of (*A*-*B*) pairs. The Gibbs energy of a binary solution can be written as:

$$G = n_A G_A^o + n_B G_B^o - T\Delta S^{config} + (n_{AB}/2)\Delta g_{AB} \tag{6.2}$$

where n_i is the number of moles of *i* atoms, and n_{ij} is the number of moles of (*i*-*j*) pairs. ΔS^{config} is the configurational entropy of mixing given by a random distribution of the three types of pairs (*AA*, *BB*, and *AB*) in the one-dimensional Ising approximation, and is given as:

$$\Delta S^{config} = -R(n_A \ln x_A + n_B \ln x_B) - R\left[n_{AA} \ln\left(\frac{x_{AA}}{Y_A^2}\right) + n_{BB} \ln\left(\frac{x_{BB}}{Y_B^2}\right) + n_{AB} \ln\left(\frac{x_{AB}}{2Y_A Y_B}\right)\right] \tag{6.3}$$

where x_i is the mole fraction of *i* atoms, x_{ij} is the pair fraction, and Y_i is the coordination equivalent fraction defined as:

$$x_i = n_i/(n_A + n_B) \tag{6.4}$$

$$x_{ij} = n_{ij}/(n_{AA} + n_{BB} + n_{AB}) \tag{6.5}$$

$$Y_i = x_{ii} + \frac{1}{2}(x_{ij}) \tag{6.6}$$

The excess Gibbs energy, Δg_{AB}, is always expanded as a polynomial in terms of pair fractions and is given as:

$$\Delta g_{AB} = \Delta g_{AB}^0 + \sum_{i\geq 1} g_{AB}^{i0}(x_{AA})^i + \sum_{j\geq 1} g_{AB}^{0j}(x_{BB})^j \tag{6.7}$$

where Δg^{0}_{AB}, g^{i0}_{AB}, and g^{0j}_{AB} are the model parameters which can be a function of temperature. The coordination number of component *i*, Z_i, is related to the number of atoms and the number of pairs by: $Z_i n_i = 2n_{ii} + \sum_{j \neq i} n_{ij}$.

In multicomponent system, composition dependent coordination numbers of element *A* were introduced to provide flexibility and permit the independent chosen of the composition of maximum short range ordering in each binary subsystem,

$$\frac{1}{Z_A} = \frac{1}{2n_{AA} + \sum_{i \neq A} n_{Ai}} \left(\frac{2n_{AA}}{Z^{A}_{AA}} + \sum_{i \neq A} \frac{n_{Ai}}{Z^{A}_{Ai}} \right) \tag{6.8}$$

where Z^{A}_{Ai} is the value of Z_A when all the nearest neighbors of atom *A* are atoms *i*. The maximum short range ordering in each binary subsystem is determined by the ratio of Z^{A}_{AB} / Z^{B}_{BA} .

In MQM, the Gibbs energy of a ternary liquid solution can be predicted by the geometric extrapolation model from the Gibbs energy of sub-binary solutions. Typically, the asymmetric Kohler extrapolation technique or asymmetric Toop extrapolation technique can be used. Considering the thermodynamic properties of each sub-binary liquid phase, the Toop type of extrapolation technique [53, 54] is applied to the Al-Cr-Si system with Al as an asymmetric component. The liquid solutions of Al-Cr and Al-Si are less negatively deviated from idea solution behavior, while the liquid Cr-Si is very negatively deviated from idea solution behavior. The Gibbs energy of the ternary liquid A-B-C solution can be expressed as follows:

$$G = n_A G^{o}_{A} + n_B G^{o}_{B} + n_C G^{o}_{C} - T\Delta S^{config} + (n_{AB}/2)\Delta g_{AB} + (n_{AC}/2)\Delta g_{AC} + (n_{BC}/2)\Delta g_{BC} \tag{6.9}$$

where each pair formation energy term can be extrapolated as [53, 54]:

$$\Delta g_{AB} = \Delta g^{0}_{AB} + \sum_{(i+j) \geq 1} g^{ij}_{AB} x^{i}_{AA} (x_{BB} + x_{BC} + x_{CC})^{j}$$

$$+\sum_{\substack{i\geq 0\\ j\geq 0\\ k\geq 1}} g^{ijk}_{AB(C)} x^{i}_{AA}(x_{BB}+x_{BC}+x_{CC})^{j}\left(\frac{Y_C}{Y_B+Y_C}\right)^{k} \tag{6.10}$$

and

$$\Delta g_{BC} = \Delta g^{0}_{BC} + \sum_{(i+j)\geq 1} g^{ij}_{BC}\left(\frac{x_{BB}}{x_{BB}+x_{CC}+x_{BC}}\right)^{i}\left(\frac{x_{CC}}{x_{BB}+x_{CC}+x_{BC}}\right)^{j}$$
$$+\sum_{\substack{i\geq 0\\ j\geq 0\\ k\geq 0}} g^{ijk}_{BC(A)}\left(\frac{x_{BB}}{x_{BB}+x_{CC}+x_{BC}}\right)^{i}\left(\frac{x_{CC}}{x_{BB}+x_{CC}+x_{BC}}\right)^{j} Y^{k}_{A} \tag{6.11}$$

where *A* is Al, asymmetric component in the ternary solution, and *B* and *C* are Cr and Si, symmetric components, respectively. The ternary parameters, $g^{ijk}_{AB(C)}$ and $g^{ijk}_{BC(A)}$, can be also added to make more accurate description of the Gibbs energy of the liquid solution.

6.3.2 Solid phases

6.3.2.1 fcc_A1, bcc_A2, and diamond_A4 phases

The molar Gibbs energies of the bcc_A2, fcc_A1, and diamond_A4 (Si) phases are described using the Bragg-Williams random mixing model in the form of Redlich-Kister (R-K) polynomial [56]:

$${}^{o}G^{\phi}_{m} = \sum_{i=1}^{3} x_i\, {}^{o}G^{\phi}_{i} + RT\sum_{i=1}^{3} x_i \ln x_i + \sum_{i=1}^{3}\sum_{j>i}^{3} x_i x_j L^{\phi}_{ij} + \sum_{i=1}^{3}\sum_{j>i}^{3}\sum_{k>j}^{3} x_i x_j x_k L^{\phi}_{ijk} + \Delta G^{mag} \tag{6.12}$$

where x_i is the mole fraction of element *i*, ${}^{o}G^{\phi}_{i}$ is the molar Gibbs energy of pure element *i* with the ϕ state, *R* is gas constant, *T* is temperature in Kelvin, L^{ϕ}_{ij} is the binary interaction parameter,

L_{ijk}^{ϕ} is the ternary interaction parameter, and ΔG^{mag} is a term to taken into account the effect of magnetic contribution to the Gibbs energy. Further, L_{ij}^{ϕ} is expanded into the form of $\sum_{v=0} L_{ij}^{v}(x_i - x_j)^v$ and L_{ijk}^{ϕ} is written as $x_i L_{ijk}^{i} + x_j L_{ijk}^{j} + x_k L_{ijk}^{k}$.

The magnetic contribution term ΔG^{mag} which given by the Hillert-Jarl-Inden model [57] is presented as:

$$\Delta G^{mag} = RT \ln(\beta^{\varphi} + 1) g(\tau^{\varphi}) \tag{6.13}$$

where τ is given by T/T^*, T^* is the critical temperature for magnetic transition. That is, the Curie temperature T_C for ferromagnetic materials or Neel temperature T_N for antiferromagnetic materials. β is the average magnetic moment per mole of atoms expressed in Bohr magnetons. $g(\tau^{\varphi})$ is a polynomial function derived by Hillert and Jarl [57].

6.3.2.2 Other solid solution phases

The well-known compound energy formalism (CEF) [58] was utilized for the description of all the solid phases. The $CrSi_2$ phase is a binary solid solution phase in the Cr-Si system which has considerable Al solubility in the Al-Cr-Si system. A sub-lattice model of $(Cr, Si)_1(Cr, Si)_2$ [7] was used for the binary $CrSi_2$ phase. It may be more reasonable to introduce Al in both sub-lattices because Al atoms mainly substitute Si atoms in this solution according to the phase diagram information. However, Al atom was only introduced in the second sub-lattice to simplify the model, that is the sub-lattice model of $(Cr, Si)_1(Al, Cr, Si)_2$ was utilized for the $CrSi_2$ solution. For the binary β_Cr_5Si_3 phase, the model $Cr_5(Cr, Si)_3$ [7] was accepted. The Cr_3Si phase shows considerable solubility in the ternary system, and was modeled as $(Cr, Si)_3(Al, Cr, Si)_1$ to reproduce a reasonable solubility range in the ternary system. Similarly, the $AlCr_2$, Al_4Cr, γ_H, and γ_L phases were modeled as $(Al, Cr, Si)_2(Al, Cr)_1$, $(Al, Va, Si)_4(Cr)_1$, $(Al, Cr)_2(Al, Cr)_3(Al)_2(Cr)_6$, and

$(Al, Si)_{12}(Cr)_5(Al, Cr, Si)_9$, respectively. The ternary solid solution τ3 is modeled as $(Al, Si)_{11}Cr_4$. As an example, the Gibbs energy of γ_L using CEF is presented as follows:

$$
\begin{aligned}
{}^{o}G_m^{\gamma\_L} &= \sum_{i=1}\sum_{j=1} y_i^{'} y_{Cr}^{''} y_j^{'''}\, {}^{o}G_{i:Cr:j}^{\gamma\_L} + 12RT\sum_{i=1} y_i^{'} \ln y_i^{'} + 9RT\sum_{i=1} y_i^{'''} \ln y_i^{'''} \\
&+ \sum_{i=1}\sum_{j>i}\sum_{k=1} y_i^{'} y_j^{'} y_k^{'''} \sum_{v=0} (y_i^{'} - y_j^{'})^v L_{ij:Cr:k}^{v} + \sum_{i=1}\sum_{j>i}\sum_{k=1} y_k^{'} y_i^{'''} y_j^{'''} \sum_{v=0} (y_i^{'''} - y_j^{'''})^v L_{k:Cr:ij}^{v}
\end{aligned}
\tag{6.14}
$$

where $y_i^{'}$, $y_i^{''}$, and $y_i^{'''}$ are the site fraction of element *i* in the first, second, and third sub-lattice, respectively. ${}^{o}G_{i:Cr:j}^{\gamma\_L}$ is the molar Gibbs energy of the hypothetical compound $i_{12}Cr_5j_9$. $L_{ij:Cr:k}^{v}$ and $L_{k:Cr:ij}^{v}$ are the interaction parameters between *i* and *j* element in the first and third sub-lattice, respectively.

6.3.3 Pure elements and stoichiometric compounds

The temperature dependence of the Gibbs energies of the pure elements and stoichiometric compounds are expressed as:

$$
G_i^o(T) = \Delta H_{298.15}^o + \int_{298.15}^{T} C_P dT - T\left(S_{298.15}^o + \int_{298.15}^{T} \frac{C_P}{T} dT\right) \tag{6.15}
$$

where $\Delta H_{298.15}^o$ and $S_{298.15}^o$ are the molar enthalpy of formaiton and entropy of element *i* at 298.15 K and 1 bar, and C_P is the heat capacity of *i*.

In the present assessment, the Gibbs energy data for the pure elements are taken from the SGTE pure element database compiled by Dinsdale [59]. The Gibbs energies of the stoichiometric compounds are optimized from the experimental heat capacity data, enthalpy of formation, entropy of formation, and phase diagram data. If there is no heat capacity data available, the Neumann-Kopp relation was applied to estimate the heat capacity of that compound. No magnetic

contribution for the binary and ternary compounds were considered in the present ternary Al-Cr-Si system.

6.4 Results and discussions

The thermodynamic parameters for the Cr-Si and Al-Cr-Si system were optimized on the basis of the critically evaluated thermodynamic and phase diagram information available in the literature. All the thermodynamic calculations were performed using the FactSage software [60]. The binary Cr-Si system was firstly revised based on the available experimental data. Then, the ternary Al-Cr-Si system was modeled by combining the thermodynamic descriptions of the Al-Cr [5] and Al-Si [6] systems with the thermodynamic optimization of the Cr-Si system. All the optimized thermodynamic parameters are presented in Table 6.2.

6.4.1 The Cr-Si system

The calculated phase diagram of the Cr-Si system in the present study is presented in Fig. 6.1 along with all the reliable experimental data in the literature. The presently calculated phase diagram is almost the same as the diagram optimized by Chen et al. [7]. All the liquidus and solidus in the system are well reproduced. The homogeneity ranges of bcc_A2 (Cr), Cr_3Si, and $CrSi_2$ are also well reproduced. The finally obtained thermodynamic parameters of the Cr-Si system are presented in Table 6.2. The calculated invariant reactions are listed in Table 6.3. The experimental values and those calculated by Chen et al. [7] are also shown for comparison. The present invariant temperatures are in excellent agreement with the experimental data and the previous optimization results by Chen et al. [7] (within ±5 °C).

The integral and partial enthalpies of mixing of the liquid Cr-Si phase at 1723 °C calculated from the present optimization is presented in Fig. 6.2 along with the experimental data by Esin et al. [38]. The results from the previous assessment by Chen et al. [7] are also plotted for comparison. The integral enthalpy of mixing of the liquid phase shows an asymmetric shape with a minimum of about -35 kJ/mol at 60 at.% Cr. The calculated results from the present study using MQM are

much accurately reproducing the experimental data for both integral and partial enthalpies in this system than the results from Chen et al. [7] using the Bragg-Williams random mixing model. This indicates that MQM has an advantage in the accurate description of the liquid properties with apparent short range ordering. Both coordination number of Cr and Si in the liquid Cr-Si system were set to be 6, and several model parameters were optimized to reproduce these data and phase diagram simultaneously.

The heat capacities of the Cr_5Si_3, $CrSi_2$, Cr_3Si, and CrSi compounds are presented in Fig. 6.3. It can be seen that the measured heat capacity data by Golutvin and Liang [26] show systematic deviation from the experimental data for both the low and high temperature heat capacity. As a result, the data by Golutvin and Liang [26] were considered as less accurate in the current optimization. In the previous optimization by Chen et al. [7], the descriptions of these heat capacities were directly taken from the former assessment by Coughanowr et al. [10]. As shown in Fig. 6.3(a), the assessed parameters by Coughanowr et al. [10] can only represent the heat capacity data of Cr_5Si_3 above 400 K, but the present optimization considers the data even below to obtain a more accurate heat capacity function. Similar inaccuracy can be found in the previous assessment [10] for $CrSi_2$, while the present results can accurately reproduce the experimental data. Since there is no reliable high temperature heat capacity data for Cr_3Si, the Neumann-Kopp relation was used to give a prediction of the heat capacity of this phase. As can be seen in Fig. 6.3(c) that the predicted high temperature heat capacity of Cr_3Si from the Neumann-Kopp relation show consistency with the low temperature heat capacity data by Surikov et al. [29], Kalishevich et al. [28], and Pan et al. [61]. Th heat capacity of the CrSi compound is presented in Fig. 6.3(d) compared with the experimental data from Kalishevich et al. [28], Golutvin and Liang [26], and Kalishevich et al. [62]. The solid line calculated from the heat capacity function optimized by Coughanowr et al. [10] is in excellent agreement with the experimental data. As a result, the heat capacity expression from Coughanowr et al. [10] was accepted in the present optimization.

The heat contents of the intermetallic compounds are shown in Fig. 6.4. Fig. 6.4(a) is the calculated heat contents of the Cr_5Si_3 phase compared with the experimental data from Kailshevich et al. [27] and Schlesinger [30]. Both the present assessment and that by Chen et al. [7] can give a very good description of the experimental data. It should be noted that neither the measurements

by Kailshevich et al. [27] nor Schlesinger [19] detected the α_Cr_5Si_3 to β_Cr_5Si_3 phase transformation. The optimized enthalpy of transformation from α_Cr_5Si_3 to β_Cr_5Si_3 in this study is slightly larger than that by Chen et al. [7], but there is no experimental data to be compared. The heat contents of $CrSi_2$ and CrSi are presented in Figs. 6.4(b) and 6.4(c), respectively. For all the heat contents of Cr_5Si_3, $CrSi_2$, and CrSi, both the calculated values from the present work and Chen et al. [7] are in good agreement with the available experimental data. But, as shown in Fig. 6.3, the heat capacity functions in the present optimization are more accurate than those of the previous assessment [7].

Figs. 6.5(a) and (b) are the calculated enthalpy and entropy of formation at 298.15 K of all the intermetallic compounds compared with the experimental data. During the optimization, the enthalpy of formation data measured by Meschel and Kleppa [13] and Topor and Kleppa [35] were considered as more reliable than the indirect data from emf and vapor pressure measurements. Similarly, entropy at 298 K calculated from the low temperature heat capacity measured by adiabatic calorimetry was considered as more trustful than the indirect values. But it should be noted that the low temperature heat capacities of Cr_5Si_3, $CrSi_2$, and CrSi were only measured above 54 K, which may induce a certain error in the calculation of their entropy at 298 K. while the heat capacity of Cr_3Si is available from 10 K, so its entropy at 298 K should be more accurate.

Although great effect was put, it is hard to reproduce the enthalpy of formation and entropy of formation along with a good description of phase diagram. In particular, the experimental entropy of formations at 298 K of Cr_5Si_3 and CrSi are too large, which makes the Gibbs energies of these two compounds very negative at high temperature and induces high melting points. In order to obtain an optimum result, a certain deviation of entropy at 298 K of these two compounds were necessary. As can be seen in Fig. 6.5(a), the enthalpy of formation data was well reproduced. The entropy of formations at 298 K for Cr_3Si and $CrSi_2$ are well reproduced as can be seen in Fig. 6.5(b), but those of Cr_5Si_3 and CrSi are several units off from the values derived from the low temperature heat capacity data. Even in the previous assessment by Chen et al. [7], the same discrepancy was observed.

The chemical potential diagrams of Cr in the bcc_A2 standard state and Si in the diamond_A4 standard state are shown in Fig. 6.6(a) and Fig. 6.6(b), respectively. In these diagrams, the two-phase field is represented by a line, three-phase field is shown as a cross point of three two-phase lines. The calculated chemical potential diagrams of Cr and Si by the present optimization are very close to those of Chen et al. [7]. However, the calculated diagrams are quite different from the experimental data obtained from emf and vapor pressure measurements. It should be also noted that there are large discrepancies between the experimental data. These data are also inconsistent with the enthalpy of formation and entropy at 298 K as discussed above in Fig. 6.5. Based on the present optimization, the activities of bcc_A2 Cr and liquid Si are calculated at 1000 °C in Fig. 6.7. The calculated activities in line scale and logarithm scale are shown in Figs. 6.7(a) and (b), respectively. There are no experimental data to be compared with the present predictions. As expected, the activities show very negative deviation from ideal solution behavior.

6.4.2 The Al-Cr-Si system

The finally obtained thermodynamic parameters for the Al-Cr-Si system in the present optimization together with the related thermodynamic parameters of the sub-binaries are listed in Table 6.2. Figs. 6.8(a) and 6.8(b) present the calculated Al-Cr [5] and Al-Si [6] phase diagrams, respectively. The Toop type of extrapolation technique was utilized for the liquid phase of the Al-Cr-Si system with Al as the asymmetric element. And the calculated ternary invariant reactions involving the liquid phase are presented in Table 6.4. The agreement between the calculated and the measured invariant reactions is satisfactory. The calculated isothermal section at 1100 °C compared with the experimental data from Gupta [48] is presented in Fig. 6.9(a). The only stable ternary phase τ4 at 1100 °C is modeled as $Al_{116}Cr_{63}Si_{21}$. The measured single phase, two phase, and three phase region is reasonably reproduced by the calculated isothermal section. The solubility of Al in Cr_2Si reaches 12 at.% Al at 1100 °C. Fig. 6.9(b) is the calculated isothermal section at 1000 °C. The Al_4Cr, γ_L, α_Cr_5Si_3, and $CrSi_2$ phases have ternary extension. And the τ3-$(Al, Si)_{11}Cr_4$ phase has already become stable. The phase relation in the Al rich side is still reasonably predicted. In Fig. 6.9(c), the isothermal section at 900 °C is shown. One more ternary compound, τ2-Al_9Cr_3Si, shows presence at this temperature. The liquid phase region and the Al_4Cr + liquid two phase region are reasonably described. Besides, the phase stability range of $CrSi_2$ is

also reasonably reproduced. Thus, the topology relation at this temperature should be reliable. Isothermal section at 800 °C is presented in Fig. 6.9(d) along with the experimental data from Chen et al. [51] and Gupta [48]. A general agreement between the calculated phase diagram and the measured phase relation by Chen et al. [51] is obtained except the Al rich region. However, the reliability of the phase relation proposed by Chen et al. [51] is not high since it is only tentatively given. Similarly, the predicted phase relation is generally in agreement with the measured one by Zhou et al. [52] except for the Al rich corner. According to the measurement by Zhou et al. [52], the $Al_{11}Cr_2$ phase is not detected at 700 °C and the stability of the liquid phase in the Al-Cr binary is quite high. But, the $Al_{11}Cr_2$ phase is treated as stable down to room temperature and liquid is less stable in the Al rich side in the Al-Cr binary system, which can be the reason for this discrepancy. Two isoplethal sections are presented in Fig. 6.10. Fig. 6.10(a) is the calculated isoplethal section with 4 wt.% Si compared with the measured one from Esslinger et al. [47]. Fig. 6.10(b) is the calculated isoplethal section with 5 wt.% Cr together with the experimental data from Esslinger et al. [47]. The agreement is satisfactory. The calculated liquidus projection is shown in Fig. 6.11, and the enlarged part to show the Al rich side of the liquidus projection is shown in Fig. 6.12. According to the present model prediction, the primary phase regions of the binary Cr-Si compounds show large extension to the Al-Si side due to the high melting temperature feature of these phases. The Al rich ternary invariant temperatures change dramatically with composition which indicates the liquidus surface in the Al rich region is very steep.

6.5 Summary

A comprehensive evaluation of all the thermodynamic and phase diagram information for the Cr-Si and Al-Cr-Si systems were carried out. A set of self-consistent thermodynamic parameters for the Cr-Si system and Al-Cr-Si system was optimized to represent all the available and reliable phase diagrams and thermodynamic properties of these systems. The modified quasi-chemical model was applied to describe the thermodynamic properties of the liquid phase. The compound energy formalism was used to describe the solid phases. Most of the reliable experimental data in the Cr-Si and Al-Cr-Si systems can be back calculated using the thermodynamic parameters obtained in the present optimization.

Acknowledgement

The authors would like to thank the financial support from NSERC-Automotive Partnership Canada program in Canada. Senlin Cui would also like to thank the McGill Engineering Doctorate Award (MEDA) from McGill University for financial support.

References

1. Kloc, L., S. Spigarelli, E. Cerri, E. Evangelista, and T.G. langdon, *An evaluation of the creep properties of two Al-Si alloys produced by rapid solidification processing.* Metall. Mater. Trans. A, 1996. **27A**(12): p. 3871-3879.
2. Kato, E. and S. Murakawa, *Influence of Cr and Be or Mn and Be on the shape change of iron compound and impact properties of Al-Si alloy castings.* Imono, 1994. **66**(1): p. 10-14.
3. Hou, L.G., C. Cui, and J.S. Zhang, *Optimizing microstructures of hypereutectic Al-Si alloys with high Fe content via spray forming technique.* Mater. Sci. Eng., A, 2010. **A527**(23): p. 6400-6412.
4. Hou, L.G., H. Cui, Y.H. Cai, and J.S. Zhang, *Effect of (Mn+Cr) addition on the microstructure and thermal stability of spray-formed hypereutectic Al-Si alloys.* Mater. Sci. Eng., A, 2009. **A527**(1-2): p. 85-92.
5. Cui, S., I.-H. Jung, J. Kim, and J. Xin, *A coupled experimental and thermodynamic study of the Al-Cr and Al-Cr-Mg systems*, submitted to J. Alloys Compd.
6. Harvey, J.-P., *M.A.Sc. thesis.* Ecole Polytechnique, 2006.
7. Chen, H., Y. Du, and J.C. Schuster, *On the melting of Cr_5Si_3 and update of the thermodynamic description of Cr-Si.* CALPHAD Comput. Coupling Phase Diagrams Thermochem., 2009. **33**(1): p. 211-214.
8. Gokhale, A.B. and G.J. Abbaschian, *The Cr-Si (chromium-silicon) system.* Bull. Alloy Phase Diagrams, 1987. **8**(5): p. 474-84.
9. Okamoto, H., *Cr-Si (chromium-silicon).* J. Phase Equilib., 1997. **18**(2): p. 222.
10. Coughanowr, C.A. and I. Ansara, *Assessment of the Cr-Si system.* CALPHAD Comput. Coupling Phase Diagrams Thermochem., 1994. **18**(2): p. 125-40.

11. Okamoto, H., *Cr-Si (chromium-silicon).* J. Phase Equilib., 2001. **22**(5): p. 593.
12. Du, Y. and J.C. Schuster, *Experimental reinvestigation of the CrSi-Si partial system and update of the thermodynamic description of the entire Cr-Si system.* J. Phase Equilib., 2000. **21**(3): p. 281-286.
13. Meschel, S.V. and O.J. Kleppa, *Standard enthalpies of formation of some 3d transition metal silicides by high temperature direct synthesis calorimetry.* J. Alloys Compd., 1998. **267**(1-2): p. 128-135.
14. Kurnakov, N.N., *Investigation of the system chromium-silicon.* Izv. Sekt. Fiz.-Khim. Anal., Inst. Obshch. Neorg. Khim., Akad. Nauk SSSR, 1948. **16**(No. 4): p. 77-84.
15. Kieffer, R., F. Benesovsky, and H. Schroth, *The system chromium-silicon and solid solutions of silicides.* Z. Metallkd., 1953. **44**: p. 437-42.
16. Goldschmidt, H.J. and J.A. Brand, *The constitution of the chromium-niobium-silicon system.* J. Less-Common Met., 1961. **3**: p. 34-43.
17. Dudkin, L.D. and E.S. Kuznetsova, *Electrophysical properties of chromium and manganese disilicides.* Poroshk. Metall. (Kiev), 1962. **2**(No. 6): p. 20-31.
18. Dubrovskaya, L.B. and P.V. Gel'd, *Limits of the region of homogeneity and the nature of chromium bisilicide.* Zh. Neorg. Khim., 1963. **8**(7): p. 1639-44.
19. Svechnikov, V.N., Y.A. Kocherzhinskii, and L.M. Yupko, *Chromium-silicon phase diagram.* Sb. Nauchn. Rab. Inst. Metallofiz., Akad. Nauk Ukr. SSR, 1964. **No. 19**: p. 212-18.
20. Chang, Y.A., *Phase relations in the system chromium-silicon.* Trans. Met. Soc. AIME (Amer. Inst. Mining, Met., Petrol. Eng.), 1968. **242**(8): p. 1509-15.
21. Voronov, B.K., L.D. Dudkin, N.I. Kiryukhina, and N.N. Trusova, *Chromium-silicon system in the disilicide region.* Poroshk. Metall. (Kiev), 1967. **7**(1): p. 73-80.
22. Kocherzhinsky, Y.A., V.Z. Turkevich, V.I. Vasilenko, and A.V. Zolotukhin, *Thermophysical devices for high temperature measurements.* J. Therm. Anal., 1995. **44**(5): p. 1067-71.
23. Pyatkova, T.M., V.I. Surikov, A.K. Shtolyts, V.L. Zagryazhskii, and P.V. Gel'd, *β-Phase homogeneity region of a chromium-silicon system and mutual solubility of Cr_3Si and V_3Si.* Izv. Akad. Nauk SSSR, Neorg. Mater., 1971. **7**(10): p. 1755-8.

24. Würker, W., K. Roy, and J. Hesse, *Diffusion and solid solubility of chromium in silicon.* Mater. Res. Bull., 1974. **9**(7): p. 971-7.
25. Jurisch, M. and G. Behr, *Growth and perfection of chromium-silicon (Cr_3Si) single crystals.* Acta Phys. Acad. Sci. Hung., 1979. **47**(1-3): p. 201-7.
26. Golutvin, Y.M. and C.i.-K. Liang, *Heats of formation, heat contents, and heat capacities of chromium silicides.* Zh. Fiz. Khim., 1961. **35**: p. 129-41.
27. Kalishevich, G.I., P.V. Gel'd, and R.P. Krentsis, *Specific heat, enthalpy, and entropy of Cr_5Si_3 and $CrSi_2$.* Teplofiz. Vys. Temp., 1966. **4**(5): p. 653-9.
28. Kalishevich, G.I., P.V. Gel'd, and R.P. Krentsis, *Standard heat capacities, entropies, and enthalpies of silicon, chromium, and chromium silicides.* Zh. Fiz. Khim., 1965. **39**(12): p. 2999-3001.
29. Surikov, V.I., G.I. Kalishevich, and P.V. Gel'd, *Thermodynamic characteristics of chromium-silicon (Cr_3Si), chromium-germanium (Cr_3Ge), vanadium-silicon (V_3Si), and vanadium-germanium (V_3Ge) compounds.* Zh. Fiz. Khim., 1975. **49**(2): p. 555-6.
30. Schlesinger, M.E., *Thermodynamics of solid transition-metal silicides.* Chem. Rev., 1990. **90**(4): p. 607-28.
31. Eremenko, V.N., G.M. Lukashenko, V.R. Sidorko, and A.M. Khar'kova, *Thermodynamic properties of chromium silicides.* Porosh. Met., 1972. **12**(7): p. 61-5.
32. Lukashenko, G.M., V.P. Sidorko, and L.M. Yupko, *Thermodynamic properties of chromium silicides.* Poroshk. Metall. (Kiev), 1986(9): p. 73-6.
33. Chart, T.G., *Thermodynamic properties of the tungsten-silicon and chromium-silicon systems.* Met. Sci., 1975. **9**(11): p. 504-9.
34. Eremenko, V.N., G.M. Lukashenko, and V.R. Sidorko, *Thermodynamic properties of the chromium silicides, $CrSi_2$ and CrSi.* Zh. Fiz. Khim., 1971. **45**(8): p. 1996-8.
35. Topor, L. and O.J. Kleppa, *Standard enthalpy of formation of chromium silicide ($CrSi_2$) by high-temperature mixing calorimetry.* J. Chem. Thermodyn., 1987. **19**(1): p. 69-75.
36. Riegert, J.P., A. Vermande, and I. Ansara, *Thermodynamic properties of the mixture of the liquid chromium-silicon system at 1900 K.* High Temp. - High Pressures, 1973. **5**(2): p. 231-7.
37. Myers, C.E., R.J. Kematick, and G.A. Murray, *Thermodynamic activities, phase equilibria and stabilities in transition metal-silicon systems by high temperature Knudsen cell mass*

spectrometry. Proceedings of International Conference on User Applications of Alloy Phase Diagrams, 1987: p. 105-108.

38. Esin, Y.O., P.V. Gel'd, Y.V. Gorbunov, V.I. Vasil'ev, and A.B. Galeznik, *Enthalpies of formation of molten chromium-silicon alloys.* Zh. Fiz. Khim., 1976. **50**(10): p. 2656-7.
39. Liang, Y., C. Guo, C. Li, and Z. Du, *A Thermodynamic Description of the Al-Cr-Si System.* J. Phase Equilib. Diffus., 2009. **30**(5): p. 462-479.
40. Hu, B., W.-W. Zhang, Y. Peng, Y. Du, S. Liu, and Y. Zhang, *Thermodynamic reassessment of the Al-Cr-Si system with the refined description of the Al-Cr system.* Thermochim. Acta, 2013. **561**: p. 77-90.
41. Mondolfo, L.F., *Metallography of Aluminum Alloys.* 1943.
42. Pratt, J.N. and G.V. Raynor, *The intermetallic compounds in the alloys of aluminum and silicon with chromium, manganese, iron, cobalt, and nickel.* J. Inst. Met., 1951. **79**(Paper No. 1306): p. 211-32.
43. Pratt, J.N. and G.V. Raynor, *Intermetallic compounds in ternary aluminum rich alloys containing transitional metals.* Proc. R. Soc. London, Ser. A, 1951. **205**: p. 103-18.
44. Robinson, K., *The structure of β(AlCrSi).* Acta Crystallogr., 1953. **6**: p. 667.
45. Robinson, K., *The structure of α-(AlCrSi), $Cr_4Si_4Al_{13}$.* Acta Crystallogr., 1953. **6**: p. 854-9.
46. Brukl, C., H. Nowotny, and F. Benesovsky, *The ternary systems V-Al-Si, Nb-Al-Si, Cr-Al-Si, Mo-Al-Si, and Cr(Mo)-Al-Si.* Monatsh. Chem., 1961. **92**: p. 967-80.
47. Esslinger, P., F. Quatrehomme, and H. Bleidorn, *The aluminum corner of the aluminum-chromium-silicon system.* Z. Metallkd., 1965. **56**(10): p. 735-9.
48. Gupta, S.P., *Formation of intermetallic compounds in the Cr-Al-Si ternary system.* Mater. Charact., 2004. **52**(4/5): p. 355-370.
49. Weitzer, F., H. Chen, and J.C. Schuster, *Crystal-structure refinement of τ3-$Cr_4(Al,Si)_{11}$ by full-profile Rietveld analysis.* Powder Diffr., 2007. **22**(3): p. 253-255.
50. Weitzer, F., H. Chen, Y. Du, and J.C. Schuster, *The crystal structure of a new triclinic ternary phase: τ3-$Cr_4(Al,Si)_{11}$.* Intermetallics, 2005. **14**(2): p. 224-226.
51. Chen, H.-L., F. Weitzer, J.C. Schuster, Y. Du, and H. Xu, *The isothermal section of the Al-Cr-Si system at 800 °C and the crystal structure of τ2-(Cr_3Al_9Si).* J. Alloys Compd., 2007. **436**(1-2): p. 313-318.

52. Zhou, Z., Z. Li, X. Wang, Y. Liu, Y. Wu, M. Zhao, and F. Yin, *700 °C isothermal section of Al-Cr-Si ternary phase diagram.* Thermochim. Acta, 2014. **577**: p. 59-65.
53. Pelton, A.D. and P. Chartrand, *The modified quasi-chemical model: Part II. Multicomponent solutions.* Metall. Mater. Trans. A, 2001. **32A**(6): p. 1355-1360.
54. Pelton, A.D., S.A. Degterov, G. Eriksson, C. Robelin, and Y. Dessureault, *The modified quasichemical model I - binary solutions.* Metall. Mater. Trans. B, 2000. **31B**(4): p. 651-659.
55. Robelin, C., P. Chartrand, and A.D. Pelton, *Thermodynamic evaluation and optimization of the ($NaNO_3$ + KNO_3 + Na_2SO_4 + K_2SO_4) system.* J. Chem. Thermodyn., 2015. **83**: p. 12-26.
56. Redlich, O. and A.T. Kister, *Thermodynamics of nonelectrolytic solutions. Algebraic representation of thermodynamic properties and the classification of solutions.* Ind. Eng. Chem., 1948. **40**: p. 84,5-8.
57. Hillert, M. and M. Jarl, *A model for alloying effects in ferromagnetic metals.* CALPHAD Comput. Coupling Phase Diagrams Thermochem., 1978. **2**(3): p. 227-38.
58. Hillert, M., *The compound energy formalism.* J. Alloys Compd., 2001. **320**(2): p. 161-176.
59. Dinsdale, A.T., *SGTE data for pure elements.* CALPHAD Comput. Coupling Phase Diagrams Thermochem., 1991. **15**(4): p. 317-425.
60. Bale, C.W., P. Chartrand, S.A. Degterov, G. Eriksson, K. Hack, R. Ben Mahfoud, J. Melancon, A.D. Pelton, and S. Petersen, *FactSage thermochemical software and databases.* CALPHAD Comput. Coupling Phase Diagrams Thermochem., 2002. **26**(2): p. 189-228.
61. Pan, V.M., A.D. Shevchenko, I.G. Mikhailov, V.E. Yachmenev, and G. Behr, *Heat capacity of chromium-silicon (Cr_3Si) single crystals in the temperature range 6-300 K.* Fiz. Nizk. Temp. (Kiev), 1980. **6**(2): p. 236-9.
62. Kalishevich, G.I., P.V. Gel'd, and Y.V. Putintsev, *Heat capacity, enthalpy, and entropy of chromium and nickel monosilicides.* Tr. Ural. Politekh. Inst., 1968. **No. 167**: p. 152-4.
63. Dauben, C.H., D.H. Templeton, and C.E. Myers, *The crystal structure of Cr_5Si_3.* J. Phys. Chem., 1956. **60**: p. 443-5.
64. Boren, B., *X-ray study on alloys of silicon with chromium, manganese, cobalt and nickel.* Arkiv. Kemi, Mineral. Geol., 1933. **11A**(No. 10): p. 28 pp.

65. Dasgupta, T., J. Etourneau, B. Chevalier, S.F. Matar, and A.M. Umarji, *Structural, thermal, and electrical properties of $CrSi_2$.* J. Appl. Phys., 2008. **103**(11): p. 113516/1-113516/7.
66. Chen, H., *PhD thesis, Central South University, Changsha, China.* 2008.
67. Grobner, J., H.L. Lukas, and F. Aldinger, *Thermodynamic Calculation of the Ternary System Al-Si-C.* CALPHAD Comput. Coupling Phase Diagrams Thermochem., 1996. **20**(2): p. 247-254.

Table captions

Table 6.1 Summary of the crystal structure information of the stable compounds in the Cr-Si and Al-Cr-Si systems.

Table 6.2 Summary of the optimized model parameters for the Al-Cr-Si system (J mol^{-1} or J mol^{-1} K^{-1}).

Table 6.3 Summary of the invariant reactions in the Cr-Si system.

Table 6.4 Summary of the invariant reactions involving the liquid phase in the Al-Cr-Si system.

Figure captions

Fig. 6.1 Calculated phase diagram of the Cr-Si system along with the experimental data.

Fig. 6.2 (a) Calculated enthalpy of mixing of the Cr-Si liquid phase at 1723 ºC along with the experimental data. (b) Calculated partial enthalpy of mixing of Cr and Si at 1723 ºC along with the experimental data.

Fig. 6.3 Calculated heat capacities of compounds in the binary Cr-Si system along with the experimental data. (a) Cr_5Si_3, (b) $CrSi_2$, (c) Cr_3Si, and (d) CrSi.

Fig. 6.4 Calculated heat contents of compounds in the binary Cr-Si system along with the experimental data. (a) Cr_5Si_3, (b) $CrSi_2$, and (c) CrSi.

Fig. 6.5 Calculated (a) enthalpy of formation and (b) entropy of formation of compounds in the binary Cr-Si system at 25 °C along with the experimental data.

Fig. 6.6 Calculated (a) chemical potential diagram of Cr with respect to bcc_A2 Cr and (b) chemical potential diagram of Si with respect to diamond_A4 Si along with the experimental data.

Fig. 6.7 Calculated activities of Cr with respect to bcc_A2 Cr and Si with respect to liquid Si at 1000 °C. (a) Line scale, and (b) logarithm scale.

Fig. 6.8 Calculated phase diagram of (a) the Al-Cr system by Cui et al. [5] and (b) the Al-Si system by Harvey [6].

Fig. 6.9 Calculated isothermal sections of the Al-Cr-Si system along with the experimental data at different temperatures. (a) 1100 °C, (b) 1000 °C, (c) 900 °C, (d) 800 °C, and (e) 700 °C.

Fig. 6.10 Calculated isoplethal sections in the Al-Cr-Si system along with the experimental data. (a) At 4 wt.% Si and (b) 5 wt.% Cr.

Fig. 6.11 Calculated liquidus projection of the Al-Cr-Si system.

Fig. 6.12 Enlarged part of the liquidus projection of the Al rich Al-Cr-Si system.

Table 6.1 Summary of the crystal structure information of the stable compounds in the Cr-Si and Al-Cr-Si systems.

Phase	Space group	System	Prototype	Pearson symbol	Lattice parameters (nm)			Comment	Ref.
					a	b	c		
Cr_3Si	Pm-3n	Cubic	Cr_3Si	cP8	0.45580(2)				[15, 25]
β_Cr_5Si_3									
α_Cr_5Si_3	I4/mcm	Tetragonal	W_5Si_3	tI38	0.9170	0.4636			[63]
CrSi	$P2_13$	Cubic	FeSi	cP8	0.4620				[64]
$CrSi_2$	$P6_222$	Hexagonal	$CrSi_2$	hP9	0.442758(7)		0.636805(11)		[65]
τ1-$Al_{13}Cr_4Si_4$	F-43m	Cubic	$Al_{13}Cr_4Si_4$	cF84	1.0927				[66]
τ2-Al_9Cr_3Si	$P6_3/mmc$	Hexagonal	Al_9Mn_3Si		0.7535		0.7839		[66]
τ3-$(Al, Si)_{11}Cr_4$	P-1	Triclinic	$Al_{11}Mn_4$	aP30	0.5126	0.8980	0.5047	α=89.775° β=100.711° γ=106.605°	[66]
τ4-$Al_{58}Cr_{31.5}Si_{10.5}$	$Pn2_1a$	Orthorhombic	Al_3Mn		1.4842	1.2452	1.2501		[66]

Table 6.2 Summary of the optimized model parameters for the Al-Cr-Si system (J mol^{-1} or J mol^{-1} K^{-1}).

Phase	Thermodynamic parameters	Ref.
Liquid (Al, Cr, Si)	$Z^{Al}_{AlAl} = Z^{Cr}_{CrCr} = Z^{Si}_{SiSi} = Z^{Al}_{AlCr} = Z^{Cr}_{CrAl} = Z^{Cr}_{CrSi} = Z^{Si}_{SiCr} = 6;\ Z^{Al}_{AlSi} = Z^{Si}_{SiAl} = 5$	
	$\Delta g_{Al,Cr} = -6250.02 - 4.707T - (4978.96 + 4.728T)x_{AlAl} + (836.8 + 1.883T)x^2_{AlAl}$ $-1602.81x_{CrCr}$	[5]
	$\Delta g_{Al,Si} = -4622.28 - 0.03T + (836.80 - 1.17T)x_{AlAl}$	[6]
	$\Delta g_{Cr,Si} = -29288.00 + 4.184T + (-30124.80 + 8.033T)x_{CrCr} + (1799.12 - 1.799T)x_{SiSi}$ $+1255.20x^2_{SiSi}$	This work
	$g^{001}_{Al,Cr,(Si)} = -1673.6 - 1.255T$, $g^{001}_{Al,Si,(Cr)} = -7543.75 + 9.623T$, $g^{001}_{Cr,Si,(Al)} = 16736$	This work
fcc_A1 $(Al, Cr, Si)_1(Va)_1$	${}^0L_{Al,Cr:Va} = -57135.57$	[5]
	${}^0L_{Al,Si:Va} = -3143.78 + 0.39T$	[67]
	${}^0L_{Cr,Si:Va} = 0$	This work
	${}^0L_{Al,Cr,Si:Va} = 680751.6$	[39]
bcc_A2 $(Al, Cr, Si)_1(Va)_3$	${}^0L_{Al,Cr:Va} = -56356.8 - 6.32T$ ${}^1L_{Al,Cr:Va} = -7654.74$	[5]
	${}^0L_{Al,Si:Va} = 2092$	[6]
	${}^0L_{Cr,Si:Va} = -77728.33 - 2.38T$ ${}^1L_{Cr,Si:Va} = 53247.56 - 13.59T$	This work

	${}^{0}L_{Al,Cr,Si:Va} = 627600$ ${}^{1}L_{Al,Cr,Si:Va} = 125520$	
Diamond_A4 $(Al, Cr, Si)_1$	${}^{o}G_{Cr} = 5000 + {}^{o}G_{Cr}^{bcc}$	[39]
	${}^{0}L_{Al,Si:Va} = 121614.16 - 47.55T$	[39]
Al_4Cr $(Cr)_1(Al, Va, Si)_4$	${}^{o}G_{Cr:Va} = 25000 + {}^{o}G_{Cr}^{bcc}$	[40]
	${}^{o}G_{Cr:Si} = -55115.83 + 29.29T + 4{}^{o}G_{Si}^{dia} + {}^{o}G_{Cr}^{bcc}$	This work
	${}^{o}G_{Cr:Al} = -84930.410 + 3.81T + 4{}^{o}G_{Al}^{fcc} + {}^{o}G_{Cr}^{bcc}$ ${}^{0}L_{Cr:Al,Va} = 28226.270$	[5]
γ_L $(Al, Si)_{12}(Cr)_5(Al, Cr, Si)_9$	${}^{o}G_{Al:Cr:Al} = -357006.160 + 20.163T + 21{}^{o}G_{Al}^{fcc} + 5{}^{o}G_{Cr}^{bcc}$ ${}^{o}G_{Al:Cr:Cr} = -320932.548 - 109.516T + 12{}^{o}G_{Al}^{fcc} + 14{}^{o}G_{Cr}^{bcc}$	[5]
	${}^{o}G_{Al:Cr:Si} = 12{}^{o}G_{Al}^{fcc} + 5{}^{o}G_{Cr}^{bcc} + 9{}^{o}G_{Si}^{dia}$ ${}^{o}G_{Si:Cr:Al} = 12{}^{o}G_{Si}^{dia} + 5{}^{o}G_{Cr}^{bcc} + 9{}^{o}G_{Al}^{fcc}$ ${}^{o}G_{Si:Cr:Cr} = -430952.00 + 12{}^{o}G_{Si}^{dia} + 14{}^{o}G_{Cr}^{bcc}$ ${}^{o}G_{Si:Cr:Si} = 5{}^{o}G_{Cr}^{bcc} + 21{}^{o}G_{Si}^{dia}$	This work
	${}^{0}L_{Al:Cr:Al,Cr} = -632060.437 + 29.071T$	[40]
γ_H	${}^{o}G_{Al:Al:Cr:Al} = -124435.30 + 11{}^{o}G_{Al}^{fcc} + 2{}^{o}G_{Cr}^{bcc}$ ${}^{o}G_{Cr:Cr:Cr:Al} = 2357.31 - 103.77T + 6{}^{o}G_{Al}^{fcc} + 7{}^{o}G_{Cr}^{bcc}$	[40]

$(Al, Cr, Si)_2(Al, Cr)_3(Cr)_2(Cr, Si)_6$	${}^{o}G_{Cr:Al:Cr:Al} = 9{}^{o}G_{Al}^{fcc} + 4{}^{o}G_{Cr}^{bcc}$	
	${}^{o}G_{Al:Cr:Cr:Al} = -243506.24 - 42.08T + 8{}^{o}G_{Al}^{fcc} + 5{}^{o}G_{Cr}^{bcc}$	[5]
	${}^{o}G_{Al:Al:Cr:Si} = 5{}^{o}G_{Al}^{fcc} + 2{}^{o}G_{Cr}^{bcc} + 6{}^{o}G_{Si}^{dia}$	This work
	${}^{o}G_{Al:Cr:Cr:Si} = -228446.40 - 20.92T + 2{}^{o}G_{Al}^{fcc} + 5{}^{o}G_{Cr}^{bcc} + 6{}^{o}G_{Si}^{dia}$	
	${}^{o}G_{Cr:Al:Cr:Si} = 3{}^{o}G_{Al}^{fcc} + 4{}^{o}G_{Cr}^{bcc} + 6{}^{o}G_{Si}^{dia}$	
	${}^{o}G_{Cr:Cr:Cr:Si} = 7{}^{o}G_{Cr}^{bcc} + 6{}^{o}G_{Si}^{dia}$	
	${}^{o}G_{Si:Al:Cr:Al} = 9{}^{o}G_{Al}^{fcc} + 2{}^{o}G_{Cr}^{bcc} + 2{}^{o}G_{Si}^{dia}$	
	${}^{o}G_{Si:Al:Cr:Si} = 3{}^{o}G_{Al}^{fcc} + 2{}^{o}G_{Cr}^{bcc} + 8{}^{o}G_{Si}^{dia}$	
	${}^{o}G_{Si:Cr:Cr:Al} = 6{}^{o}G_{Al}^{fcc} + 5{}^{o}G_{Cr}^{bcc} + 2{}^{o}G_{Si}^{dia}$	
	${}^{o}G_{Si:Cr:Cr:Si} = 5{}^{o}G_{Cr}^{bcc} + 8{}^{o}G_{Si}^{dia}$	
	${}^{0}L_{Al,Cr:*:Cr:Al} = -183139.262$	[5]
	${}^{0}L_{*:Al,Cr:Cr:Al} = -63705.751 - 25.221T$	
$AlCr_2$ $(Al, Cr, Si)_1(Al, Cr)_2$	${}^{o}G_{Al:Al} = 10000 + 3{}^{o}G_{Al}^{fcc}$	[5]
	${}^{o}G_{Cr:Cr} = 10000 + 3{}^{o}G_{Cr}^{bcc}$	
	${}^{o}G_{Al:Cr} = -36594.81 - 14.91T + {}^{o}G_{Al}^{fcc} + 2{}^{o}G_{Cr}^{bcc}$	
	${}^{o}G_{Cr:Al} = 52331.31 + 16.84T + 2{}^{o}G_{Al}^{fcc} + {}^{o}G_{Cr}^{bcc}$	
	${}^{0}L_{Al,Cr:*} = -8922.60$	

	${}^{0}L_{*:Al,Cr} = -38108.20$	
	${}^{o}G_{Si:Cr} = -79496 + 2{}^{o}G_{Cr}^{bcc} + {}^{o}G_{Si}^{dia}$	This work
	${}^{o}G_{Si:Al} = 41840 + 2{}^{o}G_{Al}^{fcc} + {}^{o}G_{Si}^{dia}$	
Al_7Cr $(Al)_7(Cr)$	${}^{o}G_{Al:Cr} = -107000 + 14.81T + 7{}^{o}G_{Al}^{fcc} + {}^{o}G_{Cr}^{bcc}$	[5]
$Al_{11}Cr_2$ $(Al)_{11}(Cr)_2$	${}^{o}G_{Al:Cr} = -195000 + 16.99T + 11{}^{o}G_{Al}^{fcc} + 2{}^{o}G_{Cr}^{bcc}$	[5]
Cr_3Si $(Cr, Si)_3(Cr, Si, Al)$	${}^{o}G_{Cr:Cr} = 20000 + 10T + 4{}^{o}G_{Cr}^{bcc}$ ${}^{o}G_{Si:Cr} = 561830.45 - 61.08T + 3{}^{o}G_{Si}^{dia} + {}^{o}G_{Cr}^{bcc}$ ${}^{o}G_{Si:Si} = 415925.96 - 65.94T + 4{}^{o}G_{Si}^{dia}$	[7]
	${}^{o}G_{Cr:Si} = -120883.71 + 2.72T + 3{}^{o}G_{Cr}^{bcc} + {}^{o}G_{Si}^{dia}$ ${}^{o}G_{Cr:Al} = -37045.14 - 8.37T + 3{}^{o}G_{Cr}^{bcc} + {}^{o}G_{Al}^{fcc}$ ${}^{o}G_{Si:Al} = 58576.00 + 12.55T + 3{}^{o}G_{Si}^{dia} + {}^{o}G_{Al}^{fcc}$ ${}^{0}L_{Cr,Si:*} = -376560$	This work
β_Cr_5Si_3 $Cr_5(Cr, Si)_3$	${}^{o}G_{Cr:Cr} = 40000 + 8{}^{o}G_{Cr}^{bcc}$ ${}^{o}G_{Cr:Si} = -278741.218 + 1286.49\,T - 220.2616\,T\ln T + 0.0133976\,T^2$ $-8.62375\times10^{-6}T^3 + 1310079.996T^{-1} \quad (298.15 < T < 1900)$ ${}^{o}G_{Cr:Si} = -444894.574 + 2312.20\,T - 345.244576\,T\ln T \quad (1900 < T < 9000)$ ${}^{0}L_{Cr:Cr,Si} = -4697.84$	This work

α_Cr_5Si_3 $Cr_5(Al, Si)_3$	$^oG_{Cr:Si} = -346143.123 + 1324.31T - 220.2616\,T\ln T + 0.0133976\,T^2$ $-8.62375\times10^{-6}T^3 + 1310079.996T^{-1}$ $(298.15 < T < 1900)$ $^oG_{Cr:Si} = -512296.479 + 2350.02\,T - 345.244576\,T\ln T$ $(1900 < T < 9000)$ $^oG_{Cr:Al} = 4184 + 2.09T + 5{}^oG_{Cr}^{bcc} + 3{}^oG_{Al}^{fcc}$	This work
CrSi (Cr)(Si)	$^oG_{Cr:Si} = -83345.088 + 315.458\,T - 51.62865\,T\ln T - 0.00447355\,T^2 + 391330\,T^{-1}$	This work
$CrSi_2$ (Cr, Si)(Al, Cr, Si)$_2$	$^oG_{Cr:Al} = -43932.00 + 83.68T + {}^oG_{Cr}^{bcc} + 2{}^oG_{Al}^{fcc}$ $^oG_{Cr:Cr} = 219200.00 + 3{}^oG_{Cr}^{bcc}$ $^oG_{Cr:Si} = -107085.92 + 394.42\,T - 65.62604\,T\ln T - 0.01148279\,972T^2$ $-1.77861666\times10^{-9}T^3 + 365453.69752T^{-1}$ $^oG_{Si:Al} = 418.40 + {}^oG_{Si}^{dia} + 2{}^oG_{Al}^{fcc}$ $^oG_{Si:Cr} = 224822.01 - 27.60T + {}^oG_{Si}^{dia} + 2{}^oG_{Cr}^{bcc}$ $^oG_{Si:Si} = 84525.00 - 26.28\,T + 3{}^oG_{Si}^{dia}$ $^0L_{Cr,Si:*} = 1535.45$ $^0L_{Cr:Al,Si} = -137992.50 - 12.55\,T$ $^1L_{Cr:Al,Si} = 37848.46 - 8.368T$	This work
τ1 $(Al)_{13}(Cr)_4(Si)_4$	$^oG_{Al:Cr:Si} = -479880.77 + 107.42\,T + 13{}^oG_{Al}^{fcc} + 4{}^oG_{Cr}^{bcc} + 4{}^oG_{Si}^{dia}$	This work
τ2 $(Al)_9(Cr)_3(Si)$	$^oG_{Al:Cr:Si} = -260327.34 + 4.219\,T + 9{}^oG_{Al}^{fcc} + 3{}^oG_{Cr}^{bcc} + {}^oG_{Si}^{dia}$	This work

τ3 $(Al, Si)_{11}(Cr)_4$	${}^{o}G_{Al:Cr} = -274943.2 + 11{}^{o}G_{Al}^{fcc} + 4{}^{o}G_{Cr}^{bcc}$ ${}^{o}G_{Si:Cr} = -259864.10 + 209.20T + 4{}^{o}G_{Cr}^{bcc} + 11{}^{o}G_{Si}^{dia}$ ${}^{0}L_{Al,Si:Cr} = -379484.6 + 251.04T$ ${}^{1}L_{Al,Si:Cr} = 515301.44 - 83.68T$	This work
τ4 $(Al)_{116}(Cr)_{63}(Si)_{21}$	${}^{o}G_{Al:Cr:Si} = -2982221.91 - 1337.295T + 116{}^{o}G_{Al}^{fcc} + 63{}^{o}G_{Cr}^{bcc} + 21{}^{o}G_{Si}^{dia}$	This work

Table 6.3 Summary of the invariant reactions in the Cr-Si system.

Reaction type	Reaction (at.% Si)			Temperature °C	Method [a]	Ref.
Eutectic	Liquid = Cr_3Si + bcc_A2					
	15.5	23.2	11.6	1700±10	DTA	[19]
				1709±8	DTA	[20]
				1700±10	DTA	[22]
				1684	Cal.	[10]
				1701	Cal.	[12]
				1699	Cal.	[7]
				1699	Cal.	This work
Congruent	Liquid = Cr_3Si					
				1770±10	DTA	[19]
				⩾1766	DTA	[20]
				1770±10	DTA	[22]
				1777	Cal.	[10]
				1780	Cal.	[12]
				1774	Cal.	[7]
				1778	Cal.	This work
Eutectic	Liquid + Cr_3Si = β_Cr_5Si_3					
	34.3	25.0	37.5	1680±10	DTA	[19]
				1664±4	DTA	[20]
				1680±10	DTA	[22]
				1677	Cal.	[10]
				1664	Cal.	[12]
				1659	Cal.	[7]
				1661	Cal.	This work
Congruent	Liquid = β_Cr_5Si_3					
				1720±5	DTA	[19]
				⩾1668	DTA	[20]
				1720±5	DTA	[22]

				1678	Cal.	[10]
				1666	Cal.	[12]
Peritectic	Liquid + β_Cr_5Si_3 = α_Cr_5Si_3					
				1519	Cal.	[12]
				1509	Cal.	[7]
				1508	Cal.	This work
Eutectoid	β_Cr_5Si_3 = α_Cr_5Si_3 + Cr_3Si					
				1488	Cal.	[12]
				1501	Cal.	[7]
				1502	Cal.	This work
Peritectic	Liquid + α_Cr_5Si_3 = CrSi					
	54.2	37.5	50.0	1475±10	DTA	[19]
				1432±5	DTA	[20]
				1425±4	DTA	[12]
				1445	Cal.	[10]
				1424	Cal.	[12]
				1425	Cal.	[7]
				1424	Cal.	This work
Eutectic	Liquid = CrSi + $CrSi_2$					
	58.3	50.0	66.7	1445±10	DTA	[19]
				1402±4	DTA	[20]
				1445±10	DTA	[22]
				1404±4	DTA	[12]
				1436	Cal.	[10]
				1408	Cal.	[12]
				1407	Cal.	[7]
				1409	Cal.	This work
Congruent	Liquid = $CrSi_2$					
				1475±5	DTA	[19]
				1437±3	DTA	[20]

				1475±5	DTA	[22]
				1438±2	DTA	[12]
				1468	Cal.	[10]
				1439	Cal.	[12]
				1441	Cal.	[7]
				1443	Cal.	This work
Eutectic	Liquid = (Si) + $CrSi_2$					
				1330	TA	[15]
	85.4	0.00	66.7	1355±10	DTA	[19]
				1308±5	DTA	[20]
				1355±10	DTA	[22]
				1328±1	DTA	[12]
				1334	Cal.	[10]
				1328	Cal.	[12]
				1323	Cal.	[7]
				1323	Cal.	This work

[a] TA = Thermal Analysis; DTA = Differential Thermal Analysis; Cal. = Calphad.

Table 6.4 Summary of the invariant reactions involving the liquid phase in the Al-Cr-Si system.

Reaction type	Reaction			Temperature °C	Ref.
	at.% Al	at.% Cr	at.% Si		
Quasi-Peritectic	Liquid + β_Cr_5Si_3 = Cr_3Si + α_Cr_5Si_3				
	12.28	57.83	29.89	1517	This work
				1501	[39]
				1507	[40]
Quasi-Peritectic	Liquid + CrSi = $CrSi_2$ + α_Cr_5Si_3				
	10.46	41.68	47.86	1363	This work
				1360	[20]
				1320	[40]
				1360	[66]
Quasi-Peritectic	Liquid + bcc_A2 = Cr_3Si + γ_H				
	50.44	44.80	4.76	1275	This work
				1265	[20]
				1295	[40]
				1298	[66]
Quasi-Peritectic	Liquid + Cr_3Si = α_Cr_5Si_3 + γ_H				
	51.64	42.11	6.25	1268	This work
				1194	[20]
				1248	[40]
				1189	[66]
Peritectic	Liquid + α_Cr_5Si_3 + γ_H = $Al_{116}Cr_{63}Si_{21}$ (τ4)				
	61.41	27.10	11.49	1185	This work
Quasi-Peritectic	Liquid + α_Cr_5Si_3 = $Al_{116}Cr_{63}Si_{21}$ (τ4) + $CrSi_2$				
	61.38	26.98	11.65	1184	This work
Peritectic	Liquid + $Al_{116}Cr_{63}Si_{21}$ (τ4) + γ_H = $(Al,Si)_{11}Cr_4$ (τ3)				

	76.53	15.22	3.25	1040	This work
				1058	[20]
				1067	[40]
				1041	[66]
Quasi-Peritectic	Liquid + $Al_{116}Cr_{63}Si_{21}$ (τ4) = $(Al,Si)_{11}Cr_4$ (τ3) + $CrSi_2$				
	74.84	14.30	10.86	1039	This work
				1053	[20]
				1066	[40]
				1047	[66]
Peritectic	Liquid + γ_H + $(Al,Si)_{11}Cr_4$ (τ3) = Al_4Cr				
	77.73	14.92	7.35	1034	This work
				1035	[20]
				1050	[40]
				1036	[66]
Quasi-Peritectic	Liquid + γ_H = γ_L + Al_4Cr				
	78.96	14.94	6.10	1033	This work
				1041	[40]
Quasi-Peritectic	Liquid + $(Al,Si)_{11}Cr_4$ (τ3) = Al_4Cr + $CrSi_2$				
	78.15	7.35	14.50	963	TW
				991	[20]
				936	[40]
				983	[66]
Peritectic	Liquid + Al_4Cr + $CrSi_2$ = $Al_{13}Cr_4Si_4$ (τ1)				
	82.63	1.58	15.80	802	This work
				808	[20]
				804	[40]
				710	[47]
				710	[48]
				806	[66]

Quasi-Peritectic	Liquid + Al_4Cr = $Al_{13}Cr_4Si_4$ (τ1) + $Al_{11}Cr_2$				
	87.19	1.22	11.60	764	This work
				715	[20]
				758	[40]
				680-710	[48]
				785	[66]
Quasi-Peritectic	Liquid + $Al_{11}Cr_2$ = $Al_{13}Cr_4Si_4$ (τ1) + Al_7Cr				
	88.40	0.75	10.86	732	This work
				693	[20]
				702	[40]
				680	[47]
				722	[66]
Quasi-Peritectic	Liquid + $CrSi_2$ = $Al_{13}Cr_4Si_4$ (τ1) + Si				
	79.12	0.17	20.72	699	This work
				608	[20]
				722	[40]
				590	[47]
Quasi-Peritectic	Liquid + Al_7Cr = fcc_A1 + $Al_{13}Cr_4Si_4$ (τ1)				
	90.17	0.44	9.79	596	This work
				635	[20]
				615	[40]
				625	[47]
				634	[66]
Eutectic	Liquid = fcc_A1 + (Si) + $Al_{13}Cr_4Si_4$ (τ1)				
	87.77	0.02	12.21	579	This work
				577	[20]
				577	[40]
				575	[47]
				574	[66]

Figures

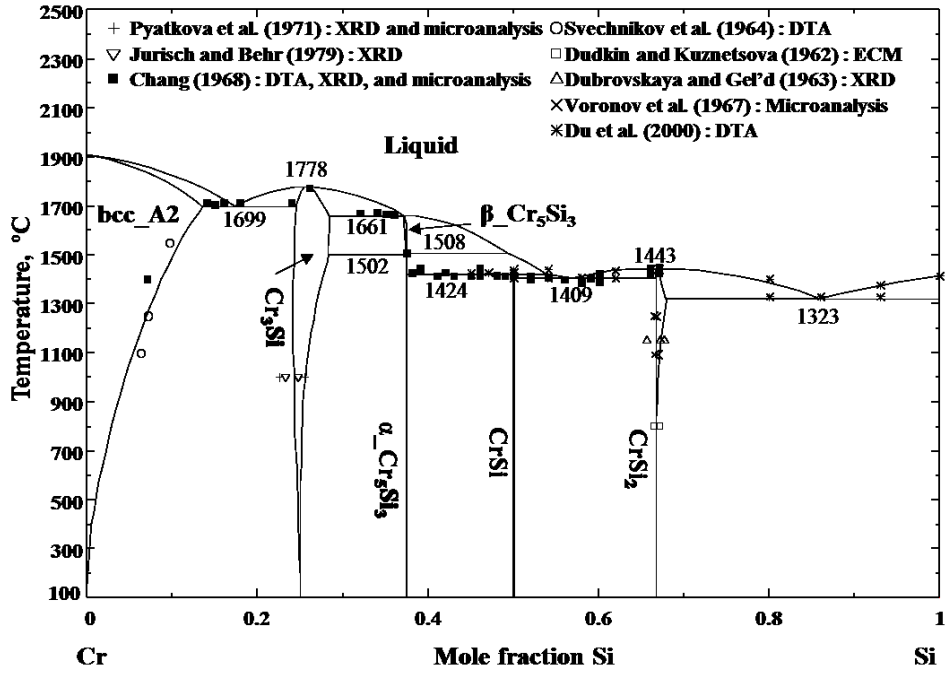

Fig. 6.1 Calculated phase diagram of the Cr-Si system along with the experimental data.

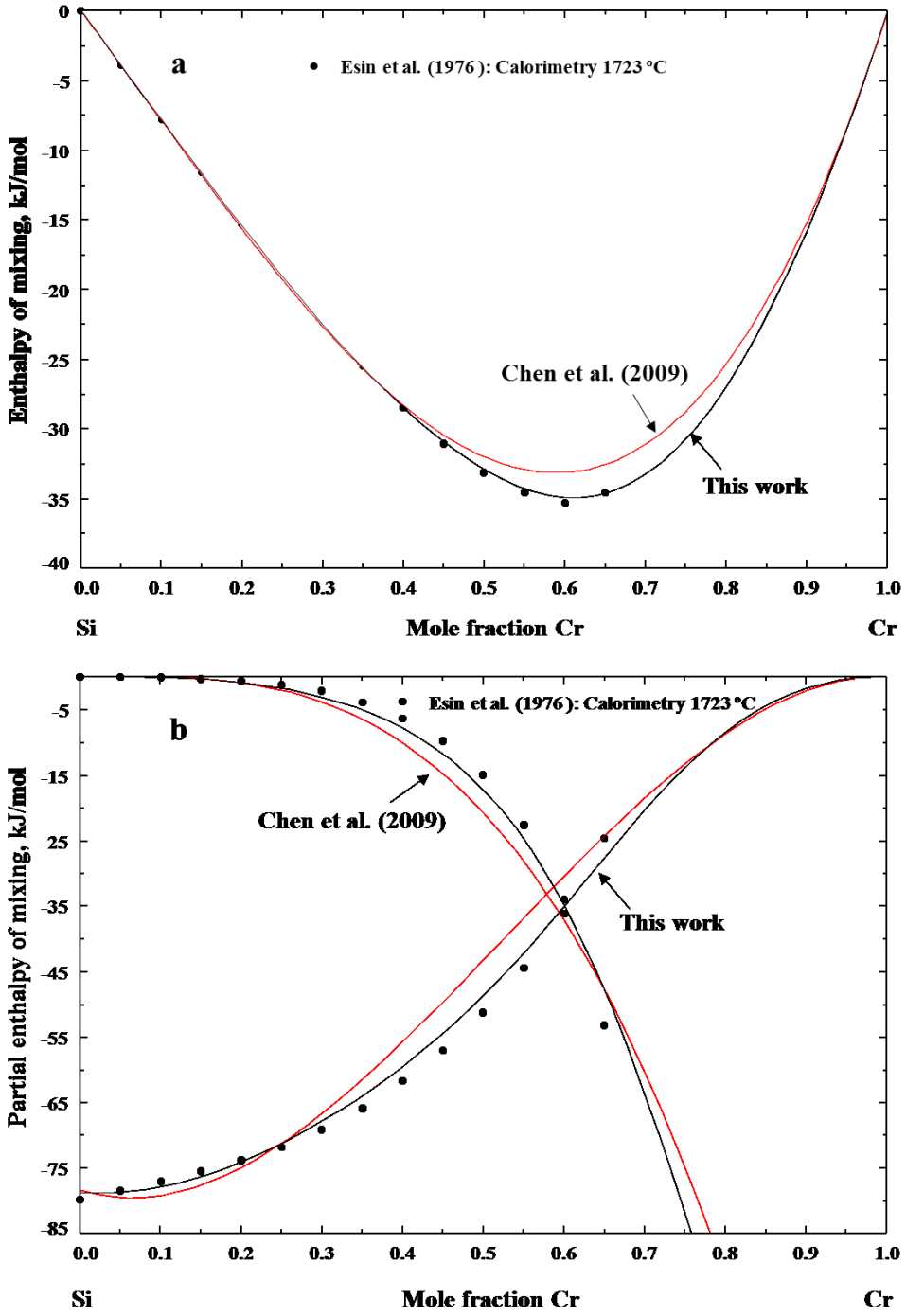

Fig. 6.2 (a) Calculated enthalpy of mixing of the Cr-Si liquid phase at 1723 ºC along with the experimental data. (b) Calculated partial enthalpy of mixing of Cr and Si at 1723 ºC along with the experimental data.

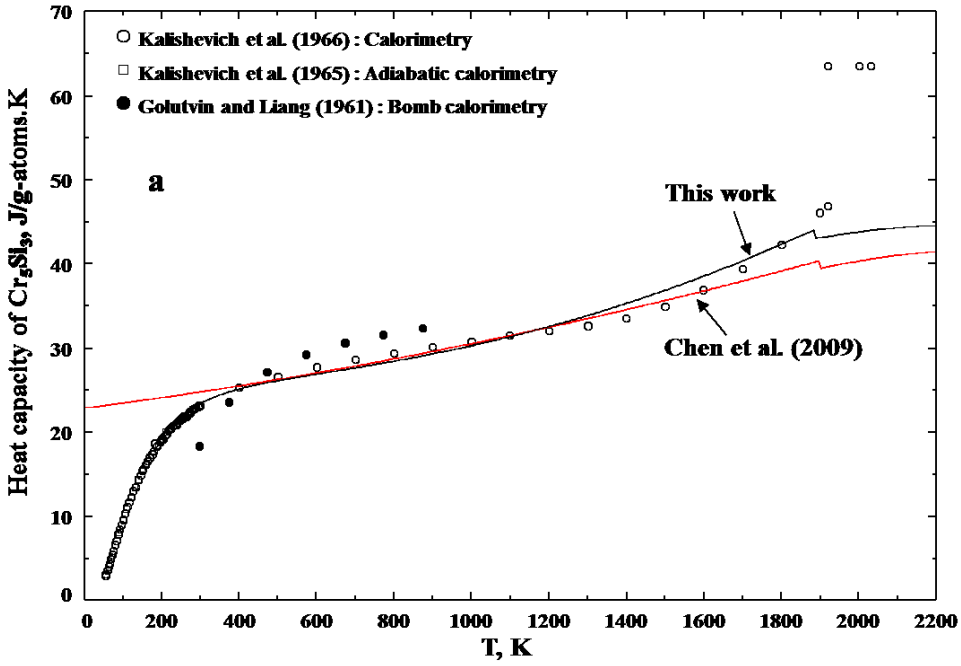
Kalishevich et al. (1966) : Calorimetry
Kalishevich et al. (1965) : Adiabatic calorimetry
Golutvin and Liang (1961) : Bomb calorimetry
a
This work
Chen et al. (2009)
Heat capacity of Cr_3Si_3, J/g-atoms.K
T, K

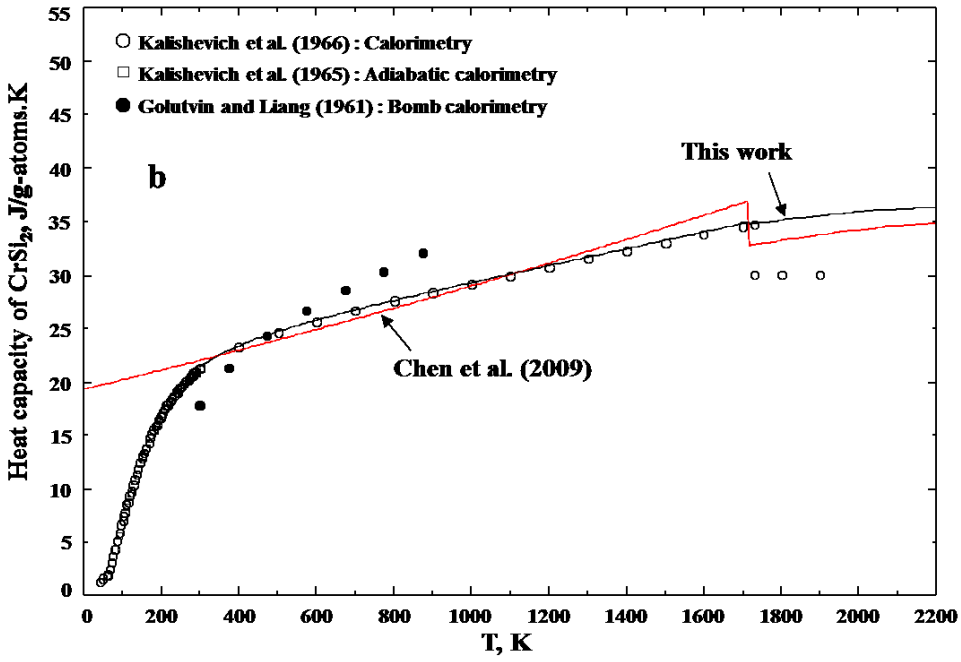
Kalishevich et al. (1966) : Calorimetry
Kalishevich et al. (1965) : Adiabatic calorimetry
Golutvin and Liang (1961) : Bomb calorimetry
b
This work
Chen et al. (2009)
Heat capacity of $CrSi_2$, J/g-atoms.K
T, K

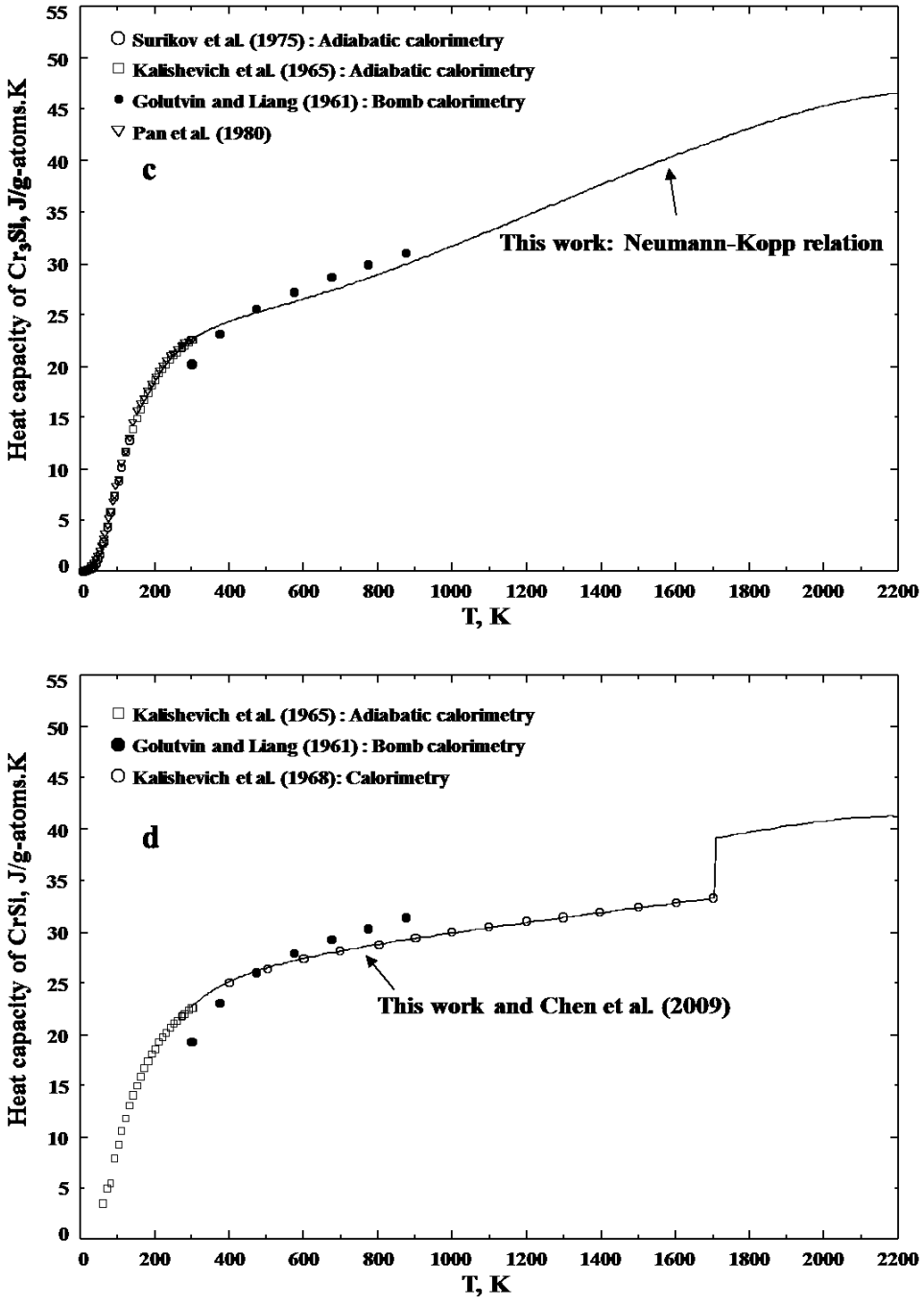

Fig. 6.3 Calculated heat capacities of compounds in the binary Cr-Si system along with the experimental data. (a) Cr_5Si_3, (b) $CrSi_2$, (c) Cr_3Si, and (d) CrSi.

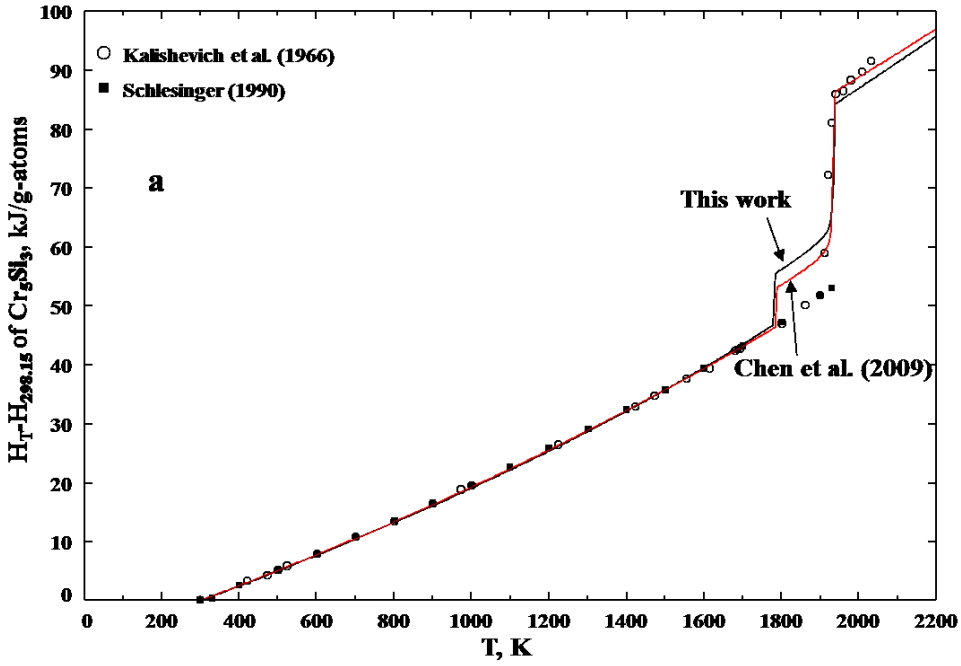
Kalishevich et al. (1966)
Schlesinger (1990)
a
This work
Chen et al. (2009)
H_T-$H_{298.15}$ of Cr_5Si_3, kJ/g-atoms
T, K

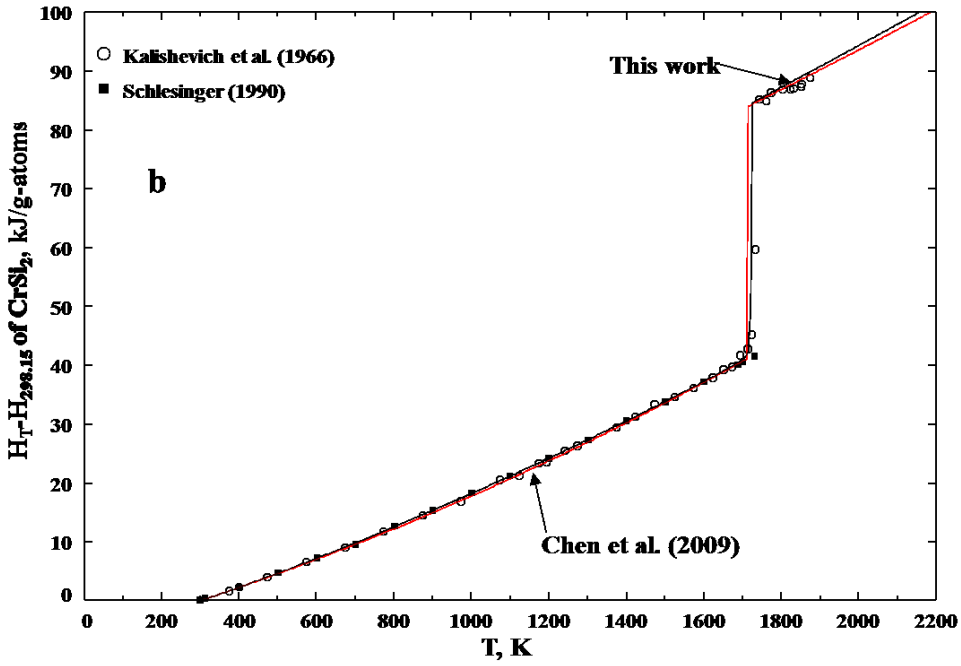
Kalishevich et al. (1966)
Schlesinger (1990)
b
This work
Chen et al. (2009)
H_T-$H_{298.15}$ of $CrSi_2$, kJ/g-atoms
T, K

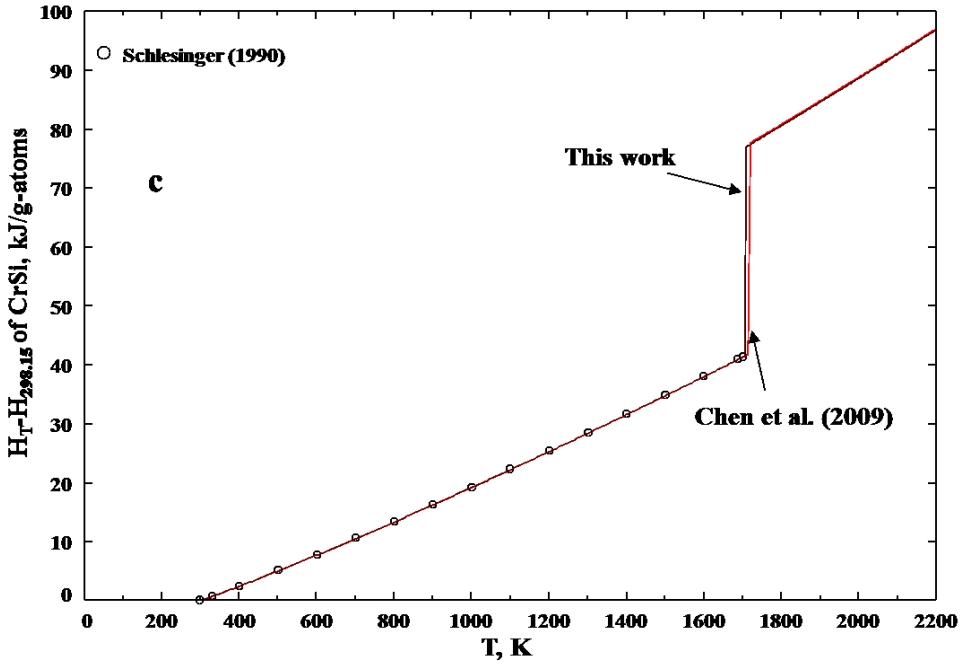

Fig. 6.4 Calculated heat contents of compounds in the binary Cr-Si system along with the experimental data. (a) Cr_5Si_3, (b) $CrSi_2$, and (c) CrSi.

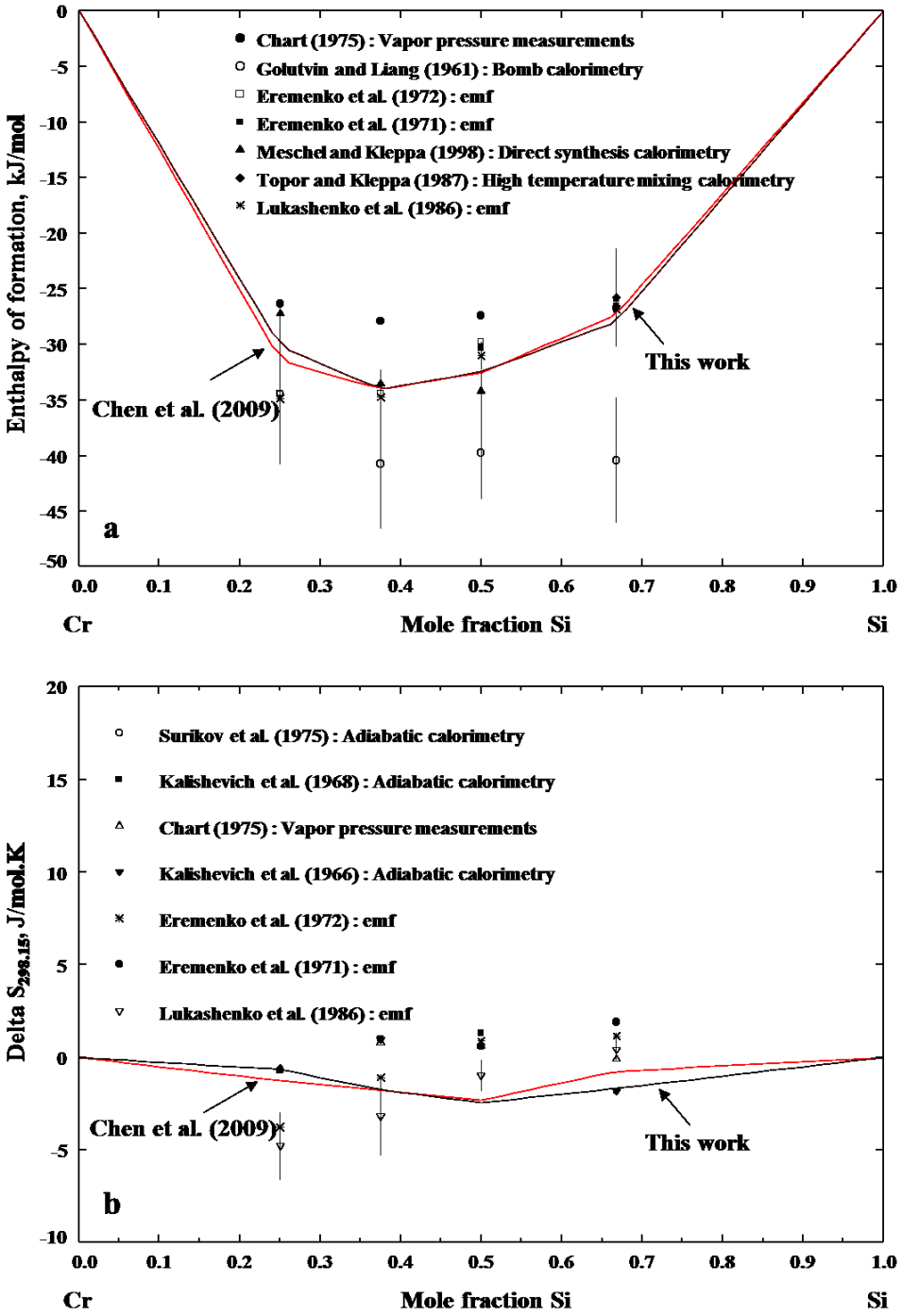

Fig. 6.5 Calculated (a) enthalpy of formation and (b) entropy of formation of compounds in the binary Cr-Si system at 25 °C along with the experimental data.

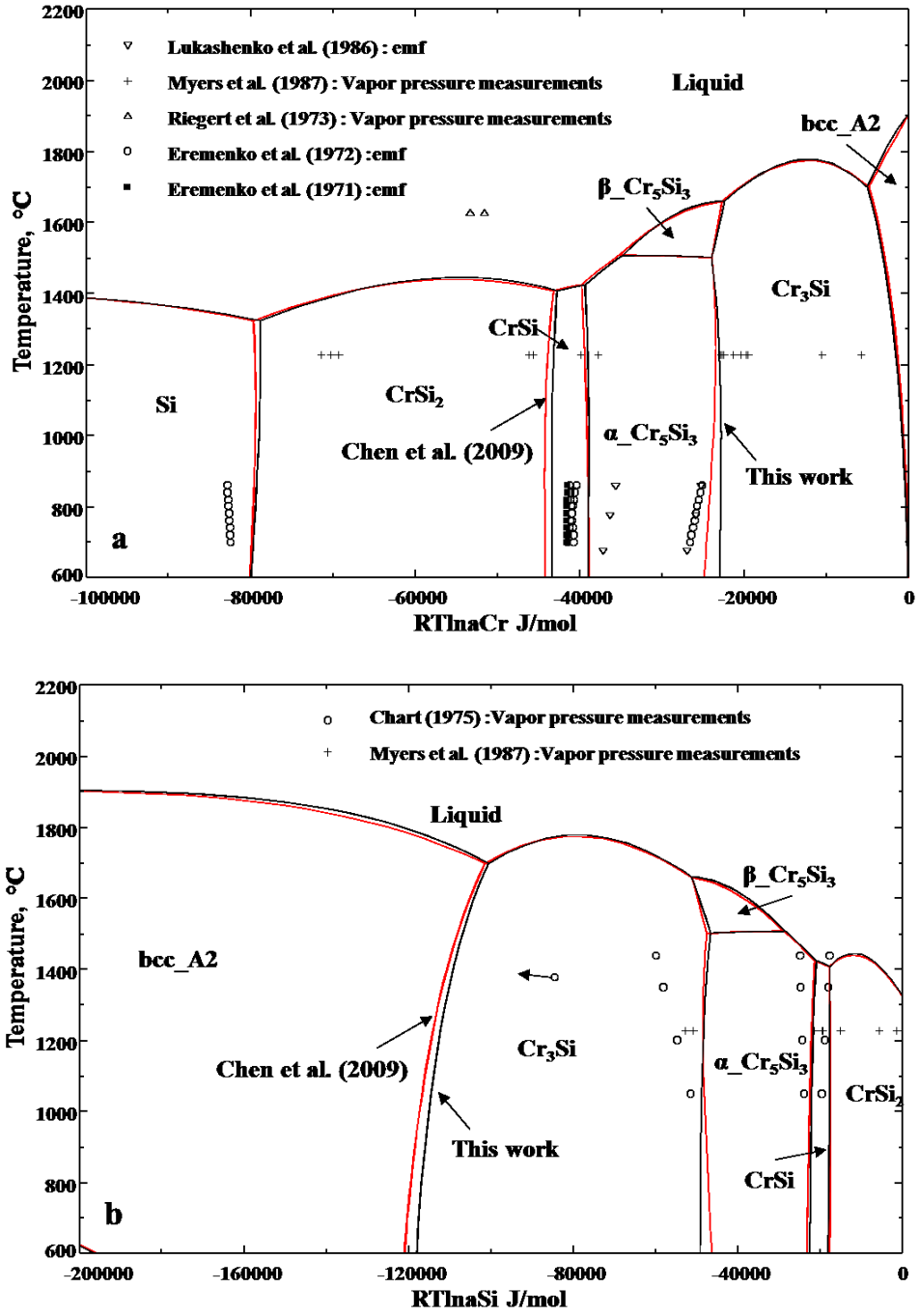

Fig. 6.6 Calculated (a) chemical potential diagram of Cr with respect to bcc_A2 Cr and (b) chemical potential diagram of Si with respect to diamond_A4 Si along with the experimental data.

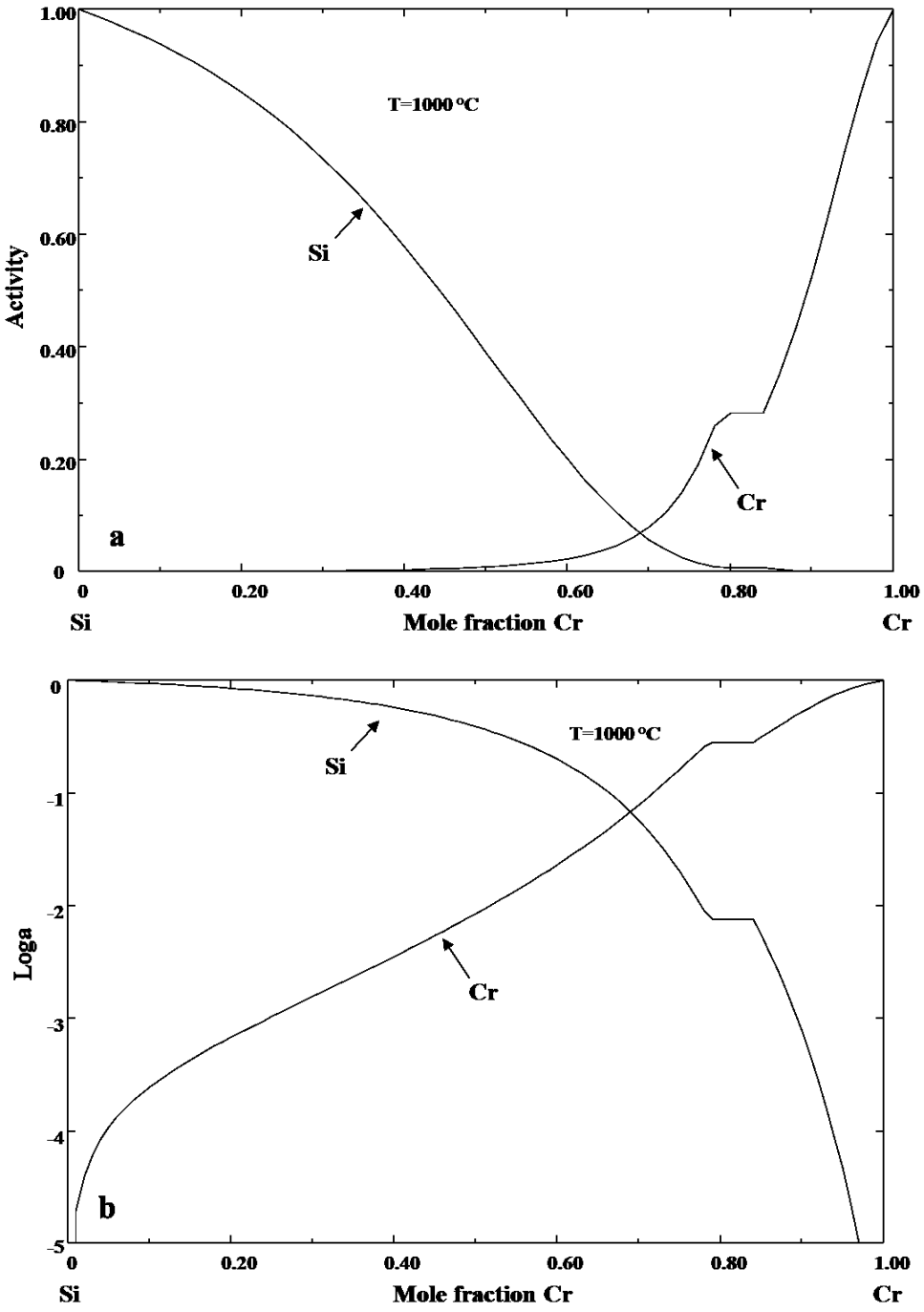

Fig. 6.7 Calculated activities of Cr with respect to bcc_A2 Cr and Si with respect to liquid Si at 1000 °C. (a) Line scale, and (b) logarithm scale.

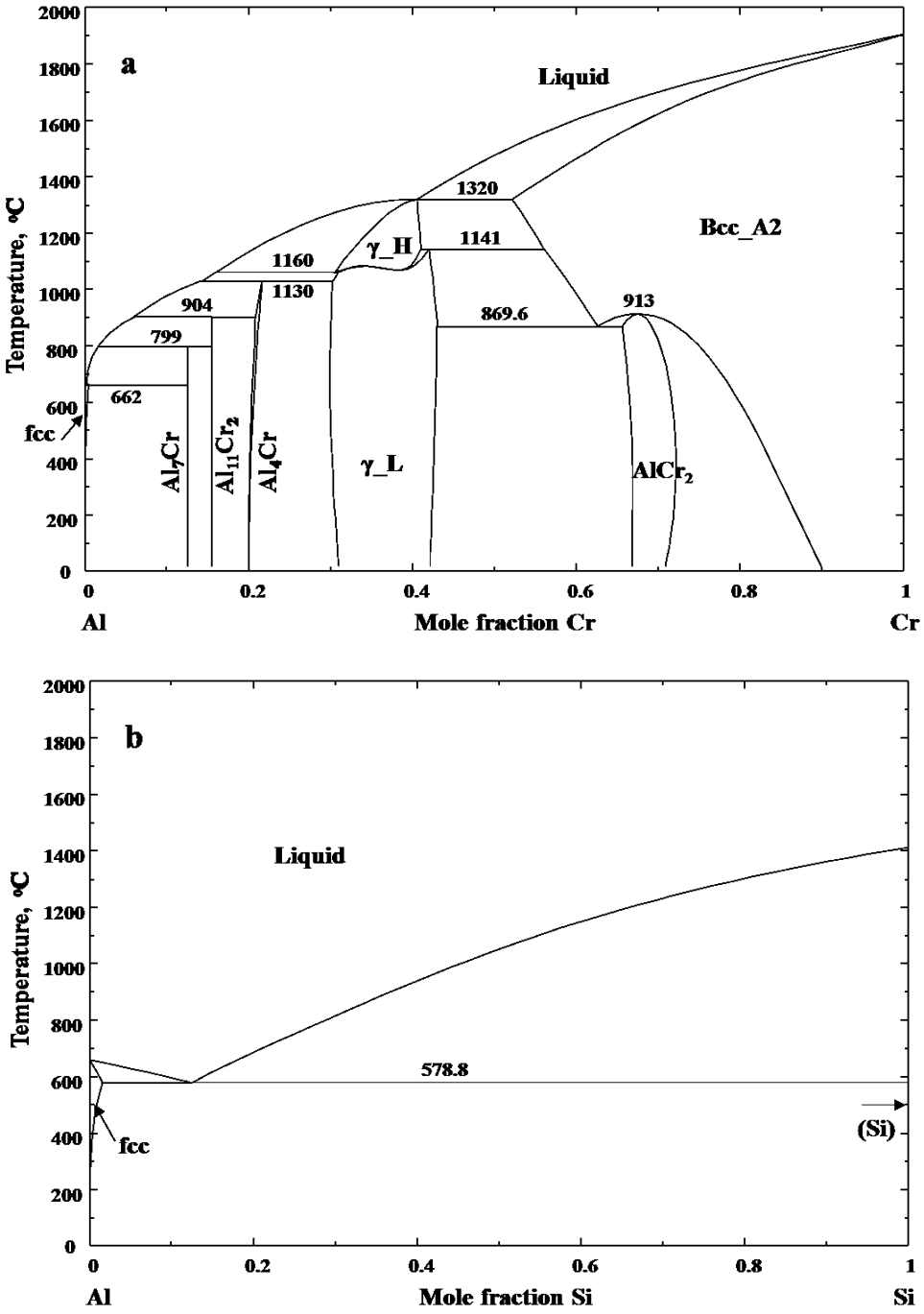

Fig. 6.8 Calculated phase diagram of (a) the Al-Cr system by Cui et al. [5] and (b) the Al-Si system by Harvey [6].

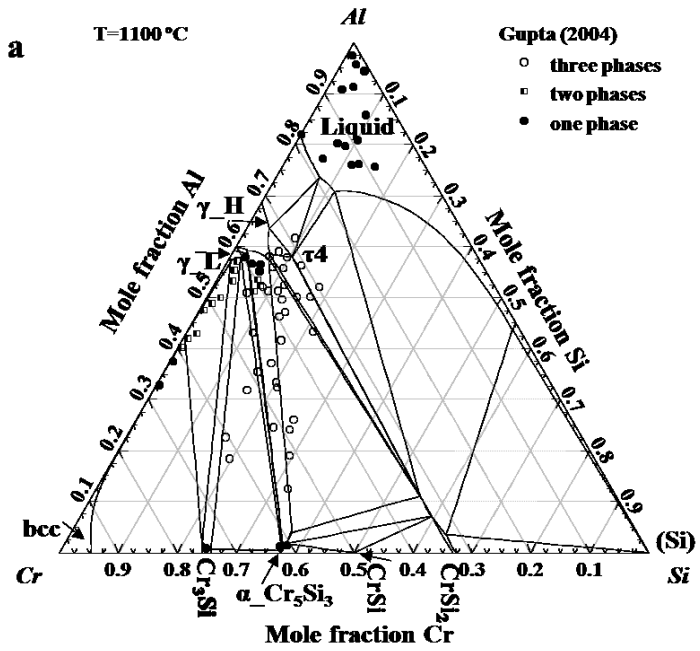
a
T=1100 °C
Gupta (2004)
three phases
two phases
one phase
Al
Liquid
γ_H
γ_L
τ4
bcc
Cr
(Si)
Si
Mole fraction Al
Mole fraction Si
Mole fraction Cr
Cr3Si
α_Cr5Si3
CrSi
CrSi2

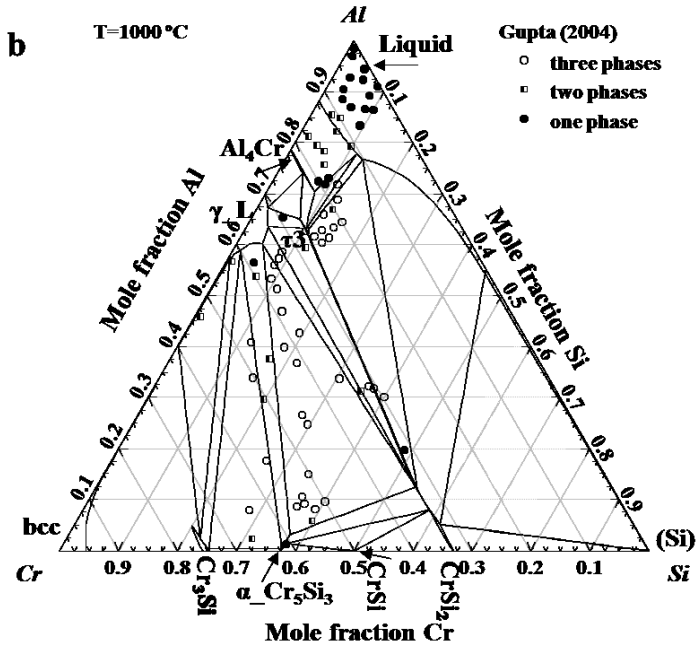
b
T=1000 °C
Gupta (2004)
three phases
two phases
one phase
Al
Liquid
Al4Cr
γ_L
τ3
bcc
Cr
(Si)
Si
Mole fraction Al
Mole fraction Si
Mole fraction Cr
Cr3Si
α_Cr5Si3
CrSi
CrSi2

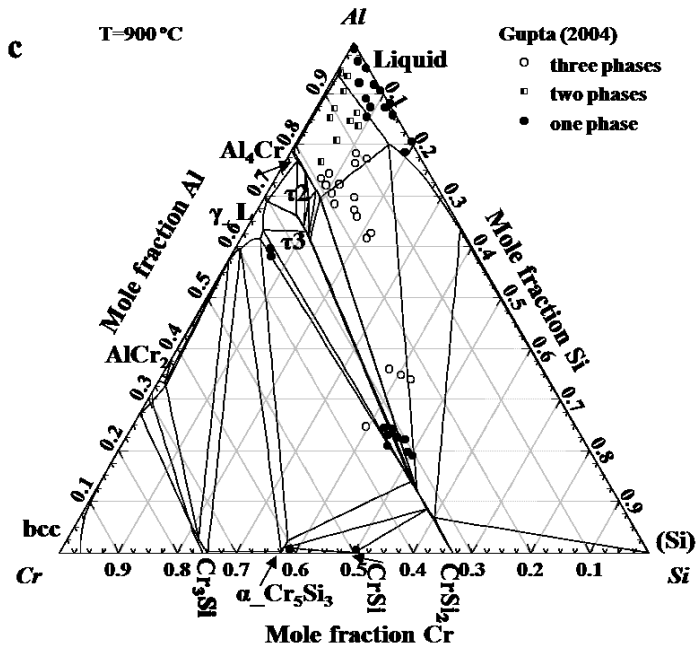
c
T=900 °C
Al
Liquid
Gupta (2004)
three phases
two phases
one phase
Al4Cr
τ2
γ
L
τ3
AlCr2
bcc
Cr
Si
(Si)
Cr3Si
α_Cr5Si3
CrSi
CrSi2
Mole fraction Al
Mole fraction Si
Mole fraction Cr

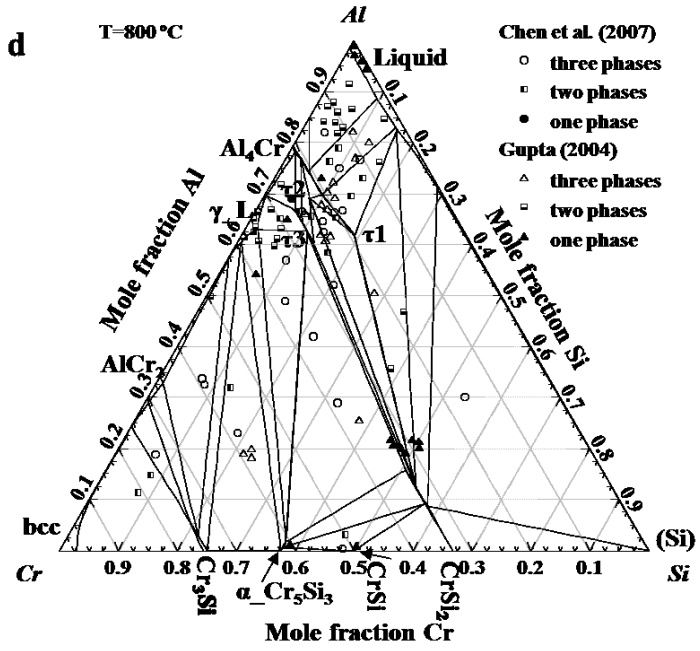
d
T=800 °C
Al
Liquid
Chen et al. (2007)
three phases
two phases
one phase
Gupta (2004)
three phases
two phases
one phase
Al4Cr
τ2
γ
L
τ3
τ1
AlCr2
bcc
Cr
Si
(Si)
Cr3Si
α_Cr5Si3
CrSi
CrSi2
Mole fraction Al
Mole fraction Si
Mole fraction Cr

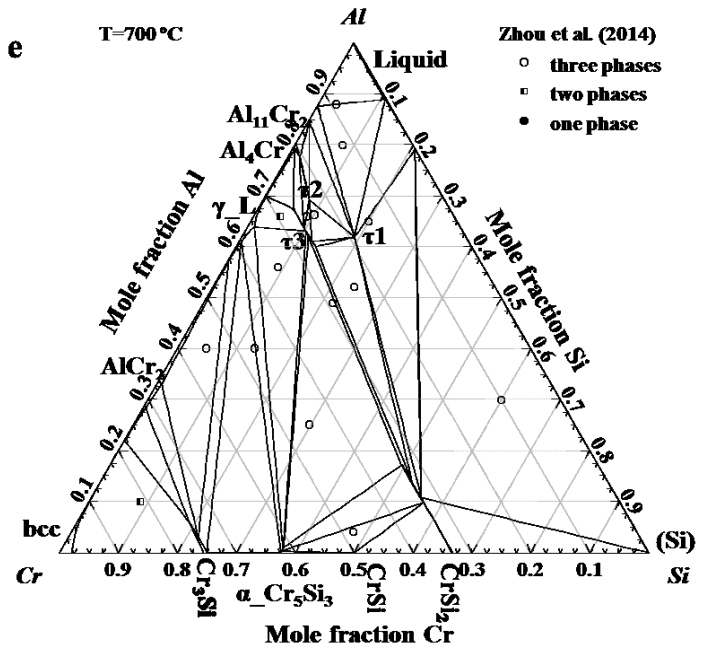

Fig. 6.9 Calculated isothermal sections of the Al-Cr-Si system along with the experimental data at different temperatures. (a) 1100 °C, (b) 1000 °C, (c) 900 °C, (d) 800 °C, and (e) 700 °C.

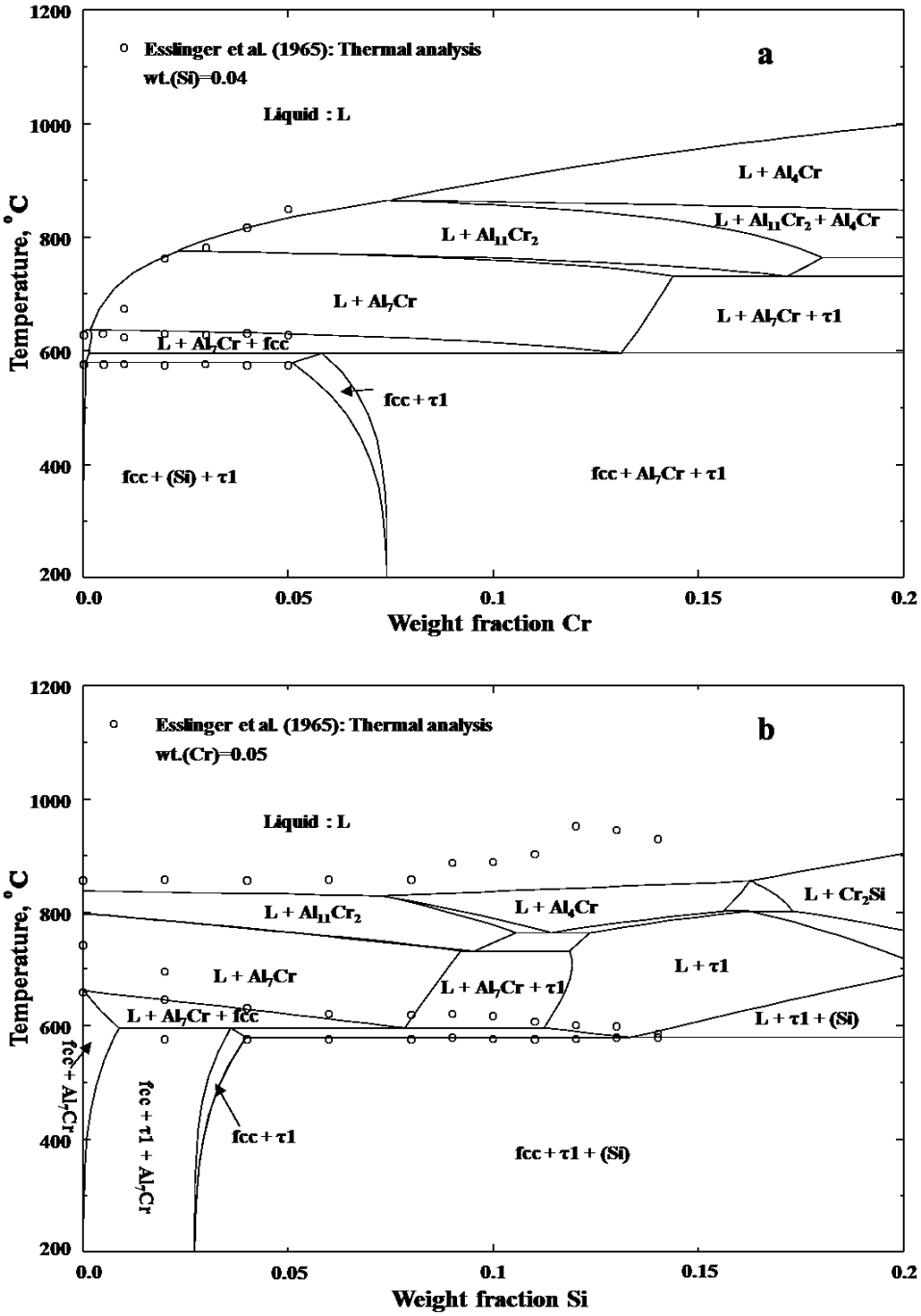

Fig. 6.10 Calculated isoplethal sections in the Al-Cr-Si system along with the experimental data. (a) At 4 wt.% Si and (b) 5 wt.% Cr.

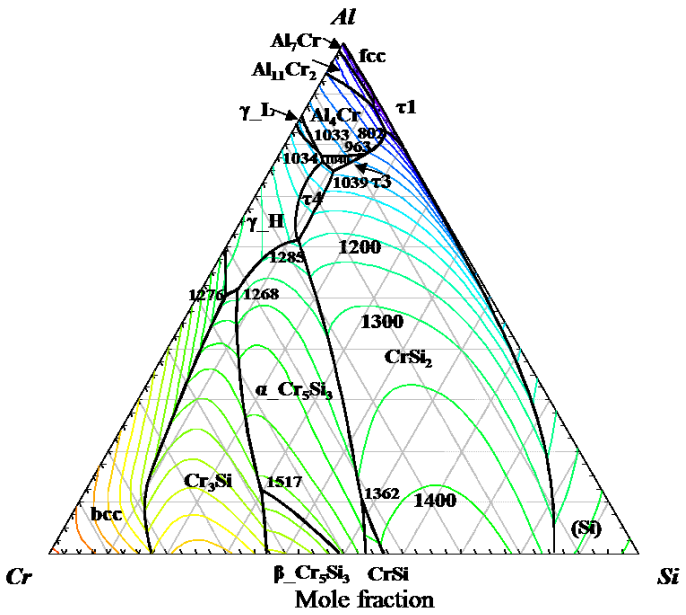

Fig. 6.11 Calculated liquidus projection of the Al-Cr-Si system.

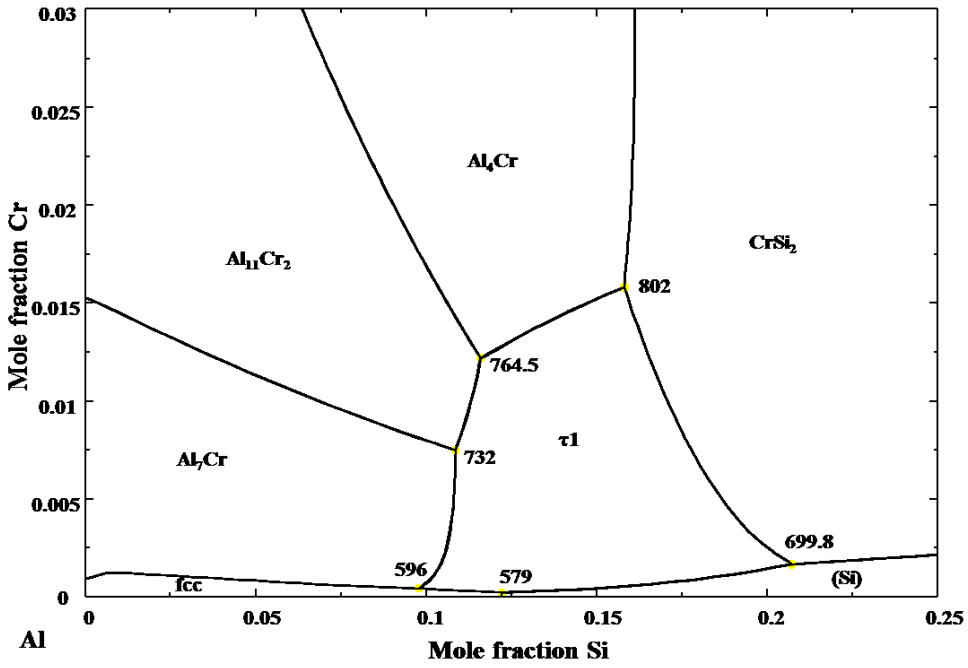

Fig. 6.12 Enlarged part of the liquidus projection of the Al rich Al-Cr-Si system.

Chapter 7 Thermodynamic modeling of the Cu-Fe-Cr and Cu-Fe-Mn systems

Senlin Cui and In-Ho Jung

Department of Mining and Materials Engineering, McGill University, 3610 University Street, Montreal, Quebec, H3A 0C5, Canada

Abstract

All the thermodynamic and phase diagram information available in the literature on the Cu-Cr system, Cu-Fe-Cr system, and Cu-Fe-Mn system were critically evaluated and optimized to obtain a set of consistent thermodynamic model parameters for the systems. The liquid solutions for the Cu-Cr, Cu-Mn, Fe-Cr, Cu-Fe-Cr, and Cu-Fe-Mn systems were described using the Modified Quasichemical Model (MQM) with pair approximation. The solid solution phases were modeled using the Bragg-Williams random mixing model. Accurate reproduction of all the reliable phase diagram and thermodynamic property data indicates the high reliability of the present thermodynamic optimizations.

Key words:

Cu-Cr alloy; Cu-Mn alloy; Fe-Cr alloy; Cu-Fe-Cr alloy; Cu-Fe-Mn alloy; phase diagram; thermodynamic modeling.

7.1 Introduction

The Cu-Fe and Cu-Cr systems are immiscible alloy systems in which the two constituent elements show little or no mutual solubility in the solid state and even in the liquid state up to a very high temperature [1]. This type of system is characterized by a large positive enthalpy of mixing in both the liquid and solid states. Due to the large entropic contribution to the free energy of mixing of liquid, liquid may become miscible at high temperature. Generally, the constitutional elements are immiscible, show the vanish of solid solubility and no intermetallic compound formation at low temperature. In spite of the impossibility for alloying of this type of system at room temperature under equilibrium condition, single phase alloys, such as amorphous phases, supersaturated crystalline solid solutions and metastable intermetallic compounds can be formed via rapid quenching process or mechanical alloying process. Cu-Fe based alloys are extensively utilized to fabricate typical immiscible alloys using mechanical alloying with high thermal and electrical conductivity and excellent magnetic properties [2-6]. The Cu rich corner of the Cu-Fe-Cr alloys is the potential candidate for the precipitation harden-able, high strength, high conductivity, softening resistant, and cost effective Cu alloys [7-9]. It is also known that the addition of transitional metallic elements such as Cr and Cu into high Mn steel can alter the stacking fault energy which determines the deformation mechanisms of α ferritic steel [10]. In addition, the Al-Cu-Fe-Cr alloys is a typical alloy to form quasi-crystalline structure for coatings and thin films [11-13]. Accurate understanding of the phase relation and thermodynamic properties of the Cu-Fe-Cr and Cu-Fe-Mn ternary systems is of fundamental importance not only for the development of Cu-Fe based alloys but also for the further development of Al-based and Fe-based alloys. Cu, Cr, Mn, and Fe are the common alloying and impurity elements in commercial Al alloys.

The Cu-Fe-Cr system was thermodynamically assessed previously by Ohtani et al. [14], Wang et al. [15], and Turchanin et al. [16] using the CALPHAD (CALculation of PHAse Diagram) method. In the work of Ohtani et al. [14], only the three isothermal sections at 1100, 1200, and 1300 °C measured by themselves were considered to determine the thermodynamic parameters. So the work is not comprehensive enough. Wang et al. [15] remodeled the Cu-Fe-Cr system by considering their new experimental phase diagram data at 800, 900, 1000, and 1100 °C. The recent

work by Dreval et al. [17] added their enthalpy of mixing of the liquid phase as input for the thermodynamic modeling. Recently, Zhou et al. [18] indicated that a stable liquid miscibility gap exists in the binary Cu-Cr system. However, none of the above thermodynamic descriptions can address it. Therefore, new thermodynamic modeling of the binary Cu-Cr system and ternary Cu-Fe-Cr system are necessary for accurate understanding.

The Cu-Fe-Mn system was optimized by Hasebe and Nishizawa [19-21], Kumar and Raghavan [22], Ohtani et al. [14], Miettinen [23], Wang et al. [15], and Zhang et al. [24]. The lattice stabilities (The Gibbs energies of pure stable and metastable elements) used by Hasebe and Nishizawa [19-21] are different from that of SGTE (Scientific Group Thermodata Europe) pure element database [25]. So their results cannot be integrated with other available database due to inconsistency in Gibbs energy of pure element. Kumar and Raghavan [22] conducted a thermodynamic calculation of the Cu-Fe-Mn system only in the Fe rich side. Ohtani et al. [14] considered only their own experimental isothermal phase diagram data at 1100, 1200, and 1300 °C, which gives a low prediction ability at low temperature. Miettinen [23] conducted a thermodynamic optimization for the Cu-Fe rich side of the Cu-Fe-Mn system. The calculated results are in good agreement only with the limited data in the Cu-Fe rich region used in his assessment. Wang et al. [26] also carried out a thermodynamic assessment to describe all the available phase diagram and thermodynamic information in the literature. Recently, Zhang et al. [24] presented another thermodynamic modeling for the Cu-Fe-Mn system with less model parameters.

The present work tends to thoroughly use the Modified Quasi-chemical Model (MQM) for the liquid phase. The aim of this study is the thermodynamic modeling of the Cu-Cr, Cu-Fe-Cr, and Cu-Fe-Mn systems, and the revision of the thermodynamic description of the liquid phase of the Fe-Cr system by Andersson and Sundman [27] and the Cu-Mn system by He et al. [28] using MQM to improve the description of each binary phase diagram and thermodynamic properties. This study is part of a comprehensive thermodynamic database development for Al alloys to design new wrought Al alloys for automotive applications.

7.2 Critical evaluation of literature information

7.2.1 The Cu-Cr system

The Cu-Cr system was previously assessed by Kaufman [29], Saunders [30], Hämäläinen et al. [31], Zeng and Hämäläinen [32], Jacob et al. [33], and Zhou et al. [18]. The major differences are the liquid miscibility gap lies in the Cr rich side of the system. Kaufman [29] modeled the Cu-Cr system for the first time with a stable liquid miscibility gap. Saunders [30] and Hämäläinen et al. [31] optimized the Cu-Cr system using the sub-regular solution model and no stable liquid miscibility gap was calculated. Zeng and Hämäläinen [32] updated the thermodynamic description of the Cu-Cr binary system by taking into account the new experimental data collected. Jacob et al. [33] refined the thermodynamic description of the Cu-Cr system by considering their activity data from electron motive force (emf) data. Recently, Zhou et al. [18] re-analyzed the Cu-Cr system to reproduce the stable liquid miscibility gap observed in their thermal analysis experiments. However, the thermodynamic properties of the liquid phase were not well reproduced. Okamoto [34-37] also provided the review of the phase diagram of the binary Cu-Cr system.

The activity of Cr in the Cu-Cr alloys was measured by Jacob et al. [33] in the temperature range from 1200 to 1600 ºC using the emf technique, Inouye et al. [38] (the Cu rich region only) from 1150 to 1300 ºC by the emf technique, and Ono et al. [39] at 1300 ºC by a Knudsen cells mass spectrometry technique. Timberg and Toguri [40] measured the activity of Cu in the Cu-Cr system at 1550 ºC using the high temperature mass spectrometric technique. These activity data show generally good agreement with each other. The enthalpy of mixing for the liquid Cu-Cr phase was reported only by Turchanin and Nikolaenko [41], who investigated the standard enthalpies of solution of Cr in liquid Cu at 1600 ºC by high temperature calorimetry.

There are three phases, fcc_A1 or (Cu), bcc_A2 or (Cr), and liquid, in the Cu-Cr system. The solubilities of Cr in (Cu) were measured by Drits et al. [42] by metallographic analysis of isothermal sections of the Cu-Cr-Hf system from 400 to 900 ºC, Zakharov and Osintsev [43] by x-ray diffraction (XRD) analysis, Doi [44] and Hibbard et al. [45] by way of microscopic

observation and electrical resistivity measurements, and Alexander [46] using microscopic analysis and chemical analysis. All these measurements are generally in good agreement.

The solubilities of Cu in (Cr) were only measured by Kuznetsov et al. [47] and Leonov et al. [48] by equilibration experiments. These two sets of data are also consistent, and the maximum solubility of Cu in (Cr) is about 0.35 at.% near 1700 °C.

Several groups of authors contributed to the measurements of the liquidus of the Cu-Cr system. Doi [44] studied the liquidus and eutectic point in the Cu rich region of the Cu-Cr system by thermal analysis. Kuznetsov et al. [47] measured the liquidus in the Cu rich corner up to 10 at.% Cr by equilibration experiments. Ono et al. [39] investigated the liquidus line in the Cu rich region by mass spectrometric measurements and differential thermal analysis (DTA). The measured liquidus line shows divergence with the previous measurements. Leonov et al. [48] studied the phase equilibrium in the Cu-Cr system from 10 to 100 at.% Cr by DTA, equilibration, XRD, and metallographic analysis. The measured phase diagram exhibits a stable liquid miscibility gap in the high Cr region. Zhou et al. [49] reported that there is a metastable liquid miscibility gap in the Cu-Cr system by examining the microstructures of splat-quenched alloy melts containing 5-70 at.% Cr. Later, Zhou et al. [18] re-examined the liquidus temperature of the Cu-Cr system from 10 to 72.7 at.% Cr using thermal analysis. Unlike their previous results, microstructure analysis showed that the Cu rich alloys exhibited dendritic solidification microstructure and the Cr rich alloys showed droplet-shaped microstructure which indicated a stable liquid miscibility gap in the Cr rich region.

The stable miscibility gap in the Cr rich part of the Cu-Cr system reported by Leonov et al. [48] and Zhou et al. [49] shows certain contradiction to the activity data measured by Jacob et al. [33] using the emf technique. The measured activity data by Jacob et al. [33] could be wrong due to no consideration of the existence of stable Cu-Cr-O oxide compounds which could be formed according to their cell configuration. Therefore, a stable liquid miscibility gap is considered in this study.

7.2.2 The Fe-Cr system

The Fe-Cr system has been thermodynamically assessed by many researchers including Chart et al. [50], Hertzman and Sundman [51], Andersson and Sundman [27], Lee [52], and recently Xiong et al. [53]. One of the most comprehensive evaluations of the thermodynamic properties and phase diagram information was conducted by Xiong et al. [53]. Lee [52] revised the liquid phase of the thermodynamic parameters obtained by Andersson and Sundman [27] in order to give a good description of the solid/liquid equilibria in the high order system. However, Lee's modification still cannot well reproduce the solid/liquid equilibria in the Fe-Cr system. The recent work by Xiong et al. [53] overcame the drawbacks of the previous assessments. However, the thermodynamic parameters obtained by Xiong et al. [53] cannot be utilized in the present study due to a different Gibbs energy of pure Fe utilized. As a result, in this study, the thermodynamic descriptions of the solid phases of the Fe-Cr system obtained by Andersson and Sundman [27] was accepted and the thermodynamic description of the liquid phase was revised using MQM. Thus, only the thermodynamic and phase equilibria data related to the liquid phase are reviewed here. More comprehensive literature review of this system can be found in the recent publication by Xiong et al. [53].

The enthalpy of mixing of the liquid Fe-Cr alloys were measured by Thiedemann et al. [54] up to 43 at.% Cr at 1627 and 1737 °C using a levitation alloying calorimetry method, Iguchi et al. [55] in the composition range of 0 to 21 at.% Cr at 1600 °C by an isoperibolic calorimeter, Shumikhin et al. [56] at 1700 °C and Batalin et al. [57] up to 40 at.% Cr at 1600 °C using solution calorimetry, and Pavars et al. [58] by analyzing the super saturation vapor pressure. The measured enthalpy of mixing data from Batalin et al. [57] and Shumikhin et al. [56] are positive, Thiedemann et al. [54] and Pavars et al. [58] indicate an ideal enthalpy of mixing, and Iguchi et al. [55] presents a negative enthalpy of mixing. During the present optimization, it was found that the ideal liquid Fe-Cr solution could give a better prediction of the thermodynamic properties of the Fe-Cr-Cu ternary solution.

The activities of the Fe-Cr alloys were measured by Maruyama and Ban-ya [59] up to 50 at.% Cr at 1600 °C by vapor pressure measurements, Mills and Grieveson [60] in the temperature

range of 1727 to 1927 °C using a technique involving electromagnetic levitation in an inert atmosphere, Pavars et al. [58] at 1600-1700 °C from 21 at.% Cr to 62 at.% Cr by vapor pressure measurements, Wada et al. [61] at 1630 °C up to 40 at.% Cr by a vaporization method using radioactive Cr, Reese et al. [62], Belton and Fruehan [63], and Gilby and Pierre [64] at 1400-1700 °C using the Knudsen cell effusion method, Fruehan [65] at 1600 °C from 11.5 to 52.2 at.% Cr and Ohtani [66] at 1540 °C up to 20 at.% Cr using the emf technique, and Hadrys et al. [67] by measuring the equilibrium distribution of Cr between Ag-Cr and Fe-Cr melts. The results from these measurements are generally in good agreement and show ideal solution behavior.

The liquid/solid equilibria were investigated by Oberhoffer and Esser [68], and Adcock [69] in the whole composition range, Putman et al. [70] in the composition range between 0 and 40 at.% Cr, Hellawell and Hume-Rothery [71] in the composition range of up to 40 at.% Cr, Schürmann and Brauckmann [72] up to 35 at.% Cr, and Kundrat et al. [73] from 0 to 25 wt.% Cr using thermal analysis, Belton and Fruehan [63] also measured liquidus and solidus using a Knudsen cell with mass spectrometry measurements. Except for the early investigation by Oberhoffer and Esser [68], all other experimental results show reasonable consistency.

7.2.3 The Cu-Mn system

The Cu-Mn system was previously assessed by Gokcen [74], Vřešťál et al. [75], Miettinen [76], Lewin et al. [77], Wang et al. [26], and He et al. [28]. Among these thermodynamic modeling, the most accurate one is by He et al. [28]. In the present study, the descriptions of the solid phases by He et al. [28] are adopted without any modification. Only the liquid phase was re-modeled using MQM instead of the original Bragg-Williams random mixing model. Since the current optimization is focused on the optimization of the liquid phase, only the experimental information related to the liquid phase is reviewed. A detailed review can be found in He et al. [28].

The enthalpy of mixing of the liquid phase in the entire composition range was measured by Turchanin and Nikolaenko [78] using an isoperibolic calorimeter at 1300 °C and Sato and Kleppa [79] using high temperature calorimetry at 1113 °C. Vřešťál et al. [75] measured the vapor pressure in the Cu-Mn system up to 70 at.% Mn using a Knudsen effusion cell coupled with mass

spectrometry at 1037-1207 °C with the composition range of 4.62-73.14 wt.% Mn. The activities of Cu and Mn at 1097 °C were calculated from the vapor pressure results.

The solidus and liquidus of the Cu-Mn system were measured by Grube et al. [80], Hellawell and Hume-Rothery [71], Wachtel et al. [81], and He et al. [28]. Grube et al. [80] measured the liquid/solid equilibria in the whole composition range by means of thermal analysis. Hellawell and Hume-Rothery [71] measured the phase equilibria in the Mn rich side up to 30 at.% Cu of the Cu-Mn system using thermal analysis. Wachtel et al. [81] measured the liquidus in the Mn rich side up to 20 at.% Cu using magnetic susceptibility measurements. He et al. [28] measured the solidus and liquidus in the Cu-Mn system using both DTA and differential scanning calorimetry (DSC). The experimental data are generally consistent with each other.

7.2.4 The Cu-Fe-Cr system

The Cu-Fe-Cr system was reviewed by Raghavan [82-84], and Turchanin and Velikanova [85]. Moriwaki [86] measured the phase equilibria in the Fe-Cr-Cu system up to 40 wt.% Cr and 40 wt.% Cu by thermal analysis, dilatation measurements, and microscopic examinations. No ternary intermetallic compounds were identified. The only invariant reaction, liquid + fcc_A1#1 (Fe) = bcc_A2 (Fe) + fcc_A1#2 (Cu), happens at 1085 °C. Salter [87] measured the isothermal sections of the Cu-Fe-Cr system (in the Cu-Fe rich side) at 900, 1100, and 1250 °C by electron probe microanalysis (EPMA). Unfortunately, mild steel was utilized as source of Fe instead of pure Fe. Ahmed et al. [88] measured the solubility of Cu in Fe in the Cu-Fe-Cr system with alloys with constant Cu contents (2 and 4 wt.% Cu) and varying Cr from 0 to 20 wt.% by the dilatometry, DTA, and XRD techniques. Jiang and Hao [89] measured the isothermal section of the Cu-Fe-Cr system at 1000 °C. Ohtani et al. [14] studied the phase diagram of the Fe-Cr-Cu system at 1000, 1200, and 1300 °C using solid-liquid diffusion couples. Fernee et al. [90] measured the solubilities of Fe and Cr in the Cu solid solution at 500-1050 °C by resistivity measurements and wavelength-dispersive X-ray spectroscopy analysis (WDS). Recently, Wang et al. [15] measured the phase equilibria in the Fe-Cr-Cu system at 800, 900, 1000, and 1200 °C using equilibrium alloys analyzed by EDS. The research of Wang et al. [26] indicated that the Cr addition in the Fe-Cu base alloys can form a core type macroscopic morphology.

The enthalpy of mixing of the ternary liquid phase was only measured by Turchanin et al. [16, 91] using calorimetry at 1600 °C from 0 to 45 at.% Cr at constant Cu/Fe atomic ratio of 3/1, 1/1, and 1/3. The partial enthalpy of mixing of Cr at 1600 °C and integral enthalpy of mixing using the Gibbs-Duhem relation were reported. Physicochemical analysis of the calorimetric samples indicated that the liquid miscibility gap is stable at the alloy composition $Cu_{0.3}Fe_{0.3}Cr_{0.4}$.

7.2.5 The Cu-Fe-Mn system

Raynor and Rivlin [92] reviewed the experimental data on the Cu-Fe-Mn system for the first time, and then Raghavan [93-96] updated the later experimental results. Another detailed literature review was from Lebrun and Perrot [97]. A brief review of phase diagram experimental data is given below. No thermodynamic properties of this ternary system were measured so far.

Parravano [98] measured the phase equilibria of the Cu-Fe-Mn system in the whole composition range at 880-1450 °C using thermal analysis and micrographic analysis. The liquidus lines at 900, 1000, 1200, 1300, 1400, and 1500 °C and isoplethal sections at 10 wt.% Mn, 20 wt.% Mn, 30 wt.% Mn, 10 wt.% Fe, 20 wt.% Fe, 30 wt.% Fe, 10 wt.% Cu, 20 wt.% Cu, and 30 wt.% Cu were given as results of his study. Later, Salter [87] measured the phase relation of the Cu-Fe-Mn system at 890, 1120, and 1250 °C using equilibrium alloys characterized by EPMA. However, mild steel was used as source of Fe, so there is possibility of error in phase diagram experiments. Hasebe and Nishizawa [19] investigated the miscibility gap of the fcc_A1 phase in the Fe-Cu-Mn system at 850 and 900 °C and the liquid/solid phase equilibria at 900, 950, and 1050 °C using diffusion couples and quenched equilibrium alloys followed by microanalysis. Ohtani et al. [14] measured the phase relations at 1100, 1200, and 1300 °C using solid/liquid diffusion couples and EDS analysis. Wang [99] measured the phase equilibrium in the Cu-Fe rich side of the Cu-Fe-Mn system at 800, 900, 1000, and 1200 °C. Recently, Zhang et al. [24] examined the phase equilibria at 800 °C and the transition temperature using four equilibrated alloys with constant 20 wt.% Cu using EPMA, XRD analysis, and DTA. The DTA measurement results by Zhang et al. [24] proved that the early measurement results by Parravano [98] are reliable.

7.3 Thermodynamic modeling

7.3.1 Pure elements

The Gibbs energy of pure element is described as below:

$$G_T = H_T - S_T T \tag{7.1}$$

$$H_T = \Delta H^o_{298.15} + \int_{298.15}^{T} C_P dT \tag{7.2}$$

$$S_T = S^o_{298.15} + \int_{298.15}^{T} \frac{C_P}{T} dT \tag{7.3}$$

where H_T and S_T are enthalpy and entropy at temperature *T*, respectively. $\Delta H^o_{298.15}$ and $S^o_{298.15}$ are the enthalpy of formation and entropy at 298.15 K, and C_p is the heat capacity. In the present assessment, the Gibbs energy data for the pure elements are all taken from the SGTE pure element database compiled by Dinsdale [25].

7.3.2 Liquid

The Gibbs energy of the liquid phase can be modeled using the Modified Quasi-chemical Model (MQM) proposed by Pelton et al. [100, 101]. In the present study, MQM was thoroughly used for the liquid solution to develop the constituent thermodynamic database of the liquid solution containing Al, Cr, Fe, Mg, Mn, and Si for new Al alloy database. The brief description of MQM is given below:

On the assumption that the following pair exchange reaction exists in the liquid:

$$(m\text{-}m) + (n\text{-}n) = 2(m\text{-}n) : \quad \Delta g_{mn} \tag{7.4}$$

where (*m*-*m*), (*n*-*n*), and (*m*-*n*) represents the first-nearest-neighbor atom pairs. The non-configurational Gibbs energy change for the formation of two moles of (*m*-*n*) pairs from (*m*-*m*) and (*n*-*n*) pairs is Δg_{mn}. The Gibbs energy of a binary solution can be written as:

$$G = n_m G_m^o + n_n G_n^o - T\Delta S^{config} + (n_{mn}/2)\Delta g_{mn} \tag{7.5}$$

where n_i is the number of moles of *i* atoms, and n_{mn} is the number of moles of (*m*-*n*) pairs. ΔS^{config} is the configurational entropy of mixing given by a random distribution of the three types of pairs in the one-dimensional Ising approximation:

$$\Delta S^{config} = -R(n_m \ln x_m + n_n \ln x_n) - R\left[n_{mm} \ln\left(\frac{x_{mm}}{Y_m^2}\right) + n_{nn} \ln\left(\frac{x_{nn}}{Y_n^2}\right) + n_{mn} \ln\left(\frac{x_{mn}}{2Y_m Y_n}\right)\right] \tag{7.6}$$

where n_{mm} is the moles of each type of pairs, x_{mn} is the pair fraction, and Y_m is the coordination equivalent fraction defined as:

$$x_{mn} = n_{mn}/(n_{mm} + n_{nn} + n_{mn}) \tag{7.7}$$

$$x_m = n_m/(n_m + n_n) \tag{7.8}$$

$$Y_m = x_{mm} + \frac{1}{2}(x_{mn}) \tag{7.9}$$

Δg_{mn} in Eq. (7.5) can be considered as the excess Gibbs energy of liquid *m*-*n* alloys, which can be expanded as a polynomial in terms of the pair fractions described as follows:

$$\Delta g_{mn} = \Delta g_{mn}^0 + \sum_{i\geq 1} g_{mn}^{i0}(x_{mm})^i + \sum_{j\geq 1} g_{mn}^{0j}(x_{nn})^j \tag{7.10}$$

where Δg_{mn}^{0}, g_{mn}^{i0}, and g_{mn}^{0j} are the model parameters which can be functions of temperature. Let Z_m be the coordination number of component *m*, the following relation holds:

$$Z_m n_m = 2n_{mm} + \sum_{n \neq m} n_{mn} .$$

In multicomponent system, composition dependent coordination number of element *m* were introduced to provide flexibility and permit the independent chosen of the composition of maximum short range ordering in each binary subsystem,

$$\frac{1}{Z_m} = \frac{1}{2n_{mm} + \sum_{i \neq m} n_{mi}} \left(\frac{2n_{mm}}{Z_{mm}^{m}} + \sum_{i \neq m} \frac{n_{mi}}{Z_{mi}^{m}} \right) \tag{7.11}$$

where Z_{mi}^{m} is the value of Z_m when all the nearest neighbors of atoms *m* are atoms *i*. The maximum short range ordering in each binary subsystem is determined by the ratio of Z_{mn}^{m} / Z_{nm}^{n}. In the present study, all the Z are set as 6. One can freely choose symmetric or asymmetric extrapolation technique to predict the Gibbs energy of the ternary system from binary model parameters depending on the energies of sub-binary systems. The detailed extrapolation technique can be found elsewhere [100, 101]. The symmetric Kohler type of extrapolation technique was used for the Cu-Fe-Mn solution. An asymmetric Toop type interpolation was used for the Cu-Fe-Cr liquid solution.

7.3.3 fcc_A1, bcc_A2, and hcp_A3 phases

The molar Gibbs energies of the fcc_A1, bcc_A2, and hcp_A3 phases are described using the Bragg-Williams random mixing model in the form of Redlich-Kister (R-K) polynomial [102]:

$${}^{o}G_m^{\phi} = \sum_{i=1}^{3} x_i {}^{o}G_i^{\phi} + RT \sum_{i=1}^{3} x_i \ln x_i + \sum_{i=1}^{3} \sum_{j>i}^{3} x_i x_j L_{ij}^{\phi} + \sum_{i=1}^{3} \sum_{j>i}^{3} \sum_{k>j}^{3} x_i x_j x_k L_{ijk}^{\phi} + \Delta G^{mag} \tag{7.12}$$

where x_i is the mole fraction of element *i*, ${}^{o}G_i^{\phi}$ is the molar Gibbs energy of pure element *i* with the ϕ state, *R* is gas constant, *T* is temperature in Kelvin, L_{ij}^{ϕ} is the binary interaction parameter, L_{ijk}^{ϕ} is the ternary interaction parameter, and ΔG^{mag} is a term for magnetic contribution to the Gibbs energy. Further, L_{ij}^{ϕ} is expanded into the form of $\sum_{v=0} L_{ij}^{v}(x_i - x_j)^v$ and L_{ijk}^{ϕ} is given as $x_i L_{ijk}^{i} + x_j L_{ijk}^{j} + x_k L_{ijk}^{k}$.

The magnetic contribution term ΔG^{mag} which given by the Hillert-Jarl-Inden model [103] is presented as:

$$\Delta G^{mag} = RT \ln(\beta^{\varphi} + 1) g(\tau^{\varphi}) \tag{7.13}$$

where τ is given by T/T^{*}; T^{*} is the critical temperature for magnetic transition. That is the Curie temperature T_C for ferromagnetic materials or Neel temperature T_N for antiferromagnetic materials. β is the average magnetic moment per mole of atom expressed in Bohr magnetons. $g(\tau^{\varphi})$ is a polynomial function derived by Hillert and Jarl [103].

7.4 Results and discussions

The optimization of the thermodynamic parameters of the Cu-Cr, Fe-Cr, Cu-Mn, Cu-Cr-Fe, and Cu-Fe-Mn systems were carried out by considering all the reliable experimental data evaluated in Section 7.2. The optimized model parameters are listed in Table 7.2. All the thermodynamic calculations were performed using the FactSage software [104]. The optimization results are discussed below.

7.4.1 The Cu-Cr system

The optimized phase diagram of the Cu-Cr system is calculated in Fig. 7.1 along with all the available phase diagram data. As can be seen in the diagram, all the experimental data are in general well reproduced in the present optimization. As summarized in Table 7.1, two invariant temperatures exist in the Cu-Cr system: Monotectic reaction of Liquid#1 = (Cr) + Liquid#2 and eutectic reaction of Liquid = (Cr) + (Cu). According to the early research by Hindrichs [105] and Siedschlag [106], monotectic reaction temperature is at around 1470 °C. However, in their study, the melting point of Cr was taken as 1550 °C which is substantially lower than 1907 °C extensively accepted nowadays [25]. Later, Leonov et al. [48] and Zhou et al. [18] reported the monotectic reaction temperature is at 1767 °C and 1747 °C, respectively. The optimized monotectic reaction temperature is at 66.2 at.% Cr and 1764 °C which is very close to the experimental data from Leonov et al. [48]. There is no controversy for the eutectic temperature in the Cu rich side. The calculated invariant temperature for the eutectic reaction liquid = (Cr) + (Cu) is 1078 °C which is very close to the measured ones, 1074-1076 °C.

It is clear that there is very limited mutual solubility in the solid state of the Cu-Cr system. As can be seen in Fig. 7.1(b), the measured solubilities of Cr in (Cu) by Ono et al. [39], Kuznetsov et al. [47], Drits et al. [42], Zakharov and Osintsev [43], Doi [44], Hibbard et al. [45], and Alexander [46] are well reproduced. The result for Cu solubility in (Cr) by Kuznetsov et al. [47] and Leonov et al. [48] are also well reproduced in Fig. 7.1(c). In both solutions, one parameter with temperature dependent term was optimized to reproduce their solubility limits.

The thermodynamic parameters for the liquid phase of the Cu-Cr system were optimized to reproduce the enthalpy of mixing of liquid, activity data, and the liquidus, simultaneously. The enthalpy of mixing of liquid at 1600 °C measured by Turchanin and Nikolaenko [41] is presented in Fig. 7.2(a) with the presently optimized results. The enthalpy of mixing is positive for the liquid phase in the Cu-Cr system, which indicates possibility of miscibility gap of the liquid phase. Partial enthalpy of mixing of liquid Cu is presented in Fig. 7.2(b). The partial enthalpy of Cu drops substantially from 120 kJ/mol at pure Cu to 0 kJ/mol at 20 at.% Cr according to the experimental data from Turchanin and Nikolaenko [41]. However, the partial enthalpy data are in consistent with their own mixing enthalpy data in Fig. 7.2(a). That is, if these partial enthalpy data are correct, the mixing enthalpy should be much positive.

The calculated activities of Cu and Cr are presented in Fig. 7.3. Fig. 7.3(a) is the calculated activities of Cu and Cr at 1550 °C in the present optimization compared with the experimental data from Timberg and Toguri [40]. The reference states of the activities are pure liquid Cu and pure solid Cr. The activity of Cr (s) reaches 1 at about 25 at.% Cr which indicates the solubility limits of Cr in the liquid phase at 1550 °C. As is also true for the activity of Cu (l). Fig. 7.3(b) shows the activities of Cr (s) at 1150, 1200, 1250, and 1300 °C. The experimental data of Inouye et al. [38] show the Henrian activity behavior up to 1 at.% Cr concentration, which is very well reproduced in the present study. Fig. 7.3(c) shows the calculated activity of Cr (s) at 1300 and 1600 °C compared with the corresponding experimental data from Ono et al. [39] and Jacob et al. [33]. The present thermodynamic calculation result can reasonably reproduce the measured values from Ono et al. [39] at 1300 °C. However, the calculated activity of Cr (s) reaches 1 plateau at about 26 at.% Cr at 1600 °C where is liquidus of solid Cr. However, the experimental data by Jacob et al. [33] show increasing activities of Cr up to 70 at.% Cr, which is completely vibrating the liquidus of Cr in Fig. 7.1(a). Therefore, the results of Jacob et al. [33] above 25 at.% Cr were neglected in the present study.

Four model parameters with three temperature dependent terms were optimized to reproduce all the experimental data in Figs. 7.2 and 7.3 together with the phase diagram in Fig. 7.1. The dashed line in Fig. 7.1 shows the calculated metastable miscibility gap from the present optimization. This miscibility gap will be valuable to design the immiscible alloy composition.

7.4.2 The Fe-Cr system

The purpose of modeling this system is the revision of thermodynamic description of the liquid Fe-Cr solution. The descriptions of the solid solutions are taken from the assessment results of Lee [52] without any modification. The main reason to revise the description of the liquid Fe-Cr solution is to improve the solidus and liquidus at the high Cr region, which will be discussed below again.

The presently calculated enthalpy of mixing of the liquid Fe-Cr solution is shown in Fig. 7.4 along with the experimental data from Thiedemann et al. [54], Batalin et al. [57], Iguchi et al. [55], Shumikhin et al. [56], and Pavars et al. [58]. The experimental data show either positive enthalpy of mixing [56, 57] or negative enthalpy of mixing [55]. It is hard to evaluate which set of data is more reliable.

In the present optimization, the almost ideal enthalpy of mixing data for the liquid phase were taken into consideration since the activities of Cr and Fe also behavior nearly ideal solution. The present optimization of the ternary Fe-Cr-Cu system also shows that ideal enthalpy of mixing gives more accurate prediction. It should be noted that the previous assessment by Lee [52] used the slightly negative enthalpy of mixing data. It can be seen from Fig. 7.4 that the present work gives a generally good fit to the measurement according to Thiedemann et al. [54]. Figs. 7.5(a) to (c) show the calculated activities of Cr and Fe compared with the related experimental data. The activities of Fe and Cr at 1927 °C with pure liquid Fe and Cr as reference states are shown in Fig. 7.5(a). The activities of Fe and Cr at 1700 and 1600 °C with pure solid Cr and liquid Fe as reference states are shown in Figs. 7.5(b) and (c), respectively. Like the enthalpy of mixing data in Fig. 7.4, the activity data are also scattered near ideal behavior. The experimental activities data of Fe and Cr are well reproduced within the experimental error range in the present study.

Fig. 7.6(a) presents the calculated Fe-Cr phase diagram according to the current revision. It can be seen from Fig. 7.6(b) that the present revision is much more reasonable than that by Lee [52] in comparison with the experimental phase diagram data in the Cr rich region. The calculated liquidus in the present study shows a minimum at about 21.1 at.% Cr and 1509 °C.

Three MQM model parameters with two temperature dependent terms were optimized to describe the liquid phase in this study. In particular, the liquidus in the Cr rich region is much improved, which is important for the Fe-Cr alloy phase diagram.

7.4.3 The Cu-Mn system

Fig. 7.7 presents the calculated activities of Cu and Mn at 1097 °C from this study compared with the experimental data from Vřešťál et al. [75]. Both reference states of pure liquid Cu and Mn are used. The calculation results from the work of He et al. [28] are also appended for a comparison. Even though the Gibbs energy of the liquid phase was revised in the present study using MQM, the calculated activities from the current revision are almost the same as those by He et al. [28], as can be seen in Fig. 7.7. In addition, as can be seen in Fig. 7.8, the enthalpy of mixing of liquid in this study is nearly the same as that of He et al. [28], and well reproduces the experimental data by Sato and Kleppa [79]. The calculated phase diagram of the Cu-Mn system shown in Fig. 7.9 from the present study is also well reproducing the experimental data like the previous work by He et al. [28]. The optimized liquid parameters are listed in Table 7.2.

7.4.4 The Cu-Fe-Cr system

The thermodynamic descriptions of the Cu-Fe binary system from Shubhank and Kang [107], and the present Cu-Cr and Fe-Cr systems are combined together to describe the Cu-Fe-Cr system. The calculated phase diagram of the Cu-Fe system is shown in Fig. 7.10. Table 7.2 shows the obtained thermodynamic parameters for the Cu-Fe-Cr system.

Turchanin et al. [16] measured the partial enthalpy of mixing of Cr along x_{Cu}/x_{Fe} = 3/1, 1/1, and 1/3 from 0 to 45 at.% Cr at 1600 °C, and calculated the integral enthalpy of mixing using the following Gibbs-Duhem equation:

$$\Delta H = (1-x_{Cr})\left[\Delta H_{x_{Cr}=0} + \int_0^{x_{Cr}} \frac{\Delta \bar{H}_{Cr}}{(1-x_{Cr})^2} dx_{Cr}\right]_{x_{Cu}/x_{Fe}} \tag{7.14}$$

According to this equation, integral enthalpy of mixing depends on the value $\Delta H_{x_{Cr}=0}$ which is the integral enthalpy of mixing of the binary Cu-Fe system. Since the binary Cu-Fe enthalpy utilized by Turchanin et al. [16] to calculate the ternary enthalpy of mixing is different from that used in the current work, a correction of the integral enthalpy of mixing by Turchanin et

al. [16] was done using the binary enthalpy description from Shubhank and Kang [107] to keep the consistency in the ternary system. The corrected data are plotted in Fig. 7.11.

In the present study, it was found that the asymmetric Toop extrapolation technique with Fe as asymmetric component provides a better description of the thermodynamic and phase diagram information of the ternary liquid phase. The solid lines in Figs. 7.11(a) to (c) are the calculated enthalpy of mixing from the present optimization. It is manifest that the calculated enthalpy of mixing can well describe these experimental data. The partial enthalpy of mixing data measured by Turchanin et al. [16] are quite scatter. The present study can reproduce the general trend of these partial enthalpy of mixing data, as can be seen in Figs. 7.12(a) to (c).

Isothermal sections at 800, 900, 1000, 1050, 1100, 1200, 1250, 1300, and 1600 °C are presented in Figs. 7.13(a) to (k). The experimental data from Wang et al. [15], Salter [87], Jiang et al. [89], Fernee et al. [90], and Ohtani et al. [14] are plotted with the calculated phase diagrams. The experimental data from Jiang et al. [89] and Salter [87] overstated the stable range of fcc_A1 compared to the binary Fe-Cu system, as can be seen in Figs. 7.13(b) and (c). The measured phase boundary data from Wang et al. [15], Fernee et al. [90], Ohtani et al. [14], and Salter [87] above 1000 °C show excellent agreement with each other, and well reproduced in this study. The calculated solubility limits of Cu at 800 and 900 °C are slightly lower than those by Wang et al. [15]. This discrepancy is originated from the binary Fe-Cu assessment results from Shubhank and Kang [107]. The stable liquid miscibility gap observed by Turchanin et al. [16] in the $Cu_{0.3}Fe_{0.3}Cr_{0.4}$ alloy can be well predicted in the present calculation at 1600 °C as can be seen in Fig. 7.13(i).

Isoplethal sections with 5 wt.% Cr, 10 wt.% Cr, and 20 wt.% Cr are calculated in Figs. 7.14(a) to (c). The calculated isoplethal sections are compared with the experimental data from Moriwaki [86]. In general, the solidus and liquidus data measured by thermal analysis are very well reproduced. The solubility of Cu in the fcc_A1 phase are also well calculated at 5 and 10 wt.% Cr sections. The two and three phases in the Fe rich region of 20 wt.% Cr section are inconsistent with the phase diagram information in Fig. 7.13(e) reported by Ohtani et al. [14]. So the measured phase diagram data by Moriwaki [86] in the low temperature range by microscopic analysis seems

to have error. Therefore, only the thermal analysis data measured by Moriwaki [86] were considered during the current assessment. Figs. 7.15(a) to (c) present the calculated isoplethal sections with 20, 30, and 40 wt.% Cu with the corresponding experimental data from Moriwaki [86]. All the experimental data are well reproduced in the present calculations. It should be noted that Moriwaki [86] did not reported a stable liquid miscibility gap. However, from the flat liquidus in Fig. 7.14 and Fig. 7.15, the strong possibility of a stable miscibility gap can be expected. The calculated miscibility gap in this study can be seen in the liquidus projection in Fig. 7.16. The miscibility gap is calculated to be expanded from binary Cu-Cr system toward the Fe-Cu system.

In the present thermodynamic optimization, one small ternary parameters of liquid were introduced to reproduce all the thermodynamic and phase diagram data related to the liquid phase. In addition, ternary parameters for the bcc_A2 solution were optimized to reproduce the homogeneity range of the bcc_A2 phase.

7.4.5 The Cu-Fe-Mn system

The binary thermodynamic descriptions for the Cu-Mn and Fe-Mn systems from He et al. [28] and Huang [108] are accepted with revision of the liquid phase using MQM. The calculated Fe-Mn phase diagram is shown in Fig. 7.17. Like the Cu-Fe system, the liquid phases of the Cu-Mn and Fe-Mn binary systems show almost ideal solution behavior. Thus, the Kohler-type symmetric extrapolation technique was applied for the liquid phase in order to give a good prediction of the liquid properties for the ternary Cu-Fe-Mn solution. Since there are no thermodynamic property data for the liquid phase, three ternary thermodynamic parameters for the liquid phase were introduced to reproduce the phase boundaries related to the liquid phase. Similarly, all the thermodynamic parameters for the solid phases were also optimized from the phase diagram information. Three ternary thermodynamic parameters were optimized for the fcc_A1 phase. Two positive ternary parameters were utilized to destabilize the bcc_A2 phase. The finally obtained thermodynamic description for the Cu-Fe-Mn system is presented in Table 7.2.

The calculated isothermal sections with the experimental data at 800, 850, 900, 950, 1000, 1050, 1100, 1200, 1250, 1300, and 1400 °C are presented in Fig. 7.18. Except for the cub_A13

(Mn), bcc_A2 (Fe), fcc_A1 (Cu) solutions, there is no formation of other ternary phase. It should be noted that the fcc_A1 phase decomposes into fcc_A1#1 and fcc_A1#2 with Fe rich and Cu rich solution originated from a stable miscibility gap of the fcc solution in the Cu-Fe system. The stable fcc miscibility gap extends to the high Mn side as shown in Fig. 7.18. The calculated boundary of the miscibility gap overestimates the measured data from Zhang et al. [24], Wang et al. [99], and Hasebe and Nishizawa [19]. This is because of the solubilities of Fe in (Cu) and Cu in (Fe) phase in the present Cu-Fe description are lower than the experimental data by Zhang et al. [24] and Wang et al. [99]. In fact, the mutual solubility of the fcc Fe-Cu solution, that is miscibility gap, in the binary Fe-Cu are well studied, as can be seen in the optimization results by Shubhank and Kang [107]. As is known, it is very difficult to determine the exact size of the miscibility gap due to slow kinetics. So, it is believed that the experimental data are less accurate in particular at low temperature. The general trend of the fcc miscibility gap is very well reproduced by ternary parameters. Liquid phase already forms at 900 °C in the Cu-Fe-Mn system. As the temperature increases to 950 °C, the stability of the liquid phase increases. The shape of liquidus in the ternary system determined by Hasebe and Nishizawa [19], Wang [26], Ohtani et al. [14], Salter [87], and Parravano [109] are all well reproduced as shown in Fig. 7.18.

Isoplethal sections with 10, 20, and 30 wt.% Cu are shown in Figs. 7.19(a), (b), and (c), respectively. It can be seen from Fig. 7.19, both liquidus and solidus determined by Parravano [109] are very well reproduced. A group of isoplethal sections with constant Fe content of 10, 20, and 30 wt.% are shown in Fig. 7.20. The calculated vertical sections are well consistent with the experimental data by Parravano [109]. Figs. 7.21(a)-(c) are the isoplethal sections with 10 wt.% Mn, 20 wt.% Mn, and 30 wt.% Mn, respectively. As shown in these figures, the experimental information is very well reproduced in the calculated phase diagram. From Figs. 7.19-7.21, it is interesting to notice that the topology relation of the phase diagram does not change much in each type of phase diagram.

The predicted liquidus projection of the Cu-Fe-Mn system from this study is shown in Fig. 7.22. A wide primary crystalline region of the fcc_A1 phase (Fe-Mn rich fcc phase) is calculated, as shown in Fig. 7.22. The critical temperature for liquid converts completely into solid fcc_A1#1 and fcc_A1#2 is calculated at 870 °C which is quite close to the assessed value 880 °C by Raynor

and Rivlin [92]. The maximum temperature for liquid + bcc_A2 = fcc_A1 (Fe, Mn) is at 1538 °C according to the current thermodynamic calculation.

7.5 Summary

A comprehensive evaluation and optimization of all the thermodynamic and phase diagram information for the Cu-Cr, Cu-Fe-Mn, and Cu-Fe-Cr systems was carried out to obtain a set of consistent thermodynamic database to describe the Gibbs energies of all the solid and liquid phases in these systems. The miscibility gap in the Cu-Cr liquid phase is evaluated to be a stable liquid miscibility gap. In the course of the present study, the thermodynamic descriptions of the liquid Fe-Cr and Cu-Mn phases were revised using MQM. MQM was applied to describe the thermodynamic properties of the liquid phase. The solid phases are described using the Bragg-Williams random mixing model. The optimized model parameters can be used with Gibbs energy minimization code to calculate any section of phase diagram and thermodynamic properties of the Cu-Fe-Cr and Cu-Fe-Mn systems.

Acknowledgement

The authors would like to thank the financial support from NSERC-Automotive Partnership Canada program in Canada. Senlin Cui would also like to thank the McGill Engineering Doctorate Award (MEDA) from McGill University for financial support.

References

1. Ma, E., *Alloys created between immiscible elements.* Prog. Mater. Sci., 2005. **50**(4): p. 413-509.
2. Bachmaier, A., M. Kerber, D. Setman, and R. Pippan, *The formation of supersaturated solid solutions in Fe-Cu alloys deformed by high-pressure torsion.* Acta Mater., 2012. **60**(3): p. 860-871.

3. Kakisawa, H., K. Minagawa, and K. Halada, *Tensile behavior change depending on the microstructure of a Fe-Cu alloy produced from rapidly solidified powder.* Mater. Sci. Eng., A, 2003. **A340**(1-2): p. 175-180.
4. Kim, Y.S., J.S. Song, and S.I. Hong, *Thermo-mechanical processing and properties of Cu-Fe-Cr microcomposites.* J. Mater. Process. Technol, 2002. **130-131**: p. 278-282.
5. Fultz, B., C.C. Ahn, S. Spooner, L.B. Hong, J. Eckert, and W.L. Johnson, *Incipient chemical instabilities of nanophase Fe-Cu alloys prepared by mechanical alloying.* Metall. Mater. Trans. A, 1996. **27A**(10): p. 2934-2946.
6. Maggio, R., G. Ischia, M. Bortolotti, F. Rossi, and A. Molinari, *The microstructure and mechanical properties of Fe-Cu materials fabricated by pressure-less-shaping of nanocrystalline powders.* J. Mater. Sci., 2007. **42**(22): p. 9284-9292.
7. Fernee, H., J. Nairn, and A. Atrens, *Cold-worked high-strength high-conductivity Cu-Fe-Cr alloys resistant to softening.* J. Mater. Sci., 2001. **36**(22): p. 5497-5510.
8. Fernee, H., J. Nairn, and A. Atrens, *Precipitation hardening of Cu-Fe-Cr alloys. Part I. Mechanical and electrical properties.* J. Mater. Sci., 2001. **36**(11): p. 2711-2719.
9. Fernee, H., J. Nairn, and A. Atrens, *Precipitation hardening of Cu-Fe-Cr alloys. Part II. Microstructural characterization.* J. Mater. Sci., 2001. **36**(11): p. 2721-2741.
10. Reeh, S., D. Music, M. Ekholm, I.A. Abrikosov, and J.M. Schneider, *Elastic properties of fcc Fe-Mn-X (X = Cr, Co, Ni, Cu) alloys from first-principles calculations.* Phys. Rev. B Condens. Matter Mater. Phys., 2013. **87**(22): p. 224103/1-224103/6.
11. Daniels, M.J., J.S. Zabinski, H. Wu, C.R.M. Grovenor, and J.C. Bilello, *Microstructure and chemistry of annealed Al-Cu-Fe-Cr quasicrystalline approximant coatings.* J. Mater. Res., 2005. **20**(1): p. 176-182.
12. Sordelet, D.J., S.D. Widener, Y. Tang, and M.F. Besser, *Characterization of a commercially produced Al-Cu-Fe-Cr quasicrystalline coating.* Mater. Sci. Eng., A, 2000. **A294-296**: p. 834-837.
13. Fikar, J., R. Schaller, and N. Baluc, *Mechanical spectroscopy of decagonal Al-Cu-Fe-Cr quasicrystalline coatings.* Philos. Mag., 2004. **84**(33): p. 3571-3584.
14. Ohtani, H., H. Suda, and K. Ishida, *Solid/liquid equilibria in Fe-Cu based ternary systems.* ISIJ Int., 1997. **37**(3): p. 207-216.

15. Wang, C.P., X.J. Liu, I. Ohnuma, R. Kainuma, and K. Ishida, *Phase equilibria in Fe-Cu-X (X: Co, Cr, Si, V) ternary systems.* J. Phase Equilib., 2002. **23**(3): p. 236-245.
16. Turchanin, M.A., A.A. Bondar, L.A. Dreval, A.R. Abdulov, and P.G. Agraval, *Mixing Enthalpies of Melts and Thermodynamic Assessment of the Cu-Fe-Cr System.* Powder Metall. Met. Ceram., 2014. **53**(1-2): p. 70-90.
17. Dreval, L.A., A.R. Abdulov, P.G. Agraval, and M.A. Turchanin, *Study and modeling of the mixing enthalpy of liquid Cu-Fe-Cr system alloys.* Rasplavy, 2010(5): p. 81-87.
18. Zhou, Z.M., J. Gao, F. Li, Y.P. Wang, and M. Kolbe, *Experimental determination and thermodynamic modeling of phase equilibria in the Cu-Cr system.* J. Mater. Sci., 2011. **46**(21): p. 7039-7045.
19. Hasebe, M. and T. Nishizawa, *Applications of phase diagram in metallurgy and ceramics.* National Bureau of Standards SP-496, 1978. **2**: p. 911-954.
20. Nishizawa, T. and M. Hasebe, *Computer calculation of phase diagrams of iron alloys.* Tetsu to Hagane, 1981. **67**(14): p. 2086-97.
21. Nishizawa, T. and M. Hasebe, *Computer calculation of phase diagrams of iron alloys. 1.* Tetsu to Hagane, 1981. **67**(11): p. 1887-98.
22. Kumar, K.C.H. and V. Raghavan, *The bcc.-fcc. equilibrium in ternary iron alloys - III.* J. Alloy Phase Diagrams, 1989. **5**(3): p. 201-20.
23. Miettinen, J., *Thermodynamic description of the Cu-Fe-Mn system at the Cu-Fe side.* CALPHAD Comput. Coupling Phase Diagrams Thermochem., 2003. **27**(2): p. 141-145.
24. Zhang, L., Y. Du, Q. Chen, H. Xu, F. Zheng, C. Tang, and H. Chen, *Thermodynamic description of the Cu-Fe-Mn system with key experiments and its practical applications.* Int. J. Mater. Res., 2008. **99**(12): p. 1306-1318.
25. Dinsdale, A.T., *SGTE data for pure elements.* CALPHAD Comput. Coupling Phase Diagrams Thermochem., 1991. **15**(4): p. 317-425.
26. Wang, C.P., X.J. Liu, I. Ohnuma, R. Kainuma, and K. Ishida, *Thermodynamic assessments of the Cu-Mn-X (X: Fe, Co) systems.* J. Alloys Compd., 2007. **438**(1-2): p. 129-141.
27. Andersson, J.O. and B. Sundman, *Thermodynamic properties of the chromium-iron system.* CALPHAD Comput. Coupling Phase Diagrams Thermochem., 1987. **11**(1): p. 83-92.

28. He, C., Y. Du, H.-L. Chen, S. Liu, H. Xu, Y. Ouyang, and Z.-K. Liu, *Thermodynamic modeling of the Cu-Mn system supported by key experiments.* J. Alloys Compd., 2008. **457**(1-2): p. 233-238.
29. Kaufman, L., *Coupled phase diagrams and thermochemical data for transition metal binary systems. III.* CALPHAD Comput. Coupling Phase Diagrams Thermochem., 1978. **2**(2): p. 117-46.
30. Saunders, N., *Thermodynamic characterization of copper-chromium system.* Mater. Sci. Technol., 1987. **3**(8): p. 671-3.
31. Hämäläinen, M., K. Jaaskelainen, R. Luoma, M. Nuotio, P. Taskinen, and O. Teppo, *A thermodynamic analysis of the binary alloy systems copper-chromium, copper niobium and copper-vanadium.* CALPHAD Comput. Coupling Phase Diagrams Thermochem., 1990. **14**(2): p. 125-37.
32. Zeng, K. and Hämäläinen, *Thermodynamic analysis of stable and metastable equilibria in the Cu-Cr system.* CALPHAD Comput. Coupling Phase Diagrams Thermochem., 1995. **19**(1): p. 93-104.
33. Jacob, K.T., S. Priya, and Y. Waseda, *A thermodynamic study of liquid Cu-Cr alloys and metastable liquid immiscibility.* Z. Metallkd., 2000. **91**(7): p. 594-600.
34. Okamoto, H., *Cr-Cu (chromium-copper).* J. Phase Equilib., 1997. **18**(2): p. 220.
35. Okamoto, H., *Cr-Cu (chromium-copper).* J. Phase Equilib., 2001. **22**(6): p. 691-692.
36. Okamoto, H., *Cr-Cu (Chromium-Copper).* J. Phase Equilib. Diffus., 2012. **33**(4): p. 342-343.
37. Okamoto, H., *Supplemental Literature Review of Binary Phase Diagrams: Bi-Ce, Bi-Er, C-Ce, C-La, C-Pr, Cd-I, Cr-Cu, Cu-Er, Er-Sb, F-Sm, F-Yb, and Fe-Gd.* J. Phase Equilib. Diffus., 2013. **34**(4): p. 350-362.
38. Inouye, T.K., H. Fujiwara, and M. Iwase, *Activities of chromium in molten copper at dilute concentrations by solid-state electrochemical cell.* Metall. Trans. B, 1991. **22B**(4): p. 475-80.
39. Ono, K., S. Nishi, and T. Oishi, *A thermodynamic study of the liquid copper-tin and copper-chromium alloys by the Knudsen cell-mass filter combination.* Trans. Jpn. Inst. Met., 1984. **25**(11): p. 810-14.

40. Timberg, L. and J.M. Toguri, *A thermodynamic study of (copper + chromium) by mass spectrometry.* J. Chem. Thermodyn., 1982. **14**(2): p. 193-9.
41. Turchanin, M.A. and I.V. Nikolaenko, *Enthalpies of solution of vanadium and chromium in liquid copper by high temperature calorimetry.* J. Alloys Compd., 1996. **235**(1): p. 128-32.
42. Drits, M.E., L.L. Rokhlin, N.R. Bochvar, E.V. Lysova, V.M. Rozenberg, A.K. Nikolaev, and N.B. Shparo, *Solubility of chromium and hafnium in copper in solid state.* Izv. Vyssh. Uchebn. Zaved., Tsvetn. Metall., 1975(2): p. 122-5.
43. Zakharov, M.V. and O.E. Osintsev, *The copper corner in the phase diagram of the copper-chromium-nickel system.* Izv. Vyssh. Ucheb. Zaved., Tsvet. Met., 1967. **10**(5): p. 152-5.
44. Doi, T., *Cooper alloys containing chromium. I. The copper-side phase diagram.* Nippon Kinzoku Gakkaishi, 1957. **21**: p. 337-40.
45. Hibbard, W.R., Jr., F.D. Rosi, H.T. Clark, Jr., and R.I. O'Herron, *The constitution and properties of copper rich copper-chromium and copper-nickel-chromium alloys.* Am. Inst. Mining Met. Engrs., Inst. Metals Div., Metals Technol., 1948. **15**(No. 2, Tech. Pub. No. 2317): p. 12 pp.
46. Alexander, W.O., *Copper rich nickel-aluminum-copper alloys. II. The constitution of the copper-nickel-rich alloys.* J. Inst. Met., 1938. **63**(Adv. copy No. 815): p. 21 pp.
47. Kuznetsov, G.M., V.N. Fedorov, and A.L. Rodnyanskaya, *Study of the phase diagram of the copper-chromium system.* Izv. Vyssh. Uchebn. Zaved., Tsvetn. Metall., 1977(3): p. 84-6.
48. Leonov, M.P., N.R. Bochvar, and V.G. Ivanchenko, *Chromium-copper phase diagram.* Dokl. Akad. Nauk SSSR, 1986. **290**(4): p. 888-90 [Phys Chem].
49. Zhou, Z.M., J. Gao, F. Li, Y.K. Zhang, Y.P. Wang, and M. Kolbe, *On the metastable miscibility gap in liquid Cu-Cr alloys.* J. Mater. Sci., 2009. **44**(14): p. 3793-3799.
50. Chart, T., F. Putland, and A. Dinsdale, *Calculated phase equilibriums for the chromium-iron-nickel-silicon system. I. Ternary equilibriums.* CALPHAD Comput. Coupling Phase Diagrams Thermochem., 1980. **4**(1): p. 27-46.
51. Hertzman, S. and B. Sundman, *A thermodynamic analysis of the iron-chromium system.* CALPHAD Comput. Coupling Phase Diagrams Thermochem., 1982. **6**(1): p. 67-80.

52. Lee, B.J., *Revision of thermodynamic descriptions of the iron-chromium and iron-nickel liquid phases.* CALPHAD Comput. Coupling Phase Diagrams Thermochem., 1993. **17**(3): p. 251-68.

53. Xiong, W., P. Hedström, M. Selleby, J. Odqvist, M. Thuvander, and Q. Chen, *An improved thermodynamic modeling of the Fe-Cr system down to zero kelvin coupled with key experiments.* CALPHAD Comput. Coupling Phase Diagrams Thermochem., 2011. **35**(3): p. 355-366.

54. Thiedemann, U., M. Rösner-Kuhn, D.M. Matson, G. Kuppermann, K. Drewes, M.C. Flemings, and M.G. Frohberg, *Mixing enthalpy measurements in the liquid ternary system iron-nickel-chromium and its binaries.* Steel Res., 1998. **69**(1): p. 3-7.

55. Iguchi, Y., S. Nobori, K. Saito, and T. Fuwa, *A calorimetric study of heats of mixing of liquid iron alloys. Iron-chromium, iron-molybdenum, iron-tungsten, iron-vanadium, iron-niobium, and iron-tantalum.* Tetsu to Hagane, 1982. **68**(6): p. 633-40.

56. Shumikhin, V.S., A.K. Biletskii, G.I. Batalin, and V.P. Anishin, *Study on thermodynamic and kinetic parameters of dissolution of solid materials in carbon-containing iron melts.* Arch. Eisenhuettenwes., 1981. **52**(4): p. 143-6.

57. Batalin, G.I., V.P. Kurach, and V.S. Sudavtsova, *Heats of mixing of molten alloys of iron-chromium and iron-titanium systems.* Zh. Fiz. Khim., 1984. **58**(2): p. 481-3.

58. Pavars, I., B.A. Baum, and P.V. Gel'd, *Thermophysical and thermodynamic characteristics of molten alloys of iron with chromium.* Teplofiz. Vys. Temp., 1970. **8**(1): p. 72-6.

59. Maruyama, N. and S. Ban-Ya, *Measurement of activities in iron-copper, iron-chromium and iron-tin alloys by a transportation method.* Nippon Kinzoku Gakkaishi, 1980. **44**(12): p. 1422-31.

60. Mills, K.C. and P. Grieveson, *Activities of iron and chromium in liquid iron + chromium alloys.* J. Chem. Thermodyn., 1976. **8**(6): p. 545-50.

61. Wada, H., Y. Kawai, and T. Saito, *Activity of chromium in liquid iron-chromium system.* Sci. Repts. Research Inst., Tohoku Univ. Ser. A, 1961. **13**(No. 2): p. 96-104.

62. Reese, R.B., R.A. Rapp, and G.R. St. Pierre, *The chemical activities of iron and chromium in binary iron-chromium alloys.* Trans. Met. Soc. AIME (Amer. Inst. Mining, Met., Petrol. Eng.), 1968. **242**(8): p. 1719-26.

63. Belton, G.R. and R.J. Fruehan, *Mass-spectrometric determination of activities in iron-chromium and iron-chromium-nickel alloys.* Met. Trans., 1970. **1**: p. 781-7.
64. Gilby, S.W. and G.R. St. Pierre, *Equilibrium vapor compositions and activities of components for iron-chromium-nickel alloys at 1600.deg.* Trans. AIME, 1969. **245**(8): p. 1749-58.
65. Fruehan, R.J., *Activities in the liquid iron-chromium-oxygen system.* Trans. Met. Soc. AIME (Amer. Inst. Mining, Met., Petrol. Eng.), 1969. **245**: p. 1215-18.
66. Ohtani, M., *Activities of chromium and carbon in molten iron-chromium-carbon alloys.* Tetsu to Hagane, 1956. **42**: p. 1095-1011.
67. Hadrys, H.G., M.G. Frohberg, J.F. Elliott, and C.H.P. Lupis, *Activities in the liquid iron-chromium-carbon(satd.), iron-phosphorus-carbon(satd.), and iron-chromium-phosphorus systems at 1600.deg.* Met. Trans., 1970. **1**: p. 1867-74.
68. Oberhoffer, P. and H. Esser, *Iron-chromium equilibrium diagram.* Stahl Eisen, 1927. **47**: p. 2021-31.
69. Adcock, F., *Alloys of iron research. X. Chromium-iron constitutional diagram.* J. Iron Steel Inst., London, 1931. **No. 2**: p. 1-48.
70. Putman, J.W., D.R. Potter, and N.J. Grant, *The ternary system Cr-Mo-Fe system.* Transaction of the A. S. M., 1951. **43**: p. 824-852.
71. Hellawell, A. and W. Hume-Rothery, *The constitution of alloys of iron and manganese with transition elements of the first long period.* Phil. Trans. Roy. Soc. London, Ser. A, 1957. **249**: p. 417-59.
72. Schürmann, E. and J. Brauckmann, *Studies of the melting equilibria in the iron corner of the ternary system iron-chromium-nickel.* Arch. Eisenhuettenwes., 1977. **48**(1): p. 3-7.
73. Kundrat, D.M., M. Chochol, and J.F. Elliott, *Phase relationships in the iron-chromium-carbon system at solidification temperatures.* Metall. Trans. B, 1984. **15**(4): p. 663-76.
74. Gokcen, N.A., *The Cu-Mn (copper-manganese) system.* J. Phase Equilib., 1993. **14**(1): p. 76-83.
75. Vřešťál, J., J. Stepankova, and P. Broz, *Thermodynamics of the copper-manganese system. Knudsen-cell mass spectrometric study of the liquid Cu-Mn system and calculation of the phase diagram.* Scand. J. Metall., 1996. **25**(5): p. 224-231.

76. Miettinen, J., *Thermodynamic description of the Cu-Mn-Si system in the copper-rich corner.* CALPHAD Comput. Coupling Phase Diagrams Thermochem., 2003. **27**(4): p. 395-401.
77. Lewin, K., S. Du, and S. Seetharaman, *Thermodynamic study of the Cu-Mn system.* Scand. J. Metall., 1993. **22**(6): p. 310-16.
78. Turchanin, M.A. and I.V. Nikolaenko, *Enthalpies of formation of liquid (copper + manganese) alloys.* Metall. Mater. Trans. B, 1997. **28B**(3): p. 473-478.
79. Sato, S. and O.J. Kleppa, *Thermochemistry of liquid alloys of transition metals: I. The systems manganese-copper and manganese-tin.* Metall. Trans., B, 1979. **10B**(1): p. 63-6.
80. Grube, G., E. Oestreicher, and O. Winkler, *The copper-manganese system.* Z. Elektrochem. Angew. Phys. Chem., 1939. **45**: p. 776-84.
81. Wachtel, E., P. Terzieff, and J. Bahle, *Construction and magnetic properties of manganese-rich copper-manganese and manganese-tin alloys.* Monatsh. Chem., 1986. **117**(12): p. 1349-66.
82. Raghavan, V., *Cr-Fe-Mn (chromium-iron-manganese).* J. Phase Equilib., 2003. **24**(3): p. 259-260.
83. Raghavan, V., *Cr-Fe-Mn (Chromium-Iron-Manganese).* J. Phase Equilib., 1994. **15**(5): p. 530-1.
84. Raghavan, V., *The Cr-Cu-Fe (Chromium-Copper-Iron) system.* Phase Diagram of Ternary Iron Alloys, Part 6, Ind. Inst. Metals, Calcutta, 1992: p. 687-88.
85. Turchanin, M. and T. Velikanova, *Chromium-copper-iron.* in: Landolt-Boernstein, Numerical Data and Functional Relationships in Science and Technology, W. Martiensen (ed.), New Series. Group IV: Physical Chemistry, G. Effenberg and S. Ilyenko (eds.), Ternary Alloy Systems, Phase Diagrams, Crystallographic and Thermodynamic Data, Springer-Verlag, Berlin, Heidelberg, 2006. **11C2**: p. 183-209.
86. Moriwaki, K., *The equilibrium diagram of the ternary system iron-chromium-copper.* Tetsu to Hagane, 1939. **25**: p. 396-403.
87. Salter, W.J.M., *Effect of chromium on solubility of copper in mild steel.* J. Iron Steel Inst., London, 1967. **205**(Pt. 11): p. 1156-60.

88. Ahmed, M., F. Thuemmler, and G. Zapf, *Metallographic examinations on iron-chromium-copper alloys obtained by powder-metallurgical processes.* Arch. Eisenhuettenw., 1970. **41**(8): p. 797-803.
89. Jiang, M. and S.M. Hao, *The Determination and Illustration of a 1000 °C Isothermal Phase Diagram of Fe-Ni-Co-Cu System.* Proc. 6th Nat. Symp. Phase Diagram, 1990: p. 150-152.
90. Fernee, H., J. Nairn, and A. Atrens, *Cu rich corner of the Cu-Fe-Cr phase diagram.* J. Mater. Sci. Lett., 2001. **20**(24): p. 2213-2215.
91. Dreval, L.A., M. Turchanin, A.R. Abdulov, and A.A. Bondar, *Thermodynamic assessment of the Cu-Fe-Cr phase diagram.* Chemistry of Metals and Alloys, 2010. **3**: p. 132-139.
92. Raynor, G.V. and V.G. Rivlin, Phase equilibria in iron ternary alloys, 1988. **4**: p. 345.
93. Raghavan, V., *Cu-Fe-Mn (Copper-Iron-Manganese).* J. Phase Equilib., 1994. **15**(5): p. 542.
94. Raghavan, V., *Cu-Fe-Mn (copper-iron-manganese).* J. Phase Equilib., 2002. **23**(3): p. 259.
95. Raghavan, V., *Cu-Fe-Mn (Copper-Iron-Manganese).* J. Phase Equilib. Diffus., 2008. **29**(6): p. 520-522.
96. Raghavan, V., *Cu-Fe-Mn (copper-iron-manganese).* J. Phase Equilib. Diffus., 2009. **30**(4): p. 381-383.
97. Lebrun, N. and P. Perrot, *Copper-Iron-Manganese.* Landolt-Börnstein New Series IV/11D3, 2008: p. 1-20.
98. Parravano, N., *Ternary Alloys of Iron-Nickel-Manganese, Nickel-Manganese-Copper, and Iron-Manganese-Copper.* Intern. Z. Metallog., 1913. **4**: p. 171-202.
99. Wang, C.P., *PhD thesis*, *Tohoku University*, *Japan*, 2001.
100. Pelton, A.D. and P. Chartrand, *The modified quasi-chemical model: Part II. Multicomponent solutions.* Metall. Mater. Trans. A, 2001. **32A**(6): p. 1355-1360.
101. Pelton, A.D., S.A. Degterov, G. Eriksson, C. Robelin, and Y. Dessureault, *The modified quasichemical model I - binary solutions.* Metall. Mater. Trans. B, 2000. **31B**(4): p. 651-659.
102. Redlich, O. and A.T. Kister, *Thermodynamics of nonelectrolytic solutions. Algebraic representation of thermodynamic properties and the classification of solutions.* Ind. Eng. Chem., 1948. **40**: p. 84,5-8.
103. Hillert, M. and M. Jarl, *A model for alloying effects in ferromagnetic metals.* CALPHAD Comput. Coupling Phase Diagrams Thermochem., 1978. **2**(3): p. 227-38.

104. Bale, C.W., P. Chartrand, S.A. Degterov, G. Eriksson, K. Hack, R. Ben Mahfoud, J. Melancon, A.D. Pelton, and S. Petersen, *FactSage thermochemical software and databases.* CALPHAD Comput. Coupling Phase Diagrams Thermochem., 2002. **26**(2): p. 189-228.
105. Hindrichs, G., *Some Chromium and Manganese Alloys.* Z. Anorg. Chem., 1909. **59**: p. 414-49.
106. Siedschlag, E., *Chromium-copper-nickel alloys.* Z. Anorg. Allg. Chem., 1923. **131**: p. 173-90.
107. Shubhank, K. and Y.-B. Kang, *Critical evaluation and thermodynamic optimization of Fe-Cu, Cu-C, Fe-C binary systems and Fe-Cu-C ternary system.* CALPHAD Comput. Coupling Phase Diagrams Thermochem., 2014. **45**: p. 127-137.
108. Huang, W., *An assessment of the iron-manganese system.* CALPHAD Comput. Coupling Phase Diagrams Thermochem., 1989. **13**(3): p. 243-52.
109. Parravano, N., *Ternary Alloys of Iron-Manganese-Copper.* Gazz. Chim. Ital., 1913. **42**(II): p. 513-31.
110. Paek, M.-K., *Thermodynamic assessment of the Fe-Mn system.* unpublished work.
111. Miettinen, J., *Thermodynamic description of the Cu-Al-Mn system in the copper rich corner.* CALPHAD Comput. Coupling Phase Diagrams Thermochem., 2003. **27**(1): p. 103-114.

Table captions

Table 7.1 Summary of the invariant reactions in the Cu-Cr system.

Table 7.2 Summary of the optimized model parameters for the Cu-Fe-Cr and Cu-Fe-Mn systems in the present work (J mol^{-1} or J mol^{-1} K^{-1}).

Figure captions

Fig. 7.1 Calculated phase diagram of the Cu-Cr system along with the experimental data. (a) The entire composition range, (b) the enlarged Cu rich part, and (c) the enlarged Cr rich part.

Fig. 7.2 (a) Calculated enthalpy of mixing of the Cu-Cr liquid phase along with the experimental data. (b) Calculated partial enthalpy of mixing of Cu along with the experimental data.

Fig. 7.3 Calculated activities of Cr with respect to the bcc_A2 standard and Cu with respect to the liquid standard in the Cu-Cr system along with the experimental data. (a) Activities of Cr and Cu at 1550 °C, (b) activity of Cr at 1150, 1200, 1250, and 1300 ºC, and (c) activity of Cr at 1300 and 1600 ºC.

Fig. 7.4 Calculated enthalpy of mixing of the Fe-Cr liquid phase at 1687 ºC along with the experimental data.

Fig. 7.5 Calculated activities of Fe-Cr liquid alloys along with the experimental data. (a) With respect to the liquid Fe and Cr standards at 1927 ºC, (b) with respect to the liquid Fe and bcc_A2 Cr standards at 1700 ºC, and (c) with respect to the liquid Fe and bcc_A2 Cr standards 1600 ºC.

Fig. 7.6 Calculated phase diagram of the Fe-Cr system. (a) The entire temperature range, and (b) the high temperature part along with the experimental data.

Fig. 7.7 Calculated activities of Cu and Mn with respect to the liquid standard at 1097 ºC along with the experimental data.

Fig. 7.8 Calculated enthalpy of mixing of the Cu-Mn liquid phase at 1113 ºC along with the experimental data.

Fig. 7.9 Calculated phase diagram of the Cu-Mn system along with the experimental data.

Fig. 7.10 Calcualted phase diagram of the Cu-Fe system.

Fig. 7.11 Calculated enthalpy of mixing of the Cu-Cr-Fe liquid phase at 1600 ºC along with the experimental data. (a) $Cu_{0.75}Fe_{0.25}$-Cr section, (b) $Cu_{0.50}Fe_{0.50}$-Cr section, and (c) $Cu_{0.25}Fe_{0.75}$-Cr section.

Fig. 7.12 Calculated partial enthalpy of mixing of Cr in the Cu-Cr-Fe liquid phase at 1600 ºC along with the experimental data. (a) $Cu_{0.50}Fe_{0.50}$-Cr section, (b) $Cu_{0.25}Fe_{0.75}$-Cr section, and (c) $Cu_{0.75}Fe_{0.25}$-Cr section.

Fig. 7.13 Calculated isothermal sections of the Cu-Cr-Fe system along with the experimental data at different temperatures. (a) At 800 ºC, (b) at 900 ºC, (c) at 1000 ºC, (d) at 1050 ºC, (e) at 1100 ºC, (f) at 1200 ºC, (g) at 1250 ºC, (h) at 1300 ºC, and (i) at 1600 ºC.

Table 7.1 Summary of the invariant reactions in the Cu-Cr system.

Reaction type	Reaction (at. % Si)			Temperature ºC	Method [a]	Ref.
Eutectic	Liquid#1=(Cr)+Liquid#2					
				1473	TA	[105]
				1470	TA	[106]
				1767	DTA	[48]
				1747	DTA	[18]
	79.35	99.66	50.06	1764	Cal.	This work
Eutectic	Liquid=(Cr)+(Cu)					
				1075	TA	[105]
				1076	TA	[106]
				1074.8	DTA	[44]
				1074	DTA	[48]
				1076	DTA	[18]
	1.33	99	0.70	1079	Cal.	This work

[a] TA = Thermal Analysis; DTA = Differential Thermal Analysis; Cal. = Calphad.

Table 7.2 Summary of the optimized model parameters for the Cu-Fe-Cr and Cu-Fe-Mn systems in the present work (J mol^{-1} or J mol^{-1} K^{-1}).

Phase	Thermodynamic parameters	Ref.
Liquid: (Cu, Fe, Cr, Mn)	$\Delta g_{\mathrm{Cu},Cr} = 6184.58 + 2.85T + (7618.56 - 2.39T)x_{CrCr} + (21756.80 - 12.76T)x_{CuCu} - 753.12x_{CuCu}^2$	This work
	$\Delta g_{Cu,Fe} = +12552.00 - 1.26T + 2719.60x_{FeFe} + 3556.40x_{CuCu}$	[107]
	$\Delta g_{Cu,Mn} = -1.71T - (3029.22 + 0.04T)x_{CuCu} + (4435.04 - 0.41T)x_{MnMn}$	This work
	$\Delta g_{Cr,Fe} = -242.67 - 0.29T - 205.02x_{FeFe} - (192.46 + 1.05T)x_{CrCr}$	This work
	$\Delta g_{Fe,Mn} = -1338.88 + 0.17T + 418.40x_{FeFe} - 334.72x_{MnMn}$	[110]
	$g^{001}_{Cr,Cu,(Fe)} = 3347.2$	This work
	$g^{001}_{Cu,Mn,(Fe)} = 7321.16 - 10.88T$, $g^{001}_{Cu,Fe,(Mn)} = 46233.20$, $g^{001}_{Fe,Mn,(Cu)} = 70496.22 - 54.39T$	This work
fcc_A1: (Cu, Fe, Cr, Mn)$_1$(Va)$_1$	$L_{Cu,Cr} = 70672.86 - 15.85T$	This work
	$L_{Cu,Fe} = 35564.00 - 2.60T + 1882.80(x_{Cu} - x_{Fe}) + (251 + 6.1T)(x_{Cu} - x_{Fe})^2$	[107]
	$L_{Cu,Mn} = 20235.508 - 13.2437T + (-12154.853 + 2.9399T)(x_{Cu} - x_{Mn}) + 1037.56(x_{Cu} - x_{Mn})^2$	[28]
	$L_{Fe,Cr} = 10833.00 - 7.48T + 1410.00(x_{Cr} - x_{Fe})$	[27]
	$L_{Fe,Mn} = -7762 + 3.865T - 259(x_{Fe} - x_{Mn})$	[108]

	$L_{Cu,Fe,Mn} = 27614.40\ x_{Cu} + (-117817.26\ + 98.87T)x_{Fe} + 20083.20\ x_{Mn}$	This work
bcc_A2: (Cu, Fe, Cr, Mn)$_1$(Va)$_3$	$L_{\mathrm{Cu},Cr} = 70310.40\ + 6.04T$	This work
	$L_{Cu,Fe} = 36149.8 - 2.7T + 1673.6(x_{Cu} - x_{Fe}) + (292.9 + 4.6T)(x_{Cu} - x_{Fe})^2$	[107]
	$L_{Cu,Mn} = 18366.034 - 16.2210T - 12667.53(x_{Cu} - x_{Mn})$	[28]
	$L_{Fe,Cr} = 20500\ - 9.68T$ $\beta^0 = -0.85$ $T_C^0 = 1650\ ,\ T_C^1 = -550$	[52]
	$L_{Fe,Mn} = -2759.00 + 1.24T$ $T_C^0 = 1230$	[108]
	$L_{Cr,Cu,Fe} = x_{Cr}(-16736) + x_{Cu}(-16736) + x_{Fe}(-37656)$	This work
	$L_{Cu,Fe,Mn} = 41421.60\ x_{Fe} + 16736.00\ x_{Mn}$	This work
Sigma: (Fe)$_8$(Cr)$_4$(Fe, Cr)$_{18}$	${}^oG^{\sigma}_{Fe:Cr:Fe} = 8{}^oG^{fcc}_{Fe} + 4{}^oG^{bcc}_{Cr} + 18{}^oG^{bcc}_{Fe} + 117300\ - 95.96T$ ${}^oG^{\sigma}_{Fe:Cr:Cr} = 8{}^oG^{fcc}_{Fe} + 22{}^oG^{bcc}_{Cr} + 92300\ - 95.96T$	[52]
cub_A13: (Cu, Fe, Mn)1	${}^oG_{Cu} = 2092 + {}^oG^{fcc}_{Cu}$	[111]
	$L_{Cu,Fe} = 41840$	This work
	$L_{Cu,Mn} = 42493.307 - 14.1644T$	[28]

	$L_{Fe,Mn} = -11518.00 + 2.82T$	[108]
cbcc_A12: (Cu, Fe, Mn)1	${}^{o}G_{Cu} = 3556 + {}^{o}G_{Cu}^{fcc}$	[111]
	$L_{Cu,Fe} = 12552$	This work
	$L_{Cu,Mn} = 36627.137 - 12.209T$	[28]
	$L_{Fe,Mn} = -10184$	[108]

Figures

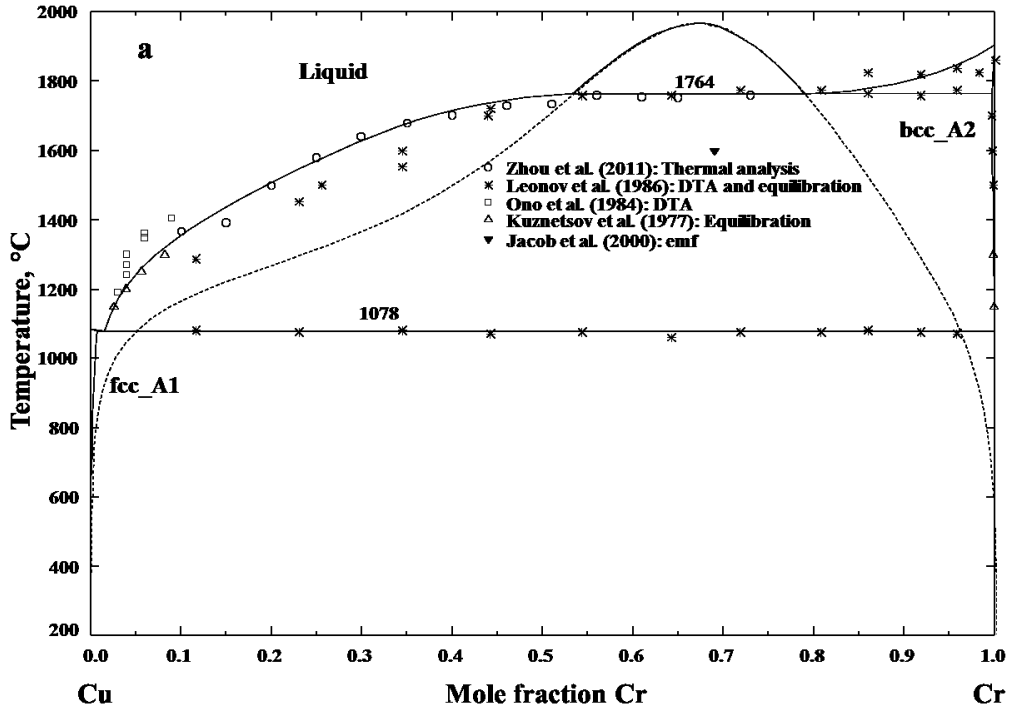
a
Liquid
1764
bcc_A2
1078
fcc_A1
Zhou et al. (2011): Thermal analysis
Leonov et al. (1986): DTA and equilibration
Ono et al. (1984): DTA
Kuznetsov et al. (1977): Equilibration
Jacob et al. (2000): emf
Temperature, °C
Cu
Mole fraction Cr
Cr

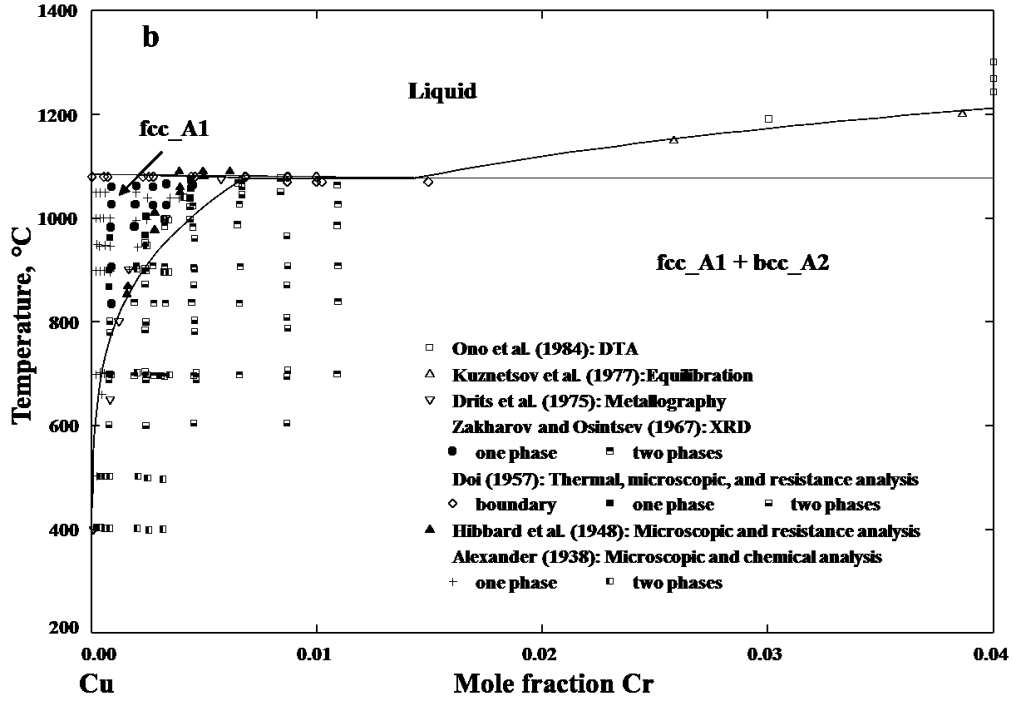
b
Liquid
fcc_A1
fcc_A1 + bcc_A2
Ono et al. (1984): DTA
Kuznetsov et al. (1977):Equilibration
Drits et al. (1975): Metallography
Zakharov and Osintsev (1967): XRD
one phase
two phases
Doi (1957): Thermal, microscopic, and resistance analysis
boundary
one phase
two phases
Hibbard et al. (1948): Microscopic and resistance analysis
Alexander (1938): Microscopic and chemical analysis
one phase
two phases
Temperature, °C
Cu
Mole fraction Cr

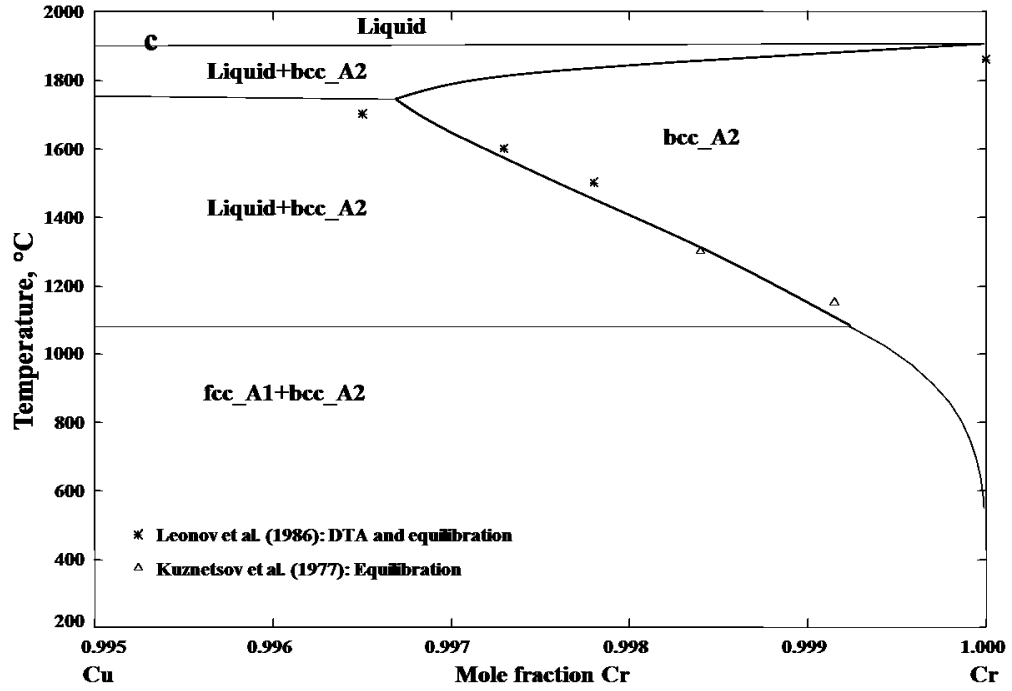

Fig. 7.1 Calculated phase diagram of the Cu-Cr system along with the experimental data. (a) The entire composition range, (b) the enlarged Cu rich part, and (c) the enlarged Cr rich part.

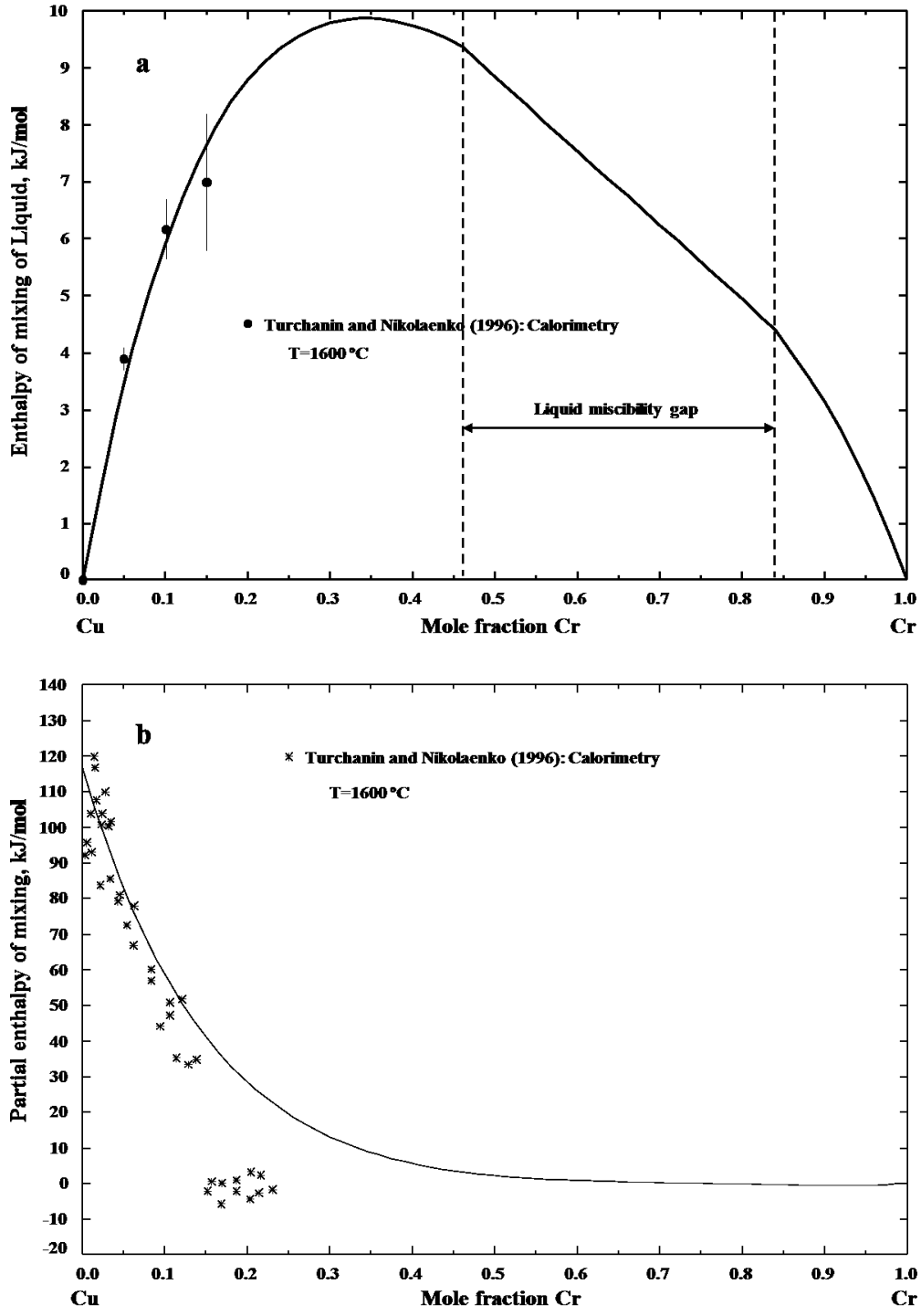

Fig. 7.2 (a) Calculated enthalpy of mixing of the Cu-Cr liquid phase along with the experimental data. (b) Calculated partial enthalpy of mixing of Cu along with the experimental data.

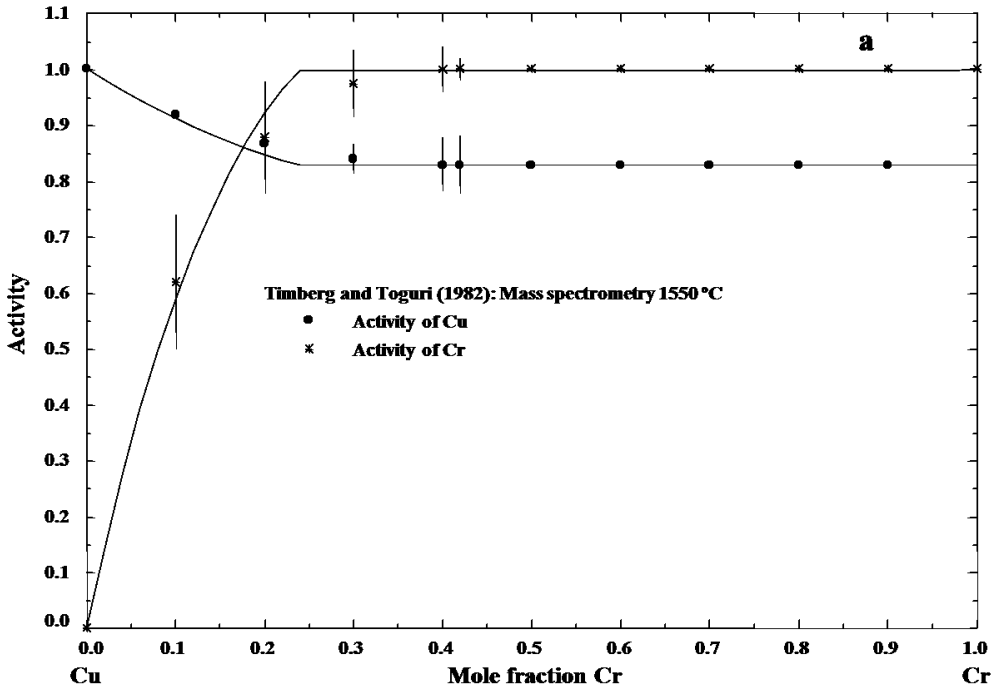
a
Timberg and Toguri (1982): Mass spectrometry 1550 °C
Activity of Cu
Activity of Cr
Activity
Mole fraction Cr
Cu
Cr

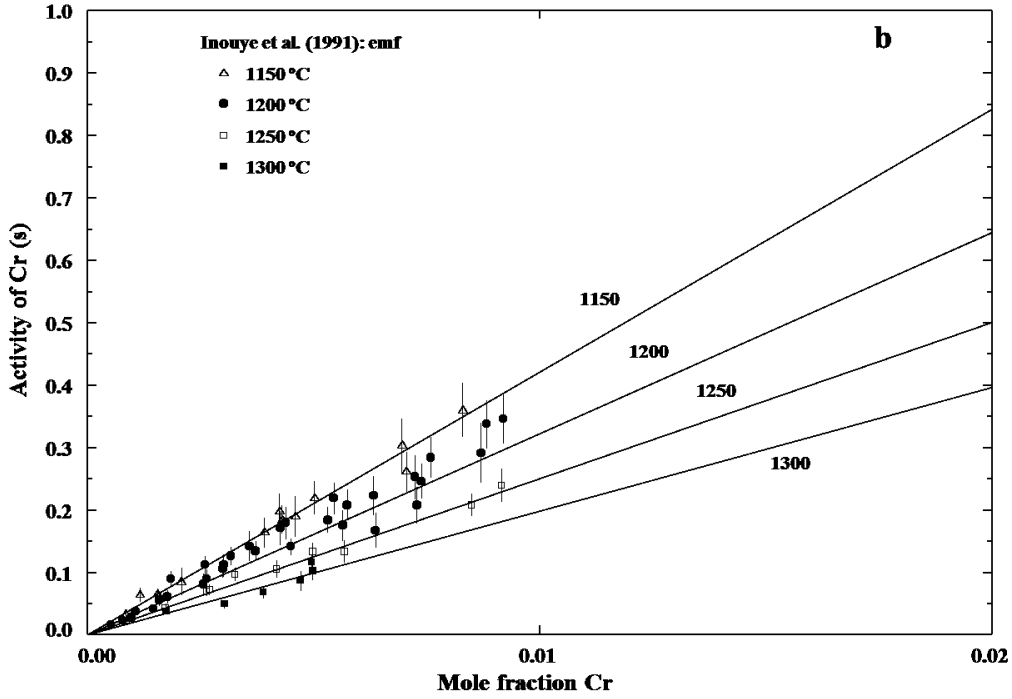
b
Inouye et al. (1991): emf
1150 °C
1200 °C
1250 °C
1300 °C
1150
1200
1250
1300
Activity of Cr (s)
Mole fraction Cr

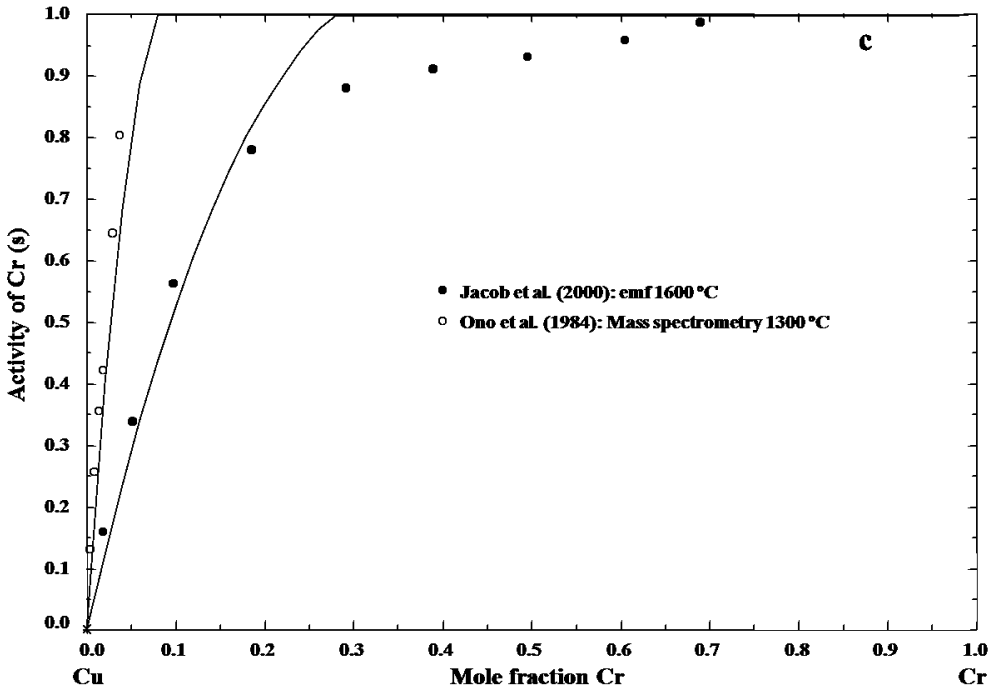

Fig. 7.3 Calculated activities of Cr with respect to the bcc_A2 standard and Cu with respect to the liquid standard in the Cu-Cr system along with the experimental data. (a) Activities of Cr and Cu at 1550 ºC, (b) activity of Cr at 1150, 1200, 1250, and 1300 ºC, and (c) activity of Cr at 1300 and 1600 ºC.

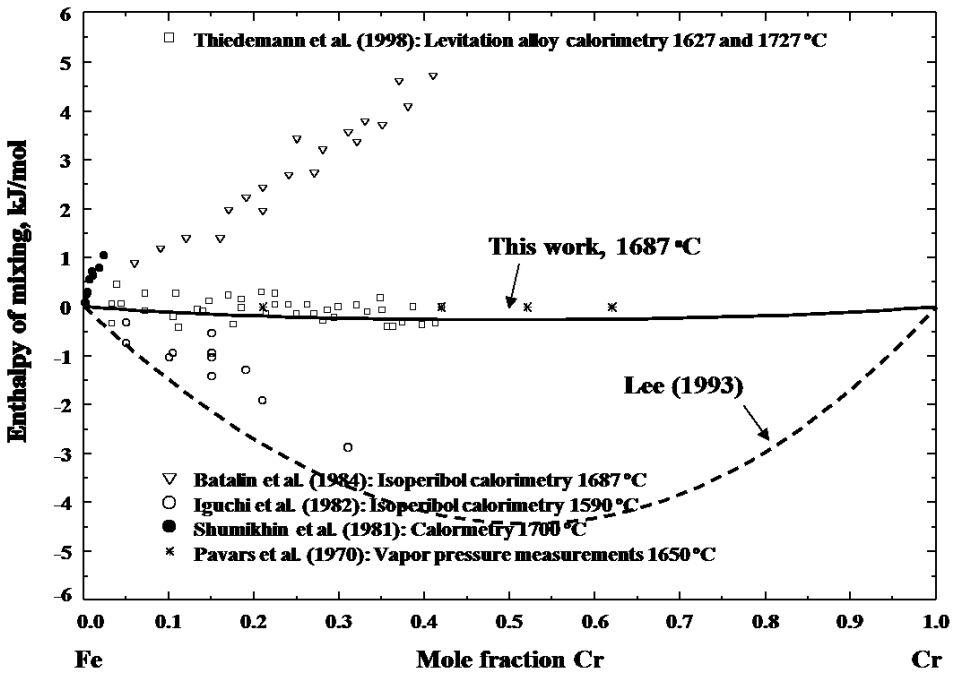

Fig. 7.4 Calculated enthalpy of mixing of the Fe-Cr liquid phase at 1687 ºC along with the experimental data.

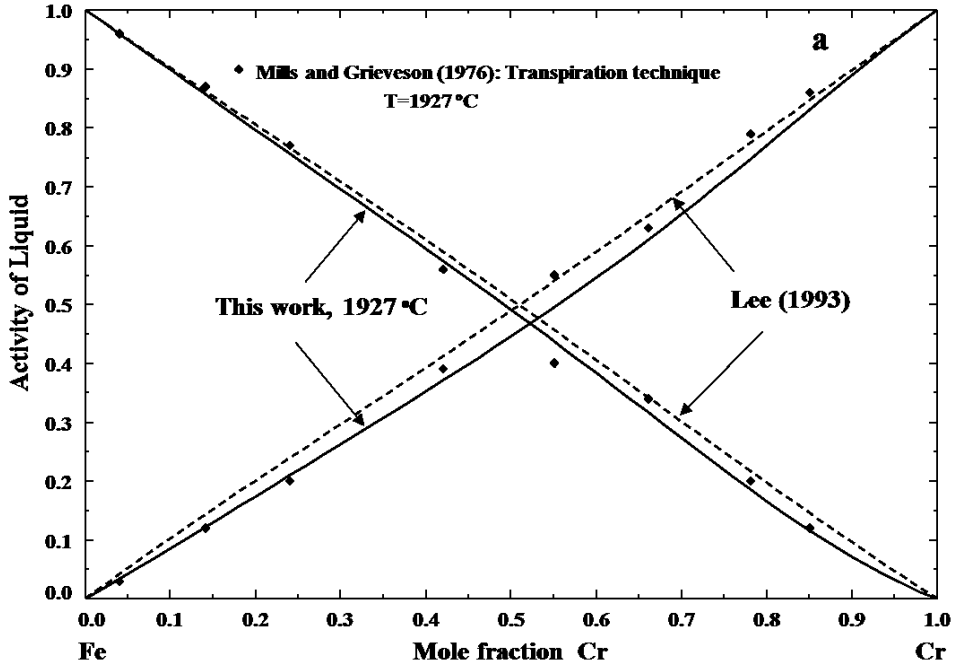
a
Mills and Grieveson (1976): Transpiration technique
T=1927 °C
This work, 1927 °C
Lee (1993)
Activity of Liquid
Mole fraction Cr
Fe
Cr

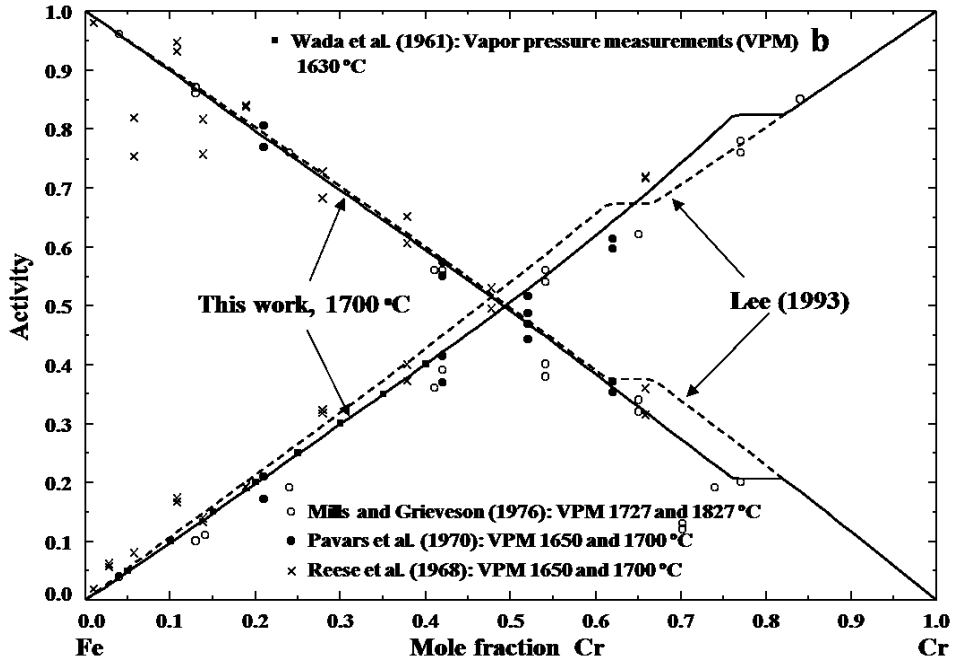
b
Wada et al. (1961): Vapor pressure measurements (VPM)
1630 °C
This work, 1700 °C
Lee (1993)
Mills and Grieveson (1976): VPM 1727 and 1827 °C
Pavars et al. (1970): VPM 1650 and 1700 °C
Reese et al. (1968): VPM 1650 and 1700 °C
Activity
Mole fraction Cr
Fe
Cr

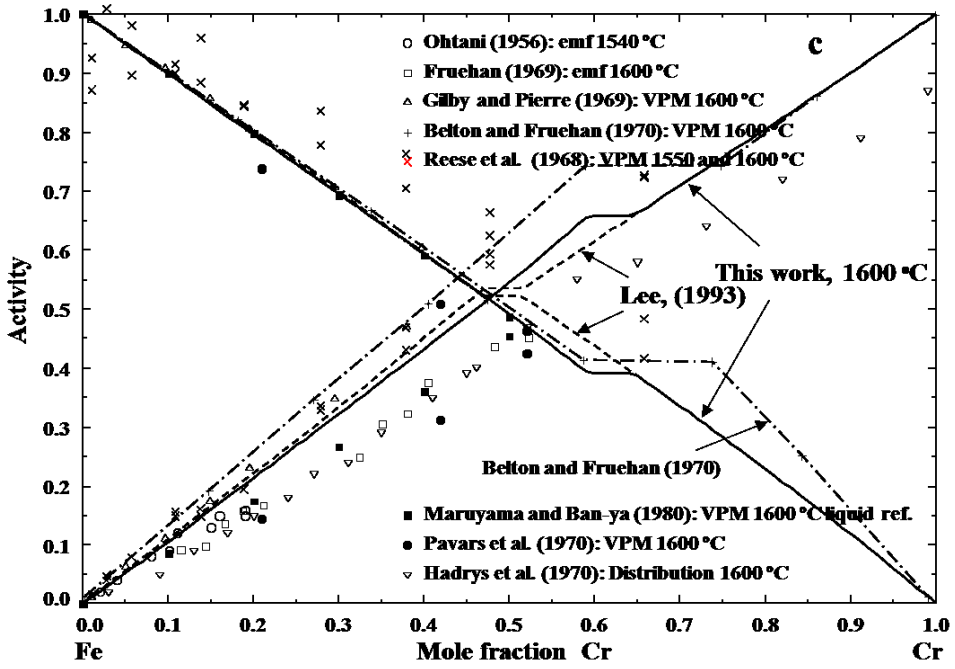

Fig. 7.5 Calculated activities of Fe-Cr liquid alloys along with the experimental data. (a) With respect to the liquid Fe and Cr standards at 1927 ºC, (b) with respect to the liquid Fe and bcc_A2 Cr standards at 1700 ºC, and (c) with respect to the liquid Fe and bcc_A2 Cr standards 1600 ºC.

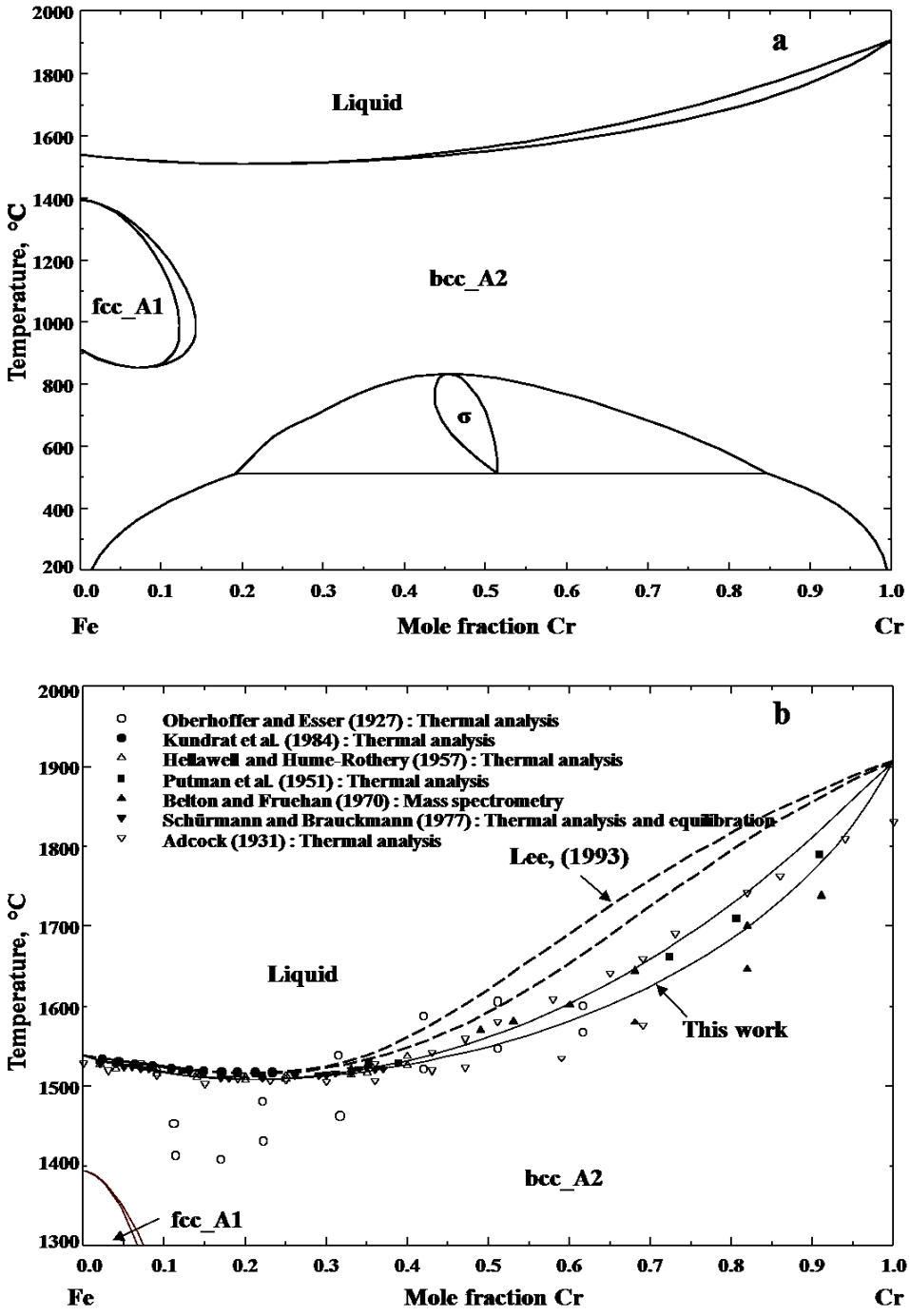

Fig. 7.6 Calculated phase diagram of the Fe-Cr system. (a) The entire temperature range, and (b) the high temperature part along with the experimental data.

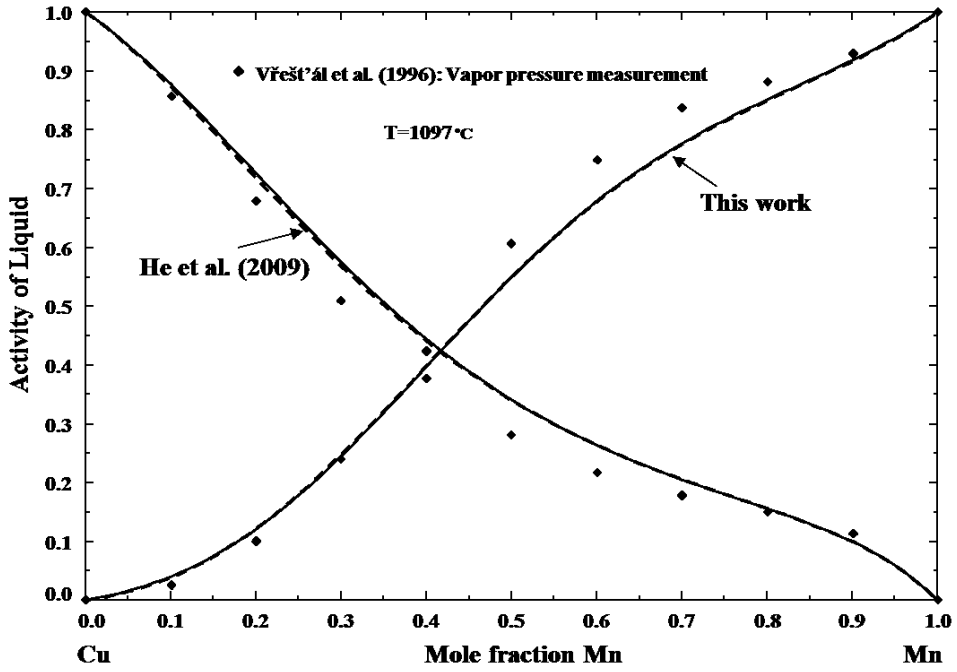

Fig. 7.7 Calculated activities of Cu and Mn with respect to the liquid standard at 1097 ºC along with the experimental data.

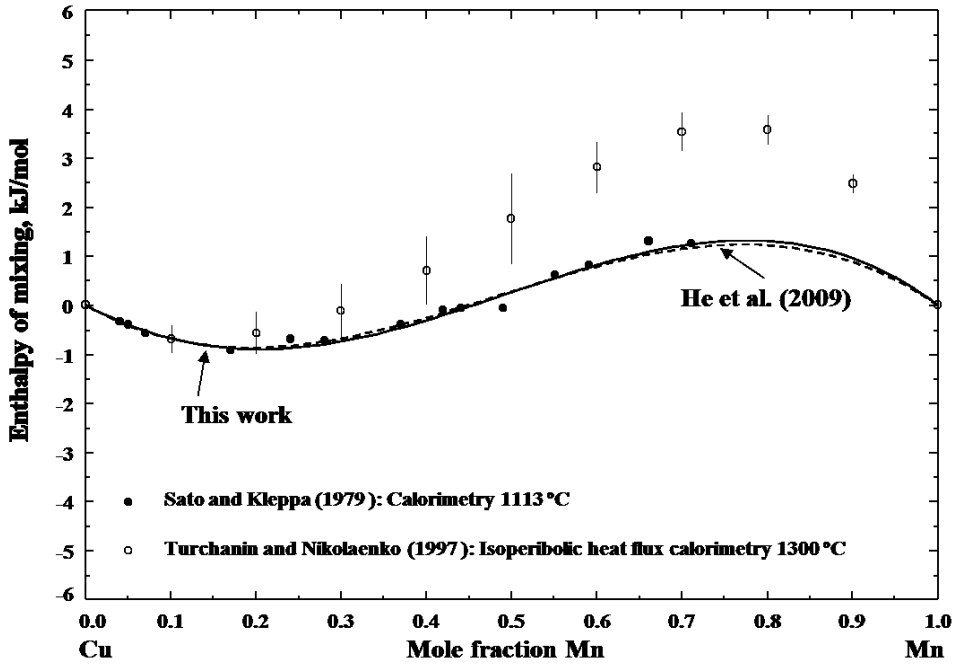

Fig. 7.8 Calculated enthalpy of mixing of the Cu-Mn liquid phase at 1113 ºC along with the experimental data.

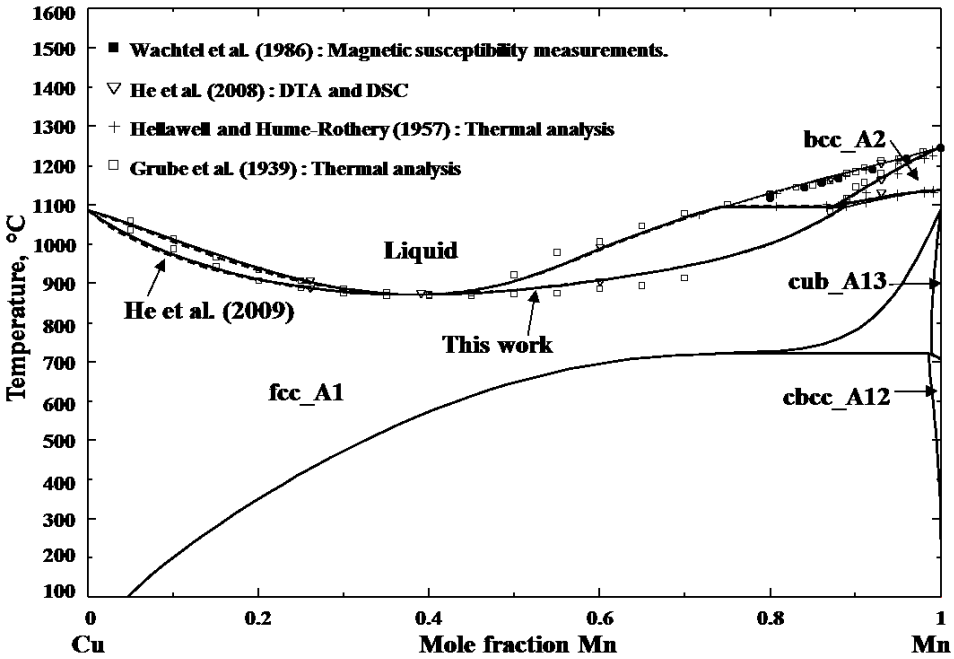

Fig. 7.9 Calculated phase diagram of the Cu-Mn system along with the experimental data.

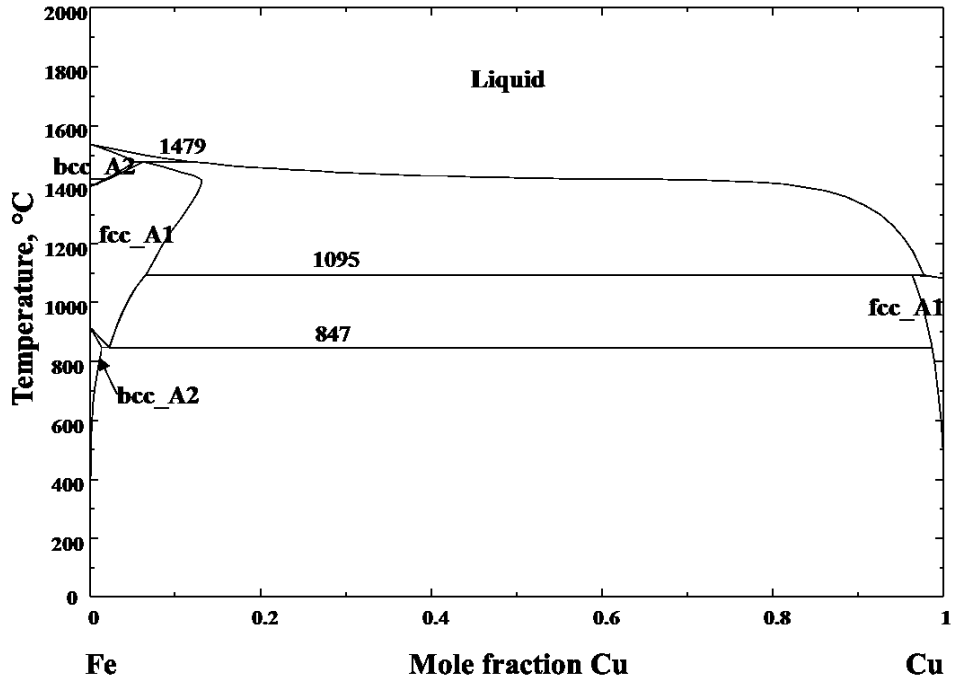

Fig. 7.10 Calcualted phase diagram of the Cu-Fe system.

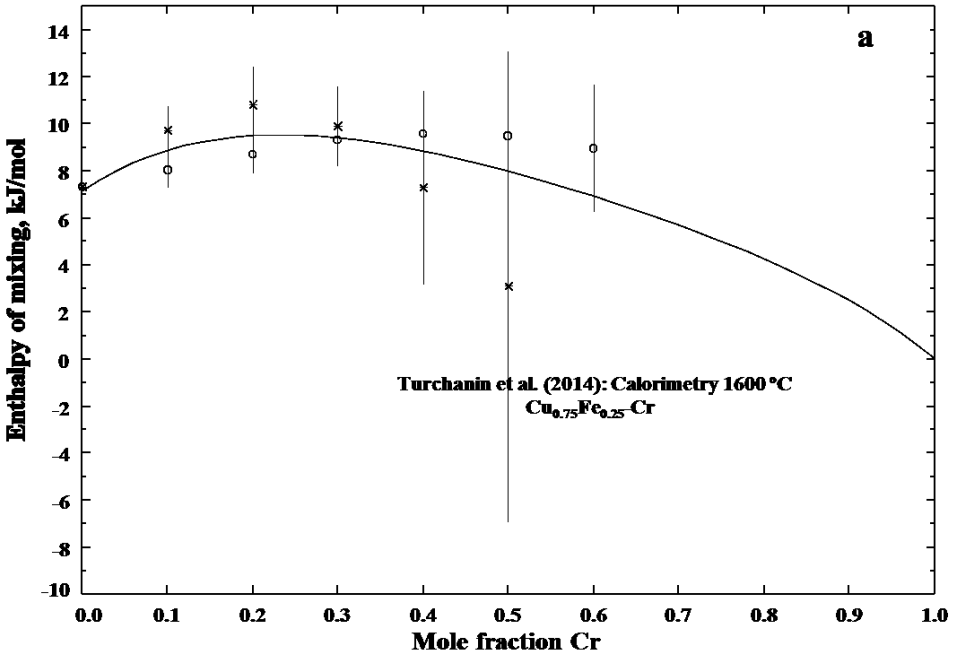
a
Enthalpy of mixing, kJ/mol
Mole fraction Cr
Turchanin et al. (2014): Calorimetry 1600 °C
Cu0.75Fe0.25–Cr

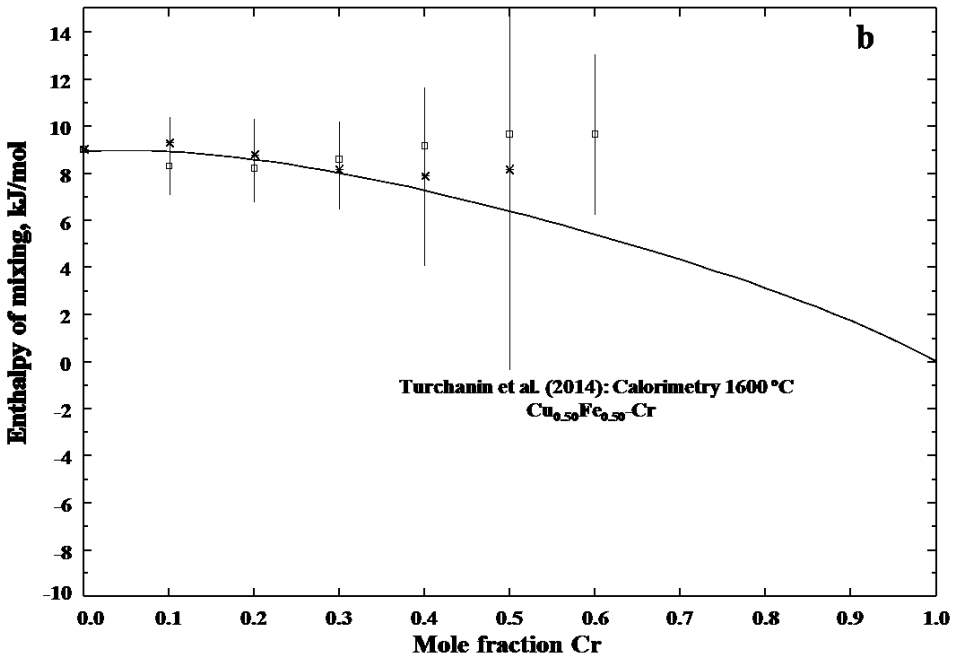
b
Enthalpy of mixing, kJ/mol
Mole fraction Cr
Turchanin et al. (2014): Calorimetry 1600 °C
Cu0.50Fe0.50–Cr

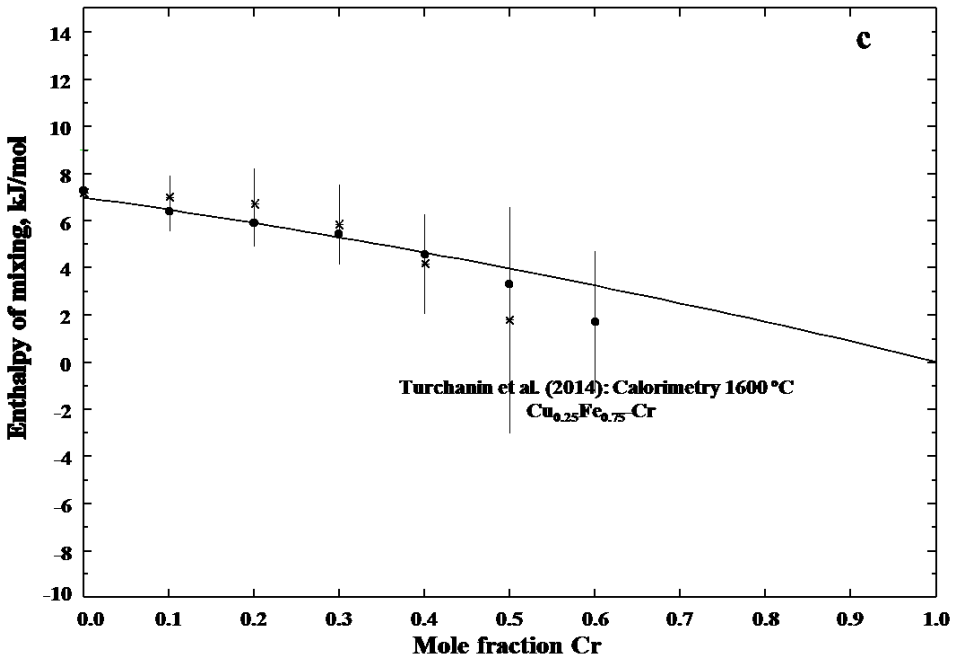

Fig. 7.11 Calculated enthalpy of mixing of the Cu-Cr-Fe liquid phase at 1600 ºC along with the experimental data. (a) $Cu_{0.75}Fe_{0.25}$-Cr section, (b) $Cu_{0.50}Fe_{0.50}$-Cr section, and (c) $Cu_{0.25}Fe_{0.75}$-Cr section.

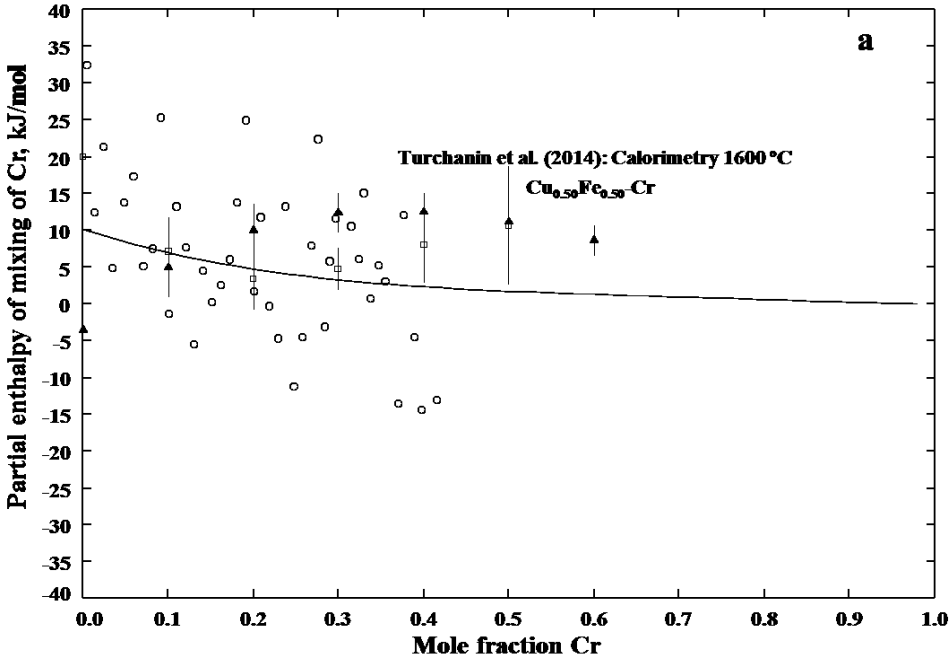
a
Turchanin et al. (2014): Calorimetry 1600 °C
Cu0.50Fe0.50–Cr
Partial enthalpy of mixing of Cr, kJ/mol
Mole fraction Cr

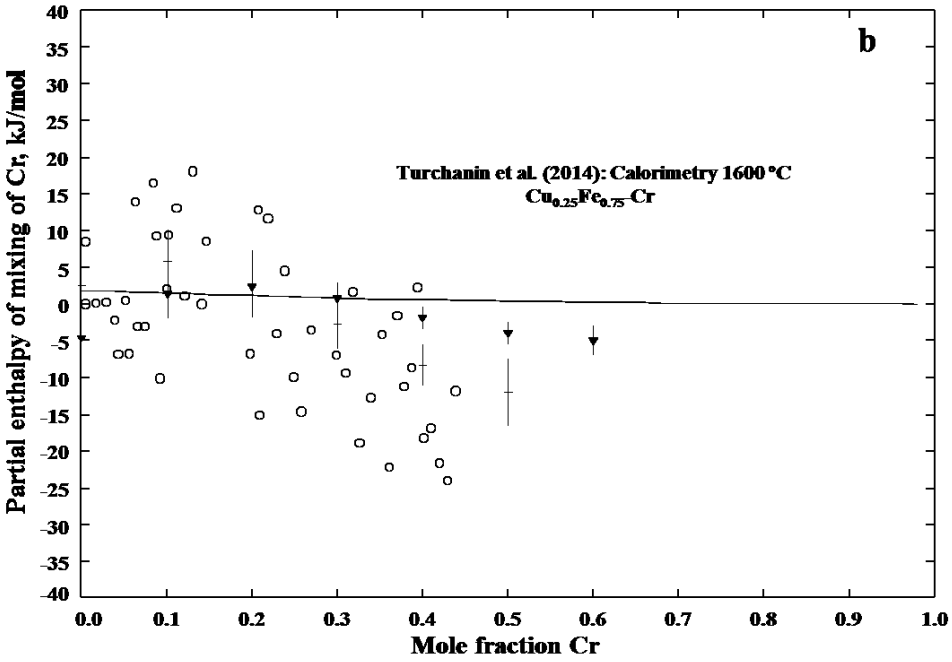
b
Turchanin et al. (2014): Calorimetry 1600 °C
Cu0.25Fe0.75–Cr
Partial enthalpy of mixing of Cr, kJ/mol
Mole fraction Cr

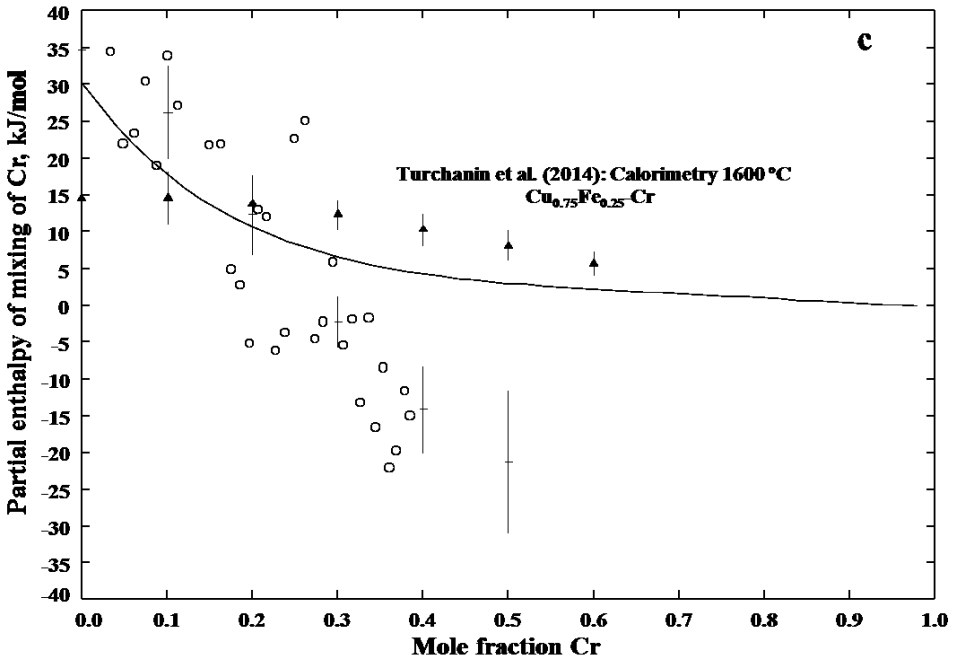

Fig. 7.12 Calculated partial enthalpy of mixing of Cr in the Cu-Cr-Fe liquid phase at 1600 ºC along with the experimental data. (a) $Cu_{0.50}Fe_{0.50}$-Cr section, (b) $Cu_{0.25}Fe_{0.75}$-Cr section, and (c) $Cu_{0.75}Fe_{0.25}$-Cr section.

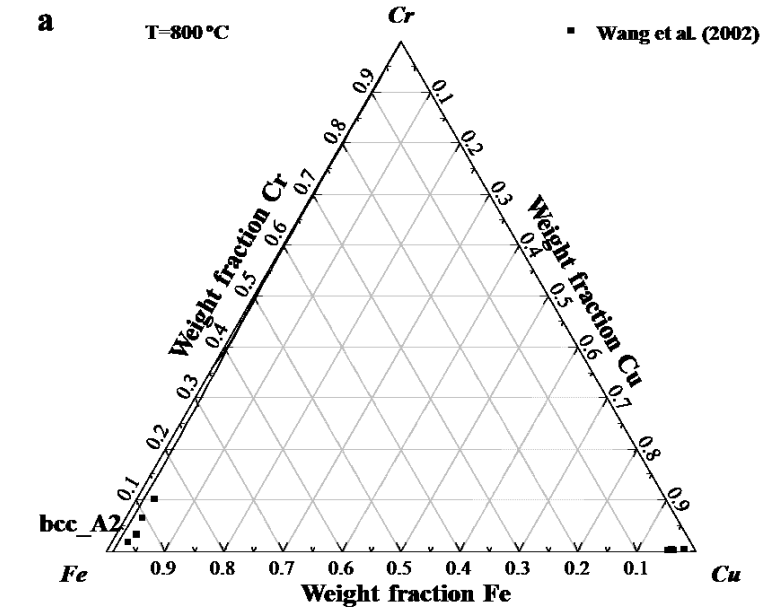
a
T=800 °C
Wang et al. (2002)
Cr
Weight fraction Cr
Weight fraction Cu
bcc_A2
Fe
Cu
Weight fraction Fe

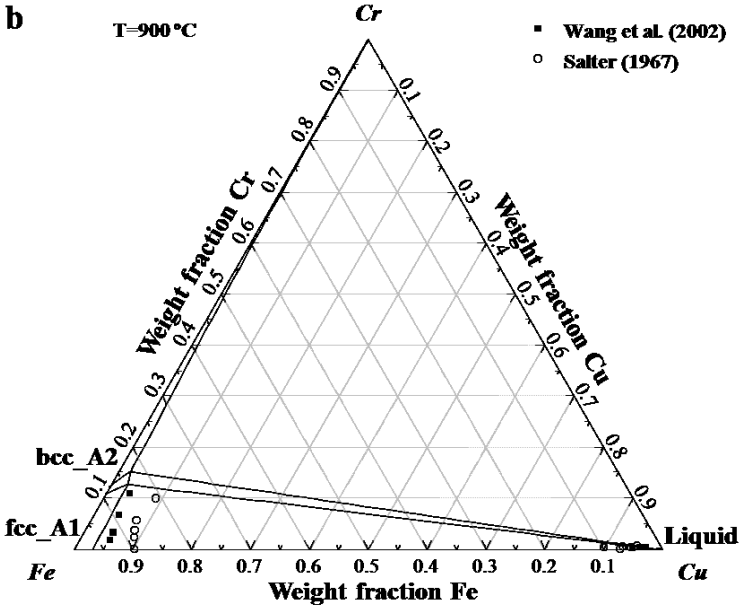
b
T=900 °C
Wang et al. (2002)
Salter (1967)
Cr
Weight fraction Cr
Weight fraction Cu
bcc_A2
fcc_A1
Liquid
Fe
Cu
Weight fraction Fe

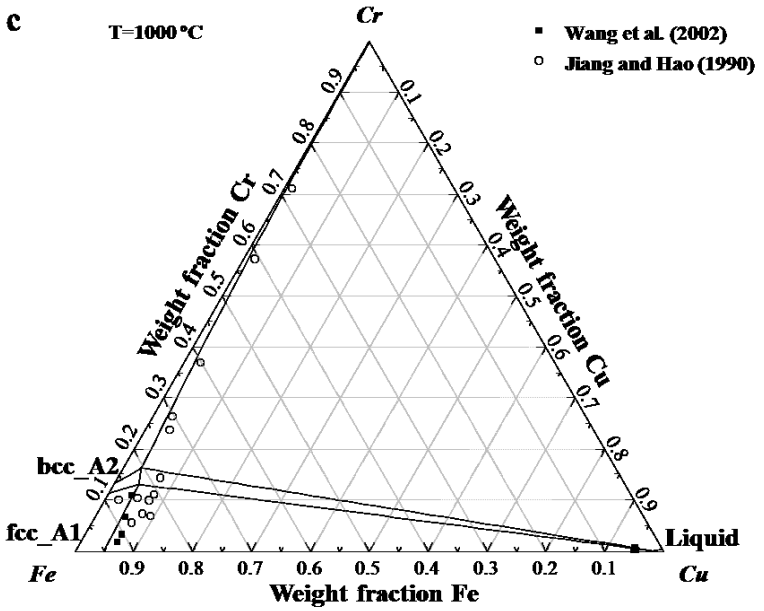
c
T=1000 °C
Cr
Wang et al. (2002)
Jiang and Hao (1990)
Weight fraction Cr
Weight fraction Cu
bcc_A2
fcc_A1
Liquid
Fe
Cu
Weight fraction Fe

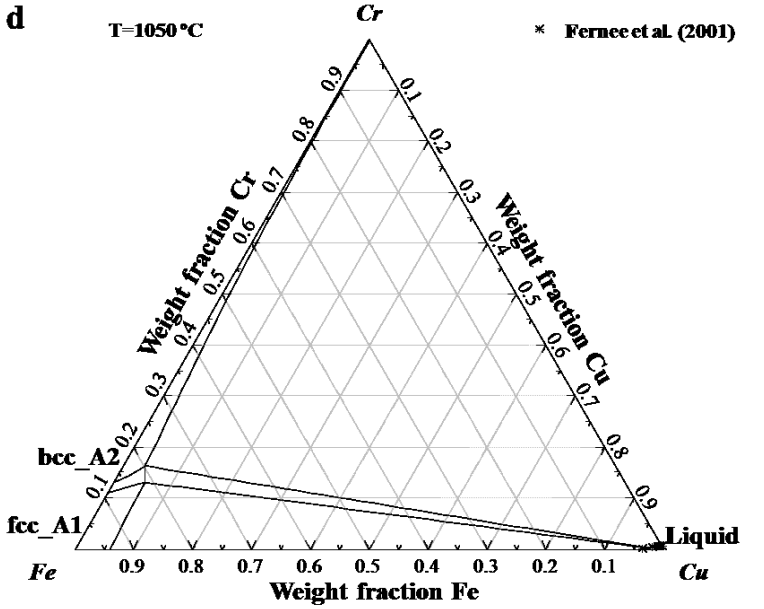
d
T=1050 °C
Cr
Fernee et al. (2001)
Weight fraction Cr
Weight fraction Cu
bcc_A2
fcc_A1
Liquid
Fe
Cu
Weight fraction Fe

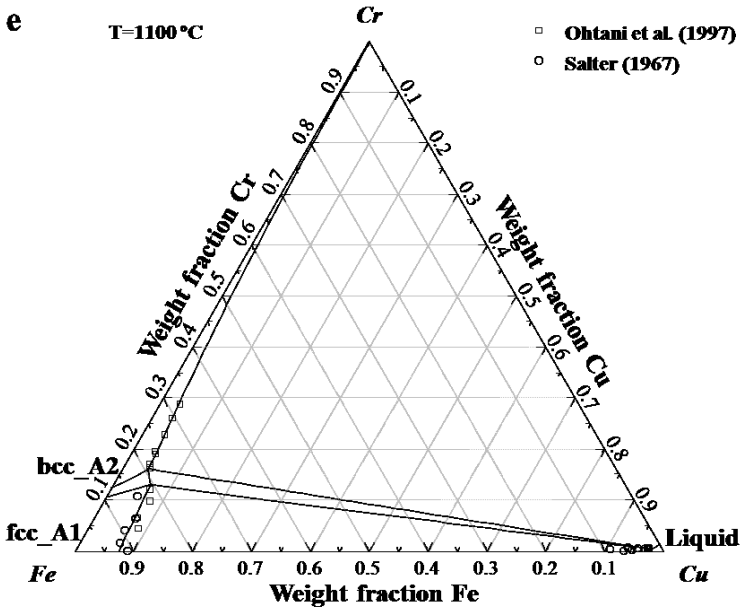
e
T=1100 °C
Cr
Ohtani et al. (1997)
Salter (1967)
Weight fraction Cr
Weight fraction Cu
bcc_A2
fcc_A1
Liquid
Fe
Cu
Weight fraction Fe

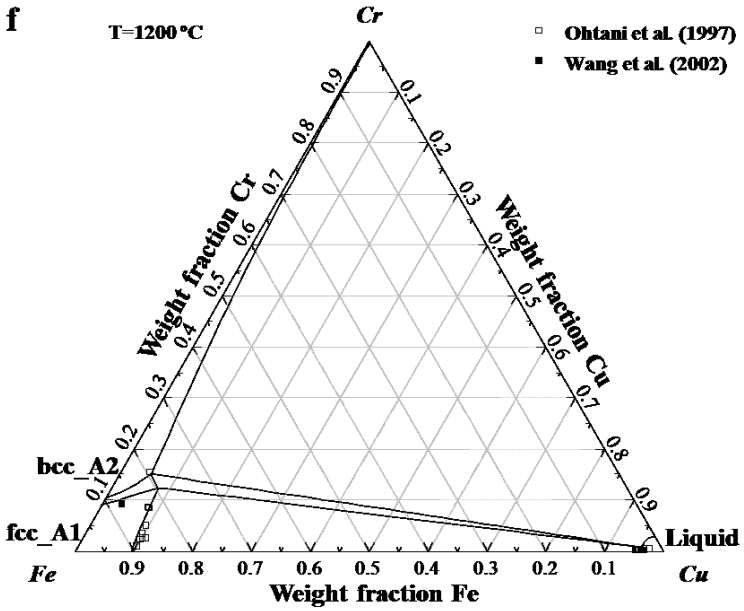
f
T=1200 °C
Cr
Ohtani et al. (1997)
Wang et al. (2002)
Weight fraction Cr
Weight fraction Cu
bcc_A2
fcc_A1
Liquid
Fe
Cu
Weight fraction Fe

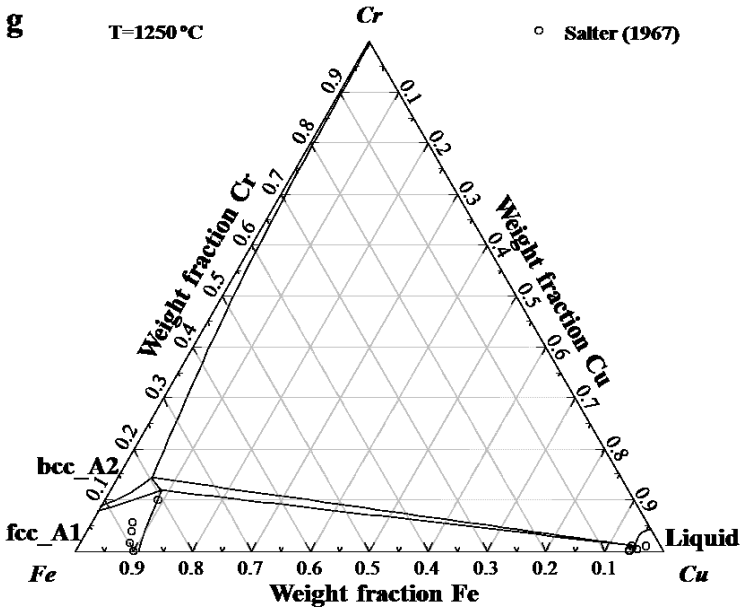
g
T=1250 °C
Salter (1967)
Cr
Weight fraction Cr
Weight fraction Cu
bcc_A2
fcc_A1
Liquid
Fe
Cu
Weight fraction Fe

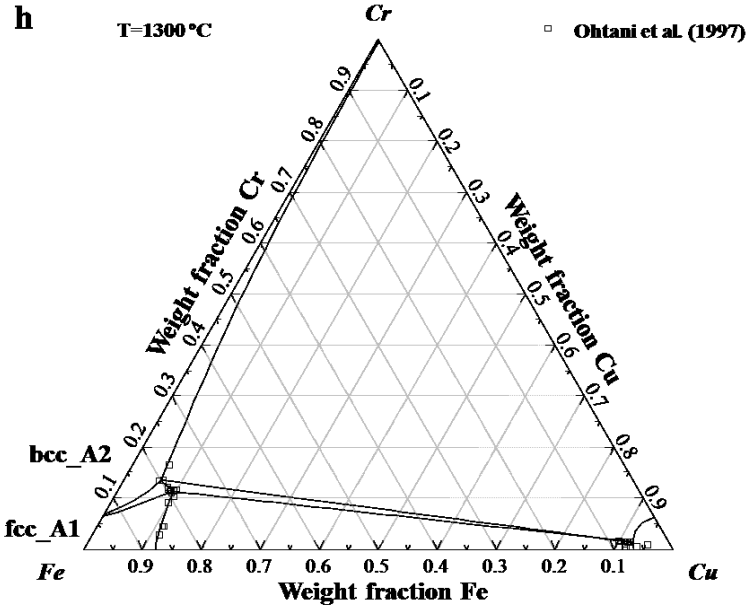
h
T=1300 °C
Ohtani et al. (1997)
Cr
Weight fraction Cr
Weight fraction Cu
bcc_A2
fcc_A1
Fe
Cu
Weight fraction Fe

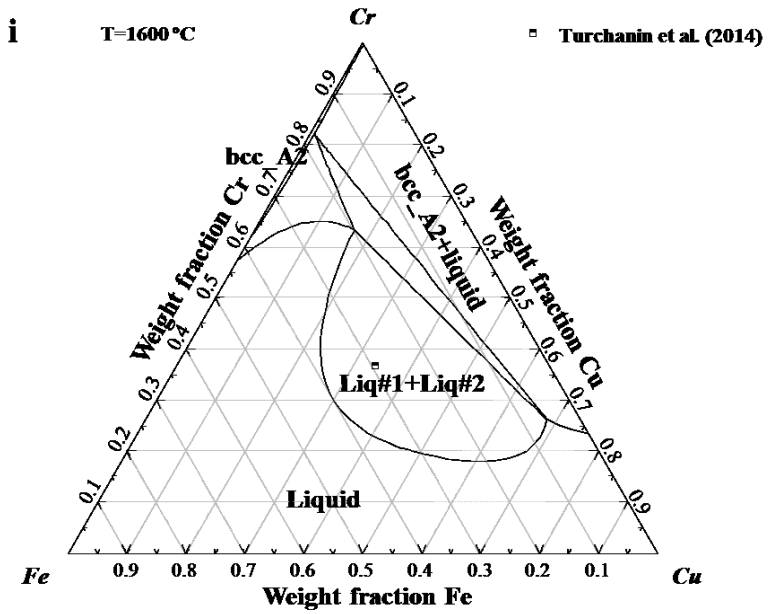

Fig. 7.13 Calculated isothermal sections of the Cu-Cr-Fe system along with the experimental data at different temperatures. (a) At 800 ºC, (b) at 900 ºC, (c) at 1000 ºC, (d) at 1050 ºC, (e) at 1100 ºC, (f) at 1200 ºC, (g) at 1250 ºC, (h) at 1300 ºC, and (i) at 1600 ºC.

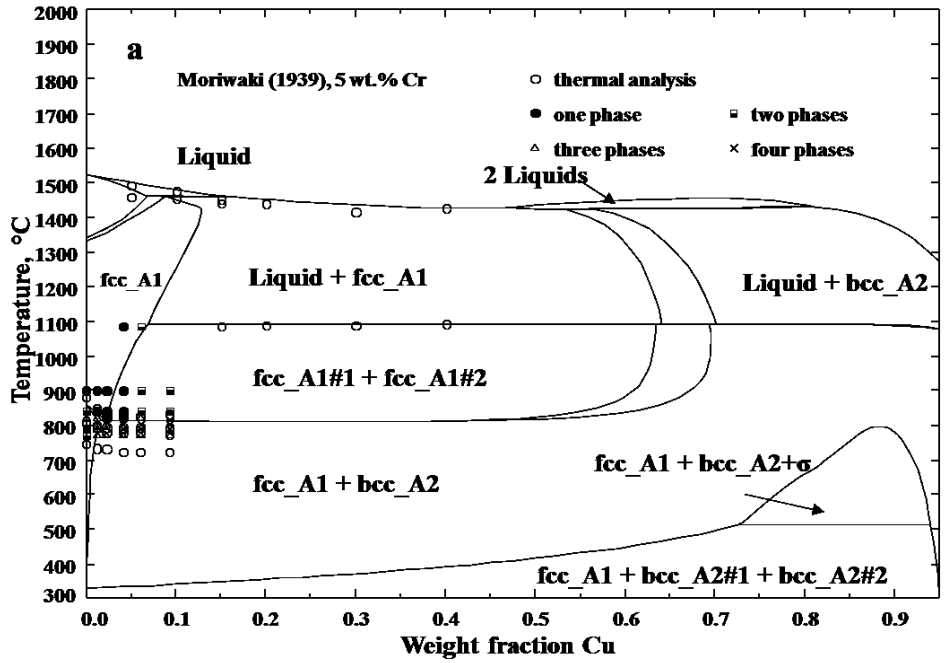
a
Moriwaki (1939), 5 wt.% Cr
thermal analysis
one phase
two phases
three phases
four phases
Liquid
2 Liquids
fcc_A1
Liquid + fcc_A1
Liquid + bcc_A2
fcc_A1#1 + fcc_A1#2
fcc_A1 + bcc_A2
fcc_A1 + bcc_A2+σ
fcc_A1 + bcc_A2#1 + bcc_A2#2
Temperature, °C
Weight fraction Cu

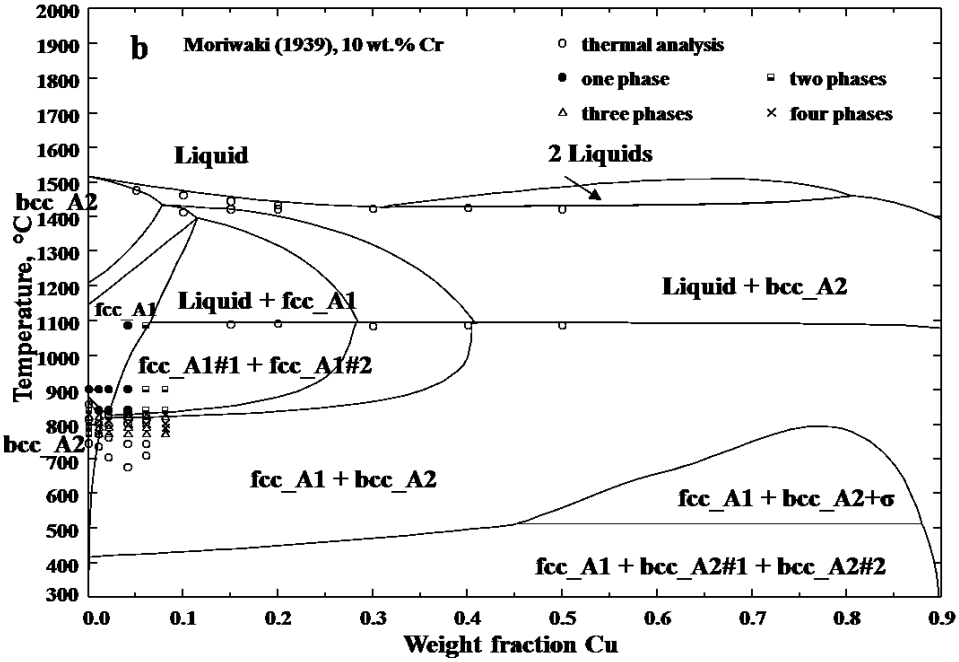
b
Moriwaki (1939), 10 wt.% Cr
thermal analysis
one phase
two phases
three phases
four phases
Liquid
2 Liquids
bcc_A2
fcc_A1
Liquid + fcc_A1
Liquid + bcc_A2
fcc_A1#1 + fcc_A1#2
bcc_A2
fcc_A1 + bcc_A2
fcc_A1 + bcc_A2+σ
fcc_A1 + bcc_A2#1 + bcc_A2#2
Temperature, °C
Weight fraction Cu

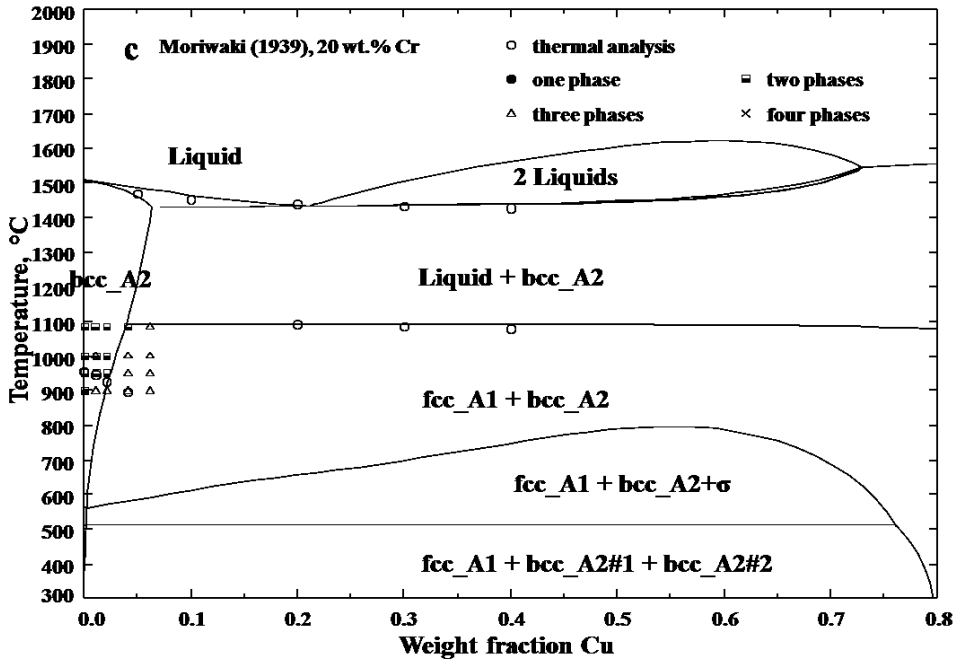

Fig. 7.14 Calculated isoplethal sections of the Cu-Cr-Fe system along with the experimental data. (a) At 5 wt.% Cr, (b) at 10 wt.% Cr, and (c) at 20 wt.% Cr.

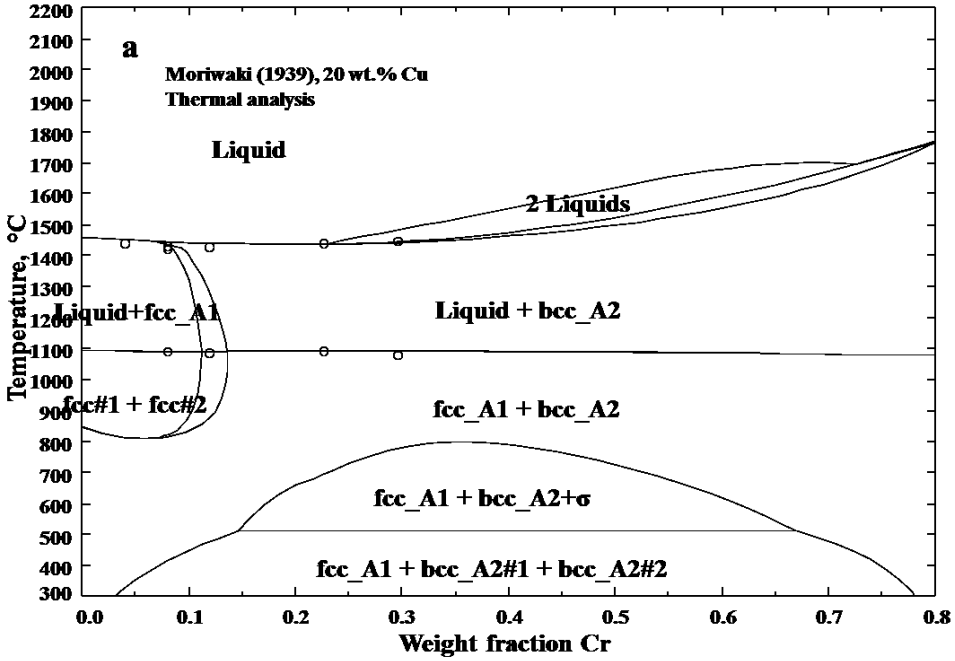
a
Moriwaki (1939), 20 wt.% Cu
Thermal analysis
Liquid
2 Liquids
Liquid+fcc_A1
Liquid + bcc_A2
fcc#1 + fcc#2
fcc_A1 + bcc_A2
fcc_A1 + bcc_A2+σ
fcc_A1 + bcc_A2#1 + bcc_A2#2
Temperature, °C
Weight fraction Cr

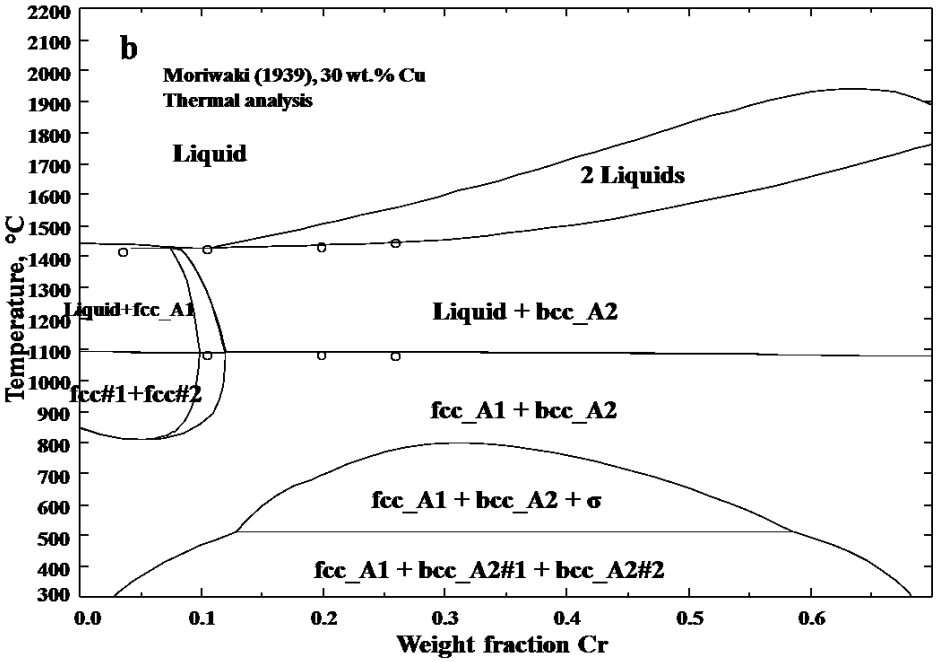
b
Moriwaki (1939), 30 wt.% Cu
Thermal analysis
Liquid
2 Liquids
Liquid+fcc_A1
Liquid + bcc_A2
fcc#1+fcc#2
fcc_A1 + bcc_A2
fcc_A1 + bcc_A2 + σ
fcc_A1 + bcc_A2#1 + bcc_A2#2
Temperature, °C
Weight fraction Cr

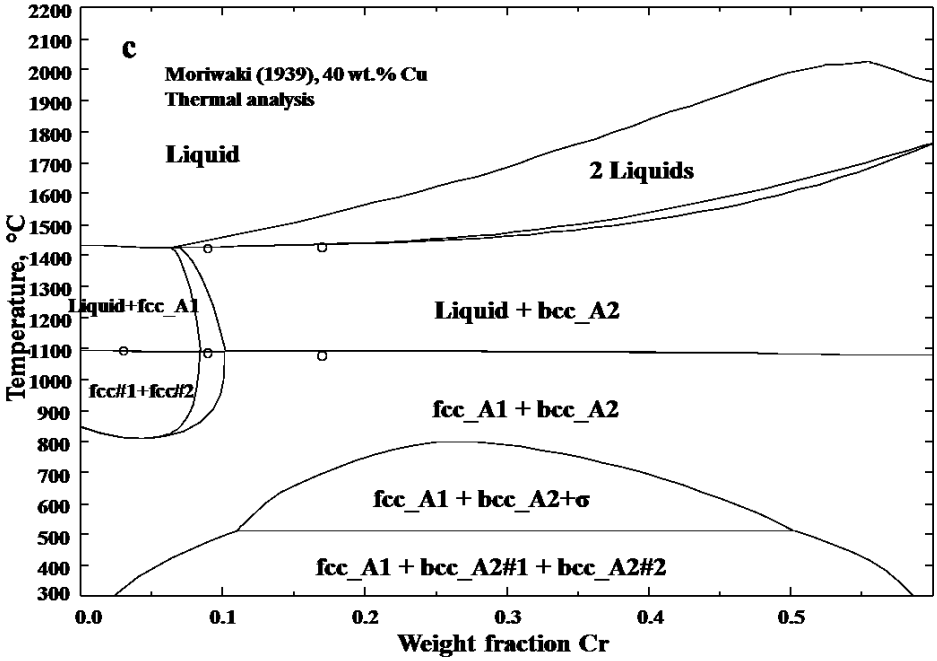

Fig. 7.15 Calculated isoplethal sections of the Cu-Cr-Fe system along with the experimental data with different Cu contents. (a) At 20 wt.% Cu, (b) at 30 wt.% Cu, and (c) at 40 wt.% Cu.

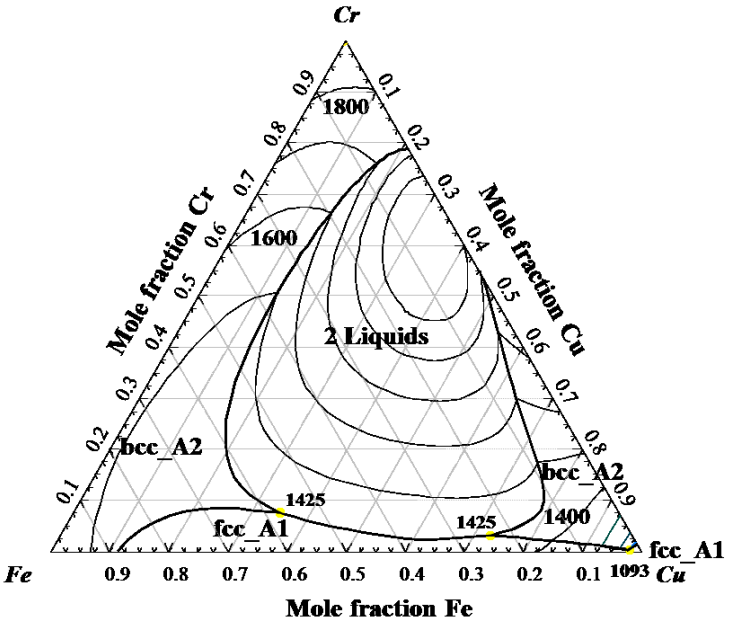

Fig. 7.16 Calculated liquidus projection of the Cu-Cr-Fe system.

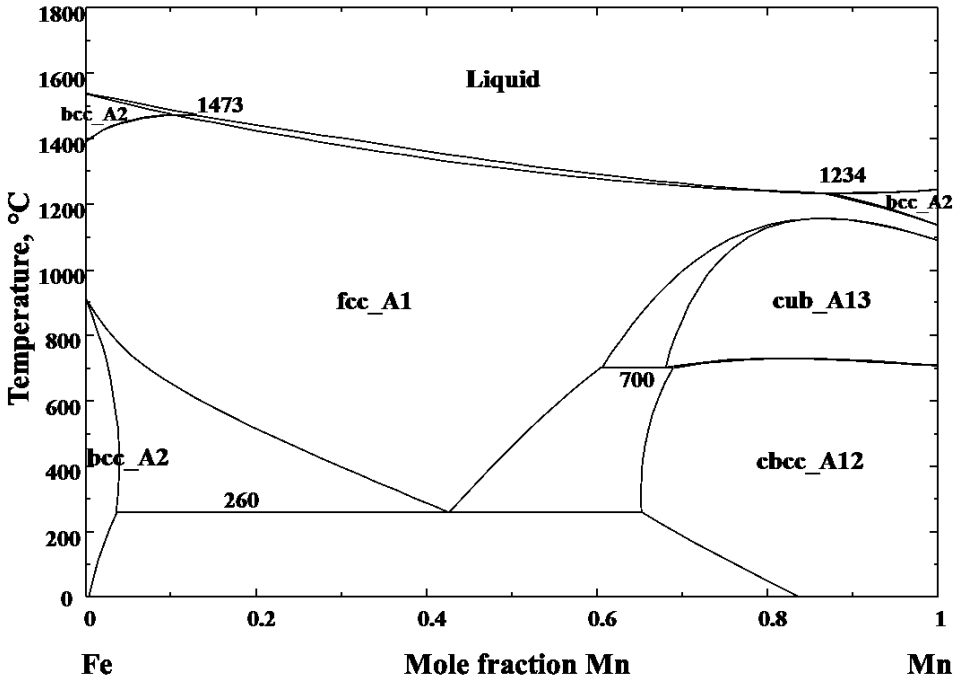

Fig. 7.17 Calculated phase diagram of the Fe-Mn system.

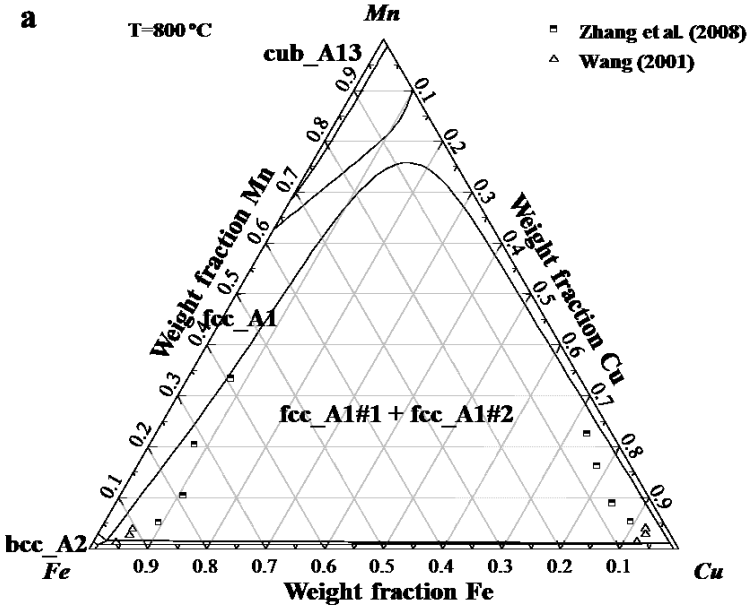
a
T=800 °C
Mn
cub_A13
Zhang et al. (2008)
Wang (2001)
Weight fraction Mn
Weight fraction Cu
fcc_A1
fcc_A1#1 + fcc_A1#2
bcc_A2
Fe
Cu
Weight fraction Fe

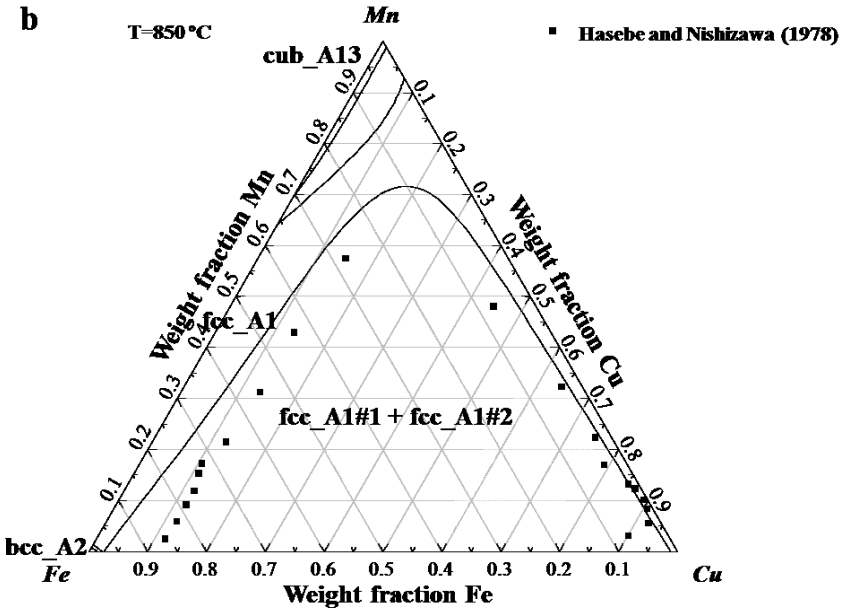
b
T=850 °C
Mn
Hasebe and Nishizawa (1978)
cub_A13
Weight fraction Mn
Weight fraction Cu
fcc_A1
fcc_A1#1 + fcc_A1#2
bcc_A2
Fe
Cu
Weight fraction Fe

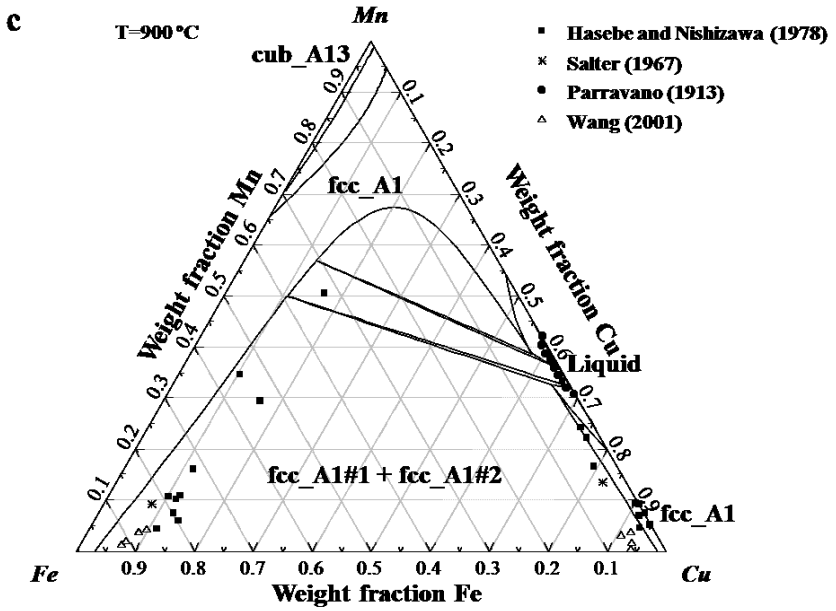
c
T=900 °C
Mn
cub_A13
Hasebe and Nishizawa (1978)
Salter (1967)
Parravano (1913)
Wang (2001)
fcc_A1
Weight fraction Mn
Weight fraction Cu
Liquid
fcc_A1#1 + fcc_A1#2
fcc_A1
Fe
Cu
Weight fraction Fe

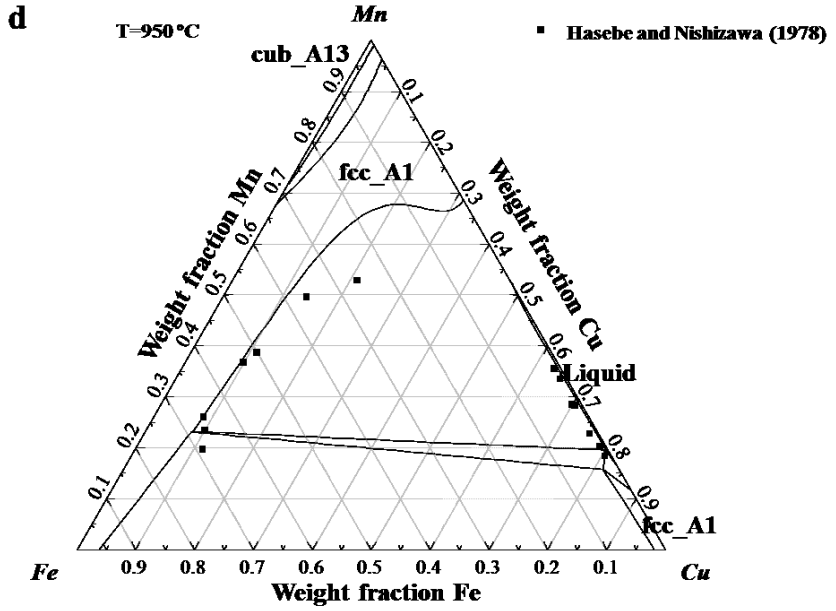
d
T=950 °C
Mn
cub_A13
Hasebe and Nishizawa (1978)
fcc_A1
Weight fraction Mn
Weight fraction Cu
Liquid
fcc_A1
Fe
Cu
Weight fraction Fe

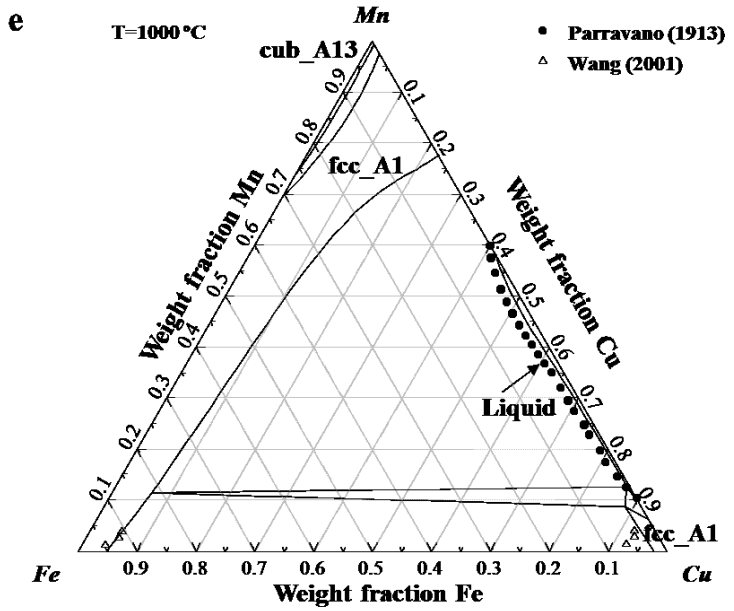
e
T=1000 °C
Mn
cub_A13
Parravano (1913)
Wang (2001)
fcc_A1
Weight fraction Mn
Weight fraction Cu
Liquid
fcc_A1
Fe
Cu
Weight fraction Fe

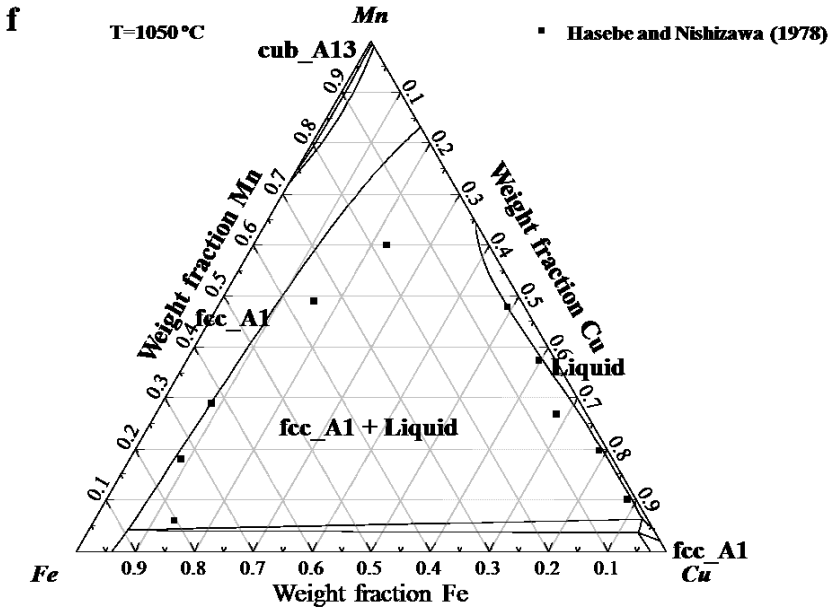
f
T=1050 °C
Mn
cub_A13
Hasebe and Nishizawa (1978)
Weight fraction Mn
Weight fraction Cu
fcc_A1
Liquid
fcc_A1 + Liquid
fcc_A1
Fe
Cu
Weight fraction Fe

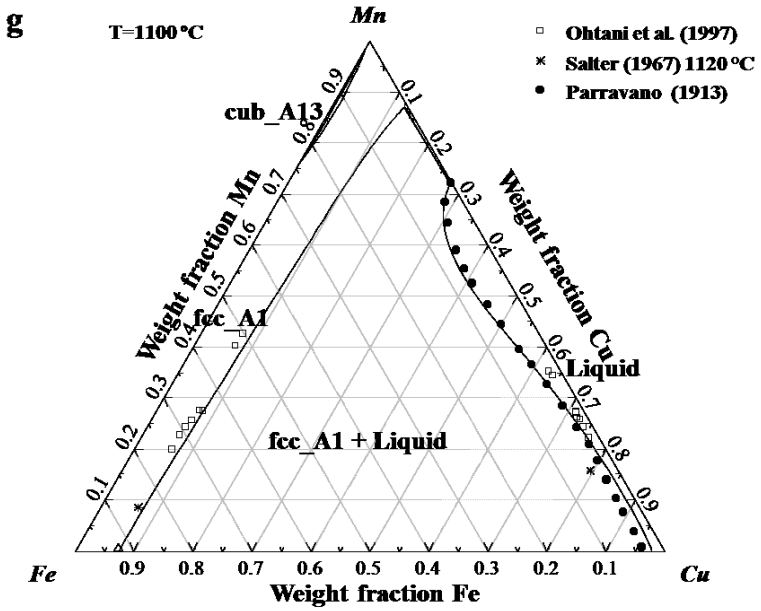
g
T=1100 °C
Mn
Ohtani et al. (1997)
Salter (1967) 1120 °C
Parravano (1913)
cub_A13
fcc_A1
Liquid
fcc_A1 + Liquid
Weight fraction Mn
Weight fraction Cu
Fe
Cu
Weight fraction Fe

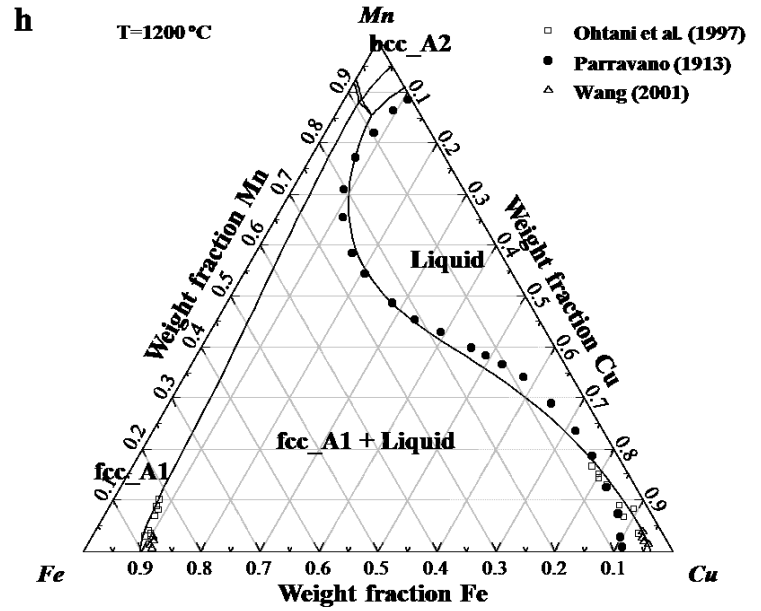
h
T=1200 °C
Mn
bcc_A2
Ohtani et al. (1997)
Parravano (1913)
Wang (2001)
Liquid
fcc_A1 + Liquid
fcc_A1
Weight fraction Mn
Weight fraction Cu
Fe
Cu
Weight fraction Fe

i

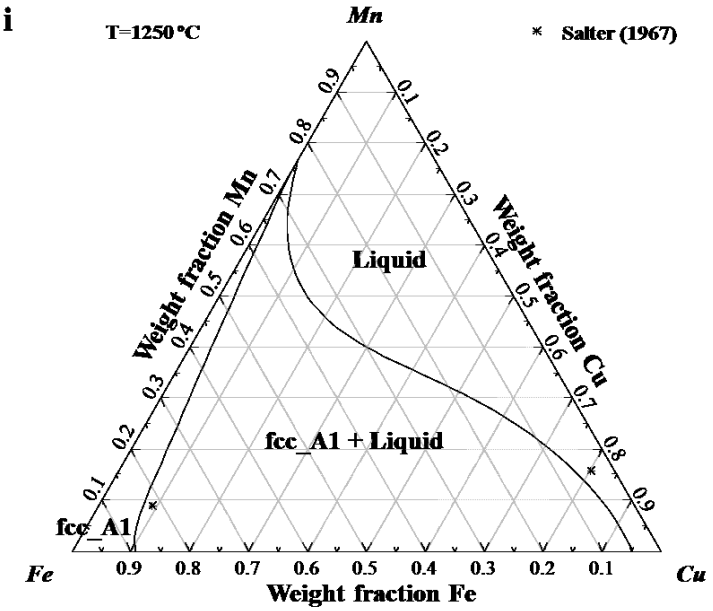
T=1250 °C
Mn
Salter (1967)
Liquid
fcc_A1 + Liquid
fcc_A1
Weight fraction Mn
Weight fraction Cu
Weight fraction Fe
Fe
Cu

j

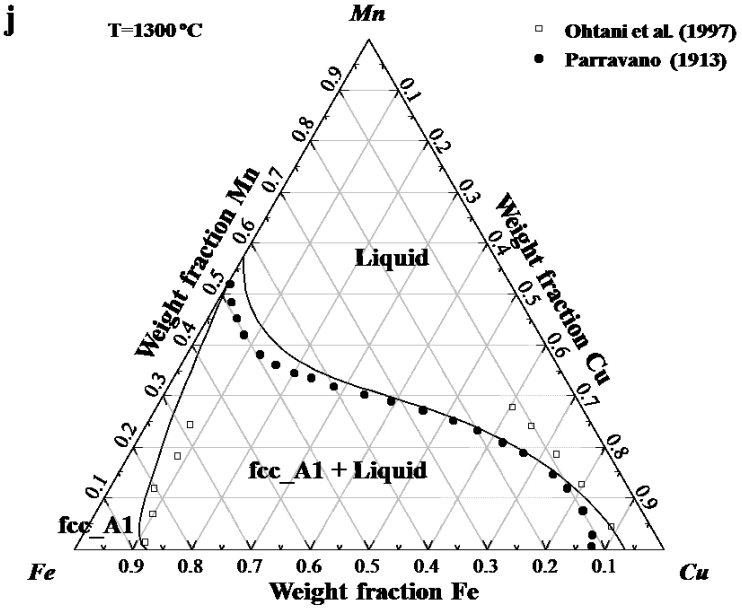
T=1300 °C
Mn
Ohtani et al. (1997)
Parravano (1913)
Liquid
fcc_A1 + Liquid
fcc_A1
Weight fraction Mn
Weight fraction Cu
Weight fraction Fe
Fe
Cu

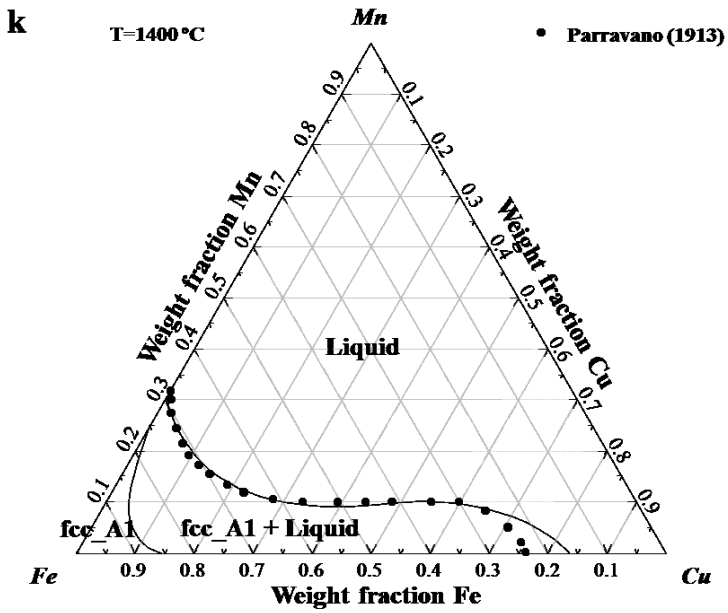

Fig. 7.18 Calculated isothermal sections of the Cu-Fe-Mn system along with the experimental data at different temperatures. (a) At 800 ºC, (b) at 850 ºC, (c) at 900 ºC, (d) at 950 ºC, (e) at 1000 ºC, (f) at 1050 ºC, (g) at 1100 ºC, (h) at 1200 ºC, (i) at 1250 ºC, (j) at 1300 ºC, and (k) at 1400 ºC.

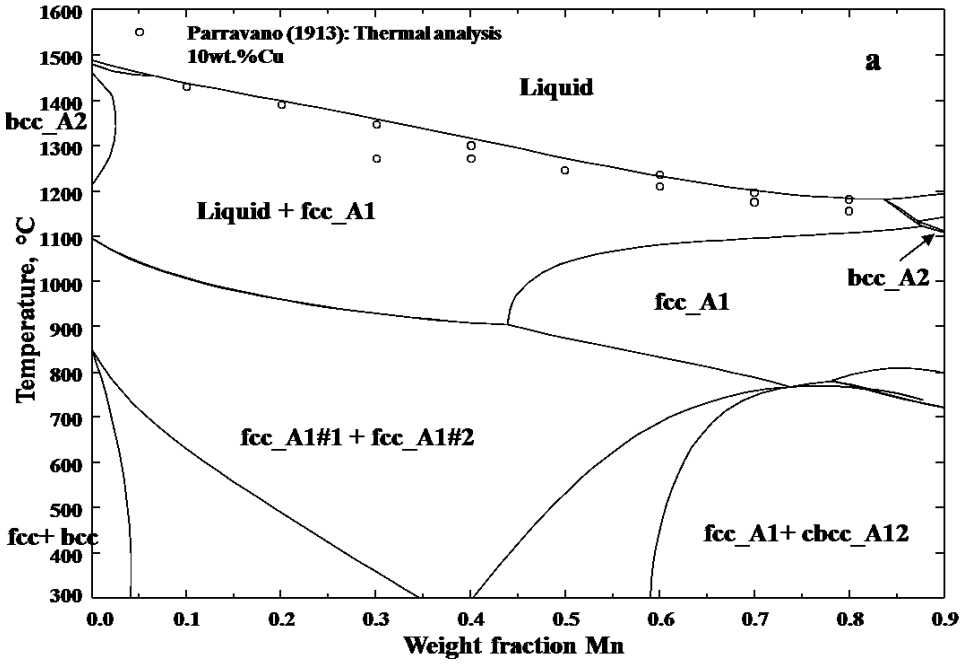
Parravano (1913): Thermal analysis
10wt.%Cu
a
Liquid
bcc_A2
Liquid + fcc_A1
bcc_A2
fcc_A1
fcc_A1#1 + fcc_A1#2
fcc+ bcc
fcc_A1+ cbcc_A12
Temperature, °C
Weight fraction Mn

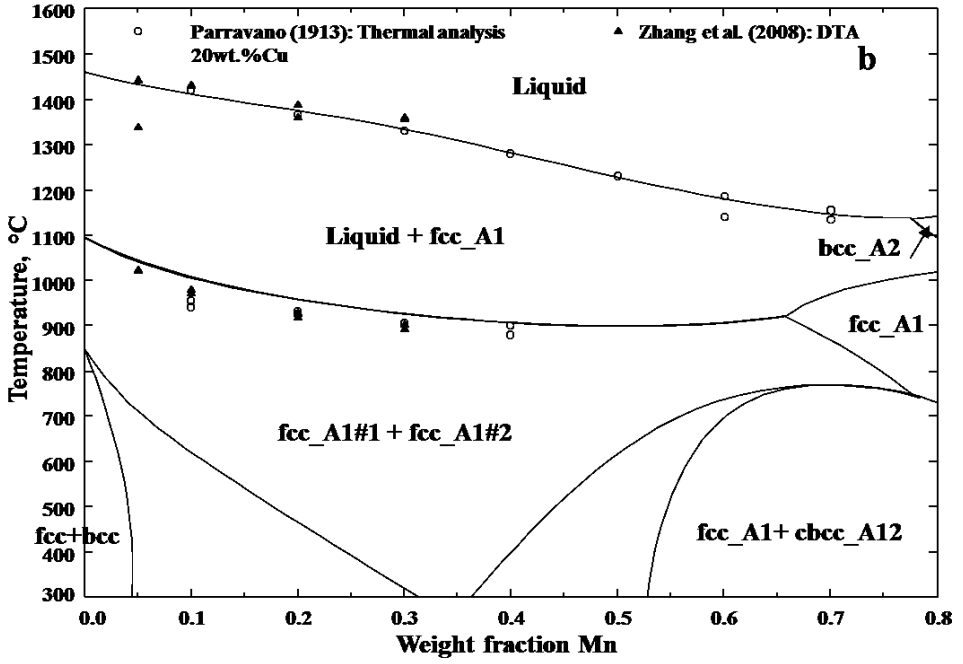
Parravano (1913): Thermal analysis
Zhang et al. (2008): DTA
20wt.%Cu
b
Liquid
Liquid + fcc_A1
bcc_A2
fcc_A1
fcc_A1#1 + fcc_A1#2
fcc+bcc
fcc_A1+ cbcc_A12
Temperature, °C
Weight fraction Mn

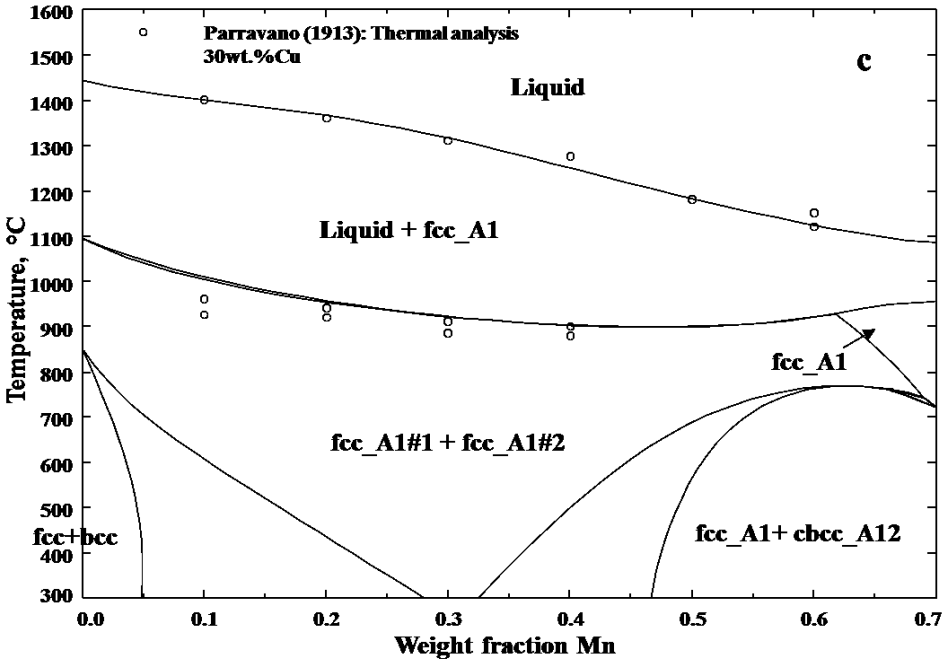

Fig. 7.19 Calculated isoplethal sections of the Cu-Fe-Mn system along with the experimental data. (a) At 10 wt.% Cu, (b) at 20 wt.% Cu, and (c) at 30 wt.% Cu.

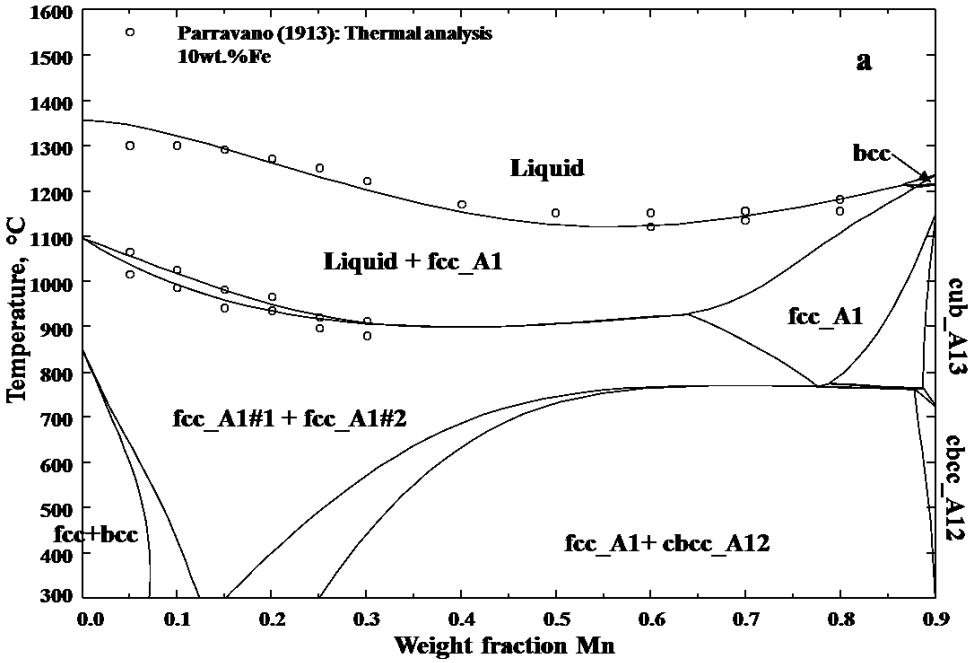
Parravano (1913): Thermal analysis
10wt.%Fe
a
Liquid
bcc
Liquid + fcc_A1
fcc_A1
cub_A13
fcc_A1#1 + fcc_A1#2
cbcc_A12
fcc+bcc
fcc_A1+ cbcc_A12
Temperature, °C
Weight fraction Mn

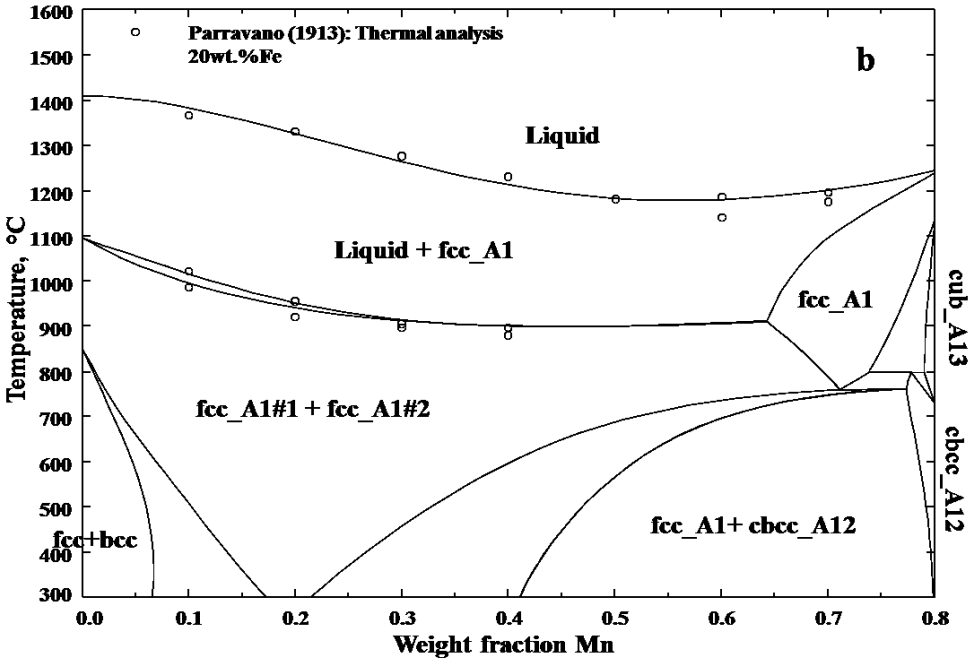
Parravano (1913): Thermal analysis
20wt.%Fe
b
Liquid
Liquid + fcc_A1
fcc_A1
cub_A13
fcc_A1#1 + fcc_A1#2
cbcc_A12
fcc+bcc
fcc_A1+ cbcc_A12
Temperature, °C
Weight fraction Mn

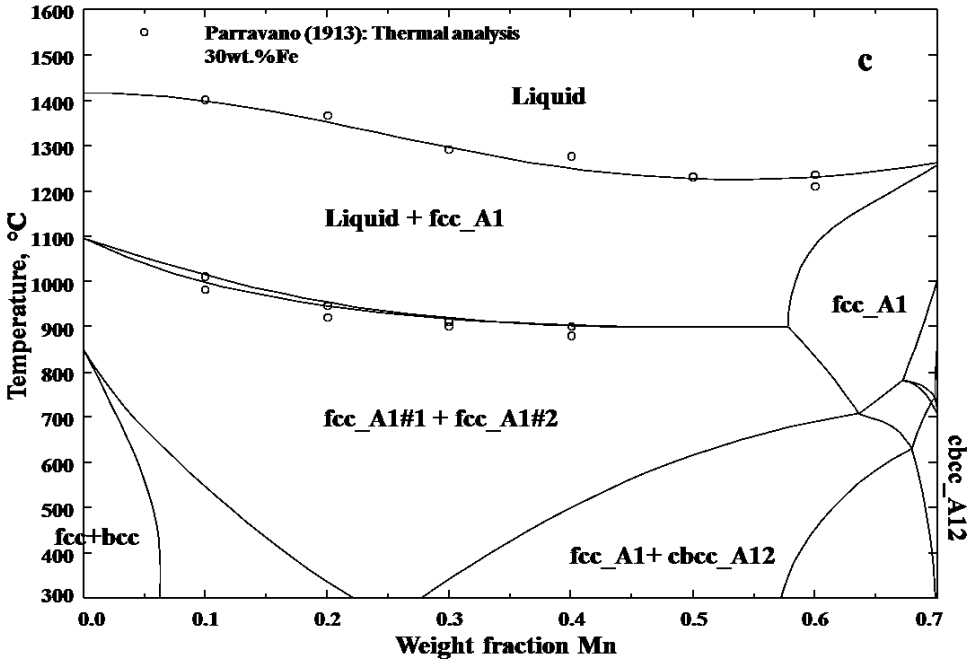

Fig. 7.20 Calculated isoplethal sections of the Cu-Fe-Mn system along with the experimental data. (a) At 10 wt.% Fe, (b) at 20 wt.% Fe, and (c) at 30 wt.% Fe.

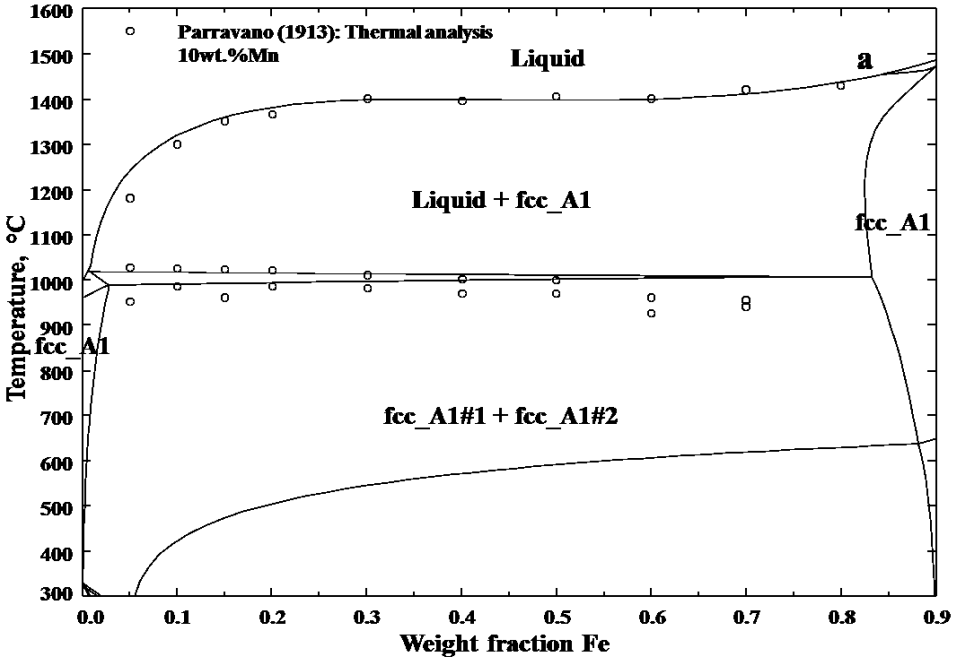
Parravano (1913): Thermal analysis
10wt.%Mn
Liquid
a
Liquid + fcc_A1
fcc_A1
fcc_A1
fcc_A1#1 + fcc_A1#2
Temperature, °C
Weight fraction Fe
1600
1500
1400
1300
1200
1100
1000
900
800
700
600
500
400
300
0.0
0.1
0.2
0.3
0.4
0.5
0.6
0.7
0.8
0.9

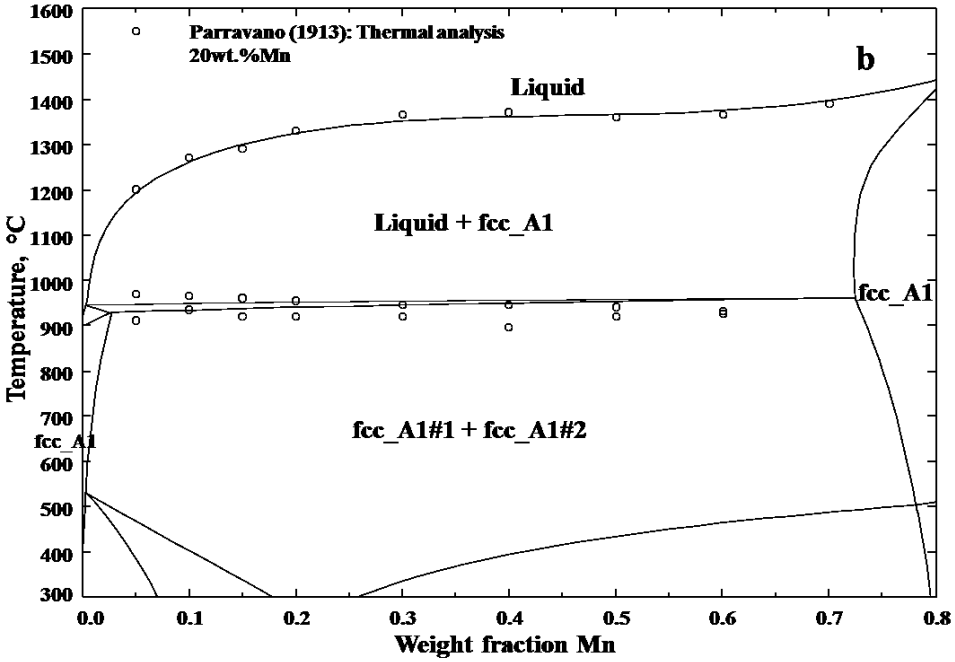
Parravano (1913): Thermal analysis
20wt.%Mn
b
Liquid
Liquid + fcc_A1
fcc_A1
fcc_A1
fcc_A1#1 + fcc_A1#2
Temperature, °C
Weight fraction Mn
1600
1500
1400
1300
1200
1100
1000
900
800
700
600
500
400
300
0.0
0.1
0.2
0.3
0.4
0.5
0.6
0.7
0.8

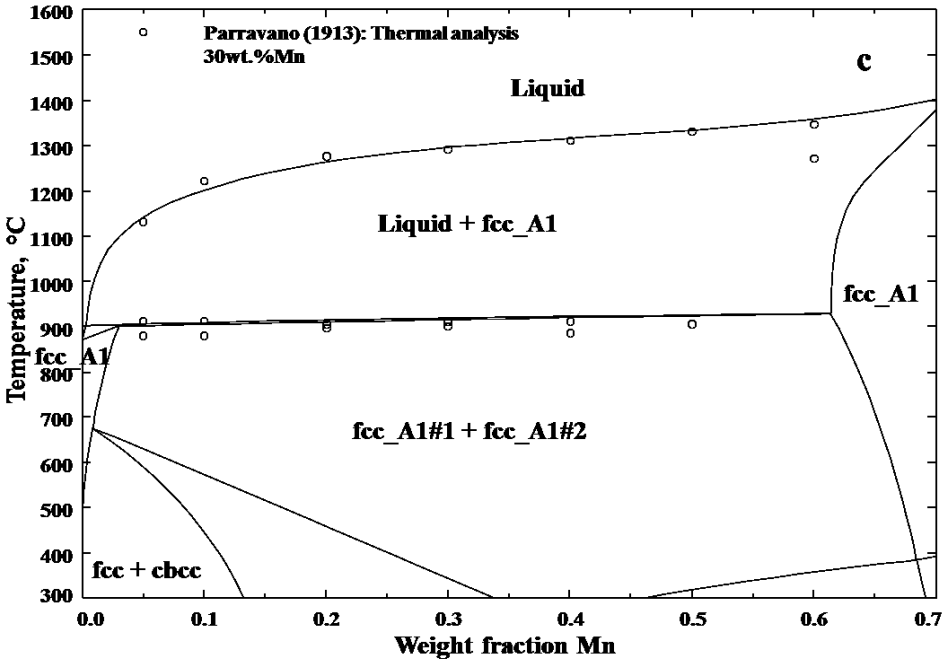

Fig. 7.21 Calculated isoplethal sections of the Cu-Fe-Mn system along with the experimental data. (a) At 10 wt.% Mn, (b) at 20 wt.% Mn, and (c) at 30 wt.% Mn.

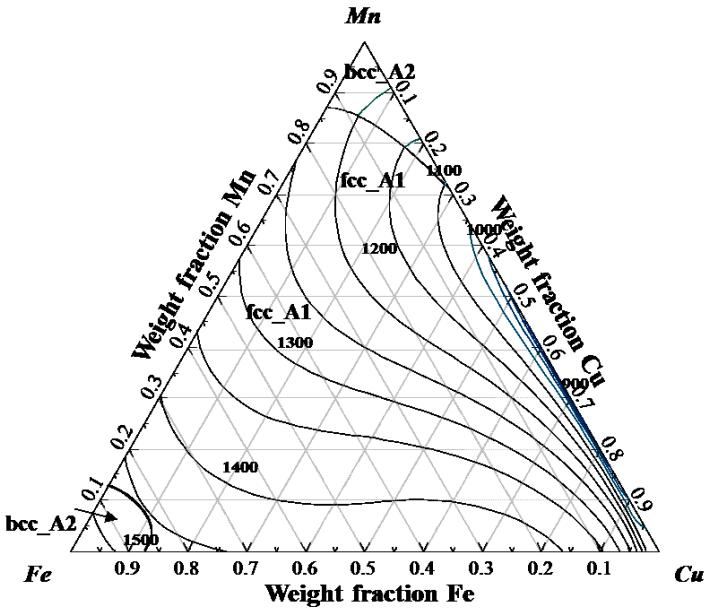

Fig. 7.22 Calculated liquidus projection of the Cu-Fe-Mn system along with the experimental data.

Chapter 8 Thermodynamic modeling of the Al-Cr-Cu system and thermodynamic revision of the Al-Cu-Mn system

Senlin Cui

Department of Mining and Materials Engineering, McGill University, 3610 University Street, Montreal, Quebec, H3A 0C5, Canada

Abstract

The phase diagram information available in the literature for the Al-Cu-Cr and Al-Cu-Mn systems is reviewed. Thermodynamic modeling for the Al-Cu-Cr ternary system is conducted on the basis of the critically evaluated phase diagram data. The Gibbs energy of the liquid phase is modeled using the Modified Quasi-chemical Model (MQM) in pair approximation. The solid phases are modeled using the Compound Energy Formalism (CEF). And the liquid phase of the Al-Cu-Mn system is revised using the MQM model. Comprehensive comparison between the model-predicted and the experimentally measured phase diagram indicates that the obtained thermodynamic descriptions for the Al-Cu-Cr and Al-Cu-Mn systems are reliable.

Key words:

The Al-Cu-Cr system; the Al-Cu-Mn system; phase diagram; thermodynamic modeling.

8.1 Introduction

The Al-Cu-Cr and Al-Cu-Mn systems are known to have metastable icosahedral quasicrystal phase formation [1]. Decagonal crystalline phases can also form in Al-Cu-Cr alloys [2, 3]. The Al-Cu-Cr and Al-Cu-Mn systems are two of the basic sub-ternary systems in the Al 6xxx serial alloys. As a part of a thermodynamic database development for Al 6xxx serial alloy, the Al-Cu-Cr and Al-Cu-Mn systems are also optimized. The Al-Cu-Cr system has never been optimized before. While the Al-Cu-Mn system was previously optimized by He [4]. Considering the fact that all the solid thermodynamic parameters of the three sub-binaries: the Al-Cu, Al-Mn, and Cu-Mn systems are the same as the currently developed thermodynamic database, only a revision of the liquid phase is needed. Consequently, the present work focuses on the thermodynamic modeling of the Al-Cu-Cr system and the revision of the thermodynamic description of the Al-Cu-Mn system.

8.2 Critical evaluation of literature information

8.2.1 The Al-Cu-Cr system

The Al-Cu-Cr system is reviewed by Raghavan [5, 6]. The available experimental data are reviewed below.

Initially, Zarechnyuk et al. [7] reported the phase equilibria at the Al rich side of the Al-Cu-Cr system at 400 °C according to powder x-ray diffraction (XRD). The three phase equilibrium between (Al), Al_7Cr, and Al_2Cu was presented. In their experiments, 99.98% Al, 99.99% Cu, and 99.99% Cr were used as starting materials. Meanwhile, Prevarskiy and Skolozdra [8] measured the isothermal sections of the Al-Cr-Cu system at 600 °C and 800 °C via XRD measurements. However, only the isothermal section at 600 °C was reported. Four quaternary compounds are shown at 600 °C: A (Al-15 at.% Cr-13 at.% Cu), B (Al-15 at.% Cr-18 at.% Cu), C (Al-20 at.% Cr-5 to 10 at.% Cu), and D (Al-23 at.% Cr-20 at.% Cu). Only C and D are found at 800 °C. The compound B has a hexagonal structure with a=1.82 nm, c=1.271 nm, and c/a=0.99. The samples

were made from 99.9% Cr, 99.99% Cu, and 99.98% Al by arc melting under purified argon gas. After that the samples were annealed at 600 °C for 400 hours and 800 °C for 200 hours. Recently, Sugiyama et al. [9] measured the structures of the ξ-$Al_{72.6}Cu_{11.0}Cr_{16.4}$ and β-$Al_{67.4}Cu_{14.3}Cr_{18.3}$ phases by means of single crystal XRD analysis. The ξ phase was found to have a relatively wide range of chemical composition of $Al_{80\text{-}65}Cu_{5\text{-}20}Cr_{15}$ (P63/m, a=1.7714 nm, c=1.2891 nm) and the β phase has a NaTl type structure with more Cr rich chemical composition around $Al_{65}Cu_{17.5}Cr_{17.5}$ (F43m, a=1.8161nm). Most recently, Grushko et al. [10, 11] studied the phase diagram of the Al-Cu-Cr system via scanning electron microscope (SEM) analysis, transmission electron microscope (TEM) analysis, XRD, and differential thermal analysis (DTA). The samples were prepared using levitation induction melting of 99.999% Al, 99.95% Cu, and 99.99% Cr under argon atmosphere. The temperature range of the investigation was from 1000 °C to 600 °C. The Al-Cr γ phase extends up to 18 at.% Cu in the ternary. The ξ phase (a=1.77nm, c=1.26nm) has a wide solubility range extending between about $Al_{82}Cu_2Cr_{16}$, $Al_{75}Cu_4Cr_{21}$, and $Al_{71}Cu_{11}Cr_{18}$ which melts below 1000 °C. The κ (a=1.82nm) phase refers to the β phase of Sugiyama et al. [9] extends from $Al_{65}Cu_{15}Cr_{20}$ to $Al_{58}Cu_{26}Cr_{16}$ which melts above 842 °C. Another phase designated as β with a composition around $Al_{46}Cu_{36}Cr_{18}$ forms by a peritectic reaction at about 906 °C and decomposes at about 815 °C. At 700 °C, the phase ϕ around $Al_{70.5}Cu_{18}Cr_{11.5}$ and the ψ phase around $Al_{65}Cu_{25}Cr_{10}$ present. One another phase $Al_{61}Cu_{35.5}Cr_{3.5}$ forms below 638 °C.

The measured experimental data from Prevarskiy and Skolozdra [8] is inconsistent with the high temperature data by Grushko et al. [10, 11]. Thus, only the recent data by Grushko et al. [10, 11] was included in the current optimization.

8.2.2 The Al-Cu-Mn system

The Al-Cu-Mn ternary system was previously evaluated by Lukas [12]. A thermodynamic modeling in the Cu rich side of the Al-Cu-Mn system was done by Miettinen [13] and later another thermodynamic modeling is conducted by He [4] in the whole composition range. As discussed before, the ternary interaction parameters of the liquid phase from He [4] need to be revised. Here only the experimental data related to current revision are reviewed.

Köster and Gödecke [14] studied the phase equilibria in the Al-Cu-Mn system via equilibrium alloys characterized by microscopic analysis, DTA, and XRD in the temperature range from 950 to 500 °C. West and Thomas [15] measured the Cu rich part of Al-Cu-Mn system up to 30 wt.% Mn and 18 wt.% Al within the temperature range of 400-800 °C. Recently, Kainuma et al. [16] measured the phase equilibria in the Cu rich side in the temperature range of 550-800 °C by means of energy dispersion x-ray spectrometry analysis (EDS), DSC, and XRD.

8.3 Thermodynamic modeling

8.3.1 Pure elements and stoichiometric compounds

The Gibbs energies of the pure elements are taken from the SGTE database [17]:

$$G_i(T) - H_i^{SER} = a + bT + cT\ln T + dT^2 + eT^{-1} + fT^3 + gT^7 + hT^{-9} \tag{8.1}$$

where H_i^{SER} is the mole enthalpy of the element *i* at 298.15 K and 1 bar in its standard element reference (SER) state.

The Gibbs free energies of stoichiometric compounds can be expressed as:

$$G_T = H_T - S_T T \tag{8.2}$$

$$H_T = \Delta H^o_{298.15} + \int_{298.15}^{T} C_p dT \tag{8.3}$$

$$S_T = S^o_{298.15} + \int_{298.15}^{T} \frac{C_P}{T} dT \tag{8.4}$$

where H_T and S_T are enthalpy and entropy at temperature *T* in Kelvin, $\Delta H^o_{298.15}$ is the enthalpy of formation at 298.15 K, C_P is the heat capacity, and $S^o_{298.15}$ is the entropy at 298.15 K.

8.3.2 Liquid phase

The Gibbs energy of liquid is modeled using the Modified Quasi-chemical Model (MQM) proposed by Pelton et al. [18, 19]. The model is described as follows:

The following pair exchange reaction exists if we assume the atoms *m* and *n* in the liquid phase occupy a quasi-lattice:

$$(m\text{-}m)+(n\text{-}n)=2(m\text{-}n)\ :\ \Delta g_{mn} \tag{8.5}$$

where (*m*-*m*), (*n*-*n*), and (*m*-*n*) are the first-nearest-neighbor atom pairs. Δg_{mn} is the non-configurational Gibbs energy change for the formation of two moles of (*m*-*n*) pairs. The Gibbs energy of a binary solution is presented as:

$$G = n_m G_m^o + n_n G_n^o - T\Delta S^{config} + \left(n_{mn}/2\right)\Delta g_{mn} \tag{8.6}$$

where n_i and n_{mn} are the number of moles of *i* atoms and (*m*-*n*) pairs, respectively. The configurational entropy of mixing (ΔS^{config}) is given as:

$$\Delta S^{config} = -R\left(n_m \ln x_m + n_n \ln x_n\right) - R\left[n_{mm}\ln\left(\frac{x_{mm}}{Y_m^2}\right) + n_{nn}\ln\left(\frac{x_{nn}}{Y_n^2}\right) + n_{mn}\ln\left(\frac{x_{mn}}{2Y_mY_n}\right)\right] \tag{8.7}$$

where x_i is the mole fraction of *i* atoms, x_{mn} is the pair fraction, and Y_m is the coordination equivalent fraction.

The excess Gibbs energy, Δg_{mn}, is always expanded as a polynomial in terms of pair fractions:

$$\Delta g_{mn} = \Delta g^{0}_{mn} + \sum_{i\geq 1} g^{i0}_{mn}\left(x_{mm}\right)^{i} + \sum_{j\geq 1} g^{0j}_{mn}\left(x_{nn}\right)^{j} \tag{8.8}$$

where Δg^{0}_{mn}, g^{i0}_{mn}, and g^{0j}_{mn} are the model parameters which can be a function of temperature. The coordination number of component *m*, Z_m, is related to the number of atoms and the number of pairs by: $Z_m n_m = 2n_{mm} + \sum_{n\neq m} n_{mn}$. In the present work, all Z are set as 6. With the introduction of composition dependent coordination number, one can independently choose the composition of maximum short range ordering in each binary subsystem,

$$\frac{1}{Z_m} = \frac{1}{2n_{mm} + \sum_{j\neq m} n_{mj}} \left(\frac{2n_{mm}}{Z^{m}_{mm}} + \sum_{j\neq m} \frac{n_{mj}}{Z^{m}_{mj}} \right) \tag{8.9}$$

where Z^{m}_{mi} is the value of Z_m when all the nearest neighbors of atoms *m* are atoms *i*. The ratio of Z^{m}_{mn}/Z^{n}_{nm} determines the maximum short range ordering in each binary subsystem. Symmetric or asymmetric extrapolation technique can be utilized to predict thermodynamic properties in ternary system.

8.3.3 Solid phases

8.3.3.1 fcc_A1, bcc_A2, hcp_A3, cbcc_A12, and cub_A13 phases

Redlich-Kister (R-K) polynomial [20] is applied to describe the molar Gibbs energies of these phases:

$${}^{o}G^{\phi}_{m} = \sum_{i=1}^{3} x_i \, {}^{o}G^{\phi}_{i} + RT\sum_{i=1}^{3} x_i \ln x_i + \sum_{i=1}^{3}\sum_{j>i}^{3} x_i x_j L^{\phi}_{ij} + \sum_{i=1}^{3}\sum_{j>i}^{3}\sum_{k>j}^{3} x_i x_j x_k L^{\phi}_{ijk} + \Delta G^{mag} \tag{8.10}$$

where ${}^{o}G_i^{\phi}$ is the molar Gibbs energy of pure *i* with the ϕ state, *R* is gas constant, *T* is temperature in Kelvin, L_{ij}^{ϕ} is the binary interaction parameter expended as $\sum_{v=0} L_{ij}^{v}(x_i - x_j)^v$, L_{ijk}^{ϕ} is the ternary interaction parameter further given as $x_i L_{ijk}^{i} + x_j L_{ijk}^{j} + x_k L_{ijk}^{k}$, and ΔG^{mag} is the magnetic contribution term. The magnetic contribution term ΔG^{mag} which given by the Hillert-Jarl-Inden model [21] is presented as:

$$\Delta G^{mag} = RT\ln(\beta^{\varphi}+1)g(\tau^{\varphi}) \tag{8.11}$$

where τ is given by T/T^* (T^* is the critical temperature for magnetic transition). β is the average magnetic moment per mole of atom expressed in Bohr magnetons. $g(\tau^{\varphi})$ is a polynomial function derived by Hillert and Jarl [21].

8.3.3.2 Other solid solution phases

The so-called compound energy formulism [22] is utilized for the descriptions of all the other solid phases. All the thermodynamic parameters of the solid phases for the Al-Cu-Mn system are directly taken from the work of He [4]. In the Al-Cu-Cr system, the γ_H_AlCu phase is modeled as $(Al, Cr)_4(Al, Cr, Cu)(Cu)_8$, the γ_L_AlCr phase is modeled as $(Al)_{12}(Cr, Cu)_5(Al, Cr, Cu)_9$. The Al_4Cr phase is modeled as $(Al, Va, Cu)_4(Cr)$. Two ternary compounds with homogeneity range, ζ and κ, are modeled as $(Al, Cu)_{41}(Cr)$ and $(Al, Cu)_4(Cr)$, respectively. As an example, the Gibbs energy of the γ_L_AlCr phase is presented here:

$$\begin{aligned}
{}^{o}G_m^{\gamma_L_AlCr} &= \sum_{i=1}\sum_{j=1} y_{Al}^{'} y_i^{''} y_j^{'''}\, {}^{o}G_{Al:i:j} + 5RT\sum_{i=1} y_i^{''}\ln y_i^{''} + 9RT\sum_{i=1} y_i^{'''}\ln y_i^{'''} \\
&+ \sum_{i=1}\sum_{j>i}\sum_{k=1} y_i^{''} y_j^{''} y_k^{'''} \sum_{v=0} (y_i^{''} - y_j^{''})^v L_{Al:ij:k}^{v} \\
&+ \sum_{i=1}\sum_{j>i}\sum_{k=1} y_i^{'''} y_j^{'''} y_k^{''} \sum_{v=0} (y_i^{'''} - y_j^{'''})^v L_{Al:k:ij}^{v} + \ldots
\end{aligned} \tag{8.12}$$

where $y_i^{'}$, $y_i^{''}$, and $y_i^{'''}$ are the site fraction of *i* on the first, second, and third sub-lattice, respectively. ${}^{o}G_{Al:i:j}$ is the Gibbs energy of formation of the hypothetical compound $Al_{12}i_5j_9$. $L^{v}_{Al:ij:k}$, and $L^{v}_{Al:k:ij}$ are the interaction parameters.

8.4 Results and discussions

The Al-Cu-Cr and Al-Cu-Mn systems are optimized using a trial and error method. All the thermodynamic calculations are conducted by using the FactSage software [23]. The Al-Cu system assessed by Saunders [24], the Cu-Cr system assessed by Cui and Jung [25], the Al-Cr system assessed by Cui et al. [26], the Al-Mn system revised by Cui and Jung [27], and the Cu-Mn system by Cui and Jung [25] are accepted to model the two ternary systems. The finally obtained thermodynamic parameters for the Al-Cu-Cr and Al-Cu-Mn ternary systems are presented in Table 8.1 and Table 8.2, respectively. The optimization results are presented as follows:

8.4.1 The Al-Cu-Cr system

A Toop-type of extrapolation technique is applied for the liquid phase. During the current modeling, the β, ψ, and ϕ phases are assigned with a stoichiometric composition of $Al_{92}Cu_{67}Cr_{41}$, $Al_{65}Cu_{25}Cr_{10}$, and $Al_{141}Cu_{36}Cr_{23}$, respectively. The calculated isothermal sections are presented in Figs. 8.1(a) to (f). Fig. 8.1(a) is the isothermal section at 1000 °C. In order to reproduce the phase relation, ternary solubilities are introduced for the Al_4Cr, γ_L, and bcc_A2 phases. The isothermal section at 900 °C is presented in Fig. 8.1(b). At this temperature, two new ternary phases: the β and ζ phases already become stable. The β phase is treated as a stoichiometric compound for simplification. While the ζ phase is treated as a ternary solution phase. As the temperature decreases to 800 °C, the β phase already decomposed, and another ternary solution phase κ is stable. In the 700 °C section, two other ternary compounds ϕ and ψ also presence. The homogeneity range of ζ decreases substantially as the temperature decreases to 600 °C. At 400 °C, only ϕ and ψ are still stable. The calculated invariant temperature related to liquid for the Al-Cu-Cr system is presented in Table 8.3. The calculated liquidus projection for the Al-Cu-Cr system is

presented in Fig. 8.2. Fig. 8.2(a) is the liquidus projection in the whole composition range. The enlarged parts to show the Al rich side are shown in Figs. 8.2(b) and (c).

8.4.2 The Al-Cu-Mn system

Toop type of asymmetric extrapolation technique is used for the liquid phase of the Al-Cu-Mn system with Al treated as the asymmetric element. Since all the thermodynamic parameters are taken from He [4], here only the isothermal section at 950 °C and the liquidus projection are presented in Fig. 8.3 and Fig. 8.4, respectively. Fig. 8.4(a) is the liquidus projection in the whole composition range. And the enlarged parts to show the Al rich side are shown in Fig. 8.4(b) and Fig. 8.4(c). It can be seen from the diagram that the experimental data at 950 °C was reasonably reproduced. All the ternary invariant equilibrium temperatures related to the liquid phase are presented in Table 8.4 with reasonable agreement with the experimentally measured ones.

8.5 Summary

A comprehensive evaluation of all the phase diagram information for the Al-Cu-Cr system is conducted. The thermodynamic description of the liquid phase for the Al-Cu-Mn system is revised. The modified quasi-chemical model is applied to describe the thermodynamic properties of the liquid phase. The solid phases are described using compound energy formalism. A comparison between the calculated and measured phase diagram information indicates that the currently obtained thermodynamic description of the Al-Cu-Cr and Al-Cu-Mn systems are reliable.

Acknowledgement

The author would like to thank the financial support from NSERC-Automotive Partnership Canada program in Canada and the McGill Engineering Doctorate Award (MEDA) from McGill University for financial support.

References

1. Ebalard, S. and F. Spaepen, *Long-range chemical ordering in aluminum-copper-iron, aluminum-copper-manganese, and aluminum-copper-chromium quasicrystals.* J. Mater. Res., 1990. **5**(1): p. 62-73.
2. Tcherdyntsev, V.V., T.A. Sviridova, A.P. Shevchukov, and S.D. Kaloshkin, *Formation of decagonal quasicrystals in mechanically alloyed Al-Cu-Cr powders.* Z. Kristallogr., 2008. **223**(11-12): p. 751-755.
3. Qi, Y.H., Z.P. Zhang, Z.K. Hei, and C. Dong, *The microstructure analysis of Al-Cu-Cr phases in $Al_{65}Cu_{20}Cr_{15}$ quasicrystalline particles/Al base composites.* J. Alloys Compd., 1999. **285**(1-2): p. 221-228.
4. He, C., *PhD thesis. Central South University, Changsha, China*, 2008.
5. Raghavan, V., *Al-Cr-Cu (aluminum-chromium-copper).* J. Phase Equilib. Diffus., 2008. **29**(2): p. 169-170.
6. Raghavan, V., *Al-Cr-Cu (Aluminum-Chromium-Copper).* J. Phase Equilib. Diffus., 2012. **33**(1): p. 53-54.
7. Zarechnyuk, O.S., A.N. Malinkovich, E.A. Lalayan, and V.Y. Markiv, *X-ray diffraction study of aluminum rich alloys of the aluminum-copper chromium- aluminum-copper-zirconium, and aluminum-chromium zirconium ternary and aluminum-copper-chromium-zirconium quaternary systems.* Izv. Akad. Nauk SSSR, Metal., 1967(6): p. 201-4.
8. Prevarskii, A.P. and R.V. Skolozdra, *Chromium-copper-aluminum system.* Izv. Akad. Nauk SSSR, Metal., 1972(1): p. 193-5.
9. Sugiyama, K., H. Saito, and K. Hiraga, *On the crystal structures of the Al-Cu-Cr alloy system.* J. Alloys Compd., 2002. **342**(1-2): p. 148-152.
10. Grushko, B., E. Kowalska-Strzeciwilk, B. Przepiorzynski, and M. Surowiec, *An investigation of the Al-Cu-Cr phase diagram: Phase equilibria at 800-1000 °C.* J. Alloys Compd., 2006. **417**(1-2): p. 121-126.
11. Grushko, B., B. Przepiorzynski, D. Pavlyuchkov, S. Mi, E. Kowalska-Strzeciwilk, and M. Surowiec, *Complex intermetallics in Al-Cu-Cr system.* J. Alloys Compd., 2007. **442**(1-2): p. 114-116.

12. Raghavan, V., *The Fe-Mg-Si (Iron-Magnesium-Silicon).* Phase Diagrams of Ternary Iron Alloys. Part 6B, Indian Institute of Metals, Calcutta,, 1992: p. 942-947.
13. Miettinen, J., *Thermodynamic description of the Cu-Al-Mn system in the copper rich corner.* CALPHAD Comput. Coupling Phase Diagrams Thermochem., 2003. **27**(1): p. 103-114.
14. Köster, W. and T. Gödecke, *Ternary system copper-manganese-aluminum.* Z. Metallkd., 1966. **57**(12): p. 889-901.
15. West, D.R.F. and D.L. Thomas, *The constitution of copper rich alloys of the copper-manganese-aluminum system.* J. Inst. Met., 1956. **85**(Pt. 3): p. 97-104;Paper No 1727.
16. Kainuma, R., N. Satoh, X.J. Liu, I. Ohnuma, and K. Ishida, *Phase equilibria and Heusler phase stability in the Cu rich portion of the Cu-Al-Mn system.* J. Alloys Compd., 1998. **266**(1-2): p. 191-200.
17. Dinsdale, A.T., *SGTE data for pure elements.* CALPHAD Comput. Coupling Phase Diagrams Thermochem., 1991. **15**(4): p. 317-425.
18. Pelton, A.D. and P. Chartrand, *The modified quasi-chemical model: Part II. Multicomponent solutions.* Metall. Mater. Trans. A, 2001. **32A**(6): p. 1355-1360.
19. Pelton, A.D., S.A. Degterov, G. Eriksson, C. Robelin, and Y. Dessureault, *The modified quasichemical model I - binary solutions.* Metall. Mater. Trans. B, 2000. **31B**(4): p. 651-659.
20. Redlich, O. and A.T. Kister, *Thermodynamics of nonelectrolytic solutions. Algebraic representation of thermodynamic properties and the classification of solutions.* Ind. Eng. Chem., 1948. **40**: p. 84,5-8.
21. Hillert, M. and M. Jarl, *A model for alloying effects in ferromagnetic metals.* CALPHAD Comput. Coupling Phase Diagrams Thermochem., 1978. **2**(3): p. 227-38.
22. Hillert, M., *The compound energy formalism.* J. Alloys Compd., 2001. **320**(2): p. 161-176.
23. Bale, C.W., P. Chartrand, S.A. Degterov, G. Eriksson, K. Hack, R. Ben Mahfoud, J. Melancon, A.D. Pelton, and S. Petersen, *FactSage thermochemical software and databases.* CALPHAD Comput. Coupling Phase Diagrams Thermochem., 2002. **26**(2): p. 189-228.
24. Saunders, N., *the Al-Cu system.* Cost 507 - Thermochemical database for light metal alloys, 1991. **2**: p. 28-33.

25. Cui, S. and I.-H. Jung, *Thermodynamic modeling of Cu-Fe-Cr and Cu-Fe-Mn systems.* to be submited.
26. Cui, S., I.-H. Jung, J. Kim, and J. Xin, *A coupled experimental and thermodynamic study of the Al-Cr-Mg ternary system.* submitted to J. Alloys Compd.
27. Cui, S. and I.-H. Jung, *Thermodynamic modeling of the Al-Cr-Mn ternary system.* submitted to Metall. Mater. Trans. A.
28. Hu, B., W.-W. Zhang, Y. Peng, Y. Du, S. Liu, and Y. Zhang, *Thermodynamic reassessment of the Al-Cr-Si system with the refined description of the Al-Cr system.* Thermochim. Acta, 2013. **561**: p. 77-90.
29. Kim, M.-S. and Y.-B. Kang, *Thermodynamic Modeling of the Fe-Mn-C and the Fe-Mn-Al Systems Using the Modified Quasichemical Model for Liquid Phase.* J. Phase Equilib. Diffus., 2015. **36**(5): p. 453-470.
30. Du, Y., J. Wang, J. Zhao, J.C. Schuster, F. Weitzer, R. Schmid-Fetzer, M. Ohno, H. Xu, Z.-k. Liu, S. Shang, and W. Zhang, *Reassessment of the Al-Mn system and a thermodynamic description of the Al-Mg-Mn system.* Int. J. Mater. Res., 2007. **98**(9): p. 855-871.
31. He, C., Y. Du, H.-L. Chen, S. Liu, H. Xu, Y. Ouyang, and Z.-K. Liu, *Thermodynamic modeling of the Cu-Mn system supported by key experiments.* J. Alloys Compd., 2008. **457**(1-2): p. 233-238.

Table captions

Figure captions

Fig. 8.1 Calculated isothermal sections in the Al-Cu-Cr system along with the experimental data. (a) At 1000 °C, (b) at 900 °C, (c) at 800 °C, (d) at 700 °C, (e) at 600 °C, and (f) at 400 °C.

Fig. 8.2 Calculated liquidus projection of the Al-Cu-Cr system.

Fig. 8.3 Calculated isothermal section in the Al-Cu-Mn system at 950 °C along with the experimental data.

Fig. 8.4 Calculated liquidus projection of the Al-Cu-Mn system.

Table 8.1 Summary of optimized model parameters for the Al-Cu-Cr system (J mol^{-1} or J mol^{-1} K^{-1}).

Phase	Thermodynamic parameters	Ref.
Liquid (Al, Cr, Cu)	$\Delta g_{Al,Cr} = -6250.02 - 4.707T + (-4978.96 - 4.728T)x_{AlAl} + (836.8 + 1.883 \cdot T)x_{AlAl}^2$ $-1602.81x_{CrCr}$	[26]
	$L_{Al,Cu} = -66622 + 8.1T + (46800 - 90.8T + 10T\ln T)(x_{Al} - x_{Cu}) - 2812(x_{Al} - x_{Cu})^2$	[24]
	$\Delta g_{\mathrm{Cu},Cr} = 6184.58 + 2.85T + (7618.56 - 2.39T)x_{CrCr}$ $+ (21756.80 - 12.76 \cdot T)x_{CuCu} - 753.12x_{CuCu}^2$	[25]
	$g^{001}_{Al,Cr,(Cu)} = 418.00$, $g^{001}_{Al,Cu,(Cr)} = 2092.00$	This work
fcc_A1 (Al, Cr, Cu)$_1$(Va)$_1$	${}^0L_{Al,Cr:Va} = -57135.57$	[26]
	$L_{Al,Cu:Va} = -53520 + 2T + (38590 - 2T)(x_{Al} - x_{Cu}) + 1170(x_{Al} - x_{Cu})^2$	[24]
	$L_{Cu,Cr:Va} = 70672.86 - 15.85T$	[25]
bcc_A2 (Al, Cr, Cu)$_1$(Va)$_3$	${}^0L_{Al,Cr:Va} = -56356.8 - 6.32T$ ${}^1L_{Al,Cr:Va} = -7654.74$	[26]
	$L_{Al,Cu:Va} = -73554 + 4.0T + (51500 - 11.84T)(x_{Al} - x_{Cu})$	[24]
	$L_{\mathrm{Cu},Cr:Va} = 70310.40 + 6.04T$	[25]
	$L_{Al,Cr,Cu:Va} = x_{Al}(-142256.00) + x_{Cr}(-142256.00)$	This work
hcp_A3 (Al, Cr, Cu)$_1$(Va)$_1$	${}^0L_{Al,Cr:Va} = -35000.00 + 6.00T$	[26]

Al_4Cr $(Cr)_1(Al, Va, Cu)_4$	${}^oG_{Cr:Al} = -84930.410 + 3.81T + 4{}^oG_{Al}^{fcc} + {}^oG_{Cr}^{bcc}$ ${}^0L_{Cr:Al,Va} = 28226.270$	[26]
	${}^0G_{Cr:Cu} = 34999.16 + 2.93T + 4{}^oG_{Cu}^{fcc} + {}^oG_{Cr}^{bcc}$ ${}^0L_{Cr:Al,Cu} = -129323.26$	This work
γ_L $(Al)_{12}(Cr, Cu)_5(Al, Cr, Cu)_9$	${}^oG_{Al:Cr:Al} = -357006.160 + 20.163T + 21{}^oG_{Al}^{fcc} + 5{}^oG_{Cr}^{bcc}$ ${}^oG_{Al:Cr:Cr} = -320932.548 - 109.516T + 12{}^oG_{Al}^{fcc} + 14{}^oG_{Cr}^{bcc}$	[26]
	${}^oG_{Al:Cr:Cu} = -497896.00 + 12{}^oG_{Al}^{fcc} + 5{}^oG_{Cr}^{bcc} + 9{}^oG_{Cu}^{fcc}$ ${}^oG_{Al:Cu:Al} = 21{}^oG_{Al}^{fcc} + 5{}^oG_{Cu}^{fcc}$ ${}^oG_{Al:Cu:Cu} = -507519.20 + 12{}^oG_{Al}^{fcc} + 14{}^oG_{Cu}^{fcc}$ ${}^oG_{Al:Cu:Cr} = -355640.00 + 12{}^oG_{Al}^{fcc} + 9{}^oG_{Cr}^{bcc} + 5{}^oG_{Cu}^{fcc}$ ${}^0L_{Al*:Al,Cu} = -137925.56$ ${}^0L_{Al:Cu:Al,Cr} = -632060.437 + 29.071T$ ${}^0L_{Al*:Cr,Cu} = -64287.16$	This work
	${}^0L_{Al:Cr:Al,Cr} = -632060.437 + 29.071T$	[28]
γ_H $(Al, Cr)_2(Al, Cr)_3(Cr)_2(Al)_6$	${}^oG_{Al:Al:Cr:Al} = -124435.30 + 11{}^oG_{Al}^{fcc} + 2{}^oG_{Cr}^{bcc}$ ${}^oG_{Cr:Cr:Cr:Al} = 2357.31 - 103.77T + 6{}^oG_{Al}^{fcc} + 7{}^oG_{Cr}^{bcc}$ ${}^oG_{Cr:Al:Cr:Al} = 9{}^0G_{Al}^{fcc} + 4{}^oG_{Cr}^{bcc}$	[28]
	${}^oG_{Al:Cr:Cr:Al} = -243506.24 - 42.08T + 8{}^oG_{Al}^{fcc} + 5{}^oG_{Cr}^{bcc}$	[26]

	${}^{0}L_{Al,Cr:*:Cr:Al} = -183139.262$ ${}^{0}L_{*:Al,Cr:Cr:Al} = -63705.751 - 25.221T$	
$AlCr_2$ $(Al, Cr)_1(Al, Cr)_2$	${}^{o}G_{Al:Al} = 10000 + 3{}^{o}G_{Al}^{fcc}$ ${}^{o}G_{Cr:Cr} = 10000 + 3{}^{o}G_{Cr}^{bcc}$ ${}^{o}G_{Al:Cr} = -36594.81 - 14.91T + {}^{o}G_{Al}^{fcc} + 2{}^{o}G_{Cr}^{bcc}$ ${}^{o}G_{Cr:Al} = 52331.31 + 16.84T + 2{}^{o}G_{Al}^{fcc} + {}^{o}G_{Cr}^{bcc}$ ${}^{0}L_{Al,Cr:*} = -8922.60$ ${}^{0}L_{*:Al,Cr} = -38108.20$	[26]
Al_7Cr $(Al)_7(Cr)_1$	${}^{o}G_{Al:Cr} = -107000 + 14.81 \cdot T + 7{}^{o}G_{Al}^{fcc} + {}^{o}G_{Cr}^{bcc}$	[26]
$Al_{11}Cr_2$ $(Al)_{11}(Cr)_2$	${}^{o}G_{Al:Cr} = -195000 + 16.99 \cdot T + 11{}^{o}G_{Al}^{fcc} + 2{}^{o}G_{Cr}^{bcc}$	[26]
AlCu_δ $(Al)_2(Cu)_3$	${}^{o}G_{Al:Cu} = -106700 + 3T + 2{}^{o}G_{Al}^{fcc} + 3{}^{o}G_{Cu}^{fcc}$	[24]
AlCu_ε $(Al, Cu)_1(Cu)_1$	${}^{o}G_{Al:Cu} = -36976 + 1.2T + {}^{o}G_{Al}^{fcc} + {}^{o}G_{Cu}^{fcc}$ ${}^{o}G_{Cu:Cu} = 2{}^{o}G_{Cu}^{bcc}$ $L_{Al,Cu:Cu}^{0} = 7600 - 24T$ $L_{Al,Cu:Cu}^{1} = -72000$	[24]
AlCu_η $(Al, Cu)_1(Cu)_1$	${}^{o}G_{Al:Cu} = -40560 + 3.14T + {}^{o}G_{Al}^{fcc} + {}^{o}G_{Cu}^{fcc}$	[24]

	${}^{o}G_{Cu:Cu} = 2{}^{o}G_{Cu}^{bcc}$ $L^{0}_{Al,Cu:Cu} = -25740 - 20T$	
AlCu_θ $(Al)_1(Al, Cu)_2$	${}^{o}G_{Al:Al} = 3{}^{o}G_{Al}^{bcc}$ ${}^{o}G_{Al:Cu} = -47406 + 6.75T + {}^{o}G_{Al}^{fcc} + 2{}^{o}G_{Cu}^{fcc}$ $L^{0}_{Al:Al,Cu} = 2211$	[24]
γ_L $(Al)_4(Al, Cu)_1(Cu)_8$	${}^{o}G_{Al:Al:Cu} = -300716 + 390T - 52T\ln T + 5{}^{o}G_{Al}^{fcc} + 8{}^{o}G_{Cu}^{fcc}$	[24]
	${}^{o}G_{Al:Cu:Cu} = -280501 + 379.6T - 52T\ln T + 4{}^{o}G_{Al}^{fcc} + 9{}^{o}G_{Cu}^{fcc}$	[24]
γ_H $(Al, Cr)_4(Al, Cr, Cu)_1(Cu)_8$	${}^{o}G_{Al:Al:Cu} = -219258 - 45.5T + 5{}^{o}G_{Al}^{fcc} + 8{}^{o}G_{Cu}^{fcc}$ ${}^{o}G_{Al:Cu:Cu} = -200460 - 58.5T + 4{}^{o}G_{Al}^{fcc} + 9{}^{o}G_{Cu}^{fcc}$	[24]
	${}^{o}G_{Al:Cr:Cu} = 4{}^{o}G_{Al}^{fcc} + {}^{o}G_{Cr}^{bcc} + 8{}^{o}G_{Cu}^{fcc}$ ${}^{o}G_{Cr:Al:Cu} = {}^{o}G_{Al}^{fcc} + 4{}^{o}G_{Cr}^{bcc} + 8{}^{o}G_{Cu}^{fcc}$ ${}^{o}G_{Cr:Cr:Cu} = 5{}^{o}G_{Cr}^{bcc} + 8{}^{o}G_{Cu}^{fcc}$ ${}^{o}G_{Cr:Cu:Cu} = 418400.00 + 4{}^{o}G_{Cr}^{bcc} + 9{}^{o}G_{Cu}^{fcc}$	This work
Al_9Cu_{11} $(Al)_9(Cu)_{11}$	${}^{o}G_{Al:Cu} = -420000 + 17.8T + 9{}^{o}G_{Al}^{fcc} + 11{}^{o}G_{Cu}^{fcc}$	[24]
β $(Al)_{92}(Cu)_{67}(Cr)_{41}$	${}^{o}G_{Al:Cu:Cr} = -3416247.19\ 6 - 976.0664\,T + 92{}^{o}G_{Al}^{fcc} + 67{}^{o}G_{Cu}^{fcc} + 41{}^{o}G_{Cr}^{bcc}$	This work
ψ $(Al)_{65}(Cu)_{25}(Cr)_{10}$	${}^{o}G_{Al:Cu:Cr} = -1891168 + 65{}^{o}G_{Al}^{fcc} + 25{}^{o}G_{Cu}^{fcc} + 10{}^{o}G_{Cr}^{bcc}$	This work

ϕ $(Al)_{141}(Cu)_{36}(Cr)_{23}$	${}^{o}G_{Al:Cu:Cr} = -3555897.32\ 1 + 25.804T + 141{}^{o}G_{Al}^{fcc} + 36{}^{o}G_{Cu}^{fcc} + 23{}^{o}G_{Cr}^{bcc}$	This work
κ $(Al, Cu)_4(Cr)$	${}^{o}G_{Al:Cr} = -71123.21 + 3.89T + 4{}^{o}G_{Al}^{fcc} + {}^{o}G_{Cr}^{bcc}$ ${}^{o}G_{Cu:Cr} = 41598.29 + 25.10T + 4{}^{o}G_{Cu}^{fcc} + {}^{o}G_{Cr}^{bcc}$ $L_{Al,Cu:Cr}^{0} = -257835.00 - 41.84T$	This work
ζ $(Al, Cu)_{41}(Cr)_9$	${}^{o}G_{Al:Cr} = -751028 + 41{}^{o}G_{Al}^{fcc} + 9{}^{o}G_{Cr}^{bcc}$ ${}^{o}G_{Cu:Cr} = 279909.6 + 41{}^{o}G_{Cu}^{fcc} + 9{}^{o}G_{Cr}^{bcc}$ $L_{Al,Cu:Cr}^{0} = -857720 - 920.48T$	This work

Table 8.2 Summary of optimized model parameters for the Al-Cu-Mn system (J mol^{-1} or J mol^{-1} K^{-1}).

Phase	Thermodynamic parameters	Ref.
Liquid (Al, Cu, Mn)	$\Delta g_{Al,Mn} = -17572.8 + 6.07T + (-4602.40 + 1.17T)x_{AlAl}^2 + (-4184.00 + 1.67T)x_{MnMn}^2$	[29]
	$L_{Al,Cu} = -66622 + 8.1T + (46800 - 90.8T + 10T\ln T)(x_{Al} - x_{Cu}) - 2812(x_{Al} - x_{Cu})^2$	[24]
	$\Delta g_{Cu,Mn} = -1.71T + (-3029.22 - 0.04T)x_{CuCu} + (4435.04 - 0.41T)x_{MnMn}$	[25]
	$g^{001}_{Cu,Mn,(Al)} = 50270.76 - 20.920T$, $g^{001}_{Al,Mn,(Cu)} = 3765.60$, $g^{001}_{Al,Cu,(Mn)} = -4184$	This work
fcc_A1 $(Al, Cu, Mn)_1(Va)_1$	${}^0L_{Al,Mn:Va} = -69938.0 + 27.17958T$, ${}^1L_{Al,Mn:Va} = 8248.9$	[30]
	$L_{Al,Cu:Va} = -53520 + 2T + (38590 - 2T)(x_{Al} - x_{Cu}) + 1170(x_{Al} - x_{Cu})^2$	[24]
	$L_{Cu,Mn:Va} = +18366.034 - 16.2210T - 12667.53(x_{Cu} - x_{Mn})$	[31]
	$L_{Al,Cu,Mn:Va} = 87381.347x_{Cu}$	[4]
bcc_A2 $(Al, Cu, Mn)_1(Va)_3$	${}^0L_{Al,Mn:Va} = -111336.2 + 44.48059T$ ${}^1L_{Al,Mn:Va} = -68691.8 + 44.52653T$	[30]
	$L_{Al,Cu:Va} = -73554 + 4.0T + (51500 - 11.84T)(x_{Al} - x_{Cu})$	[24]
	$L_{Cu,Mn:Va} = 18366.034 - 16.2210T - 12667.53(x_{Cu} - x_{Mn})$	[31]
	$L_{Al,Cu,Mn:Va} = x_{Al}(-493652.52 + 381.14365T) + x_{Cu}(98000 + 35T) + x_{Mn}(33905.10)$	[4]
hcp_A3 $(Al, Cu, Mn)_1(Va)_1$	${}^0L_{Al,Mn:Va} = -95264.1 + 33.09659T$ ${}^1L_{Al,Mn:Va} = -56880.6 + 43.14119T$	[30]

	${}^{2}L_{Al,Mn:Va} = 14430.2$	
	$L_{Al,Cu,Mn:Va} = x_{Al}(-287942.88 + 67.72T) + x_{Cu}(-42429.944) + x_{Mn}(-113691.832 + 67.72T)$	This work
AlCu_δ $(Al)_2(Cu)_3$	${}^{o}G_{Al:Cu} = -106700 + 3T + 2{}^{o}G_{Al}^{fcc} + 3{}^{o}G_{Cu}^{fcc}$	[24]
AlCu_ε $(Al, Cu)_1(Cu)_1$	${}^{o}G_{Al:Cu} = -36976 + 1.2T + {}^{o}G_{Al}^{fcc} + {}^{o}G_{Cu}^{fcc}$ ${}^{o}G_{Cu:Cu} = 2{}^{o}G_{Cu}^{bcc}$ $L_{Al,Cu:Cu}^{0} = 7600 - 24T$ $L_{Al,Cu:Cu}^{1} = -72000$	[24]
AlCu_η $(Al, Cu)_1(Cu)_1$	${}^{o}G_{Al:Cu} = -40560 + 3.14T + {}^{o}G_{Al}^{fcc} + {}^{o}G_{Cu}^{fcc}$ ${}^{o}G_{Cu:Cu} = 2{}^{o}G_{Cu}^{bcc}$ $L_{Al,Cu:Cu}^{0} = -25740 - 20T$	[24]
AlCu_θ $(Al)_1(Al, Cu)_2$	${}^{o}G_{Al:Al}^{0} = 3{}^{o}G_{Al}^{bcc}$ ${}^{o}G_{Al:Cu}^{0} = -47406 + 6.75T + {}^{o}G_{Al}^{fcc} + 2{}^{o}G_{Cu}^{fcc}$ $L_{Al:Al,Cu}^{0} = 2211$	[24]
γ_L_AlCu $(Al)_4(Al, Cu)_1(Cu,Mn)_8$	${}^{o}G_{Al:Al:Cu} = -300716 + 390T - 52T\ln T + 5{}^{o}G_{Al}^{fcc} + 8{}^{o}G_{Cu}^{fcc}$	[24]
	${}^{o}G_{Al:Cu:Cu} = -280501 + 379.6T - 52T\ln T + 4{}^{o}G_{Al}^{fcc} + 9{}^{o}G_{Cu}^{fcc}$	[24]
	${}^{o}G_{Al:Cu:Mn} = -205000 + 118.1417T + 4{}^{o}G_{Al}^{fcc} + {}^{o}G_{Cu}^{fcc} + 8{}^{o}G_{Mn}^{cbcc}$ ${}^{o}G_{Al:Al:Mn} = -148230.872 + 38.1784T + 5{}^{o}G_{Al}^{fcc} + 8{}^{o}G_{Mn}^{cbcc}$	[4]

	$L^{0}_{Al:Cu:Cu,Mn} = -49597.5263$	
γ_H_AlCu $(Al)_4(Al, Cu)_1(Cu, Mn)_8$	${}^{o}G_{Al:Al:Cu} = -219258 - 45.5T + 5{}^{o}G^{fcc}_{Al} + 8{}^{o}G^{fcc}_{Cu}$ ${}^{o}G_{Al:Cu:Cu} = -200460 - 58.5T + 4{}^{o}G^{fcc}_{Al} + 9{}^{o}G^{fcc}_{Cu}$	[24]
	${}^{o}G_{Al:Cu:Mn} = -110000 + 4{}^{o}G^{fcc}_{Al} + {}^{o}G^{fcc}_{Cu} + 8{}^{o}G^{cbcc}_{Mn}$ ${}^{o}G_{Al:Al:Mn} = 5{}^{o}G^{fcc}_{Al} + 8{}^{o}G^{cbcc}_{Mn}$ $L^{0}_{Al:Al,Cu:Mn} = -40000$	[4]
Al_9Cu_{11}	${}^{o}G_{Al:Cu} = -420000 + 17.8T + 9{}^{o}G^{fcc}_{Al} + 11{}^{o}G^{fcc}_{Cu}$	[24]
cub_A13 $(Al, Mn, Cr)_1(Va)_1$	${}^{0}L_{Al,Mn:Va} = -118512.30 + 52.74T$ ${}^{1}L_{Al,Mn:Va} = -3174.9$	[30]
	$L_{Al,Cu,Mn:Va} = x_{Al}(-231422.565) + x_{Mn}(-67890.8332)$	[4]
cbcc_A12 $(Al, Cr, Mn)_1(Va)_1$	${}^{0}L_{Al,Mn:Va} = -63000 + 21T$	[30]
$Al_{11}Mn_4$ $(Al)_{11}(Mn)_4$	${}^{o}G_{Al:Mn} = -350550 + 97.89915T + 11{}^{o}G^{fcc}_{Al} + 4{}^{o}G^{cbcc}_{Mn}$	[30]
$Al_{29}Mn_{10}$ $(Al, Mn)_{29}(Mn)_{10}$	${}^{o}G_{Al:Mn} = -744944.46 + 130.36T + 29{}^{o}G^{fcc}_{Al} + 10{}^{o}G^{cbcc}_{Mn}$ ${}^{o}G_{Mn:Mn} = 195000.01 + 39{}^{o}G^{cbcc}_{Mn}$ ${}^{0}L_{Al,Mn:Mn} = -664034.27$	[30]
$Al_{99}Mn_{23}$ $(Al)_{99}(Mn)_{23}$	${}^{o}G_{Al:Mn} = -2510049 + 837.903T + 99{}^{o}G^{fcc}_{Al} + 23{}^{o}G^{cbcc}_{Mn}$	[29]

Al_6Mn $(Al)_6(Mn)_1$	${}^{o}G_{Al:Mn} = -109091 + 35.22T + 6{}^{o}G_{Al}^{fcc} + {}^{o}G_{Mn}^{cbcc}$	[30]
G_$Al_{12}Mn$ $(Al)_{12}(Mn)_1$	${}^{o}G_{Al:Mn} = -35528.44 + 11.84T + 12{}^{o}G_{Al}^{fcc} + {}^{o}G_{Mn}^{cbcc}$	[30]
γ_L $(Al)_{12}(Mn)_5$(Al, Cu, Mn)$_9$	${}^{o}G_{Al:Mn:Al} = -199849.60 - 60.25T + 21{}^{o}G_{Al}^{fcc} + 5{}^{o}G_{Mn}^{cbcc}$ ${}^{o}G_{Al:Mn:Mn} = -791382.68 + 290.39T + 12{}^{o}G_{Al}^{fcc} + 14{}^{o}G_{Mn}^{cbcc}$ ${}^{0}L_{Al:Mn:Al,Mn} = -522188.30 + 244.35T$ ${}^{1}L_{Al:Mn:Al,Mn} = 38014.60$	[27]
	${}^{o}G_{Al:Mn:Cu} = -486333.607 - 14.6742T + 12{}^{o}G_{Al}^{fcc} + 5{}^{o}G_{Mn}^{cbcc} + 9{}^{o}G_{Cu}^{fcc}$ ${}^{0}L_{Al:Mn:Al,Cu} = -571477.603 + 300.146T$ ${}^{0}L_{Al:Mn:Cu,Mn} = 76914.1887$	[4]
γ_H (Al, $Mn)_2$(Al, $Mn)_3(Mn)_2(Al)_6$	${}^{o}G_{Al:Al:Mn:Al} = 11{}^{o}G_{Al}^{fcc} + 2{}^{o}G_{Mn}^{cbcc}$ ${}^{o}G_{Mn:Al:Mn:Al} = -264550.14 + 42.15T + 9{}^{o}G_{Al}^{fcc} + 4{}^{o}G_{Mn}^{cbcc}$ ${}^{o}G_{Mn:Mn:Mn:Al} = -238387.58 + 12.55T + 6{}^{o}G_{Al}^{fcc} + 7{}^{o}G_{Mn}^{cbcc}$ ${}^{o}G_{Al:Mn:Mn:Al} = 8{}^{o}G_{Al}^{fcc} + 5{}^{o}G_{Mn}^{cbcc}$ ${}^{0}L_{Al:Al,Mn:Mn:Al} = -215919.50 + 158.99T$ ${}^{0}L_{Mn:Al,Mn:Mn:Al} = -215919.50 + 158.99T$	[27]
τ1 $(Al)_{28}(Cu)_4(Mn)_7$	${}^{o}G_{Al:Mn:Cu} = -801485.683 + 60.545T + 28{}^{o}G_{Al}^{fcc} + 4{}^{o}G_{Mn}^{cbcc} + 7{}^{o}G_{Cu}^{fcc}$	[4]

τ2 $(Al)_{11}(Cu)_5(Mn)_3$	${}^{o}G_{Al:Mn:Cu} = -413240.075 + 26.4T + 11{}^{o}G_{Al}^{fcc} + 5{}^{o}G_{Mn}^{cbcc} + 3{}^{o}G_{Cu}^{fcc}$	[4]
τ3 $(Al)_1(Cu)_3(Mn)_2$	${}^{o}G_{Al:Mn:Cu} = -79525.752 + {}^{o}G_{Al}^{fcc} + 3{}^{o}G_{Mn}^{cbcc} + 2{}^{o}G_{Cu}^{fcc}$	[4]

Table 8.3 Summary of invariant reactions involving the liquid phase in the Al-Cu-Cr ternary system.

Reaction type	Reaction			Temperature °C	Ref.
	at.% Al	at.% Cr	at.% Cu		
Peritectic	Liquid + bcc_A2#1 + γ_H = γ_L				
	60.34	34.77	4.83	1288	This work
Quasi-Peritectic	Liquid + fcc_A1 = bcc_A2#1 + bcc_A2#2				
	19.39	3.17	77.44	1002	This work
Quasi-Peritectic	Liquid + bcc_A2#1 = bcc_A2#2 + γ_H				
	27.33	4.15	68.52	993	This work
Peritectic	Liquid + Al_4Cr + γ_L = ξ				
	81.26	8.66	10.08	992	This work
Quasi-Peritectic	Liquid + bcc_A2 = γ_H_AlCu + γ_L				
	37.55	4.47	57.98	967	This work
Peritectic	Liquid + γ_H_AlCu + γ_L = β				
	40.23	2.91	56.86	935	This work
Quasi-Peritectic	Liquid + γ_H_AlCu = bcc_A2 + β				
	42.87	0.027	57.10	927	This work
Quasi-Peritectic	Liquid + β = bcc_A2 + γ_L				
	41.58	2.31	56.11	916	This work
Quasi-Peritectic	Liquid + Al_4Cr = $Al_{11}Cr_2$ + ξ				
	91.86	4.23	3.91	886	This work
Quasi-Peritectic	Liquid + bcc_A2 = AlCu_ε + γ_L				
	48.03	0.99	50.99	844	This work
Peritectic	Liquid + γ_L + AlCu_ε = κ				
	49.63	0.85	49.52	832	This work
Quasi-Peritectic	Liquid + γ_L = ξ + κ				
	59.73	0.75	39.52	823	This work
Peritectic	Liquid + ξ + κ = ψ				

	60.10	0.32	39.56	756	This work
Quasi-Peritectic	Liquid + κ = AlCu_ε + ψ				
	57.51	0.25	42.23	741	This work
Peritectic	Liquid + ξ + ψ = ϕ				
	68.06	0.16	31.78	720	This work
Quasi-Peritectic	Liquid + ξ = ϕ + $Al_{11}Cr_2$				
	74.20	0.10	25.69	691	This work
Quasi-Peritectic	Liquid + $Al_{11}Cr_2$ = Al_7Cr + ϕ				
	76.00	0.03	23.98	635	This work
Quasi-Peritectic	Liquid + AlCu_ε = ϕ + AlCu_η				
	65.43	0.009	34.56	625	This work
Quasi-Peritectic	Liquid + AlCu_η = AlCu_θ + ψ				
	68.146	0.004	31.85	596	This work
Quasi-Peritectic	Liquid + ψ = AlCu_θ + ϕ				
	72.85	0.006	27.14	588	This work
Quasi-Peritectic	Liquid + ϕ = AlCu_θ + Al_7Cr				
	75.99	0.005	24.01	578	This work
Eutectic	Liquid = AlCu_θ + Al_7Cr + fcc_A1				
	82.47	0.002	17.53	548	This work

Table 8.4 Summary of invariant reactions involving the liquid phase in the Al-Cu-Mn ternary system.

Reaction type	Reaction			Temperature °C	Method	Ref.
	at.% Al	at.% Mn	at.% Cu			
Peritectic	Liquid + bcc_A2#1 + γ_H = γ_L					
	74.55	25.00	0.45	1039	Cal.	This work
Quasi-Peritectic	Liquid + γ_H = $Al_{29}Mn_{10}$ + γ_L					
	78.60	21.37	0.03	1003	Cal.	This work
Peritectic	Liquid + γ_L + $Al_{29}Mn_{10}$ = τ1					
	80.83	17.27	1.90	965	Cal.	This work
				956	Cal.	[4]
				970	TA	[14]
Quasi-Peritectic	Liquid + $Al_{29}Mn_{10}$ = Al_4Cr + τ1					
	85.18	13.45	1.37	917	Cal.	This work
				914	Cal.	[4]
				825	TA	[14]
Quasi-Peritectic	Liquid + γ_L = bcc_A2 + τ1					
	54.60	2.84	42.57	833	Cal.	This work
				834	Cal.	[4]
				830	TA	[14]
Quasi-Peritectic	Liquid + bcc_A2 = AlCu_ε + γ_L					
	55.91	0.77	43.32	758	Cal.	This work
				757	Cal.	[4]
Quasi-Peritectic	Liquid + Al_4Cr = $Al_{99}Mn_{23}$ + τ1					
	94.48	1.26	4.27	691	Cal.	This work
				680	Cal.	[4]
				703	TA	[14]
Quasi-Peritectic	Liquid + $Al_{99}Mn_{23}$ = Al_6Mn + τ1					
	94.46	1.00	4.55	674	Cal.	This work

				671	Cal.	[4]
				625	TA	[14]
Quasi-Peritectic	Liquid + AlCu_ε = AlCu_η + τ1					
	65.44	0.04	34.52	625	Cal.	This work
				625	Cal.	[4]
				622	TA	[14]
Quasi-Peritectic	Liquid + Al_6Mn = τ1 + fcc_A1					
	92.75	0.33	6.92	618	Cal.	This work
				615.6	Cal.	[4]
				628	TA	[14]
Quasi-Peritectic	Liquid + AlCu_η = AlCu_θ + τ1					
	68.15	0.024	31.83	596	Cal.	This work
				596	Cal.	[4]
				582	TA	[14]
Eutectic	Liquid = AlCu_θ + fcc_A1 + τ1					
	82.48	0.026	17.49	548	Cal.	This work
				547.5	Cal.	[4]
				547	TA	[14]

Figures

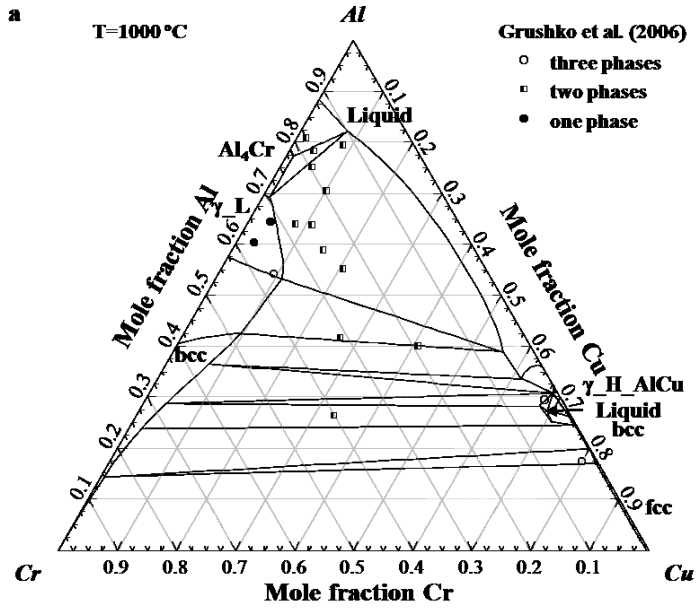
a
T=1000 °C
Al
Grushko et al. (2006)
three phases
two phases
one phase
Liquid
Al4Cr
γ_L
bcc
γ_H_AlCu
Liquid
bcc
fcc
Mole fraction Al
Mole fraction Cu
Cr
Cu
Mole fraction Cr

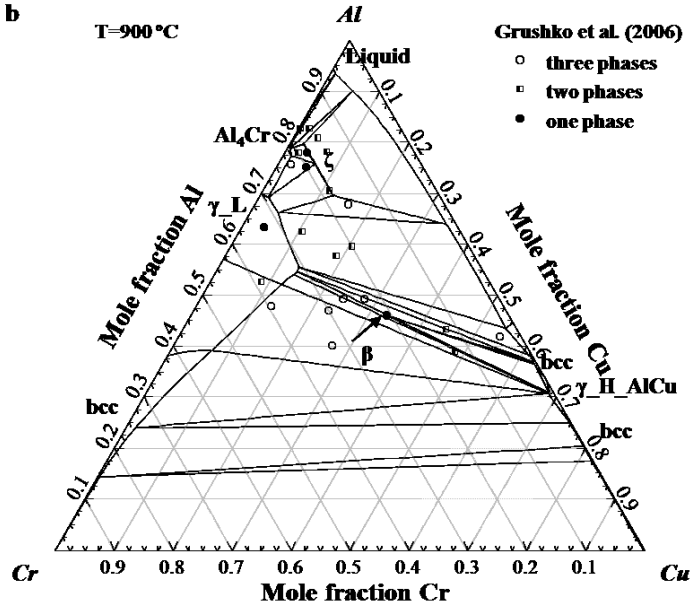
b
T=900 °C
Al
Grushko et al. (2006)
three phases
two phases
one phase
Liquid
Al4Cr
ζ
γ_L
β
bcc
bcc
γ_H_AlCu
bcc
Mole fraction Al
Mole fraction Cu
Cr
Cu
Mole fraction Cr

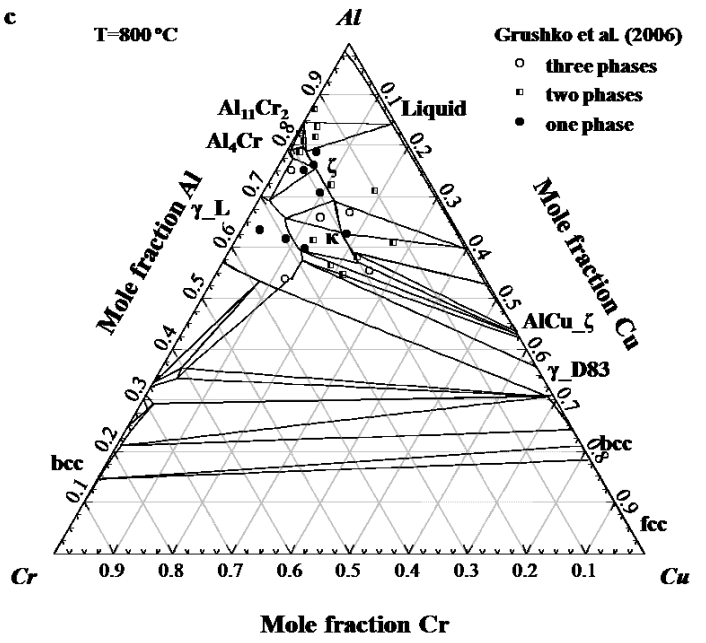
c
T=800 °C
Al
Grushko et al. (2006)
three phases
two phases
one phase
Al11Cr2
Al4Cr
Liquid
ζ
γ_L
κ
AlCu_ζ
γ_D83
bcc
bcc
fcc
Mole fraction Al
Mole fraction Cu
Cr
Cu
Mole fraction Cr

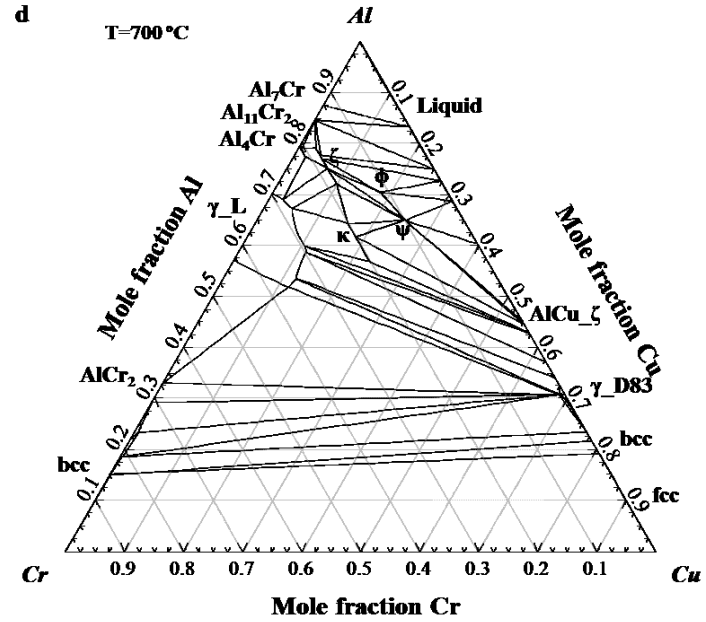
d
T=700 °C
Al
Al7Cr
Al11Cr2
Al4Cr
Liquid
ε
Φ
γ_L
κ
ψ
AlCu_ζ
AlCr2
γ_D83
bcc
bcc
fcc
Mole fraction Al
Mole fraction Cu
Cr
Cu
Mole fraction Cr

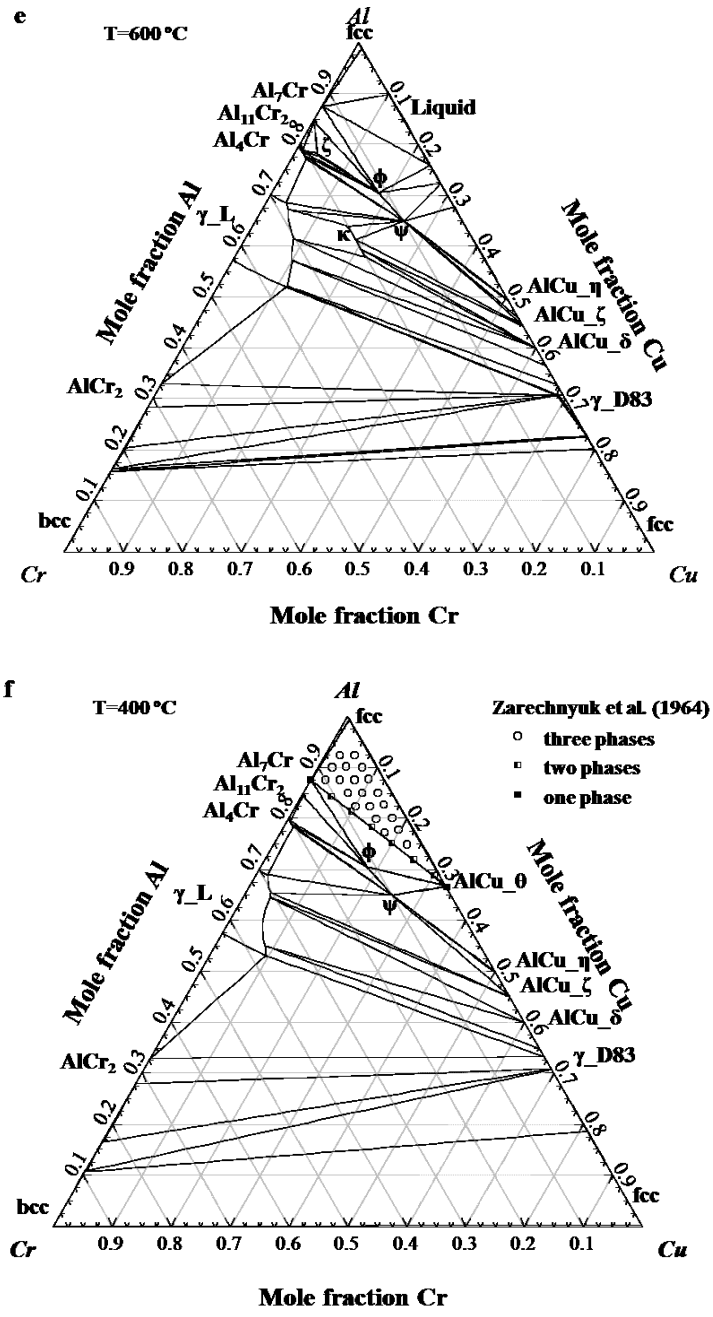

Fig. 8.1 Calculated isothermal sections in the Al-Cu-Cr system along with the experimental data. (a) At 1000 °C, (b) at 900 °C, (c) at 800 °C, (d) at 700 °C, (e) at 600 °C, and (f) at 400 °C.

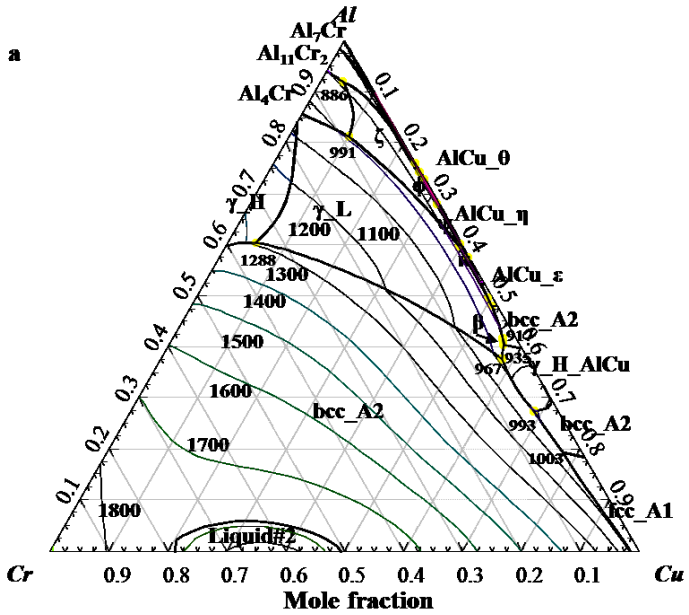
a
Al
Al7Cr
Al11Cr2
Al4Cr
886
991
ζ
AlCu_θ
AlCu_η
γ_H
γ_L
1200
1100
1288
1300
1400
1500
1600
1700
1800
bcc_A2
AlCu_ε
β
910
935
967
γ_H_AlCu
993
1003
bcc_A2
bcc_A1
Liquid#2
Cr
Cu
Mole fraction

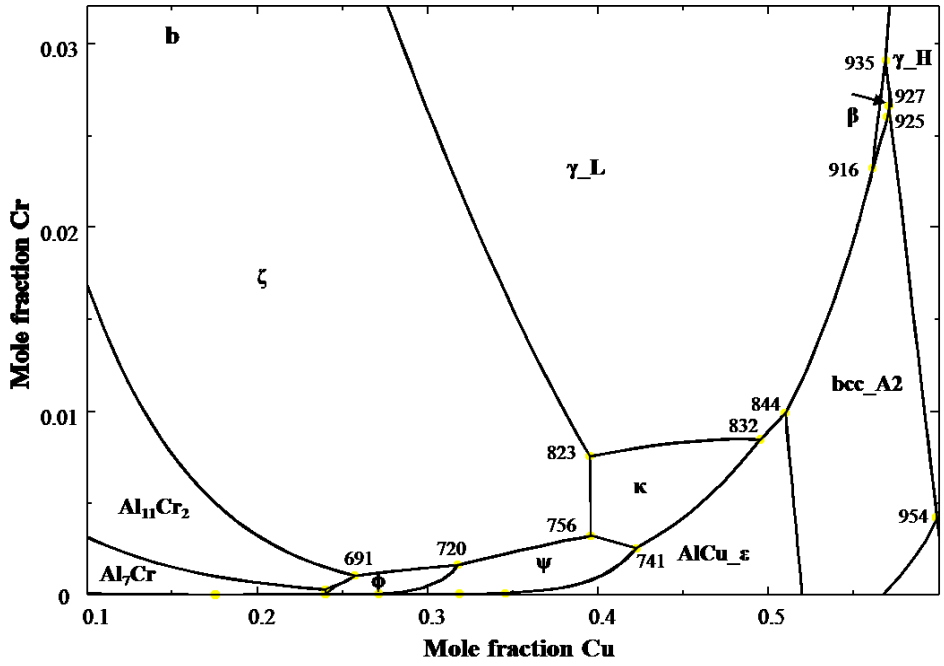
b
Mole fraction Cr
Mole fraction Cu
γ_L
ζ
935
γ_H
927
β
925
916
844
832
bcc_A2
823
κ
Al11Cr2
756
954
691
720
741
AlCu_ε
Al7Cr
Φ
ψ

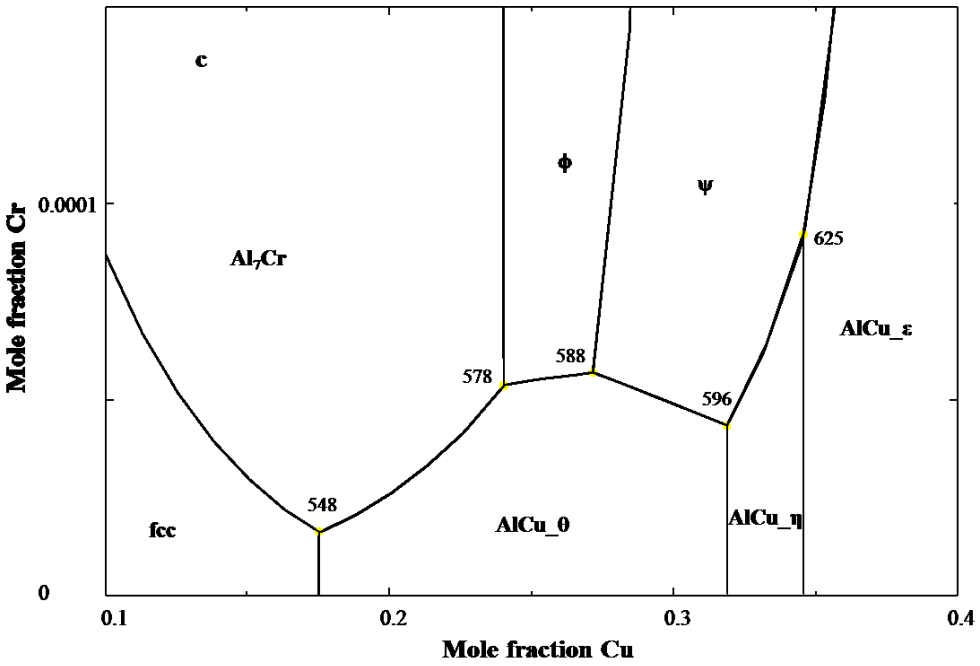

Fig. 8.2 Calculated liquidus projection of the Al-Cu-Cr system.

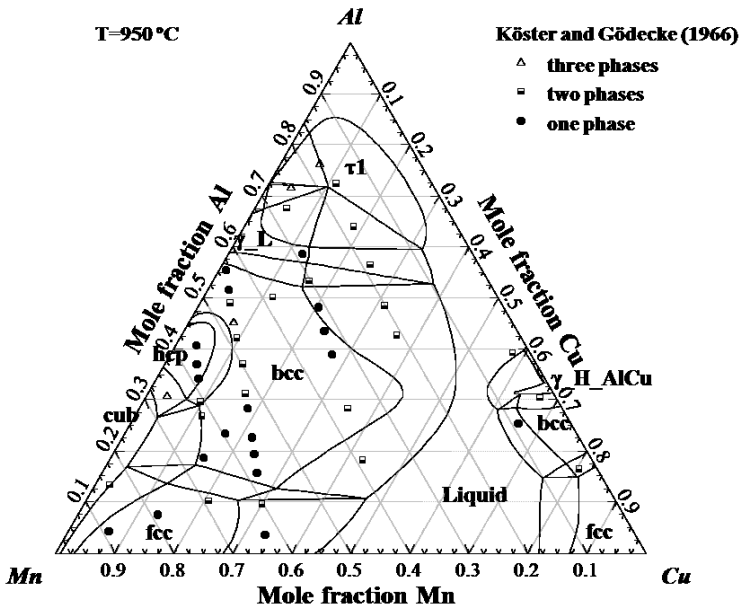

Fig. 8.3 Calculated isothermal section in the Al-Cu-Mn system at 950 °C along with the experimental data.

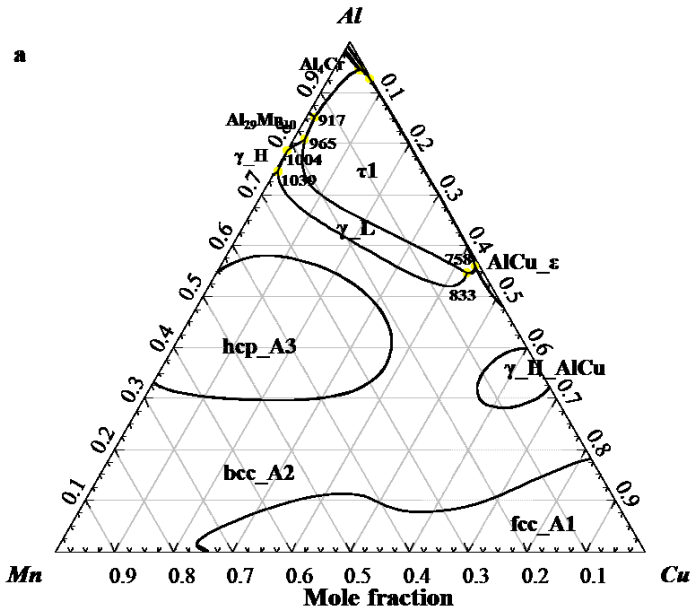
a
Al
Mn
Cu
Mole fraction
Al4Cr
Al29Mn20
γ_H
917
965
1004
1039
τ1
γ_L
758
833
AlCu_ε
γ_H_AlCu
hcp_A3
bcc_A2
fcc_A1

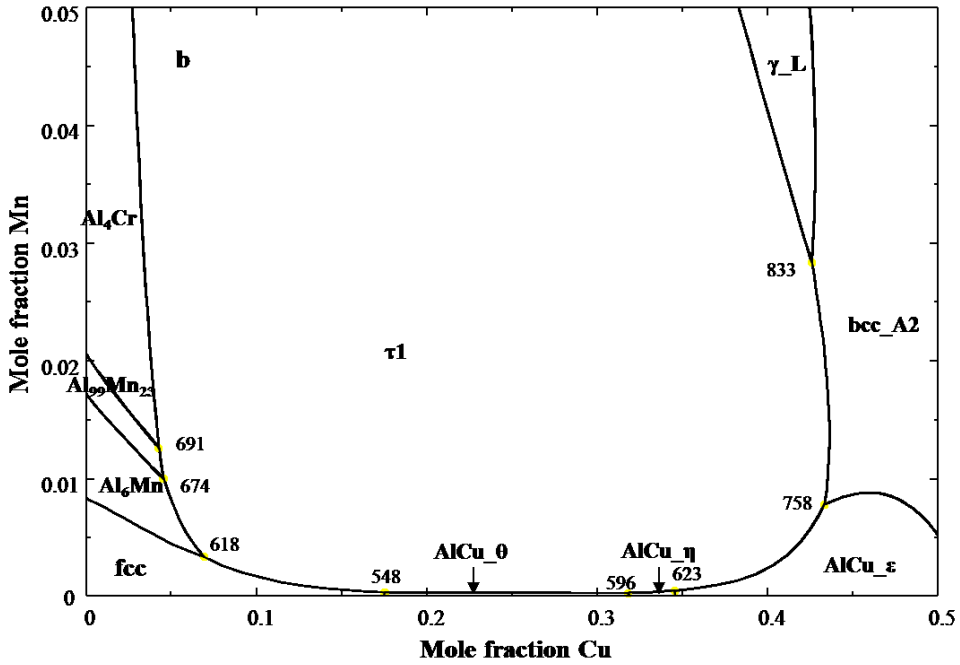
b
Mole fraction Mn
Mole fraction Cu
Al4Cr
Al99Mn25
Al6Mn
691
674
618
548
596
623
758
833
τ1
γ_L
bcc_A2
fcc
AlCu_θ
AlCu_η
AlCu_ε

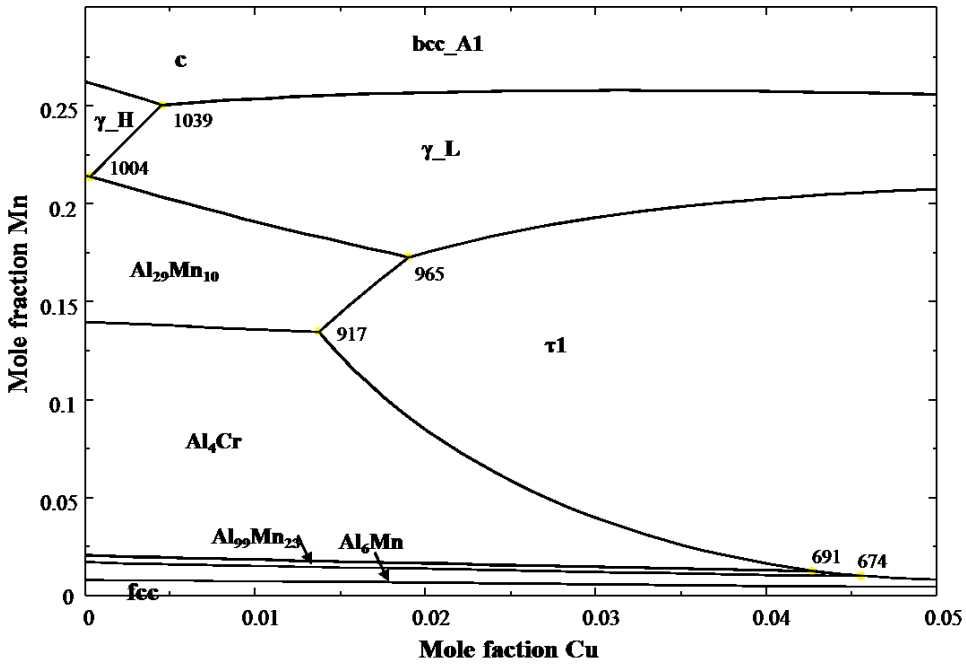

Fig. 8.4 Calculated liquidus projection of the Al-Cu-Mn system.

Chapter 9 Thermodynamic modeling of the quaternary Al-Cu-Mg-Si system

Senlin Cui and In-Ho Jung

Department of Mining and Materials Engineering, McGill University, 3610 University Street, Montreal, Quebec, H3A 0C5, Canada

Abstract

Based on the critically evaluated thermodynamic and phase diagram information available in the literature, thermodynamic modeling of the Cu-Mg, Al-Cu-Mg, Al-Cu-Si, and Cu-Mg-Si systems were conducted using the CALPHAD (CALculation of PHAse Diagrams) technique. The liquid phase was described using the Modified Quasi-chemical Model (MQM), and the solid solution phases were modeled with the Compound Energy Formalism (CEF). Based on the newly obtained and the previously published thermodynamic descriptions of the subsystems, a set of self-consistent thermodynamic description for the Al-Cu-Mg-Si quaternary system was constructed. Comprehensive comparison between the calculated and measured thermodynamic and phase diagram information indicated that most of the reliable experimental data in the quaternary system can be satisfactorily reproduced by the present thermodynamic description. The optimized thermodynamic parameters can be used for the calculation of the phase diagram and thermodynamic properties of any composition and temperature range in the Al rich Al-Cu-Mg-Si quaternary system.

Key words:

Cu-Mg system; Al-Cu-Mg system; Al-Cu-Si system; Cu-Mg-Si system; Al-Cu-Mg-Si system; phase diagram; thermodynamic modeling; CALPHAD.

9.1 Introduction

Aluminum alloys have constantly expanded their usage in construction, automotive, ship building, and aerospace industries. With the increasing demand of improving fuel efficiency and reducing the weight of vehicle, in particular, the resurgence of research on aluminum alloys for automobile application happens. The heat treatable Al-Mg-Si-(Cu) alloys (6xxx series) have attractive properties such as high strength, formability, weldability, corrosion resistance, and low cost. Al-Mg-Si-(Cu) alloys are the most commonly used extruded materials with many applications in automotive components.

The mechanical properties of 6xxx series aluminum alloys are directly related to its microstructure. As both the composition of matrix and the distributions of the precipitations are two key factors which determine the mechanical properties of alloys, the proper selection of composition and processing conditions is important. In order to design the composition of 6xxx series aluminum alloys to cater the need for extruded aluminum front rail, knowledge of the solubility of different alloying elements such as Mg, Si, Mn, Fe, and Cu in Al alloy and different possible precipitate phases such as Mg_2Si, Q ($Al_3Cu_2Mg_9Si_7$), S (Al_2CuMg), etc., at various temperature and composition ranges are indispensable. CALPHAD (CALculation of PHAse Diagram) -type thermodynamic database can provide accurate phase diagram information for multicomponent system which can be used for new alloy design.

The present work aims to conduct a thermodynamic optimization for the Al-Cu-Mg-Si quaternary system. The phase diagram and thermodynamic data in the Cu-Mg, Al-Cu-Mg, Al-Cu-Si, Cu-Mg-Si, and Al-Cu-Mg-Si systems available in the literature were first critically evaluated and thermodynamically optimized. Thereafter, the newly optimized thermodynamic model parameters of the Al-Cu-Mg, Al-Cu-Si, and Cu-Mg-Si systems were combined with the previous thermodynamic parameters of the Al-Mg-Si system to fully describe the Al-Cu-Mg-Si quaternary system. A comprehensive comparison between the calculated and the experimental data was presented to verify the reliability of the current thermodynamic description for the Al rich region of the Al-Cu-Mg-Si system.

9.2 Critical evaluation of literature information

The available literature data for the Cu-Mg, Al-Cu-Mg, Al-Cu-Si, and Al-Cu-Mg-Si systems includes phase diagram information, thermodynamic data, and first principles calculations data. Details of these data are reviewed below. All the phases in the Al rich Al-Cu-Mg-Si system with their short names are listed in Table 9.1.

9.2.1 The Cu-Mg system

The binary Cu-Mg system was previously assessed by Coughanowr et al. [1], Zuo and Chang [2], and Zhou et al. [3]. Coughanowr et al. [1] and Zuo and Chang [2] modeled the liquid phase using the Bragg-Williams random mixing model, while Zhou et al. [3] utilized the association model for the liquid phase with four associates (Cu, Mg, Cu_2Mg, $CuMg_2$).

Major phase diagram data of the Cu-Mg system were reported by Urazova [4], Jones [5], Sahmen [6], Bagnoud and Feschotte [7], Rogelberg [8], Hansen [9], Stepanov and Kornilov [10], and Sederman [11]. These data are generally in good agreement except for the liquidus between Cu_2Mg and $CuMg_2$. While a significant solubility of Mg in fcc Cu (about 7 at.% Mg) is reported, the solubility of Cu in hcp Mg is reported to be less than 0.2 at.%. Laves_C15 (Cu_2Mg) phase has certain homogeneity range, but $CuMg_2$ is reported to be a stoichiometric compound. The detailed literature review for the phase diagram data can be found in the reference by Nayeb-Hashemi and Clark [12].

The enthalpies of formation of C15 (Cu_2Mg) and $CuMg_2$ were measured by King and Kleppa [13] and Feufel and Sommer [14] using solution calorimetry, Smith and Christian [15] using a Knudsen effusion cell for vapor pressure measurements between 117 and 827 ºC, and Eremenko et al. [16] using electromotive force (emf) measurements between 450 and 600 ºC. The direct measurements by Feufel and Sommer [14] and King and Kleppa [13] using solution calorimetry are consistent. Zhou et al. [3] calculated the formation enthalpies of the end member compounds of $CuMg_2$ and C15 (Cu_2Mg) via first principles calculations with a generalized

gradient approximation (GGA). However, the calculated results are quite different from those experimental data measured by solution calorimetry. In the present study, the direct enthalpy data from solution calorimetry by Feufel and Sommer [14] and King and Kleppa [13] were considered as the most reliable data for the enthalpy of formation of each compound.

Heat capacities of the intermetallic compounds were measured by Schimpff [17] for Cu_2Mg and $CuMg_2$ from -150 to 50 ºC and Schübel [18] for Cu_2Mg from -150 to 400 ºC using adiabatic calorimetry, and Feufel and Sommer [14] for $CuMg_2$ and Cu_2Mg from 70 to 490 ºC using differential scanning calorimetry (DSC). Besides, Sommer et al. [19] determined the heat capacity of $Mg_{0.855}Cu_{0.145}$ alloy between 327 and 627 ºC using DSC.

Juneja et al. [20] measured the vapor pressure of Mg in the composition range of 0.9 to 0.17 at.% Mg at the temperature range of 682 to 977 ºC by means of the boiling point method. Hino et al. [21] determined the activity of Mg at 600, 700, and 800 ºC by measuring the vapor pressure. And the activity of Cu was derived from the Gibbs-Duhem relationship. Similarly, Grag et al. [22] measured the vapor pressure of Mg from 11 to 90 at.% Mg between 572 and 1072 ºC, and derived the activities of Mg and Cu at 927 ºC. Arita et al. [23] determined the activity of Mg in the Cu_2Mg and $CuMg_2$ two phase region at 327 ºC by measuring the vapor pressure of metal-hydrogen equilibrium reactions. Eremenko et al. [16] measured the chemical potential of Mg in the Mg_2Cu and Cu_2Mg compounds at 450 to 600 ºC by emf measurements. Smith and Christian [15] also computed the chemical potential of Mg in the Mg_2Cu and Cu_2Mg phases at 127 to 827 ºC from their Knudsen effusion measurements.

Batalin et al. [24] and Sommer et al. [25] used the solution calorimetry technique to determine the integral enthalpy of solution in the liquid phase at 827 ºC and 847 ºC, respectively. However, these two sets of data show certain divergence in the Cu rich region. The experimental data from Sommer et al. [25] were preferred in the present study as their data are more consistent with other experimental information in this binary system and the ternary thermodynamic information in the Al-Cu-Mg system.

9.2.2 The Al-Cu-Mg system

The Al-Cu-Mg system was previously assessed by Chen et al. [26], Buhler et al. [27], and Gable et al. [28]. Chen et al. [26] presented a thermodynamic optimization for the Al-Cu-Mg system. However, the Laves_C14, Laves_C15, and Laves_C16 phases were treated as one phase. Buhler et al. [27] conducted a thermodynamic modeling of the Al-Cu-Mg system in the frame of COST 507 project [29] by fitting the previously evaluated experimental phase diagram and thermodynamic data available in the literature. With the aid of their own experimental data, Gable et al. [28] refined the thermodynamic description of this system to ensure the accurate description of the phase diagram in the Al rich corner of the Al-Cu-Mg-Ag quaternary system.

The phase diagram of the Al rich corner of the Al-Cu-Mg system was firstly investigated by Nishimura [30] using thermal analysis and microscopic examination. Laves and Witte [31] studied the $MgCu_2$-$MgAl_2$ section in the Al-Cu-Mg system by thermal analysis, microanalysis, and XRD analysis. Urazov and Petrov [32, 33] determined the isoplethal sections along 80 wt.% Al, 70 wt.% Al, 60 wt.% Al, 20 wt.% Cu, and from Al to S compound using thermal analysis. Three ternary phases, S (Al_2CuMg), τ (Al_6CuMg_4), and U ($Al_2Cu_4Mg_3$) were identified. The invariant reaction temperatures of Liquid = fcc_Al + AlCu_θ + S at 500 ºC, Liquid = fcc_Al + τ + AlMg_β at 445 ºC, Liquid + S = fcc_Al + τ at 465 ºC, and Liquid + U + S = τ at 520 ºC were determined. Urazov and Mirgalovskaya [34] reported the Laves phase at 400 ºC, but the reported shape of the laves phase in the high Al region is very strange. Garmong and Rhodes [35] measured the ternary invariant reaction of Liquid = Al + AlCu_θ + S to be located at Al-33.1 wt.% Cu-6.25 wt.% Mg and 506 ºC. Brommelle and Phillips [36] investigated the phase diagram of the Al rich Al-Cu-Mg system over the range of 0-40 wt.% Cu and 0-35 wt.% Mg by thermal analysis and microscopic phase identification. Several vertical sections and one isothermal section at 430 ºC were studied. The eutectic reaction of Liquid = fcc_A1 + AlCu_θ + S occurred at the composition of 33.0 wt.% Cu and 6.1 wt.% Mg and 507 ºC, the peritectic point for Liquid + fcc_A1 + S = τ is 26.0 wt.% Mg and 10.0 wt.% Cu at 467 ºC, and the Liquid = fcc_A1 + τ + AlMg_β is 2.7 wt.% Cu and 32.0 wt.% Mg at 451 ºC. The isothermal section at 400 ºC was studied by Mel'nik and Kinzhibalo [37] using x-ray diffraction analysis (XRD) and microscopic analysis. Laves_C14, Laves_C36, and Laves_C15 were identified. Huang and Chen [38] measured the phase equilibria

in the Al rich corner of the Al-Cu-Mg system using DTA, electron probe microanalysis (EPMA), XRD, and optical microanalysis. The invariant temperature between liquid, fcc_A1, AlCu_θ, and S phase was measured to be 503 ºC. The solubilities of Cu and Mg in Al of sections with a Cu/Mg ratio from 2.16 to 0.042 at 300, 400, and 450 ºC were investigated by Zamotorin [39] using quenching experiments. Recently, Gable et al. [28] measured the vertical sections of the Al-Cu-Mg system at 1.0, 2.5, and 4.0 wt.% Cu with up to 1 wt.% Mg using DTA.

The thermodynamic data available for the Al-Cu-Mg system are limited to Predel and Ruge [40], Notin et al. [41], Sommer (1992), Soares et al. [42], and Kim et al. [43]. Predel and Ruge [40] measured the formation enthalpies of the Laves phase in the Al-Cu-Mg system by solution calorimetry. The shape of the measured enthalpy of formation shows an abnormal change at high Al content. Thus, the high Al concentration part of the enthalpy of formation data was excluded during the present assessment. Notin et al. [41] measured the formation enthalpy of S phase (Al_2CuMg) at 298 K by solution calorimetry. In the study of Chen et al. [26], the unpublished enthalpy of mixing data of the liquid phase along $Al_{0.65}Cu_{0.35}$-Mg and $Al_{0.75}Mg_{0.25}$-Cu sections at 700 ºC by Sommer (1992) was presented. Kim et al. [43] measured the enthalpy of mixing of the liquid Al-Cu-Mg ternary alloys along the $Al_{0.25}Mg_{0.75}$-Cu, $Al_{0.75}Mg_{0.25}$-Cu, $Al_{0.5}Mg_{0.5}$-Cu, and $Al_{0.65}Cu_{0.35}$-Mg sections at 713 ºC using a high temperature mixing calorimeter. The activity of Mg in the Al-Cu-Mg liquid alloys was measured by Soares et al. [42] at 1000, 1020, and 1130 ºC using an isopiestic method. These thermodynamic data are all taken into account in the current assessment.

9.2.3 The Al-Cu-Si system

Thermodynamic assessment was previously conducted by Pan et al. [44] in the Al rich corner, Miettinen [45] in the Cu rich corner, and He et al. [46] in the whole composition range. However, the thermodynamic description of the subsystems used by He et al. [46] are different from those in the present work. Thus, a new thermodynamic assessment for the Al-Cu-Si system was carried out. The Al-Cu-Si system was previously reviewed by Lukas [47], Lukas and Lebrun [48], Villars et al. [49], and Raghavan [50-52]. Therefore, only the important literature information

related to the present thermodynamic modeling is briefly reviewed in this section. For the detailed literature review, ref. [47] and ref. [48] can be referred.

Philips [53] determined two vertical sections contain 4 wt.% Cu and 1 wt.% Si using equilibration experiments. Hisatsune [54] and Matsuyama [55] investigated the entire system using thermal analysis and microstructural analysis, and many isothermal sections and isoplethal sections. However, the measured isothermal sections by Hisatsune [54] and Matsuyama [55] are inconsistent. Recently, Riani et al. [56] measured the isothermal section at 500 ºC in the whole composition range by means of XRD, optical microanalysis (OM), and SEM measurements. One ternary compound with the composition of 1.5 at.% Al and 21 at.% Si was identified to have the same crystal structure as the $Cu_{15}Si_4$ phase. As discussed by the authors, however, this phase is stabilized due to the presence of minor amount of impurities, and is not incorporated in the current assessment. The AlCu_γ phase can dissolve about 11.5 at.% Si. The hcp_A3 phase has a stable range in the Cu rich corner. He et al. [46] determined the isothermal sections at 500 ºC and 600 ºC using XRD and SEM analysis. They reported no ternary phase at 500 and 600 ºC. The fcc_A1 phase has a large solubility of about 10 at.% Si and 20 at.% Al. The stability of the hcp_A3 phase in the Cu rich side was also noticed. The AlCu_γ phase has a solubility of 11 at.% Si at 500 ºC and 13 at.% Si at 600 ºC, respectively. In addition, the vertical section at about 15 at.% Si was also measured by DTA. Later, the phase equilibrium in the Al-Cu-Si system at 500 ºC and 700 ºC were investigated by Ponweiser and Richter [57] using OM, powder XRD, DTA, and EPMA measurements. The experimental results confirmed the phase diagram previously reported by Riani et al. [56] and He et al. [46]. The AlCu_γ phase extends to the ternary for about 9.8 at.% Si. The hcp_A3 phase was also found to have a stable range in the Cu rich corner. At 700 ºC, the AlCu_γ phase extends up to 11 at.% Si. The hcp_A3 phase extends from the Al-Si side continuously almost to the Al-Cu side. A new phase τ was found to form between 500 and 700 ºC. Ponweiser and Richter [57] also investigated two isopleths, at 10 and 40 at.% Si, using DTA, but only the phase relation with 40 at.% Si was well determined. The measured phase relations by Riani et al. [56], He et al. [46], and Ponweiser and Richter [57] are generally in agreement except for the phase relation in the Cu rich region. The stability range of the τ phase reported by Ponweiser and Richter [57] is still not yet well known and also this Cu rich phase will not affect the multi-

component system at the Al rich side, this phase is decided to be excluded from the present modeling.

Beloborodova et al. [58] measured the enthalpy of mixing of the liquid phase along the $Al/Cu_{0.35}Si_{0.65}$ and $Al/Cu_{0.5}Si_{0.5}$ sections at 1472 ºC using high temperature isoperibolic calorimetry. Witusiewicz et al. [59] measured the enthalpies of the liquid Al-Cu-Si alloys along the $Al_{0.5}Si_{0.5}$/Cu, $Al_{0.8}Si_{0.2}$/Cu, and $Al_{0.2}Si_{0.8}$/Cu sections at 1302 ± 3 ºC by high temperature calorimetry. Later, Kanibolotsky et al. [60] investigated the thermodynamic properties of the liquid Al-Cu-Si alloys by emf measurements (at 647-977 ºC) and high temperature isoperibolic calorimetry (at 1477 ºC). The partial enthalpy of mixing of Al in the $Si_{0.15}Cu_{0.85}$/Al, $Si_{0.3}Cu_{0.7}$/Al, $Si_{0.5}Cu_{0.5}$/Al, $Si_{0.65}Cu_{0.35}$/Al, and $Si_{0.85}Cu_{0.15}$/Al alloys and activiy of Al in $Si_{0.15}Cu_{0.85}$/Al, $Si_{0.3}Cu_{0.7}$/Al, and $Si_{0.879}Cu_{0.121}$/Al were measured by Kanibolotsky et al. [60]. Besides, they reported the integral enthalpy of mixing for $Si_{0.15}Cu_{0.85}$/Al and $Si_{0.3}Cu_{0.7}$/Al alloys at 900 ºC. As these data are inconsistent [46, 61], the enthalpy of mixing data from Witusiewicz et al. [59] were considered most highly in the present study among all the enthalpy data.

9.2.4 The Cu-Mg-Si system

The Cu-Mg-Si system was previously assessed by the European COST 507 project [29] and Miettinen and Vassilev [62] in the Cu rich region. A review of this ternary system was conducted by Bochvar et al. [63]. According to Bochvar et al. [63], there are three ternary compounds E (Cu_3Mg_2Si), D ($Cu_{16}Mg_6Si_7$), and $(Cu_{0.8}Si_{0.2})_2(Mg_{0.88}Cu_{0.12})$. Only E and D phases are considered in the present assessment, because the stable temperature range of $(Cu_{0.8}Si_{0.2})_2(Mg_{0.88}Cu_{0.12})$ is not yet known.

Ganesan et al. [64, 65] measured the thermodynamic properties of the Cu-Mg-Si alloys with a constant copper and silicon ratio of 7/3 by a combination of different methods. The enthalpy of mixing was measured using an isoperibolic calorimeter. The activity of Mg at 900 °C was measured by isopiestic vapor pressure measurement with a wide composition range of Mg.

Witte [66] reported the phase diagram of the $MgCu_2$-$MgSi_2$ section using thermal analysis measurements. Aschan [67] investigated the phase equilibriums in the Cu-Mg-Si system by microscopic analysis, powder XRD analysis, and thermal analysis. The results of their thermal analysis are presented in the form of tables. According to the table, Fe impurity is presented in the thermal analysis samples. Recently, Ganesan et al. [64] measured the phase equilibrium along Cu/Si = 7/3 by means of thermal analysis. As the results of Aschan [67] contain non-negligible amount of Fe impurities, their results were considered as less reliable, and taken only for the purpose of checking the liquidus surface. The results from Witte [66] and Ganesan et al. [64] are more reliable.

9.2.5 The Al-Cu-Mg-Si system

The previous thermodynamic assessments of the Al-Cu-Mg-Si system include Lacaze et al. [68], Yan et al. [69], Pan et al. [61], and Chang et al. [70].

Petrov and Nagorskaya [71] investigated the Al rich corner of the Al-Cu-Mg-Si quaternary diagram down to 50 wt.% Al by means of cooling curves taken with a Kurnakov pyrometer and microscopic examinations. Several isoplethal sections were presented. Three quaternary eutectic reaction temperatures and compositions were determined: Liquid = fcc_A1 + AlCu_θ + Si + Mg_2Si (505 °C), Liquid = fcc_A1 + AlCu_θ + S + Mg_2Si (500 °C), and Liquid = fcc_A1 + τ + AlMg_β + Mg_2Si (444 °C). And three quaternary peritectic reaction temperatures and compositions were measured: Liquid + Mg_2Si = fcc_A1 + Si + Q (521 °C), Liquid + Mg_2Si = fcc_A1 + AlCu_θ + Q (510 °C), and Liquid + S = fcc_A1 + Mg_2Si + τ (464 °C). Schrader [72] and Mondolfo [73] reexamined the quaternary eutectic and peritectic reactions. The measured invariant temperatures are generally in good agreement with those by Petrov and Nagorskaya [71] except for the reaction temperature for Liquid + Mg_2Si = fcc_A1 + Si + Q is 541°C according to Schrader [72]. Mondolfo [73] further determined the reaction should be Liquid + Mg_2Si + Si = fcc_A1 + Q. Lacaze et al. [68] investigated the invariant reaction temperatures of Liquid = fcc_A1 + AlCu_θ + Q + Si (506.5 °C), Liquid = fcc_A1 + Mg_2Si + AlCu_θ + Q (510 °C), and Liquid = fcc_A1 + Mg_2Si + AlCu_θ + S (500 °C) by thermal analysis. The sequences of deposition for some of these alloys were determined by unidirectional solidification followed by quenching, and the compositions of

these quaternary invariant points were measured by microanalysis. Beside, Chakrabarti and Murray [74] measured the invariant temperatures by means of DSC.

Axon [75-77] measured the phase equilibrium of Al-Cu-Mg-Si alloys containing 0-7 wt.% Mg, 0-7 wt.% Cu and constant 0.6 wt.%, 1.2 wt.%, and 2 wt.% Si by microscopic examination. Smith [78] measured the phase diagram of Al-Cu-Mg-Si alloys containing 0-2 wt.% Si, 0-4 wt.% Mg, with constant 3 wt.% and 4.5 wt.% Cu by microscopic examination at 500 °C. A quaternary phase Q was reported. Pepelyan [79] measured the isothermal section at 300 °C in the Mg rich side of the Al-Cu-Mg-Si system at 0.2-1.5 wt.% Si, 0.3-6 wt.% Cu, and constant 4.5 wt.% Al by means of metallographic analysis, SEM, and XRD. Crowther [80] reported the isoplethal section from 4 wt.% Cu, 4 wt.% Mg to 4 wt.% Cu, 4 wt.% Si. All these data are considered in the present assessment.

Recently, Chang et al. [70] presented a detail discussion of the structure and formula of the Q phase. Since the phase was found by Dix et al. [81], this phase used to be named as AlCuMgSi [81] , W [71], h_AlCuMgSi [82], and Q [74, 83]. In the recent work, Q is extensively accepted as the name of this compound. This compound is assigned as $Al_5Cu_2Mg_8Si_6$ [68, 77, 84], $Al_xCu_2Mg_{12-x}Si_7$ [82], $Al_xCu_4Mg_5Si_4$ [85], and $Al_{17}Cu_9Mg_{45}Si_{29}$ [86] with a hexagonal structure [84] or space group P-6 [82]. The work by Wolverton [87] and Chang et al. [70] using first principles calculation indicate that the most stable form of the Q phase is $Al_3Cu_2Mg_9Si_7$. Thus, the Q phase was modeled as $Al_3Cu_2Mg_9Si_7$ in the present work. It should be noted that the currently accepted composition of the Q phase is very close to the reported one by Löffier et al. [86] ($Al_{17}Cu_9Mg_{45}Si_{29}$) using EDS standardless analysis. The difference is within the realm of experimental error. Löffier et al. [86] measured the heat capacity of the Q phase from 423 to 673 K using a differential calorimeter. However, according to the authors [86], the measured heat capacity is unreliable due to the high brittle feature of Q which results in inefficient contact between sample and crucible and further heat loss. Thus, the only reliable thermodynamic data available in the literature is the enthalpy of formation of the Q phase via first principles calculation by various authors as reviewed by Chang et al. [70].

9.3 Thermodynamic modeling

9.3.1 Pure elements and compounds

The Gibbs free energies of pure elements and stoichiometric compounds at a given temperature can be expressed as:

$$G_T = H_T - S_T T \tag{9.1}$$

$$H_T = \Delta H^o_{298.15} + \int_{298.15}^{T} C_P dT \tag{9.2}$$

$$S_T = S^o_{298.15} + \int_{298.15}^{T} \frac{C_P}{T} dT \tag{9.3}$$

where H_T and S_T are enthalpy and entropy at temperature T, respectively. $\Delta H^o_{298.15}$ is the enthalpy of formation at 298.15 K, and C_p is the heat capacity. $S^o_{298.15}$ is the entropy at 298.15 K. The Gibbs energy data for the pure elements are taken from the SGTE pure element database compiled by Dinsdale [88]. For stoichiometric compound, the Gibbs energy can be derived from the experimentally measured heat capacity data, enthalpy of formation at 298.15 K, and entropy of formation at 298.15 K. In case there is no reliable heat capacity data available in the literature, the Neumann-Kopp relation will be utilized.

9.3.2 Liquid

The liquid phase was modeled using the modified quasi-chemical model (MQM) suggested by Pelton et al. [89, 90]. The detailed model is described as below:

Assume the following pair exchange reaction exists in a quaternary liquid phase:

$$(m\text{-}m) + (n\text{-}n) = 2(m\text{-}n) : \quad \Delta g_{mn} \tag{9.4}$$

where (*m*-*m*), (*n*-*n*), and (*m*-*n*) represents the first-nearest-neighbor atom pairs. The non-configurational Gibbs energy change for the formation of two moles of (*m*-*n*) pairs is Δg_{mn}. Then the Gibbs energy of the solution is given by:

$$G = \sum_{m=1}^{4} n_m G_m^o - T\Delta S^{config} + \sum_{n>m}^{4}\sum_{m=1}^{4} n_{mn}(\Delta g_{mn}/2) \tag{9.5}$$

where n_m is the number of moles of *m* atoms, and n_{mn} is the number of moles of the (*m*-*n*) pairs. ΔS^{config} is the configurational entropy of mixing given by a random distribution of the (*m*-*m*), (*n*-*n*), and (*m*-*n*) pairs in the one-dimensional Ising approximation:

$$\Delta S^{config} = -R\sum_{m=1}^{4} n_m \ln x_m - R\left[\sum_{m=1}^{4} n_{mm} \ln\left(\frac{x_{mm}}{Y_m^2}\right) + \sum_{n>m}^{4}\sum_{m=1}^{4} n_{mn} \ln\left(\frac{x_{mn}}{2Y_m Y_n}\right)\right] \tag{9.6}$$

where n_{nm} is the number of moles of each type of pairs, x_{mn} is the pair fraction, and Y_m is the coordination equivalent fraction defined as:

$$x_{mn} = n_{mn} \Big/ \left(\sum_{i=1}^{4} n_{ii} + \sum_{\substack{i=1 \\ j>i}}^{4} n_{ij}\right) \tag{9.7}$$

$$x_m = n_m \Big/ \sum_{i=1}^{4} n_i \tag{9.8}$$

$$Y_m = x_{mm} + \frac{1}{2}\sum_{n\neq m} x_{mn} \tag{9.9}$$

Δg_{mn} is the excess Gibbs energy of the liquid *m*-*n* alloys, which can be expanded as a polynomial in terms of pair fractions described as:

$$\Delta g_{mn} = \Delta g_{mn}^0 + \sum_{i\geq 1} g_{mn}^{i0}(x_{mm})^i + \sum_{j\geq 1} g_{mn}^{0j}(x_{nn})^j \tag{9.10}$$

where Δg^{0}_{mn}, g^{i0}_{mn}, and g^{0j}_{mn} are the adjustable parameters which can be functions of temperature. Let Z_m be the coordination number of component *m*, the following relation holds: $Z_m n_m = 2n_{mm} + \sum_{n \neq m} n_{mn}$. In order to provide flexibility and permits the independent chosen of the composition of maximum short range order in each binary subsystem, composition dependent coordination numbers of element *m* were introduced:

$$\frac{1}{Z_m} = \frac{1}{2n_{mm} + \sum_{j \neq m} n_{mj}} \left(\frac{2n_{mm}}{Z^m_{mm}} + \sum_{j \neq m} \frac{n_{mj}}{Z^m_{mj}} \right) \tag{9.11}$$

where Z^m_{mi} is the value of Z_m when all the nearest neighbors of atoms *m* are atoms *i*. The maximum short range ordering in each binary subsystem is determined by the ratio of Z^m_{mn} / Z^n_{nm}. The user can freely choose symmetric or asymmetric extrapolation technique in the ternary system. For details, readers can refer to [89, 90].

9.3.3 fcc_A1, bcc_A2, hcp_A3, and diamond_A4 phases

The molar Gibbs energies of the bcc_A2, fcc_A1, hcp_A3, and diamond_A4 phases are described using the Bragg-Williams random mixing model in the form of Redlich-Kister (R-K) polynomial:

$${}^{o}G^{\phi}_{m} = \sum_{i=1}^{4} x_i \, {}^{o}G^{\phi}_{i} + RT \sum_{i=1}^{4} x_i \ln x_i + \sum_{i=1}^{4} \sum_{j>i}^{4} x_i x_j L^{\phi}_{ij} + \sum_{i=1}^{4} \sum_{j>i}^{4} \sum_{k>j}^{4} x_i x_j x_k L^{\phi}_{ijk} \tag{9.12}$$

where x_i is the mole fraction of element *i*, ${}^{o}G^{\phi}_{i}$ is the molar Gibbs energy of pure element *i* with the ϕ state, *R* is gas constant, *T* is temperature in Kelvin, L^{ϕ}_{ij} is the binary interaction parameter,

and L_{ijk}^{ϕ} is the ternary interaction parameter. Further, L_{ij}^{ϕ} is expanded into the form of $\sum_{v=0} L_{ij}^{v}(x_i - x_j)^v$ and L_{ijk}^{ϕ} is written as $x_i L_{ijk}^{i} + x_j L_{ijk}^{j} + x_k L_{ijk}^{k}$.

9.3.4 Laves_C14, Laves_C15, and Laves_C36 phases

The Laves phases were modeled using a two sub-lattice model: (Al, Cu, Mg, Si)$_2$(Al, Cu, Mg). The Gibbs energies of the Laves phases are described using the compound energy formulism [91]:

$$
\begin{aligned}
{}^{o}G_m^{\phi} = {} & \sum_{i=1}\sum_{j=1} y_i^{'} y_j^{''}\, {}^{o}G_{i:j}^{\phi} + 2RT\sum_{i=1} y_i^{'} \ln y_i^{'} + RT\sum_{j=1} y_j^{''} \ln y_j^{''} + \sum_{i<j}\sum_{k=1} y_i^{'} y_j^{'} y_k^{''} \sum_{v=0} (y_i^{'} - y_j^{'})^v L_{ij:k}^{v} \\
& + \sum_{k=1}\sum_{i<j} y_k^{'} y_i^{''} y_j^{''} \sum_{v=0} (y_i^{''} - y_j^{''})^v L_{k:ij}^{v} + \sum_{i<j}\sum_{m<n} y_i^{'} y_j^{'} y_m^{''} y_n^{''} L_{ij:mn}
\end{aligned}
\tag{9.13}
$$

where $y_i^{'}$ and $y_j^{''}$ are the site fraction of *i* and *j* elements in the first and second sub-lattice, respectively. ${}^{o}G_{ij}^{\phi}$ is the molar Gibbs energy of end member compound i_2j. $L_{ij:k}^{v}$ is the interaction parameter for elements *i* and *j* in the first sub-lattice when the second sub-lattice is fully occupied by element *k*, and $L_{k:ij}^{v}$ is the interaction parameter of element *i* and *j* in the second sub-lattice when the first sub-lattice is fully occupied by element *k*. $L_{ij:mn}$ is the reciprocal parameter and can be expanded as $L_{ij:mn}^{0} + (y_i^{'} - y_j^{'})L_{ij:mn}^{1} + (y_m^{''} - y_n^{''})L_{ij:mn}^{2}$.

9.3.5 τ phase

The prototype of τ is $Mg_{32}(Al, Zn)_{49}$. The Zn atoms are substituted by Cu atoms in the Al-Cu-Mg ternary system. Considering the stability of τ in the Al-Cu-Mg-Zn quaternary system, Buhler et al. [27] proposed a simplified sub-lattice model for τ based on the crystallographic structure. The model is given by $(Mg)_{26}(Mg, Al)_6(Al, Cu, Mg)_{48}Al$. The present work accepts this

well-defined model for τ on the purpose of building a huge thermodynamic databank. The molar Gibbs energy of τ is then presented as:

$$
\begin{aligned}
{}^{o}G_{m}^{\tau} &= \sum_{i=1}\sum_{j=1} y_i^{''} y_j^{'''} {}^{o}G_{Mg:i:j:Al}^{\phi} + 6RT\sum_{i=1} y_i^{''} \ln y_i^{''} + 48RT\sum_{j=1} y_j^{'''} \ln y_j^{'''} \\
&+ \sum_{i<j}\sum_{k=1} y_i^{''} y_j^{''} y_k^{'''} \sum_{v=0} (y_i^{''} - y_j^{''})^{v} L_{Mg:ij:k:Al}^{v} + \sum_{k=1}\sum_{i<j} y_k^{''} y_i^{'''} y_j^{'''} \sum_{v=0} (y_i^{'''} - y_j^{'''})^{v} L_{Mg:k:ij:Al}^{v} \\
&+ \sum_{i<j}\sum_{m<n} y_i^{''} y_j^{''} y_m^{'''} y_n^{'''} L_{Mg:ij:mn:Al}
\end{aligned}
\tag{9.14}
$$

where $y_i^{''}$ and $y_j^{'''}$ are the site fraction of i and j elements in the second and third sub-lattice respectively. ${}^{o}G_{Mg:i:j:Al}^{\phi}$ is the Gibbs energy of hypothetical compound $Mgi_6j_{48}Al$, $L_{Mg:ij:k:Al}^{v}$ and $L_{Mg:k:ij:Al}^{v}$ are the interaction parameter for the elements in the second and third sub-lattice, respectively. $L_{Mg:ij:mn:Al}$ is the reciprocal parameter.

9.3.6 γ_L phase

γ_L is the low temperature form of the Al_4Cu_9 phase. As γ_L shows considerable Si solubility in the ternary Al-Cu-Si system, Si is introduced in the first sub-lattice and the model becomes: $(Al, Si)_4(Al, Cu)(Cu)_8$. The molar Gibbs energy can be expressed as:

$$
\begin{aligned}
{}^{o}G_{m}^{\gamma\_L} &= \sum_{i=1}\sum_{j=1} y_i^{'} y_j^{''} {}^{o}G_{i:j:Cu}^{\phi} + 4RT\sum_{i=1} y_i^{'} \ln y_i^{'} + RT\sum_{j=1} y_j^{''} \ln y_j^{''} \\
&+ \sum_{i<j}\sum_{k=1} y_i^{'} y_j^{'} y_k^{''} \sum_{v=0} (y_i^{'} - y_j^{'})^{v} L_{ij:k:Cu}^{v} + \sum_{k=1}\sum_{i<j} y_k^{'} y_i^{''} y_j^{''} \sum_{v=0} (y_i^{''} - y_j^{''})^{v} L_{k:ij:Cu}^{v} \\
&+ \sum_{i<j}\sum_{m<n} y_i^{'} y_j^{'} y_m^{''} y_n^{''} L_{ij:mn:Cu}
\end{aligned}
\tag{9.15}
$$

where $y_i^{'}$ and $y_j^{''}$ are the site fraction of *i* and *j* elements in the first and second sub-lattice respectively. ${}^{o}G_{i:j:Cu}^{\phi}$ is the molar Gibbs energy of the hypothetical compound i_4jCu_8. $L_{ij:k:Cu}^{v}$, $L_{k:ij:Cu}^{v}$, and $L_{ij:mn:Cu}$ are the interaction parameters and reciprocal parameter.

9.3.7 S phase

The addition of Si in Al-Cu-Mg alloys can enhance the amount of S (Al_2CuMg) formed [92] and there is solubility of Si in the S phase [93]. As a result, the S phase was modeled with $(Al, Si)_2(Cu)(Mg)$. The Gibbs energy of this phase is thus expressed as:

$$
\begin{aligned}
{}^{o}G_m^S &= y_{Al}^{'}\,{}^{o}G_{Al:Cu:Mg}^S + y_{Si}^{'}\,{}^{o}G_{Si:Cu:Mg}^S + 2RT\sum_{i=1} y_i^{'}\ln y_i^{'} \\
&+ y_{Al}^{'}y_{Si}^{'}\sum_{v=0} L_{AlSi:Cu:Mg}^{v}(y_{Al}-y_{Si})^{v}
\end{aligned}
\tag{9.16}
$$

where $y_i^{'}$, ${}^{o}G_{i:j:k}^{\phi}$, and L^{v} are the site fraction of *i* element, the molar Gibbs energy of the hypothetical compound i_2jk, and the interaction parameter, respectively.

9.3.8 Other phases

Other binary solid phases which do not show ternary solubility are directly taken from binary systems.

9.4 Results and discussions

The optimization of the thermodynamic parameters was conducted with the aid of the FactSage software. The thermodynamic descriptions for the Al-Cu, Al-Mg, Al-Si, Cu-Si, Mg-Si, and Al-Mg-Si systems are taken from the work of Saunders [94], Chartrand [95], Harvey [96],

Kang and Jung [97], and Harvey [96], respectively. The calculated phase diagrams of the Al-Cu system, the Al-Mg system, the Al-Si system, the Cu-Si system, and the Mg-Si system are shown in Fig. 9.1. The Cu-Mg, Al-Cu-Mg, Al-Cu-Si, and Cu-Mg-Si systems are assessed in the present work based on the critically evaluated phase diagram and thermodynamic data in section 9.2. The optimized thermodynamic model parameters for all the phases in the Al-Cu-Mg-Si system are presented in Table 9.2. In the subsequent section, the optimization result will be discussed system by system.

9.4.1 The Cu-Mg system

The calculated Cu-Mg phase diagram together with the experimental data from Urazova [4], Sahmen [6], Jones [5], Sederman [11], Rogelberg [8], and Bagnoud and Feschotte [7] is shown in Fig. 9.2(a). The calculated phase diagram can reproduce most of the experimental phase diagram data. The calculated invariant reactions are shown in Table 9.3 compared with the corresponding experimental values and the previous assessment results from Coughanowr et al. [1], Zuo and Chang [2], and Zhou et al. [3]. It can be seen from Table 9.3 that the present model predicted invariant temperatures can account the experiment values within a ± 5 °C error range. The enlarged Mg rich part of the Cu-Mg phase diagram is shown in Fig. 9.2(b) to show the solubility of Cu in Mg. As shown in Fig. 9.2(b), the solubility measured by Jones [5] is much smaller than the other data by Hansen [9] and Stepanov and Kornilov [10]. The maximum solubility of Cu in Mg is calculated to be about 0.176 at.% Cu according to the present assessment.

Fig. 9.3 presents the thermodynamic properties of the liquid phase. Pure liquid Mg and pure liquid Cu are taken as the reference states for the calculations. Fig. 9.3(a) is the calculated enthalpy of mixing of liquid at 927 °C compared with the experimental data from Garg et al. [22], Sommer et al. [25], Batalin et al. [24], and Juneja et al. [20]. As mentioned above, the direct calorimetry results by Sommer et al. [25] were considered to be the most reliable one than all others in this study. Fig. 9.3(b) shows the calculated activities of Cu and Mg at 873 °C together with the experimental data. The activity of Mg which was derived from the partial pressure of Mg is well reproduced. It should be noted that the activity of Cu was derived from the Gibbs-Duhem relationship. While Fig. 9.3(c) and Fig. 9.3(d) presents the partial Gibbs energy of Cu and Mg,

respectively, calculated form the present study at 972 °C along with the experimental data. The agreement between the calculated values and the experimental data are quite good. Thermodynamic properties of the Cu-Mg solid phases are summarized in Fig. 9.4. The optimized heat capacities of the Cu_2Mg (Laves_C15) and $CuMg_2$ phases are compared in Figs. 9.4(a) and (b), respectively, with the experimental data from Feufel and Sommer [14], Schimpff [17], and Schübel [18]. The estimated heat capacities from the Neumann-Kopp relation is also appended for comparison. It is apparent that the Neumann-Kopp relation can give slightly higher heat capacity than the experimental data. In the current assessment, more weight was given to the heat capacity data measured by adiabatic calorimetry than that by differential scanning calorimetry (DSC). Fig. 9.4(c) shows the calculated enthalpy of formation at 298 K of the Cu_2Mg and $CuMg_2$ phases compared with the literature data. It can be seen from the figure that the experimental data from different sources show a large discrepancy. The data from Smith and Christian [15] according to vapor pressure measurements are quite positive and the first principles calculations data by Zhou et al. [3] are too negative. The solution calorimetry data by King and Kleppa [13] and Feufel and Sommer [14] are consistent with the data by Eremenko et al. [16] using emf measurements and Arita et al. [23] by vapor pressure measurements. The optimized values agree with the data from King and Kleppa [13]. The calculated entropy of formation at 298 K is shown in Fig. 9.4(d) along with the corresponding experimental data form Smith and Christian [15] and Eremenko et al. [16]. It should be noted that these data are indirect data derived from emf and vapor pressure measurements. During the calculation, the pure fcc_A1 Cu and pure hcp_A3 Mg are considered as the reference states. Fig. 9.4(e) shows the calculated diagram of the chemical potential of hcp_A3 Mg. The experimental data from Eremenko et al. [16] and Arita et al. [23] are well reproduced. In the present study, while the results by Smith and Christian [15] are inconsistent with the other experimental data. It should be noted that the results in Fig. 9.4 indicates that the optimized Gibbs energies of the two intermetallic phases are accurate.

For the liquid solution, a short range ordering at molar ratio of Cu/Mg = 2 was considered by setting the $Z_{CuMg}^{Cu} = 3$ and $Z_{MgCu}^{Mg} = 6$ to reproduce the enthalpy of mixing data in Fig. 9.3(a) and phase diagram in Fig. 9.2(a). Three model parameters with two temperature dependent terms were used to reproduce all the thermodynamic properties and phase diagram data. In the case of the Laves_C15 phase, the end member of $G_{Cu:Mg}^{o}$ was optimized first from the heat capacity and

enthalpy of formation data. The end members of $G^{o}_{Cu:Cu}$ proposed by the COST-507 project [29] was accepted. And the homogeneity range of the Laves_C15 phase was then introduced by optimized the values of $G^{o}_{Cu:Mg}$, $G^{o}_{Mg:Mg}$, $G^{o}_{Mg:Cu}$, and the interactions parameters of $L^{0}_{Cu,Mg:*}$ and $L^{0}_{*:Cu,Mg}$, simultaneously.

9.4.2 The Al-Cu-Mg system

The Kohler type of extrapolation technique was used for the ternary Al-Cu-Mg liquid phase since the thermodynamic properties of the three sub-binary systems are quite similar. Then two small ternary parameters were optimized to reproduce all the experimental data more accurately. There are several solid solutions (Laves_C14, Laves_C15, Laves_C36, and τ) and stoichiometric compounds S, U, and V in this system. However, the thermodynamic properties of these ternary phases are not well investigated. On the other hand, the thermodynamic properties of the liquid phase have been well studied. Therefore, the Gibbs energy of the liquid phase was modeled first in this study and the Gibbs energies of the solid phases were optimized to reproduce mostly the available phase diagram. Fig. 9.5 shows the calculated mixing enthalpy of liquid along several different sections. The experimental data from Kim et al. [43] and Sommer et al. (1992) are also compared with the present results. Fig. 9.5(a) to Fig. 9.5(d) presents the mixing enthalpy data of liquid along the $Al_{0.75}Mg_{0.25}$-Cu, $Al_{0.65}Mg_{0.35}$-Cu, $Al_{0.5}Mg_{0.5}$-Cu, and $Al_{0.25}Mg_{0.75}$-Cu sections, respectively. The pure liquid Mg, Cu, and Al were taken as the reference state for the calculation. The optimized thermodynamic parameters can reproduce all the experiment data very well. The calculated activity of liquid Mg from 727 to 907 ºC is compared with the corresponding experimental data measured by Soares et al. [42] as shown in Fig. 9.5(e). The current calculations slightly underestimate the experimental data.

The calculated enthalpy of formation of Laves_C15 at 25 ºC is compared in Fig. 9.6 with the solution calorimetry data measured by Predel and Ruge [40]. The measured enthalpy of formation at $x_{Al} = 0.16$ is very negative. If these negative data point was reproduced, the isothermal section at 400 °C cannot be reproduced. However, the trend of enthalpy except for the point is well reproduced in the present study.

A group of calculated phase diagrams together with the experimental data are shown in Fig. 9.7. Fig. 9.7(a) is the calculated isothermal section of the Al-Cu-Mg system at 400 °C. The phase relation reported by Mel'nik and Kinzhibalo [37] at this temperature is well represented by the present study. The section of Al-(Al_2CuMg) S is calculated in Fig. 9.7(b). The S (Al_2CuMg) phase forms via a peritectic reaction. Several isoplethal sections with constant Al concentrations (80 wt.% Al, 70 wt.% Al, and 60 wt.% Al), and constant Cu concentration (20 wt.% Cu) are presented in Figs. 9.7(c)-(f). It can be seen from these diagrams that the phase relation in a wide range of composition in this system are generally well described by the current modeling. The solubility ranges of Mg and Cu in the Al solid solution at 300, 400, and 450 °C are shown in Fig. 9.7(g). The calculated phase diagram is also shown for comparison. The agreement between the calculated and the measured phase boundary is satisfactory.

The calculated liquidus projection for the Al-Cu-Mg system is presented in Fig. 9.8. It should be noted that a significant primary area of C15 is calculated. In addition, the primary crystalline regions of C14, S, U, V, and τ are also calculated. The C36 phase does not show its primary crystalline region due to the interference by C14 and C15. The calculated invariant reaction temperatures involving the liquid phase are summarized in Table 9.4 along with the available experimental data. The calculated invariant temperature for Liquid = S + AlCu_θ + fcc_A1 is 495 °C which is reasonably in agreement with experimental measurement results (500 to 507 °C) [22, 30, 33, 36, 38, 98]. The calculated temperatures are 474 °C and 446 °C for Liquid + S = τ + fcc_A1 and Liquid + fcc_A1 = τ + AlMg_β, respectively, which are quite closed to the measured values (465 to 467 °C and 445 to 451 °C, respectively) from refs. [30, 33, 36]. The only large difference (about 38 °C) is found for the ternary peritectic invariant reaction Liquid + S + U ($Al_7Cu_3Mg_6$) = τ.

For the Laves_C14, Laves_C15, and Laves_C36 phases, the generally accepted sub-lattice model of $(Al, Cu, Mg)_2(Al, Cu, Mg)$ was used. Al is introduced in both sub-lattices to model the ternary extension of the Laves_C15 phase and the ternary Laves_C14 and Laves_C36 phases. The end-member Gibbs energy of $G^o_{Al:Al}$ defined by the COST-507 porject [29] was accepted. Other ternary parameters were optimized to reproduce the phase relations related to the Laves_C14,

Laves_C15, and Laves_C36 phases and the enthalpy of formation of the Laves_C15 phase on the basis of the nature of CEF.

9.4.3 The Al-Cu-Si system

As the thermodynamic properties of the ternary solid solutions were not investigated, and there are many thermodynamic studies for the liquid phase, the Gibbs energy of the liquid phase was optimized first to reproduce the enthalpy and phase diagram data. Then the Gibbs energies of the solid solution phases were optimized to reproduce the phase diagram. Since the thermodynamic properties of the Cu-Si and Al-Cu binary liquid systems are quite different from that of the Al-Si system, the Toop type of extrapolation technique was utilized for the ternary liquid solution and with Cu as an asymmetric element. Three small ternary parameters with temperature dependent terms were optimized to better reproduce the experimental data. In the present study, the ternary solid solutions like γ_L, bcc_A2, and hcp_A3 were optimized to reproduce the phase relations related to these phases.

Fig. 9.9 presents the calculated isothermal sections of the Al-Cu-Si system at 700 °C, 600 °C, and 500 °C with the corresponding experimental data from Ponweiser and Richter [57], He et al. [46], and Riani et al. [56]. The experimental data in the Cu rich side reported by different authors are inconsistent with each other, especially the phase stability range of the fcc_A1 phase. As the phase boundary of the fcc_A1 phase reported by Riani et al. [56] is less likely (convex shape instead of concave shape). Thus, emphasis was presented to the experiment data from He et al. [46] and Ponweiser and Richter [57]. It can be seen from Fig. 9.9 that the calculated isothermal sections can reasonably reproduce the experimental data. The reproduction of the exact phase regions of hcp_A3 and γ_L in the ternary system was very difficult, but the general phase relation was well reproduced.

The calculated isoplethal section with 1 wt.% Si from 0 to 40 wt.% Cu and isoplethal section with 4 wt.% Cu from 0 to 25 wt.% Si are presented in Figs. 9.10(a) and (b), respectively, along with the experimental data from Philips [53]. A group of isoplethal sections with 2 wt.% Si, 6 wt.% Si, 10 wt.% Si, 15 wt.% Si, 20 wt.% Si, and 40 at.% Si are calculated in Fig. 9.11 along

with the experimental data from Matsuyama [55], Hisatsune [54], and Ponweiser and Richter [57]. The experimental data are general well reproduced. The calculated phase relation in the Cu rich corner (Fig. 9.11(a)) cannot address all the experimental data because the phase relation at this region is still not yet well understood. As η, η', and η" are treated as one phase in the thermodynamic description of the Cu-Si system used in this work, the phase relation related to η' and η" in the Si rich side of Fig. 9.11(f) cannot be reproduced.

The calculated enthalpy of mixing for the liquid phase along the $Al_{0.8}Si_{0.2}$-Cu, $Al_{0.5}Si_{0.5}$-Cu, and $Al_{0.2}Si_{0.8}$-Cu sections are shown in Figs. 9.12(a) to (c), respectively, with the calorimetry data measured by Witusiewicz et al. [59] at 1302 °C. The short range ordering of the liquid Al-Cu-Si solution happens along 70 at.% Cu as can be seen from Fig. 9.12. At low Si content, the calculated enthalpy of mixing can represent the experimental values quite well. As the Si content increase, the calculated values show a certain divergence in the Cu rich side.

But, the calculated results are still acceptable. The calculated ternary invariant equilibrium involving the liquid phase are summarized in Table 9.5. Fig. 9.13 presents the calculated liquidus projection of the Al-Cu-Si system. The Cu rich side of the liquidus projection is different from that calculated from He et al. [46]. The calculated primary phase region of (Si) is very large due to the high melting feature of Si. The fcc_A1 phase primary regions are shown in the Al and Cu rich corners. It can be seen from the figure that other high melting temperature phases like, bcc_A2, γ_L, AlCu_θ, etc., also show primary phase region in the diagram. The available experimental data for the invariant equilibria in the Al rich side are also listed in Table 9.5 for comparison. The model predicted information for the ternary invariant equilibria are in good agreement with those measured values.

9.4.4 The Cu-Mg-Si system

Like the previous ternary system, the thermodynamic properties of ternary phase like D and E are not known. Therefore, the Gibbs energy of the liquid phase was first optimized based on the thermodynamic data and phase diagram and the Gibbs energies of the ternary solid phases were determined to reproduce the phase diagram data. The Gibbs energy of the liquid phase was

calculated using the symmetric Kohler type extrapolation technique. One small ternary parameter was also optimized to better reproduce the experimental data.

The calculated enthalpy of mixing of the liquid phase along the Cu/Si atomic ratio of 7/3 section at 827 °C and 697 °C are shown in Fig. 9.14 together with the corresponding experimental data from Ganesan et al. [64, 65]. The agreement between the calculated enthalpy of mixing and the measured ones is quite good. Fig. 9.15 presents the calculated activity of liquid Mg along the section of Cu/Si atomic ratio of 7/3 at 900 °C compared with the experimental data measured by Ganesan et al. [64, 65]. Even though the calculated values show certain deviation from the measured ones, the general trend of the activity is very reasonable.

Figs. 9.16(a) to (f) presents a group of isoplethal sections. Figs. 9.16(a) to (e) are the isoplethal sections with 4.5 at.% Mg, 11.5 at.% Mg, 20 at.% Mg, 31 at.% Mg, and 33.33 at.% Mg, respectively. Fig. 9.16(f) is the calculated isoplethal section with constant Mg/Si ratio of 7/3. Since the experimental samples by Aschan [67] contained Fe impurity, these data were considered as less accurate. Overall, the calculated results are in fair agreement with the experimental data. The discrepancy of liquidus of Mg_2Si in Fig. 9.16(f) is due to the very steep liquidus of Mg_2Si. For example, if the sample composition (Cu/Si ratio) is slightly changed, the liquidus of Mg_2Si can be calculated a hundred degree different (see the liquidus projection). The calculated liquidus projection of the Cu-Mg-Si system is shown in Fig. 9.17(a). The isothermal section of this ternary system at 400 °C is shown in Fig. 9.17(b). The calculated ternary invariant equilibrium reaction temperatures and compositions corresponding to the liquid phase are summarized in Table 9.6. The calculation results can reasonably predict the available experimental data from Aschan [67]. The calculated liquidus projection of the Cu-Mg-Si system is presented in Fig. 9.17.

9.4.5 The Al-Cu-Mg-Si system

No quaternary thermodynamic parameters for the solution phases were introduced. The Q phase was modeled as a stoichiometric compound, and the S phase was considered as a quaternary solution phase. The Gibbs energy of the Q phase was evaluated by fitting the enthalpy of formation data from first principles calculation and the quaternary phase diagram data. While the Gibbs

energy for the S phase were assessed from the phase diagram data. Fig. 9.18 is a series of isoplethal sections in the Al rich corner of the Al-Cu-Mg-Si quaternary system. Fig. 9.18(a) is the calculated isoplethal section at 60 wt.% Al and 8 wt.% Si compared with the experimental data measured by Petrov and Nagorskaya [71]. It can be seen that the thermal analysis data are satisfactorily addressed by the currently obtained thermodynamic parameters. Fig. 9.18(b) is the calculated isoplethal section at 80 wt.% Al and 2 wt.% Si compared with the corresponding experimental data. Similarly, isoplethal sections with 80 wt.% Al and 0.2 wt.% Si, 70 wt.% Al and 0.2 wt.% Si, 50 wt.% Al and 46.5 wt.% Cu, and 90 wt.% Al and 4 wt.% Mg compared with the experimental data are shown in Figs. 9.18(c) to (f), respectively. It is apparent that the calculated phase diagram is reasonable. Isothermal sections with constant 1.8 wt.% Si, 1.2 wt.% Si, and 0.6 wt.% Si at 500 °C are presented in Figs. 9.19(a) to (c) with the related experimental data from Smith [78]. The calculated phase diagram can account most of the experimental data with high accuracy. The calculated isothermal section with constant 2 wt.% Si, 1.2 wt.% Si, and 0.6 wt.% Si at 460 °C are shown in Figs. 9.20(a) to (c). At 460 °C, the calculated phase relation is reasonable. However, the calculated phase region for fcc_A1+ Mg_2Si + Al_2Cu + S four-phase equilibria deviates from the experimental data as the Si content decrease. This can be due to the thermodynamic description of the S phase is not accurate enough, since there is no enough thermodynamic and phase diagram information for this phase. Fig. 9.21 presents the calculated two isothermal sections with 3 wt.% Cu and 4.5 wt.% Cu respectively compared with the related experimental data. As can be seen from these two figures that the calculated phase relation is excellently agree with the measured one. The calculated quaternary five-phase invariant equilibrium temperatures in the Al rich corner of the Al-Cu-Mg-Si system are presented in Table 9.7 compared with the measured values. Even though these quaternary invariant equilibria temperatures are not utilized in the present assessment, the present calculation still can give a pretty good prediction of the temperature for these reactions. It can be seen from Table 9.7 that the present calculation agrees very well with the measured ones from Schrader [72]. The difference is within ±3 °C. From the above discussion, we can conclude that the presently obtained thermodynamic description can give a reasonable prediction of the phase equilibria in the Al rich corner of the Al-Cu-Mg-Si system.

9.5 Summaries

- The available literature phase diagram and thermodynamic data for the Cu-Mg system, Al-Cu-Mg system, Al-Cu-Si system, Cu-Mg-Si system, and Al-Cu-Mg-Si system are critically evaluated.
- Thermodynamic modeling for the Cu-Mg system, Al-Cu-Mg system, Al-Cu-Si system, and Cu-Mg-Si system are conducted based on the critically evaluated thermodynamic and phase diagram data. The modified quasi-chemical model was utilized for the liquid phase to give a better description of the short range ordering. The compound energy formalism was applied to all the other phases.
- A self-consistent set of thermodynamic database for the quaternary system was obtained by combining the currently obtained thermodynamic descriptions with the literature reported thermodynamic descriptions of other subsystems in the Al-Cu-Mg-Si quaternary system.
- Comprehensive comparison between the calculated thermodynamic properties and phase diagrams with the corresponding experimental information indicates that the currently obtained thermodynamic parameters can give a reliable description of the Al rich corner of the Al-Cu-Mg-Si quaternary system.

Acknowledgement

The authors would like to thank the financial support from NSERC-Automotive Partnership Canada program in Canada. Senlin Cui would also like to thank the McGill Engineering Doctorate Award (MEDA) from McGill University for financial support.

References

1. Coughanowr, C.A., I. Ansara, R. Luoma, M. Hamalainen, and H.L. Lukas, *Assessment of the copper-magnesium system.* Z. Metallkd., 1991. **82**(7): p. 574-81.
2. Zuo, Y. and Y.A. Chang, *Thermodynamic calculation of magnesium-copper phase diagram.* Z. Metallkd., 1993. **84**(10): p. 662-7.

3. Zhou, S., Y. Wang, F.G. Shi, F. Sommer, L.-Q. Chen, Z.-K. Liu, and R.E. Napolitano, *Modeling of thermodynamic properties and phase equilibria for the Cu-Mg binary system.* J. Phase Equilib. Diffus., 2007. **28**(2): p. 158-166.
4. Urazova, G.G., *Experimental Measurements for Cu-Mg System.* Zh. Russ. Fiz-Khim. Obschestva, 1907(39): p. p 1556-1581.
5. Jones, W.R.D., *Copper-magnesium alloys. IV. Equilibrium diagram.* J. Inst. Metals, Advance copy, 1931. **No. 574**: p. 25 pp.
6. Sahmen, R., *Alloys of Copper with Cobalt, Iron, Manganese, and Magnesium.* Z. Anorg. Chem., 1908. **57**: p. 1-33.
7. Bagnoud, P. and P. Feschotte, *Binary systems of magnesium-copper and magnesium-nickel, especially the nonstoichiometry of the $MgCu_2$ and $MgNi_2$ laves phases.* Z. Metallkd., 1978. **69**(2): p. 114-20.
8. Rogelberg, I.L., *Cu-Mg Phase Diagram.* Tr.Gos. Nauchn. -Issled., 1957(16): p. p 82-89.
9. Hansen, M., *Note on the magnesium rich magnesium copper alloys.* J. Inst. Metals (advance copy), 1927. **No. 428**: p. 8 pp.
10. Stepanov, N.I. and I.I. Kornilov, *Solubility of copper in magnesium in the solid state.* Izv. Inst. Fiz.-Khim. Anal., Akad. Nauk SSSR, 1935. **7**: p. 89-98.
11. Sederman, V.G., *Cu_2Mg phase in the copper-magnesium system.* Philos. Mag. (1798-1977), 1934. **18**: p. 343-52.
12. Nayeb-Hashemi, A.A. and J.B. Clark, *The Cu-Mg (copper-magnesium) system.* Bull. Alloy Phase Diagrams, 1984. **5**(1): p. 36-43, 103-4.
13. King, R.C. and O.J. Kleppa, *A thermochemical study of some selected Laves phases.* Acta Metall., 1964. **12**(1): p. 87-97.
14. Feufel, H. and F. Sommer, *Thermodynamic investigations of binary liquid and solid Cu-Mg and Mg-Ni alloys and ternary liquid Cu-Mg-Ni alloys.* J. Alloys Compd., 1995. **224**(1): p. 42-54.
15. Smith, J.F. and J.L. Christian, *Thermodynamics of formation of copper-magnesium and nickel-magnesium compounds from vapor-pressure measurements.* Acta Metall., 1960. **8**: p. 249-55.
16. Eremenko, V.N., G.M. Lukashenko, and R.I. Polotskaya, *Thermodynamic properties of magnesium-copper compounds.* Izv. Akad. Nauk SSSR, Metal., 1968(1): p. 210-12.

17. Schimpff, H., *Heat Capacity of Metals and Metallic Compounds.* Gottingen. Z. physik. Chem., 1910. **71**: p. 257-300.
18. Schübel, P., *The heat capacity of metals and metallic compounds between 18 and 600 K.* Z. Anorg. Chem., 1914. **87**: p. 81-119.
19. Sommer, F., G. Bucher, and B. Predel, *Thermodynamic investigations of magnesium-copper and magnesium-nickel metallic glasses.* J. Phys., Colloq. (Orsay, Fr.), 1980(C8): p. 563-6.
20. Juneja, J.M., G.N.K. Iyengar, and K.P. Abraham, *Thermodynamic properties of liquid (magnesium + copper) alloys by vapor-pressure measurements made by a boiling-temperature method.* J. Chem. Thermodyn., 1986. **18**(11): p. 1025-35.
21. Hino, M., T. Nagasaka, and R. Takehama, *Activity measurement of the constituents in liquid Cu-Mg and Cu-Ca alloys with mass spectrometry.* Metall. Mater. Trans. B, 2000. **31B**(5): p. 927-935.
22. Garg, S.P., Y.J. Bhatt, and C.V. Sundaram, *Thermodynamic study of liquid copper-magnesium alloys by vapor pressure measurements.* Met. Trans., 1973. **4**(1): p. 283-9.
23. Arita, M., Y. Ichinose, and M. Someno, *Thermodynamic properties of the titanium-copper, titanium-nickel, and magnesium-copper systems by metal-hydrogen equilibration.* Chem. Metall.--Tribute Carl Wagner, Proc. Symp., 1981: p. 153-8.
24. Batalin, G.I., V.S. Sudavtsova, and M.V. Mikhailovskaya, *Thermodynamic properties of liquid copper-magnesium alloys.* Izv. Vyssh. Uchebn. Zaved., Tsvetn. Metall., 1987(2): p. 29-31.
25. Sommer, F., J.J. Lee, and B. Predel, *Calorimetric investigations of liquid alkaline earth metal alloys.* Ber. Bunsen-Ges. Phys. Chem., 1983. **87**(9): p. 792-7.
26. Chen, S.L., Y. Zuo, H. Liang, and Y.A. Chang, *A thermodynamic description for the ternary Al-Mg-Cu system.* Metall. Mater. Trans. A, 1997. **28A**(2): p. 435-446.
27. Buhler, T., S.G. Fries, P.J. Spencer, and H.L. Lukas, *A thermodynamic assessment of the Al-Cu-Mg ternary system.* J. Phase Equilib., 1998. **19**(4): p. 317-333.
28. Gable, B.M., A.W. Zhu, G.J. Shiflet, and E.A. Starke, Jr., *Assessment of the aluminum-rich corner of the Al-Cu-Mg-(Ag) phase diagram.* CALPHAD Comput. Coupling Phase Diagrams Thermochem., 2008. **32**(2): p. 256-267.

29. Ansara, I., A. Dinsdale, T, and M. Rand, H, *COST 507.* Thermochemical database for light metal alloys, 1998. **2**.
30. Nishimura, H., *Investigation of the aluminum-rich aluminum-copper-magnesium alloy system.* Mem. Coll. Eng., Kyoto Imp. Univ., 1937. **10**: p. 18-33.
31. Laves, F. and H. Witte, *Investigations in the system Mg-Cu-Al, especially on the line $MgCu_2$-$MgAl_2$.* Metallwirtsch., Metallwiss., Metalltech., 1936. **15**: p. 15-22.
32. Urazov, G.G. and M.S. Mirgalovskaya, *The system aluminum-copper-magnesium.* Dokl. Akad. Nauk SSSR, 1952. **83**: p. 247-50.
33. Urazov, G.G. and D.A. Petrov, *The diagram of state of the system aluminum-copper-magnesium.* Zh. Fiz. Khim., 1946. **20**: p. 387-98.
34. Urazov, G.G. and M.S. Mirgalovskaya, *Ternary Intermetallic Phases in the Al-Cu-Mg System.* Izv. Sekt. Fiz.-Khim. Anal., 1949. **19**: p. 514-521.
35. Garmong, G. and C.G. Rhodes, *Structure and mechanical properties of the directionally solidified aluminum-copper-magnesium eutectic.* Met. Trans., 1972. **3**(2): p. 533-44.
36. Brommelle, N.S. and H.W.L. Phillips, *The constitution of aluminum-copper-magnesium alloys.* J. Inst. Met., 1949. **75**: p. 529-58;Paper No 1167.
37. Mel'nik, E.V. and V.V. Kinzhibalo, *Study of magnesium-aluminum-copper and magnesium-gallium-copper systems in the phase containing 33.3-100 at.% magnesium.* Izv. Akad. Nauk SSSR, Met., 1981(3): p. 201-6.
38. Huang, C.-C. and S.-W. Chen, *Phase equilibria of Al rich Al-Cu-Mg alloys.* Metall. Mater. Trans. A, 1995. **26A**(4): p. 1007-10.
39. Zamotorin, M.I., *Mutual solubility of magnesium and zinc in aluminum in the solid state.* Trudy Leningrad. Politekh. Inst., 1955(No. 180): p. 38-43.
40. Predel, B. and H. Ruge, *Enthalpies of formation in the magnesium-copper-zinc, magnesium-copper-aluminum, and magnesium-copper-tin systems as a contribution to the clarification of the bonding conditions in Laves phases.* Mater. Sci. Eng., 1972. **9**(3): p. 141-51.
41. Notin, M., M. Dirand, D. Bouaziz, and J. Hertz, *Determination of the partial molar enthalpy at infinite dilution of liquid magnesium and solid copper in pure liquid aluminum and of the enthalpy of formation of the S-phase aluminum-copper-magnesium (Al_2CuMg).* C. R. Acad. Sci., Ser. 2, 1986. **302**(2): p. 63-6.

42. Soares, D., L.F. Malheiros, M. Haemaelaeinen, and F. Castro, *Isopiestic determination of the coefficients of activity of magnesium in Al-Cu-Mg liquid alloys.* J. Alloys Compd., 1995. **220**(1-2): p. 179-81.
43. Kim, Y.B., F. Sommer, and B. Predel, *Determination of the enthalpy of mixing of liquid aluminum-copper-magnesium alloys.* Z. Metallkd., 1995. **86**(9): p. 597-602.
44. Pan, X., J.E. Morral, and H.D. Brody, *Predicting the Q-Phase in Al-Cu-Mg-Si Alloys.* J. Phase Equilib. Diffus., 2010. **31**(2): p. 144-148.
45. Miettinen, J., *Thermodynamic description of the Cu-Al-Si system in the copper rich corner.* CALPHAD Comput. Coupling Phase Diagrams Thermochem., 2007. **31**(4): p. 449-456.
46. He, C.-Y., Y. Du, H.-L. Chen, and H. Xu, *Experimental investigation and thermodynamic modeling of the Al-Cu-Si system.* CALPHAD Comput. Coupling Phase Diagrams Thermochem., 2009. **33**(1): p. 200-210.
47. Lukas, H.L., *Aluminium - Copper - Silicon.* MSIT Ternary Evaluation Program, in MSIT Workplace, Effenberg, G. (Ed.), MSI, Materials Science International Services GmbH, Stuttgart;, 1992: p. Document ID: 10.15417.1.20.
48. Lukas, H.L. and N. Lebrun, *Aluminum-Copper-Silicon.* Landolt-Bornstein New Series IV, 2005. **11A2**: p. 135-147.
49. Villars, P., A. Prince, and H. Okamoto, *Al-Cu-Si.* Handbook of Ternary Alloy Phase Diagrams, 1995. **3**: p. 3331-3351.
50. Raghavan, V., *Al-Cu-Si (aluminum-copper-silicon).* J. Phase Equilib. Diffus., 2007. **28**(2): p. 180-182.
51. Raghavan, V., *Al-Cu-Si (Aluminum-Copper-Silicon).* J. Phase Equilib. Diffus., 2010. **31**(1): p. 39-40.
52. Raghavan, V., *Al-Cu-Si (Aluminum-Copper-Silicon).* J. Phase Equilib. Diffus., 2012. **33**(1): p. 59-61.
53. Phillips, H.W.L., *The constitution of aluminum-copper-silicon alloys.* J. Inst. Met., 1953. **82**((Paper No. 1488)): p. 9-15.
54. Hisatsune, C., *Constitution of alloys of copper, aluminum and silicon.* Mem. Coll. Eng., Kyoto Imp. Univ., 1935. **9**: p. 18-47.
55. Matsuyama, K., *Ternary diagram of aluminum-copper-silicon system.* Kinzoku No Kenkyu, 1934. **11**: p. 461-90.

56. Riani, P., K. Sufryd, and G. Cacciamani, *About the Al-Cu-Si isothermal section at 500 °C and the stability of the ε-$Cu_{15}Si_4$ phase.* Intermetallics, 2009. **17**(3): p. 154-164.
57. Ponweiser, N. and K.W. Richter, *New investigation of phase equilibria in the system Al-Cu-Si.* J. Alloys Compd., 2012. **512**(1): p. 252-263.
58. Beloborodova, E.A., T.N. Zinevich, N.V. Kotova, D.S. Kanibolotskii, and V.I. Shcherbakov, *Calorimetric determination of the mixing enthalpy in the Si-Cu-Al ternary system.* Casting Processes, 1997. **6**(2): p. 3-9.
59. Witusiewicz, V.T., I. Arpshofen, H.J. Seifert, and F. Aldinger, *Enthalpy of mixing of liquid Al-Cu-Si alloys.* J. Alloys Compd., 2000. **297**(1-2): p. 176-184.
60. Kanibolotsky, D.S., O.A. Bieloborodova, V.A. Stukalo, N.V. Kotova, and V.V. Lisnyak, *Thermodynamics of liquid aluminium-copper-silicon alloys.* Thermochim. Acta, 2004. **412**(1-2): p. 39-45.
61. Pan, X.M., C. Lin, J.E. Morral, and H.D. Brody, *An assessment of thermodynamic data for the liquid phase in the Al rich corner of the Al-Cu-Si system and its application to the solidification of a 319 alloy.* J. Phase Equilib. Diffus., 2005. **26**(3): p. 225-233.
62. Miettinen, J. and G. Vassilev, *Thermodynamic assessment of the Cu-Mg-Si system in its copper rich region.* Cryst. Res. Technol., 2011. **46**(11): p. 1122-1130.
63. Bochvar, N., E. Lysova, and L. Rokhlin, *Copper - Magnesium - Silicon.* Landolt-Börnstein New Series IV/11A4, 2006: p. 224-237.
64. Ganesan, V., H. feufel, F. Sommer, and H. Ipser, *Thermochemistry of ternary liquid Cu-Mg-Si alloys.* Metall. Mater. Trans. B, 1998. **29B**(4): p. 807-813.
65. Ganesan, V. and H. Ipser, *Partial thermodynamic properties of magnesium in ternary Cu-Mg-Si alloys.* J. Non-Cryst. Solids, 1996. **205-207**(Pt. 2): p. 711-715.
66. Witte, H., *Crystal chemistry of alloys. II. System Mg-Cu-Si with special reference to the line $MgCu_2$-$MgSi_2$.* Metallwirtsch., Metallwiss., Metalltech., 1939. **18**: p. 459-63.
67. Aschan, L.J., *Ternary system Cu-Mg-Si.* Acta Polytech. Scand., Chem. Met. Ser, 1960. **No. 11**: p. 1-63.
68. Lacaze, J., G. Lesoult, O. Relave, I. Ansara, and J.P. Riquet, *Thermodynamics and solidification of aluminum-copper-magnesium-silicon alloys.* Z. Metallkd., 1987. **78**(2): p. 141-50.

69. Yan , X.-Y., Y.A. Chang , F.-Y. Xie, S.-L. Chen, F. Zhang, and S. Daniel, *Calculated phase diagrams of aluminum alloys from binary Al-Cu to multicomponent commercial alloys.* Journal of Alloys and Compounds, 2001. **320**: p. 151-160.
70. Chang, K., S. Liu, D. Zhao, Y. Du, L. Zhou, and L. Chen, *Thermodynamic description of the Al-Cu-Mg-Mn-Si quinary system and its application to solidification simulation.* Thermochim. Acta, 2011. **512**(1-2): p. 258-267.
71. Petrov, D.A. and N.D. Nagorskaya, *Constitution diagram of the aluminum-copper-magnesium-silicon system.* Zh. Obshch. Khim., 1949. **19**: p. 1994-2037.
72. Schrader, A., *Quaternary alloys.* Metall (Berlin, 1914-34), 1949. **3**: p. 110-15,150-4.
73. Mondolfo, L.F., *Aluminum Alloys: Structure and Properties*. 1976. 944 pp.
74. Chakrabarti, D.J. and J.L. Murray, *Eutectic melting in Al-Cu-Mg-Si alloys.* Mater. Sci. Forum, 1996. **217-222**(Pt. 1, Aluminium Alloys, Pt. 1): p. 177-181.
75. Axon, H.J., *Equilibrium relations at 460 °C in aluminum rich alloys containing 0-7% copper, 0-7% magnesium, and 2% silicon.* J. Inst. Met., 1955. **83**: p. 490-2;Paper No 1626.
76. Axon, H.J., *Equilibrium relations at 460 °C in aluminum rich alloys containing 0-7% copper, 0-7% magnesium, and 0-6% silicon.* J. Inst. Met., 1953. **81**: p. 449-50;Paper No 1463.
77. Axon, H.J., *Equilibrium relations at 460 °C in aluminum rich alloys containing 0-7% copper, 0-7% magnesium, and 1.2% silicon.* J. Inst. Met., 1952. **81**(Paper No. 1432): p. 209-13.
78. Smith, D.P., *The constitution of quaternary aluminum-copper-magnesium-silicon alloys at 500 °C.* Metallurgia, 1961. **63**: p. 223-30.
79. Pepelyan, A.G., *Phase equilibrium in the Mg-Al-Si-Cu system.* Magnievye Splavy Sovrem. Tekh., [Mater. Vses. Soveshch. Issled., Razrab. Primen. Magnievykh Splavov Nar. Khoz.], 2nd, 1992: p. 67-71.
80. Crowther, J., *Overheating phenomena in aluminum-copper-magnesium-silicon alloys of the Duralumin type.* J. Inst. Met., 1949. **76**: p. 201-36;Paper No 1216.
81. Dix, E.H., Jr., G.F. Sager, and B.P. Sager, *Equilibrium relations in aluminum-copper-magnesium and aluminum-copper-magnesium silicide alloys.* Am. Inst. Mining Met. Engrs., Inst. Metals Division, Tech. Pub., 1932. **472**: p. 13 pp.

82. Arnberg, L. and B. Aurivillius, *The crystal structure of aluminum-copper-magnesium-silicon [$Al_xCu_2Mg_{12-x}Si_7$, (h-AlCuMgSi)].* Acta Chem. Scand., Ser. A, 1980. **A34**(1): p. 1-5.

83. Chakrabarti, D.J. and D.E. Laughlin, *Phase relations and precipitation in Al-Mg-Si alloys with Cu additions.* Prog. Mater. Sci., 2004. **49**(3-4): p. 389-410.

84. Phragmen, G., *The phases occurring in alloys of aluminum with copper, magnesium, manganese, iron, and silicon.* J. Inst. Met., 1950. **77**(Paper No. 1262): p. 489-552.

85. Petrov, D.A., *The composition of the quaternary phase in the system Al-Cu-Mg-Si.* Acta Physicochim. URSS, 1937. **6**: p. 505-12.

86. Löffler, A., A. Zendegani, J. Gröbner, M. Hampl, R. Schmid-Fetzer, H. Engelhardt, M. Rettenmayr, F. Körmann, T. Hickel, and J. Neugebauer, *Quaternary Al-Cu-Mg-Si Q Phase: Sample Preparation, Heat Capacity Measurement and First-Principles Calculations.* J. Phase Equilib. Diffus., 2016. **37**(2): p. 119-126.

87. Wolverton, C., *Crystal structure and stability of complex precipitate phases in Al-Cu-Mg-(Si) and Al-Zn-Mg alloys.* Acta Mater., 2001. **49**(16): p. 3129-3142.

88. Dinsdale, A.T., *SGTE data for pure elements.* CALPHAD Comput. Coupling Phase Diagrams Thermochem., 1991. **15**(4): p. 317-425.

89. Pelton, A.D. and P. Chartrand, *The modified quasi-chemical model: Part II. Multicomponent solutions.* Metall. Mater. Trans. A, 2001. **32A**(6): p. 1355-1360.

90. Pelton, A.D., S.A. Degterov, G. Eriksson, C. Robelin, and Y. Dessureault, *The modified quasichemical model I - binary solutions.* Metall. Mater. Trans. B, 2000. **31B**(4): p. 651-659.

91. Frisk, K. and M. Selleby, *The compound energy formalism: applications.* J. Alloys Compd., 2001. **320**(2): p. 177-188.

92. Chen, Z., J. Zhang, J. Shu, G. Sha, J. Xia, S. Wang, and S.P. Ringer, *Effects of Si addition on the microstructure evolution of Al-Cu-Mg alloys in the $\alpha + S + T$ phase field.* Philos. Mag. Lett., 2013. **93**(11): p. 648-654.

93. Hutchinson, C.R. and S.P. Ringer, *Precipitation processes in Al-Cu-Mg alloys microalloyed with Si.* Metall. Mater. Trans. A, 2000. **31A**(11): p. 2721-2733.

94. Saunders, N., *System Al-Cu.* Cost 507 - Thermochemical database for light metal alloys, 1991. **2**: p. 28-33.

95. Chartrand, P., *Thermodynamic assessment of the Al-Mg system.* unpublished work.
96. Harvey, J.-P., *M.A.Sc. thesis. Ecole Polytechnique*, 2006.
97. Kang, D.H. and I.-H. Jung, *Thermodynamic assessmet of the Cu-Si system.* unpublished work.
98. Cooksey, J.S. and A. Hellawell, *The microstructures of ternary eutectic alloys in the systems Cd-Sn-(Pd, In, Tl), Al-Cu-(Mg, Zn, Ag), and Zn-Sn-Pb.* Journal of the institute of metals, 1967. **95**: p. 183-187.
99. Grobner, J., H.L. Lukas, and F. Aldinger, *Thermodynamic Calculation of the Ternary System Al-Si-C.* CALPHAD Comput. Coupling Phase Diagrams Thermochem., 1996. **20**(2): p. 247-254.
100. Feufel, H., T. Gödecke, H.L. Lukas, and F. Sommer, *Investigation of the Al-Mg-Si system by experiments and thermodynamic calculations.* J. Alloys Compd., 1997. **247**(1-2): p. 31-42.
101. Boudouard, M.O., *The bianry alloys of Magnesium.* Bull. Soc. Encourag. Industr., 1903. **102**(2): p. 200.
102. Phillips, H.W.L., *The constitution of alloys of aluminum with magnesium, silicon, and iron.* J. Inst. Met., 1946. **72**(Paper No. 1016): p. 151-227.
103. Murray, J.L., *Industrial applications of multicomponent aluminum phase diagrams.* J. Chim. Phys. Phys.-Chim. Biol., 1993. **90**(2): p. 151-66.

Table captions

Figure captions

Fig. 9.1 Calculated phase diagrams of (a) the Al-Cu system, (b) the Al-Mg system, (c) the Al-Si system, (d) the Cu-Si system, and (e) the Mg-Si system.

Fig. 9.2 Calculated phase diagrams of the Cu-Mg system along with the experimental data. (a) The entire composition range, and (b) enlarged Mg rich part.

Fig. 9.3 Calculated thermodynamic properties of the Cu-Mg liquid phase along with the experimental data. (a) Enthalpy of mixing at 927 ºC, (b) activity of Cu and Mg with respect to the pure liquid standard at 972 ºC, (c) chemical potential of Mg at 873 ºC, and (d) chemical potential of Cu at 873 ºC.

Fig. 9.4 Calculated thermodynamic properties of the Cu-Mg solid phases along with the experimental data. (a) Heat capacity of Cu_2Mg, (b) heat capacity of $CuMg_2$, (c) enthalpy of formation of compounds at 25 ºC, (d) entropy of formation of compounds at 25 ºC, and (e) chemical potential diagram of hcp_A3 Mg.

Fig. 9.5 Calculated thermodynamic properties of the Al-Cu-Mg liquid phase along with the experimental data. (a) Enthalpy of mixing of the $Al_{0.75}Mg_{0.25}$-Cu section at 713 ºC, (b) enthalpy of mixing of the $Al_{0.65}Mg_{0.35}$-Cu section at 713 ºC, (c) enthalpy of mixing of the $Al_{0.5}Mg_{0.5}$-Cu section at 713 ºC, (d) enthalpy of mixing of the $Al_{0.25}Mg_{0.75}$-Cu section at 713 ºC, and (e) activity of Mg with respect to the pure liquid standard at 727-857 ºC.

Fig. 9.6 Calculated enthalpy of formation of the Laves_C15 phase in the Al-Cu-Mg system at 25 ºC along with the experimental data.

Fig. 9.7 Calculated phase diagrams of the Al-Cu-Mg system along with the experimental data. (a) Isothermal section at 400 ºC, (b) isoplethal section of S-Al, (c) isoplethal section with 80 wt.% Al, (d) isoplethal section with 70 wt.% Al, (e) isoplethal section with 60 wt.% Al, (f) isoplethal section with 20 wt.% Cu, and (g) the solubility of Mg and Cu in (Al) at 300, 400, and 450 ºC.

Fig. 9.8 Calculated liquidus projection of the Al-Cu-Mg system.

Fig. 9.9 Calculated isothermal sections of the Al-Cu-Si system along with the experimental data. (a) At 700 ºC, (b) at 600 ºC, and (c) at 500 ºC.

Fig. 9.10 Calculated isoplethal sections of the Al-Cu-Si system along with the experimental data. (a) 1 wt.% Si and (b) 4 wt.% Cu

Fig. 9.11 Calculated isoplethal sections of the Al-Cu-Si system along with the experimental data. (a) Isoplethal section with 2 wt.% Si, (b) isoplethal section with 6 wt.% Si, (c) isoplethal section

with 10 wt.% Si, (d) isoplethal section with 15 wt.% Si, (e) isoplethal section with 20 wt.% Si, and (f) isoplethal section with 40 at.% Si.

Fig. 9.12 Calculated enthalpy of mixing of the Al-Cu-Si liquid phase at 1302 ºC along with the experimental data. (a) The $Al_{0.8}Si_{0.2}$-Cu section, (b) the $Al_{0.5}Si_{0.5}$-Cu section, and (c) the $Al_{0.2}Si_{0.8}$-Cu section.

Fig. 9.13 Calculated liquidus projection of the Al-Cu-Si system.

Fig. 9.14 Calculated enthalpy of mixing of the Cu-Mg-Si liquid phase of the $Cu_{0.7}Si_{0.3}$-Mg section along with the experimental data at 827 and 697 ºC.

Fig. 9.15 Calculated activity of Mg of the Cu-Mg-Si liquid phase of the $Cu_{0.7}Si_{0.3}$-Mg section at 900 ºC along with the experimental data.

Fig. 9.16 Calculated isoplethal sections of the Cu-Mg-Si system along with the experimental data. (a) Isoplethal section with 4.5 at.% Mg, (b) isoplethal section with 11.5 at.% Mg, (c) isoplethal section with 20 at.% Mg, (d) isoplethal section with 31 at.% Mg, (e) isoplethal section with 33.33 at.% Mg, and (f) isoplethal section with Cu/Si ratio of 7/3.

Fig. 9.17 (a) Calculated liquidus projection of the Cu-Mg-Si system. (b) Calculated isothermal section of the Cu-Mg-Si system at 400 °C.

Fig. 9.18 Calculated isoplethal sections in the Al rich corner of the Al-Cu-Mg-Si quaternary system along with the experimental data. (a) Isoplethal section with 60 wt.% Al and 8 wt.% Si, (b) isoplethal section with 80 wt.% Al and 2 wt.% Si, (c) isoplethal section with 80 wt.% Al and 0.2 wt.% Si, (d) isoplethal section with 70 wt.% Al and 0.2 wt.% Si, (e) isoplethal section with 50 wt.% Al and 46.5 wt.% Mg, and (f) isoplethal section with 90 wt.% Cu and 4 wt.% Mg.

Fig. 9.19 Calculated isothermal sections in the Al rich Al-Cu-Mg-Si system at 500 ºC along with the experimental data. (a) 1.8 wt.% Si, (b) 1.2 wt.% Si, and (c) 0.6 wt.% Si.

Fig. 9.20 Calculated isothermal sections in the Al rich Al-Cu-Mg-Si system at 460 ºC along with the experimental data. (a) 2 wt.% Si, (b) 1.2 wt.% Si, and (c) 0.6 wt.% Si.

Fig. 9.21 Calculated isothermal sections in the Al rich Al-Cu-Mg-Si system at 500 ºC along with the experimental data. (a) 3 wt.% Cu and (b) 4.5 wt.% Cu.

Table 9.1 List of the symbols to denote the phases in the Al-Cu-Mg-Si system.

Symbols	Phases	Pearson symbol/Space group
L	Liquid	
fcc	Solid solution based on disordered fcc_A1	cF4/Fm-3m
bcc	Solid solution based on disordered bcc_A2	cI2/Im-3m
hcp	Solid solution based on disordered hcp_A3	hP2/$P6_3$/mmc
(Si)	Solid solution based on diamond_A4	cF8/Fd-3m
AlCu_δ	Binary solid solution Al_2Cu_3	hR*/R-3m
AlCu_ε	High temperature Al_9Cu_{11} solid solution	hP4/$P6_3$/mmc
AlCu_η	Binary solid solution AlCu	mC20/C2/m
AlCu_θ	Binary solid solution Al_2Cu	tI12/I4/mcm
γ_L	Low temperature form of Al_4Cu_9 solid solution	cP52/P-43m
γ_H	High temperature form of Al_4Cu_9 solid solution	cI52/I-43m
AlCu_ζ	Binary compound phase Al_9Cu_{11}	hP42/C_2/m
AlMg_β	Binary solid solution phase Al_3Mg_2	cF112/Fd-3m
AlMg_ε	Binary compound phase $Al_{30}Mg_{23}$	hR53/R-3
AlMg_γ	Binary solid solution $Al_{12}Mg_{17}$	cI58/I-43m
C15	Solid solution Laves_C15 phase Cu_2Mg	cF24/Fd-3m
C14	Solid solution Laves_C14 phase Zn_2Mg	hP12/$P6_3$/mmc
C36	Solid solution Laves_C36 phase Ni_2Mg	hP24/$P6_3$/mmc
$CuMg_2$	Binary compound $CuMg_2$	Fddd/oF48
CuSi_γ	Binary compound $Cu_{33}Si_7$	cP20/$P4_132$
CuSi_δ	Binary compound Cu_9Si_2	t** or hP*/P63/mmc
CuSi_ε	Binary compound $Cu_{15}Si_4$	cI76/I-43d
CuSi_η	Binary compound $Cu_{19}Si_6$	Rh*/R-3m
Mg_2Si	Binary compound Mg_2Si	cF12/Fm-3m
τ	Ternary solid solution $Mg_{32}(Al, Cu)_{49}$	cI162/Im-3
U	Ternary compound $Al_7Cu_3Mg_6$	cI96/Im-3m
S	Quaternary solid solution $(Al, Si)_2CuMg$	oC16/Cmcm
V	Ternary compound $Al_5Cu_6Mg_2$	cP39/Pm-3

E	Ternary compound Cu_3Mg_2Si	hP12/$P6_3$/mmc
D	Ternary compound $Cu_{16}Mg_6Si_7$	Fm-3m/cF116
Q	Quaternary compound $Al_3Cu_2Mg_9Si_7$	

Table 9.2 Optimized thermodynamic parameters for the Al-Cu-Mg-Si system obtained in the present work (J mol^{-1} or J mol^{-1} K^{-1}).

Phase	Thermodynamic parameters	Ref.
liquid (Al, Cu, Mg, Si)(Va)	$Z_{AlAl}^{Al} = Z_{CuCu}^{Cu} = Z_{MgMg}^{Mg} = Z_{SiSi}^{Si} = Z_{AlMg}^{Al} = Z_{MgAl}^{Mg} = Z_{MgCu}^{Mg} = Z_{SiMg}^{Si} = 6$; $Z_{AlSi}^{Al} = Z_{SiAl}^{Si} = 5$; $Z_{CuMg}^{Cu} = 3$; $Z_{MgSi}^{Mg} = 4$; $Z_{CuSi}^{Cu} = 2$; $Z_{SiCu}^{Si} = 7$	
	$L_{Al,Cu} = -66622 + 8.1T + (46800 - 90.8T + 10T\ln T)(x_{Al} - x_{Cu}) - 2812(x_{Al} - x_{Cu})^2$	[94]
	$\Delta g_{Al,Mg} = -2761.44 + 1.53T + (-418.40 + 0.63T)x_{AlAl}$	[95]
	$\Delta g_{Al,Si} = -4622.28 - 0.03T + (836.80 - 1.17T)x_{AlAl}$	[96]
	$\Delta g_{Cu,Mg} = -11506.00 + 1.22T - 2594.08x_{CuCu} - (5188.16 + 2.24T)x_{MgMg}$	This work
	$\Delta g_{Cu,Si} = -30899.29 + 12.55T + (11924.40 - 13.39T)x_{CuCu} + (16401.28 - 17.15T)x_{SiSi}$	[97]
	$\Delta g_{Mg,Si} = -22670.17 + 6.92T + (3385.38 - 2.594T)x_{MgMg} - 3849.28x_{SiSi}$	[96]
	$g_{Al,Cu,(Mg)}^{001} = -4184.00 + 4.18T$, $g_{Cu,Mg,(Al)}^{001} = -37656.00 + 25.10T$	This work
	$g_{Al,Cu,(Si)}^{001} = -1255.20 - 1.67T$, $g_{Al,Si,(Cu)}^{001} = -1046.00 - 7.11T$, $g_{Cu,Si,(Al)}^{001} = -1255.20 + 0.63T$	This work
	$g_{Al,Mg,(Si)}^{001} = -10319.56$, $g_{Al,Si,(Mg)}^{001} = 7683.08$	[96]
	$g_{Mg,Si,(Cu)}^{001} = -25104.00$	This work
fcc_A1 (Al, Cu, Mg, Si)(Va)	$L_{Al,Cu} = -53520 + 2T + (38590 - 2T)(x_{Al} - x_{Cu}) + 1170(x_{Al} - x_{Cu})^2$	[94]
	$L_{Al,Mg} = 2803.66 + 0.52T + (-280.75 + 0.54T)(x_{Al} - x_{Mg})$	[95]

	$L_{Al,Si} = -3143.78 + 0.39T$	[99]
	$L_{Cu,Mg} = -21934.09 + 4.80T$	This work
	$L_{Cu,Si} = -7470.06 + 0.75T + (-84383.10 + 8.44T)(x_{Cu} - x_{Si})$	[97]
	$L_{Mg,Si} = -7148.79 + 0.89T$	[100]
	$L_{Al,Cu,Si} = (83680 - 39.75T)x_{Cu} - 836.80x_{Si}$	This work
	$L_{Al,Cu,Mg} = 83680\,x_{Al} + 83680\,x_{Cu}$	This work
	$L_{Cu,Mg,Si} = -163176\,x_{Cu}$	This work
hcp_A3 (Al, Cu, Mg, Si)(Va)	$L_{Al,Mg} = 2510.40$	[95]
	$L_{Al,Si} = -3143.78 + 0.39T$	[99]
	$L_{Cu,Mg} = -7437.60 + 25.40T$	This work
	$L_{Cu,Si} = -28001.58 + 8.07T + (-68445.56 + 1.66T)(x_{Cu} - x_{Si})$	[97]
	$L_{Mg,Si} = -7148.79 + 0.89T$	[100]
	$L_{Al,Cu,Si} = 38107\,x_{Al} - 2259360\,x_{Cu} + 9623200\,x_{Si}$	This work
bcc_A2	$L_{Al,Cu} = -73554 + 4.0T + (51500 - 11.84T)(x_{Al} - x_{Cu})$	[94]

(Al, Cu, Mg, Si)$(Va)_3$	$L_{Al,Mg} = 5020.8$	[95]
	$L_{Al,Si} = 2092$	[96]
	$L_{Cu,Mg} = -5439.2$	This work
	$L_{Cu,Si} = -120000.00 + 99.49T + (47978.99 - 125.33T)(x_{Cu} - x_{Si})$	[97]
	$L_{Mg,Si} = -7148.79 + 0.89T$	[100]
	$L_{Al,Cu,Si} = 78241\,x_{Al} - (33472 + 16.74T)x_{Cu} + 1578623\,x_{Si}$	This work
AlCu_δ $(Al)_2(Cu)_3$	$G^o_{Al:Cu} = -106700 + 3T + 2{}^oG^{fcc}_{Al} + 3{}^oG^{fcc}_{Cu}$	[94]
AlCu_ε (Al,Cu)(Cu)	$G^o_{Al:Cu} = -36976 + 1.2T + {}^oG^{fcc}_{Al} + {}^oG^{fcc}_{Cu}$ $G^o_{Cu:Cu} = 2{}^oG^{bcc}_{Cu}$ $L^0_{Al,Cu:Cu} = 7600 - 24T$ $L^1_{Al,Cu:Cu} = -72000$	[94]
AlCu_η (Al,Cu)(Cu)	$G^o_{Al:Cu} = -40560 + 3.14T + {}^oG^{fcc}_{Al} + {}^oG^{fcc}_{Cu}$ $G^o_{Cu:Cu} = 2{}^oG^{bcc}_{Cu}$ $L^0_{Al,Cu:Cu} = -25740 - 20T$	[94]
AlCu_θ $(Al)(Al,Cu)_2$	$G^o_{Al:Al} = 3{}^oG^{bcc}_{Al}$ $G^o_{Al:Cu} = -47406 + 6.75T + {}^oG^{fcc}_{Al} + 2{}^oG^{fcc}_{Cu}$ $L^0_{Al:Al,Cu} = 2211$	[94]

γ_L $(Al,Si)_4(Al,Cu)(Cu)_8$	$G^o_{Al:Al:Cu} = -300716 + 390T - 52T\ln T + 5^oG^{fcc}_{Al} + 8^oG^{fcc}_{Cu}$	[94]
	$G^o_{Al:Cu:Cu} = -280501 + 379.6T - 52T\ln T + 4^oG^{fcc}_{Al} + 9^oG^{fcc}_{Cu}$	[94]
	$G^o_{Si:Al:Cu} = 41840 + 4^oG^{dia}_{Si} + {}^oG^{fcc}_{Al} + 8^oG^{fcc}_{Cu}$	This work
	$G^o_{Si:Cu:Cu} = -41840 + 4^oG^{dia}_{Si} + 9^oG^{fcc}_{Cu}$	This work
	$L^0_{Al,Si:*:Cu} = -83680$	This work
γ_H $(Al)_4(Al,Cu)(Cu)_8$	$G^o_{Al:Al:Cu} = -219258 - 45.5\cdot T + 5^oG^{fcc}_{Al} + 8^oG^{fcc}_{Cu}$ $G^o_{Al:Cu:Cu} = -200460 - 58.5T + 4^oG^{fcc}_{Al} + 9^oG^{fcc}_{Cu}$	[94]
C15 $(Al, Cu, Mg, Si)_2(Al, Cu, Mg)$	$G^o_{Al:Al} = 15000 + 3^oG^{fcc}_{Al}$	[29]
	$G^o_{Al:Cu} = 15000 + 2^oG^{fcc}_{Al} + {}^oG^{fcc}_{Cu}$	[29]
	$G^o_{Al:Mg} = 5039.84 - 6.28T + 2^oG^{fcc}_{Al} + {}^oG^{hcp}_{Mg}$	This work
	$G^o_{Cu:Al} = 15000 + 2^oG^{fcc}_{Cu} + {}^oG^{fcc}_{Al}$	[29]
	$G^o_{Cu:Cu} = 15000 + 3^oG^{fcc}_{Cu}$	[29]
	$G^o_{Cu:Mg} = -55863.51 + 361.90T - 67.51T\ln T - 0.01538T^2 + 9.41409\times10^{-7}T^3$ $+ 134705.49\times10^{-1}T^{-1}$	This work

	$G^{o}_{Mg:Al} = 64170.01 + 2^{o}G^{hcp}_{Mg} + {}^{o}G^{fcc}_{Al}$	This work
	$G^{o}_{Mg:Cu} = 104970.96 - 16.46T + 2^{o}G^{hcp}_{Mg} + {}^{o}G^{fcc}_{Cu}$	[29]
	$G^{o}_{Mg:Mg} = 22740 + 3^{o}G^{hcp}_{Mg}$	This work
	$G^{o}_{Si:Al} = 15000 + 2^{o}G^{fcc}_{Si} + {}^{o}G^{fcc}_{Al}$	[29]
	$G^{o}_{Si:Cu} = 112500 + 2^{o}G^{fcc}_{Si} + {}^{o}G^{fcc}_{Cu}$	This work
	$G^{o}_{Si:Mg} = 75000 + 2^{o}G^{fcc}_{Si} + {}^{o}G^{hcp}_{Mg}$	This work
	$L^{0}_{Cu,Mg:*} = 16776.95$	This work
	$L^{0}_{*:Cu,Mg} = 8691.45$	This work
	$L^{0}_{Cu,Si:*} = -191096.09 - 29.29T$	This work
	$L^{0}_{Mg,Si:*} = 400714.49$	This work
	$L^{0}_{Al,Cu:Mg} = -165307.23 + 57.32T$, $L^{1}_{Al,Cu:Mg} = 79752.80$	This work
C14 $(Al, Cu, Mg)_2(Al, Cu, Mg)$	$G^{o}_{Al:Al} = 15000 + 3^{o}G^{fcc}_{Al}$	[29]
	$G^{o}_{Al:Cu} = 15000 + 2^{o}G^{fcc}_{Al} + {}^{o}G^{fcc}_{Cu}$	[29]

	$G^{o}_{Al:Mg} = 17995.15 + 8.37T + 2{}^{o}G^{fcc}_{Al} + {}^{o}G^{hcp}_{Mg}$	This work
	$G^{o}_{Cu:Al} = 15000 + 2{}^{o}G^{fcc}_{Cu} + {}^{o}G^{fcc}_{Al}$	[29]
	$G^{o}_{Cu:Cu} = 15000 + 3{}^{o}G^{fcc}_{Cu}$	[29]
	$G^{o}_{Cu:Mg} = -55779.83 + 361.90T - 67.51T\ln T - 0.01538T^{2} + 9.41409\times10^{-7}T^{3}$ $+ 134705.49\times10^{-1}T^{-1}$	This work
	$G^{o}_{Mg:Al} = 51618 + 2{}^{o}G^{hcp}_{Mg} + {}^{o}G^{fcc}_{Al}$	This work
	$G^{o}_{Mg:Cu} = 112468.06 - 16.46T + 2{}^{o}G^{hcp}_{Mg} + {}^{o}G^{fcc}_{Cu}$	This work
	$G^{o}_{Mg:Mg} = 22740 + 3{}^{o}G^{hcp}_{Mg}$	This work
	$L^{0}_{Cu,Mg:*} = 16776.95$	This work
	$L^{0}_{*:Cu,Mg} = 8691.45$	This work
	$L^{0}_{Al,Cu:Mg} = -213584.32 + 58.58T$, $L^{1}_{Al,Cu:Mg} = -5373.83 - 33.47T$	This work
C36 $(Al, Cu, Mg)_2(Al, Cu, Mg)$	$G^{o}_{Al:Al} = 15000 + 3{}^{o}G^{fcc}_{Al}$	[29]
	$G^{o}_{Al:Cu} = 15000 + 2{}^{o}G^{fcc}_{Al} + {}^{o}G^{fcc}_{Cu}$	[29]
	$G^{o}_{Al:Mg} = -9865.64 + 8.368T + 2{}^{o}G^{fcc}_{Al} + {}^{o}G^{hcp}_{Mg}$	This work

	$G^{o}_{Cu:Al} = 15000 + 2{}^{o}G^{fcc}_{Cu} + {}^{o}G^{fcc}_{Al}$	[29]
	$G^{o}_{Cu:Cu} = 15000 + 3{}^{o}G^{fcc}_{Cu}$	[29]
	$G^{o}_{Cu:Mg} = -48834.4 + 361.90T - 67.51T\ln T - 0.01538T^{2} + 9.41409\times10^{-7}T^{3}$ $+ 134705.49\times10^{-1}T^{-1}$	This work
	$G^{o}_{Mg:Al} = 55425.45 + 2{}^{o}G^{hcp}_{Mg} + {}^{o}G^{fcc}_{Al}$	This work
	$G^{o}_{Mg:Cu} = 112000.10 - 16.46T + 2{}^{o}G^{hcp}_{Mg} + {}^{o}G^{fcc}_{Cu}$	This work
	$G^{o}_{Mg:Mg} = 22740 + 3{}^{o}G^{hcp}_{Mg}$	This work
	$L^{0}_{Cu,Mg:*} = 16776.95$	This work
	$L^{0}_{*:Cu,Mg} = 8691.45$	This work
	$L^{0}_{Al,Cu:Mg} = -183926.03 + 77.24T$, $L^{1}_{Al,Cu:Mg} = 130086.32 - 43.93T$	This work
τ $(Mg)_{26}(Al, Mg)_{6}(Al, Mg, Cu)_{48}(Al)$	$G^{o}_{Mg:Al:Al:Al} = 26{}^{o}G^{hcp}_{Mg} + 55{}^{o}G^{fcc}_{Al}$	[95]
	$G^{o}_{Mg:Al:Cu:Al} = -502080 + 26{}^{o}G^{hcp}_{Mg} + 7{}^{o}G^{fcc}_{Al} + 48{}^{o}G^{fcc}_{Cu}$	This work
	$G^{o}_{Mg:Al:Mg:Al} = 8368000 + 74{}^{o}G^{hcp}_{Mg} + 7{}^{o}G^{fcc}_{Al}$	[95]
	$G^{o}_{Mg:Mg:Al:Al} = 18828 + 32{}^{o}G^{hcp}_{Mg} + 49{}^{o}G^{fcc}_{Al}$	[95]

	$G^{o}_{Mg:Mg:Cu:Al} = 158992 + 32{}^{o}G^{hcp}_{Mg} + 48{}^{o}G^{fcc}_{Cu} + {}^{o}G^{fcc}_{Al}$	This work
	$G^{o}_{Mg:Mg:Mg:Al} = 8368000 + 80{}^{o}G^{hcp}_{Mg} + {}^{o}G^{fcc}_{Al}$	[95]
	$L^{0}_{Mg:*:Al,Cu:Al} = -4649190.09 + 1922.96T$	This work
	$L^{0}_{Mg:*:Al,Mg:Al} = -3154680.02 - 379.40T$	[95]
	$L^{0}_{Mg:*:Cu,Mg:Al} = -4626720.50$	This work
AlMg_β $Al_{19}(Al, Mg)_2Mg_{12}$	$G^{o}_{Al:Al:Mg} = -82111.42 - 13.81T + 12{}^{o}G^{hcp}_{Mg} + 21{}^{o}G^{fcc}_{Al}$	[95]
	$G^{o}_{Al:Mg:Mg} = -72446.38 - 27.61T + 14{}^{o}G^{hcp}_{Mg} + 19{}^{o}G^{fcc}_{Al}$	
AlMg_γ $Mg_{10}(Al, Mg)_{24}(Al, Mg)_{24}$	$G^{o}_{Mg:Al:Al} = 178762.94 - 203T + 10{}^{o}G^{hcp}_{Mg} + 48{}^{o}G^{fcc}_{Al}$	[95]
	$G^{o}_{Mg:Al:Mg} = 359507.52 - 197.67T + 34{}^{o}G^{hcp}_{Mg} + 24{}^{o}G^{fcc}_{Al}$	
	$G^{o}_{Mg:Mg:Al} = -208741.60 + 78.46T + 34{}^{o}G^{hcp}_{Mg} + 24{}^{o}G^{fcc}_{Al}$	
	$G^{o}_{Mg:Mg:Mg} = 359154.56 - 174.64T + 58{}^{o}G^{hcp}_{Mg}$	
S $(Al, Si)_2CuMg$	$G^{o}_{Al:Cu:Mg} = -63200 + 3.11T + 2{}^{o}G^{fcc}_{Al} + {}^{o}G^{fcc}_{Cu} + {}^{o}G^{hcp}_{Mg}$	This work
	$G^{o}_{Si:Cu:Mg} = 2{}^{o}G^{dia}_{Si} + {}^{o}G^{fcc}_{Cu} + {}^{o}G^{hcp}_{Mg}$	

	$L^{0}_{Al,Si:Cu:Mg} = -75312$	
Al_9Cu_{11}	$G^{o}_{Al:Cu} = -420000 + 18.0T + 9^{o}G^{fcc}_{Al} + 11^{o}G^{fcc}_{Cu}$	[94]
Cu_9Si_2	$G^{o}_{Cu:Si} = -36809.99 - 49.32T + 9^{o}G^{fcc}_{Cu} + 2^{o}G^{dia}_{Si}$	[97]
$Cu_{15}Si_4$	$G^{o}_{Cu:Si} = -93099.98 - 66.05T + 15^{o}G^{fcc}_{Cu} + 4^{o}G^{dia}_{Si}$	[97]
$Cu_{19}Si_6$	$G^{o}_{Cu:Si} = -149913.88 - 11.55T + 19^{o}G^{fcc}_{Cu} + 6^{o}G^{dia}_{Si}$	[97]
$Cu_{33}Si_7$	$G^{o}_{Cu:Si} = -167999.95 - 139.09T + 33^{o}G^{fcc}_{Cu} + 7^{o}G^{dia}_{Si}$	[97]
$Al_{30}Mg_{23}$	$G^{o}_{Al:Mg} = -116327.71 - 72.99T + 30^{o}G^{fcc}_{Al} + 23^{o}G^{hcp}_{Mg}$	[95]
Mg_2Si	$G^{o}_{Mg:Si} = -65100 + 8.04T + 2^{o}G^{hcp}_{Mg} + {}^{o}G^{dia}_{Si}$	[100]
Cu_3Mg_2Si	$G^{o}_{Cu:Mg:Si} = -125980 - 4T + 3^{o}G^{fcc}_{Cu} + 2^{o}G^{hcp}_{Mg} + {}^{o}G^{dia}_{Si}$	This work
$Cu_{16}Si_7Mg_6$	$G^{o}_{Cu:Mg:Si} = -491510 - 30T + 16^{o}G^{fcc}_{Cu} + 6^{o}G^{hcp}_{Mg} + 7^{o}G^{dia}_{Si}$	This work
$Al_7Cu_3Mg_6$	$G^{o}_{Al:Cu:Mg} = -217887.81 + 7.56T + 7^{o}G^{fcc}_{Al} + 3^{o}G^{fcc}_{Cu} + 6^{o}G^{hcp}_{Mg}$	This work
$Al_5Cu_6Mg_2$	$G^{o}_{Al:Cu:Mg} = -288681.51 + 18.94T + 5^{o}G^{fcc}_{Al} + 6^{o}G^{fcc}_{Cu} + 2^{o}G^{hcp}_{Mg}$	This work
$Cu_2Si_7Al_3Mg_9$	$G^{o}_{Cu:Si:Al:Mg} = -375900 + 22.89T + 2^{o}G^{fcc}_{Cu} + 7^{o}G^{dia}_{Si} + 3^{o}G^{fcc}_{Al} + 9^{o}G^{hcp}_{Mg}$	This work

Table 9.3 Invariant reactions in the Cu-Mg system.

Reaction type	Reaction (at. % Cu)			Temperature °C	Method	Ref.
Eutectic	Liquid = fcc_A1 + Laves_C15 (Cu_2Mg)					
	77.5	100	66.66	890	TA	[101]
	77.0			725	TA	[4]
	76.5			728-730	TA	[6]
	76.9	93.5		722	TA	[5]
	69	93.7		725±3	TA	[7]
				725	Cal.	[1]
				725	Cal.	[2]
				725.8	Cal.	[3]
	78.7	92.6	68.26	722	Cal.	This work
Congruent	Liquid = Laves_C15					
	66.66	66.66		940	TA	[101]
				799	TA	[4]
				797	TA	[6]
				819	TA	[5]
				793±4	TA	[7]
				800	Cal.	[1]
				793	Cal.	[2]
				793	Cal.	[3]
	66.91	66.91		794	Cal.	This work
Eutectic	Liquid = $CuMg_2$ + Laves_C15					
	47.1	33.33	66.66	540	TA	[101]
	41.48			555	TA	[4]
	43.7-44.3			555	TA	[6]
	41.9			552	TA	[5]
			64.7	552±2	TA	[7]
				552.5	Cal.	[1]

				552.2	Cal.	[2]
				553.5	Cal.	[3]
	40.42	33.33	65.72	549	Cal.	This work
Congruent	Liquid = $CuMg_2$					
	33.33	33.33		550	TA	[101]
				570	TA	[4]
				568-571	TA	[6]
				568	TA	[5]
				568±2	TA	[7]
				568	Cal.	[1]
				568	Cal.	[2]
				567.5	Cal.	[3]
	33.33	33.33		562.5	Cal.	This work
Eutectic	Liquid = $CuMg_2$ + hcp_A3					
	14.1	33.33	0	472	TA	[101]
	16.0			480	TA	[4]
	14.6		0.012	485	TA	[6]
	14.5		0.012	485	TA	[5]
				488±2	TA	[7]
				486	Cal.	[1]
				485	Cal.	[2]
				484	Cal.	[3]
	15.84	33.33	0.0017	485	Cal.	This work

Table 9.4 Invariant reactions involving liquid in the Al-Cu-Mg system.

Reaction type	Reaction			Temperature °C	Method	Ref.
	at.% Al	at.% Cu	at.% Mg			
Eutectic	Liquid + bcc_A2 + γ_L = γ_H					
	39.35	56.79	3.86	874	Cal.	This work
Quasi-Peritectic	Liquid + bcc_A2 = AlCu_ε + γ_L					
	43.06	53.25	3.68	831	Cal.	This work
Quasi-Peritectic	Liquid + γ_H = γ_L + C15					
	26.42	60.60	12.97	809	Cal.	This work
Quasi-Peritectic	Liquid + γ_H = bcc_A2 + C15					
	21.30	65.46	13.24	799	Cal.	This work
Quasi-Peritectic	Liquid + bcc_A2 = fcc_A1 + C15					
	13.91	71.61	14.48	777	Cal.	This work
Quasi-Peritectic	Liquid + γ_L = AlCu_ε + C15					
	38.47	50.66	10.87	746.5	Cal.	This work
Peritectic	Liquid + AlCu_ε + C15 = V					
	42.05	47.15	10.79	725.5	Cal.	This work
Quasi-Peritectic	Liquid + AlCu_ε = V + AlCu_η					
	59.59	34.74	5.67	606	Cal.	This work
Peritectic	Liquid + C14 + C15 = S					
	60.24	20.50	19.25	576	Cal.	This work
Quasi-Peritectic	Liquid + C15 = S + V					
	61.00	25.07	13.92	567	Cal.	This work
Quasi-Peritectic	Liquid + AlCu_η = AlCu_θ + V					
	63.48	30.80	5.71	565	Cal.	This work
Quasi-Peritectic	Liquid + V = S + AlCu_θ					
	65.66	24.31	10.03	532	Cal.	This work
Eutectic	Liquid = S + AlCu_θ + fcc_A1					
	74.00	15.82	10.18	495	Cal.	This work

	78.58	13.35	8.07	500	TA	[30]
	75.39	15.07	9.55	500	TA	[33]
	74.56	17.15	8.29	507	TA	[36]
	73.37	17.13	9.50	506	TA	[98]
	74.29	17.21	8.50	506	TA	[35]
				503	DTA	[38]
Quasi-Peritectic	Liquid + C14 = S + U					
	64.81	7.62	27.57	493	Cal.	This work
Quasi-Peritectic	Liquid + C15 = hcp_A3 + C14					
	20.58	5.83	73.58	484	Cal.	This work
Peritectic	Liquid + S + U = τ					
	66.21	7.01	26.78	482	Cal.	This work
	53.62	6.69	39.68	520	TA	[33]
Eutectic	Liquid = $CuMg_2$ + hcp_A3 + C15					
	0.61	16.21	83.18	481	Cal.	This work
Quasi-Peritectic	Liquid + S = τ + fcc_A1					
	68.73	6.68	24.59	474	Cal.	This work
	66.37	4.84	28.78	465	TA	[30]
	66.35	4.37	29.28	465	TA	[33]
	65.91	4.37	29.72	467	TA	[36]
Quasi-Peritectic	Liquid + C14 = U + hcp_A3					
	26.05	3.74	70.21	455	Cal.	This work
Peritectic	Liquid + AlMg_β + AlMg_γ = τ					
	59.22	1.04	39.74	445	Cal.	This work
Quasi-Peritectic	Liquid + fcc_A1 = τ + AlMg_β					
	62.23	1.15	36.62	446	Cal.	This work
	63.85	1.25	34.89	447	TA	[30]
	63.73	0.62	35.65	445	TA	[33]
	64.04	1.12	34.84	451	TA	[36]
Quasi-Peritectic	Liquid + τ = U + AlMg_γ					

	40.49	2.32	57.18	445	Cal.	This work
Eutectic	Liquid = U + AlMg_γ + hcp_A3					
	30.38	1.92	67.70	428	Cal.	This work

Table 9.5 Invariant reactions involving liquid in the Al-Cu-Si system.

Reaction type	Reaction			Temperature °C	Method	Ref.
	at.% Al	at.% Cu	at.% Si			
Quasi-Peritectic	Liquid + fcc_A1 = hcp_A3 + bcc_A2					
	9.37	6.84	83.79	978	Cal.	This work
Quasi-Peritectic	Liquid + fcc_A1 = bcc_A2 + hcp_A3					
	0.031	16.51	83.46	851	Cal.	This work
Quasi-Peritectic	Liquid + bcc_A2 = CuSi_δ + hcp_A3					
	0.35	18.49	81.16	815	Cal.	This work
Eutectic	Liquid = CuSi_η + CuSi_δ + hcp_A3					
	0.48	18.81	80.71	812	Cal.	This work
Quasi-Peritectic	Liquid + γ_L = bcc_A2 + (Si)					
	23.89	18.10	58.01	761	Cal.	This work
Quasi-Peritectic	Liquid + bcc_A2 = γ_L + hcp_A3					
	11.39	19.28	69.33	757	Cal.	This work
Eutectic	Liquid = CuSi_η + γ_L + hcp_A3					
	9.48	21.03	69.49	731	Cal.	This work
Quasi-Peritectic	Liquid + bcc_A2 = AlCu_ε + (Si)					
	41.40	11.89	46.71	730	Cal.	This work
Eutectic	Liquid = CuSi_η + γ_L + (Si)					
	9.23	22.87	67.90	716	Cal.	This work
Quasi-Peritectic	Liquid + AlCu_ε = AlCu_η + (Si)					
	61.67	5.40	32.93	611	Cal.	This work
				615	TA	[55]
				608	TA	[54]
				606	DTA	[46]
	60.00	32.00	8.00	603	DTA	[57]
Quasi-Peritectic	Liquid + AlCu_η = AlCu_θ + (Si)					
	66.09	4.49	29.42	578	Cal.	This work
				575	TA	[55]

				573	TA	[54]
				574	DTA	[46]
	67.00	26.50	6.50	573	DTA	[57]
Eutectic	Liquid = AlCu_θ + fcc_A1 + (Si)					
	80.67	5.49	13.84	527	Cal.	This work
				522	TA	[55]
				522	TA	[54]
	80.60	5.97	13.43	524	TA	[102]
				524	DTA	[46]
	80.50	6.00	13.50	522	DTA	[57]

Table 9.6 Invariant reactions involving liquid in the Cu-Mg-Si system.

Reaction type	Reaction			Temperature °C	Method	Ref.
	at.% Cu	at.% Si	at.% Mg			
Peritectic	Liquid + fcc_A1 + bcc_A2 = hcp_A3					
	82.80	16.64	0.57	841	Cal.	This work
	84.0	15.7	0.3	824	TA	[67]
Peritectic	Liquid + CuSi_η + CuSi_δ = CuSi_ε					
	79.51	19.18	1.31	802	Cal.	This work
	77.3	18.5	4.2	763	TA	[67]
Quasi-Peritectic	Liquid + bcc_A2 = hcp_A3 + CuSi_δ					
	80.10	17.75	2.15	793.5	Cal.	This work
Peritectic	Liquid + D + E = (Si)					
	43.84	33.09	23.07	786	Cal.	This work
Peritectic	Liquid + hcp_A3 + CuSi_δ = CuSi_γ					
	78.53	17.25	4.23	765	Cal.	This work
Eutectic	Liquid = E + (Si) + Mg_2Si					
	28.67	35.63	35.70	762	Cal.	This work
Quasi-Peritectic	Liquid + hcp_A3 = fcc_A1 + CuSi_γ					
	78.26	17.06	4.68	760	Cal.	This work
	79.8	17.3	2.9	800	TA	[67]
Quasi-Peritectic	Liquid + CuSi_δ = CuSi_ε + CuSi_γ					
	76.67	18.07	5.24	752	Cal.	This work
	77.8	18.4	3.8	772	TA	[67]
Quasi-Peritectic	Liquid + CuSi_η = CuSi_ε + D					
	69.93	21.98	8.09	734	Cal.	This work
Eutectic	Liquid = fcc_A1 + C15 + E					
	74.93	8.45	16.61	724	Cal.	This work
Eutectic	Liquid = CuSi_η + (Si) + D					

	64.13	28.32	7.55	722	Cal.	This work
Quasi-Peritectic	Liquid + CuSi_ε = D + CuSi_γ					
	72.98	17.56	9.46	704	Cal.	This work
Quasi-Peritectic	Liquid + D = E + CuSi_γ					
	73.01	17.36	9.62	703	Cal.	This work
Quasi-Peritectic	Liquid + CuSi_γ = fcc_A1 + E					
	74.45	15.62	9.94	697	Cal.	This work
Quasi-Peritectic	Liquid + E = C15 + $CuMg_2$					
	38.02	0.22	61.76	556	Cal.	This work
Eutectic	Liquid = Mg_2Si + $CuMg_2$ + E					
	22.78	1.29	75.93	528	Cal.	This work

Table 9.7 Invariant reactions involving liquid in the Al rich corner of the Al-Cu-Mg-Si system.

Reaction type	Reaction			Temperature °C	Method	Ref.
	at.% Cu	at.% Mg	at.% Si			
Peritecitc	Liquid + S = fcc_A1 + Mg_2Si + τ					
				473	Cal.	This work
				464	TA	[71]
				471	TA	[72]
				467		[73]
Eutectic	Liquid = fcc_A1+ AlCu_θ + S + Mg_2Si					
				501	Cal.	This work
				500	TA	[71]
				500		[73]
				500±2	DTA	[68]
				503	Cal.	[103]
Eutectic	Liquid = fcc_A1 + τ + AlMg_β + Mg_2Si					
				446	Cal.	This work
				444	TA	[71]
				449.4	TA	[72]
				444-448		[73]
				450	Cal.	[103]
Peritectic	Liquid + Mg_2Si + (Si) = fcc_A1 + Q					
				540	Cal.	This work
				521	TA	[71]
				541.6	TA	[72]
				529		[73]

		532	DSC	[74]
Peritectic	Liquid + Mg_2Si = fcc_A1 + AlCu_θ + Q			
		515	Cal.	This work
		510	TA	[71]
		511-513	TA	[72]
		512		[73]
		510±1	DTA	[68]
		513	DSC	[74]
Eutectic	Liquid = (Si) + fcc_A1 + AlCu_θ + Q			
		512	Cal.	This work
		505	TA	[71]
		509.4	TA	[72]
		507		[73]
		506.5±1	DTA	[68]
		510	Cal.	[103]
		510	DSC	[74]

Figures

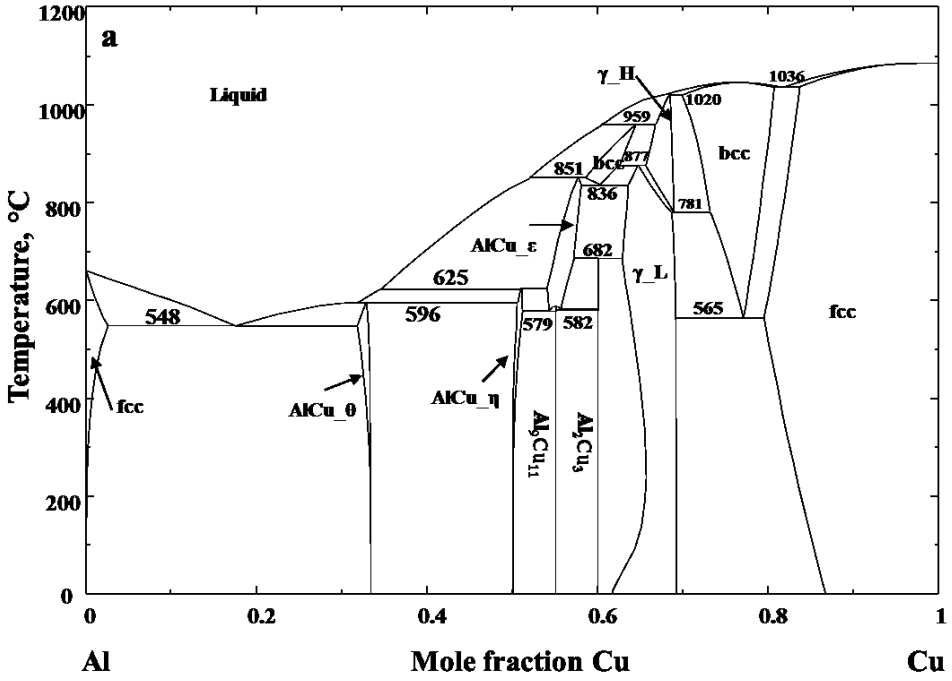
a
Liquid
γ_H
1036
1020
959
851
bcc
877
836
781
bcc
AlCu_ε
682
625
γ_L
548
596
579
582
565
fcc
fcc
AlCu_θ
AlCu_η
Al5Cu11
Al2Cu3
Temperature, °C
1200
1000
800
600
400
200
0
0
0.2
0.4
0.6
0.8
1
Al
Mole fraction Cu
Cu

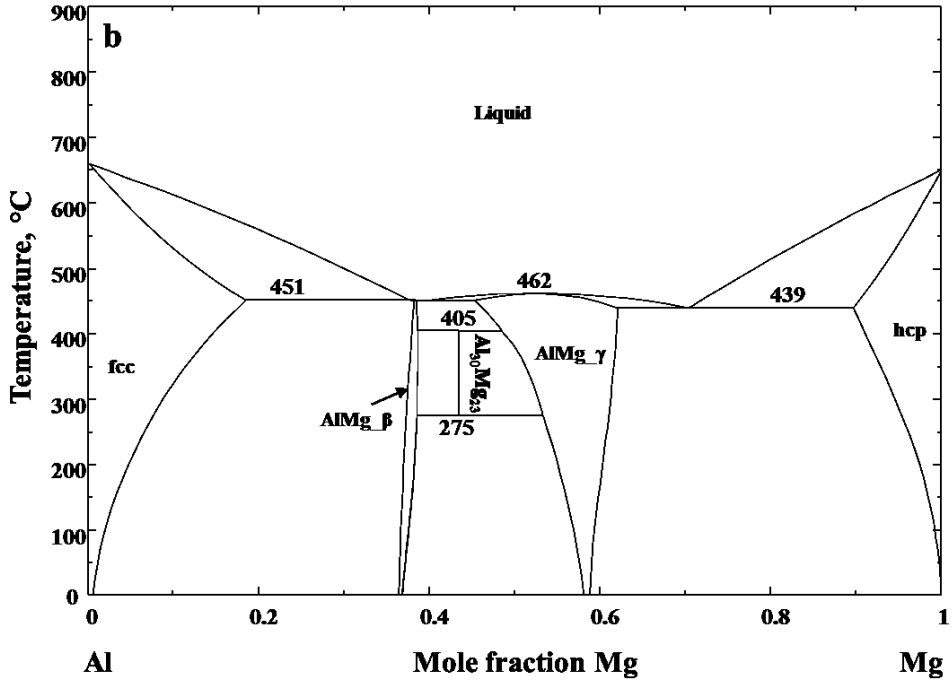
b
Liquid
451
462
439
405
hcp
fcc
AlMg_γ
Al30Mg23
AlMg_β
275
Temperature, °C
900
800
700
600
500
400
300
200
100
0
0
0.2
0.4
0.6
0.8
1
Al
Mole fraction Mg
Mg

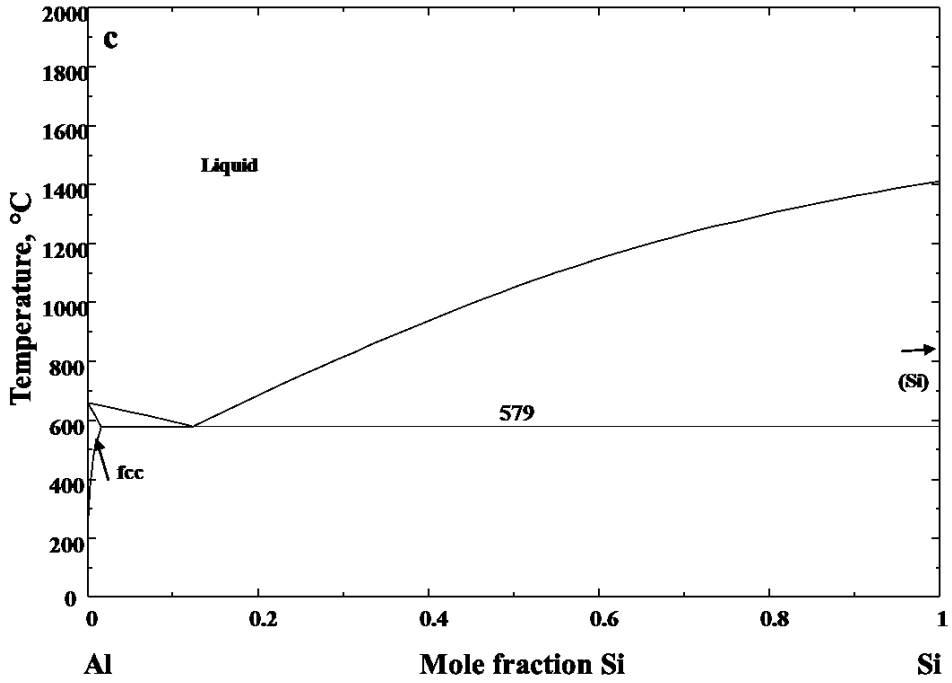
c
Liquid
579
fcc
(Si)
Temperature, °C
Al
Mole fraction Si
Si

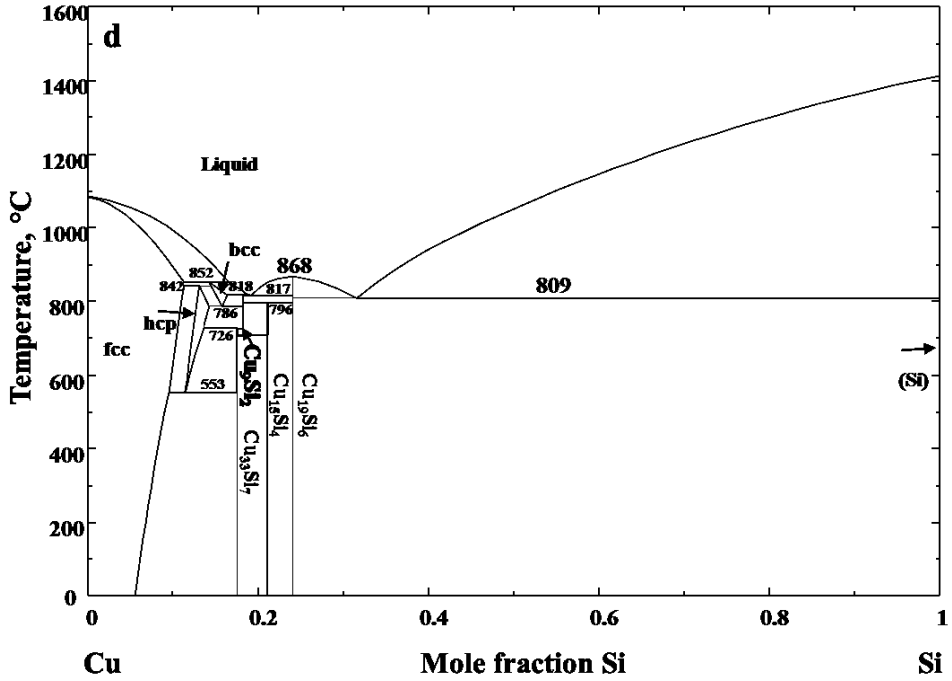
d
Liquid
bcc
868
852
842
818
817
809
796
786
hcp
726
fcc
553
(Si)
Temperature, °C
Cu
Mole fraction Si
Si

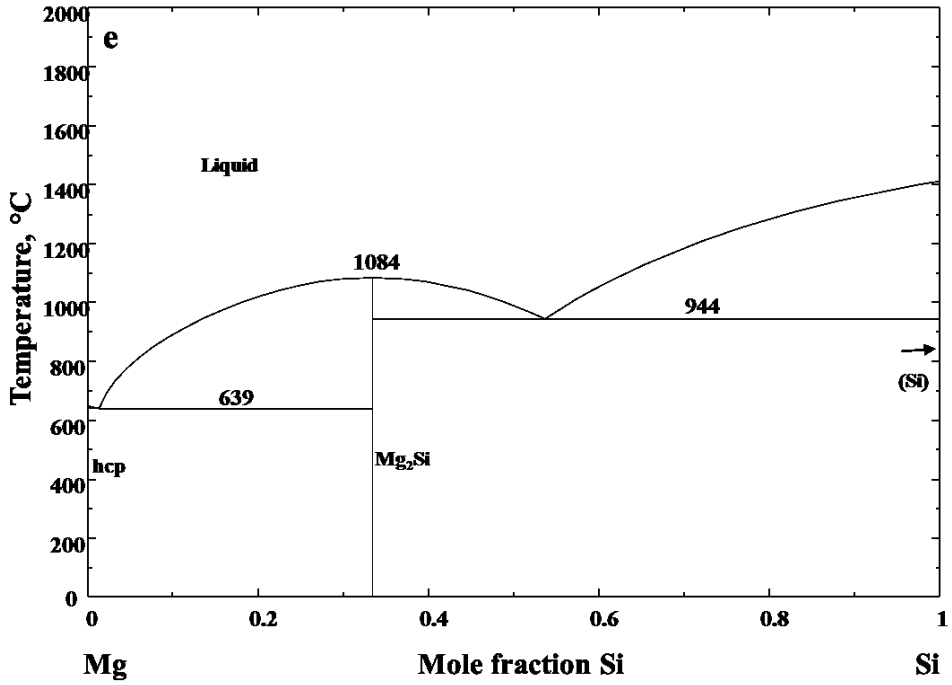

Fig. 9.1 Calculated phase diagrams of (a) the Al-Cu system, (b) the Al-Mg system, (c) the Al-Si system, (d) the Cu-Si system, and (e) the Mg-Si system.

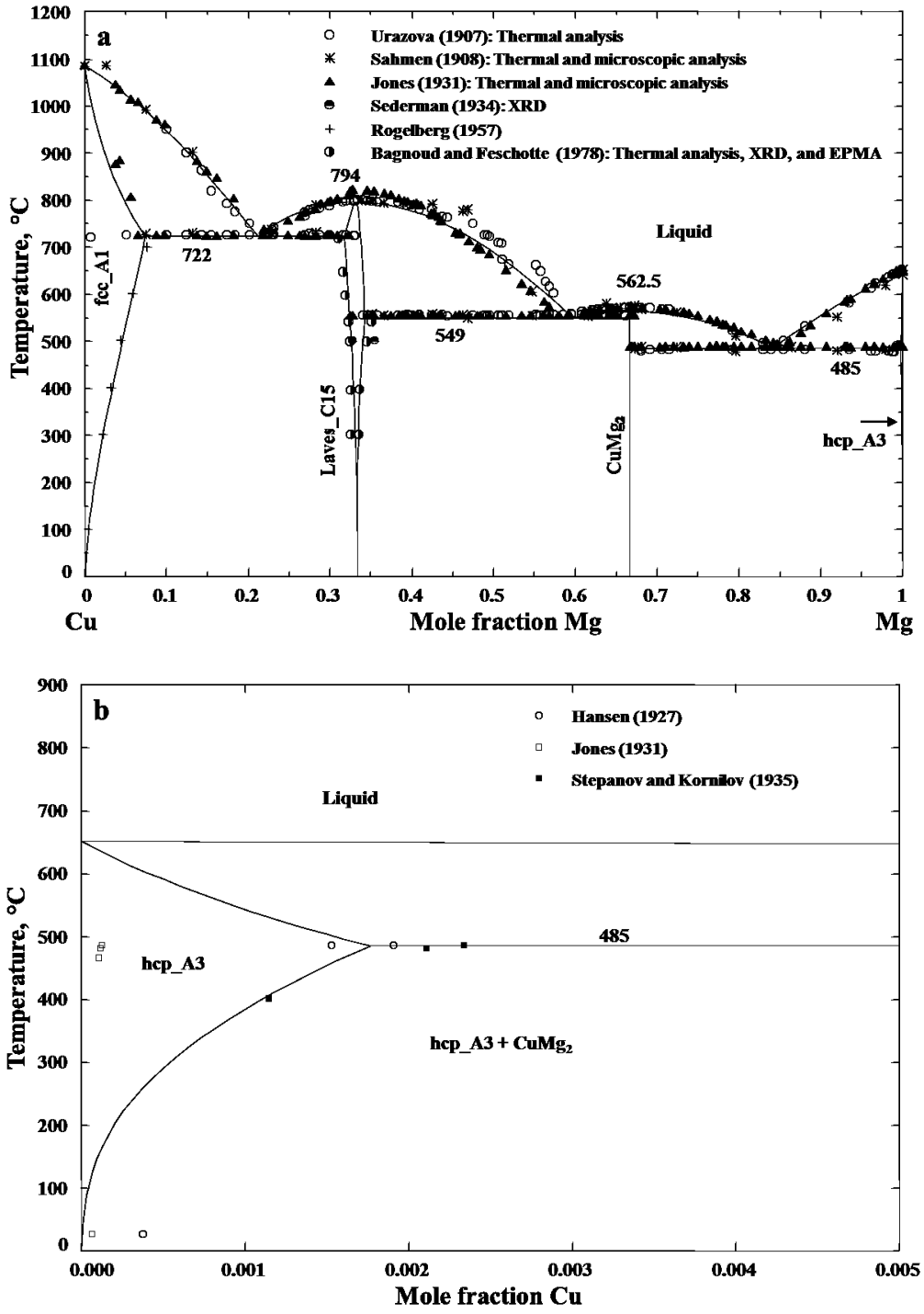

Fig. 9.2 Calculated phase diagrams of the Cu-Mg system along with the experimental data. (a) The entire composition range, and (b) enlarged Mg rich part.

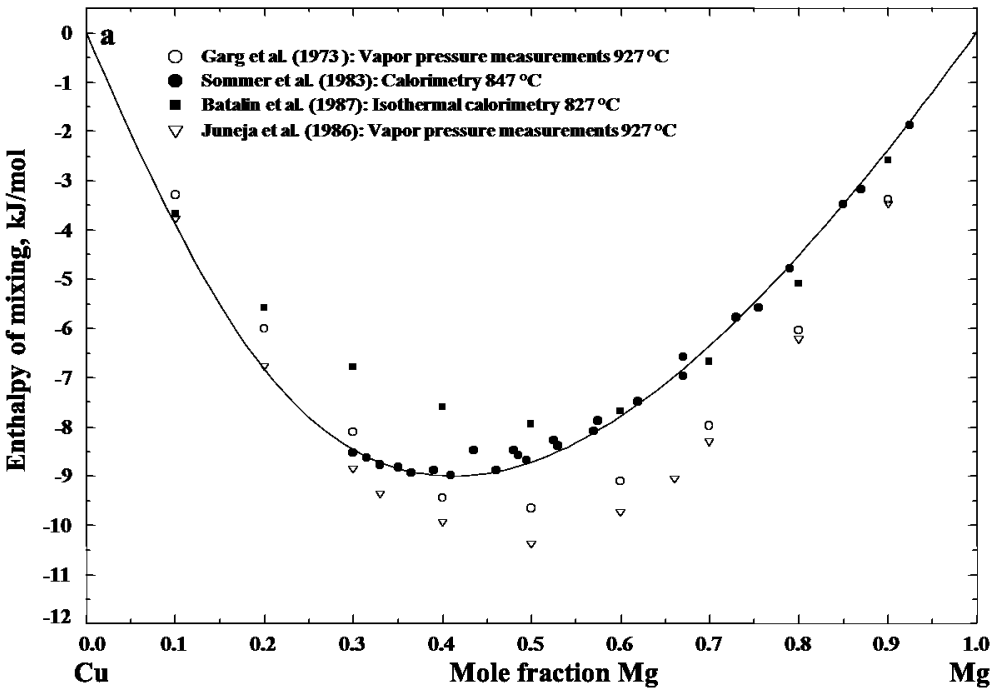
a
Garg et al. (1973): Vapor pressure measurements 927 °C
Sommer et al. (1983): Calorimetry 847 °C
Batalin et al. (1987): Isothermal calorimetry 827 °C
Juneja et al. (1986): Vapor pressure measurements 927 °C
Enthalpy of mixing, kJ/mol
0
-1
-2
-3
-4
-5
-6
-7
-8
-9
-10
-11
-12
0.0
0.1
0.2
0.3
0.4
0.5
0.6
0.7
0.8
0.9
1.0
Cu
Mole fraction Mg
Mg

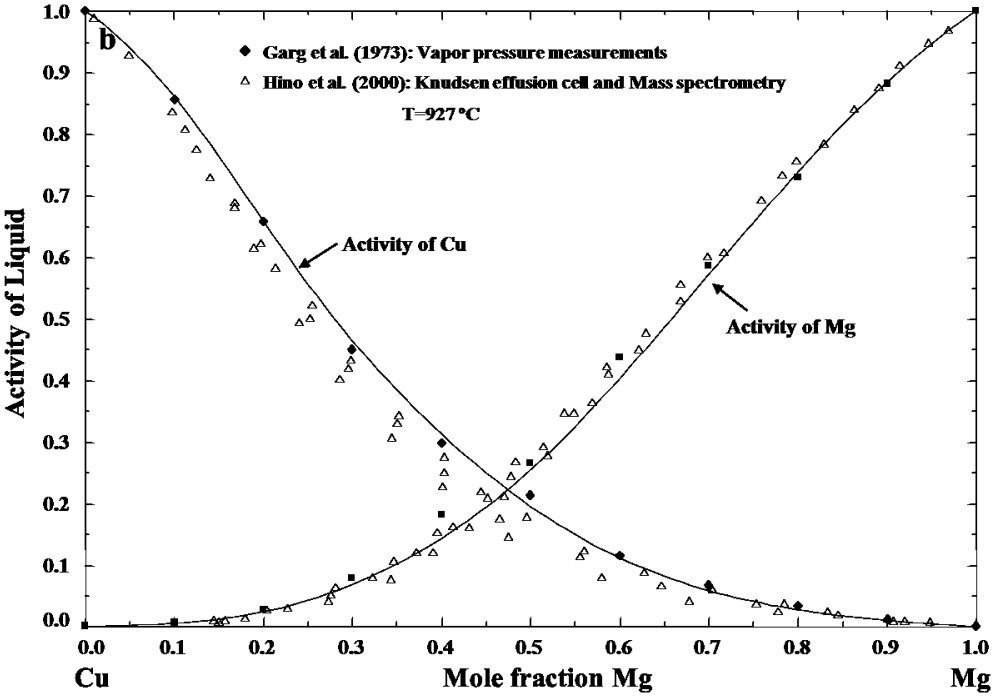
b
Garg et al. (1973): Vapor pressure measurements
Hino et al. (2000): Knudsen effusion cell and Mass spectrometry
T=927 °C
Activity of Cu
Activity of Mg
Activity of Liquid
1.0
0.9
0.8
0.7
0.6
0.5
0.4
0.3
0.2
0.1
0.0
0.0
0.1
0.2
0.3
0.4
0.5
0.6
0.7
0.8
0.9
1.0
Cu
Mole fraction Mg
Mg

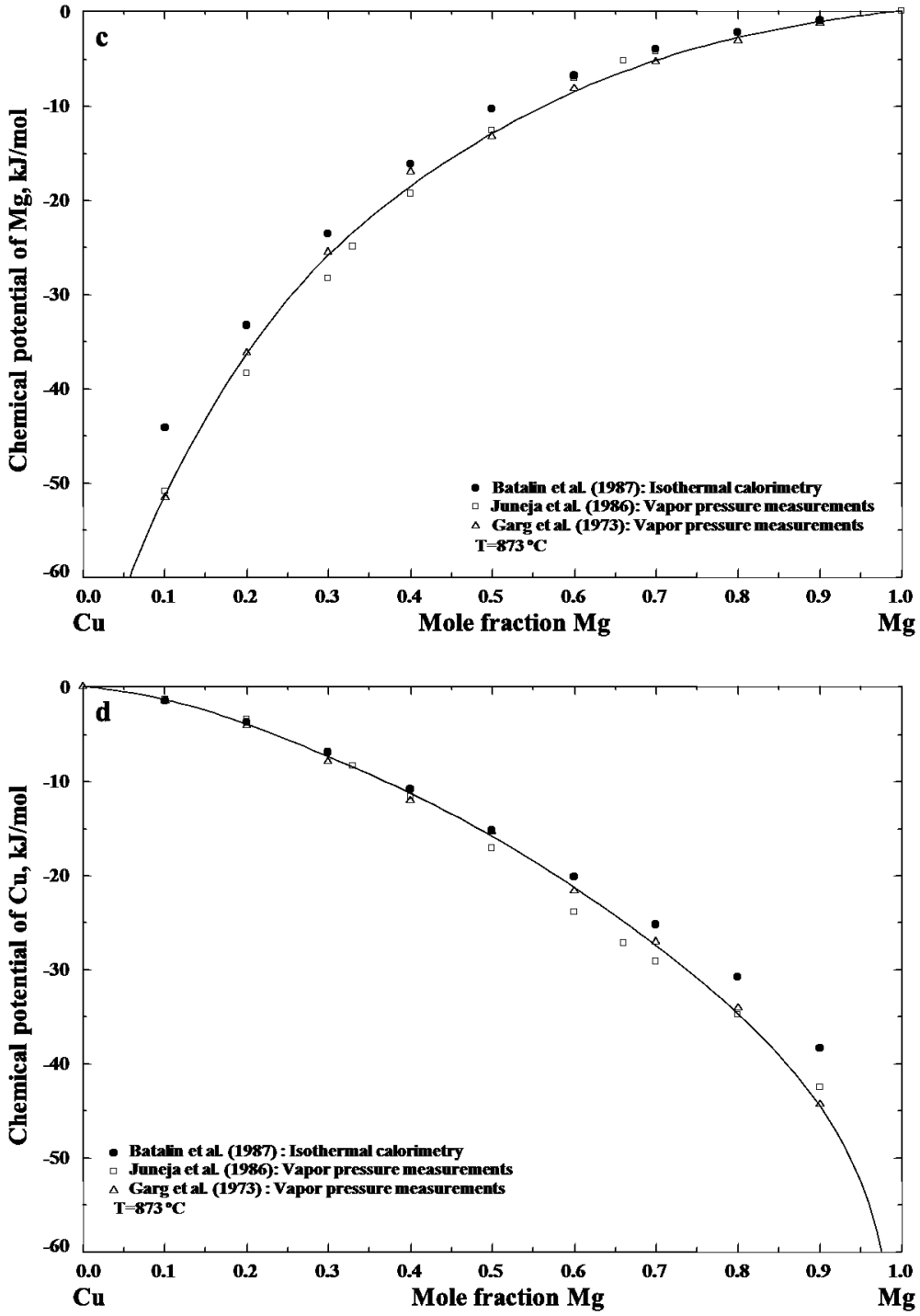

Fig. 9.3 Calculated thermodynamic properties of the Cu-Mg liquid phase along with the experimental data. (a) Enthalpy of mixing at 927 ºC, (b) activity of Cu and Mg with respect to the pure liquid standard at 972 ºC, (c) chemical potential of Mg at 873 ºC, and (d) chemical potential of Cu at 873 ºC.

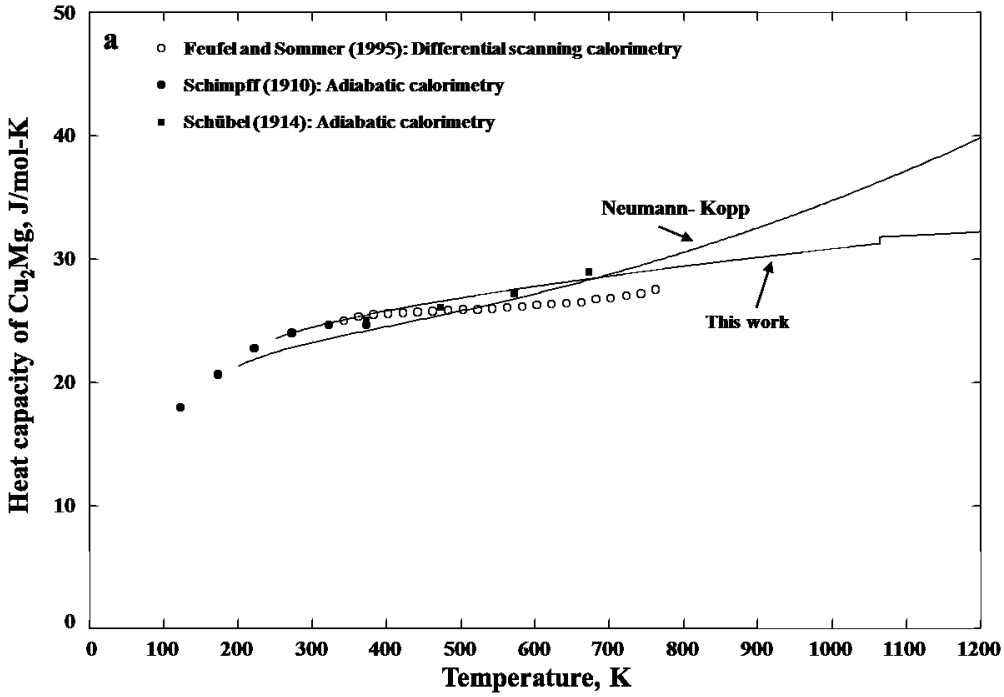
a
Feufel and Sommer (1995): Differential scanning calorimetry
Schimpff (1910): Adiabatic calorimetry
Schübel (1914): Adiabatic calorimetry
Neumann- Kopp
This work
Heat capacity of Cu2Mg, J/mol-K
Temperature, K
0
10
20
30
40
50
0
100
200
300
400
500
600
700
800
900
1000
1100
1200

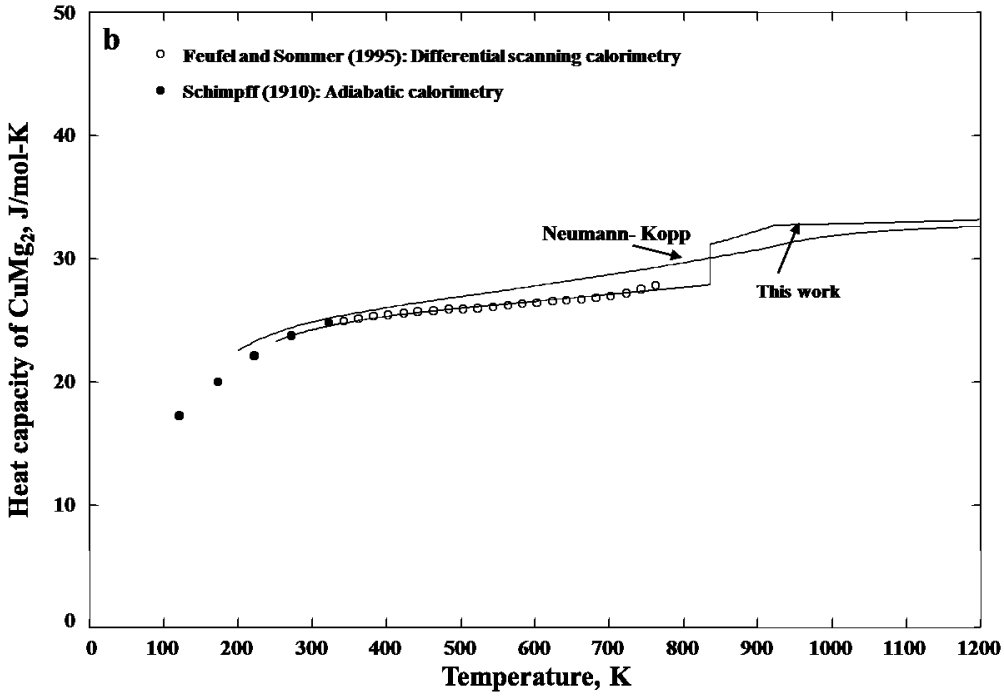
b
Feufel and Sommer (1995): Differential scanning calorimetry
Schimpff (1910): Adiabatic calorimetry
Neumann- Kopp
This work
Heat capacity of CuMg2, J/mol-K
Temperature, K
0
10
20
30
40
50
0
100
200
300
400
500
600
700
800
900
1000
1100
1200

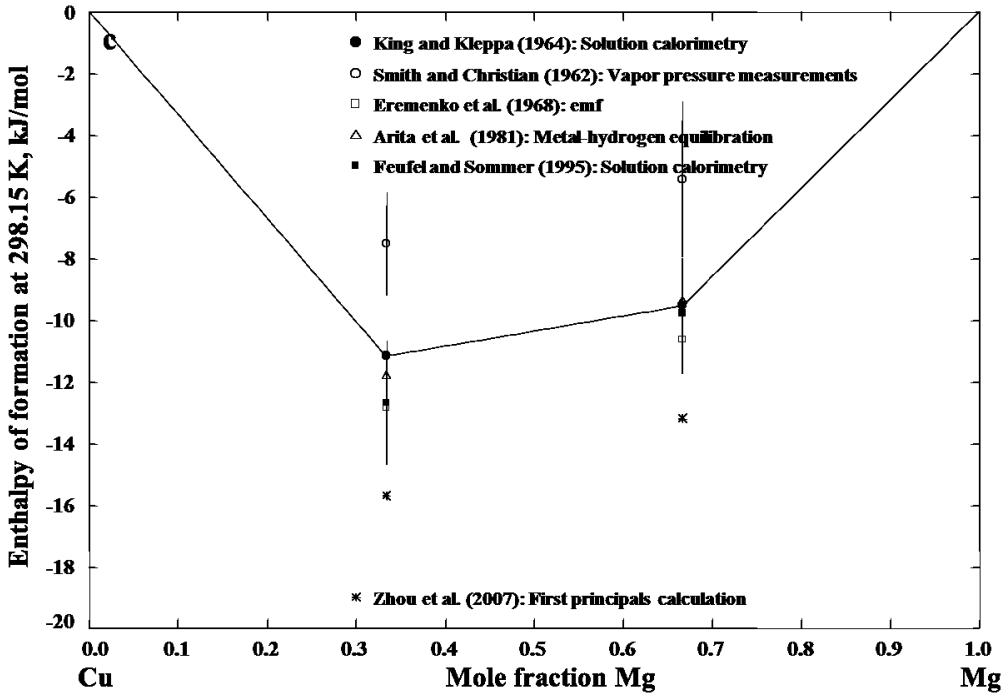
c
King and Kleppa (1964): Solution calorimetry
Smith and Christian (1962): Vapor pressure measurements
Eremenko et al. (1968): emf
Arita et al. (1981): Metal-hydrogen equilibration
Feufel and Sommer (1995): Solution calorimetry
Zhou et al. (2007): First principals calculation
Enthalpy of formation at 298.15 K, kJ/mol
0
-2
-4
-6
-8
-10
-12
-14
-16
-18
-20
0.0
0.1
0.2
0.3
0.4
0.5
0.6
0.7
0.8
0.9
1.0
Cu
Mole fraction Mg
Mg

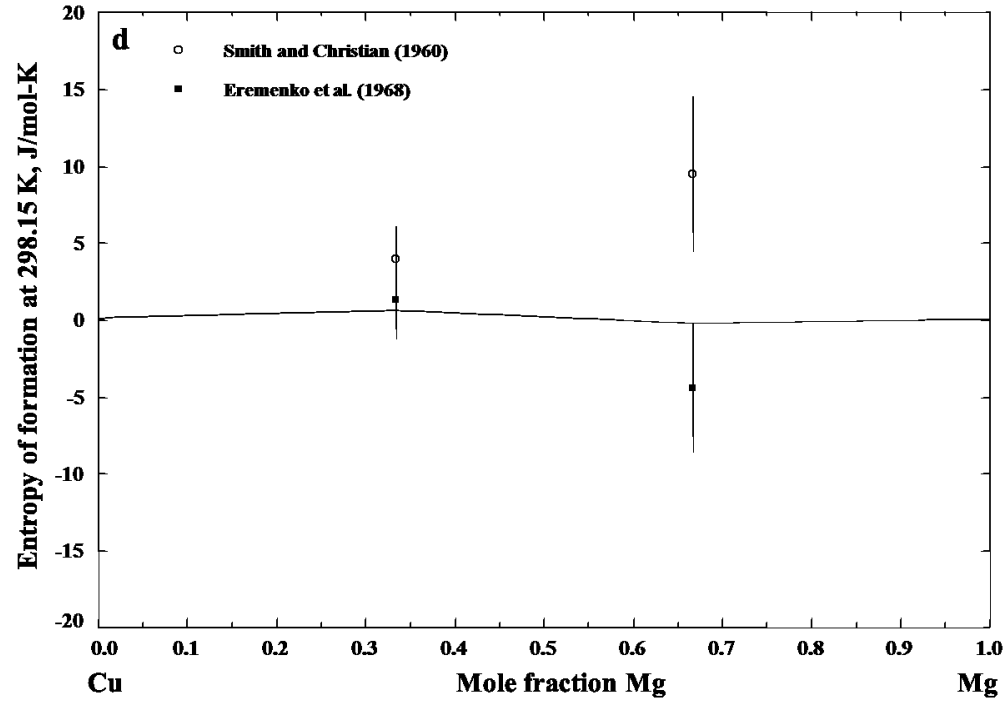
d
Smith and Christian (1960)
Eremenko et al. (1968)
Entropy of formation at 298.15 K, J/mol-K
20
15
10
5
0
-5
-10
-15
-20
0.0
0.1
0.2
0.3
0.4
0.5
0.6
0.7
0.8
0.9
1.0
Cu
Mole fraction Mg
Mg

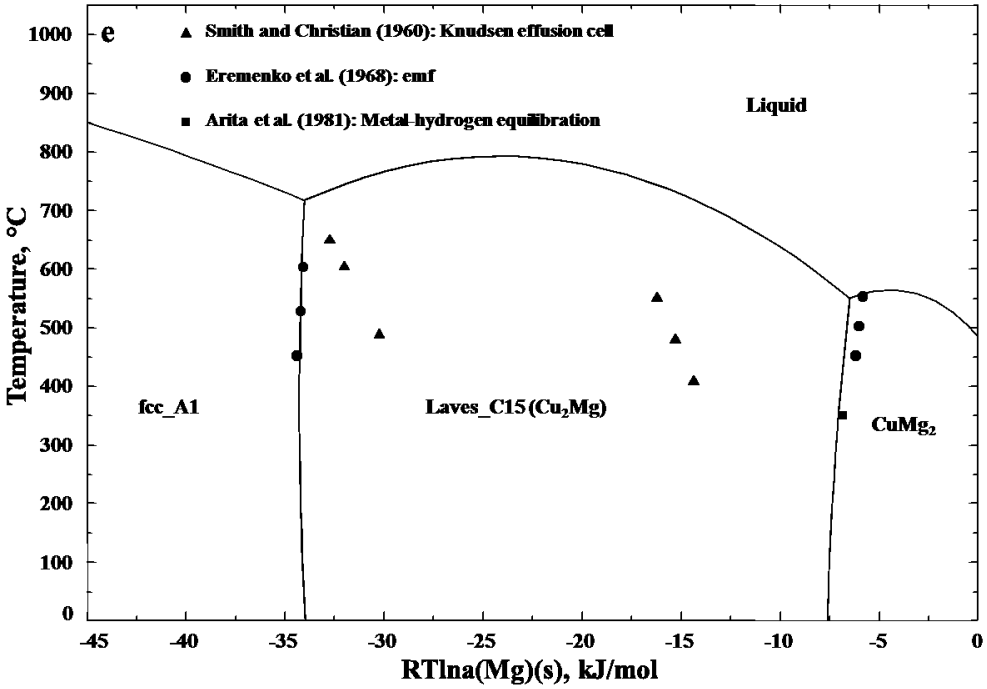

Fig. 9.4 Calculated thermodynamic properties of the Cu-Mg solid phases along with the experimental data. (a) Heat capacity of Cu_2Mg, (b) heat capacity of $CuMg_2$, (c) enthalpy of formation of compounds at 25 ºC, (d) entropy of formation of compounds at 25 ºC, and (e) chemical potential diagram of hcp_A3 Mg.

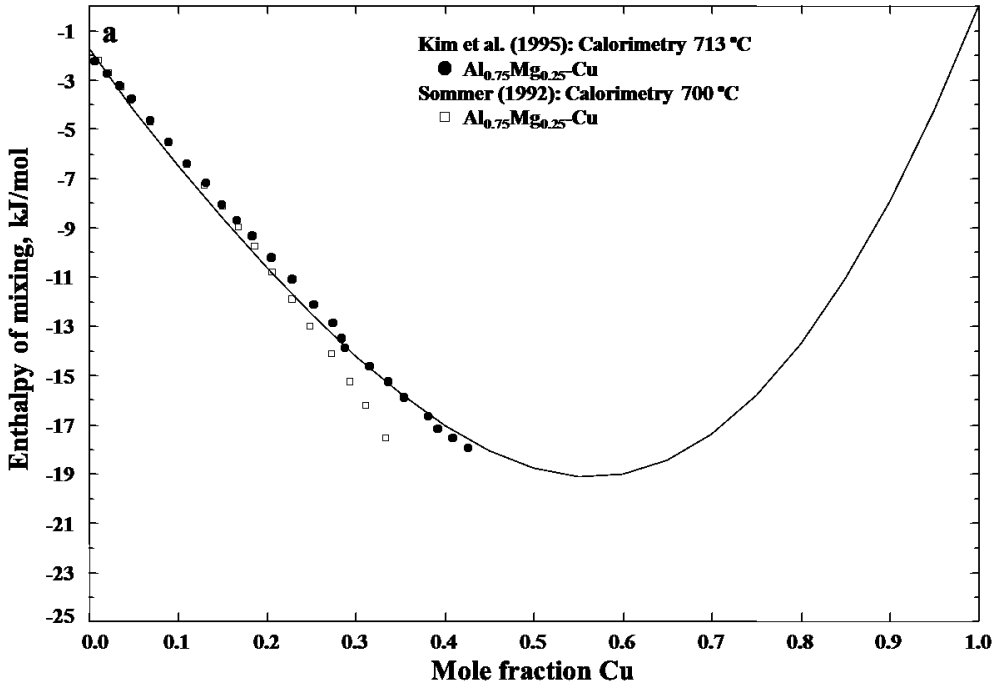
a
Kim et al. (1995): Calorimetry 713 °C
Al0.75Mg0.25–Cu
Sommer (1992): Calorimetry 700 °C
Al0.75Mg0.25–Cu
Enthalpy of mixing, kJ/mol
Mole fraction Cu

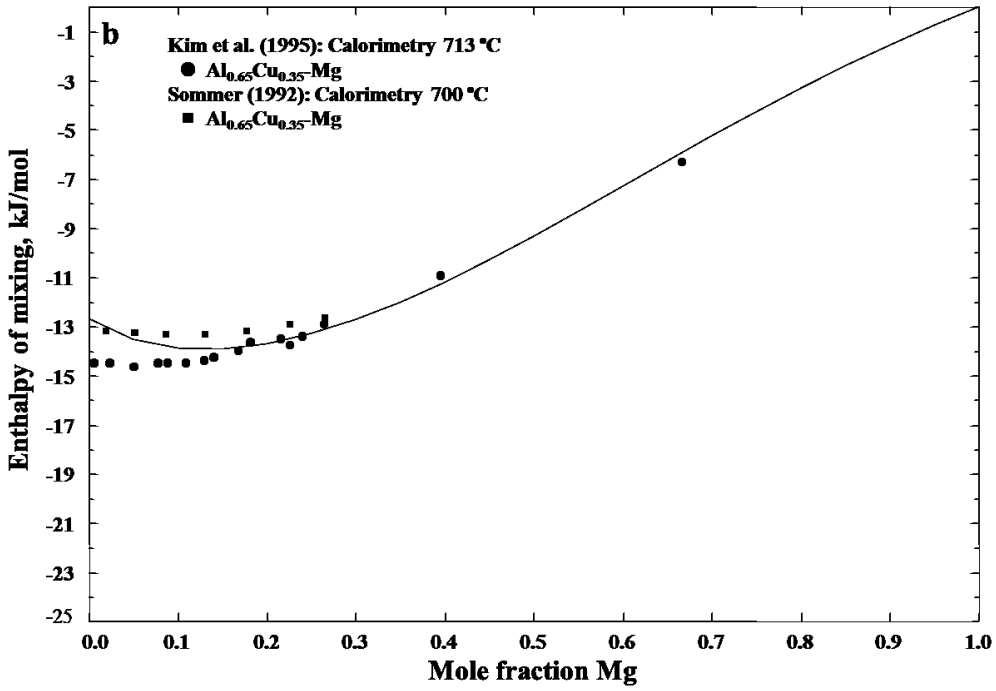
b
Kim et al. (1995): Calorimetry 713 °C
Al0.65Cu0.35–Mg
Sommer (1992): Calorimetry 700 °C
Al0.65Cu0.35–Mg
Enthalpy of mixing, kJ/mol
Mole fraction Mg

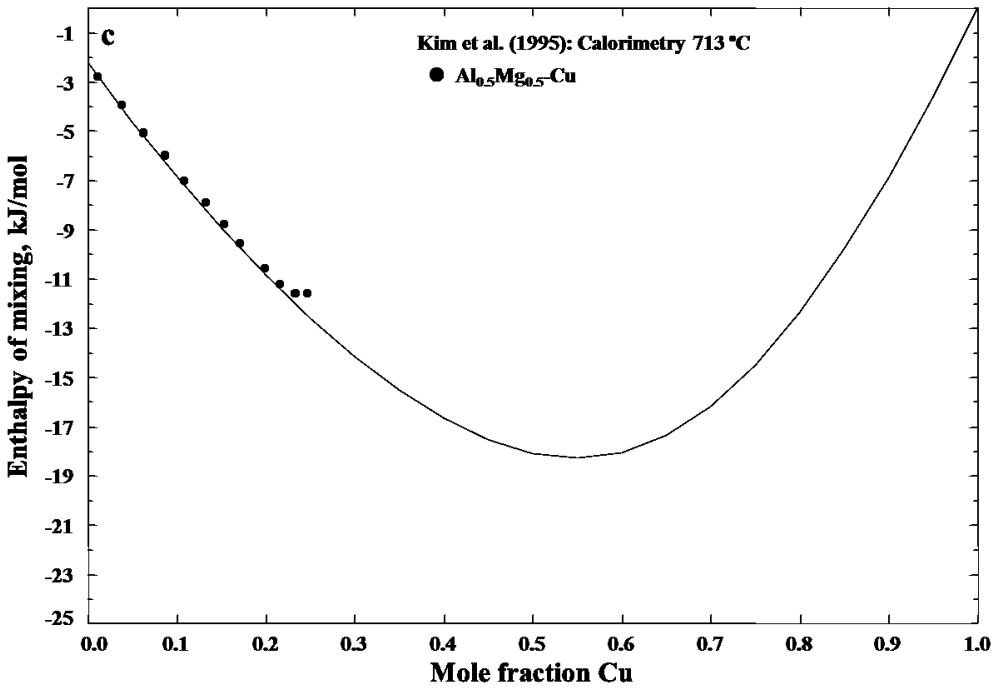
c
Kim et al. (1995): Calorimetry 713 °C
● $Al_{0.5}Mg_{0.5}$-Cu
Enthalpy of mixing, kJ/mol
-1
-3
-5
-7
-9
-11
-13
-15
-17
-19
-21
-23
-25
0.0
0.1
0.2
0.3
0.4
0.5
0.6
0.7
0.8
0.9
1.0
Mole fraction Cu

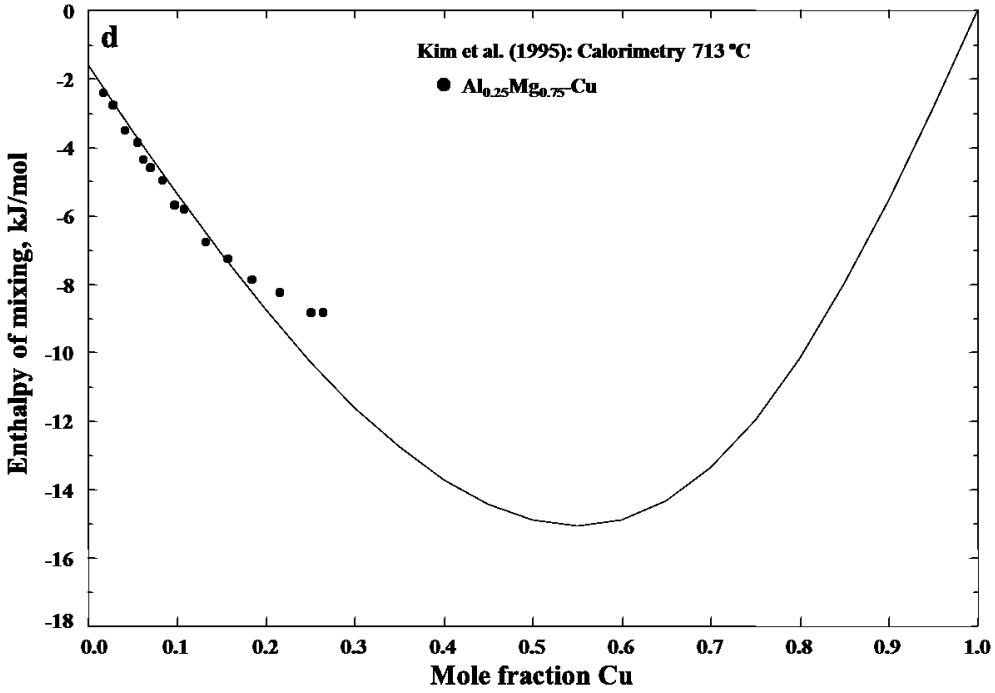
d
Kim et al. (1995): Calorimetry 713 °C
● $Al_{0.25}Mg_{0.75}$-Cu
Enthalpy of mixing, kJ/mol
0
-2
-4
-6
-8
-10
-12
-14
-16
-18
0.0
0.1
0.2
0.3
0.4
0.5
0.6
0.7
0.8
0.9
1.0
Mole fraction Cu

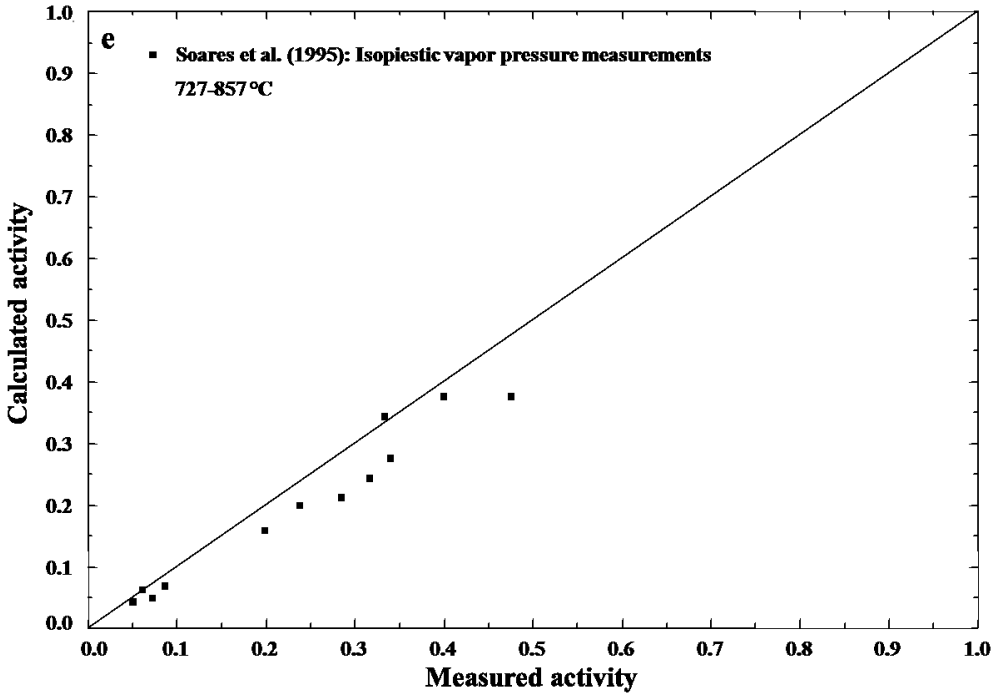

Fig. 9.5 Calculated thermodynamic properties of the Al-Cu-Mg liquid phase along with the experimental data. (a) Enthalpy of mixing of the $Al_{0.75}Mg_{0.25}$-Cu section at 713 ºC, (b) enthalpy of mixing of the $Al_{0.65}Mg_{0.35}$-Cu section at 713 ºC, (c) enthalpy of mixing of the $Al_{0.5}Mg_{0.5}$-Cu section at 713 ºC, (d) enthalpy of mixing of the $Al_{0.25}Mg_{0.75}$-Cu section at 713 ºC, and (e) activity of Mg with respect to the pure liquid standard at 727-857 ºC.

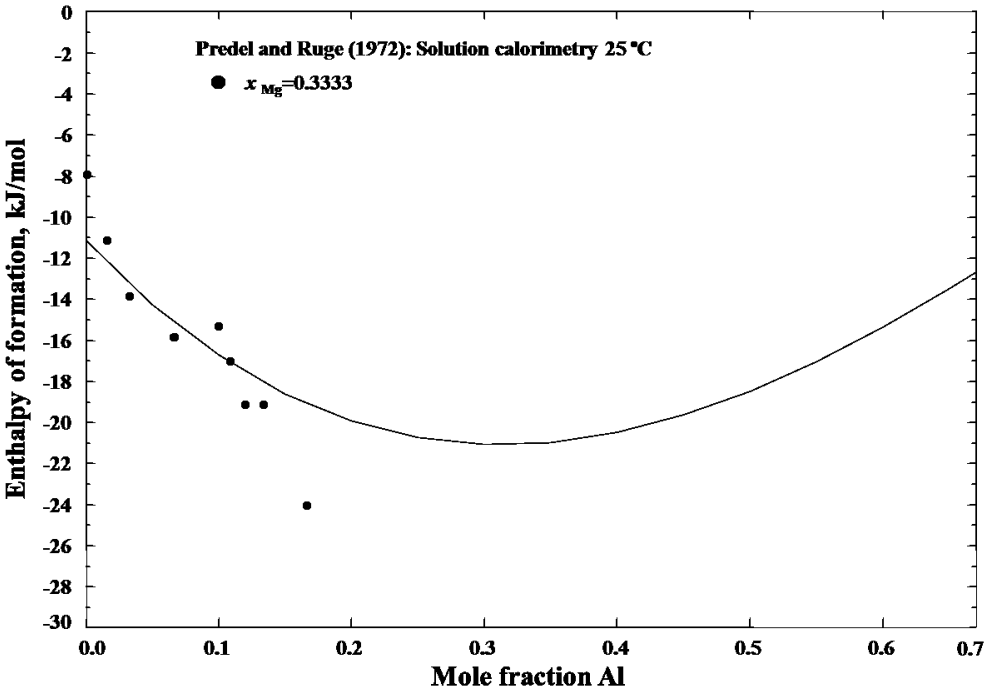

Fig. 9.6 Calculated enthalpy of formation of the Laves_C15 phase in the Al-Cu-Mg system at 25 ºC along with the experimental data.

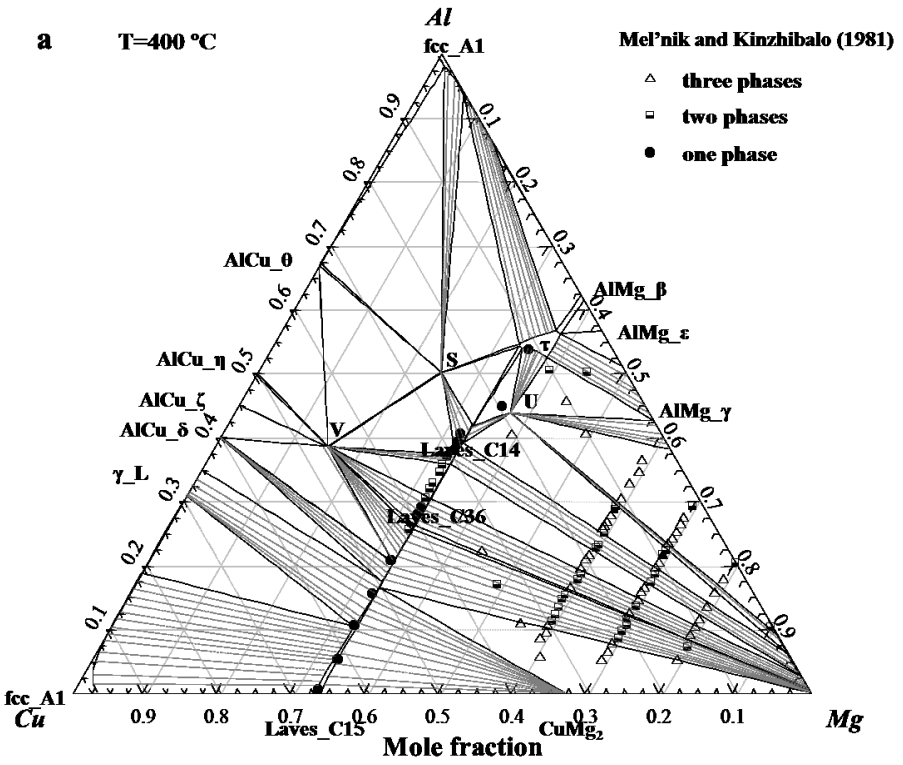
a
T=400 °C
Al
fcc_A1
Mel'nik and Kinzhibalo (1981)
three phases
two phases
one phase
AlCu_θ
AlMg_β
AlMg_ε
AlCu_η
AlCu_ζ
AlCu_δ
AlMg_γ
γ_L
S
τ
U
V
Laves_C14
Laves_C36
fcc_A1
Cu
Laves_C15
CuMg2
Mg
Mole fraction

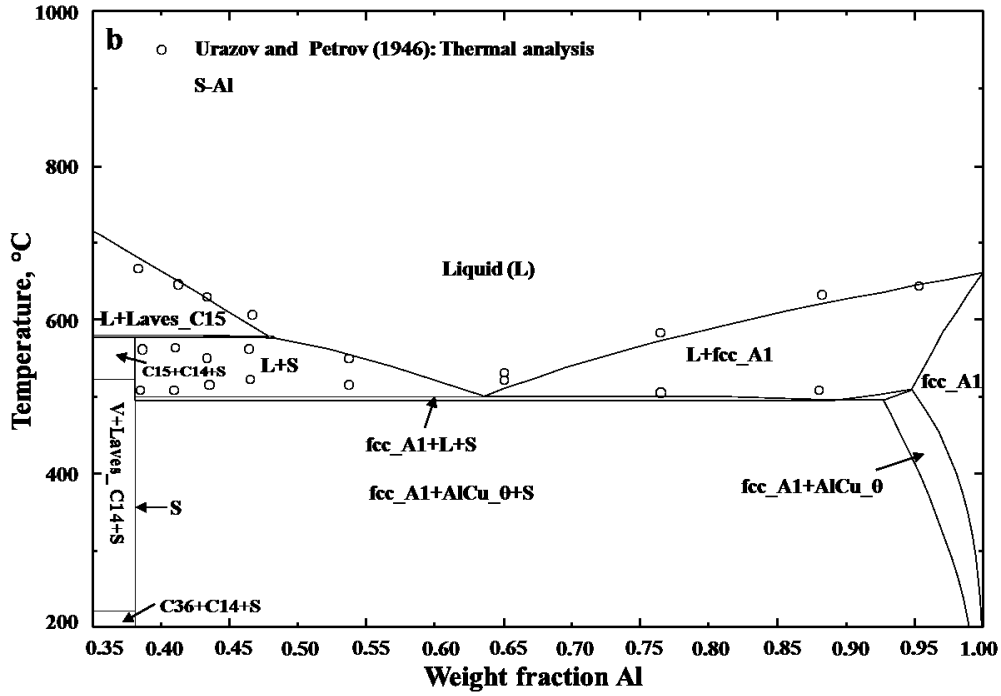
b
Urazov and Petrov (1946): Thermal analysis
S-Al
Liquid (L)
L+Laves_C15
L+S
L+fcc_A1
C15+C14+S
V+Laves_C14+S
fcc_A1+L+S
fcc_A1+AlCu_θ+S
fcc_A1+AlCu_θ
fcc_A1
S
C36+C14+S
Temperature, °C
Weight fraction Al

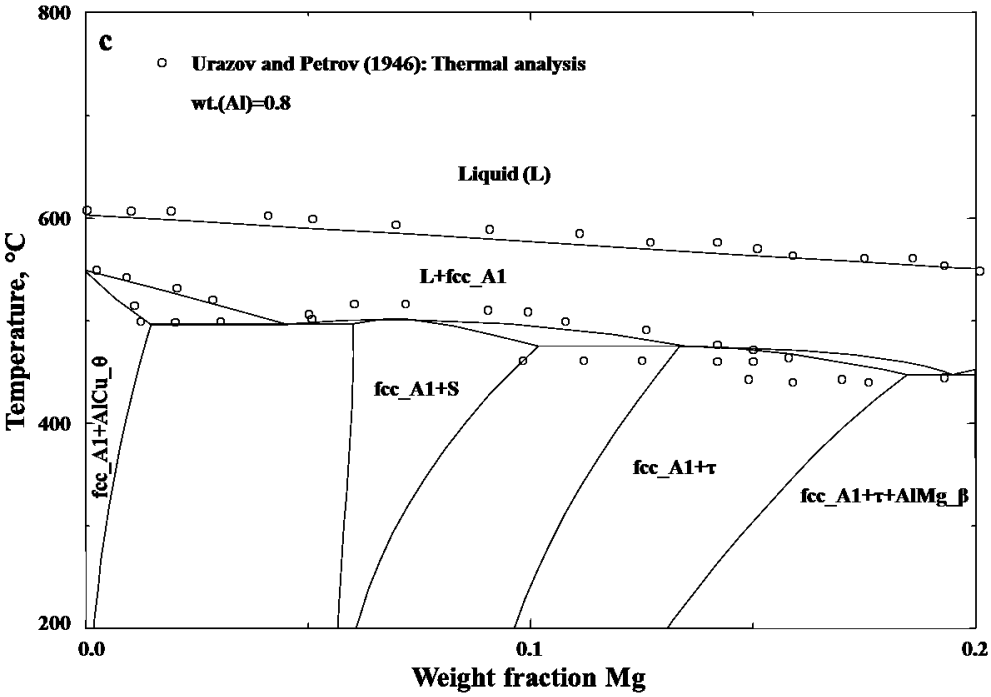
c
Urazov and Petrov (1946): Thermal analysis
wt.(Al)=0.8
Liquid (L)
L+fcc_A1
fcc_A1+AlCu_θ
fcc_A1+S
fcc_A1+τ
fcc_A1+τ+AlMg_β
Temperature, °C
Weight fraction Mg
800
600
400
200
0.0
0.1
0.2

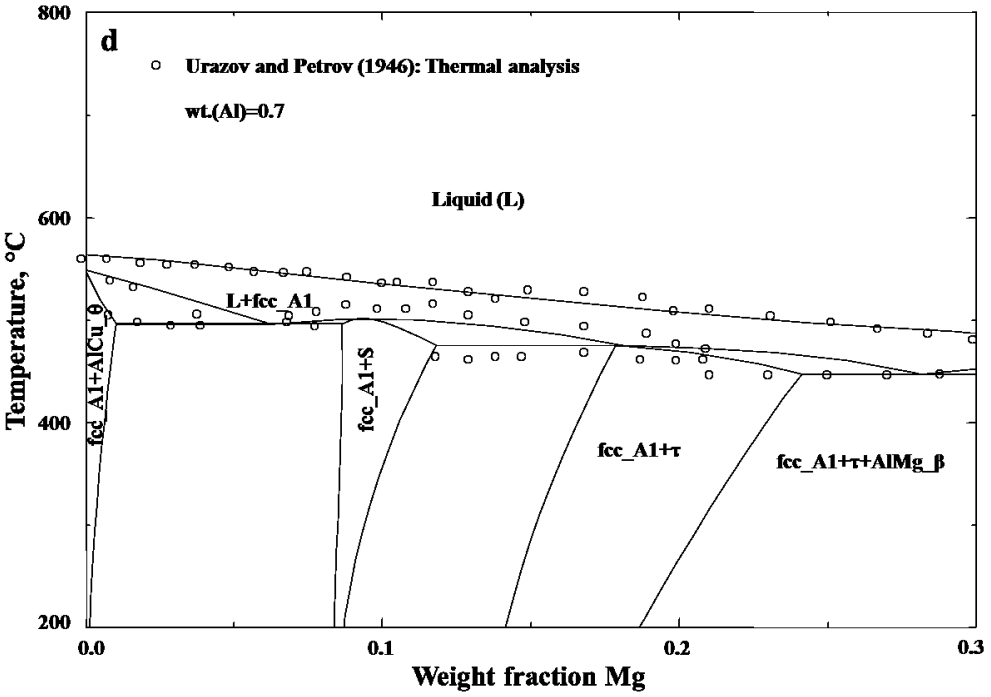
d
Urazov and Petrov (1946): Thermal analysis
wt.(Al)=0.7
Liquid (L)
L+fcc_A1
fcc_A1+AlCu_θ
fcc_A1+S
fcc_A1+τ
fcc_A1+τ+AlMg_β
Temperature, °C
Weight fraction Mg
800
600
400
200
0.0
0.1
0.2
0.3

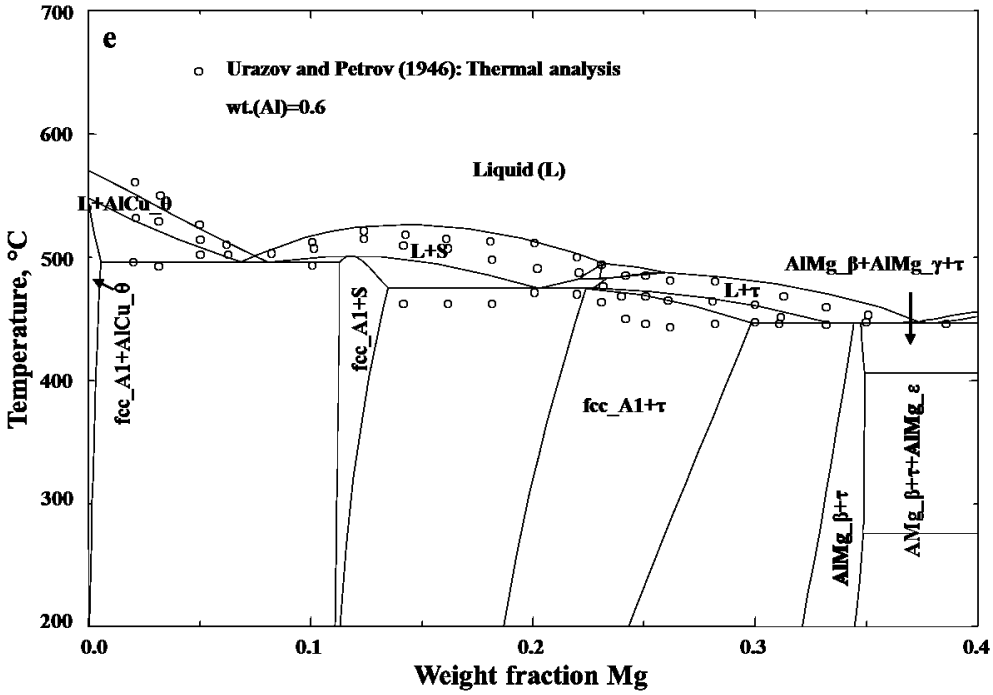
e
Urazov and Petrov (1946): Thermal analysis
wt.(Al)=0.6
Liquid (L)
L+AlCu_θ
L+S
AlMg_β+AlMg_γ+τ
L+τ
fcc_A1+AlCu_θ
fcc_A1+S
fcc_A1+τ
AlMg_β+τ
AlMg_β+τ+AlMg_ε
Temperature, °C
Weight fraction Mg
700
600
500
400
300
200
0.0
0.1
0.2
0.3
0.4

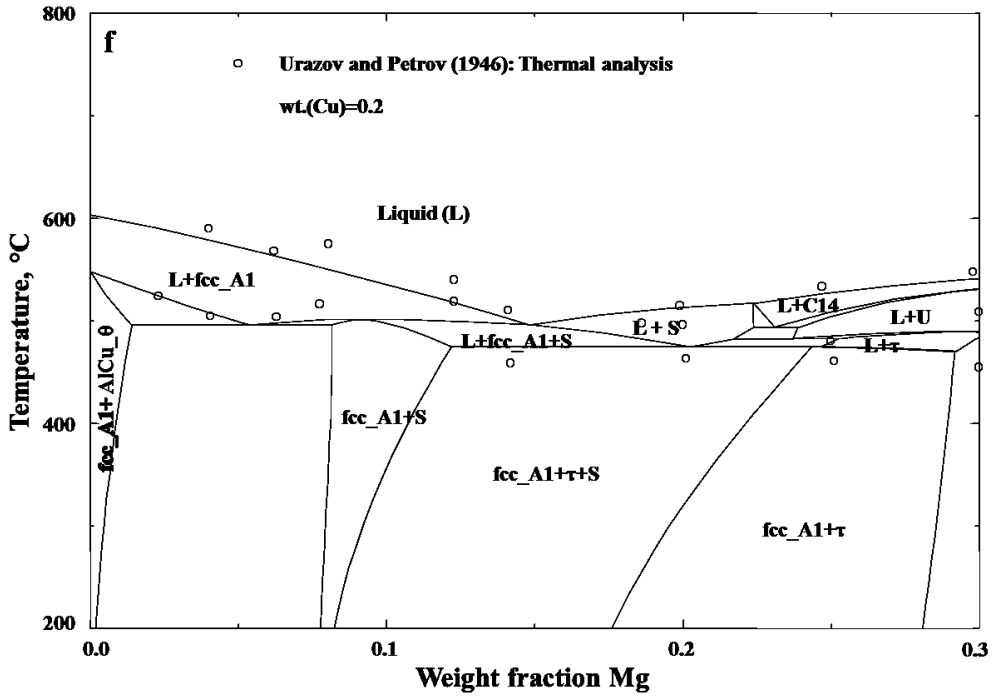
f
Urazov and Petrov (1946): Thermal analysis
wt.(Cu)=0.2
Liquid (L)
L+fcc_A1
L+C14
L+U
L + S
L+fcc_A1+S
L+τ
fcc_A1+ AlCu_θ
fcc_A1+S
fcc_A1+τ+S
fcc_A1+τ
Temperature, °C
Weight fraction Mg
800
600
400
200
0.0
0.1
0.2
0.3

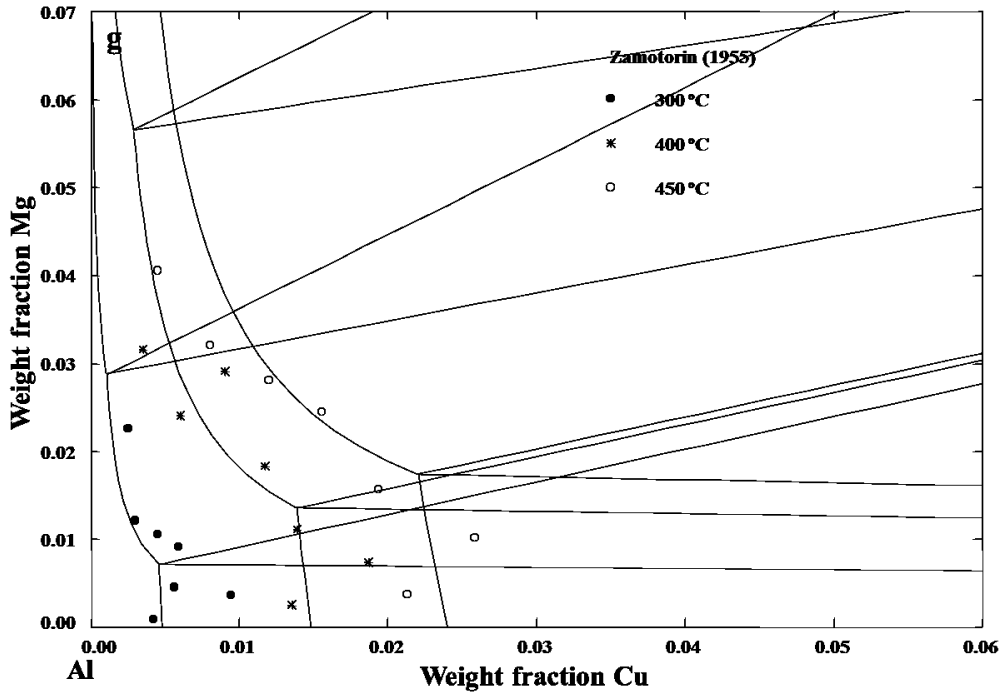

Fig. 9.7 Calculated phase diagrams of the Al-Cu-Mg system along with the experimental data. (a) Isothermal section at 400 ºC, (b) isoplethal section of the S-Al section, (c) isoplethal section with 80 wt.% Al, (d) isoplethal section with 70 wt.% Al, (e) isoplethal section with 60 wt.% Al, (f) isoplethal section with 20 wt.% Cu, and (g) the solubility of Mg and Cu in (Al) at 300, 400, and 450 ºC.

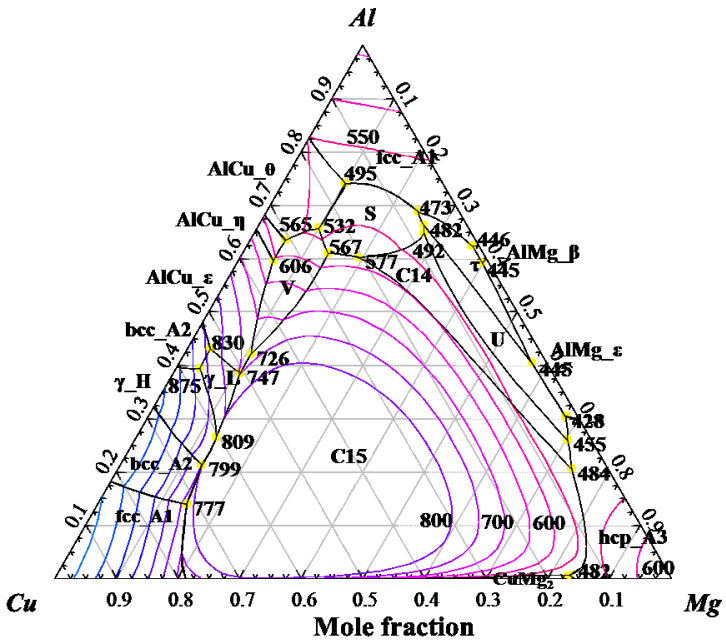

Fig. 9.8 Calculated liquidus projection of the Al-Cu-Mg system.

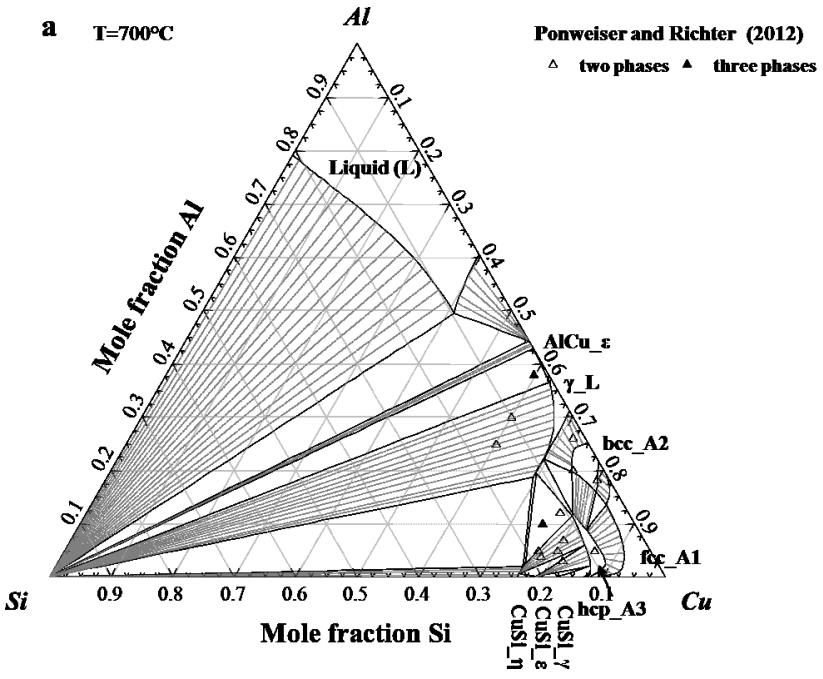
a
T=700°C
Al
Ponweiser and Richter (2012)
two phases
three phases
Liquid (L)
Mole fraction Al
AlCu_ε
γ_L
bcc_A2
fcc_A1
hcp_A3
Si
Cu
Mole fraction Si
CuSI_η
CuSI_ε
CuSI_γ

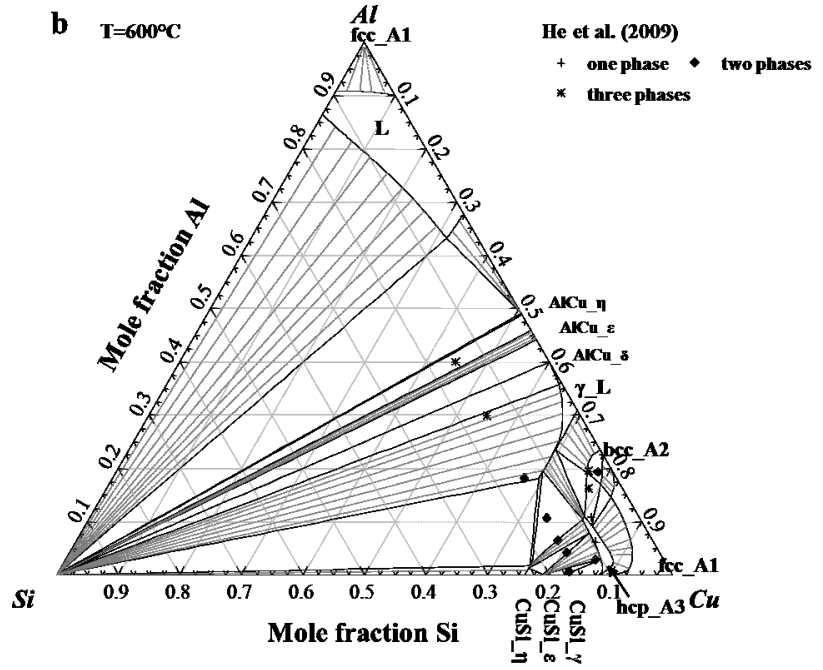
b
T=600°C
Al
fcc_A1
He et al. (2009)
one phase
two phases
three phases
L
Mole fraction Al
AlCu_η
AlCu_ε
AlCu_δ
γ_L
bcc_A2
fcc_A1
hcp_A3
Si
Cu
Mole fraction Si
CuSI_η
CuSI_ε
CuSI_γ

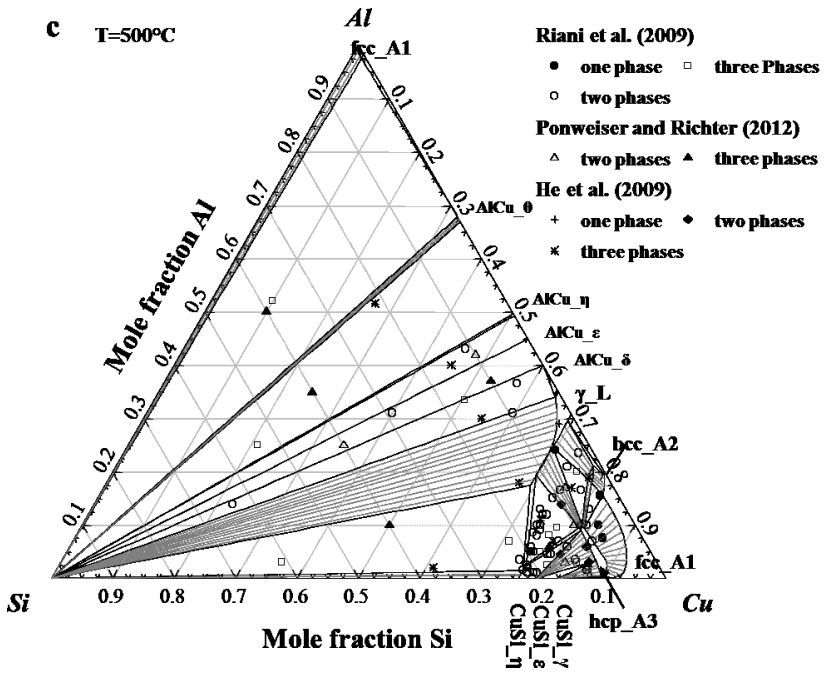

Fig. 9.9 Calculated isothermal sections of the Al-Cu-Si system along with the experimental data. (a) At 700 ºC, (b) at 600 ºC, and (c) at 500 ºC.

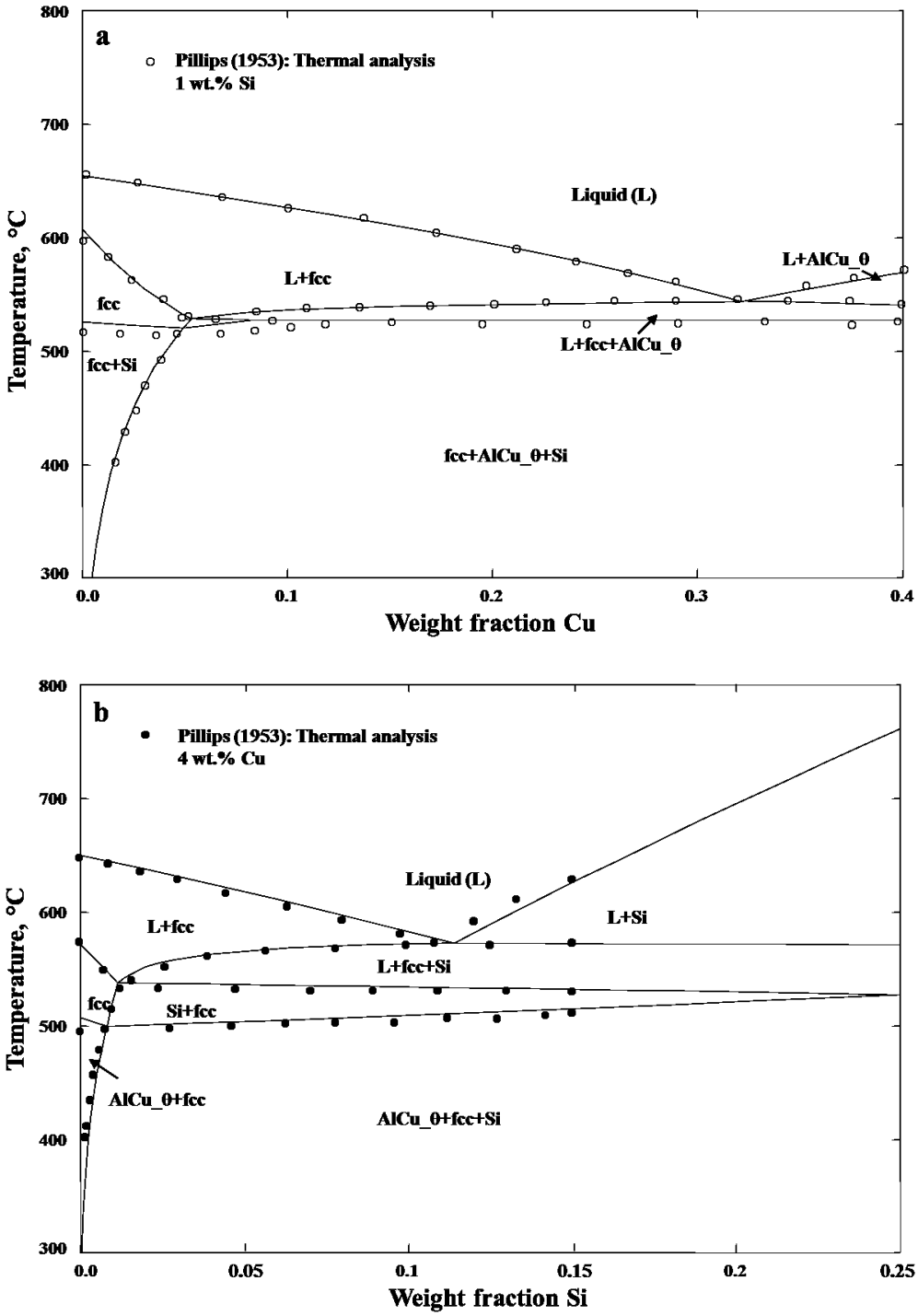

Fig. 9.10 Calculated isoplethal sections of the Al-Cu-Si system along with the experimental data. (a) 1 wt.% Si and (b) 4 wt.% Cu

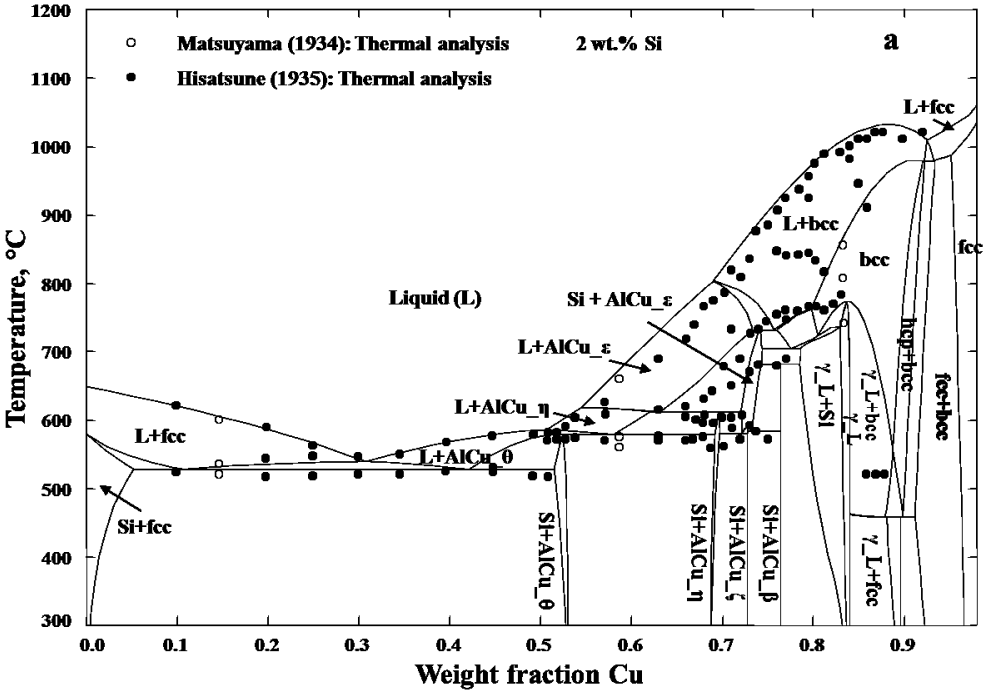
Matsuyama (1934): Thermal analysis
Hisatsune (1935): Thermal analysis
2 wt.% Si
a
Liquid (L)
Si + AlCu_ε
L+AlCu_ε
L+AlCu_η
L+AlCu_θ
L+fcc
Si+fcc
L+bcc
bcc
fcc
hcp+bcc
fcc+bcc
γ_L+Si
γ_L+bcc
γ_L
γ_L+fcc
Si+AlCu_θ
Si+AlCu_η
Si+AlCu_ζ
Si+AlCu_β
Temperature, °C
Weight fraction Cu

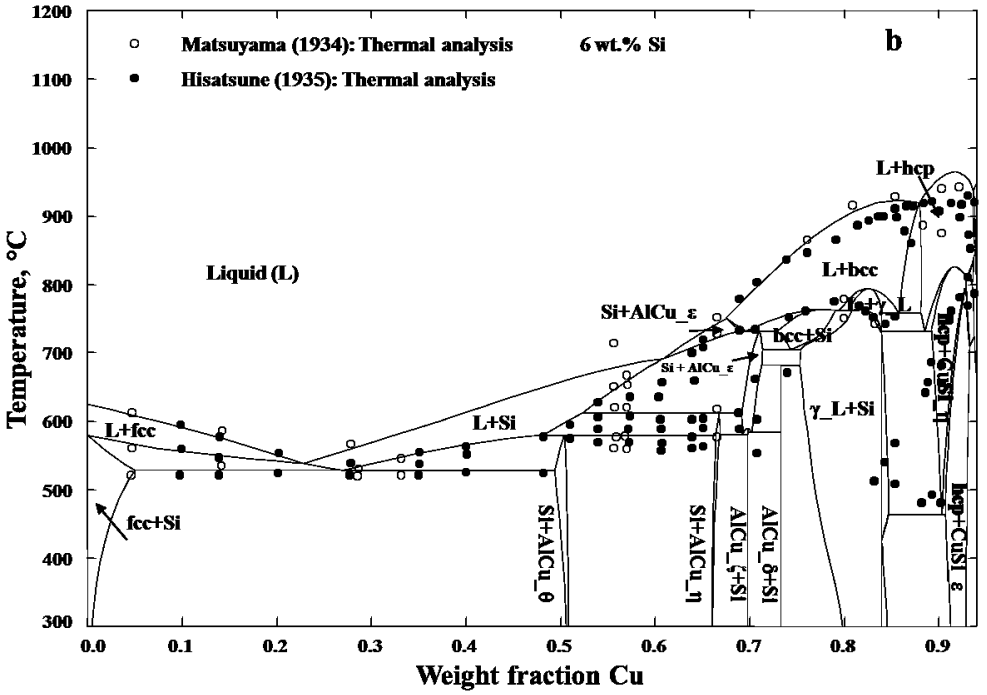
Matsuyama (1934): Thermal analysis
Hisatsune (1935): Thermal analysis
6 wt.% Si
b
Liquid (L)
L+hcp
L+bcc
Si+AlCu_ε
bcc+Si
Si + AlCu_ε
γ_L+Si
L+Si
L+fcc
fcc+Si
Si+AlCu_θ
Si+AlCu_η
AlCu_ζ+Si
AlCu_β+Si
hcp+CuSi_ε
Temperature, °C
Weight fraction Cu

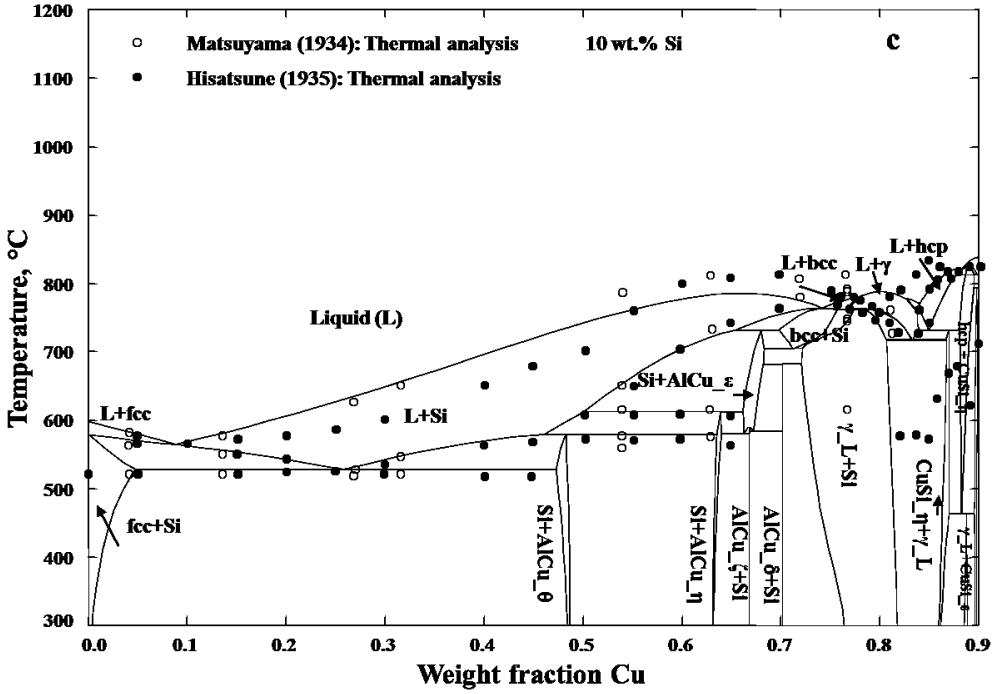
Matsuyama (1934): Thermal analysis
Hisatsune (1935): Thermal analysis
10 wt.% Si
c
Liquid (L)
L+fcc
L+Si
fcc+Si
Si+AlCu_θ
Si+AlCu_η
AlCu_ζ+Si
AlCu_δ+Si
γ_L+Si
Si+AlCu_ε
bcc+Si
L+bcc
L+γ
L+hcp
CuSi_η+γ_L
Temperature, °C
Weight fraction Cu

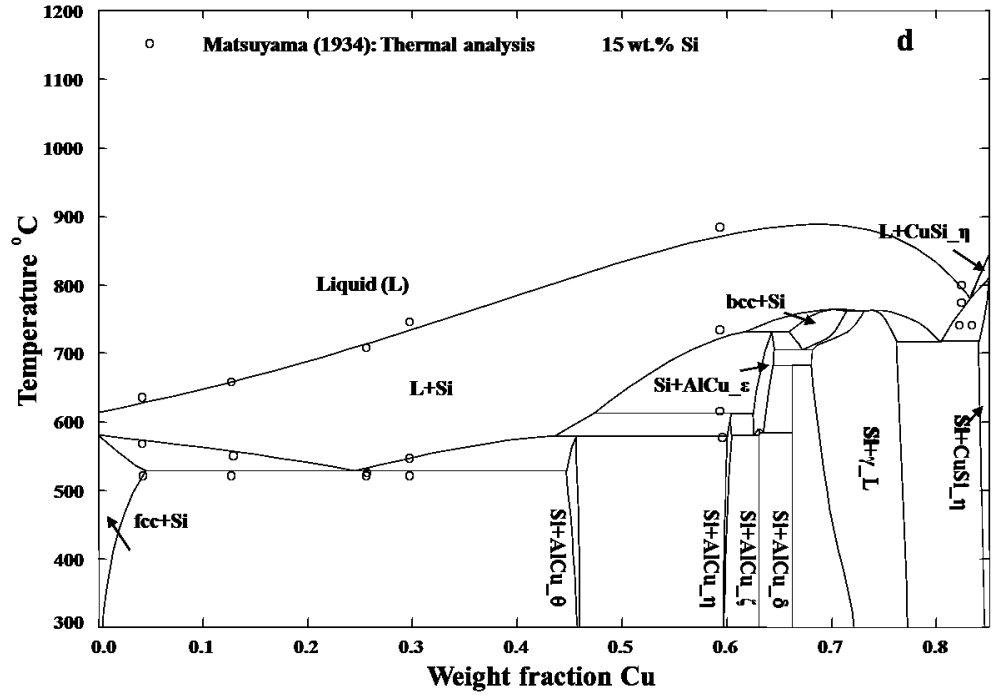
Matsuyama (1934): Thermal analysis
15 wt.% Si
d
Liquid (L)
L+Si
fcc+Si
Si+AlCu_θ
Si+AlCu_η
Si+AlCu_ζ
Si+AlCu_δ
Si+γ_L
Si+AlCu_ε
bcc+Si
L+CuSi_η
Si+CuSi_η
Temperature °C
Weight fraction Cu

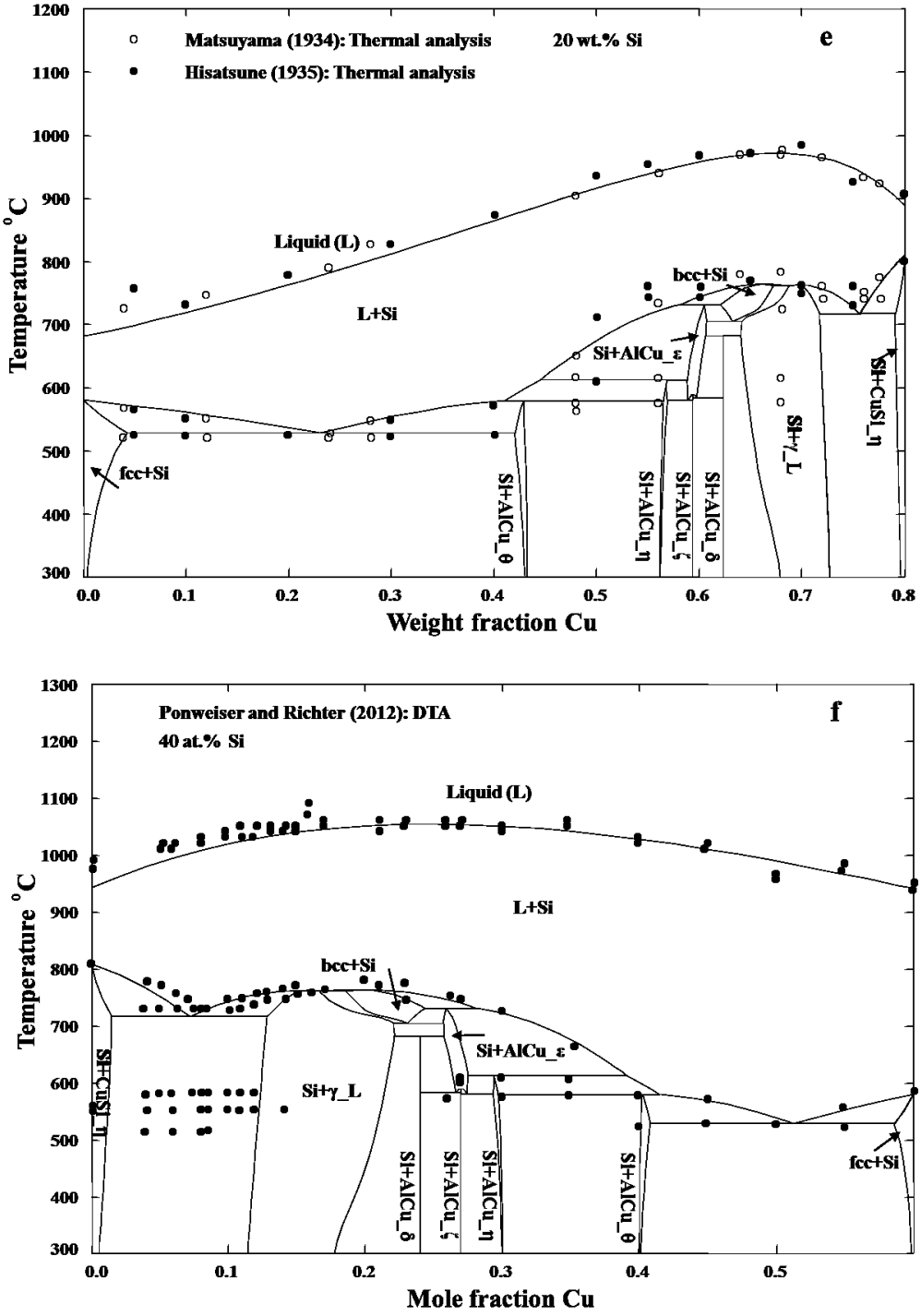

Fig. 9.11 Calculated isoplethal sections of the Al-Cu-Si system along with the experimental data. (a) Isoplethal sections with 2 wt.% Si, (b) isoplethal sections with 6 wt.% Si, (c) isoplethal sections with 10 wt.% Si, (d) isoplethal sections with 15 wt.% Si, (e) isoplethal sections with 20 wt.% Si, and (f) isoplethal sections with 40 at.% Si.

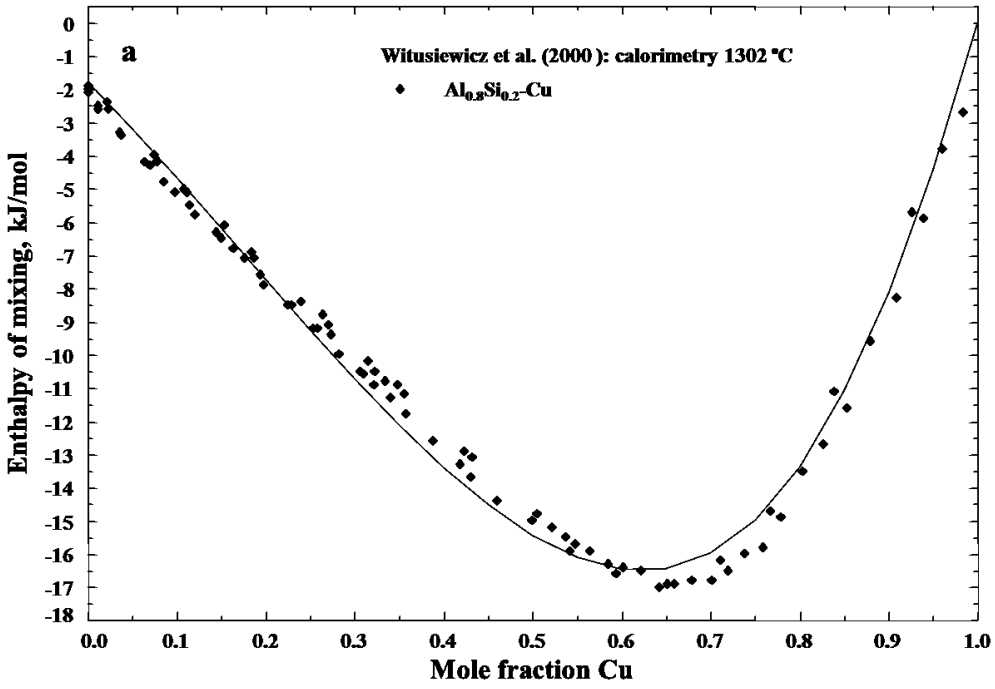
a
Witusiewicz et al. (2000): calorimetry 1302 °C
$Al_{0.8}Si_{0.2}$-Cu
Enthalpy of mixing, kJ/mol
Mole fraction Cu

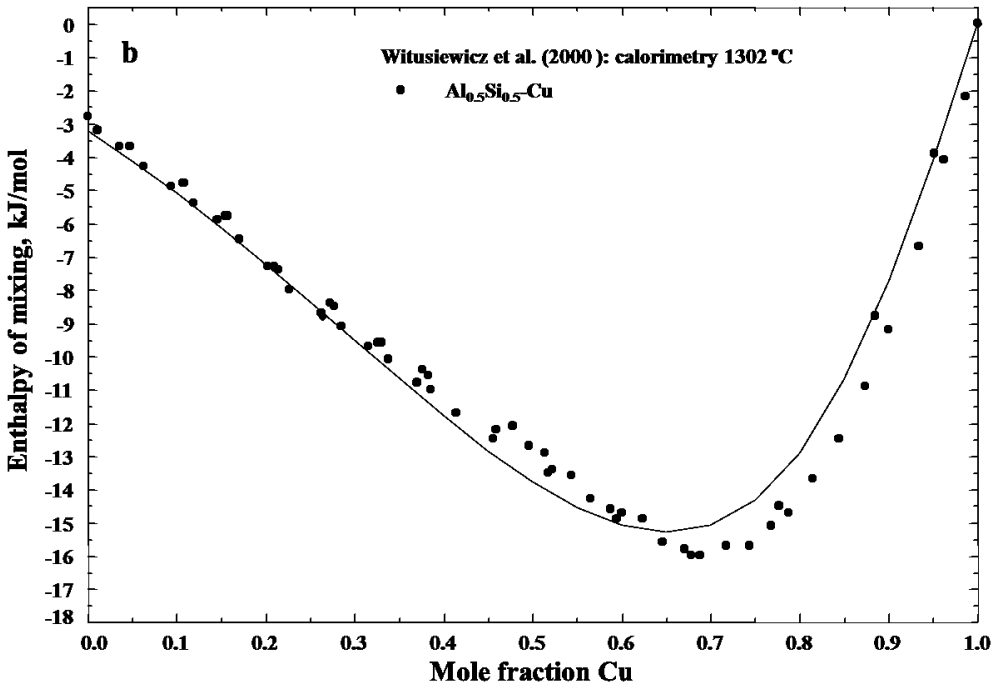
b
Witusiewicz et al. (2000): calorimetry 1302 °C
$Al_{0.5}Si_{0.5}$-Cu
Enthalpy of mixing, kJ/mol
Mole fraction Cu

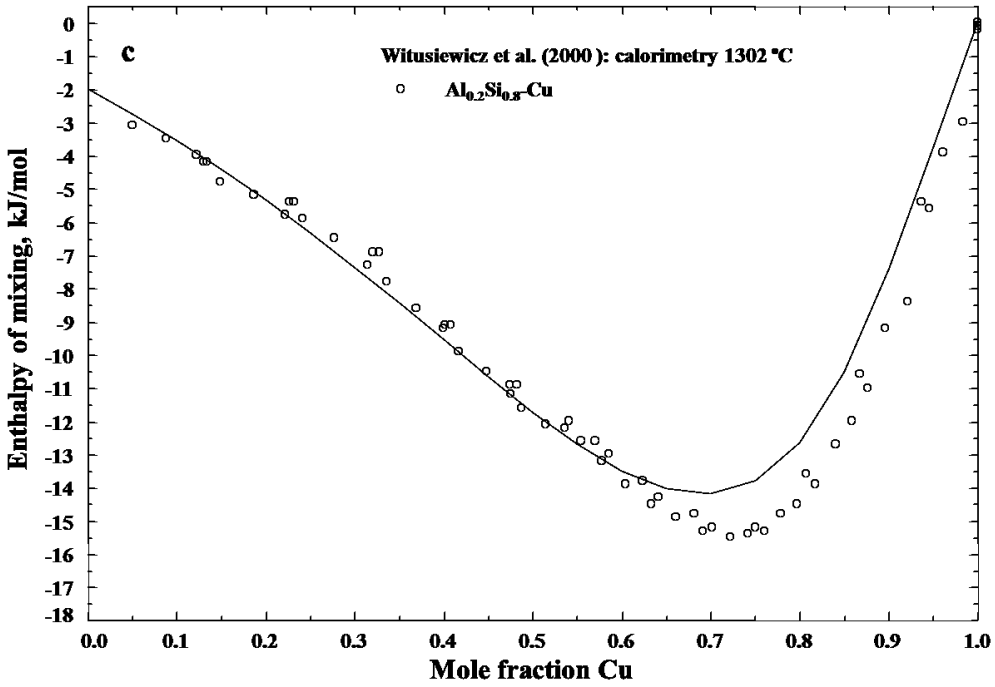

Fig. 9.12 Calculated enthalpy of mixing of the Al-Cu-Si liquid phase at 1302 ºC along with the experimental data. (a) The $Al_{0.8}Si_{0.2}$-Cu section, (b) the $Al_{0.5}Si_{0.5}$-Cu section, and (c) the $Al_{0.2}Si_{0.8}$-Cu section.

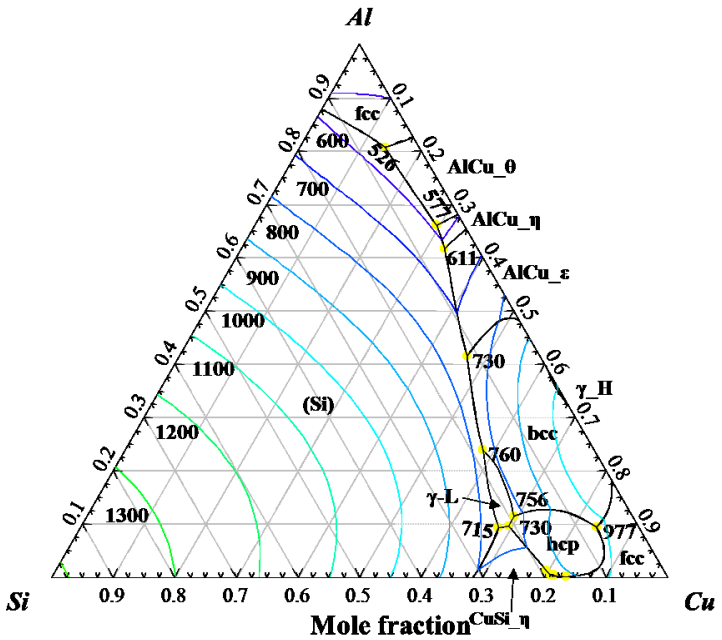

Fig. 9.13 Calculated liquidus projection of the Al-Cu-Si system.

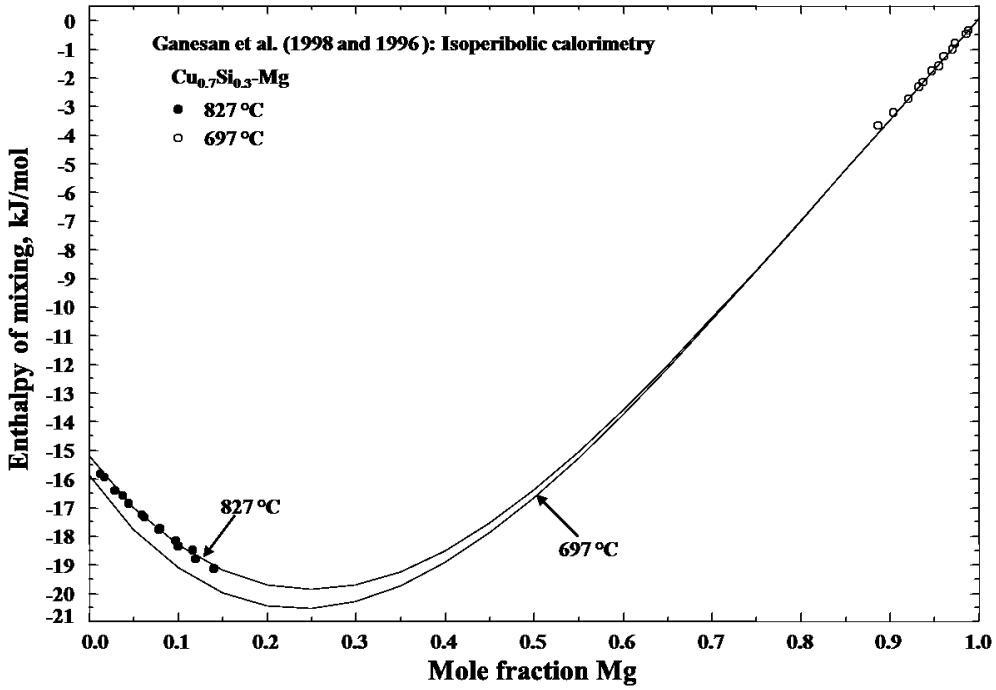

Fig. 9.14 Calculated enthalpy of mixing of the Cu-Mg-Si liquid phase of the $Cu_{0.7}Si_{0.3}$-Mg section along with the experimental data at 827 and 697 ºC.

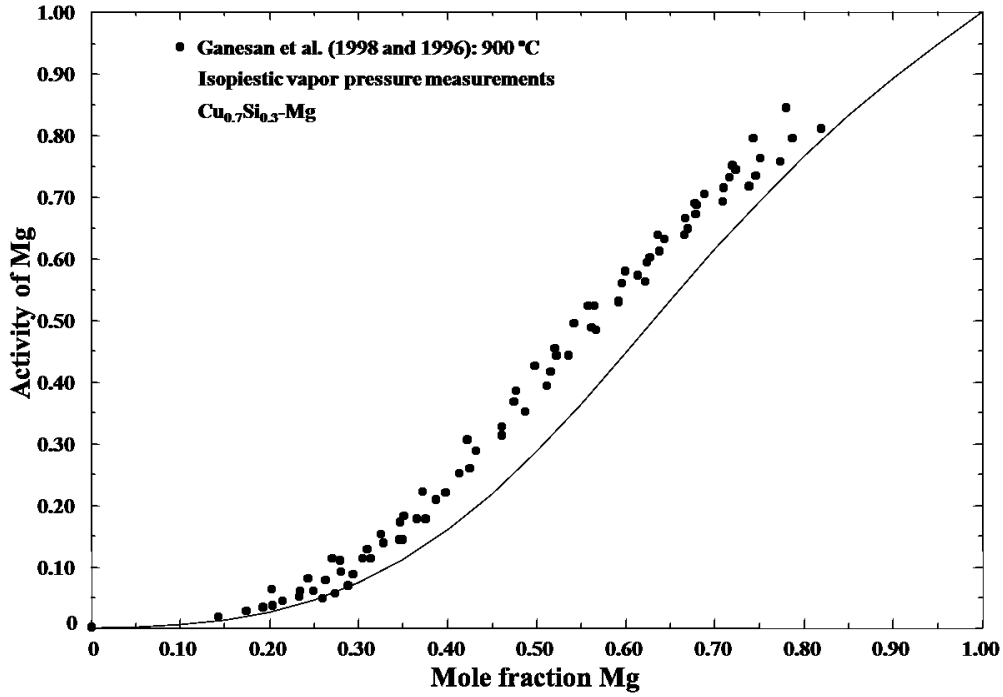

Fig. 9.15 Calculated activity of Mg of the Cu-Mg-Si liquid phase of the $Cu_{0.7}Si_{0.3}$-Mg section at 900 ºC along with the experimental data.

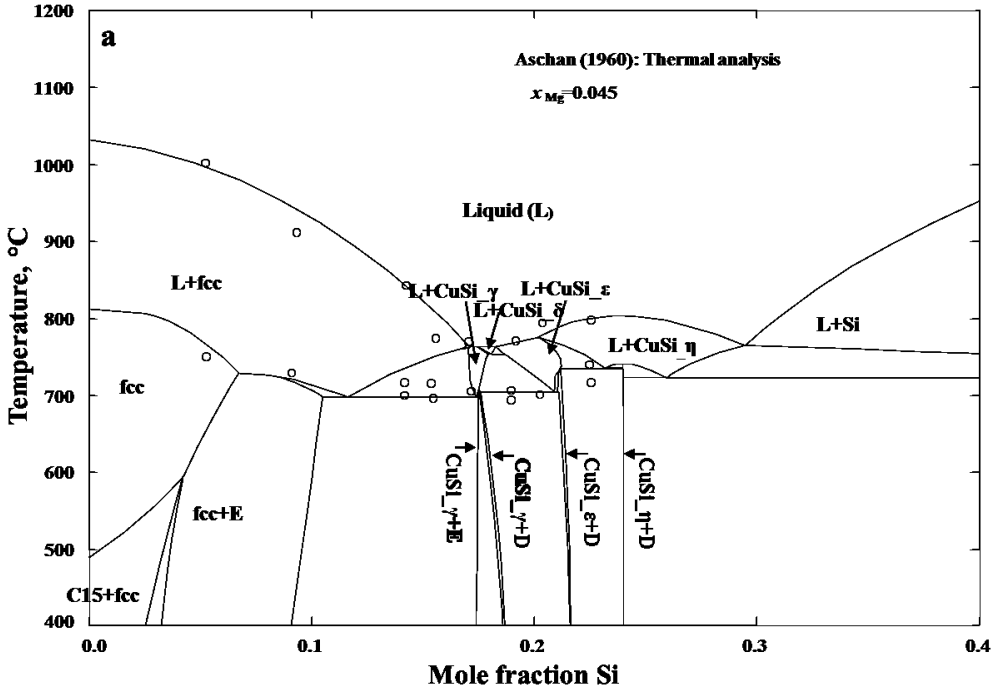
a
Aschan (1960): Thermal analysis
x_{Mg}=0.045
Liquid (L)
L+fcc
L+CuSi_γ
L+CuSi_ε
L+CuSi_δ
L+Si
L+CuSi_η
fcc
fcc+E
C15+fcc
L→CuSi_γ+E
CuSi_γ+D
CuSi_ε+D
CuSi_η+D
Temperature, °C
Mole fraction Si
1200
1100
1000
900
800
700
600
500
400
0.0
0.1
0.2
0.3
0.4

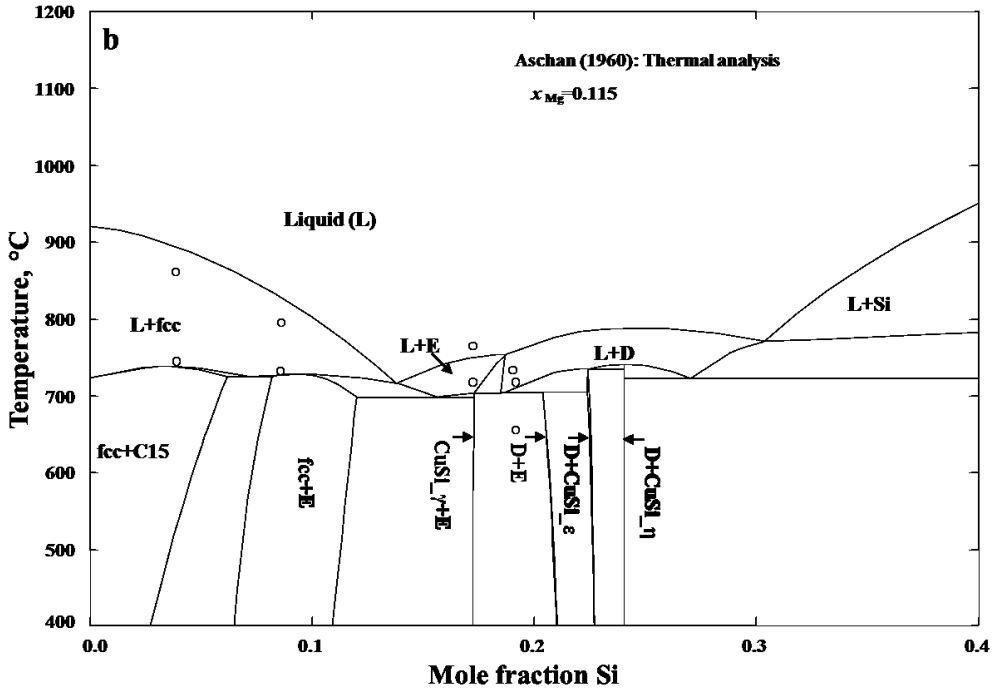
b
Aschan (1960): Thermal analysis
x_{Mg}=0.115
Liquid (L)
L+fcc
L+E
L+D
L+Si
fcc+C15
fcc+E
L→CuSi_γ+E
D+E
D+CuSi_ε
D+CuSi_η
Temperature, °C
Mole fraction Si
1200
1100
1000
900
800
700
600
500
400
0.0
0.1
0.2
0.3
0.4

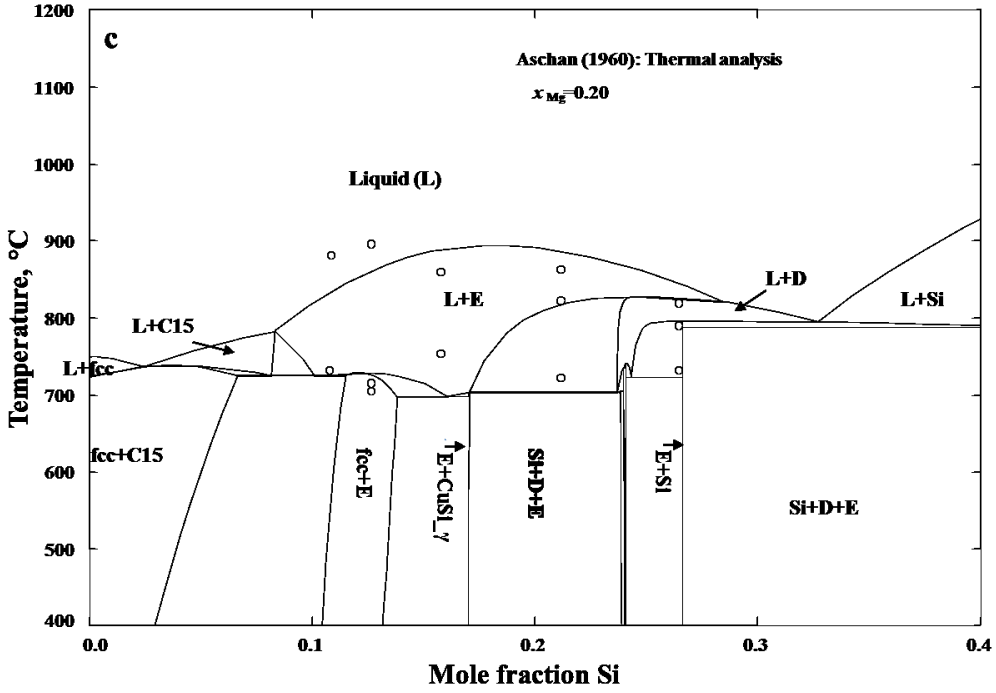
c
Aschan (1960): Thermal analysis
x_{Mg}=0.20
Liquid (L)
L+E
L+D
L+Si
L+C15
L+fcc
fcc+C15
fcc+E
E+CuSi_γ
Si+D+E
E+Si
Si+D+E
Temperature, °C
Mole fraction Si
1200
1100
1000
900
800
700
600
500
400
0.0
0.1
0.2
0.3
0.4

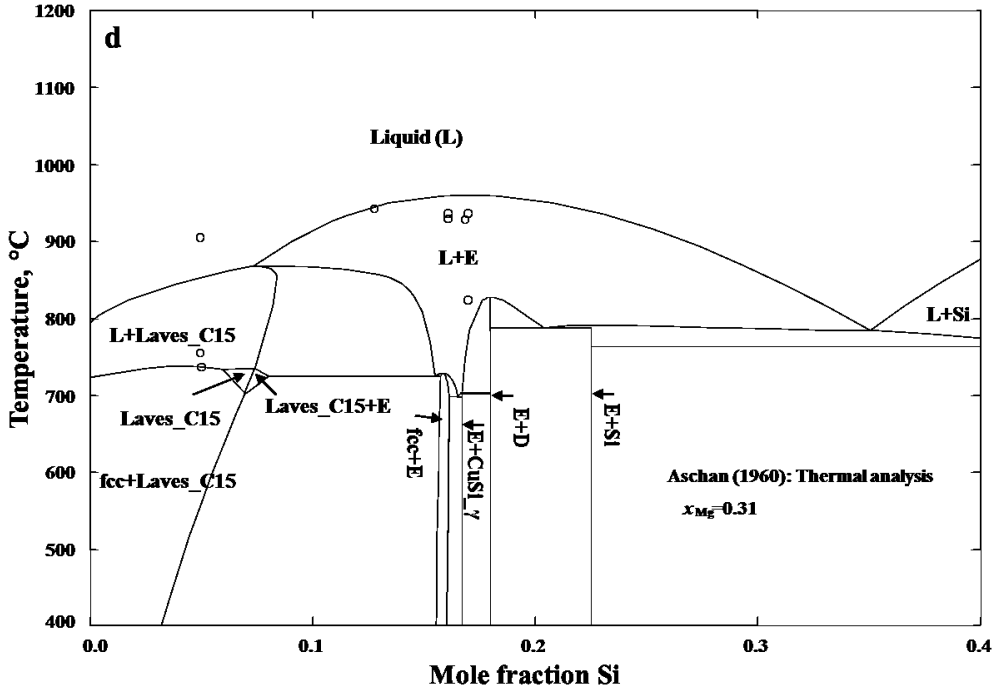
d
Liquid (L)
L+E
L+Si
L+Laves_C15
Laves_C15
Laves_C15+E
fcc+Laves_C15
fcc+E
E+CuSi_γ
E+D
E+Si
Aschan (1960): Thermal analysis
x_{Mg}=0.31
Temperature, °C
Mole fraction Si
1200
1100
1000
900
800
700
600
500
400
0.0
0.1
0.2
0.3
0.4

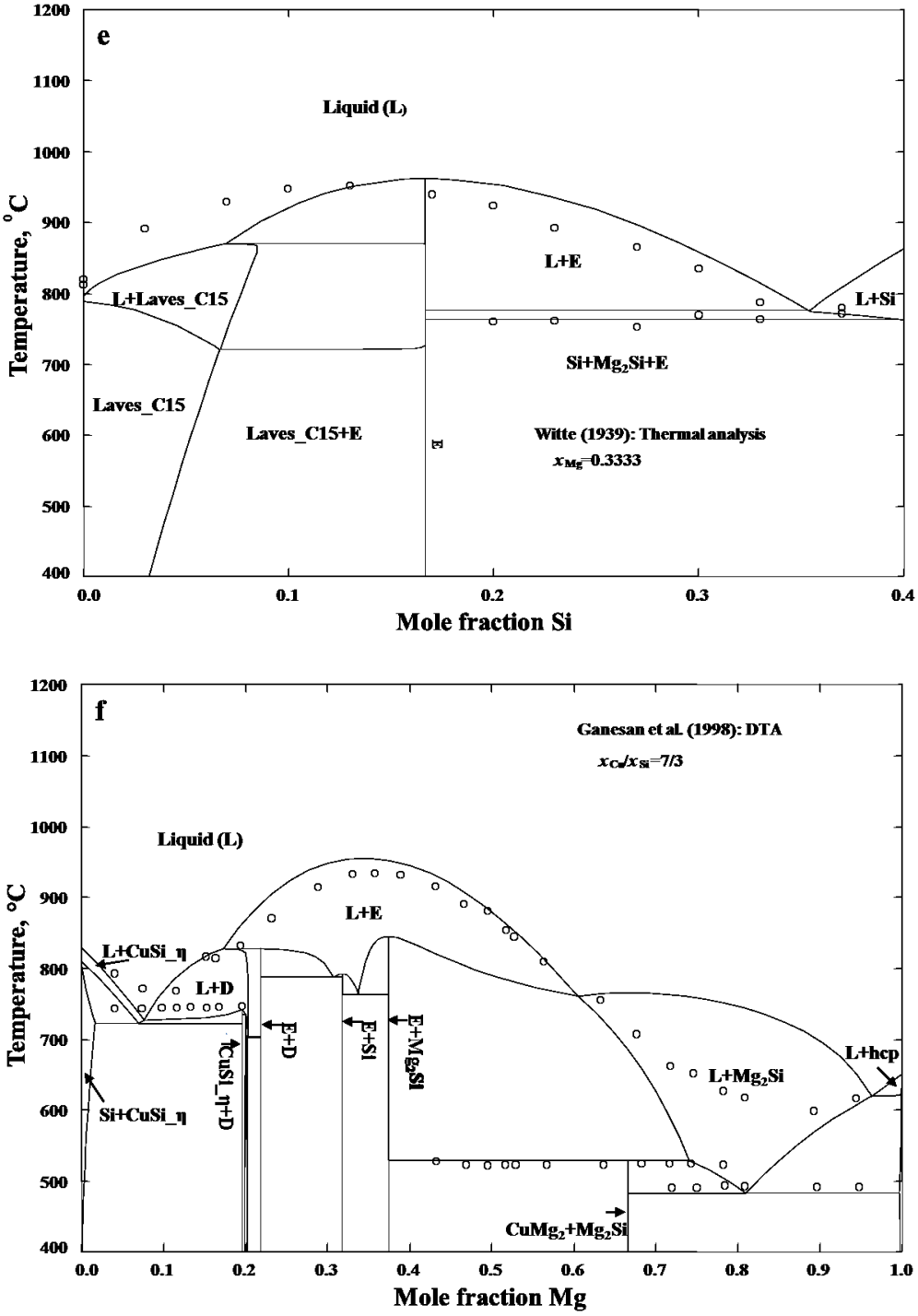

Fig. 9.16 Calculated isoplethal sections of the Cu-Mg-Si system along with the experimental data. (a) Isoplethal section with 4.5 at.% Mg, (b) isoplethal section with 11.5 at.% Mg, (c) isoplethal section with 20 at.% Mg, (d) isoplethal section with 31 at.% Mg, (e) isoplethal section with 33.33 at.% Mg, and (f) isoplethal section with Cu/Si ratio of 7/3.

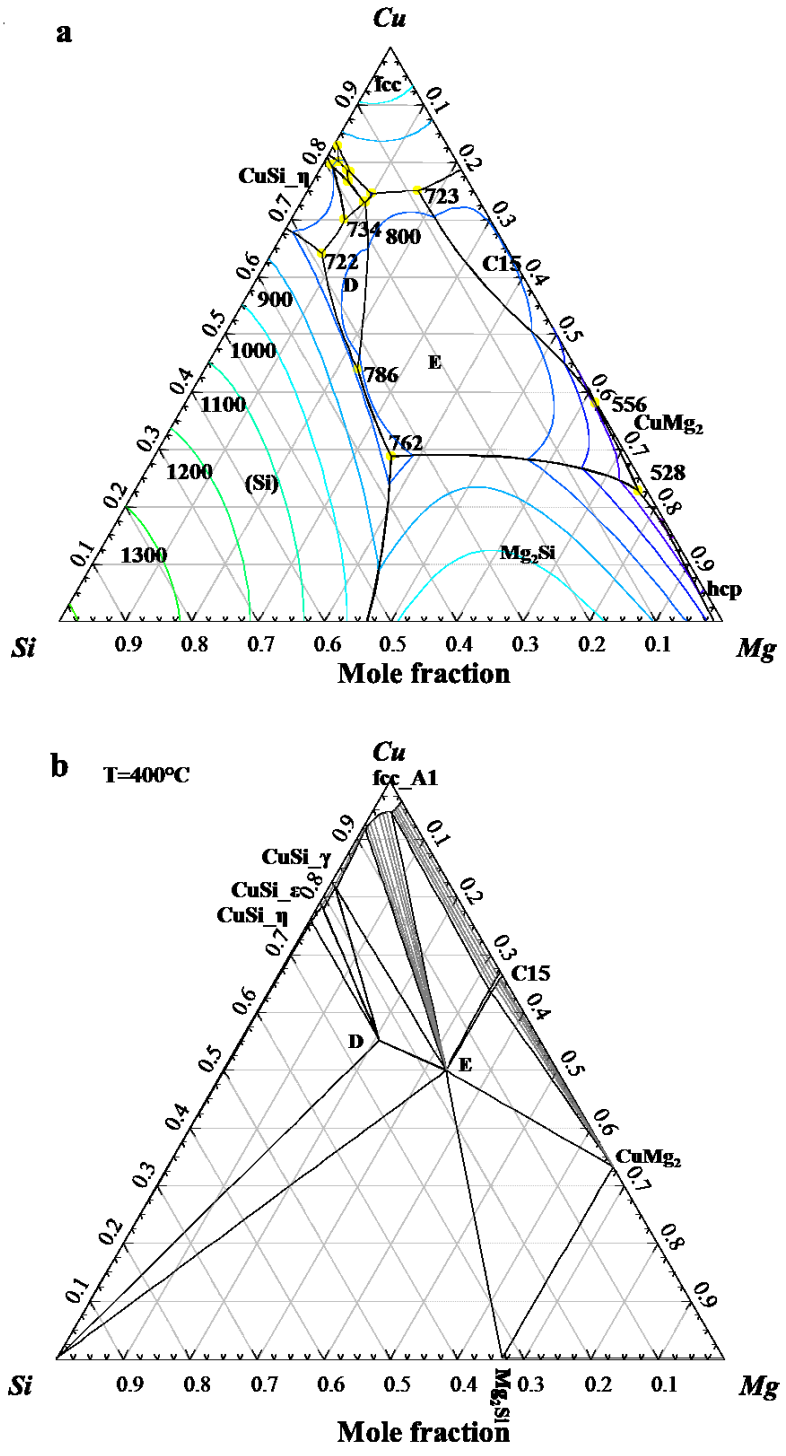

Fig. 9.17 (a) Calculated liquidus projection of the Cu-Mg-Si system. (b) Calculated isothermal section of the Cu-Mg-Si system at 400 °C.

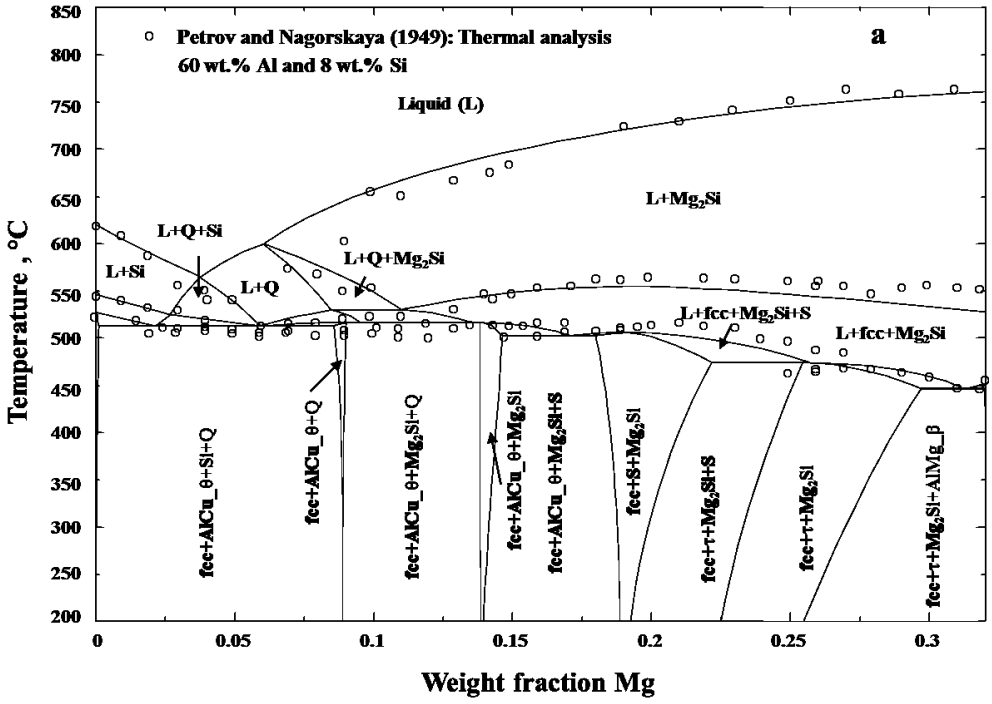
Petrov and Nagorskaya (1949): Thermal analysis
60 wt.% Al and 8 wt.% Si
a
Liquid (L)
L+Mg2Si
L+Q+Si
L+Si
L+Q
L+Q+Mg2Si
L+fcc+Mg2Si+S
L+fcc+Mg2Si
fcc+AlCu_θ+Si+Q
fcc+AlCu_θ+Q
fcc+AlCu_θ+Mg2Si+Q
fcc+AlCu_θ+Mg2Si
fcc+AlCu_θ+Mg2Si+S
fcc+S+Mg2Si
fcc+τ+Mg2Si+S
fcc+τ+Mg2Si
fcc+τ+Mg2Si+AlMg_β
Temperature , °C
Weight fraction Mg

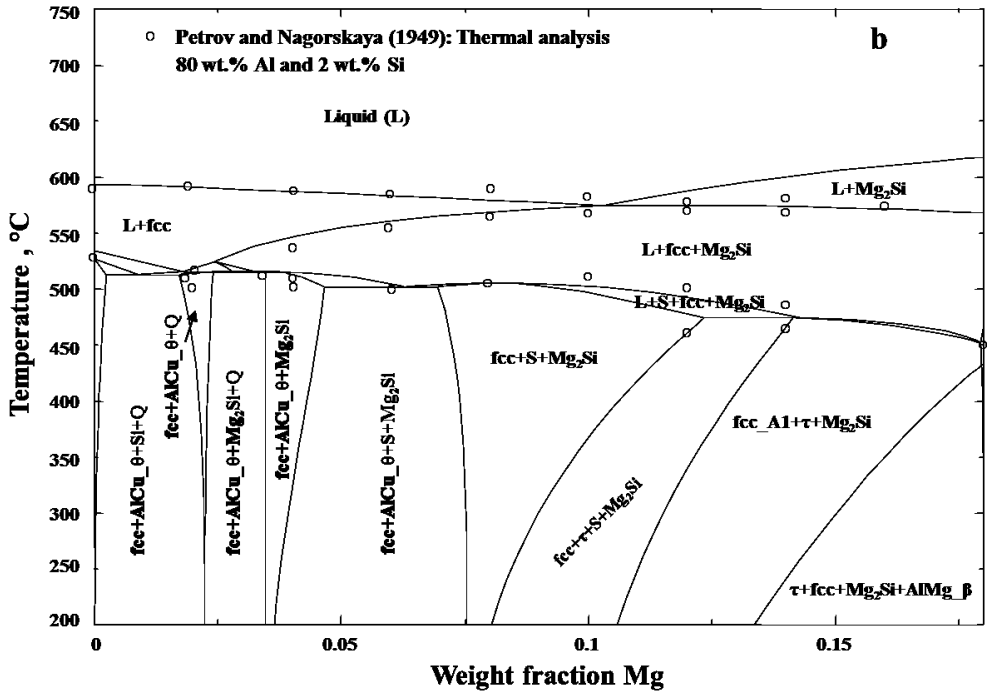
Petrov and Nagorskaya (1949): Thermal analysis
80 wt.% Al and 2 wt.% Si
b
Liquid (L)
L+Mg2Si
L+fcc
L+fcc+Mg2Si
L+S+fcc+Mg2Si
fcc+AlCu_θ+Si+Q
fcc+AlCu_θ+Q
fcc+AlCu_θ+Mg2Si+Q
fcc+AlCu_θ+Mg2Si
fcc+AlCu_θ+S+Mg2Si
fcc+S+Mg2Si
fcc_A1+τ+Mg2Si
fcc+τ+S+Mg2Si
τ+fcc+Mg2Si+AlMg_β
Temperature , °C
Weight fraction Mg

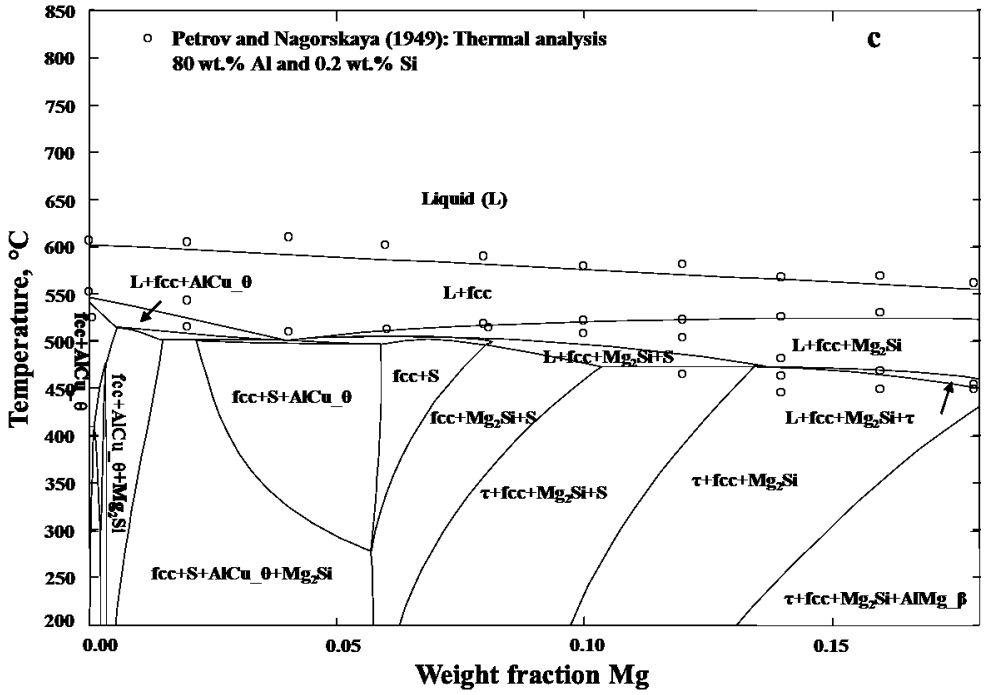
Petrov and Nagorskaya (1949): Thermal analysis
80 wt.% Al and 0.2 wt.% Si
c
Liquid (L)
L+fcc+AlCu_θ
L+fcc
L+fcc+Mg2Si
L+fcc+Mg2Si+S
fcc+S
fcc+S+AlCu_θ
fcc+Mg2Si+S
L+fcc+Mg2Si+τ
τ+fcc+Mg2Si+S
τ+fcc+Mg2Si
fcc+S+AlCu_θ+Mg2Si
τ+fcc+Mg2Si+AlMg_β
Temperature, °C
Weight fraction Mg

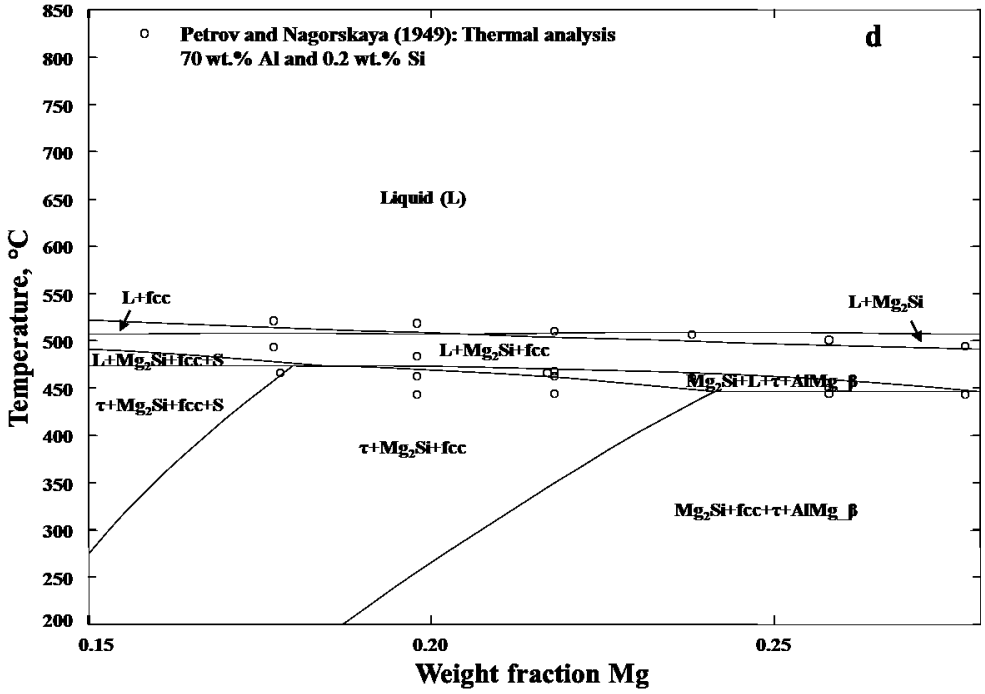
Petrov and Nagorskaya (1949): Thermal analysis
70 wt.% Al and 0.2 wt.% Si
d
Liquid (L)
L+fcc
L+Mg2Si
L+Mg2Si+fcc
L+Mg2Si+fcc+S
Mg2Si+L+τ+AlMg_β
τ+Mg2Si+fcc+S
τ+Mg2Si+fcc
Mg2Si+fcc+τ+AlMg_β
Temperature, °C
Weight fraction Mg

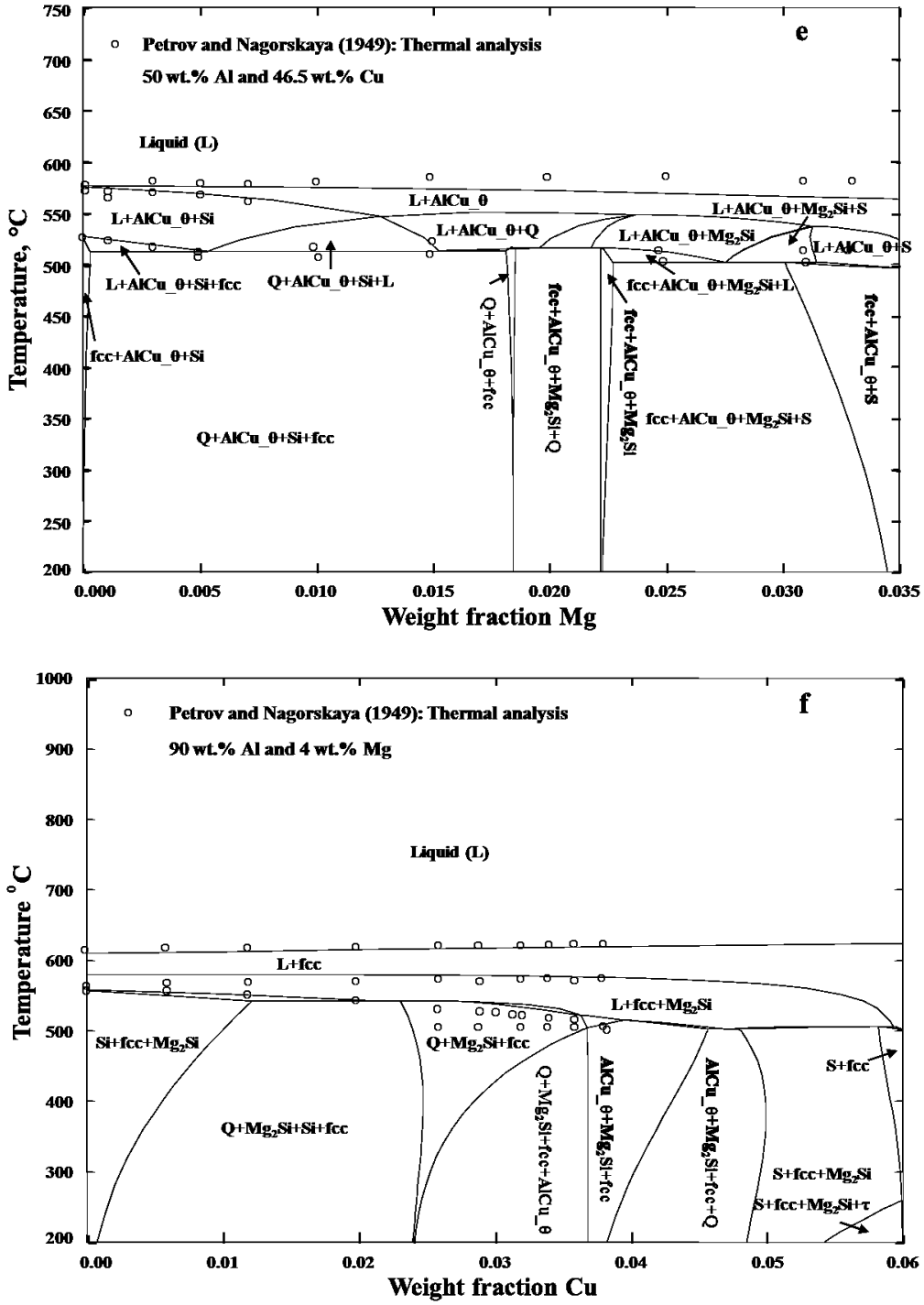

Fig. 9.18 Calculated isoplethal sections in the Al rich corner of the Al-Cu-Mg-Si quaternary system along with the experimental data. (a) Isoplethal section with 60 wt.% Al and 8 wt.% Si, (b) isoplethal section with 80 wt.% Al and 2 wt.% Si, (c) isoplethal section with 80 wt.% Al and 0.2 wt.% Si, (d) isoplethal section with 70 wt.% Al and 0.2 wt.% Si, (e) isoplethal section with 50 wt.% Al and 46.5 wt.% Mg, and (f) isoplethal section with 90 wt.% Cu and 4 wt.% Mg.

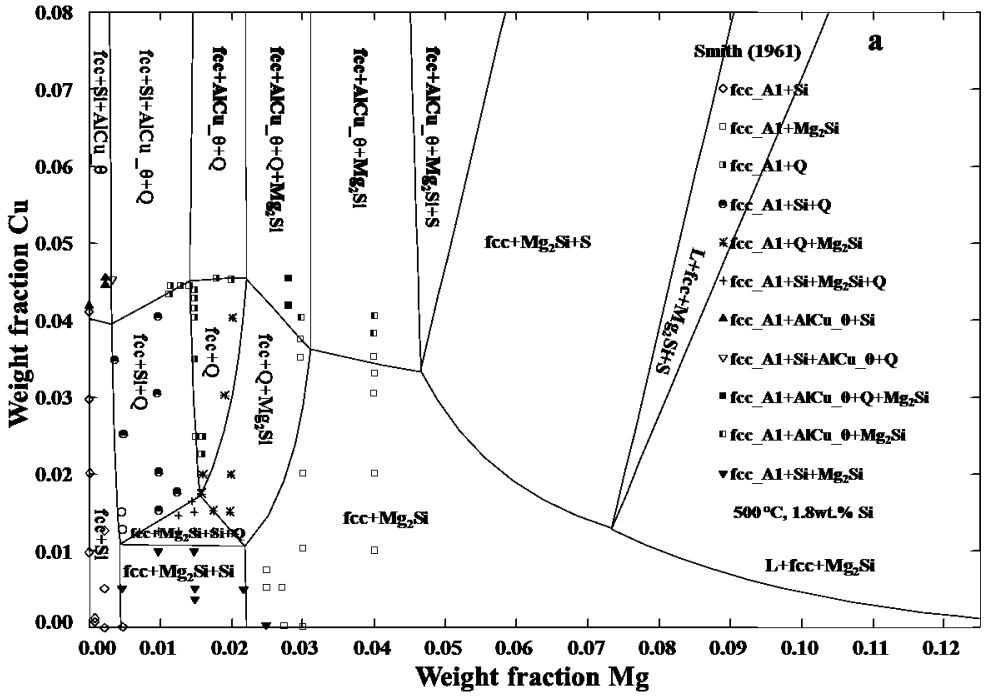
a
Smith (1961)
fcc_A1+Si
fcc_A1+Mg2Si
fcc_A1+Q
fcc_A1+Si+Q
fcc_A1+Q+Mg2Si
fcc_A1+Si+Mg2Si+Q
fcc_A1+AlCu_θ+Si
fcc_A1+Si+AlCu_θ+Q
fcc_A1+AlCu_θ+Q+Mg2Si
fcc_A1+AlCu_θ+Mg2Si
fcc_A1+Si+Mg2Si
500 °C, 1.8wt.% Si
fcc+Si+AlCu_θ
fcc+Si+AlCu_θ+Q
fcc+AlCu_θ+Q
fcc+AlCu_θ+Q+Mg2Si
fcc+AlCu_θ+Mg2Si
fcc+AlCu_θ+Mg2Si+S
fcc+Mg2Si+S
L+fcc+Mg2Si+S
fcc+Si
fcc+Si+Q
fcc+Q
fcc+Q+Mg2Si
fcc+Mg2Si+Si+Q
fcc+Mg2Si
fcc+Mg2Si+Si
L+fcc+Mg2Si
Weight fraction Cu
Weight fraction Mg
0.00
0.01
0.02
0.03
0.04
0.05
0.06
0.07
0.08
0.09
0.10
0.11
0.12

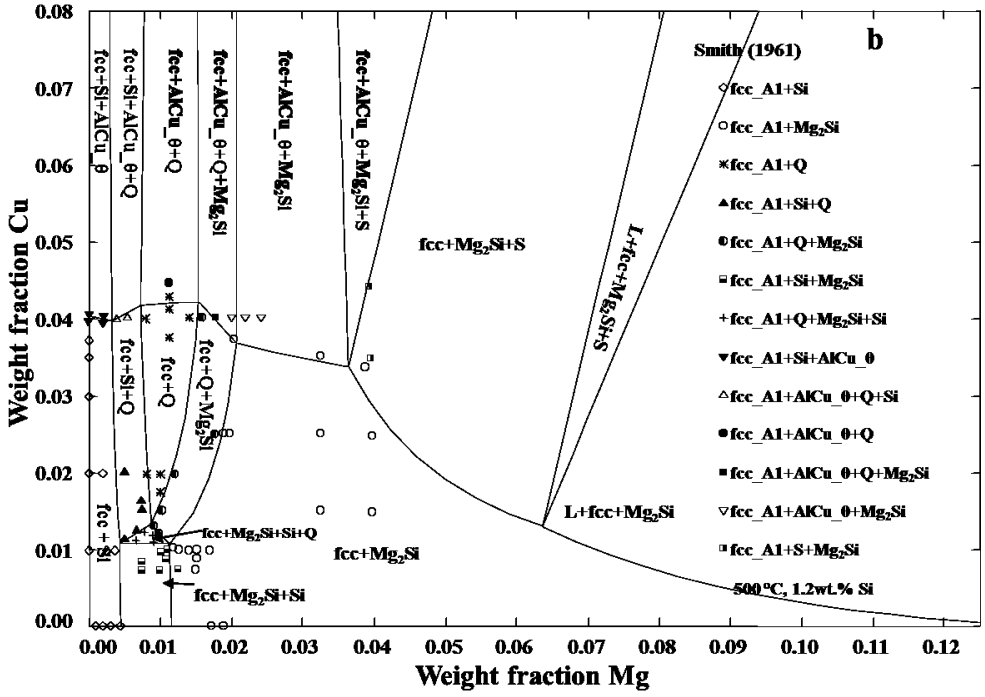
b
Smith (1961)
fcc_A1+Si
fcc_A1+Mg2Si
fcc_A1+Q
fcc_A1+Si+Q
fcc_A1+Q+Mg2Si
fcc_A1+Si+Mg2Si
fcc_A1+Q+Mg2Si+Si
fcc_A1+Si+AlCu_θ
fcc_A1+AlCu_θ+Q+Si
fcc_A1+AlCu_θ+Q
fcc_A1+AlCu_θ+Q+Mg2Si
fcc_A1+AlCu_θ+Mg2Si
fcc_A1+S+Mg2Si
500 °C, 1.2wt.% Si
fcc+Si+AlCu_θ
fcc+Si+AlCu_θ+Q
fcc+AlCu_θ+Q
fcc+AlCu_θ+Q+Mg2Si
fcc+AlCu_θ+Mg2Si
fcc+AlCu_θ+Mg2Si+S
fcc+Mg2Si+S
L+fcc+Mg2Si+S
fcc+Si
fcc+Si+Q
fcc+Q
fcc+Q+Mg2Si
fcc+Mg2Si+Si+Q
fcc+Mg2Si
fcc+Mg2Si+Si
L+fcc+Mg2Si
Weight fraction Cu
Weight fraction Mg
0.00
0.01
0.02
0.03
0.04
0.05
0.06
0.07
0.08
0.09
0.10
0.11
0.12

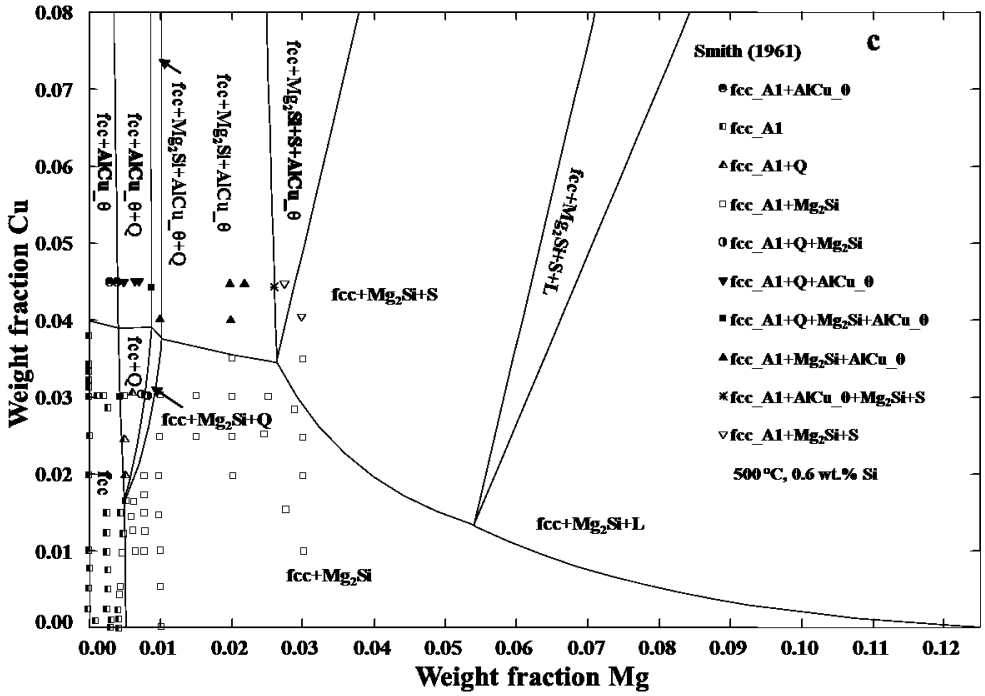

Fig. 9.19 Calculated isothermal sections in the Al rich Al-Cu-Mg-Si system at 500 ºC along with the experimental data. (a) 1.8 wt.% Si, (b) 1.2 wt.% Si, and (c) 0.6 wt.% Si.

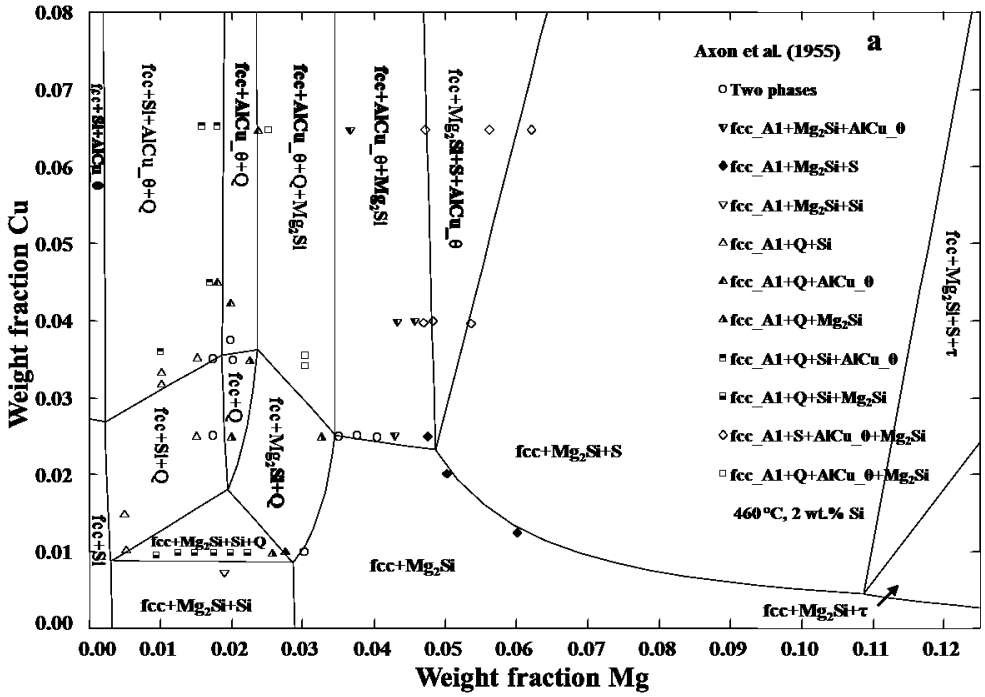
a
Axon et al. (1955)
Two phases
fcc_A1+Mg2Si+AlCu_θ
fcc_A1+Mg2Si+S
fcc_A1+Mg2Si+Si
fcc_A1+Q+Si
fcc_A1+Q+AlCu_θ
fcc_A1+Q+Mg2Si
fcc_A1+Q+Si+AlCu_θ
fcc_A1+Q+Si+Mg2Si
fcc_A1+S+AlCu_θ+Mg2Si
fcc_A1+Q+AlCu_θ+Mg2Si
460 °C, 2 wt.% Si
fcc+Mg2Si+S
fcc+Mg2Si
fcc+Mg2Si+Si
fcc+Mg2Si+τ
fcc+Mg2Si+Si+Q
Weight fraction Cu
Weight fraction Mg

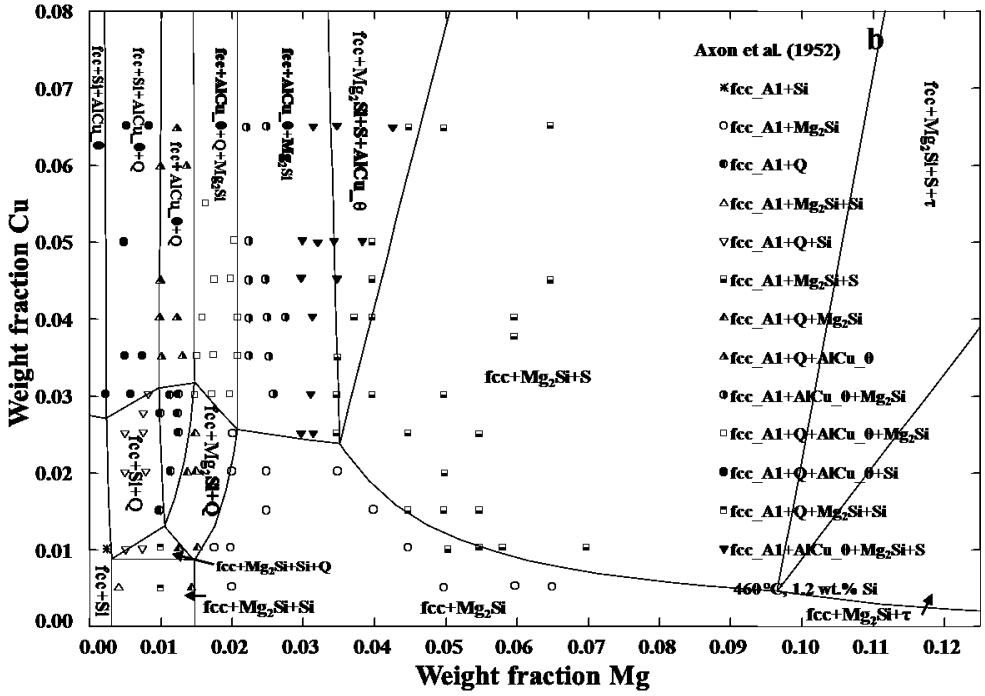
b
Axon et al. (1952)
fcc_A1+Si
fcc_A1+Mg2Si
fcc_A1+Q
fcc_A1+Mg2Si+Si
fcc_A1+Q+Si
fcc_A1+Mg2Si+S
fcc_A1+Q+Mg2Si
fcc_A1+Q+AlCu_θ
fcc_A1+AlCu_θ+Mg2Si
fcc_A1+Q+AlCu_θ+Mg2Si
fcc_A1+Q+AlCu_θ+Si
fcc_A1+Q+Mg2Si+Si
fcc_A1+AlCu_θ+Mg2Si+S
460 °C, 1.2 wt.% Si
fcc+Mg2Si+S
fcc+Mg2Si+Si+Q
fcc+Mg2Si+Si
fcc+Mg2Si
fcc+Mg2Si+τ
Weight fraction Cu
Weight fraction Mg

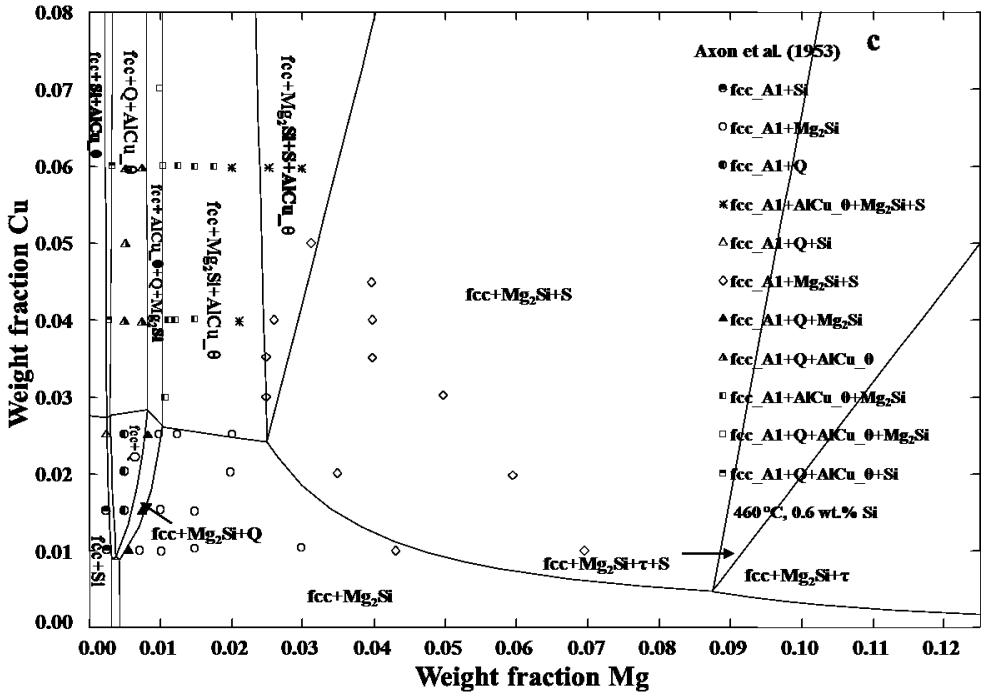

Fig. 9.20 Calculated isothermal sections in the Al rich Al-Cu-Mg-Si system at 460 ºC along with the experimental data. (a) 2 wt.% Si, (b) 1.2 wt.% Si, and (c) 0.6 wt.% Si.

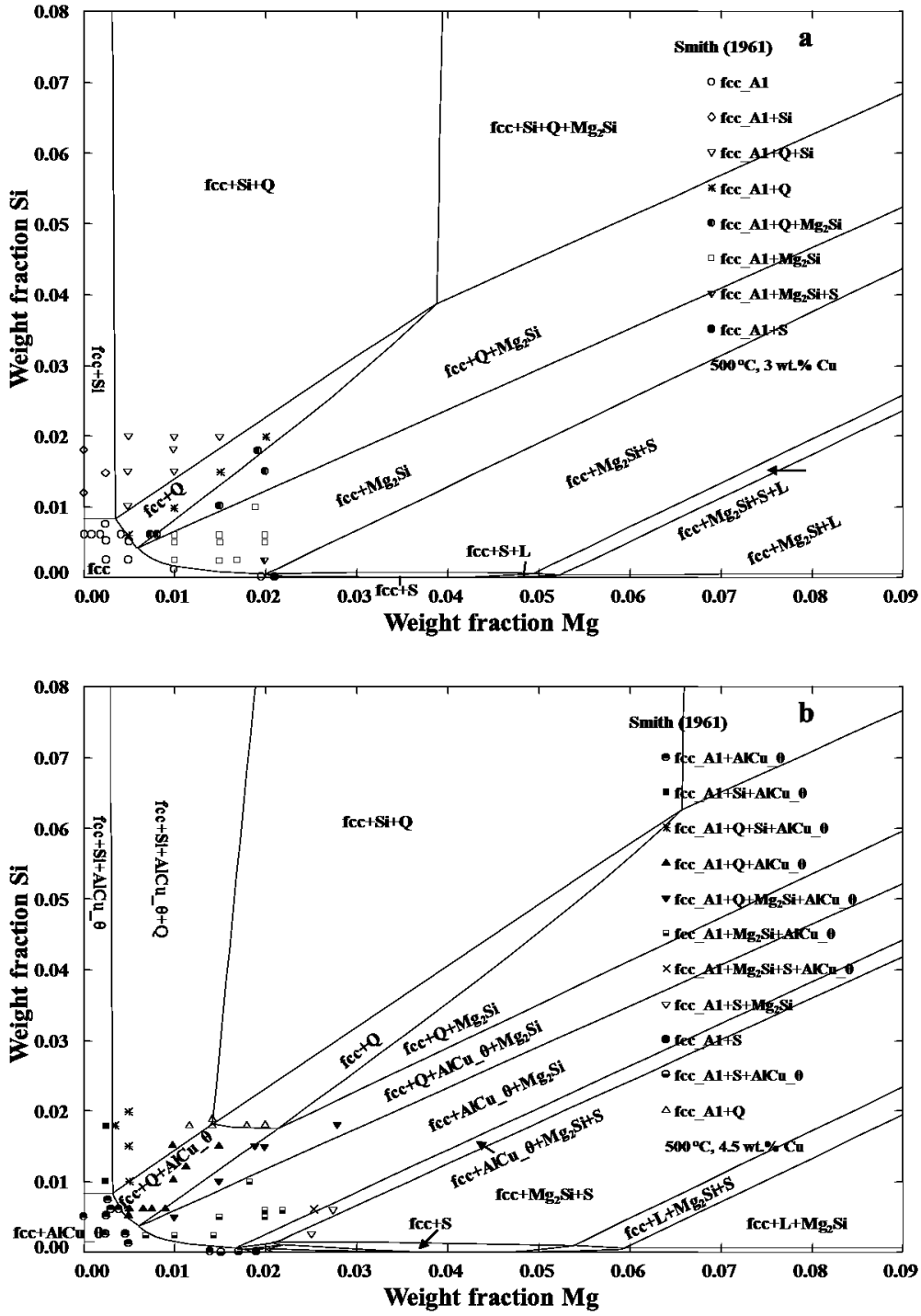

Fig. 9.21 Calculated isothermal sections in the Al rich Al-Cu-Mg-Si system at 500 ºC along with the experimental data. (a) 3 wt.% Cu and (b) 4.5 wt.% Cu.

Chapter 10 Critical reassessment of the Fe-Si system

(Submitted to CALPHAD)

Senlin Cui and In-Ho Jung

Department of Mining and Materials Engineering, McGill University, 3610 University Street, Montreal, Quebec, H3A 0C5, Canada

Abstract

The Fe-Si system has been studied extensively due to its importance in steelmaking and electrical-magnetic applications. Thermodynamic and phase diagram data of the Fe-Si system available in the literature were critically evaluated and re-optimized to improve the thermodynamic description of this system. Two sets of optimized model parameters were prepared to reproduce the available and reliable literature data. In each set of parameters, the liquid phase was described using the modified quasi-chemical model or the Bragg-Williams random mixing model. The A2/B2 and B2/D03 order-disorder transitions were also taken into account in the present study.

Key words:

The Fe-Si system; phase diagram; thermodynamic modeling; CALPHAD.

10.1 Introduction

Silicon steel (electric steel) combining low magneto-striation and high saturation magnetization has been broadly used as soft magnetic materials [1]. Silicon steel is the fundamental material for both electromagnetic energy conversion and energy transportation. The requirements for environmental conservation and energy saving have driven the expansion of the industries of green energy generation and electric vehicle production which increases the market for silicon steels. The tight controls of the composition and microstructural features are the main issues in the design of silicon steel with higher permeability and lower power loss [2]. Advanced high strength steels containing more than 1.0 wt.% Si are also commercially used in automotive industry to manufacture bodies and frames [3]. The Fe-Si system is the most fundamental binary system for the ferrosilicon production. In particular, impurity control in the liquid state and enthalpy of the liquid and solid Fe-Si alloys are important for the production and application of ferrosilicon alloy. Thus, accurate thermodynamic information of the Fe-Si system is of importance for the whole chain of the silicon steel and ferrosilicon alloy production and application.

Many thermodynamic reviews and assessments on the Fe-Si system have been performed. However, there is still room to improve the understanding and accuracy of the thermodynamic description of this system. Previously, Chart [4, 5] evaluated the thermodynamic properties related to the solid and liquid Fe-Si alloys, and reported a very early version of the calculated Fe-Si phase diagram. Kubaschewski [6] reported the most accepted version of the Fe-Si phase diagram based on the evaluation by Chart [5] and the experimental work by Schürmann and Hensgen [7]. The Fe rich part of the Fe-Si system involves the low temperature magnetic transition, A2/B2 transition, and B2/D03 transition, which makes the binary Fe-Si phase diagram as one of the most complicated binary phase diagrams in real world. Lee et al. [8] studied the A2/B2 and B2/D03 atomic ordering energy by a heat capacity integration method and further calculated the Fe-Si phase diagram. Lacaze and Sundman [9] assessed the Fe-Si system including A2/B2 transition and provided a set of thermodynamic parameters for this system. However, the B2/D03 phase transition was neglected in their assessment. This set of thermodynamic description was the most widely used one in thermodynamic database development. Later, Miettinen [10] modified the

thermodynamic descriptions of the solution phases (bcc_A2, fcc_A1, and liquid) by Lacaze and Sundman [9] for preventing an inverse liquid miscibility gap in the Fe-Si system and a better modeling of the Fe-Si-C system. Recently, Tang and Tangstad [11] slightly revised the Si rich side of the thermodynamic description from Lacaze and Sundman [9] by considering their own differential thermal analysis (DTA) results in the silicon rich side. Ohnuma et al. [12] presented a new assessment for the Fe-Si binary system where the low temperature magnetic transition, A2/B2 transition, and B2/D03 transition were all considered. However, the thermodynamic properties data of many intermetallic compounds were not fully considered in their study. Yuan et al. [13] revised the liquid phase of the thermodynamic description by Lacaze and Sundman [9] for the modeling of the Fe-Si-Zn system. In all the previous assessments, the Bragg-Williams random mixing model (BW) was used to describe the liquid phase.

The purpose of the present study is to reassess the Fe-Si system based on the critical evaluation of all the available phase diagram and thermodynamic property data of this system. Although several thermodynamic assessments have been performed, the critical review of the entire experimental data in this system is scare, so all the experimental data were collected again and reviewed. In particular, the thermodynamic data of the solid and liquid phases were more carefully evaluated. As a result of the present optimization, two sets of model parameters are presented for the case that the liquid phase was described either using BW or the Modified Quasi-chemical Model (MQM). Both the A2/B2 and B2/D03 transitions are also taken into account in the present study.

10.2 Literature review

10.2.1 Thermodynamic property data

There is abundance of experimental thermodynamic information available for the Fe-Si system in the literature. A brief summary of the thermodynamic information is given in Table 10.1.

In this section, thermodynamic information is divided into several categories and critically reviewed.

10.2.1.1 Activity data of the liquid phase

Various contributions to the measurements of the activities of Si and Fe in the liquid Fe-Si phase are available in the literature, and the selected experimental data are summarized in Fig. 10.1. Some of the activity data of Fe were derived from the activity measurements of Si using the Gibbs-Duhem relationship.

Gokcen and Chipman [14] measured the Si-O/SiO_2 equilibrium in the liquid Fe and derived the activity of Si at 1600 °C. Using the same technique, the activity of Si was measured by Matoba et al. [15] in the dilute Si region at 1570-1680 °C, Bowles et al. [16] up to 19.7 at.% Si at 1560 °C, and Cirilli et al. [17] from 3.7 to 17.9 at.% Si at 1560 °C.

The galvanic cell composed of Fe-Si|Silicate slag|pure Si was utilized to measure the activity of Si by Sanbongi and Ohtani [18] at 1460-1540 °C, Ohtani [19] in the dilute Fe-Si melts at 1540 °C, Schwerdtfeger and Engell [20] at 1470-1610 °C, and Sudavtsova et al. [21, 22] at 1600 °C. Fruehan [23] employed the Cr-Cr_2O_3(s)|ZrO_2(CaO)|Fe-Si(l), SiO_2(s) and Cr-Cr_2O_3(s)|ThO_2(Y_2O_3)|Fe-Si(l), SiO_2(s) galvanic cells to measure the activity of Si in the entire composition range of the liquid Fe-Si alloys at 1500 and 1600 °C. Slye and Fruehan [24] further investigated the activity of Si using the solid electrolyte galvanic cell of Cr-Cr_2O_3(s)|ThO_2(Y_2O_3)|Fe-Si-O-SiO_2(s) for the liquid Fe-Si alloy and reevaluated the previous experimental data by Fruehan [23], which are used in the current study. Sano and Okajima [25] also studied the activity of Si in the Fe-Si melts at 1470 and 1510 °C using a galvanic cell.

Chipman et al. [26] studied the activity of Si by measuring the equilibrium distribution of Si between liquid Ag-Si and liquid Fe-Si at 1420 °C. From the known Si activity in the liquid Ag-Si, the activity of Si in the liquid Fe-Si was calculated. Similar technique was employed for various ranges of Si contents by Chipman and Baschwitz [27] at 1420 and 1530 °C, Turkdogan et al. [28]

at 1400-1600 °C, Smith and Taylor [29] at 1450 and 1570 °C, and Murakami et al. [30, 31] up to 60 at.% Si at 1450 and 1540 °C.

Vapor pressure measurements using the Knudsen effusion cell were employed to determine the activities of Fe and Si by Yamada et al. [32] at 1600 °C. Miki et al. [33], Zaitsev et al. [34], and Hsu et al. [35] also used the same or similar technique at the temperature range from 1450 to 1600 °C. Besides, Schneider and Meyer-Jungnick [36] also measured the activity of Si at 1250 °C.

10.2.1.2 Enthalpy data of the liquid phase

The solution calorimetry method was employed to measure the enthalpy of mixing of the liquid Fe-Si alloy by Korber and Oelsen [37], Abdel-Aziz et al. [38], and Iguchi et al. [39] in the whole composition range at 1560-1600 °C. Tripolitov et al. [40] and Shumikhin et al. [41] also measured the enthalpy of mixing in the Fe rich region at 1600 °C and 1700 °C, respectively. Kanibolotsky et al. [42] measured the enthalpy of mixing at 1477 °C using high temperature isoperibolic calorimetry. The integral enthalpy of mixing of the liquid phase was also derived by Gertman and Gel'd [43], Woolley and Elliott [44], Chistyakov et al. [45], Gel'd et al. [46] from their partial enthalpy of mixing data in the temperature range between 1525 °C and 1650 °C. Fruehan [23] and Sudavtsova et al. [21, 22] calculated the enthalpy of mixing at 1600 °C from their electron motive force (emf) results. Zaitsev et al. [34] derived it from their Knudsen effusion cell vapor pressure data. Petrushevskii and Gel'd [47] calculated the enthalpy of mixing at 1600 °C based on the concept of short range order parameter. Filippov [48] investigated the secondary order phase transformation in the molten Fe-Si alloys by measuring the light radiation intensity and obtained the heat of mixing. Safonov et al. [49] calculated the enthalpy of mixing of the Fe-Si alloys at 1550 °C using a cell method. The selected enthalpy of mixing data are plotted in Fig. 10.2. The results from Filippov [48] and Abdel-Aziz et al. [38] show a large deviation from other experimental data. It should be also noticed that the indirect results of Sudavtsova et al. [21, 22] derived from their emf results are much more negative than other's data.

Many groups of researchers investigated the partial enthalpies of mixing of Fe and Si. Chipman and Grant [50] studied the partial enthalpy of Si in the molten Fe at 1600 °C using an

induction furnace as a high temperature calorimeter. Gertman and Gel'd [43] measured the partial enthalpies of Fe and Si in the whole composition range at 1525 °C using an isothermal calorimeter. Woolley and Elliott [44], Vatalin and Kozlov [51], Chistyakov et al. [45], and Gel'd et al. [46] measured the partial enthalpy in the Fe rich side in the temperature range between 1525 °C and 1650 °C by the high temperature calorimetry technique. Tripolitov et al. [40], Iguchi et al. [39], and Kanibolotsky et al. [42] derived the partial enthalpy of mixing from their integral enthalpy of mixing data between 1477 and 1600 °C. Murakami et al. [30], Chipman et al. [26], and Turkdogan et al. [28] calculated the partial enthalpy of Si and Fe from their measured equilibrium distribution data at 1600 °C. Fruehan [23] and Sudavtsova et al. [21, 22] calculated the partial enthalpies of mixing of both Fe and Si at 1600 °C from their emf data. Petrushevskii and Gel'd [47] calculated the partial enthalpy of mixing at 1600 °C on the basis of the short range order parameter. Zaitsev et al. [34] and Miki et al. [33] calculated the partial enthalpy of mixing from their measured vapor pressure data. The selected partial enthalpies of mixing of Si and Fe are presented in Figs. 10.3(a) and (b), respectively. Most of the direct experimental data are consistent with each other, and the general trend of these data can be clearly seen.

10.2.1.3 Activity data of the bcc phase

Vecher et al. [52] determined the activity of Fe in the Fe-Si alloys with 75.5 to 94.5 at.% Fe at 727 °C using a galvanic cell of Fe(s)|Fe^{2+}, KI and NaI|FeSi(s). Sakao and Elliott [53] measured the activity of Si in the bcc solution (2.8 to 8.4 at.% Si) at 1100-1350 °C using a galvanic cell of Mo, Si(s)|SiO_2-Li_2O|Fe-Si(s), Mo. The experimental data from Vecher et al. [52] and Sakao and Elliott [53] are presented in Figs. 10.4(a) and (b), respectively.

10.2.1.4 Heat capacity and heat content of the intermetallic phases

The heat capacity of alloy with composition of Fe_3Si was measured by Krentsis and Gel'd [54-57] from 55 to 1800 K, and the heat content of Fe_3Si were presented by Krentsis and Gel'd [55, 58]. The low temperature values (below 300 K) were measured by adiabatic calorimetry, while the high temperature data were determined by high temperature calorimetry.

No experimental measurement for the heat capacity of Fe_2Si was reported in the literature. Salina and Baisanov [59, 60] roughly estimated the heat capacity, heat content, and entropy of Fe_2Si by a semi-empirical equation based on melting temperature and density.

The heat capacity of Fe_5Si_3 was measured calorimetrically by Krentsis and Gel'd [54] from 55 to 300 K, Gel'd and Krentsis [56, 57] from 60 to 300 K, Krentsis et al. [61] from 55 to 1300 K, Kalishevich et al. [62] from 13 to 60 K, and Sudakova et al. [63] from 13 to 370 K, while the heat content of Fe_5Si_3 was reported by Davydov et al. [64] from 273 to 1273 K, Krentsis and Gel'd [58] from 0 to 1300 K, and Krentsis et al. [61] from 55 to 1400 K. The heat capacity curve shows a kink at 360±5 K which refers to the ferromagnetic to paramagnetic transition temperature. However, the recent measurement by Seo et al. [65] indicates a Curie temperature of 380 K.

Several groups of authors investigated the heat capacity and heat content of the FeSi compound. The heat capacity measurements were carried out by Schubel [66] from 373 to 873 K, Davydov et al. [64] from 273 to 1473 K, Krentsis and Gel'd [54] from 55 to 300 K, Krentsis et al. [61] from 55 to 1923 K, Gel'd and Krentsis [56, 57] from 60 to 300 K, and Acker et al. [67] from 11 to 400 K. On the other hand, the heat content was measured by Davydov et al. [64] from 273 to 1473 K, Krentsis and Gel'd [58] from 0 to 1300 K, Krentsis et al. [61] from 55 to 1923 K, and Ferrier and Jacobi [68] from 1123 to 1853 K. In addition, Kelley [69] derived the heat content of FeSi from 400 to 900 K by reanalyzing the experimental data measured by Schubel [66]. Acker et al. [67] also presented the optimized high temperature heat capacity and heat content of FeSi. The reported heat capacity and heat content of FeSi in the literature agree well with each other.

The heat capacity of $FeSi_2$ was measured in the temperature range from 50 to 1200 K by Krentsis et al. [54, 56, 57, 70] using low temperature adiabatic calorimetry and high temperature calorimetry. The heat contents of $FeSi_2$ from 0 to 1233 K were reported by Krentsis et al. [58, 70].

The heat capacity of Fe_3Si_7 was measured by Krentsis et al. [54, 56, 57, 70] from 50 to 1700 K, Serebrennikov and Gel'd [71] from 290 to 1400 K, Davydov et al. [64] from 273 to 1473 K, and Acker et al. [67] from 11 to 400 K. The high temperature heat capacity data derived from the heat content experiments by Krentsis et al. [70] and Serebrennikov and Gel'd [71] show a large

disagreement with each other and discontinuity with the low temperature heat capacity data measured by Krentsis et al. [54, 56, 57, 70] and Acker et al. [67] using adiabatic calorimetry. The results from Davydov et al. [64] also show strange shaped curve. Similarly, the heat content of Fe_3Si_7 was reported by Acker et al. [67] from 11 to 400 K, Krentsis et al. [70] from 50 to 1700 K, and Serebrennikov and Gel'd [71] from 273 to 1473 K using the calorimetry method. These data are generally consistent with each other.

Davydov et al. [64], Kendall and Hultgren [72], Pandey and Kohlhaas [73], Normanton and Argent [74], Pepperhoff and Ettwig [75], and Ettwig and Pepperhoff [76] also measured the heat capacities and heat contents of various Fe-Si alloys other than the intermetallic compositions using various calorimetry techniques, as listed in Table 10.1.

10.2.1.5 Enthalpy and entropy of formation of the solid phases

Korber et al. [37, 77] measured the enthalpy of formation of the solid Fe-Si alloys at room temperature in the whole composition range using a high temperature calorimeter. The enthalpy of formation of the solid Fe-Si alloys was also measured calorimetrically by Krentsis and Gel'd [55] for the Fe_3Si phase, Abdel-Aziz et al. [38] in the whole composition range of the Fe-Si system, Jounel et al. [78] for FeSi, Gorelkin et al. [79, 80] for FeSi and $FeSi_2$, and Meschel and Kleppa [81] for FeSi. Bosholm et al. [82] applied the chemical transport reaction to measure the heat of formation of Fe_3Si, Fe_5Si_3, FeSi, $FeSi_2$, and Fe_3Si_7. Recently, Liang et al. [83] calculated the heat of formation of all the compounds in the Fe-Si alloys using first principles calculations. The USPP GGA-PW91 values show best agreement with the experimental results. In addition, Vecher et al. [84, 85] derived the enthalpies of formation of the Fe_3Si, FeSi, $FeSi_2$, and Fe_3Si_7 compounds at 298 K and 1000 K from their emf data between 600 and 800 °C using a galvanic cell of $Fe|Fe^{2+}$ in fused KI+NaI|Fe-Si. Zaitsev et al. [86] calculated the enthalpy of formation of FeSi and Fe_3Si_7 using their Knudsen effusion cell data. Acker et al. [67] optimized the enthalpy of formation of FeSi and Fe_3Si_7 from their calorimetry data. The enthalpy of formation of all the compounds at 298.15 K are summarized in Table 10.5 and plotted in Fig 10.11(a). The enthalpy of formation seems quite scatter, but it is still believed that the calorimetric data are more reliable than other indirect calculations from the emf, Knudsen effusion cell, and chemical transportation results.

The most direct method to determine the entropy at 298.15 K of a solid compound is the heat capacity measurement at the low temperature using the adiabatic calorimetry technique. As shown in Fig. 10.5, the low temperature heat capacities of Fe_5Si_3, FeSi, $FeSi_2$, and Fe_3Si_7 were measured and used to determine the entropy at 298.15 K for each compound. The results are summarized in Table 10.6. In addition, the indirect estimation of the entropy of formation from other Gibbs energy measurements using the emf, Knudsen cell, and chemical transportation techniques are also listed in the table. It can be seen from Table 10.6 that the entropy at 298.15 K measured by the adiabatic calorimetry technique are generally consistent with each other, which indicates these data are of high confidence. The results derived from the indirect methods are rather scattered, as expected.

10.2.2 Phase diagram information

All the available contributions to the measurements of the Fe-Si phase diagram are listed in Table 10.2. According the literature, the stable compounds in the Fe-Si system are FeSi, Fe_2Si, Fe_5Si_3, Fe_3Si_7, and $FeSi_2$. The space group, prototype, and lattice parameters for each stable compound are presented in Table 10.3, and the invariant reactions are summarized in Table 10.4. A summary of the experimental Fe-Si phase diagram data is presented in Figs. 10.7 to 10.10.

10.2.2.1 Gamma loop

The gamma loop of the Fe-Si alloys was investigated by Ruer and Klesper [87] from 0 to 0.024 at.% Si by thermal analysis, Esser and Oberhoffer [88] from 0 to 3.54 at.% Si by dilatometry, Wever and Giani [89] from 0 to 3.61 at.% Si by magnetic analysis, thermal analysis, and optical microanalysis, Oberhoffer and Kreutzer [90] by chemical analysis, optical microanalysis, and x-ray diffraction analysis (XRD), Crangle [91] and Fischer et al. [92] using the paramagnetic susceptibility measurements, and Übelacker [93] by the magnetic susceptibility and DTA measurements. In particular, Wever and Giani [89] and Übelacker [93] measured the gamma loop in the entire composition range. As can be seen in Fig. 10.7, the experimental results from Oberhoffer and Kreutzer [90] and Crangle [91] show a large deviation from others.

10.2.2.2 Tx, Ty, and Tc lines: the second order transitions

The Tx and Ty lines refer to the bcc_A2 to bcc_B2 transition, and the bcc_B2 to bcc_D03 transition, respectively, while the Tc line corresponds to the magnetic transition. As many experiments have been carried out for these phase transformations and they are somewhat scattered, only the most accepted experimental data for the Tx, Ty, and Tc lines are plotted in Fig. 10.8. The Tx line and/or Ty line were measured by Dokken [94] using resistance measurements, Meinhardt and Krisement [95], Ettwig and Pepperhoff [76], and Inden and Pitsch [96] using neutron diffraction, Polishchuk and Selisskii [97] using high temperature XRD, Schlatte et al. [98-100] and Swann et al. [101] using transmission electron microscope (TEM) analysis, Meco and Napolitano [102] by DTA, and Ohnuma et al. [12] using diffusion couple with electron probe microanalysis (EPMA) and TEM. The experimental results of the Tx line from Dokken [94] and Meinhardt and Krisement [95] show a systematical deviation from those measured by Ettwig and Pepperhoff [76], Inden and Pitsch [96], Polishchuk and Selisskii [97], Schlatte [98-100], Swann et al. [101], and Ohnuma et al. [12]. Similar to the measured Tx line data, the measured Ty lines from Dokken [94] and Meinhardt and Krisement [95] are inconsistent with those from other researchers. The Tc line was measured by Murakami [103], Wever and Giani [89], Lecocq and Lecocq [104], Osawa and Murata [105], and Haughton and Becker [106] using magnetic analysis, Dokken [94] using resistance measurements, Meinhardt and Krisement [95] using neutron diffraction, Pepperhoff and Ettwig [75] and Ettwig and Pepperhoff [76] using calorimetry, Inden and Pitsch [96] using both calorimetry and neutron diffraction, and Meco and Napolitano [102] and Köster [107] using DTA. The measured magnetic transition temperatures are consistent with each other.

The transformation between A2 and B2 (Tx) occurs homogenously both above and below the Curie temperature. However, there are discrepancies for the B2 and D03 phase transformation (Ty) in the literature. Swann et al. [101] found that the B2/D03 ordering reaction occurs homogeneously above Tc but becomes a first order transition below Tc. Schlatte et al. [98-100] indicated that there is a two phase region (B2+D03) above the Curie temperature and disappeared in high temperature (above 700 °C). That is, the order disorder transition at high temperature is a second order transition, but it becomes a first order transition at low temperature. Ohnuma et al.

[12] further confirmed the two phase region (B2+D03) above the Tc line has a horn shape. On the other hand, the TEM and XRD results from Ustinovshikov and Sapegina [108] indicates that two phase regions of A2+B2 and A2+D03 are stable instead of B2 and D03 single phase regions. Lecocq and Lecocq [104] reported that B2/D03 transition has a maximum temperature of about 1150 °C near the Fe_3Si composition from their magnetic analysis results, which is inconsistent with other studies [12, 98-100]. The current optimization prefers that the B2/D03 transformation is a second order transition at high temperature and a first order transition in low temperature with a two phase region above Tc as suggested by Ohnuma et al. [12].

The calculated Tx line according to the current optimization and the evaluated Ty line are presented in Fig. 10.8(a) with the selected experiment data from Ohnuma et al. [12], Schlatte et al. [98-100], Inden and Pitch [96], Ettwig and Pepperhoff [76], Polishchuk and Selisskii [97], and Meco and Napolitano [102]. It can be seen from the figure that both the Tx and Ty lines are accurately described. In Fig. 10.8(b), the measured magnetic transition line (Tc) is presented together with the presently calculated magnetic transition temperature of the bcc_A2 phase. The agreement is satisfactory.

10.2.2.3 Phase diagram

The solubility of Fe in the solid Si was measured by many researchers as shown in Fig. 10.9: Struthers [109] using the radio isotope Fe^{59}, Lee et al. [110] and Colas and Weber [111] by the electron paramagnetic resonance (EPR) technique, Feichtinger [112] using the Hall's method and EPR method, Weber and Riotte [113] and Wiehl et al. [114] using the instrumental neutron activation analysis (INAA) and the EPR technique, Nakashima et al. [115] by the deep level transition spectroscopy (DTLS) and the Hall's method, and McHugo et al. [116] using the INNA method. The experimental solubility of Fe measured by Feichtinger [112] is slightly larger than the optimized solubility in the present study. This may happen due to the difficulty in the measurement of the solubility under equilibrium with the liquid phase.

The experimental study for the homogeneity range of the intermetallic compounds is very limited. Abrikosov [117] and Sidorenko et al. [118, 119] measured the homogeneity range of

Fe_3Si_7 using the emf measurements and XRD analysis, respectively. Although the non-negligible homogeneity range was observed, the two experimental results are quite different. Thus, the Fe_3Si_7 phase was treated as a stoichiometric compound in the present study. Similarly, the homogeneity range of FeSi was measured by Vainshtein et al. [120] to be 50.4-50.7 at.% Si from the Mössbauer spectrum analysis, and Wachtel and Mager [121] to be 49.7 to 50.8 at.% of Si at 1150 °C using the magneto thermal measurements. As the homogeneity range of FeSi is less than 1 at.% Si, the FeSi phase was also treated as a stoichiometric compound in this study. Köster and Gödecke [122] reported that the Fe_2Si phase has a certain homogeneity range. However, the later work by Schürmann and Hensgen [7] indicated that Fe_2Si is a stoichiometric compound. No homogeneity range for other intermetallic phases has been reported.

Numerous phase diagram studies were carried out for the Fe-Si system, and the selected phase diagram data are plotted in Fig. 10.10. The earlier Fe-Si phase diagram measurements include Guerlter and Tammann [123], Ruer and Klesper [87], Murakami [103, 124], Kurnakow and Urasov [125], and Bamberger et al. [126]. Haughton and Becker [106] systematically investigated the phase equilibrium in the Fe-Si alloys for the first time by a combination of thermal analysis, magnetic analysis, the dilatometry technique, and quenching experiment followed by optical microanalysis. The phase diagram in the Si rich region was almost established since then. Further measurements of the Si rich side of the Fe-Si phase diagram are Piton and Fay [127] in the region near the Fe_3Si_7 compound from 955 to 1220 °C and 64-75 at.% Si by DTA, Wachtel and Mager [121] for the FeSi-Si partial system from 600 to 1400 °C by magneto thermal measurements, Wefers [128] for the FeSi-Si sub-system by DTA and quenching experiment followed by optical microanalysis and XRD phase determination, and Tang and Tangstad [11] from 72 to 100 at.% Si using DTA. All these experimental data in the Si rich region are generally consistent with each other.

Greiner and Jette [129] studied the phase diagram from 24 to 50 at.% Si using quenching experiments followed by XRD phase analysis. Their results indicate that the Fe_3Si_2 (Fe_5Si_3) compound is unstable below 825 °C. In addition, the phase boundaries of bcc/FeSi and bcc/Fe_3Si_2 (Fe_5Si_3) were determined from 825 to 1030 °C. Osawa and Murata [105] confirmed that the formerly reported Fe_3Si_2 to be Fe_5Si_3 according to their phase diagram measurements from 0 to 80

at.% Si using dilatometry, thermal analysis, magnetic analysis, XRD analysis, and optical microanalysis. Übelacker and Lecocq [130] reported the stability range of Fe_5Si_3 to be from 800 to 1406 °C using magnetic analysis. Weill [131] reexamined the Fe rich region using quenching experiments followed by XRD phase analysis and reported a revised phase diagram from 0 to 45 at.% Si, which is close to the well accepted diagram nowadays. The phase diagram in the Fe rich region was also investigated by Übelacker [132, 133] from pure Fe to FeSi using magnetic susceptibility measurements, dilatometry, and thermal analysis, Köster and Gödecke [122] and Köster [107] from 10 to 40 at.% Si at 900-1200 °C using DTA and quenching experiments followed by SEM and XRD analysis, Schürmann and Hensgen [7] from 0 to 50 at.% Si by DTA, thermal analysis, and equilibration, and Meco and Napolitano [102] from 0 to 30 at.% Si by DTA. The experimental data from Übelacker [132, 133], Köster and Gödecke [122], Köster [107], and Schürmann and Hensgen [7] are consistent with each other, but the results from Meco and Napolitano [102] are rather different from others.

10.3 Thermodynamic modeling

10.3.1 Unary phases and stoichiometric compounds

For the pure elements and stoichiometric compounds their Gibbs free energies at a given temperature (T in K) can be expressed as:

$$G_T^o = H_T^o - S_T^o T \tag{10.1}$$

$$H_T^o = \Delta H_{298.15}^o + \int_{298.15}^{T} C_P dT \tag{10.2}$$

$$S_T^o = S_{298.15}^o + \int_{298.15}^{T} \frac{C_P}{T} dT \tag{10.3}$$

where H_T and S_T are enthalpy and entropy at temperature T, $\Delta H_{298.15}^o$ is the enthalpy of formation at 298.15 K, $S_{298.15}^o$ is the entropy at 298.15 K, and C_P is the heat capacity.

The thermodynamic properties of the pure elements Fe and Si were taken from the SGTE database complied by Dinsdale [134]. In the present study all the intermetallic compounds Fe_5Si_3, Fe_2Si, FeSi, $FeSi_2$, and Fe_3Si_7 were treated as stoichiometric compounds. The heat capacities of Fe_5Si_3, FeSi, $FeSi_2$, and Fe_3Si_7 were evaluated from the heat capacity and heat content data in the literature. As there is no available experimental heat capacity and heat content data for Fe_2Si, the heat capacity of Fe_2Si was assumed to follow the Neumann-Kopp relation. $\Delta H^{o}_{298.15}$ and $S^{o}_{298.15}$ of each compound were determined based on the experimental thermodynamic data and phase diagram data. The magnetic contributions to the Gibbs energy of the bcc and Fe_5Si_3 phase were described using the model proposed by Hillert-Jarl-Inden [135]:

$$\Delta G_{mag} = RT\ln(\beta+1)g(\tau) \tag{10.4}$$

where R is gas constant, τ is T/T^*. T^* is the critical temperature for magnetic ordering (Curie temperature, Tc), and β is the average magnetic moment per atom of the alloy expressed in Bohr magnetons. The polynomial function $g(\tau)$ was derived by Hillert and Jarl [135].

10.3.2 Solid solutions

The fcc_A1 and bcc_A2 phases were modeled as completely disordered solutions. The Gibbs energies of the disordered phases were described by BW with the Redlich-Kister (R-K) polynomial [136]:

$$\begin{aligned} {}^{o}G^{\phi} = {}^{o}G^{\phi}_{Fe}x_{Fe} + {}^{o}G^{\phi}_{Si}x_{Si} + RT(x_{Fe}\ln x_{Fe} + x_{Si}\ln x_{Si}) \\ + x_{Fe}x_{Si}\sum_{i=0}^{n} L^{i,\phi}_{Fe,Si}(x_{Fe}-x_{Si})^{i} \end{aligned} \tag{10.5}$$

where the ${}^{o}G^{\phi}_{Fe}$ and ${}^{o}G^{\phi}_{Si}$ are the molar Gibbs energies of pure Fe and Si of the ϕ phase, respectively, and x_{Fe} and x_{Si} are the mole fraction of Fe and Si, respectively. $L^{i,\phi}_{Fe,Si}$ are the interaction parameters between Fe and Si in the ϕ solution.

The order-disorder transition includes chemical contribution and magnetic contribution which can be modeled by the split compound energy formalism. The B2 order contribution to the Gibbs energy can be described with a two sub-lattice model: $(Fe, Si)_{0.5}(Fe, Si)_{0.5}(Va)_3$, and that of both the B2 and D03 phases can be described using a four sub-lattice model: $(Fe, Si)_{0.25}(Fe, Si)_{0.25}(Fe, Si)_{0.25}(Fe, Si)_{0.25}(Va)_3$ simultaneously. The details of these models for the order-disorder phase transition in the Fe-Si system can be found in the recent paper by Ohnuma et al. [12]. In the present study, the ordering parameters of B2 were optimized based on the experimental data. However, the ordering parameters for D03 were taken from Ohnuma et al. [12] without any modification.

10.3.3 Liquid phase

The liquid phase was modeled by using BW and MQM [137, 138]. BW for binary solution is already introduced in Eq. (10.5). In MQM with pair approximation, the atoms Fe and Si are assumed to distribute over a quasi-lattice site in the liquid phase. The following pair exchange reaction can be considered in the binary liquid Fe-Si solution:

$$(Fe\text{-}Fe) + (Si\text{-}Si) = 2(Fe\text{-}Si) : \Delta g_{FeSi} \tag{10.6}$$

where $(i\text{-}j)$ represents a first-nearest-neighbor pair of i and j. Δg_{FeSi} is the Gibbs energy to form two moles of $(Fe\text{-}Si)$ pairs from the $(Fe\text{-}Fe)$ and $(Si\text{-}Si)$ pairs. Then the Gibbs energy of the solution can be given by:

$$G = n_{Fe}G^{o}_{Fe} + n_{Si}G^{o}_{Si} - T\Delta S^{config} + \left(n_{FeSi}/2\right)\Delta g_{FeSi} \tag{10.7}$$

where n_{Fe} and n_{Si} are the numbers of moles of the Fe and Si atoms in the solution, and n_{FeSi} is the number of moles of $(Fe\text{-}Si)$ pairs. ΔS^{config} is the configurational entropy of mixing given by a random distribution of the $(Fe\text{-}Fe)$, $(Si\text{-}Si)$, and $(Fe\text{-}Si)$ pairs in the one-dimensional Ising approximation:

$$\Delta S^{config} = -R\left(n_{Fe}\ln x_{Fe} + n_{Si}\ln x_{Si}\right) - R\left[n_{FeFe}\ln\left(\frac{x_{FeFe}}{Y_{Fe}^2}\right) + n_{SiSi}\ln\left(\frac{x_{SiSi}}{Y_{Si}^2}\right) + n_{FeSi}\ln\left(\frac{x_{FeSi}}{2Y_{Fe}Y_{Si}}\right)\right] \quad (10.8)$$

where n_{ij}, x_{ij}, and Y_i are the number of moles of each type of pairs, pair fractions, and coordination equivalent fractions, respectively. Let Z_i be the coordination number of *i* given by $Z_i n_i = 2n_{ii} + n_{ij}$ $(i \neq j)$. Further x_{ij} and Y_i are defined as:

$$x_{ij} = \frac{n_{ij}}{n_{ii} + n_{jj} + n_{ij}} \quad (10.9)$$

$$Y_i = x_{ii} + \frac{1}{2}x_{ij} \quad (10.10)$$

Δg_{FeSi} is the model parameter to reproduce the Gibbs energy of the liquid Fe-Si solution, which is expanded as a polynomial in terms of the pair fractions:

$$\Delta g_{FeSi} = \Delta g^0_{FeSi} + \sum_{i\geq 1} g^{i0}_{FeSi}\left(x_{FeFe}\right)^i + \sum_{j\geq 1} g^{0j}_{FeSi}\left(x_{SiSi}\right)^j \quad (10.11)$$

where Δg^0_{FeSi}, g^{i0}_{FeSi}, and g^{0j}_{FeSi} are the adjustable parameters which can be functions of temperature.

10.4 Optimization results and discussions

In the present work, two sets of thermodynamic parameters were optimized. In the first set of thermodynamic description, the liquid phase was described by MQM. The B2 order phase was modeled, while the D03 ordered phase was not considered for practical application in the present project. The expansion of the D03 phase to multicomponent system would be very complex. In the second optimization using BW for the liquid solution, both the B2 and D03 phases were considered like the work by Ohnuma et al. [12].

The thermodynamic parameters for the liquid phase and all stoichiometric compounds were first optimized from the available thermodynamic properties. The parameters for the Fe_5Si_3, FeSi, $FeSi_2$, and Fe_3Si_7 phases were obtained from the experimental heat capacity, enthalpy of formation and entropy data at 298.15 K, and phase diagram, and that for Fe_2Si was fixed from the phase diagram information. The parameters for the fcc_A1 phase were obtained from the experimental gamma loop information, while the thermodynamic parameters for the bcc_A2 phase were evaluated from the activity data, magnetic transition temperature, and phase diagram information. In addition, the ordering parameters for B2 were evaluated from the Tx line, and the ordering parameters for the D03 phase were directly taken from the work of Ohnuma et al. [12] without any modification. Then, the final optimization was performed to reproduce all the available and reliable experimental data in the Fe-Si system. The optimization of the parameters was conducted with the help of the FactSage software [139] (the set of parameters with MQM for liquid solution) and the Thermo-Calc academic version [140] (the set of parameters with BW for liquid solution). The final optimized thermodynamic parameters are listed in Table 10.8 and Table 10.9. Depending on the selection of the liquid model, the optimized thermodynamic parameters of the solid phases are slightly different. The optimization results are discussed below.

The calculated phase diagrams from the two sets of optimized model parameters are presented in Fig. 10.10 along with the selected experimental data. Fig. 10.10(a) shows the calculated diagram with MQM. It can be seen that the computed phase diagram can give a good description of the selected experimental data except for the phase boundary of the ordered bcc solution related to Fe_2Si and Fe_5Si_3, and the eutectoid temperature of Fe_5Si_3 = bcc_B2 (D03) + FeSi. This is because the D03 ordered phase was not considered in this optimization. The phase boundary of the bcc solution can be more pushed toward the Si side, and the eutectoid temperature can be pushed up, if the D03 phase is considered as shown in Fig. 10.10(b). Another way to reproduce the eutectoid temperature is to change $\Delta H^{o}_{298.15}$ and $S^{o}_{298.15}$ of compound Fe_5Si_3, which will make these values deviate largely from the available experimental data. Therefore, it was not attempted to improve these discrepancies due to the ignorance of the D03 phase. The calculated phase diagram from the second set of parameters in which the liquid phase is described using BW is presented in Fig. 10.10(b). In this description, the phase boundary of D03 was better reproduced.

The calculated invariant reactions according to the current optimizations are compared with the experimental results in Table 10.4. All the calculated invariant reactions are in good agreement with the experimental results.

The enlarged phase diagram near the gamma loop is shown in Fig. 10.7 and the bcc order/disorder transitions are shown in Fig. 10.8. The currently optimized gamma loop can reproduce the latest experimental data from Fischer et al. [92] using the magnetic susceptibility measurements. The Tc line and Tx line are well reproduced. The temperature dependence of the Fe solubility in (Si) (the solvus of solid Si phase) and the liquidus of the Si-rich region are well reproduced in the present study as shown in Fig. 10.9 and Fig. 10.10. However, the solidus data of Si from Feichtinger [112], Weber and Riotte [113], Wiehl et al. [114], and Struthers [109] are inconsistent with each other, and the presently calculated solubility is rather lower than the experimental value. As the solidus of Si is difficult to measure, and the results from the present optimization should be reasonable because the temperature dependence of solvus in the solid state is well reproduced in a wide temperature range.

The calculated activity and enthalpy data of the liquid phase from the presently optimized model parameters are compared with the experimental data in Figs. 10.1 to 10.3. The previous assessment results by Lacaze and Sundman [9] are also plotted for comparisons. The calculate activity of Fe in the liquid standard state from the previous and present study are very similar. However, there is noticeable difference between the previous and present works in the activity of Si as shown in Fig. 10.1(a), although both results still agree with the experimental data within the experimental scatter. A large difference can be found in the enthalpy of mixing of the liquid phase at 1600 °C as shown in Fig. 10.2. Lacaze and Sundman's assessment follows the results of Sudavtsova et al. [21, 22] derived from emf data and Filippov [48] derived from light radiation in the Si-rich region. It should be noted that both these experimental data are indirect results and show a large deviation from other calorimetric data, and therefore they are less reliable. According to the experimental results determined by calorimetry, the enthalpy of mixing has a minimum of about -40 kJ/mol at about 0.45 x_{Si}, which is well reproduced in the present study. Due to the same reason, the current optimization can more accurately reproduce the partial enthalpy of mixing data in Fig. 10.3.

Figure 10.4 shows the activities of Fe and Si in the bcc solid solution in comparison with the experimental data. The optimized activity of Fe (with respect to the bcc_A2 Fe reference state) in the bcc phase is shown in Fig. 10.4(a). Although the present calculation shows reasonable agreement with the experimental data by Vecher et al. [52] up to 0.1 x_{Si}, the calculated results are much lower than the experimental data in the composition range between 0.1 and 0.3 x_{Si}. As can be seen from the figure that the experimental data show constant activity of Fe between 0.1 and 0.2 x_{Si}, which can only happen in a two phase region. This is inconsistent with the phase diagram data in Fig. 10.10. Therefore, the results of Vecher et al. [52] are questionable. On the other hand, the calculated activities of Si at 1100 to 1350 °C in the present study with respect to the diamond Si state are in excellent agreement with the experimental results by Sakao and Elliott [53] as shown in Fig. 10.4(b). The previous results by Lacaze and Sundman [9] show a gradual deviation from the experimental data as temperature increase.

The experimental heat content and heat capacity data of the stoichiometric compounds were not carefully considered in the previous assessments by others [9-13]. It was found that the heat capacities of these compounds show noticeable deviation from the Neumann-Kopp relation which was used in the previous assessments, as shown in Fig. 10.5. As a result, in the present study, the heat capacities of Fe_5Si_3, FeSi, $FeSi_2$, and Fe_3Si_7 were fitted to the experimental data. The heat capacity of the Fe_2Si compound where there is no experimental data available in the literature was estimated using the Neumann-Kopp relation. Fig. 10.5 shows the optimized heat capacities in the present study in comparison with the experimental data. In the case of Fe_5Si_3, the magnetic transition at 360 K was also considered. The corresponding heat contents of these four intermetallic compounds are shown in Fig. 10.6. It should be noted that the calculated enthalpies of fusion of these compounds from the present thermodynamic descriptions are more accurate than the results from Lacaze and Sundman [9]. For example, the enthalpy of fusion of FeSi and Fe_3Si_7 are well reproduced in the present study, while the results of the previous assessment are lower than the experimental results. The discrepancies in the previous assessment mainly result from the less accurate enthalpy of mixing of liquid, as shown in Fig. 10.2. A summary of the enthalpies of fusion of the intermetallic phases is also given in Table 10.7.

The calculated enthalpy of formation of the Fe-Si system at 298.15 K is presented in Fig. 10.11(a). The previous assessment by Lacaze and Sundman [9] considered the data from Korber et al. [37, 77] as the most reliable ones. But, in the present study, the later experimental data from Meschel and Kleppa [81] and Jounel et al. [78] were considered as more reliable. In fact, once the enthalpy of the liquid phase is fixed as shown in Fig. 10.2, and the heat capacities and heat contents of compounds are determined as shown in Figs. 10.5 and 10.6, the enthalpies of formation of these compounds should be consistently determined by reproducing the enthalpies of fusion of these compounds. A more detailed comparison is shown in Table 10.5.

Table 10.6 shows the optimized entropy of compounds at 298.15 K in the present work compared with the experimental data and previous assessments. The entropies of Fe_5Si_3, FeSi, Fe_3Si_7, and $FeSi_2$ are experimentally available from the low temperature heat capacity measurements. In particular, the present optimization with MQM description for the liquid phase can reproduce the entropy for compounds much accurately. It should be noted that the present optimization with BW for the liquid phase is still inferior to the results with MQM in term of reproduction of $S^o_{298.15}$ of compounds as shown in Table 10.6, since more effect was put to the phase diagram information for the optimization with BW. Fig 10.11(b) shows the calculated entropy of formation at 298.15 K in the present work compared with the literature data and previous assessment. It can be seen from the figure that the present work shows a certain improvement.

In general, two sets of model parameters with MQM and BW were obtained for the Fe-Si system. Both sets of optimized parameters provide more accurate description of the system than the previous assessments, in particular, for the thermodynamic properties of the solid and liquid phases. The configuration entropy of the liquid solution can be more accurately described by MQM considering the pair exchange reaction than by BW considering random mixing. Such an advantage of MQM can give the flexibility and accuracy in the optimization of binary liquid solution which has a strong negative deviation from the ideal solution behavior, like the Fe-Si solution. This advantage of MQM also provides a more accurate description of the thermodynamic properties of the solid phases.

10.5 Summary

All the literature for the Fe-Si system available were critically reviewed. Two sets of thermodynamic parameters for the Fe-Si system were then carried out by taken into account the selected phase diagram and thermodynamic properties of each phases. The set of parameters with the liquid Fe-Si phase described by the modified quasi-chemical model is suitable for the updating of the FactSage-FTlite database. While the other set of parameters with the Bragg Williams random mixing model for the liquid solution can be used for general purpose. Both sets of optimized parameters can provide more accurate description of the Fe-Si system than the previous assessments in particular for the thermodynamic properties of the solid and liquid phases.

Acknowledgement

The authors would like to thank the financial support from NSERC-Automotive Partnership Canada program in Canada. Senlin Cui would also like to thank the McGill Engineering Doctorate Award (MEDA) from McGill University for financial support and Thermo-Calc AB for accessing of the academic version of Thermo-Calc software.

References

1. Shin, S., R. Schafer, and B.C. De Cooman, *Three-dimensional visualization of the magnetic microstructure in bulk Fe-6.6 pct Si.* Metall. Mater. Trans. A, 2013. **44**(9): p. 4239-4247.
2. McHenry, M.E., M.A. Willard, and D.E. Laughlin, *Amorphous and nanocrystalline materials for applications as soft magnets.* Prog. Mater. Sci., 1999. **44**(4): p. 291-433.
3. Liu, L.L., Q.Q. Guo, S. Liu, C.S. Ni, and Y. Niu, *Anomalous oxidation of Fe-Si alloys under a low oxygen pressure at 800 °C.* Corros. Sci., 2015. **98**: p. 507-515.
4. Chart, T.G., *Critical assessment of the thermodynamic properties of the system iron-silicon.* High Temp.-High Pressures, 1970. **2**(4): p. 461-70.

5. Chart, T.G., *Critical assessment of thermodynamic data for the iron-silicon system*. 1982, Natl. Phys. Lab., Div. Mater. Appl., Teddington, UK. p. 5-1/5-35.
6. Kubaschewski, O., *Iron - Binary Phase Diagrams*. 1982. 185 pp.
7. Schürmann, E. and U. Hensgen, *Studies of the melting equilibria in the system iron-silicon.* Arch. Eisenhuettenwes., 1980. **51**(1): p. 1-4.
8. Lee, B.J., S.K. Lee, and D.N. Lee, *Formulation of the A2/B2/D03 atomic ordering energy and a thermodynamic analysis of the iron-silicon system.* CALPHAD Comput. Coupling Phase Diagrams Thermochem., 1987. **11**(3): p. 253-70.
9. Lacaze, J. and B. Sundman, *An assessment of the iron-carbon-silicon system.* Metall. Trans. A, 1991. **22A**(10): p. 2211-23.
10. Miettinen, J., *Reassessed thermodynamic solution phase data for ternary Fe-Si-C system.* CALPHAD Comput. Coupling Phase Diagrams Thermochem., 1998. **22**(2): p. 231-256.
11. Tang, K. and M. Tangstad, *A thermodynamic description of the Si rich Si-Fe system.* Acta Metall. Sin. (Engl. Lett.), 2012. **25**(4): p. 249-255.
12. Ohnuma, I., S. Abe, S. Shimenouchi, T. Omori, R. Kainuma, and K. Ishida, *Experimental and thermodynamic studies of the Fe-Si binary system.* ISIJ Int., 2012. **52**(4): p. 540-548.
13. Yuan, Y., F. Pan, D. Li, and A. Watson, *The re-assessment of the Mg-Zn and Fe-Si systems and their incorporation in thermodynamic descriptions of the Al-Mg-Zn and Fe-Si-Zn systems.* CALPHAD Comput. Coupling Phase Diagrams Thermochem., 2014. **44**: p. 54-61.
14. Gokcen, N.A. and J. Chipman, *Silicon-oxygen equilibrium in liquid iron.* J. Met., 1952. **4**(Trans.): p. 171-81.
15. Matoba, S., K. Gunji, and T. Kuanwa, *Silicon-oxygen equilibrium in molten iron.* Trans. Natl. Rec. Inst. Metals (Tokyo), 1961. **3**(No. 2): p. 81-90.
16. Bowles, P.J., H.F. Ramstad, and F.D. Richardson, *Activities of silicon in metals and alloys.* J. Iron Steel Inst., London, 1964. **202**: p. 113-21.
17. Cirilli, V., F. Abbattista, G. Chiantaretto, B. Alfonsi, and M. Palladino, *Effect of Group V elements on the activity of silicon dissolved in molten iron at 1560 °C.* Chim. Ind. (Milan), 1968. **50**(1): p. 33-41.

18. Sanbongi, K. and M. Ohtani, *Activities of coexisting elements in molten iron. II. Activity of silicon in a molten iron-silicon system.* Science Repts. Research Inst. Tohoku Univ., 1953. **5**(Ser. A): p. 350-7.
19. Ohtani, M., *Activities of silicon and carbon in molten Fe-Si-C alloys.* Science Repts. Research Insts. Tohoku Univ., Ser. A, 1955. **7**: p. 487-501.
20. Schwerdtfeger, K. and H.J. Engell, *Free energy of formation of silicon dioxide and the activities of silicon in liquid iron and cobalt.* Arch. Eisenhuettenwes., 1964. **35**(6): p. 533-40.
21. Batalin, G.I. and V.S. Sudavtsova, *Thermodynamic properties of iron-silicon molten alloys.* Zh. Fiz. Khim., 1975. **49**(7): p. 1672-5.
22. Sudavtsova, V.S., G.I. Batalin, and V.I. Ul'yanov, *Thermodynamic properties of liquid iron-silicon alloys.* Izv. Akad. Nauk SSSR, Neorg. Mater., 1975. **11**(1): p. 66-71.
23. Fruehan, R.J., *Thermodynamic properties of liquid iron-silicon alloys.* Met. Trans., 1970. **1**: p. 865-70.
24. Slye, W.E. and R.J. Fruehan, *The activity of silicon in liquid Fe-Si and Fe-Si-Cr alloys at 1600 °C.* Electr. Furn. Conf. Proc., 1999. **57th**: p. 401-412.
25. Sano, K. and K. Okajima, *Thermodynamic studies by use of galvanic cells of the formation of molten silicon alloys. III. System iron-silicon.* Mem. Fac. Eng., Nagoya Univ., 1956. **8**: p. 254-6.
26. Chipman, J., J.C. Fulton, N. Gokcen, and G.R. Caskey, Jr., *Activity of silicon in liquid iron-silicon and iron-carbon-silicon alloys.* Acta Metall., 1954. **2**: p. 439-50.
27. Chipman, J. and R. Baschwitz, *The activity of silicon in liquid Fe-Si-C alloys.* Trans. Am. Inst. Min., Metall. Pet. Eng., 1963. **227**: p. 473-8.
28. Turkdogan, E.T., P. Grieveson, and J.F. Beisler, *Kinetic and equilibrium considerations for the silicon reaction between silicate melts and graphite-saturated iron. II. Reaction kinetics of silica reduction.* Trans. Am. Inst. Min., Metall. Pet. Eng., 1963. **227**(6): p. 1265-74.
29. Smith, G. and J. Taylor, *Activity of silicon in liquid iron solutions.* J. Iron Steel Inst., London, 1964. **202**: p. 577-80.
30. Murakami, S., S. Ban-Ya, and T. Fuwa, *Activity of silicon in liquid iron and the effect of carbon on the activity of silicon.* Tetsu To Hagane, 1967. **53**(7): p. 779-783.

31. Murakami, S., S. Banya, and T. Fuwa, *Activity of silicon in molten iron and the effect of carbon on the activity of silicon.* Tetsu To Hagane, 1970. **56**(5): p. 536-45.
32. Yamada, K., H. Abe, and E. Kato, *Mass spectrometric study of the activity in liquid iron-silicon alloys at 1600°C.* Tetsu To Hagane, 1980. **66**(5): p. 488-95.
33. Miki, T., K. Morita, and M. Yamawaki, *Measurements of thermodynamic properties of iron in molten silicon by Knudsen effusion method.* J. Mass Spectrom. Soc. Jpn., 1999. **47**(2): p. 72-75.
34. Zaitsev, A.I., M.A. Zemchenko, and B.M. Mogutnov, *Thermodynamic properties of silicon-iron mixtures {(1 - x)Si + xFe}(l).* J. Chem. Thermodyn., 1991. **23**(9): p. 831-49.
35. Hsu, C.-C., A.Y. Polyakov, and A.M. Samarin, *Component activity in liquid binary alloys of the iron-silicon system.* Izv. Vyssh. Uchebn. Zaved., Chern. Metall., 1961(No. 1): p. 12-20.
36. Schneider, A. and W. Meyer-Jungnick, *Activities in the system iron-silicon.* Angew. Chem., 1955. **67**: p. 306.
37. Korber, F. and W. Oelsen, *The effect of the silicide, carbide and phosphide formation in iron melts on their equilibria with oxides.* Mitt. Kaiser-Wilhelm-Inst. Eisenforsch. Duesseldorf, 1936. **18**(No. 9): p. 109-30.
38. Abdel-Aziz, A.E.-H.K., A.A. Vertman, and A.M. Samarin, *Thermochemistry of Fe and Ni melts.* Izv. Akad. Nauk SSSR, Met., 1966(3): p. 19-30.
39. Iguchi, Y., Y. Tozaki, M. Kakizaki, T. Fuwa, and S. Ban-Ya, *A calorimetric study of heats of mixing of liquid iron alloys.* Tetsu To Hagane, 1981. **67**(7): p. 925-32.
40. Tripolitov, A.I., Y.T. Loginov, A.Y. Stomakhin, and A.F. Filippov, *Iron-silicon melts studied with the aid of a high-temperature calorimeter.* Izv. Vyssh. Ucheb. Zaved., Chern. Met., 1968. **11**(11): p. 53-9.
41. Shumikhin, V.S., A.K. Biletskii, G.I. Batalin, and V.P. Anishin, *Study on thermodynamic and kinetic parameters of dissolution of solid materials in carbon-containing iron melts.* Arch. Eisenhuettenwes., 1981. **52**(4): p. 143-6.
42. Kanibolotsky, D.S., O.A. Bieloborodova, N.V. Kotova, and V.V. Lisnyak, *Thermodynamics of liquid Fe-Si and Fe-Ge alloys.* J. Therm. Anal. Calorim., 2003. **71**(2): p. 583-591.

43. Gertman, Y.M. and P.V. Gel'd, *Thermochemistry of liquid melts of iron with silicon.* Zh. Fiz. Khim., 1962. **36**: p. 1477-82.
44. Woolley, F. and J.F. Elliott, *Heats of solution of aluminum, copper, and silicon in liquid iron.* Trans. Am. Inst. Min., Metall. Pet. Eng., 1967. **239**(12): p. 1872-83.
45. Chistyakov, L.S., A.Y. Stomakhin, and K.V. Grigorovich, *High-temperature calorimetric study of the enthalpy of formation of iron-silicon and nickel-chromium solutions.* Metally, 1993(4): p. 27-37.
46. Gel'd, P.V., M.G. Valishev, A.F. Ermakov, and E.D. Pletneva, *Partial and integral enthalpies of formation of liquid binary melts of iron with silicon.* Zh. Fiz. Khim., 1994. **68**(9): p. 1712-14.
47. Petrushevskii, M.S. and P.V. Gel'd, *Short-range order parameter and enthalpies of mixing of metal-silicon molten alloys with unsymmetrical properties.* Fiz. Khim. Rastvorov, 1972: p. 279-82.
48. Filippov, E.S., *Determination of the heats of phase transformations and mixing in molten metals and alloys according to light emission.* Izv. Vyssh. Ucheb. Zaved., Chern. Met., 1973(5): p. 112-18.
49. Safonov, S.O., V.F. Ukhov, and O.A. Esin, *Evaluation of the heat of mixing of binary metallic melts with a cell method.* Elektrokhim. Rasplavy, 1974: p. 148-53.
50. Chipman, J. and N.J. Grant, *The induction furnace as a high-temperature calorimeter and the heat of solution of silicon in liquid iron.* Trans. Am. Soc. Met., 1943. **31**: p. 365-379.
51. Vatalin, N.A. and Y.S. Kozlov, *Apparatus for determining partial heats of mixing of metallic alloys at high temperatures.* Tr. Inst. Met., Akad. Nauk SSSR, Ural. Nauch. Tsentr, 1972. **No. 27**(Pt. 4): p. 119-23.
52. Vecher, R.A., Y.I. Gerasimov, and V.A. Geiderikh, *Activity of iron in solid solutions of silicon and iron.* Zh. Fiz. Khim., 1965. **39**(5): p. 1229-32.
53. Sakao, H. and J.F. Elliott, *Thermodynamics of dilute bcc. iron-silicon alloys.* Metall. Trans., A, 1975. **6A**(10): p. 1849-51.
54. Krentsis, R.P. and P.V. Gel'd, *Heat capacity of iron silicides at 55-300 K.* Fiz. Met. Metalloved., 1962. **13**: p. 319-20.

55. Krentsis, R.P. and P.V. Gel'd, *Thermochemistry of iron silicides; heat capacity, enthalpy, and entropy of Fe_3Si.* Izv. Vyssh. Uchebn. Zaved., Chern. Metall., 1962. **5**(No. 11): p. 12-19.
56. Gel'd, P.V. and R.P. Krentsis, *Enthalpy and heat of fusion of iron silicides.* Eksp. Tekh. Metody Vysokotemp. Izmer., Sb. Tr. Soveshch., 2nd, 1966: p. 197-205.
57. Gel'd, P.V. and R.P. Krentsis, *Some thermophysical characteristics of iron silicides.* Fiz. Met. Metalloved., 1963. **15**: p. 63-71.
58. Krentsis, R.P. and P.V. Gel'd, *The thermochemistry of iron silicides.* Fiz.-Khim. Osnovy Proizv. Stali, Akad. Nauk SSSR, Inst. Met. Tr. 6-oi [Shestoi] Konf., Moscow, 1961. **1961**: p. 400-3.
59. Salina, V.A. and S.O. Baisanov, *The enthalpy of formation estimation of $BaSi_2$, $Mn_{11}Si_{19}$, and Fe_2Si compounds.* Bayandamalary Kaz. Resp. Ulttyk Gylym Akad., 2010(3): p. 75-78.
60. Salina, V.A. and S.O. Baisanov, *Temperature dependence of the heat capacity and the enthalpy and entropy of melting of the compounds $BaSi_2$, $Mn_{11}Si_{19}$, and Fe_2Si.* Izv. Nats. Akad. Nauk Resp. Kaz., Ser. Khim., 2010(2): p. 7-10.
61. Krentsis, R.P., P.V. Gel'd, and G.I. Kalishevich, *The thermochemistry of iron silicides-the heat capacity, enthalpy, and entropy of FeSi and Fe_5Si_3.* Izv. Vyssh. Uchebn. Zaved., Chern. Metall., 1963. **6**(9): p. 161-8.
62. Kalishevich, G.I., N.P. Sudakova, A.V. Mikhel'son, P.V. Gel'd, and V.I. Surikov, *Heat capacity of manganese silicide (Mn_5Si_3), iron silicide (Fe_5Si_3), and chromium silicide (Cr_5Si_3) at low temperatures.* Fiz. Tverd. Tela (Leningrad), 1974. **16**(7): p. 2123-5.
63. Sudakova, N.P., G.I. Kalishevich, and R.P. Krentsis, *Thermal properties of the iron-silicon system η-phase.* Izv. Akad. Nauk SSSR, Neorg. Mater., 1976. **12**(2): p. 354-5.
64. Davydov, K.N., P.V. Gel'd, and N.N. Serebrennikov, *Heat capacity and thermal expansion of silicon alloys containing iron, chromium, and manganese.* Fiz.-Khim. Osnovy Proizvodstva Stali, Akad. Nauk S.S.S.R., Inst. Met. im A. A. Baikova, Trudy 3-ei Konf., 1957: p. 350-69.
65. Seo, K., S. Lee, Y. Jo, M.-H. Jung, J. Kim, D.G. Churchill, and B. Kim, *Room Temperature Ferromagnetism in Single-Crystalline Fe_5Si_3 Nanowires.* J. Phys. Chem. C, 2009. **113**(17): p. 6902-6905.

66. Schubel, P., *The heat capacity of metals and metallic compounds between 18 and 600 K.* Z. Anorg. Chem., 1914. **87**: p. 81-119.
67. Acker, J., K. Bohmhammel, G.J.K. van den Berg, J.C. van Miltenburg, and C. Kloc, *Thermodynamic properties of iron silicides FeSi and α-$FeSi_2$.* J. Chem. Thermodyn., 1999. **31**(12): p. 1523-1536.
68. Ferrier, A. and H. Jacobi, *Heat capacity of iron-silicon alloy between 850 and 1580 °C.* C. R. Hebd. Seances Acad. Sci., Ser. C, 1966. **263**(22): p. 1325-8.
69. Kelley, K.K., *Data on theoretical metallurgy. XIII. High-temperature, heat-capacity, and entropy data for the elements and inorganic compounds.* Bull. - U. S., Bur. Mines, 1960. **No. 584**: p. 232 pp.
70. Krentsis, R.P., P.V. Gel'd, and G.I. Kalishevich, *Thermochemistry of iron silicides. Heat capacity, enthalpy, and entropy of iron silicides.* Izv. Vyssh. Uchebn. Zaved., Chern. Metall., 1963. **6**(11): p. 146-52.
71. Serebrennikov, N.N. and P.V. Gel'd, *Heat capacity of ζ-phase of the system iron-silicon.* Dokl. Akad. Nauk SSSR, 1954. **97**: p. 695-8.
72. Kendall, W.B. and R. Hultgren, *High-temperature heat contents of some binary iron alloys.* Trans. Am. Soc. Met., 1961. **53**: p. 207-14.
73. Pandey, R.K. and R. Kohlhaas, *High-temperature specific heat and magnetic suspectibility of iron-silicon alloys.* Indian J. Phys., 1968. **42**(1): p. 20-32.
74. Normanton, A.S. and B.B. Argent, *A calorimetric study of dilute solutions of nickel, silicon, and vanadium in iron.* Met. Sci., 1976. **10**(7): p. 243-8.
75. Pepperhoff, W. and H.H. Ettwig, *Specific heats of iron-silicon alloys.* Z. Angew. Phys., 1967. **22**(6): p. 496-9.
76. Ettwig, H.H. and W. Pepperhoff, *Ordering transitions in body centered cubic iron-silicon alloys. III. Heat capacity.* Z. Metallk., 1972. **63**(8): p. 453-6.
77. Korber, F., W. Oelsen, and H. Lichtenberg, *The thermochemistry of alloys. II. Direct determination of heats of formation of the ternary alloys iron-nickel-aluminum, iron-cobalt-aluminum, copper-nickel-aluminum, iron-aluminum-silicon and of a series of alloys of the system copper-manganese-aluminum.* Mitt. Kaiser-Wilhelm-Inst. Eisenforsch. Duesseldorf, 1937. **19**: p. 131-59.

78. Jounel, B., J.C. Mathieu, and P. Desre, *Calorimetric measurement of the heat of formation of iron silicide by dissolution in aluminum.* C. R. Acad. Sci., Paris, Ser. C, 1968. **266**(11): p. 773-6.
79. Gorelkin, O.S., A.S. Dubrovin, O.D. Kolesnikova, and N.A. Chirkov, *Determination of the heats of formation of intermetallic compounds in an isothermal calorimeter by a sintering method.* Zh. Fiz. Khim., 1972. **46**(3): p. 754-5.
80. Gorelkin, O.S., A.S. Subrovin, O.D. Kolesnikova, Y.Y. Demidov, and N.A. Chirkov, *Thermochemistry of alloys containing aluminum, silicon, and boron.* Proizvod. Ferrosplavov, 1972. **No. 1**: p. 123-37.
81. Meschel, S.V. and O.J. Kleppa, *Standard enthalpies of formation of some 3d transition metal silicides by high temperature direct synthesis calorimetry.* J. Alloys Compd., 1998. **267**(1-2): p. 128-135.
82. Bosholm, O., H. Oppermann, and S. Dabritz, *Chemical vapour transport of intermetallic phases. Part 2. The system Fe-Si.* Z. Naturforsch., B Chem. Sci., 2000. **55**(7): p. 614-626.
83. Liang, Y.F., S.L. Shang, J. Wang, Y. Wang, F. Ye, J.P. Lin, G.L. Chen, and Z.K. Liu, *First-principles calculations of phonon and thermodynamic properties of Fe-Si compounds.* Intermetallics, 2011. **19**(10): p. 1374-1384.
84. Vecher, R.A., V.A. Geiderikh, and Y.I. Gerasimov, *Thermodynamic properties of iron-silicon alloys.* Dokl. Akad. Nauk SSSR, 1965. **164**(4): p. 835-8.
85. Vecher, R.A., V.A. Geiderikh, and Y.I. Gerasimov, *Thermodynamic properties of alloys of iron and silicon.* Symposium on Thermodynamics with Emphasis on Nuclear Materials and Atomic Transport in Solids, 1966. **1**: p. 171-180.
86. Zaitsev, A.I., M.A. Zemchenko, and B.M. Mogutnov, *Thermodynamic properties of iron silicides and phase equilibria in the silicon-iron system.* J. Chem. Thermodyn., 1991. **23**(10): p. 933-40.
87. Ruer, R. and R. Klesper, *The gamma-delta transformation in pure iron and the influence upon it of carbon, silicon, cobalt and copper.* Ferrum, 1914. **11**: p. 258-61.
88. Esser, H. and P. Oberhoffer, *The binary systems silicon-iron; iron-phosphorus; iron-manganese.* Phys. Ber., 1925. **7**: p. 106.
89. Wever, F. and P. Giani, *The iron-silicon system.* Mitt. Kaiser-Wilhelm-Inst. Eisenforsch. Duesseldorf, 1925. **7**: p. 59-68.

90. Oberhoffer, P. and C. Kreutzer, *The system iron-silicon, iron-chromium, and iron-phosphorus.* Arch. Eisenhuettenwes., 1929. **2**: p. 449-56.
91. Crangle, J., *Magnetic method for the determination of γ-loops in binary iron alloys and its application to the iron-silicon system.* Br. J. Appl. Phys., 1954. **5**: p. 151-4.
92. Fischer, W.A., K. Lorenz, H. Fabritius, A. Hoffmann, and G. Kalwa, *Phase transformations in pure iron alloys with a magnetic balance.* Arch. Eisenhuettenwes., 1966. **37**(1): p. 79-86.
93. Übelacker, E., *Determination of magnetic susceptibility of pure iron and of iron-silicon alloys; determination of phase diagrams for Fe-Si containing 0-10% Si.* Compt. Rend., 1965. **261**(4(Groupe 7)): p. 976-9.
94. Dokken, R.N., *A resistance-measurement study of ordering in iron-silicon alloys. FeSi- and Fe_3Si-type superstructures.* Trans. Am. Inst. Min., Metall. Pet. Eng., 1965. **233**(6): p. 1187-9.
95. Meinhardt, D. and O. Krisement, *Long-range ordering in the iron-silicon system.* Arch. Eisenhuettenwes., 1965. **36**(4): p. 293-9.
96. Inden, G. and W. Pitsch, *Ordering reactions in body centered cubic iron-silicon solid solutions. II. Experimental determination of the atomic configurations.* Z. Metallk., 1972. **63**(5): p. 253-8.
97. Polishchuk, V.E. and Y.P. Selisskii, *High-temperature x-ray study of iron-silicon system alloys.* Fiz. Metal Metalloved., 1970. **29**(5): p. 1101-4.
98. Schlatte, G., G. Inden, and W. Pitsch, *Ordering reactions in body centered cubic iron-silicon solid solutions. IV. Theroy with simultaneous consideration of chemical and magnetic interactions.* Z. Metallk., 1974. **65**(2): p. 94-100.
99. Schlatte, G. and W. Pitsch, *Ordering reactions in bcc iron-silicon solid solutions. V. Electronmicroscopic observations.* Z. Metallkd., 1975. **66**(11): p. 660-8.
100. Schlatte, G., *Completion of the phase diagram of the iron-silicon systems in the iron-rich range.* Phys. Status Solidi A, 1974. **23**(1): p. K91-K92.
101. Swann, P.R., L. Granas, and B. Lehtinen, *The B2 and D03 ordering reactions in iron-silicon alloys in the vicinity of the curie temperature.* Met. Sci., 1975. **9**(2): p. 90-6.
102. Meco, H. and R.E. Napolitano, *Liquidus and solidus boundaries in the vicinity of order-disorder transitions in the Fe-Si system.* Scr. Mater., 2004. **52**(3): p. 221-226.

103. Murakami, T., *The equilibrium diagram of the iron-silicon system.* Science Reports Tohoku Imp. Univ., 1921. **10**: p. 79-92.
104. Lecocq, Y. and P. Lecocq, *Solid solution of silicon in iron.* Colloq. Int. Centre Nat. Rech. Sci., 1967. **No. 157**: p. 165-9.
105. Osawa, A. and T. Murata, *The equilibrium diagram of the iron-silicon system.* Nippon Kinzoku Gakkaishi, 1940. **4**: p. 228-42.
106. Haughton, J.L. and M.L. Becker, *Alloys of iron research. IX. The constitution of the alloys of iron with silicon.* J. Iron Steel Inst., London, 1930. **No. 7**: p. 1-18.
107. Köster, W., *Micro- and crystal structure of iron-silicon alloys containing up to 40 at.% silicon.* Trans. Iron Steel Inst. Jpn., 1974. **14**(6): p. 387-94.
108. Ustinovshikov, Y. and I. Sapegina, *Morphology of ordering Fe-Si alloys.* J. Mater. Sci., 2004. **39**(3): p. 1007-1016.
109. Struthers, J.D., *Solubility and diffusivity of gold, iron, and copper in silicon.* J. Appl. Phys., 1956. **27**: p. 1560.
110. Lee, Y.H., R.L. Kleinhenz, and J.W. Corbett, *EPR of a thermally induced defect in silicon.* Appl. Phys. Lett., 1977. **31**(3): p. 142-4.
111. Colas, E.G. and E.R. Weber, *Reduction of iron solubility in silicon with oxygen precipitates.* Appl. Phys. Lett., 1986. **48**(20): p. 1371-3.
112. Feichtinger, H., *Electrical and kinetic properties of thermally activated iron in silicon.* Acta Phys. Austriaca, 1979. **51**(3-4): p. 161-84.
113. Weber, E. and H.G. Riotte, *The solution of iron in silicon.* J. Appl. Phys., 1980. **51**(3): p. 1484-8.
114. Wiehl, N., U. Herpers, and E. Weber, *Study on the solid solubility of transition metals in high-purity silicon by instrumental neutron activation analysis and anti-Compton spectrometry.* J. Radioanal. Chem., 1982. **72**(1-2): p. 69-78.
115. Nakashima, H., T. Isobe, Y. Yamamoto, and K. Hashimoto, *Diffusion coefficient of iron in silicon at room temperature.* Jpn. J. Appl. Phys., Part 1, 1988. **27**(8): p. 1542-3.
116. McHugo, S.A., R.J. McDonald, A.R. Smith, D.L. Hurley, and E.R. Weber, *Iron solubility in highly boron-doped silicon.* Appl. Phys. Lett., 1998. **73**(10): p. 1424-1426.
117. Abrikosov, N.K., *Iron-silicon system in the $FeSi_2$ compound range.* Izv. Sekt. Fiz.-Khim. Anal., Inst. Obshch. Neorg. Khim., Akad. Nauk SSSR, 1956. **27**: p. 157-63.

118. Sidorenko, F.A., P.V. Gel'd, and P.S. Rempel, *Stability region of α-lebeauite.* Izv. Vyssh. Uchebn. Zaved., Chern. Metall., 1962. **5**(No. 4): p. 102-8.

119. Sidorenko, F.A. and B.S. Rabinovich, *The region of iron monosilicide stability.* Tr. Ural. Politekh. Inst. im. S. M. Kirova, 1965. **No. 144**: p. 71-3.

120. Vainshtein, E.E., P.M. Valov, F.A. Sidorenko, and T.S. Shubina, *Moessbauer spectra of iron in the ε-phase homogeneity region of iron-silicon systems.* Fiz. Met. Metalloved., 1967. **23**(2): p. 367-9.

121. Wachtel, E. and T. Mager, *Constitution of the ferrosilicon-silicon partial system.* Z. Metallk., 1970. **61**(10): p. 762-6.

122. Köster, W. and T. Gödecke, *Iron-silicon system.* Z. Metallk., 1968. **59**(8): p. 602-5.

123. Guertler, W. and G. Tammann, *Compounds of the iron with silicon. [machine translation].* Z. f. anorg. Ch., 1905. **47**: p. 163-79.

124. Murakmi, T., *Further investigation of the equil. diagram of the iron-silicon system.* Sci. Rep. Tohoku Imp. Univ., Ser. 1, 1927. **16**: p. 475-89.

125. Kurnakov, N. and G. Urazov, *Toxic properties of commercial ferrosilicon.* Z. Anorg. Allg. Chem., 1922. **123**: p. 89-131.

126. Bamberger, M., O. Einerl, and J. Nussbaum, *Study of technical ferrosilicon.* Stahl Eisen, 1925. **45**: p. 141-4.

127. Piton, J.P. and M.F. Fay, *Phase changes in alloys wih compositions near $FeSi_2$.* C. R. Acad. Sci., Paris, Ser. C, 1968. **266**(8): p. 514-16.

128. Wefers, K., *Decomposition of ferrosilicon alloys. The partial system FeSi-Si.* Metall (Berlin, 1914-34), 1963. **17**: p. 446-51.

129. Greiner, E.S. and E.R. Jette, *X-ray study on the constitution of iron-silicon alloys containing from 14 to 33.4 per cent silicon.* Trans. Am. Inst. Min., Metall. Pet. Eng., 1937. **125**: p. 473-81.

130. Übelacker, E. and P. Lecocg, *Phase Fe_5Si_3 in its paramagnetic state.* C. R. Seances Acad. Sci., Ser. C, 1966. **262**(10): p. 793-5.

131. Weill, A., *The iron-silicon diagram up to 30% of silicon and its practical applications.* Rev. met., 1945. **42**: p. 266-70.

132. Übelacker, E., *Phase diagram of the iron-silicon system and of the Fe_3Si ordered state.* Colloq. Int. Centre Nat. Rech. Sci., 1967. **No. 157**: p. 171-3.

133. Übelacker, E., *Paramagnetic study of iron-silicon and iron-germanium alloys.* Mem. Sci. Rev. Met., 1967. **64**(4): p. 183-90.
134. Dinsdale, A.T., *SGTE data for pure elements.* CALPHAD Comput. Coupling Phase Diagrams Thermochem., 1991. **15**(4): p. 317-425.
135. Hillert, M. and M. Jarl, *A model for alloying effects in ferromagnetic metals.* CALPHAD Comput. Coupling Phase Diagrams Thermochem., 1978. **2**(3): p. 227-38.
136. Redlich, O. and A.T. Kister, *Thermodynamics of nonelectrolytic solutions. Algebraic representation of thermodynamic properties and the classification of solutions.* Ind. Eng. Chem., 1948. **40**: p. 84,5-8.
137. Pelton, A.D., S.A. Degterov, G. Eriksson, C. Robelin, and Y. Dessureault, *The modified quasichemical model I - binary solutions.* Metall. Mater. Trans. B, 2000. **31B**(4): p. 651-659.
138. Pelton, A.D. and P. Chartrand, *The modified quasi-chemical model: Part II. Multicomponent solutions.* Metall. Mater. Trans. A, 2001. **32**(6): p. 1355-1360.
139. http://www.factsage.com.
140. http://www.thermocalc.com.
141. Kohlhaas, R. and R.K. Pandey, *The physical properties of an iron-silicon alloy with 3.34% silicon in the high-temperature region.* Z. Angew. Phys., 1966. **21**(4): p. 365-7.
142. Sanfourche, A., *Iron-silicon alloys.* Rev. metal., 1919. **16**: p. 217-24.
143. Lihl, F. and H. Ebel, *X-ray examination of the structure of iron-rich alloys of the iron-silicon system.* Arch. Eisenhuettenwes., 1961. **32**: p. 489-91.
144. Warlimont, H., *Electron microscopic investigation of the equilibriums and transformations of the α-iron-silicon phases.* Z. Metallk., 1968. **59**(8): p. 595-602.
145. Stroganov, A.I., L.V. Slepova, and A.V. Puzyrev, *Temperature intervals of the solidification of chromium and silicon technical alloys.* Izv. Vyssh. Uchebn. Zaved., Chern. Metall., 1976(10): p. 64-7.
146. Ustinovshchikov, Y.I. and I.V. Sapegina, *Ordering of Fe-Si phases.* Inorg. Mater., 2005. **41**(1): p. 24-31.
147. Khalaff, K. and K. Schubert, *Crystal structure of iron silicide (Fe_2Si)(h).* J. Less-Common Metals, 1974. **35**(2): p. 341-5.

148. Weill, A.R., *Structure of the η phase of the Fe-Si system.* Nature (London, U. K.), 1943. **152**: p. 413.

149. Watanabe, H., H. Yamamoto, and E. Ito, *Neutron diffraction study of the intermetallic compound FeSi.* J. Phys. Soc. Jpn., 1963. **18**(7): p. 995-9.

150. Sidorenko, F.A. and P.V. Gel'd, *The nature of ε-phase in the system Fe-Si.* Izv. Vyssh. Uchebn. Zaved., Chern. Metall., 1963. **6**(7): p. 140-8.

151. Phragmen, G., *Iron-silicon alloys.* Jernkontorets Ann., 1923: p. 121-31.

152. Bucksch, R., *Structural data on the β-phase of ferrous silicide.* Z. Naturforsch., A, 1967. **22**(12): p. 2124.

153. Dusausoy, Y., J. Protas, R. Wandji, and B. Roques, *Crystal structure of the iron disilicide, β-$FeSi_2$.* Acta Crystallogr., Sect. B, 1971. **27**(Pt. 6): p. 1209-18.

154. Yamane, H. and T. Yamada, *Effects of stacking fault on the diffraction intensities of β-$FeSi_2$.* J. Alloys Compd., 2009. **476**(1-2): p. 282-287.

155. Imai, M., Y. Isoda, and H. Udono, *Thermal expansion of semiconducting silicides β-$FeSi_2$ and Mg_2Si.* Intermetallics, 2015. **67**: p. 75-80.

156. Sidorenko, F.A., P.V. Gel'd, and L.B. Dubrovskaya, *Nature of the ζ-α phase of the Fe-Si system.* Fiz. Met. Metalloved., 1959. **8**: p. 735-39.

157. Gel'd, P.V. and N.N. Serebrennikov, *Dilatometric investigation of the ζ-phase of the iron-silicon system.* Dokl. Akad. Nauk SSSR, 1954. **97**: p. 827-30.

Table captions

Figure captions

Fig. 10.1 Calculated activities of (a) Si and (b) Fe in the liquid Fe-Si at 1600 °C with respect to their liquid states compared with the experimental data.

Fig. 10.2 Calculated enthalpy of mixing of liquid at 1600 °C compared with the experimental data.

Fig. 10.3 Calculated partial enthalpy of mixing of liquid at 1600 °C compared with the experimental data. (a) Partial enthalpy of Si and (b) partial enthalpy of Fe.

Fig. 10.4 Calculated activities in the bcc alloys compared with the experimental data. (a) Activities of Fe at 727 °C with respect to the bcc_A2 state and (b) activities of Si at 1100-1350 °C with respect to the diamond Si state.

Fig. 10.5 Calculated heat capacities of (a) Fe_5Si_3, (b) FeSi, (c) $FeSi_2$, and (d) Fe_3Si_7 compared with the experimental data.

Fig. 10.6 Calculated heat contents of (a) Fe_5Si_3, (b) FeSi, (c) $FeSi_2$, and (d) Fe_3Si_7 compared with the experimental data.

Fig. 10.7 Calculated gamma loop in the present study compared with the experimental data.

Fig. 10.8 The order-disorder transition of the bcc phase. (a) The A2/B2 (Tx) transition temperature and B2/D03 (Ty) transition temperature, and (b) the Curie temperature (Tc) of magnetic transition compared with the experimental data. The Tx line and Tc line are calculated from the present study, and the Ty line is an evaluated line from the experimental data.

Fig. 10.9 Calculated solubility of Fe in (Si) compared the with experimental data.

Fig. 10.10 Calculated phase diagram from the present optimization compared with the selected experimental data. Optimization with the liquid phase by (a) MQM and (b) BW.

Fig. 10.11 Calculated (a) enthalpy of formation at 298.15 K and (b) entropy of formation at 298.15 K compared with the experimental data.

Table 10.1 Summary of the experimental studies for the thermodynamic properties in the Fe-Si system.

Type of experimental data	Experimental method [a]	Ref.
Formation enthalpy at 298.15 K and enthalpy of mixing at 1600 °C	Calorimetry	[37]
Formation enthalpy at 298.15 K	Calorimetry	[77]
Partial enthalpy of mixing of Si at 1600 °C	Calorimetry	[50]
Activity of Si in liquid at 1600 °C	Si, O/SiO_2 equilibrium in molten Fe	[14]
Activity of Si in liquid at 1460-1540 °C	emf	[18]
Activity of Si and Fe at 1420 °C	Distribution of Si between liquid Fe-Si and Ag-Si	[26]
Activity of Si in liquid at 1250 °C		[36]
Activity of Si in liquid at 1540 °C	emf	[19]
Activity of Si in liquid at 1470 and 1510 °C	emf	[25]
Activity of Si in liquid at 1570-1680 °C	Si, O/SiO_2 equilibrium in molten Fe	[15]
Activity of Si and Fe in liquid at 1550 and 1600 °C	Vapor pressure measurements	[35]
Enthalpy and partial enthalpy of mixing at 1525 °C	Isothermal calorimetry	[43]
Activity of Si in liquid at 1420 and 1530 °C	Distribution of Si between liquid Fe-Si and Ag-Si	[27]
Activity of Si at 1400-1600 °C	Solubility of Si_3N_4 and distribution of Si between liquid Fe-Si and Ag-Si	[28]
Activity of Si and Fe in liquid at 1470-1610 °C	emf	[20]
Activity of Si in liquid at 1560 °C	$SiO+H_2=[Si]+H_2O$ equilibrium	[16]
Activity of Si in liquid at 1450 and 1570 °C	Distribution of Si between liquid Fe-Si and Ag-Si	[29]

Formation enthalpy at 298.15 K and enthalpy of mixing at 1600 °C	Isothermal calorimetry	[38]
Partial enthalpy of mixing at 1600 °C	High temperature calorimetry	[44]
Activity of Si at 1450 and 1540 °C	Distribution of Si between liquid Fe-Si and Ag-Si	[30]
Activity of Si in liquid at 1560 °C	$SiO+H_2=[Si]+H_2O$ equilibrium	[17]
Enthalpy and partial enthalpy of mixing of Si at 1600 °C	High temperature calorimetry	[40]
Activity of Si at 1450 and 1540 °C	Distribution of Si between liquid Fe-Si and Ag-Si	[31]
Activity of Si and Fe at 1500 and 1600 °C	emf	[23]
Enthalpy of mixing at 1600 °C	Calculated based on short range ordering	[47]
Partial enthalpy of mixing of Si and Fe at 1525 °C	High temperature calorimetry	[51]
Enthalpy of mixing	Light radiation intensity measurement	[48]
Enthalpy of mixing at 1550 °C	Calculated based on a cell method	[49]
Activity of Fe and Si at 1600 °C	emf	[21]
Activity of Fe and Si at 1600 °C	emf	[22]
Activity of Si in bcc phase at 1100-1350 °C	emf	[53]
Activity of Fe in bcc phase at 727 °C	emf	[52]
Activity of Fe in liquid at 1450-1550 °C	Knudsen effusion measurement	[33]
Enthalpy and partial enthalpy of mixing of Fe and Si at 1477 °C	High temperature isoperibolic calorimeter	[42]
Activity of Si and Fe in liquid at 1600 °C	Knudsen effusion measurement	[32]
Enthalpy of Fe and Si at 1561 °C	Isoperibolic calorimetry	[39]
Enthalpy of mixing at 1700 °C	High temperature vacuum isothermal calorimetry	[41]
Activity of Si at 1600 °C	Knudsen effusion measurement	[34]

Partial enthalpy of mixing of Fe and Si at 1600 °C	Calorimetry	[45]
Partial enthalpy of mixing of Fe and Si at 1650 °C	Calorimetry	[46]
Activity of Si in liquid at 1600 °C	emf	[24]
Heat capacity of FeSi at 373-873 K	Calorimetry	[66]
Heat content and heat capacity of Fe_3Si_7 at 290-1400 K	Calorimetry	[71]
Heat content and heat capacity of Fe-Si alloys with 99.6, 69.5, 51.1, 38.8, 2.04, 3.38, 7.88, 36.68, 44.62, 51.87, 53.25, 61.42, 80.30, 87.89, 92.86 and 95.76 at.% Si at 273-1556 K	Calorimetry	[64]
Heat capacity of Fe-12 at.% Si alloy at 298-1400 K	Calorimetry	[72]
Heat content and heat capacity of $FeSi_2$ and Fe_3Si_7 at 50-1700 K (66.67 and 70.84 at.% Si)	(Adiabatic) calorimetry	[70]
Enthalpy of formation of $FeSi_2$, Fe_3Si_7, FeSi, and Fe_3Si at 298.15 and 1000 K (emf: 600-800 °C)	emf	[84]
Enthalpy of formation of $FeSi_2$, Fe_3Si_7, FeSi, and Fe_3Si at 298.15 and 1000 K	emf	[85]
Heat capacity of Fe-Si alloy with 6.43 at.% Si at 293-1273 K	Calorimetry	[141]
Heat capacity and entropy of Fe_3Si, Fe_5Si_3, FeSi, $FeSi_2$, and Fe_3Si_7 at 55-300 K	Low temperature adiabatic calorimetry	[54]
Heat content of Fe_3Si, Fe_5Si_3, FeSi, and $FeSi_2$ at 0-1400 K and entropy at 298.15 K	Adiabatic calorimetry	[58]
Heat content of FeSi at 1123-1853 K	Drop calorimetry	[68]

Heat content, heat capacity, and entropy of Fe_3Si at 55-1800 K and heat of formation at 293.15 K	Calorimetry	[55]
Heat capacity, heat content, and entropy of FeSi and Fe_5Si_3 at 55-1923 K	Calorimetry	[61]
Heat capacity of Fe_3Si, Fe_5Si_3, FeSi, $FeSi_2$, and Fe_3Si_7 at 60-300 K	Adiabatic Calorimetry	[57]
Heat capacity and entropy of Fe_3Si, Fe_5Si_3, FeSi, $FeSi_2$, and Fe_3Si_7 at 60-300 K	Adiabatic Calorimetry	[56]
Enthalpy of formation of FeSi at 298.15 K	Isothermal calorimetry	[79]
Enthalpy of formation of FeSi at 293.15 K	Calorimetry	[78]
Heat capacity of Fe-Si alloys with 2.37, 4.05, 6.44, and 8.56 at.% Si at 400-1870 K	Adiabatic calorimetry	[73]
Heat capacity of Fe_5Si_3 at 13-60 K	Vacuum adiabatic calorimetry	[62]
Heat capacity of Fe_5Si_3 at 13-370 K	Adiabatic Calorimetry	[63]
Heat content, heat capacity, and entropy of Fe- 0.67, 2.61, 4.83 at.% Si alloys at 600-1600 K	(Adiabatic) calorimetry	[74]
Enthalpy of formation of FeSi and $FeSi_2$ at 298.15 K	Isothermal calorimetry	[80]
Enthalpy of formation of FeSi at 298.15 K	High temperature direct synthesis calorimetry	[81]
Gibbs energy of formation of FeSi, Fe_2Si, and Fe_3Si_7 at 1351-1664 K	Knudsen effusion technique	[86]
Heat capacity, enthalpy, entropy, and Gibbs energy of FeSi and Fe_3Si_7 at 11-400 K	Low temperature adiabatic calorimetry	[67]
Enthalpy and entropy of formation of Fe-Si compounds at 298.15 K	Chemical transport reaction with iodine	[82]

[a] emf = electron motive force.

Table 10.2 Summary of the phase diagram studies in the Fe-Si system.

Type of experimental data [a]	Experimental method [b]	Ref.
Liquidus and solidus from 0 to 100 at.% Si	MA, TA, OM	[123]
Phase diagram from 0 to 0.024 at.% Si (γ loop and liquidus)	TA	[87]
Phase diagram from 0 to 39.86 at. % Si and 66.53 to 74.89 at.% Si	TA	[142]
Phase diagram and Tc from 0 to 49.14 at.% Si	MA, TA, OM	[103]
Liquidus and solidus equilibrium from 0 to 100 at.% Si	TA, OM	[125]
Phase diagram from 0 to 3.54 at.% Si (γ loop)	DT	[88]
Phase diagram from 0 to 27.38 at.% Si (γ loop and Tc)	MA, TA, OM	[89]
Phase diagram from 52.25 to 84.58 at.% Si	TA	[126]
Phase diagram from 49.48 to 100 at.% Si	TA, OM, XRD	[124]
Phase diagram from 0 to 5.91 at.% Si (γ loop)	CA, OM, XRD	[90]
Phase diagram from 0 to 100 at.% Si	TA, MA, DT, HA, OM	[106]
Phase diagram from 24 to 50 at.% Si	XRD	[129]
Phase diagram from 0 to 80 at.% Si	DT, TA, MA, XRD, OM	[105]
Phase diagram from 0 to 45 at.% Si	XRD	[131]
Phase diagram from 0 to 4.18 at.% Si (γ loop)	MA	[91]
Phase diagram from 60 to 80 at.% Si	OM, XRD, emf	[117]
Solubility of Fe in (Si)	Radio isotope Fe^{59}	[109]
Phase diagram from 3.7 to 23.4 at.% Si	XRD	[143]

Homogeneity range of Fe_3Si_7	XRD, OM	[118]
Phase diagram from 57 to 100 at.% Si	DTA, TA, XRD, OM	[128]
Homogeneity range of FeSi	XRD	[119]
Tx, Ty, and Tc lines	RM	[94]
Tx, Ty, and Tc lines	ND	[95]
Phase diagram from 0.4 to 9.25 at.% Si (γ loop)	MSM, DTA	[93]
Phase diagram from 0 to 4 at.% Si (γ loop)	MSM	[92]
Stability of Fe_5Si_3	MA	[130]
Tc line and order-disorder transition	MA	[104]
Homogeneity range of FeSi (50.4-50.7 at.% Si)	MS	[120]
Tc line	Calorimetry	[75]
Phase diagram from 15 to 30 at.% Si	DT, MSM, TA	[132]
Phase diagrams from 0 to 50 at.% Si	MSM, DTA	[133]
Phase diagram from 30 to 40 at.% Si	DTA, HA, OM	[122]
Phase diagram from 7.4 to 17.1 at.% Si	SEM, TEM	[144]
Phase diagram from 64 to 75 at.% Si	DTA	[127]
Phase diagram from 50 to 100 at.% Si	MTA	[121]
Tx and Ty lines	HTXRD	[97]
Tx, Ty, and Tc lines	Calorimetry	[76]
Tx, Ty, Tc, and solidus lines	ND, Calorimetry	[96]

Phase diagram from 10 to 40 at.% Si	DTA, SEM, XRD, MA	[107]
Tx and Ty lines	TEM	[98-100]
Tx and Ty lines	TEM	[101]
Phase diagram from 33 to 100 at.% Si	TA	[145]
Solubility of Fe in (Si)	EPR	[110]
Solubility of Fe in (Si)	Hall effect, EPR	[112]
Solubility of Fe in (Si)	NAA, EPR	[113]
Phase diagram from 0 to 50 at.% Si	TA, DTA, HA	[7]
Solubility of Fe in (Si)	INAA, EPR	[114]
Solubility of Fe in (Si)	EPR	[111]
Solubility of Fe in (Si)	Hall effect, DLTS	[115]
Solubility of Fe in (Si)	INAA	[116]
Phase diagram from 0 to 30 at % Si (liquidus/solidus)	DTA	[102]
Phase diagram from 0 to 30 at.% Si (order-disorder)	TEM, SEM, XRD	[108, 146]
Tx and Ty lines	DC, EPMA, SEM, TEM	[12]
Phase diagram from 72 to 100 at.% Si	DTA	[11]

[a] Tx: A2/B2 transition temperature, Ty: B2/$D0_3$ transition temperature, Tc: magnetic transition temperature.

[b] TA = Thermal Analysis; OM = Optical Microanalysis; MA = Magnetic Analysis; XRD = X-Ray Diffraction Analysis; CA = Chemical Analysis; DT = Dilatometry; HA = Homogeneous Alloy; emf = electron motive force; DTA = Differential Thermal Analysis; RM = Resistance Measurement; ND = Neutron Diffraction; MSM = Magnetic Susceptibility Measurement; MS = Mössbauer Spectrometry, MTA = Magneto Thermal Analysis;

HTXRD = High Temperature X-Ray Diffraction Analysis; SEM = Scanning Electron Microscopy; TEM = Transmission Electron Microscopy; EPR = Electron Paramagnetic Resonance; NAA = Neutron Activation Analysis; DC = Diffusion Couple; EPMA = Electron Probe Microanalysis; INAA = Instrumental Neutron Activation Analysis; DLTS = Deep Level Transient Spectrum.

Table 10.3 Summary of the crystal structure information for the stable compounds in the Fe-Si system.

Phase	Structure	Prototype	Lattice parameters (nm)			Ref.
			A	b	c	
Fe_2Si	Cubic	CsCl	0.281			[147]
Fe_5Si_3	Hexagonal	Mn_5Si_3	0.67416		0.47079	[148]
			0.67449		0.94209	[105]
FeSi	Cubic	FeSi	0.4517			[149]
			0.4478			[105]
			0.44883			[119]
			0.44882			[150]
			0.448			[151]
			0.448663			[67]
$FeSi_2$	Orthorhombic	$FeSi_2$	0.98792	0.77991	0.78388	[152]
			0.9863	0.7791	0.7833	[153]
			9.8764(3)	7.7985(2)	7.8359(2)	[154]
			9.8752(1)	7.7922(1)	7.8372(1)	[155]
Fe_3Si_7	Tetragonal		0.26853		0.511965	[105]
			0.26932		0.5136	[156]
			0.269		0.508	[151]
			0.268739		0.513034	[67]

Table 10.4 Summary of the invariant reactions in the Fe-Si system (Abbreviation of the experimental methods can be found in Table 10.2.).

Reaction type	Reaction (at.% Si)			Temperature °C	Method	Ref.
Eutectic	Liquid = Fe_3Si_7 + (Si)					
				1245	TA	[123]
	75.46			1245	TA	[125]
	71.18			1215	TA	[126]
				1225	TA	[124]
	74.10			1145	DT, TA	[106]
				1145	DT, TA	[105]
	70.00			1207	emf	[117]
	73.30			1205	DTA, TA	[128]
	72.87	72.47		1207	DTA	[127]
	73.5	71.42		1202	MTA	[121]
				1207	TA	[145]
				1207	Calphad	[4]
				1207		[6]
	72.56	69.99	1	1205	Calphad	[9]
	73.51	69.99	1	1211	Calphad	[12]
	71.86	69.99	1	1214	Calphad (MQM)	This work
	74.40	69.99	1	1208	Calphad (BW)	This work
Congruent	Liquid = Fe_3Si_7					
	66.89			1225	TA	[124]
	70.81			1223	DT, TA	[106]
				1220	DT, TA	[105]
				1216	emf	[117]
				1216	DTA, TA	[128]
	70.5			1220	DTA	[127]
	70.0			1220	MTA	[121]
				1220	Calphad	[4]

				1220		[6]
	70.00	70.00		1209	Calphad	[9]
	70.00	70.00		1217	Calphad	[12]
	70.00	70.00		1215	Calphad (MQM)	This work
	70.00	70.00		1219	Calphad (BW)	This work
Eutectic	Liquid = FeSi + Fe_3Si_7					
				1245	TA	[123]
	70.78			1243	TA	[125]
	62.59			1200	TA	[126]
	61.93			1220	TA	[124]
	67.42			1213	DT, TA	[106]
				1215	DT, TA	[105]
				1212	emf	[117]
	67.42			1210	DTA, TA	[128]
	66.70		69.36	1212	DTA	[127]
	67	50.71	69.2	1206	MTA	[121]
				1212	TA	[145]
				1212	Calphad	[4]
				1212		[6]
	67.18	50.00	69.99	1204	Calphad	[9]
	63.37	50.00	69.99	1210	Calphad	[12]
	66.74	50.00	69.99	1211	Calphad (MQM)	This work
	66.68	50.00	69.99	1212	Calphad (BW)	This work
Eutectoid	Fe_3Si_7 = $FeSi_2$ + (Si)					
	72.71			960	emf	[117]
				930	DTA, TA	[128]
	70.61			955	DTA	[127]
	69.5			940	MTA	[121]
				937	DTA	[11]
				955	Calphad	[4]

				927		[6]
	69.99	66.67	1	960	Calphad	[9]
	69.99	66.67	1	937	Calphad	[12]
	69.99	66.67	1	948	Calphad (MQM)	This work
	69.99	66.67	1	955	Calphad (BW)	This work
Peritectoid	$FeSi + Fe_3Si_7 = FeSi_2$					
				908	DT	[157]
		69.54		955	emf	[117]
				998	DTA, TA	[128]
		69.77		986	DTA	[127]
	50.80	70		982	MTA	[121]
				986	Calphad	[4]
				982		[6]
	50.00	69.99	66.67	1003	Calphad	[9]
	50.00	69.99	66.67	981	Calphad	[12]
	50.00	69.99	66.67	996	Calphad (MQM)	This work
	50.00	69.99	66.67	986	Calphad (BW)	This work
Congruent	Liquid = FeSi					
				1443	TA	[123]
				1420	TA	[103]
				1463	TA	[125]
				1410	DT, TA	[106]
				1400	DT, TA	[105]
				1410	MTA	[121]
				1410	DT, TA	[7]
				1410	Calphad	[4]
				1410		[6]
	50.00	50.00		1409	Calphad	[9]
	50.00	50.00		1398	Calphad	[12]
	50.00	50.00		1410	Calphad (MQM)	This work

	50.00	50.00		1409	Calphad (BW)	This work
Eutectic	Liquid = Fe_2Si + FeSi					
				1235	TA	[123]
				1203	TA	[103]
	35.95			1239	TA	[125]
	33.20			1195	DT, TA	[106]
				1200	DT, TA	[105]
				1205	DTA	[133]
	35.11	34.08	49.39	1202	TA	[122]
	34.6			1202	DTA	[107]
				1195	TA	[145]
	35.66	33.33		1204	TA, DTA	[7]
				1202	Calphad	[4]
				1203		[6]
	35.72	33.33	50.00	1203	Calphad	[9]
	34.73	33.33	50.00	1200	Calphad	[12]
	35.76	33.33	50.00	1202	Calphad (MQM)	This work
	34.32	33.33	50.00	1208	Calphad (BW)	This work
Congruent	Liquid = Fe_2Si					
				1251	TA	[123]
				1215	TA	[122]
				1215	DTA	[107]
				1210	TA, DTA	[7]
				1215	Calphad	[4]
				1212		[6]
	33.33	33.33		1215	Calphad	[9]
	33.33	33.33		1202	Calphad	[12]
	33.33	33.33		1215	Calphad (MQM)	This work
	33.33	33.33		1210	Calphad (BW)	This work
Eutectic	Liquid = bcc_B2 + Fe_2Si					

	31.69	29.9	33.35	1190	TA	[122]
	32.4	30.4		1194	DTA	[107]
	32.51	29.81	33.33	1205	TA, DTA	[7]
				1200		[6]
	30.51	27.24	33.33	1198	Calphad	[9]
	32.81	30.78	33.33	1202	Calphad	[12]
	30.49	26.57	33.33	1202	Calphad (MQM)	This work
	30.70	27.87	33.33	1199	Calphad (BW)	This work
Peritectoid	$Fe_2Si + FeSi = Fe_5Si_3$					
				1020	TA	[103]
				1045	TA	[125]
				1030	DT, TA	[106]
				1030	DT, TA	[105]
				1030	XRD	[131]
				1046	MA	[130]
				1046	DTA	[133]
	33.91			1090	TA	[122]
	34.45			1098	DTA	[107]
				1056	TA, DTA	[7]
				1090	Calphad	[4]
				1060		[6]
	33.33	50.00	37.50	1091	Calphad	[9]
	33.33	50.00	37.50	1061	Calphad	[12]
	33.33	50.00	37.50	1095	Calphad (MQM)	This work
	33.33	50.00	37.50	1055	Calphad (BW)	This work
Eutectoid	$Fe_2Si = bcc\_B2 + Fe_5Si_3$					
	33.29	30.54		1040	TA	[122]
	33.35	31.2		1045	DTA	[107]
				1044	TA, DTA	[7]
				1040	Calphad	[4]

	33.33	29.88	37.5	1050	Calphad	[9]
	33.33	31.39	37.5	1029	Calphad	[12]
	33.33	28.50	37.5	1045	Calphad (MQM)	This work
	33.33	28.79	37.5	1047	Calphad (BW)	This work
Eutectoid	Fe_5Si_3 = bcc_B2 + FeSi					
				825	XRD	[129]
				825	XRD	[131]
				800	MA	[130]
				825	Calphad	[4]
				825		[6]
				825	Calphad	[9]
	37.50	30.03	50.00	775	Calphad	[12]
	37.50	26.83	50.00	825	Calphad (BW)	This work

Table 10.5 Summary of enthalpy of formation at 298.15 K of all the compounds in the Fe-Si system.

Compound	Enthalpy (kJ mol^{-1})	Method	Ref.
(Fe_3Si)	~ -90	Calorimetry	[37, 77]
	-76.57	Calorimetry	[55]
	-102.09±4.60	Emf	[84]
	-93.72±2.51	Emf	[85]
	~ -97	Isothermal calorimetry	[38]
	-100.42	Chemical transport reaction with iodine	[82]
Fe_2Si	~ -78	Calorimetry	[37, 77]
	~ -84	Isothermal calorimetry	[38]
	-52.96	Calphad	[9]
	-73.48	Calphad	[12]
	-53.89	Calphad (MQM)	This work
	-59.86	Calphad (BW)	This work
Fe_5Si_3	-220	Calorimetry	[37, 77]
	-209.20	Chemical transport reaction with iodine	[82]
	-195.40	Calphad	[9]
	-228.05	Calphad	[12]
	-234.74	Calphad (MQM)	This work
	-242.78	Calphad (BW)	This work
FeSi	~ -73	Calorimetry	[37, 77]
	-76.99±3.77	Emf	[84]
	-73.64±3.77	Emf	[85]
	~ -61	Isothermal calorimetry	[38]
	-78.66±3.77	Isothermal calorimetry (293 K)	[78]
	-75.31±8.35	Calorimetry	[79]
	-74.48±8.35	Calorimetry	[80]
	-71.80	Calphad	[86]
	-77.20±3.60	High temperature direct synthesis calorimetry	[81]
	-73.89	Calphad	[67]

	-77.40	Chemical transport reaction with iodine	[82]
	-63.61	Calphad	[9]
	-70.26	Calphad	[12]
	-76.41	Calphad (MQM)	This work
	-77.88	Calphad (BW)	This work
$FeSi_2$	~ -75	Calorimetry	[37, 77]
	-89.12±7.53	Emf	[84]
	-81.17±7.53	Emf	[85]
	~ -82	Isothermal calorimetry	[38]
	-88.66	Calorimetry	[80]
	-100.42	Chemical transport reaction with iodine	[82]
	-73.00	Calphad	[9]
	-109.56	Calphad	[12]
	-96.94	Calphad (MQM)	This work
	-101.78	Calphad (BW)	This work
Fe_3Si_7	~ -220	Calorimetry	[37, 77]
	-197.26	Emf	[84]
	-180.93±30.15	Emf	[85]
	~ -250	Isothermal calorimetry	[38]
	-232.21	Calphad	[86]
	-238.24	Calphad	[67]
	-169.04	Calphad	[9]
	-212.25	Calphad	[12]
	-247.84	Calphad (MQM)	This work
	-199.36	Calphad (BW)	This work

Table 10.6 Summary of entropy at 298.15 K of all the compounds in the Fe-Si system.

Compound	Entropy (J mol^{-1} K^{-1})	Method	Ref.
(Fe_3Si)	103.59	Adiabatic calorimetry	[54-56, 58]
	101.25	Chemical transport reaction with iodine	[82]
Fe_2Si	103.16	Calphad	[9]
	92.55	Calphad	[12]
	106.39	Calphad (MQM)	This work
	101.96	Calphad (BW)	This work
Fe_5Si_3	209.61	Adiabatic calorimetry	[54, 56]
	208.65	Adiabatic calorimetry	[58, 61]
	213.6	Adiabatic calorimetry	[63]
	237.23	Chemical transport reaction with iodine	[82]
	238.59	Calphad	[9]
	228.48	Calphad	[12]
	209.1	Calphad (MQM)	This work
	202.88	Calphad (BW)	This work
FeSi	46.02	Adiabatic calorimetry	[54, 56, 58, 61]
	46.02	Chemical transport reaction with iodine	[82]
	45.57±0.5	Adiabatic calorimetry	[67]
	51.23	Calphad	[9]
	51.51	Calphad	[12]
	46.024	Calphad (MQM)	This work
	45.28	Calphad (BW)	This work
Fe_3Si_7	208.32	Adiabatic calorimetry	[54]
	206.69±2.15	Adiabatic calorimetry	[67]
	243.97	Chemical transport reaction with iodine	[82]
	251.46	Calphad	[9]
	242.33	Calphad	[12]
	207.3	Calphad (MQM)	This work
	248.9	Calphad (BW)	This work

$FeSi_2$	55.48	Adiabatic calorimetry	[54, 58]
	55.23	Chemical transport reaction with iodine	[82]
	64.04	Calphad	[9]
	42.43	Calphad	[12]
	55.48	Calphad (MQM)	This work
	52.36	Calphad (BW)	This work

Table 10.7 Summary of melting enthalpy of all the compounds in the Fe-Si system.

Compound	Enthalpy (J mol^{-1})	Method	Ref.
(Fe_3Si)	55.98	Calorimetry	[55]
	57.32	Calorimetry	[57]
Fe_2Si	37.00	Calphad	[86]
	35.77	Calphad	[9]
	63.78	Calphad	[12]
	36.86	Calphad (MQM)	This work
	46.16	Calphad (BW)	This work
FeSi	68.91	Calorimetry	[61]
	70.29	Calorimetry	[57]
	66.94±1.46	Calorimetry	[68]
	61.44	Calphad	[86]
	53.64	Calphad	[9]
	67.09	Calphad	[12]
	65.26	Calphad (MQM)	This work
	70.81	Calphad (BW)	This work
Fe_3Si_7	321.62	Calorimetry	[70]
	315.37	Calorimetry	[57]
	337.91	Calphad	[86]
	234.20	Calphad	[9]
	340.48	Calphad	[12]
	353.00	Calphad (MQM)	This work
	315.64	Calphad (BW)	This work

Table 10.8 Optimized model parameters for the Fe-Si system with MQM liquid description (J mol^{-1} or J mol^{-1} K^{-1}).

Phase	Thermodynamic parameters
liquid (Fe, Si)	$Z^{Si}_{Si,Si} = Z^{Fe}_{Fe,Fe} = Z^{Fe}_{Fe,Si} = Z^{Si}_{Fe,Si} = 6$ $\Delta g_{Fe,Si} = -33710.49 + 2.26T + (-12552 + 5.02T)x_{FeFe}$ $+ (-8368 + 4.82T)x^2_{FeFe} + (-3054.32 + 6.49T)x_{SiSi}$
fcc_A1 $(Fe, Si)_1(Va)_1$	${}^0L_{Fe,Si} = -115254.05 - 2.19T$ ${}^1L_{Fe,Si} = -84776.91 + 44.33T$ ${}^2L_{Fe,Si} = 20007.03$
bcc_A2 $(Fe, Si)_1(Va)_3$	${}^0L_{Fe,Si} = -154013.56 + 32.29T$ ${}^1L_{Fe,Si} = -63511.47 + 13.25T$ ${}^2L_{Fe,Si} = 35727.58$ ${}^1Tc = 504$
bcc_B2 $(Fe, Si)_{0.5}(Fe, Si)_{0.5}(Va)_3$	$\Delta G^{B2}_{Fe:Si} = \Delta G^{B2}_{Si:Fe} = -10464.8$; $\Delta G^{B2}_{Fe:Fe} = \Delta G^{B2}_{Si:Si} = 0$
Fe_2Si $(Fe)_2(Si)_1$	$\Delta H^o_{298} = -53889.7$, $S^o_{298} = 106.4$ $C_p = 2\ C_p(Fe_{(bcc)}) + C_p(Si_{(diamond)})$
Fe_5Si_3 $(Fe)_5(Si)_3$	$\Delta H^o_{298} = -234740$, $S^o_{298} = 209.1$ $C_p = 180.30693 + 8.5911943\ 10^{-2}T - 1060721.6T^{-2} + 2.6645942\ 10^{-7}T^2$ $\beta = 2.32$, $Tc = 360$, $P = 0.28$
FeSi $(Fe)_1(Si)_1$	$\Delta H^o_{298} = -76410$, $S^o_{298} = 46.024$ $C_p = 48.56656315 + 1.47211235\ 10^{-2}T - 428219.9934T^{-2} - 1.751134669\ 10^{-6}T^2$
$FeSi_2$ $(Fe)_1(Si)_2$	$\Delta H^o_{298} = -96940.44$, $S^o_{298} = 55.48$ $C_p = 79.0298507 - 1.814692\ 10^{-2}T - 999009.042T^{-2} + 1.782\ 10^{-5}T^2$
Fe_3Si_7 $(Fe)_3(Si)_7$	$\Delta H^o_{298} = -247842.42$, $S^o_{298} = 207.3$ $C_p = 214.2176 + 1.0992713\ 10^{-1}T - 2345706.9T^{-2} - 2.3033434\ 10^{-5}T^2$

Table 10.9 Optimized model parameters for the Fe-Si system with BW liquid description (J mol^{-1} or J mol^{-1} K^{-1}).

Phase	Thermodynamic parameters
liquid $(Fe, Si)_1$	${}^0L_{Fe,Si} = -153321.91+25.11T$ ${}^1L_{Fe,Si} = -32952.45+10.83T$ ${}^2L_{Fe,Si} = +26297.75$
fcc_A1 $(Fe, Si)_1(Va)_1$	${}^0L_{Fe,Si} = -115254.05 - 2.19T$ ${}^1L_{Fe,Si} = -84776.91 + 44.33T$ ${}^2L_{Fe,Si} = +20007.03$
Diamond_A4 $(Fe, Si)_1$	${}^oG_m^{Fe} = +{}^oG_{Fe}^{bcc} + 1000$ ${}^0L_{Fe,Si} = +113000 - 0.5T$
bcc_A2 $(Fe, Si)_1(Va)_3$	${}^0L_{Fe,Si} = -154013.56 + 32.29T$ ${}^1L_{Fe,Si} = -63511.47 + 13.25T$ ${}^2L_{Fe,Si} = +35727.58$ ${}^1Tc = +504$
bcc_B2 $(Fe, Si)_{0.5}(Fe, Si)_{0.5}(Va)_3$	$\Delta G_{Fe:Si}^{B2} = \Delta G_{Si:Fe}^{B2} = -10675.2$; $\Delta G_{Fe:Fe}^{B2} = \Delta G_{Si:Si}^{B2} = 0$ $\Delta Tc_{Fe:Si}^{B2} = \Delta Tc_{Si:Fe}^{B2} = -210$; $\Delta Tc_{Fe:Fe}^{B2} = \Delta Tc_{Si:Si}^{B2} = 0$ $\Delta\beta_{Fe:Si}^{B2} = \Delta\beta_{Si:Fe}^{B2} = -0.75$; $\Delta\beta_{Fe:Fe}^{B2} = \Delta\beta_{Si:Si}^{B2} = 0$
D03 $(Fe, Si)_{0.25}(Fe, Si)_{0.25}(Fe, Si)_{0.25}(Fe, Si)_{0.25}(Va)_3$	$\Delta G_{Fe_3Si}^{D03} = -3350.0$; $\Delta Tc_{Fe_3Si}^{D03} = +65$; $\Delta\beta_{Fe_3Si}^{D03} = +0.2$
Fe_2Si $(Fe)_2(Si)_1$	${}^oG_m^{Fe_2Si} = +2\cdot{}^oG_{Fe}^{bcc} + {}^oG_{Si}^{dia} - 78160 - 9.4274\ T$
Fe_5Si_3 $(Fe)_5(Si)_3$	${}^oG_m^{Fe_5Si_3} = -301755.4 + 1030.47T - 180.31T\ln(T)$ $+ 530360.8T^{-1} - 0.04296T^{-2} - 4.441\cdot10^{-8}T^3$ $\beta = 2.32$, $Tc = 360$, $P = 0.28$

FeSi $(Fe)_1(Si)_1$	${}^{o}G_m^{FeSi} = -94437.05 + 286.72T - 48.57T\ln(T)$ $+ 214110T^{-1} - 0.007361T^2 + 2.9186 \cdot 10^{-7}T^3$
$FeSi_2$ $(Fe)_1(Si)_2$	${}^{o}G_m^{FeSi_2} = -128043.76 + 477.95T - 79.0298 \cdot \ln(T)$ $+ 499504.521T^{-1} + 0.009073T^2 - 2.9710^{-6}T^3$
Fe_3Si_7 $(Fe)_3(Si)_7$	${}^{o}G_m^{Fe_3Si_7} = -275773.79 + 1230.78T - 214.2176T\ln(T)$ $+ 1172853.45T^{-1} - 0.05496T^2 + 3.8389 \cdot 10^{-6}T^3$

Figures

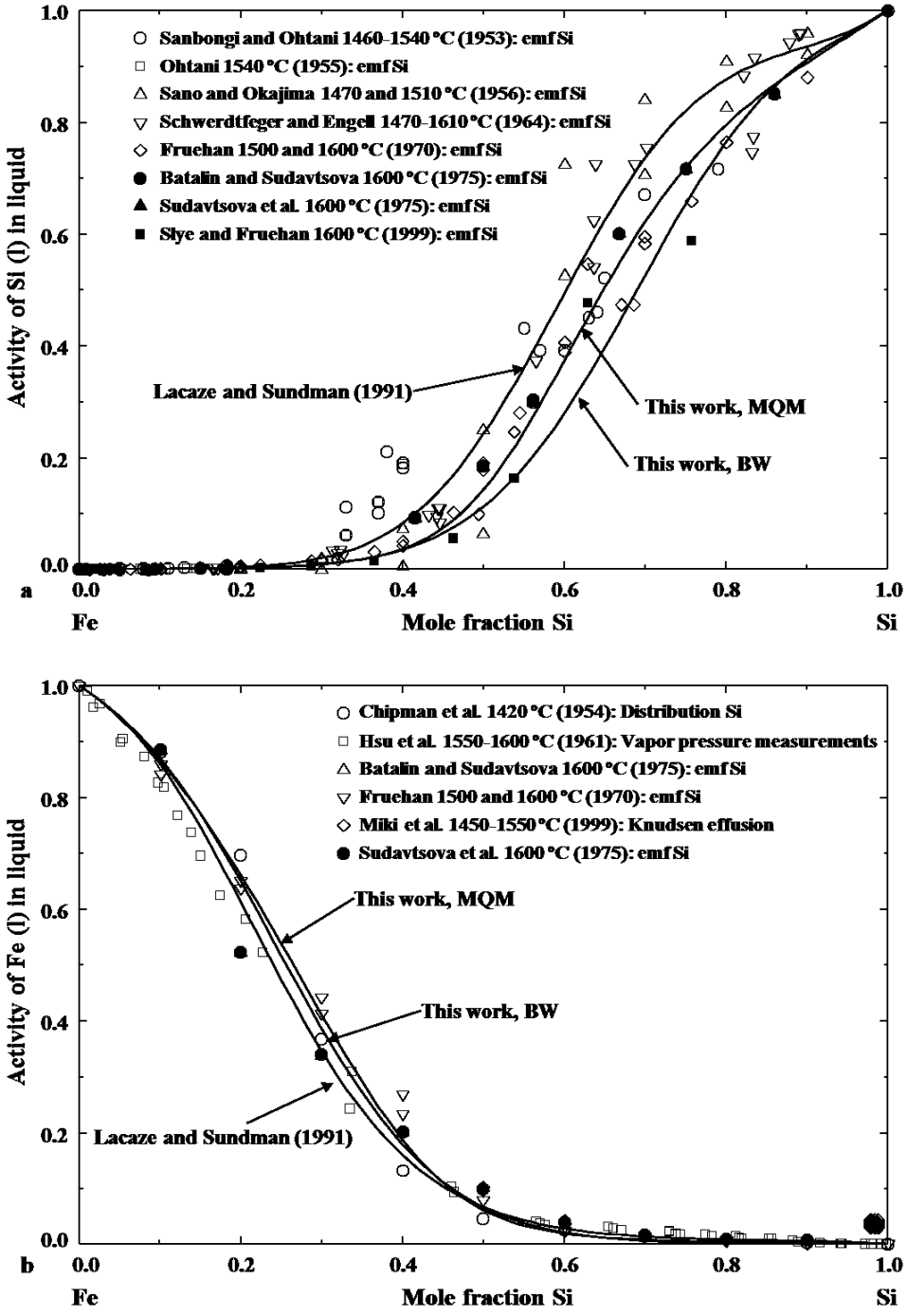

Fig. 10.1 Calculated activities of (a) Si and (b) Fe in the liquid Fe-Si at 1600 °C with respect to their liquid states compared with the experimental data.

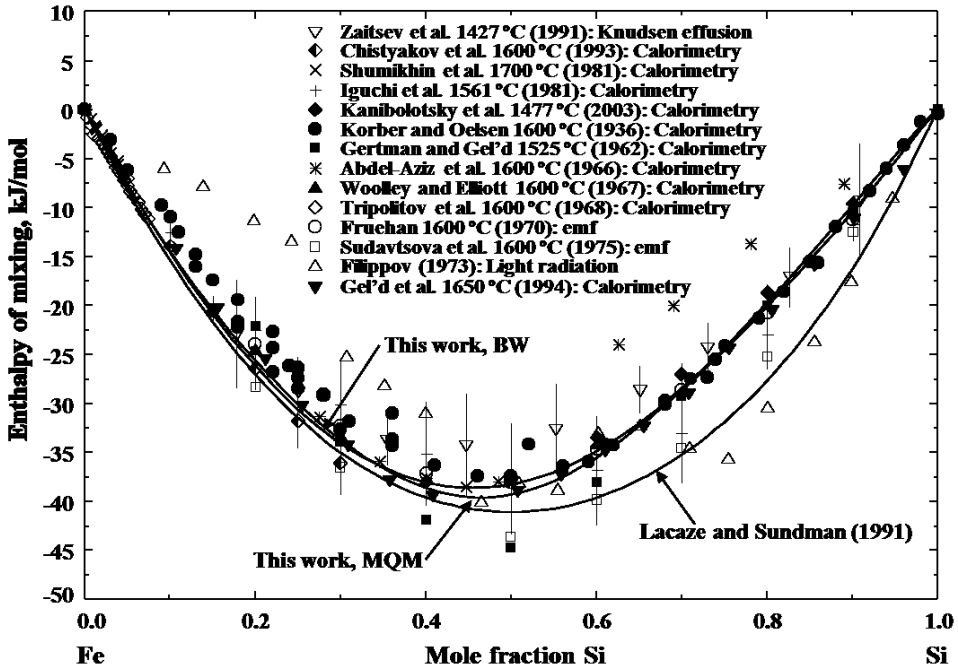

Fig. 10.2 Calculated enthalpy of mixing of liquid at 1600 °C compared with the experimental data.

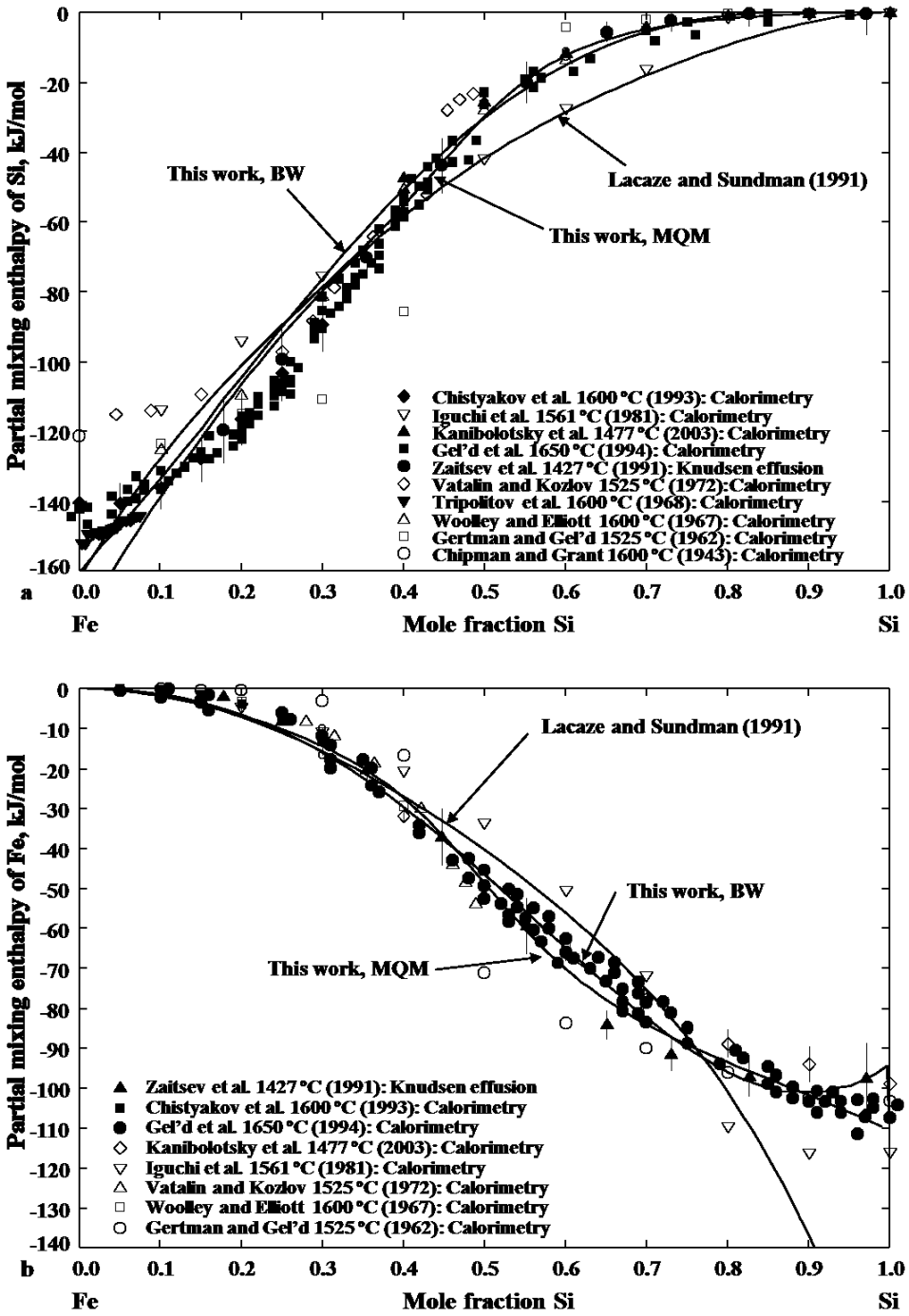

Fig. 10.3 Calculated partial enthalpy of mixing of liquid at 1600 °C compared with the experimental data. (a) Partial enthalpy of Si and (b) partial enthalpy of Fe.

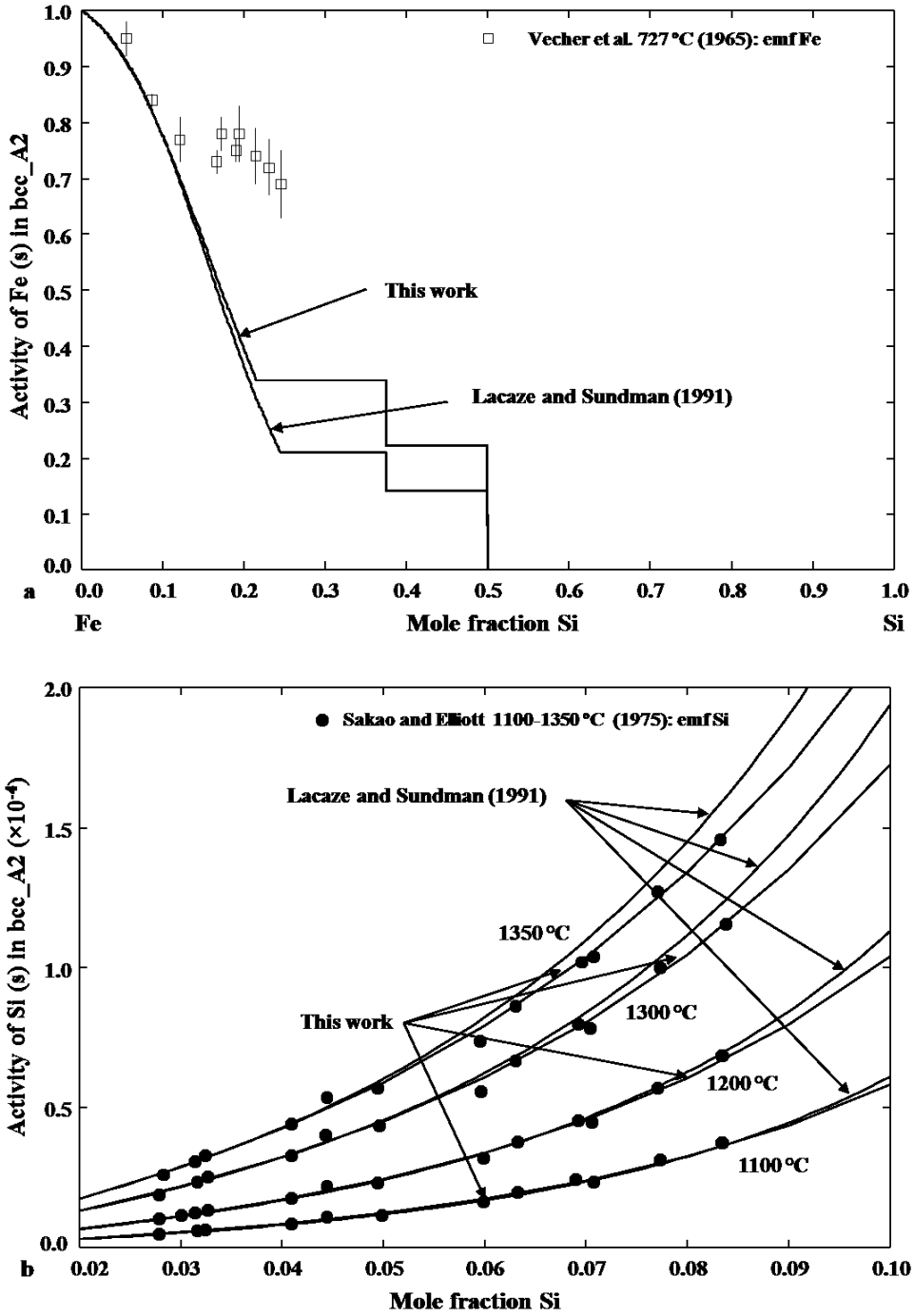

Fig. 10.4 Calculated activities in the bcc alloys compared with the experimental data. (a) Activities of Fe at 727 °C with respect to the bcc_A2 state and (b) activities of Si at 1100-1350 °C with respect to the diamond Si state.

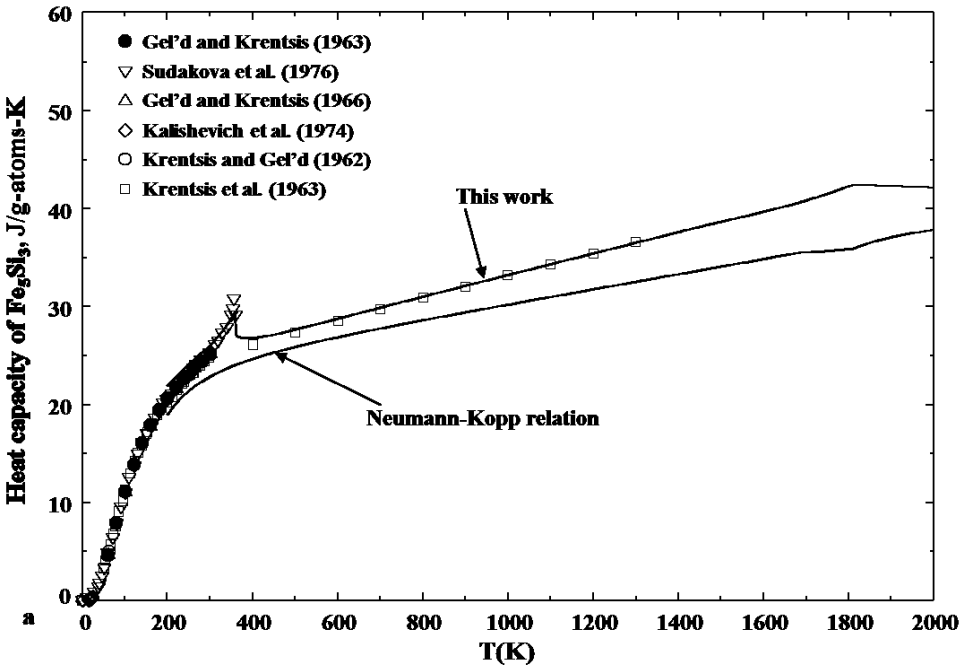
Gel'd and Krentsis (1963)
Sudakova et al. (1976)
Gel'd and Krentsis (1966)
Kalishevich et al. (1974)
Krentsis and Gel'd (1962)
Krentsis et al. (1963)
This work
Neumann-Kopp relation
Heat capacity of Fe_3Si_3, J/g-atoms-K
T(K)
a

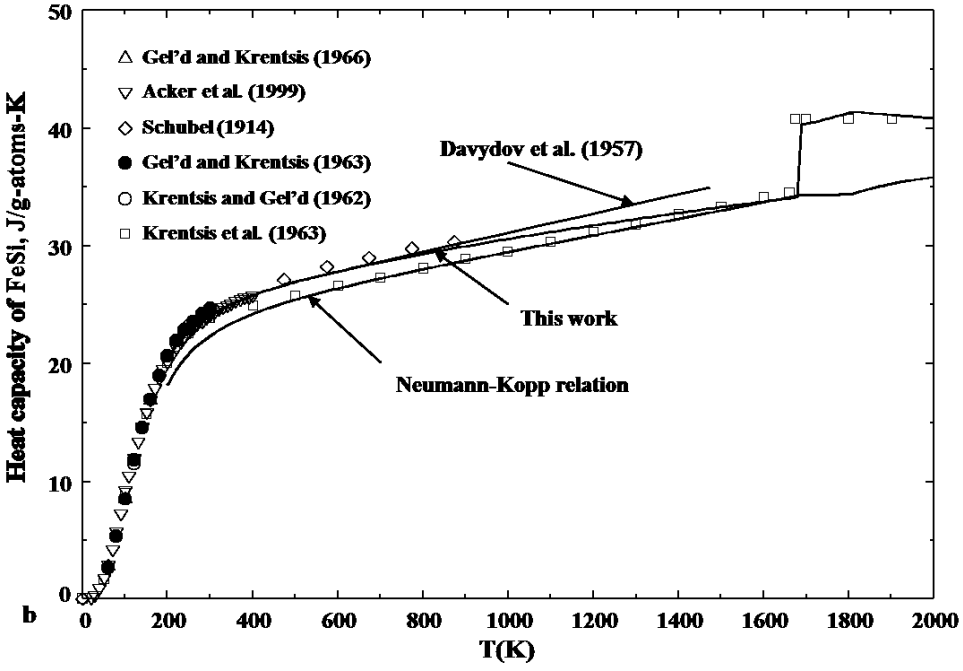
Gel'd and Krentsis (1966)
Acker et al. (1999)
Schubel (1914)
Gel'd and Krentsis (1963)
Krentsis and Gel'd (1962)
Krentsis et al. (1963)
Davydov et al. (1957)
This work
Neumann-Kopp relation
Heat capacity of FeSi, J/g-atoms-K
T(K)
b

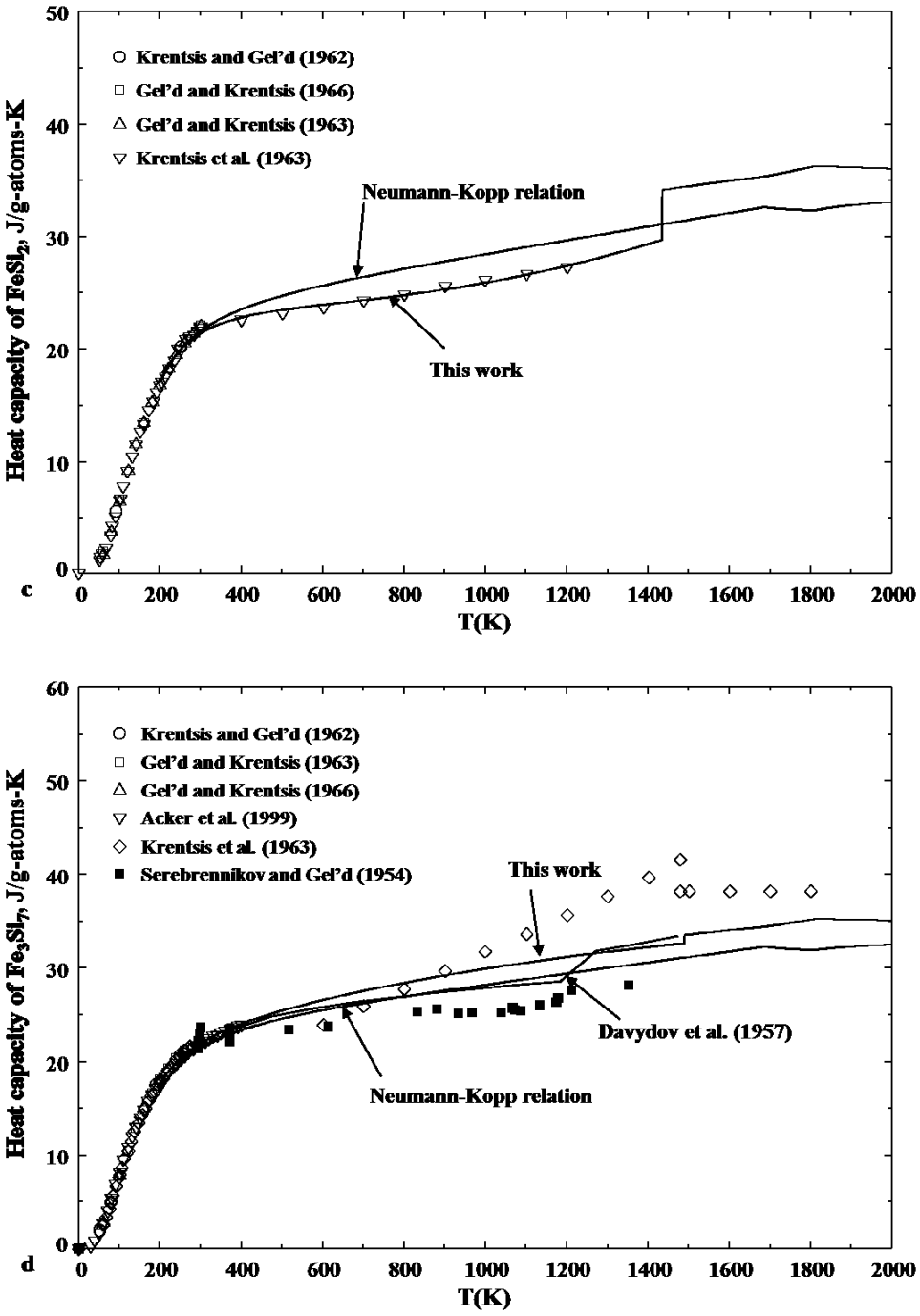

Fig. 10.5 Calculated heat capacities of (a) Fe_5Si_3, (b) FeSi, (c) $FeSi_2$, and (d) Fe_3Si_7 compared with the experimental data.

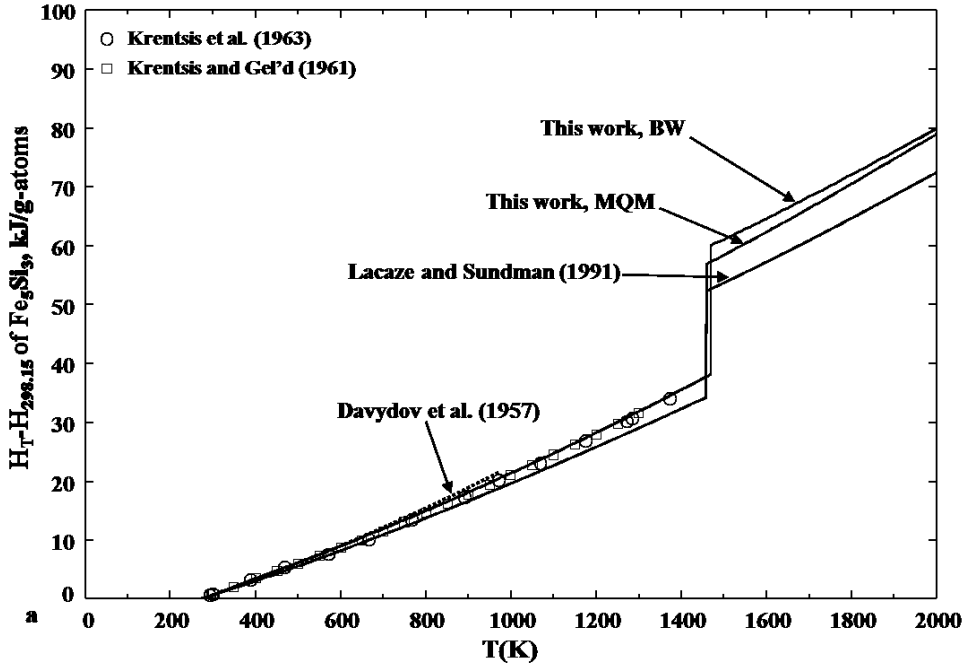
Krentsis et al. (1963)
Krentsis and Gel'd (1961)
This work, BW
This work, MQM
Lacaze and Sundman (1991)
Davydov et al. (1957)
H_T-$H_{298.15}$ of Fe_3Si_3, kJ/g-atoms
T(K)
a

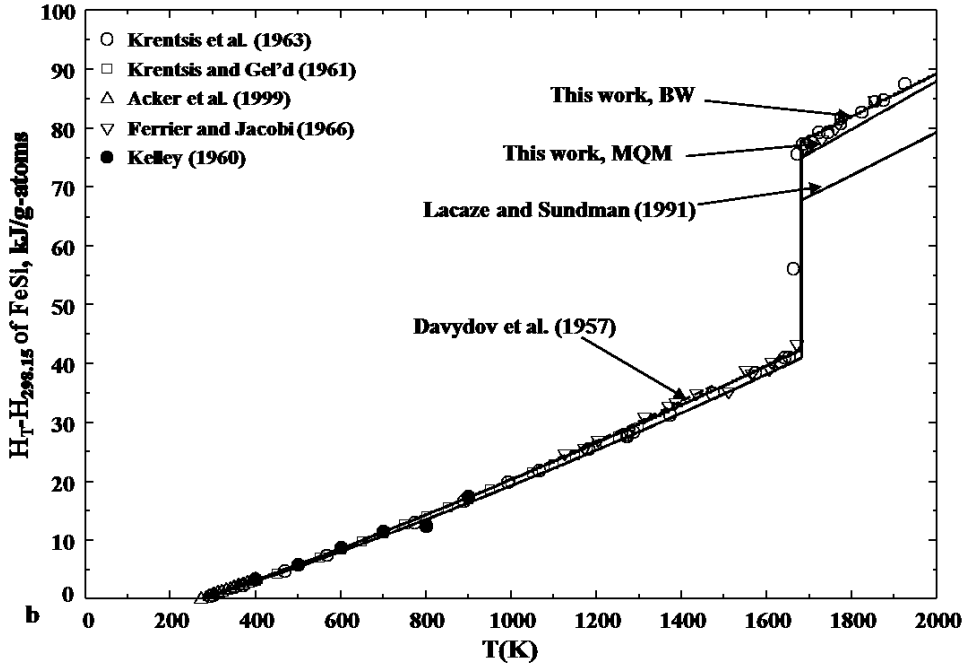
Krentsis et al. (1963)
Krentsis and Gel'd (1961)
Acker et al. (1999)
Ferrier and Jacobi (1966)
Kelley (1960)
This work, BW
This work, MQM
Lacaze and Sundman (1991)
Davydov et al. (1957)
H_T-$H_{298.15}$ of FeSi, kJ/g-atoms
T(K)
b

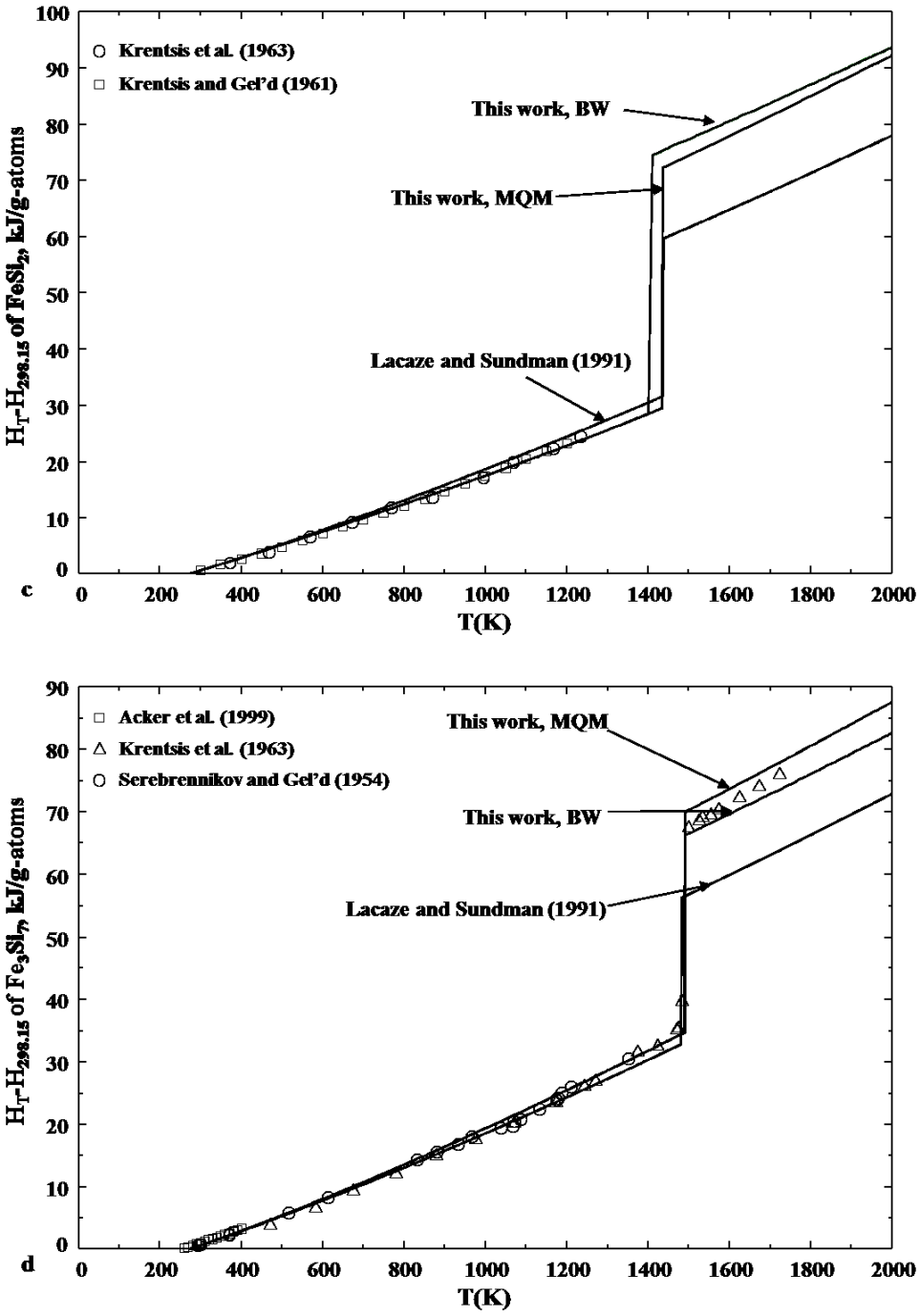

Fig. 10.6 Calculated heat contents of (a) Fe_5Si_3, (b) FeSi, (c) $FeSi_2$, and (d) Fe_3Si_7 compared with the experimental data.

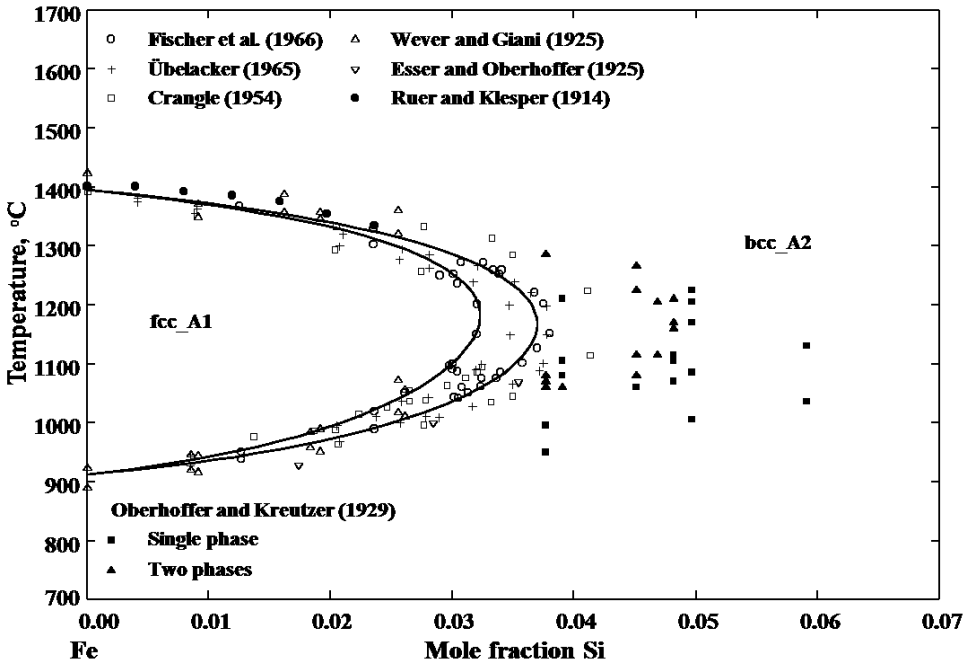

Fig. 10.7 Calculated gamma loop in the present study compared with the experimental data.

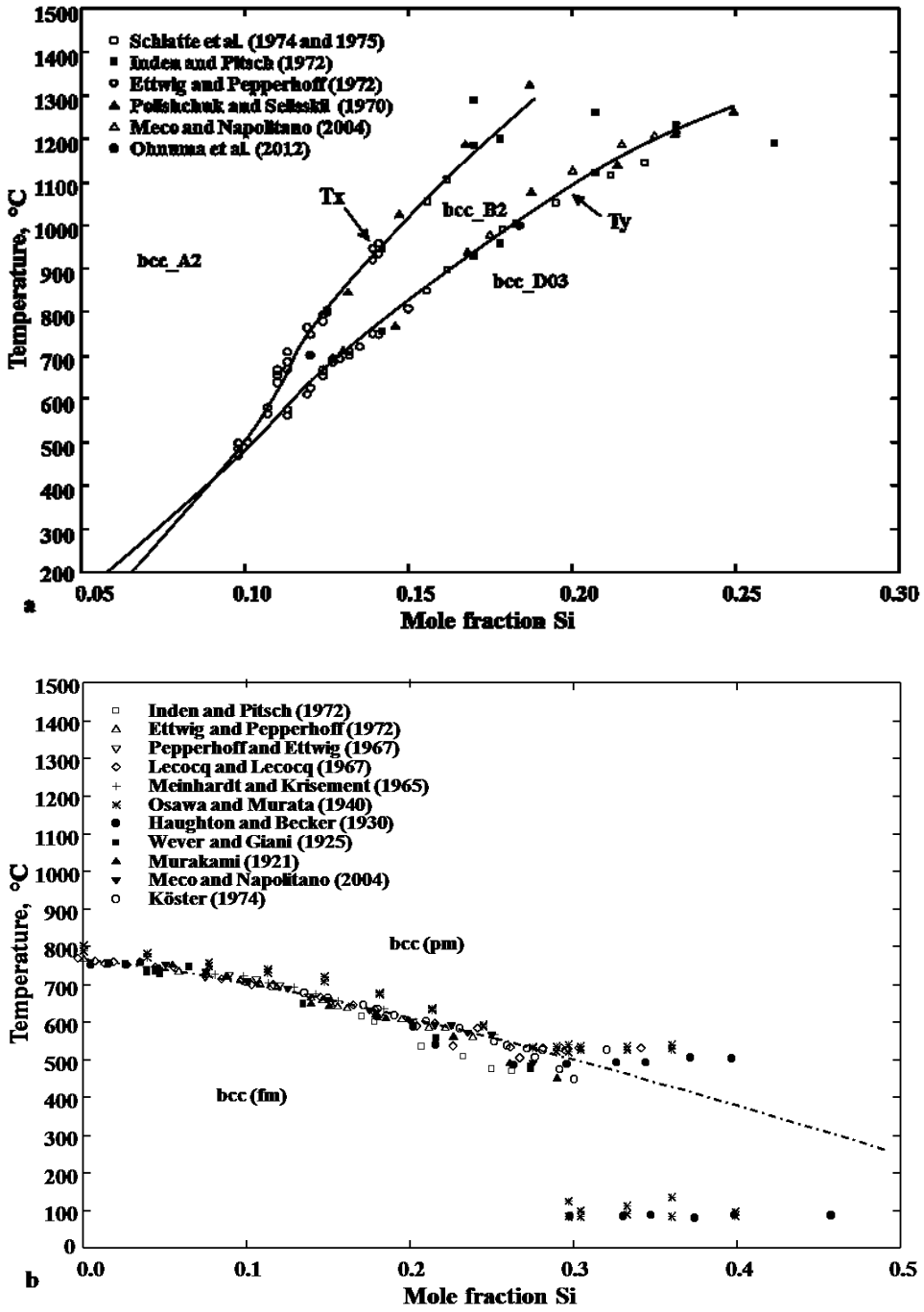

Fig. 10.8 The order-disorder transition of the bcc phase. (a) The A2/B2 (Tx) transition temperature and B2/D03 (Ty) transition temperature, and (b) the Curie temperature (Tc) of magnetic transition compared with the experimental data. The Tx line and Tc line are calculated from the present study, and the Ty line is an evaluated line from the experimental data.

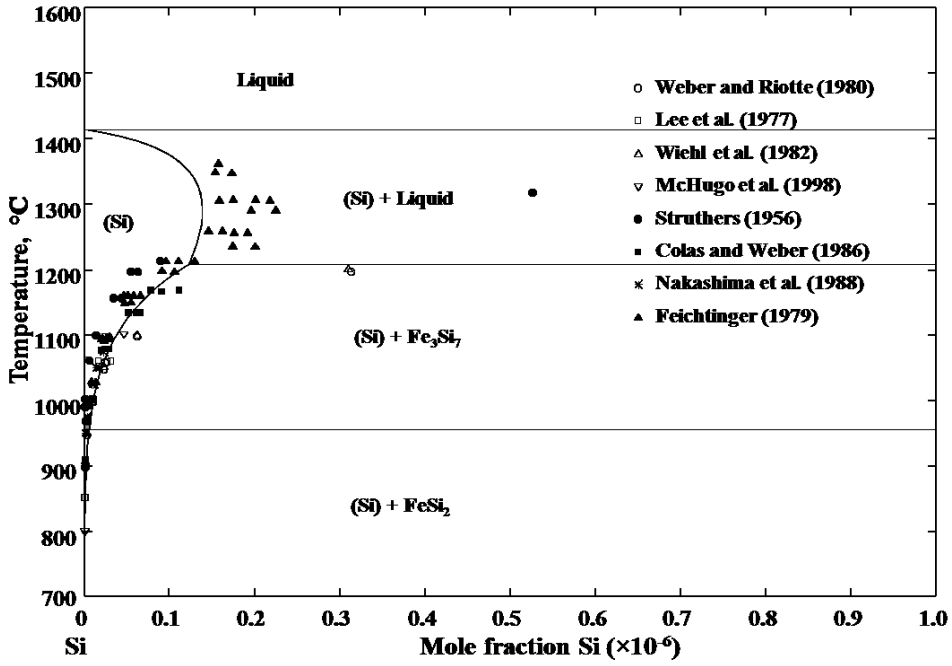

Fig. 10.9 Calculated solubility of Fe in (Si) compared with the experimental data.

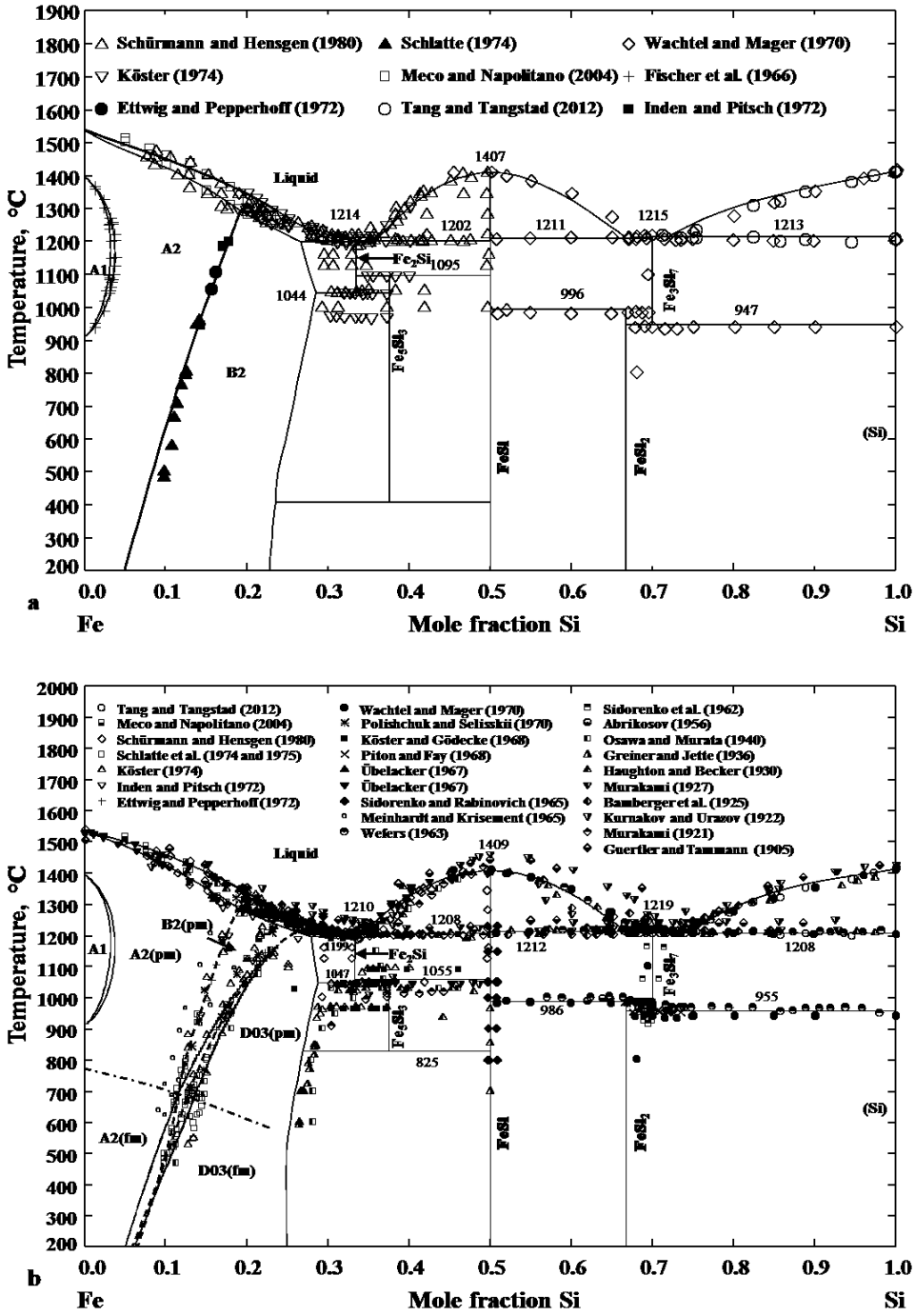

Fig. 10.10 Calculated phase diagram from the present optimization compared with the selected experimental data. Optimization with the liquid phase by (a) MQM and (b) BW.

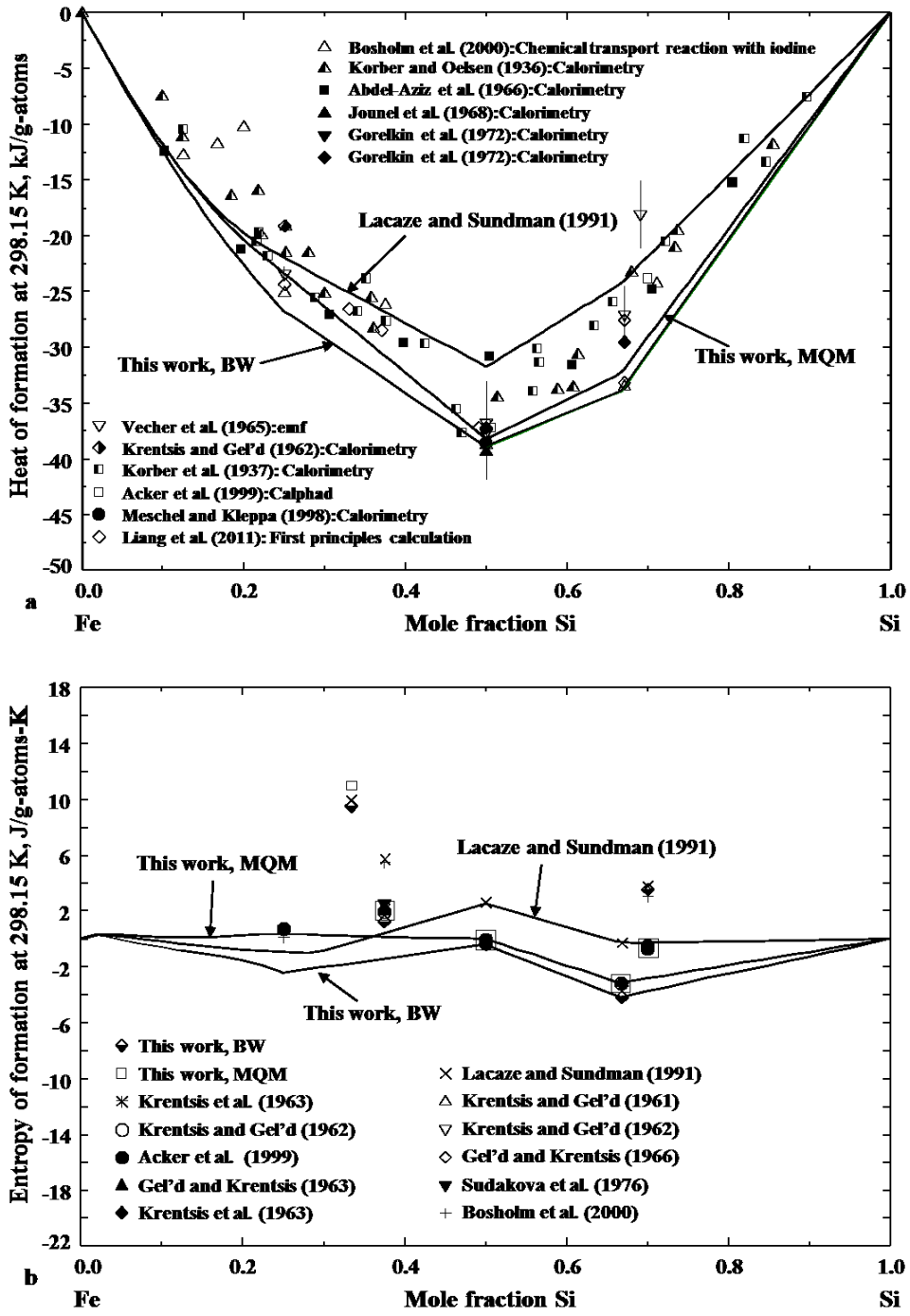

Fig. 10.11 Calculated (a) enthalpy of formation at 298.15 K and (b) entropy of formation at 298.15 K compared with the experimental data.

Chapter 11 Thermodynamic modeling of the Fe-Si-Cr and Fe-Si-Mg systems

Senlin Cui and In-Ho Jung

Department of Mining and Materials Engineering, McGill University, 3610 University Street, Montreal, Quebec, H3A 0C5, Canada

Abstract

Thermodynamic modeling for the Fe-Si-Cr and Fe-Si-Mg ternary systems were conducted on the basis of the critical evaluation and optimization of all the thermodynamic and phase diagram data in the literature. The Gibbs energy of the liquid phase was described using the Modified Quasi-chemical Model (MQM) in pair approximation. The obtained thermodynamic descriptions of the Fe-Si-Cr and Fe-Si-Mg systems can be used to calculate any sections of the phase diagrams and thermodynamic properties of these two systems with high accuracy from room temperature to above the melting temperature of the system.

Key words:

Fe-Cr-Si alloys; Fe-Mg-Si alloys; phase diagram; thermodynamic modeling.

11.1 Introduction

Silicon steels as soft magnetic materials are widely used in energy transportation and electromagnetic energy conversion due to their combined low magneto-striation and high saturation magnetization [1]. In order to satisfy the various requirements related to work condition, silicon steels with different compositions have been developed [2]. Cr and Mg are commonly added in the Fe-Si alloys to modify the microstructure and mechanical and magnetic properties. Cr can promote the formation of the CrSi and $CrSi_2$ compounds with high thermal stability that benefits to the high temperature applications of Fe-Si electrical steel [2]. It is also known that Mg addition in the molten steel can produce uniform spinel oxide ($MgAl_2O_4$), which acts as the nucleation sites for TiN to further induce the formation of fine equi-axied structure [3, 4]. In addition, Mg can be used for the refinement of austenite grain size [5] and magnesium treatment can improve the hydrogen-induced cracking resistance and possibly hot cracking resistance [6].

The microstructure of alloys is critically related to its thermochemistry and kinetics. Reliable thermodynamic and phase diagram information is of fundamental importance for the understanding of the microstructure evolution and mechanical and magnetic properties of electric steel. The Fe-Si-Cr and Fe-Si-Mg systems are two important subsystems within the silicon steel system. The purpose of the present study is to optimize the Fe-Si-Cr and Fe-Si-Mg systems.

Recently, the present authors [7] identified that the thermodynamic description of the Fe-Si system [8] widely used in thermodynamic database of steel has room for improvement, and presented a revised critical optimization of the Fe-Si system. In the present study, the revised modeling results of the Fe-Si system is used for the description of the Fe-Si-Cr and Fe-Si-Mg systems for the accurate descriptions of all the available thermodynamic and phase diagram information in the two systems.

11.2 Critical evaluation of literature information

11.2.1 The Fe-Si-Cr system

The Fe-Si-Cr system was previously reviewed by Raghavan [9], and later updated by Raghavan [10-12]. Chart et al. [13] conducted the first version of thermodynamic modeling for the Fe-Si-Cr system with the consideration of only the isothermal section at 900 °C. Lindholm [14] optimized the Fe-Si-Cr system, but the optimization results are not satisfactory, for example, the calculated liquidus temperature is much lower than the experimental data and the distribution of Si between solid and liquid showed considerable error. Later, Miettinen [15] revised the liquid, bcc, and fcc phases of the Fe-Si-Cr system to improve the quality of the thermodynamic description. However, the optimization was only limited to the low Si region. So far, no comprehensive thermodynamic modeling of the Fe-Si-Cr system has been performed.

The phase diagrams of this ternary system were measured by Anderson and Jette [16], Yajima [17], Gladyshevskii and Borusevich [18], Yamaguchi et al. [19], Wethmar et al. [20], Awais and Hayes [21, 22], Yamamoto et al. [23], and Li et al. [24]. More specifically, Yajima [17] determined the liquidus projection in the Fe rich region of the Fe-Si-Cr system by thermal analysis and microscopic examination. Anderson and Jette [16] studied the phase equilibria in the Fe-Si-Cr system at 600, 800, and 1000 °C using x-ray diffraction (XRD) analysis of the equilibrated alloy samples, but, no isothermal phase diagram sections were given. Gladyshevskii and Borusevich [18] measured the isothermal section at 900 °C by XRD and microscopic analysis. The existence of a continuous solid solution between CrSi and FeSi was confirmed, and a large Cr solubility in the Fe_5Si_3 phase was determined. The homogeneity range of the σ phase was also measured. Awais and Hayes [21, 22] investigated the phase equilibrium in the Fe-Fe_5Si_3-Cr_3Si-Cr region at 947 and 1047 °C by optical microscopic analysis, scanning electron microscopy (SEM) analysis, energy dispersive x-ray microanalysis (EDS), and XRD analysis of the equilibrated alloy samples. Yamamoto et al. [23] measured the isoplethal section at constant 10 at.% Cr and the isothermal section at 600 °C in the Fe rich region related to the bcc_A2 and bcc_D03 phases by means of SEM analysis, transmission electron microscopy (TEM) analysis, and electron probe microanalysis (EPMA). Li et al. [24] measured the isothermal section at 700 °C by means of SEM, EDS, and XRD measurements. They found that both the σ and D03 phases have large ternary extension, the FeSi and CrSi phases form a continuous solid solution, and Fe_5Si_3 and Cr_5Si_3 have

mutual solubilities. In addition, Yamaguchi et al. [19] reported that the Si addition in the Fe-Cr alloys enhanced the critical point of the miscibility gap of the bcc Fe-Cr solution by differential thermal analysis (DTA). Wethmar et al. [20] measured the liquidus temperature along the Cr/Fe atomic ratio of 4.0, 2.33, 1.5, and 1.0 using DTA and quenching experiments.

The measured liquidus projection by Yajima [17], isothermal section at 900 °C by Gladyshevskii and Borusevich [18], isothermal sections at 947 and 1047 °C by Awais and Hayes [21], and isothermal section at 700 °C by Li et al. [24] are utilized in the current optimization.

The enthalpy of mixing of the liquid phase was investigated by Igushev et al. [25] and Petrushevskii et al. [26]. Igushev et al. [25] measured the enthalpy of mixing in the molten Fe-Si-Cr alloys along the Fe/Cr atomic ratio of 4.55, 1.86, 0.93, and 0.64 by high temperature calorimetry. Petrushevskii et al. [26] calculated the enthalpy of mixing of the Fe-Si-Cr system at 1600 °C by a self-developed equation which can take into account short range ordering. The calculated data from Petrushevskii et al. [26] are reasonably consistent with the measured ones by Igushev et al. [25].

11.2.2 The Fe-Si-Mg system

The ternary Fe-Si-Mg system has been reviewed several times by Raghavan [27-29]. Another systematic review was performed by Lebrun et al. [30]. A thermodynamic modeling was recently conducted by Du et al. [31].

The phase relation in the Fe-Mg-Si system was previously measured by Zwicker [32], Guichelaar [33], Ageev and Archugov [34], Pierre et al. [35], Löffler et al. [36], and Normann et al. [37]. Zwicker [32] reported the liquidus projection of the Fe-Mg-Si system measured by thermal analysis, followed by microscopic and XRD phase analysis. The FeSi phase was assumed to have a large primary phase region. Guichelaar [33] measured the miscibility gap between the Fe and Mg rich liquid in the Fe-Mg-Si system at 1545 °C using vapor pressure measurements. Later, Ageev and Archugov [34] measured the solubility of Mg in the Fe rich region of the Fe-Mg-Si system at 1600 °C under argon atmosphere. Recently, Pierre et al. [35] measured the solid-liquid

phase equilibrium in the Fe-Mg-Si system at 727 °C by powder mixture reaction to equilibrium and the diffusion couple technique coupled with powder XRD, optical microscopy, SEM, and EPMA analysis. No ternary compound was found in the ternary system. All the stable compounds and solutions in the Mg-Si and Fe-Si systems were in equilibrium with the Mg rich liquid phase. Most recently, Löffler et al. [36] determined the phase equilibrium of the Fe-Mg-Si system at 800 and 1000 °C using equilibrated alloys and the diffusion couple technique. According to the measurements, the Fe_5Si_3 phase was stabilized to lower temperature with the addition of Mg. In addition, the solubilities of Fe in the liquid Mg-Si solution were measured at 670, 710, and 750 °C by Normann et al. [37] using the atomic absorption spectroscopy and EPMA.

Lepinskikh et al. [38] measured of the activity of Mg in the Fe-Si-Mg system along the Fe/Si atomic ratio of 0.165, 0.61, and 2.8 at 1300-1350 °C by the electromotive force (emf) technique. Then, isothermal activities of Fe and Si were calculated by the Darken-Wager method. However, according to the present evaluation, the experiments with Fe/Si atomic ratios of 0.61 and 2.8 were within the liquid miscibility gap, and therefore the calculated values are erroneous. Only the activity data with the Fe/Si atomic ratio of 0.165 were considered in the present optimization.

11.3 Thermodynamic modeling

11.3.1 Pure elements and stoichiometric compounds

The Gibbs energies of pure elements, Fe, Si, Mg, and Cr, were taken from the SGTE database complied by Dinsdale [39] in the form:

$$^{o}G_i(T) = a + bT + cT\ln T + dT^2 + eT^{-1} + fT^3 + gT^7 + hT^{-9} \quad (11.1)$$

The Gibbs free energies of stoichiometric compounds can be expressed as:

$$G_T = H_T - S_T T \quad (11.2)$$

$$H_T = \Delta H^o_{298.15} + \int_{298.15}^{T} C_P dT \tag{11.3}$$

$$S_T = S^o_{298.15} + \int_{298.15}^{T} \frac{C_P}{T} dT \tag{11.4}$$

where H_T and S_T are the enthalpy and entropy at temperature T in Kelvin, $\Delta H^o_{298.15}$ is the enthalpy of formation at 298.15 K, C_p is the heat capacity, and $S^o_{298.15}$ is the entropy at 298.15 K. The Gibbs energies of stoichiometric compounds can be thus described using C_p, $S^o_{298.15}$, and $\Delta H^o_{298.15}$. The heat capacity expression of each compound can be obtained by numerical fitting of the experimental heat content data and heat capacity data. If no experimental data available, the Neumann-Kopp relation can be used to estimate the heat capacity.

11.3.2 Liquid phase

In the present study, the Gibbs energy of liquid is described using the Modified Quasi-chemical Model (MQM) proposed by Pelton et al. [40, 41]. Assume the atoms *m* and *n* in the liquid phase occupy a quasi-lattice, then, the following pair exchange reaction can be considered:

$$(m\text{-}m)+(n\text{-}n)=2(m\text{-}n): \quad \Delta g_{mn} \tag{11.5}$$

where (*m*-*m*), (*n*-*n*), and (*m*-*n*) are the first-nearest-neighbor atom pairs. Δg_{mn} is the non-configurational Gibbs energy change for the formation of two moles of (*m*-*n*) pairs. The Gibbs energy of a binary solution is presented as:

$$G = n_m G^o_m + n_n G^o_n - T\Delta S^{config} + (n_{mn}/2)\Delta g_{mn} \tag{11.6}$$

where n_i and n_{mn} are the number of moles of *i* atoms and (*m*-*n*) pairs, respectively. ΔS^{config} is the configurational entropy of mixing given as:

$$\Delta S^{config} = -R\left(n_m \ln x_m + n_n \ln x_n\right) - R\left[n_{mm} \ln\left(\frac{x_{mm}}{Y_m^2}\right) + n_{nn} \ln\left(\frac{x_{nn}}{Y_n^2}\right) + n_{mn} \ln\left(\frac{x_{mn}}{2Y_m Y_n}\right)\right] \tag{11.7}$$

where x_i is the mole fraction of *i* atoms, x_{mn} and Y_m are the pair fraction and the coordination equivalent fraction, respectively.

The excess Gibbs energy, Δg_{mn}, is expanded as a polynomial in terms of pair fractions and is given as:

$$\Delta g_{mn} = \Delta g_{mn}^0 + \sum_{i\geq 1} g_{mn}^{i0} (x_{mm})^i + \sum_{j\geq 1} g_{mn}^{0j} (x_{nn})^j \tag{11.8}$$

where Δg_{mn}^0, g_{mn}^{i0}, and g_{mn}^{0j} are the model parameters which can be a function of temperature. The coordination number of component *m*, Z_m, is related to the number of atoms and the number of pairs by: $Z_m n_m = 2n_{mm} + \sum_{n\neq m} n_{mn}$. With the introduction of composition dependent coordination numbers, one can independently choose the composition of maximum short range ordering in each binary subsystem,

$$\frac{1}{Z_m} = \frac{1}{2n_{mm} + \sum_{i\neq m} n_{mi}} \left(\frac{2n_{mm}}{Z_{mm}^m} + \sum_{i\neq m} \frac{n_{mi}}{Z_{mi}^m}\right) \tag{11.9}$$

where Z_{mi}^m is the value of Z_m when all the nearest neighbors of atoms *m* are atoms *i*. The ratio of Z_{mn}^m / Z_{nm}^n determines the maximum short range ordering in each binary subsystem. Symmetric or asymmetric extrapolation technique [40, 41] can be utilized to predict the thermodynamic properties of a ternary system from the binary model parameters depending on the nature of each ternary system. It is also possible to introduce ternary model parameters to better reproduce the experimental data if necessary. The details about ternary extrapolation of MQM and ternary parameters can be found elsewhere [40, 41].

11.3.3 Solid phases

11.3.3.1 Solid solution phases: fcc_A1, bcc_A2, hcp_A3, and diamond_A4

The Bragg-Williams random mixing model in the form of Redlich-Kister (R-K) polynomial [42] is applied to describe the molar Gibbs energies of the bcc_A2, fcc_A1, hcp_A3, and diamond_A4 phases:

$$ {}^{o}G_m^{\phi} = \sum_{i=1}^{3} x_i {}^{o}G_i^{\phi} + RT\sum_{i=1}^{3} x_i \ln x_i + \sum_{i=1}^{3}\sum_{j>i}^{3} x_i x_j L_{ij}^{\phi} + \sum_{i=1}^{3}\sum_{j>i}^{3}\sum_{k>j}^{3} x_i x_j x_k L_{ijk}^{\phi} + \Delta G^{mag} \qquad (11.10) $$

where x_i is the mole fraction of element *i*, ${}^{o}G_i^{\phi}$ is the molar Gibbs energy of pure element *i* with the ϕ state, *R* is gas constant, *T* is temperature in Kelvin, L_{ij}^{ϕ} is the binary interaction parameter, L_{ijk}^{ϕ} is the ternary interaction parameter, and ΔG^{mag} is the magnetic contribution term. Further, L_{ij}^{ϕ} is expanded in the form of $\sum_{v=0} L_{ij}^{v}(x_i - x_j)^v$ and L_{ijk}^{ϕ} is written as $x_i L_{ijk}^{i} + x_j L_{ijk}^{j} + x_k L_{ijk}^{k}$.

The magnetic contribution term ΔG^{mag} which given by the Hillert-Jarl-Inden model [43] is presented as:

$$ \Delta G^{mag} = RT\ln(\beta^{\varphi} + 1)g(\tau^{\varphi}) \qquad (11.11) $$

where τ is given by T/T^{*} (T^{*} is the critical temperature for magnetic transition.). β is the average magnetic moment per mole of atom expressed in Bohr magnetons. $g(\tau^{\varphi})$ is a polynomial function derived by Hillert and Jarl [43].

11.3.3.2 bcc_B2 phase

The Gibbs energy of the ordered bcc_B2 phase is described using a two sub-lattice model with equal number of sites: (Fe, Si, M)$_{0.5}$(Fe, Si, M)$_{0.5}$, where M = Cr and Mg for the Fe-Si-Cr and Fe-Si-Mg systems, respectively. The Gibbs energy of the bcc phase is expressed as:

$$G_m = G_m^{ord}(y_i^{'}, y_i^{''}) + G_m^{dis}(x_i) - G_m^{ord}(x_i, x_i) \tag{11.12}$$

where $y_i^{'}$ and $y_i^{''}$ are the site fractions. $G_m^{dis}(x_i)$ is the disordered part of the Gibbs energy in the form of Eq. (11.10). $G_m^{ord}(y_i^{'}, y_i^{''})$ is the Gibbs energy described using a two sub-lattice model: (Fe, Si, M)$_{0.5}$(Fe, Si, M)$_{0.5}$.

$$G_m^{ord}(y_i^{'}, y_i^{''}) = \sum_{i=1}\sum_{j=1} y_i^{'} y_j^{''} G_{ij}^{ord} + \frac{1}{2}\sum_{i=1}\sum_{j=1} RT y_j^i \ln(y_j^i)$$

$$+ \sum_{i=1}\sum_{j>i}\sum_{k=1} y_i^{'} y_j^{'} y_k^{''} \sum_{v=0} (y_i^{'} - y_j^{'})^v L_{ij:k}^v + \sum_{i=1}\sum_{j>i}\sum_{k=1} y_k^{'} y_i^{''} y_j^{''} \sum_{v=0} (y_i^{''} - y_j^{''})^v L_{k:ij}^v \tag{11.13}$$

and $G_m^{ord}(x_i, x_i)$ is the value of $G_m^{ord}(y_i^{'}, y_i^{''})$ when $y_i^{'} = x_i$ and $y_i^{''} = x_i$ which means the alloys is completely disordered.

11.3.3.3 Other solid solution phases

The well-known Compound Energy Formulism [44] is utilized for the description of all the other solid phases. There is no binary phase with apparent ternary extension in the Fe-Si-Mg system. In the Fe-Si-Cr system, the FeSi and CrSi compounds form a continuous solid solution with a simple sub-lattice model: (Fe, Cr)Si. Consider the fact that the Fe_5Si_3 phase has considerable Cr solubility and the Cr_5Si_3 phase has considerable Fe solubility, sub-lattice model: (**Fe**, Cr)$_5$Si$_3$ and (**Cr**, Fe)$_5$Si$_3$ are utilized, respectively, for the Fe_5Si_3 and Cr_5Si_3 phases. Si is introduced in the second sub-lattice of the σ phase in the Fe-Cr binary system to describe its considerable ternary extension and the model becomes (Fe)$_8$(Fe, Cr, Si)$_{18}$(Cr)$_4$. The Gibbs energy of the σ phase, for example, is expressed as:

$$ {}^{o}G_{m}^{\sigma} = \sum_{i=1} y_i^{''}\, {}^{o}G_{Fe:i:Cr}^{\sigma} + RT\sum_{i=1} y_i^{''} \ln y_i^{''} + \sum_{i=1}\sum_{j>i} y_i^{''} y_j^{''} L_{Fe:ij:Cr}^{\sigma} \quad (11.14) $$

where ${}^{o}G_{Fe:i:Cr}^{\sigma}$ is the Gibbs energy of the end member $Fe_8i_{18}Cr_4$, $y_i^{''}$ is the site fraction of *i* in the second sub-lattice, and $L_{Fe:ij:Cr}^{\sigma}$ is the interaction parameter as a function of composition and temperature. ${}^{o}G_{Fe:i:Cr}^{\sigma}$ and $L_{Fe:ij:Cr}^{\sigma}$ are the model parameters.

11.4 Results and discussions

The optimization of the Fe-Si-Cr and Fe-Si-Mg systems were carried out on the basis of the critically evaluated experimental data. All the thermodynamic calculations are conducted by the FactSage software [45]. The binary descriptions of the Fe-Si system by Cui and Jung [7], the Fe-Cr system revised by Cui and Jung [46], the Cr-Si system by Cui and Jung [47], the Mg-Si system by Harvey [48], and the Fe-Mg system by Chartrand [49] were accepted to model the ternary systems in this study. The calculated phase diagrams for the Fe-Si, Fe-Cr, Cr-Si, Mg-Si, and Fe-Mg systems are shown in Fig. 11.1. It should be noted that there are two assessments of the Fe-Si system done by the present authors [7]. In the first assessment, the ordered and disordered solution phases (bcc_A2, bcc_B2, and D03) were considered with the liquid phase described by the Bragg-Williams random mixing model. In the second version of assessment, the liquid phase was described using MQM, the bcc_A2 and bcc_B2 solutions without the D03 phase were considered. This is due to the incapability of FactSage to handle the four sub-lattice solution model for order-disorder transition using CEF. In this study, the second version was adopted due to MQM description for the liquid solution. The finally optimized thermodynamic parameters for the ternary Fe-Si-Cr and Fe-Si-Mg systems are presented in Table 11.1 and Table 11.2, respectively. The optimization results are presented below along with the experimental data.

11.4.1 The Fe-Si-Cr system

While there are extensive solid solutions in the ternary system, no thermodynamic data related to the solid phases have been determined. Therefore, the Gibbs energy of the liquid phase

was firstly modeled based on the available thermodynamic data. Then the full optimization of the entire system was carried out based on the phase diagram data. The Kohler type of extrapolation technique was found to give a better prediction of the enthalpy of mixing data before adding any ternary parameters. One small ternary parameter with temperature dependence was introduced to give a better representation of the liquid enthalpy data. The calculated enthalpy of mixing of the liquid phase is presented in Fig. 11.2 together with the measured experimental data from Igushev et al. [25]. The calculated enthalpy of mixing from the previous assessment by Miettinen [15] is also appended for comparison. Figs. 11.2(a) to (d) are the enthalpy of mixing of the liquid Fe-Si-Cr alloys along the sections with constant Fe/Cr atomic ratio of 4.55, 1.86, 0.93, and 0.46, respectively. It can be seen from these figures that the present optimization can reproduce the enthalpy of mixing data in a wide range of composition, and better than the results from the previous assessment [15].

The calculated isothermal section at 700 °C is compared with the recent experimental data measured by Li et al. [24] in Fig. 11.3(a). According to Li et al. [24], the D03 ordered phase has a large stability range. However, the D03 phase is not considered in the current optimization, instead the bcc_B2 phase is considered in the region of the D03 phase. They reported that the (Fe, Cr)Si phase did not form a continuous solid solution in the CrSi rich region but formed a $CrSi_2$ + (Fe, Cr)Si + Cr_5Si_3 three phase equilibrium. This result is hard to believe because CrSi is a stable compound in the Cr-Si system as shown in Fig. 11.1(e). Therefore, this three phase equilibrium is neglected in the present optimization. The calculated σ phase region is smaller than the experimental data, but consider the σ phase region at 900 °C and 947 °C (see Figs. 11.3(b) and (c)), this σ phase region at 700 °C seems too large. The high temperature phase relation at 900, 947, and 1047 °C are similar to that at 700 °C as can be seen from Figs. 11.3(b) to (d). The phase equilibrium at 900 °C by Gladyshevskii and Borusevich [18] are well reproduced in the present study. The result by Awais and Hayes [21, 22] are also reasonably reproduced.

The liquidus projection for the Fe-Si-Cr system is shown in Fig. 11.4. The calculated result from the assessment by Lindholm [14] is also appended in Fig. 11.4 as dotted lines. The bcc and (Fe, Si)Cr primary phase regions were very well represented by the present assessment. Yajima [17] did not distinguish the Fe_5Si_3 and Cr_5Si_3 phases, but the current calculation indicates that these

data should be related to the primary phase region of the Fe_5Si_3 phase. The calculated Cr_3Si primary phase region is larger than that measured by Yajima [17]. On the other hand, the primary phase region of the σ phase is noticeably smaller than the measured one.

In the present optimization, the ordered bcc_B2 solution parameters were optimized to reproduce the homogeneity range of the solution. The thermodynamic parameters for the bcc_B2 Fe-Cr phase were taken from the previously assessment by Lindholm [14], and the binary Cr-Si parameters were optimized in this study to reproduce phase diagram. In the case of bcc_A2, all the binary parameters were taken from each binary system, and ternary parameters were introduced to reproduce the homogeneity range of the bcc phase. The complete line solution of (Cr, Fe)Si was treated as an ideal solution. The α_Cr_5Si_3 solution with Fe_5Si_3 solubility was modeled as $(Cr, Fe)_5Si_3$, and the end member Gibbs energy of Fe_5Si_3 and one interaction parameter was optimized to reproduce the ternary extension. On the other hand, β_Cr_5Si_3 was treated as a binary Cr-Si solution because there is no experimental data showing the ternary extension. The ternary extension of the Fe_5Si_3 phase was treated as $(Fe, Cr)_5Si_3$ and the end member Gibbs energy of Cr_5Si_3 was optimized without any interaction parameter to reproduce the experimental data. To reproduce the small solubility of Fe in the Cr_3Si solution, the end member Gibbs energy of Fe_3Cr was taken from the assessment by Lindholm [14]. And the Gibbs energy of Fe_3Si and one positive interaction parameter were optimized. For the σ phase, the end member Gibbs energy of $Fe_8Cr_4Si_{18}$ and two interaction parameters were optimized to reproduce the solubility. Overall, the optimization results in this study are much improved than the previous results by Lindholm [14]. However, there is a certain room to be further improved. In particular, the thermodynamic description of the σ phase can be improved in the future by considering a more complex sub-lattice model.

11.4.2 The Fe-Si-Mg system

The ternary extension of the Fe_5Si_3 phase was not considered in the current optimization, since it dissolves less than 1 at.% Mg. The Toop-type of extrapolation technique was applied for the liquid phase with Si as asymmetric component due to a large miscibility gap in the Mg-Fe

liquid. One ternary parameter is optimized to adjust the extension of the binary miscibility gap to the ternary system. No ternary compound was considered in this study, as shown in the experiment.

The calculated liquid miscibility gap is presented in Figs. 11.5(a) and (b). The calculated miscibility gap for the liquid phase at 1600 °C is presented in Fig. 11.5(a) and agrees well with the measured one from Ageev and Archugov [34]. The calculated isothermal section at 1454 °C is shown in Fig. 11.5(b) in comparison with the measured phase equilibria data from Guichelaar et al. [33]. The calculated miscibility gap can give an accurate reproduction of the experimental data. Fig. 11.5(c) to Fig. 11.5(e) are the calculated isothermal sections of the Fe-Mg-Si system at 1000, 800, and 727 °C, respectively, with the experimental data from Löffler et al. [36] and Pierre et al. [35]. At 1000 °C, the calculated Liquid + FeSi + Fe_3Si_7 three phase equilibrium triangle show acceptable result compared to the experimental data. At 800 °C, the Mg_2Si phase already becomes stable. The calculated phase equilibria agree with the measured data. This is also true for the isothermal section at 727 °C. As the solubility of the third element in the binary compound is very low, the phase relation is actually determined by the stability of the binary compounds.

The calculated activity of Mg along the section with Mg/Fe ratio of 0.165 at 1350 °C is presented in Fig. 11.6, and shows a reasonable agreement with the experimental data by Lepinskikh et al. [38]. The calculated solubilities of Fe in the liquid Mg-Si alloy at 670, 710, and 750 °C are presented in Fig. 11.7. The experimental data from Normann et al. [37] are also appended for comparison. According to the experiments, the Fe solubility in pure Mg changes significantly with temperature. However, the solubility is nearly constant with temperature when Si content in the liquid Mg is 0.4 to 0.8 at.%. This result is rather strange. The present study can well reproduce the Fe solubility in the pure liquid Mg but not in the Mg-Si alloys.

The calculated liquidus projection of the Fe-Mg-Si system is presented in Fig. 11.8 together with the experimental data measured by Zwicker [32]. The primary phase regions of FeSi and Fe_3Si_7 are reasonably reproduced. The enlarged diagram in the Mg rich part is presented in Fig. 11.9. In general, the accuracy of the present modeling result are as good as the previous assessment by Du et al. [31]. However, Du et al. [31] needed three ternary parameters for the liquid phase, while the present study need only one small ternary parameter for liquid.

11.5 Conclusion

A comprehensive evaluation and optimization of all the thermodynamic and phase diagram information for the Fe-Si-Cr and Fe-Si-Mg systems was performed. The Modified Quasi-chemical Model was applied to describe the thermodynamic properties of the liquid phase. The solid solution phases were described using the compound energy formalism. A comparison between the calculated and measured thermodynamic and phase diagram information indicates that the currently obtained thermodynamic descriptions of the Fe-Si-Cr and Fe-Si-Mg systems are reliable. The phase diagram or thermodynamic properties in any section of these ternary systems can be calculated from the present model parameters with the Gibbs energy minimization routine.

Acknowledgement

The authors would like to thank the financial support from NSERC-Automotive Partnership Canada program in Canada. Senlin Cui would also like to thank the McGill Engineering Doctorate Award (MEDA) from McGill University for financial support.

References

1. Shin, S., R. Schafer, and B.C. De Cooman, *Three-dimensional visualization of the magnetic microstructure in bulk Fe-6.6 pct Si.* Metall. Mater. Trans. A, 2013. **44**(9): p. 4239-4247.
2. Chen, S.F., H.Y. Chang, S.J. Wang, S.H. Chen, and C.C. Chen, *Enhanced electromagnetic properties of Fe-Cr-Si alloy powders by sodium silicate treatment.* J. Alloys Compd., 2015. **637**: p. 30-35.
3. Isobe, K., *Effect of Mg addition on solidification structure of low carbon steel.* ISIJ Int., 2010. **50**(12): p. 1972-1980.
4. Kimura, K., S. Fukumoto, G.-i. Shigesato, and A. Takahashi, *Effect of Mg addition on equiaxed grain formation in ferritic stainless steel.* ISIJ Int., 2013. **53**(12): p. 2167-2175.

5. Zhu, K., J. Yang, R.-z. Wang, and Z.-g. Yang, *Effect of Mg addition on inhibiting austenite grain growth in heat affected zones of Ti-bearing low carbon steels.* J. Iron Steel Res. Int., 2011. **18**(9): p. 60-64.
6. Wilson, R.K., *Effect of calcium and magnesium treatment on steel weldability.* Weld. Res. (Miami), 1982(June): p. 182s-188s.
7. Cui, S. and I.-H. Jung, *Critical reassessment of the Fe-Si system.* submitted to CALPHAD.
8. Lacaze, J. and B. Sundman, *An assessment of the iron-carbon-silicon system*. Metall. Trans. A, 1991. **22**A(10): p. 2211-23.
9. Raghavan, V., *The Fe-Cr-Si system.* Phase Diagram of Ternary Iron Alloys: Part 1, 1987: p. 171-182.
10. Raghavan, V., *Cr-Fe-Si (chromium-iron-silicon).* J. Phase Equilib. Diffus., 2004. **25**(6): p. 545-546.
11. Raghavan, V., *Cr-Fe-Si (chromium-iron-silicon).* J. Phase Equilib., 2003. **24**(3): p. 265-266.
12. Raghavan, V., *Cr-Fe-Si (chromium-iron-silicon).* J. Phase Equilib., 1993. **14**(5): p. 626-8.
13. Chart, T., F. Putland, and A. Dinsdale, *Calculated phase equilibriums for the chromium-iron-nickel-silicon system. I. Ternary equilibriums.* CALPHAD Comput. Coupling Phase Diagrams Thermochem., 1980. **4**(1): p. 27-46.
14. Lindholm, M., *A thermodynamic description of the Fe-Cr-Si system with emphasis on the equilibria of the sigma (σ) phase.* J. Phase Equilib., 1997. **18**(5): p. 432-440.
15. Miettinen, J., *Thermodynamic description of solution phases of systems Fe-Cr-Si and Fe-Ni-Si with low silicon contents and with application to stainless steels.* CALPHAD Comput. Coupling Phase Diagrams Thermochem., 1999. **23**(2): p. 249-262.
16. Anderson, A.G.H. and E.R. Jette, *X-ray investigation of the iron-chromium-silicon phase diagram.* Trans. Am. Soc. Met., 1936. **24**: p. 375-418.
17. Yajima, E., *The Equilibrium Diagram of the Fe-Cr-Si System.* Nippon Kinzoku Gakkai-Si, 1941. **5**(12): p. 455-461.
18. Gladyshevskii, E.I. and L.K. Borusevich, *Cr-Fe-Si ternary system.* Izv. Akad. Nauk SSSR, Met., 1966(1): p. 159-64.

19. Yamaguchi, M., Y. Ymakoshi, and G. Mima, *Miscibility gap in iron-chromium-metal (X = copper, manganese, molybdenum, nickel, vanadium, silicon, and aluminum) system.* Proc. Int. Conf. Sci. Technol. Iron Steel, 1971. **Pt. 2**: p. 1015-19.
20. Wethmar, J.C.M., D.D. Howat, P.R. Jochens, and O.A.W. Strydom, *Liquidus temperatures in the chromium-iron-silicon system in the composition range representative of ferrochromium-silicide produced in South Africa.* J. S. Afr. Inst. Mining Met., 1973. **73**(6): p. 181-3.
21. Awais, H.B. and F.H. Hayes, *Phase relations in Fe-Cr-Si system.* Phase Transform.--96, Proc. Int. Conf., 1st, 1996: p. 62-66.
22. bin Awais, H., *Phase relations in the Fe-Fe_5Si_3-Cr_3Si-Cr region of the Fe-Cr-Si system* Thesis, UMIST, Manchester, UK 1995, 1995.
23. Yamamoto, K., Y. Kimura, and Y. Mishima, *Phase constitution and microstructure of the Fe-Si-Cr ternary ferritic alloys.* Scr. Mater., 2004. **50**(7): p. 977-981.
24. Li, Z., Z. Zhou, X. Wang, Y. Liu, Y. Wu, M. Zhao, and F. Yin, *Experimental study of the phase relations in the Fe-Cr-Si ternary system at 700 °C.* Int. J. Mater. Res., 2014. **105**(9): p. 840-846.
25. Igushev, V.F., N.V. Tolstoguzov, and V.A. Rudenko, *Enthalpies of iron-chromium-silicon molten alloys.* Izv. Vyssh. Uchebn. Zaved., Chern. Metall., 1975(6): p. 46-50.
26. Petrushevskii, M.S., P.V. Gel'd, and Y.O. Esin, *Calculation of enthalpies of formation of molten iron-chromium-silicon alloys.* Izv. Vyssh. Uchebn. Zaved., Chern. Metall., 1978(6): p. 5-8.
27. Raghavan, V., *The Fe-Mg-Si (Iron-Magnesium-Silicon).* Phase Diagrams of Ternary Iron Alloys. Part 6B, Indian Institute of Metals, Calcutta,, 1992: p. 942-947.
28. Raghavan, V., *Fe-Mg-Si (iron-magnesium-silicon).* J. Phase Equilib., 2002. **23**(2): p. 175-176.
29. Raghavan, V., *Fe-Mg-Si (iron-magnesium-silicon).* J. Phase Equilib. Diffus., 2012. **33**(3): p. 236-237.
30. Lebrun, N., C. Baetzner, A. Stamou, J. Robinson, and L. Rokhlin, *Iron-Magnesium-Silicon.* Landolt-Börnstein New Series IV/11D4, 2008: p. 1-17.
31. Du, Y., J.R. Zhao, C. Zhang, H.L. Chen, and L.J. Zhang, *Thermodynamic modeling of the Fe-Mg-Si system.* J. Min. Metall., Sect. B, 2007. **43**(1): p. 39-56.

32. Zwicker, U., *Reactions of magnesium alloys with molten cast iron.* Z. Metallkd., 1954. **45**: p. 31-5.
33. Guichelaar, P.J., P.K. Trojan, T. McCluhan, and R.A. Flinn, *New technique for vapor pressure measurement applied to the iron-silicon-magnesium system.* Met. Trans., 1971. **2**(12): p. 3305-13.
34. Ageev, Y.A. and S.A. Archugov, *Solubility of magnesium in molten iron and some iron-base binary alloys.* Izv. Akad. Nauk SSSR, Met., 1984(3): p. 78-80.
35. Pierre, D., M. Peronnet, F. Bosselet, J.C. Viala, and J. Bouix, *Solid-liquid phase equilibria at 727 °C in the ternary system Fe-Mg-Si.* J. Phase Equilib., 2000. **21**(1): p. 78-86.
36. Löffler, F., G. Sauthoff, and M. Palm, *Phase equilibria in the Fe-Mg-Si system.* Int. J. Mater. Res., 2011. **102**(8): p. 1042-1047.
37. Normann, H.H., H. Thoresen, J.E. Tibballs, and C.J. Simensen, *Impurities and Mg - Base Phase Diagrams.* Proc. Conf. on Light Metals, Amsterdam, Netherlands, 1990: p. 823.
38. Lepinskikh, B.M., I.T. Sryvalin, and A.A. Tikhomirov, *Thermodynamic properties of Fe-Si-Mg melts.* Zh. Fiz. Khim., 1966. **40**(7): p. 1551-5.
39. Dinsdale, A.T., *SGTE data for pure elements.* CALPHAD Comput. Coupling Phase Diagrams Thermochem., 1991. **15**(4): p. 317-425.
40. Pelton, A.D. and P. Chartrand, *The modified quasi-chemical model: Part II. Multicomponent solutions.* Metall. Mater. Trans. A, 2001. **32A**(6): p. 1355-1360.
41. Pelton, A.D., S.A. Degterov, G. Eriksson, C. Robelin, and Y. Dessureault, *The modified quasichemical model I - binary solutions.* Metall. Mater. Trans. B, 2000. **31B**(4): p. 651-659.
42. Redlich, O. and A.T. Kister, *Thermodynamics of nonelectrolytic solutions. Algebraic representation of thermodynamic properties and the classification of solutions.* Ind. Eng. Chem., 1948. **40**: p. 84,5-8.
43. Hillert, M. and M. Jarl, *A model for alloying effects in ferromagnetic metals.* CALPHAD Comput. Coupling Phase Diagrams Thermochem., 1978. **2**(3): p. 227-38.
44. Hillert, M., *The compound energy formalism.* J. Alloys Compd., 2001. **320**(2): p. 161-176.
45. Bale, C.W., P. Chartrand, S.A. Degterov, G. Eriksson, K. Hack, R. Ben Mahfoud, J. Melancon, A.D. Pelton, and S. Petersen, *FactSage thermochemical software and databases.* CALPHAD Comput. Coupling Phase Diagrams Thermochem., 2002. **26**(2): p. 189-228.

46. Cui, S. and I.-H. Jung, *Thermodynamic modeling of Cu-Fe-Cr and Cu-Fe-Mn systems.* to be submited.
47. Cui, S. and I.-H. Jung, *Thermodynamic assessment of the Cr-Si and Al-Cr-Si systems.* to be submited.
48. Harvey, J.-P., *M.A.Sc. thesis. Ecole Polytechnique*, 2006.
49. Chartrand, P., *Thermodynamic assessment of the Fe-Mg system.* unpublished work.
50. Andersson, J.O. and B. Sundman, *Thermodynamic properties of the chromium-iron system.* CALPHAD Comput. Coupling Phase Diagrams Thermochem., 1987. **11**(1): p. 83-92.
51. Liang, Y., C. Guo, C. Li, and Z. Du, *A Thermodynamic Description of the Al-Cr-Si System.* J. Phase Equilib. Diffus., 2009. **30**(5): p. 462-479.
52. Chen, H., Y. Du, and J.C. Schuster, *On the melting of Cr_5Si_3 and update of the thermodynamic description of Cr-Si.* CALPHAD Comput. Coupling Phase Diagrams Thermochem., 2009. **33**(1): p. 211-214.
53. Lee, B.J., *Revision of thermodynamic descriptions of the iron-chromium and iron-nickel liquid phases.* CALPHAD Comput. Coupling Phase Diagrams Thermochem., 1993. **17**(3): p. 251-68.
54. Chartrand, P., *Thermodynamic assessment of the Al-Mg system.* unpublished work.

Table captions

Table 11.1 Summary of the optimized model parameters for the Fe-Si-Cr system (J mol^{-1} or J mol^{-1} K^{-1}).

Table 11.2 Summary of the optimized model parameters for the Fe-Si-Mg system (J mol^{-1} or J mol^{-1} K^{-1}).

Figure captions

Fig. 11.1 Calculated phase diagram of (a) the Fe-Si system, (b) the Fe-Cr system, (c) the Fe-Mg system, (d) the Mg-Si system, and (e) the Cr-Si system.

Fig. 11.2 The calculated enthalpy of mixing of the Fe-Si-Cr liquid phase from pure liquid Fe, Cr, and Si along with the experimental data. (a) Fe/Cr atomic ratio of 4.55, (b) Fe/Cr atomic ratio of 1.86, (c) Fe/Cr atomic ratio of 0.93, and (d) Fe/Cr atomic ratio of 0.46.

Fig. 11.3 The calculated isothermal sections of the Fe-Si-Cr system along with the experimental data at different temperatures. (a) 700 °C, (b) 900 °C, (c) 947 °C, and (d) 1047 °C.

Fig. 11.4 The calculated liquidus projection of the Fe-Si-Cr system along with the experimental data.

Fig. 11.5 The calculated isothermal sections of the Fe-Si-Mg system along with the experimental data at different temperatures. (a) 1600 °C, (b) 1454 °C, (c) 1000 °C, (d) 800 °C, and (e) 727 °C.

Fig. 11.6 The calculated activity of Mg with respect to the liquid Mg standard of the Mg/Fe ratio of 0.165 section at 1350 °C along with the experimental data.

Fig. 11.7 The calculated solubilities of Fe and Si in liquid Mg at 670, 710, and 750 °C along with the experimental data.

Fig. 11.8 The calculated liquidus projection of the Fe-Si-Mg system.

Fig. 11.9 Enlarged part of the liquidus projection of the Mg rich Fe-Si-Mg system.

Table 11.1 Summary of the optimized model parameters for the Fe-Si-Cr system (J mol^{-1} or J mol^{-1} K^{-1}).

Phase	Thermodynamic parameters	Ref.
Liquid (Fe, Si, Cr)	$Z_{FeFe}^{Fe} = Z_{CrCr}^{Cr} = Z_{SiSi}^{Si} = Z_{FeCr}^{Fe} = Z_{FeSi}^{Fe} = Z_{CrFe}^{Cr} = Z_{CrSi}^{Cr} = Z_{SiFe}^{Si} = Z_{SiCr}^{Si} = 6$	
	$\Delta g_{Fe,Si} = -33710.49 + 2.26T + (-12552 + 5.02T)x_{FeFe}$ $+ (-8368 + 4.82T)x_{FeFe}^2 + (-3054.32 + 6.49T)x_{SiSi}$	[7]
	$\Delta g_{Cr,Fe} = -242.67 - 0.29T - 205.02x_{FeFe} - (192.46 + 1.05T)x_{CrCr}$	[46]
	$\Delta g_{Cr,Si} = -29288.00 + 4.184T + (-30124.80 + 8.033T)x_{CrCr} + (1799.12 - 1.799T)x_{SiSi}$ $+ 1255.20x_{SiSi}^2$	[47]
	$g_{Fe,Si,(Cr)}^{001} = 23760.94 - 17.78T$	This work
fcc_A1 $(Fe, Si, Cr)_1(Va)_1$	${}^0L_{Fe,Si} = -115254.05 - 2.19T$ ${}^1L_{Fe,Si} = -84776.91 + 44.33T$ ${}^2L_{Fe,Si} = 20007.03$	[7]
	$L_{Fe,Cr} = 10833.00 - 7.48 \cdot T + 1410.00(x_{Cr} - x_{Fe})$	[50]
	${}^0L_{Cr,Si:Va} = 0$	[47]
bcc_A2 $(Fe, Si, Cr)_1(Va)_3$	${}^0L_{Fe,Si} = -154013.56 + 32.29T$ ${}^1L_{Fe,Si} = -63511.47 + 13.25T$ ${}^2L_{Fe,Si} = 35727.58$ ${}^1Tc = 504$	[7]
	$L_{Fe,Cr} = 20500 - 9.68T$	[50]

	$\beta^0 = -0.85$	
	${}^0L_{Cr,Si:Va} = -77728.33 - 2.38T$	[47]
	${}^1L_{Cr,Si:Va} = 53247.56 - 13.59T$	
	${}^0L_{Cr,Fe,Si:Va} = -59914.88 + 4.18T$	This work
	${}^1L_{Cr,Fe,Si:Va} = -66944.00 + 4.18T$	
	${}^2L_{Cr,Fe,Si:Va} = -48701.76 + 8.37T$	
bcc_B2 $(Fe, Si, Cr)_{0.5}(Fe, Si, Cr)_{0.5}(Va)_3$	$\Delta G^{B2}_{Fe:Si} = \Delta G^{B2}_{Si:Fe} = -10464.8\ ;\ \Delta G^{B2}_{Fe:Fe} = \Delta G^{B2}_{Si:Si} = 0$	[7]
	$\Delta G^{B2}_{Fe:Cr} = \Delta G^{B2}_{Cr:Fe} = 1500.00\ ;\ \Delta G^{B2}_{Fe:Fe} = \Delta G^{B2}_{Cr:Cr} = 0$	[14]
	$\Delta G^{B2}_{Cr:Si} = \Delta G^{B2}_{Si:Cr} = -20307.044 + 5.44T$	This work
Diamond_A4 $(Fe, Si, Cr)_1$	${}^oG_{Cr} = 5000 + {}^oG^{bcc}_{Cr}$	[51]
Cr_3Si $(Cr, Fe, Si)_3(Cr, Si)$	${}^oG_{Cr:Cr} = 20000 + 10T + 4{}^oG^{bcc}_{Cr}$	[52]
	${}^oG_{Si:Cr} = 561830.45 - 61.08T + 3{}^oG^{dia}_{Si} + {}^oG^{bcc}_{Cr}$	
	${}^oG_{Si:Si} = 415925.96 - 65.94T + 4{}^oG^{dia}_{Si}$	
	${}^oG_{Cr:Si} = -120883.71 + 2.72T + 3{}^oG^{bcc}_{Cr} + {}^oG^{dia}_{Si}$	[47]
	${}^0L_{Cr,Si:*} = -376560$	
	${}^oG_{Fe:Cr} = 8000 + 3{}^oG^{bcc}_{Fe} + {}^oG^{bcc}_{Cr}$	[14]
	${}^oG_{Fe:Si} = -50479.96 + 3{}^oG^{bcc}_{Fe} + {}^oG^{dia}_{Si}$	This work

	${}^{0}L_{Fe,Cr:Si} = 18368.00$	
β_Cr_5Si_3 $Cr_5(Cr, Si)_3$	${}^{o}G_{Cr:Cr} = 40000 + 8{}^{o}G_{Cr}^{bcc}$ ${}^{o}G_{Cr:Si} = -278741.218 + 1286.49\,T - 220.2616\,T\ln T + 0.0133976\,T^2 - 8.62375\times10^{-6}T^3$ $+1310079.996T^{-1}$ (298.15<T<1900) ${}^{o}G_{Cr:Si} = -444894.574 + 2312.20\,T - 345.244576\,T\ln T$ (1900<T<9000) ${}^{0}L_{Cr:Cr,Si} = -4697.84$	[47]
α_Cr_5Si_3 $(Fe, Cr)_5Si_3$	${}^{o}G_{Cr:Si} = -346143.123 + 1324.31\,T - 220.2616\,T\ln T + 0.0133976\,T^2 - 8.62375\times10^{-6}T^3$ $+1310079.996T^{-1}$ (298.15<T<1900) ${}^{o}G_{Cr:Si} = -512296.479 + 2350.02\,T - 345.244576\,T\ln T$ (1900<T<9000)	[47]
	${}^{o}G_{Fe:Si} = -259408.00 + 41.84T + 5{}^{o}G_{Fe}^{bcc} + 3{}^{o}G_{Si}^{dia}$ ${}^{0}L_{Fe,Cr:Si} = -77973.31 + 66.94T$	This work
CrSi (Cr, Fe)(Si)	${}^{o}G_{Cr:Si} = -83345.088 + 315.458\,T - 51.62865\,T\ln T - 0.00447355\,T^2 + 391330\,T^{-1}$	[47]
	${}^{o}G_{Fe:Si} = -92965.21 + 285.98\,T - 48.57\,T\ln T - 0.00736056\,175T^2 + 214109.996\,7T^{-1}$ $+2.9186\times10^{-7}T^3$	[7]
$CrSi_2$ $(Cr, Si)(Cr, Si)_2$	${}^{o}G_{Cr:Cr} = 219200.00 + 3{}^{o}G_{Cr}^{bcc}$ ${}^{o}G_{Cr:Si} = -107085.92 + 394.42\,T - 65.62604\,T\ln T - 0.01148279\,972T^2$ $-1.77861666\times10^{-9}T^3 + 365453.69752T^{-1}$ ${}^{o}G_{Si:Cr} = 224822.01 - 27.60T + {}^{o}G_{Si}^{dia} + 2{}^{o}G_{Cr}^{bcc}$	[47]

	${}^{o}G_{Si:Si} = 84525.00 - 26.28T + 3{}^{o}G_{Si}^{dia}$ ${}^{0}L_{Cr,Si:*} = 1535.45$	
Fe_5Si_3 $(Fe, Cr)_5Si_3$	${}^{o}G_{Fe:Si} = -293714.15 + 1024.25T - 180.30693T\ln T - 0.04295597\ 15T^2$ $-4.44099\times10^{-8}T^3 + 530360.8T^{-1}$ $\beta = 2.32$, $Tc = 360$, $P = 0.28$	[7]
	${}^{o}G_{Cr:Si}^{0} = -227117.69 + 5{}^{o}G_{Cr}^{bcc} + 3{}^{o}G_{Si}^{dia}$	This work
σ $(Fe)_8(Cr)_4(Fe, Si, Cr)_{18}$	${}^{o}G_{Fe:Cr:Fe}^{\sigma} = 117300 - 95.96T + 8{}^{o}G_{Fe}^{fcc} + 4{}^{o}G_{Cr}^{bcc} + 18{}^{o}G_{Fe}^{bcc}$ ${}^{o}G_{Fe:Cr:Cr}^{\sigma} = 92300 - 95.96T + 8{}^{o}G_{Fe}^{fcc} + 22{}^{o}G_{Cr}^{bcc}$	[53]
	${}^{o}G_{Fe:Si:Cr}^{\sigma} = -1077102.73 + 259.41T + 8{}^{o}G_{Fe}^{bcc} + 4{}^{o}G_{Si}^{dia} + 18{}^{o}G_{Cr}^{bcc}$ ${}^{0}L_{Fe:Cr:Cr,Si} = -2098177.80 + 142.26T$ ${}^{0}L_{Fe,Cr:Fe:Si} = -1998177.94 + 142.26T$	This work
Fe_2Si $(Fe)_2(Si)_1$	${}^{o}G_{Fe:Si} = -53889.7 - 33.02115\ T + 2{}^{o}G_{Fe}^{bcc} + {}^{o}G_{Si}^{dia}$	[7]
$FeSi_2$ $(Fe)_1(Si)_2$	${}^{o}G_{Fe:Si} = -123204.74 + 474.83T - 79.0298507\ 3T\ln T + 0.00907346\ T^2$ $-2.97\times10^{-6}T^3 + 499504.521T^{-1}$	[7]
Fe_3Si_7 $(Fe)_3(Si)_7$	${}^{o}G_{Fe:Si} = -324261.35 + 1272.39T - 214.2176T\ln T - 0.05496356\ 5T^2$ $+3.838905\times10^{-6}T^3 + 1172853.45T^{-1}$	[7]

Table 11.2 Summary of the optimized model parameters for the Fe-Si-Mg system (J mol^{-1} or J mol^{-1} K^{-1}).

Phase	Thermodynamic parameters	Ref.
Liquid (Fe, Si, Mg)	$Z^{Fe}_{FeFe} = Z^{Mg}_{MgMg} = Z^{Si}_{SiSi} = Z^{Fe}_{FeMg} = Z^{Fe}_{FeSi} = Z^{Mg}_{MgFe} = Z^{Si}_{SiFe} = Z^{Si}_{SiMg} = 6\ ;\ Z^{Mg}_{MgSi} = 4$	
	$\Delta g_{Fe,Si} = -33710.49 + 2.26T + (-12552 + 5.02T)x_{FeFe}$ $+ (-8368 + 4.82T)x^2_{FeFe} + (-3054.32 + 6.49T)x_{SiSi}$	[7]
	$\Delta g_{Fe,Mg} = -19794.03 + 1.26T - 2477.69\,x_{FeFe} - 390.60\,x_{MgMg}$	[49]
	$\Delta g_{Mg,Si} = -22670.17 + 6.92T + (3385.38 - 2.594T)x_{MgMg} - 3849.28x_{SiSi}$	[48]
	$g^{001}_{Fe,Si,(Mg)} = 4184.00$	This work
fcc_A1 $(Fe, Si, Mg)_1(Va)_1$	${}^0L_{Fe,Si} = -115254.05 - 2.19T$ ${}^1L_{Fe,Si} = -84776.91 + 44.33T$ ${}^2L_{Fe,Si} = 20007.03$	[7]
	$L_{Fe,Mg} = 69383.98$	This work
	${}^0L_{Mg,Si} = -7148.79 + 0.89T$	[48]
bcc_A2 $(Fe, Si, Mg)_1(Va)_3$	${}^0L_{Fe,Si} = -154013.56 + 32.29T$ ${}^1L_{Fe,Si} = -63511.47 + 13.25T$ ${}^2L_{Fe,Si} = 35727.58$ ${}^1Tc = 504$	[7]
	$L_{Fe,Mg} = 65700.00$	[49]
	${}^0L_{Mg,Si} = -7148.79 + 0.89T$	[48]

bcc_B2 $(Fe, Si, Mg)_{0.5}(Fe, Si, Mg)_{0.5}(Va)_3$	$\Delta G^{B2}_{Fe:Si} = \Delta G^{B2}_{Si:Fe} = -10464.8$; $\Delta G^{B2}_{Fe:Fe} = \Delta G^{B2}_{Si:Si} = 0$	[7]
	$\Delta G^{B2}_{Fe:Mg} = \Delta G^{B2}_{Mg:Fe} = 0$; $\Delta G^{B2}_{Fe:Fe} = \Delta G^{B2}_{Mg:Mg} = 0$	[14]
	$\Delta G^{B2}_{Mg:Si} = \Delta G^{B2}_{Si:Mg} = 0$	This work
Fe_5Si_3 $(Fe)_5(Si)_3$	${}^{o}G_{Fe:Si} = -293714.15 + 1024.25T - 180.30693T\ln T - 0.04295597\ 15T^2$ $-4.44099\times10^{-8}T^3 + 530360.8T^{-1}$ $\beta = 2.32$, $Tc = 360$, $P = 0.28$	[7]
Fe_2Si $(Fe)_2(Si)_1$	${}^{o}G_{Fe:Si} = -53889.7 - 33.02115\ T + 2{}^{o}G^{bcc}_{Fe} + {}^{o}G^{dia}_{Si}$	[7]
$FeSi_2$ $(Fe)_1(Si)_2$	${}^{o}G_{Fe:Si} = -123204.74 + 474.83T - 79.0298507\ 3T\ln T + 0.00907346\ T^2$ $-2.97\times10^{-6}T^3 + 499504.521T^{-1}$	[7]
Fe_3Si_7 $(Fe)_3(Si)_7$	${}^{o}G_{Fe:Si} = -324261.35 + 1272.39T - 214.2176T\ln T - 0.05496356\ 5T^2$ $+3.838905\times10^{-6}T^3 + 1172853.45T^{-1}$	[7]
Mg_2Si $(Mg)_2(Si)$	${}^{o}G_{Mg:Si} = -65100 + 8.04T + 2{}^{o}G^{hcp}_{Mg} + {}^{o}G^{dia}_{Si}$	[54]

Figures

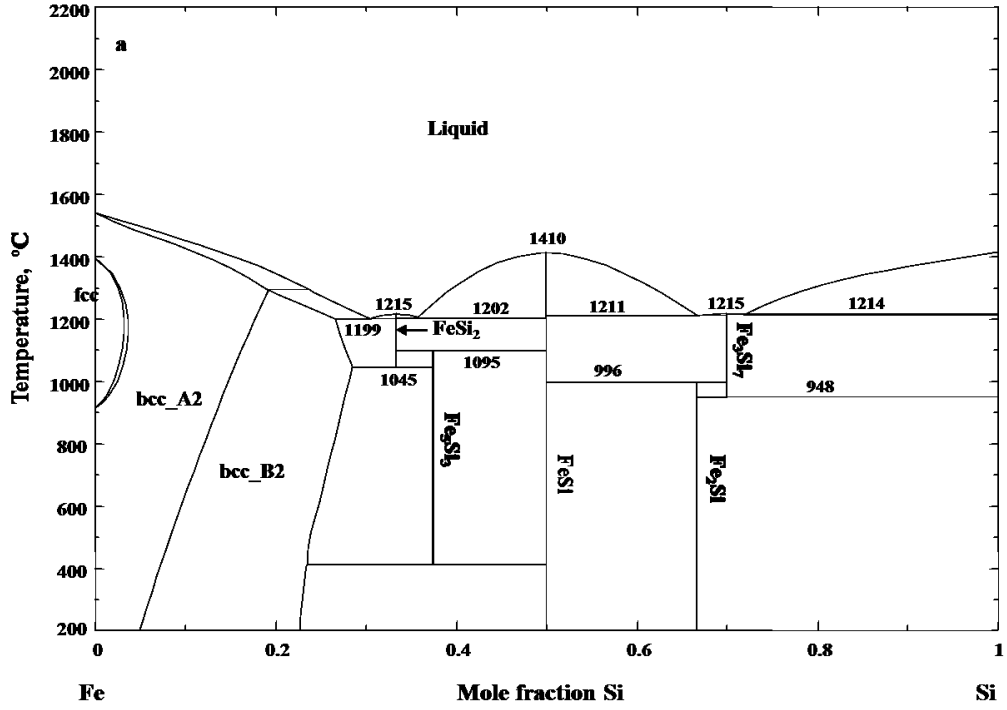
a
Liquid
fcc
bcc_A2
bcc_B2
1410
1215
1202
1211
1215
1214
1199
FeSi2
1095
996
948
1045
Fe5Si3
FeSi
Fe2Si
Fe3Si7
Temperature, °C
Fe
Mole fraction Si
Si

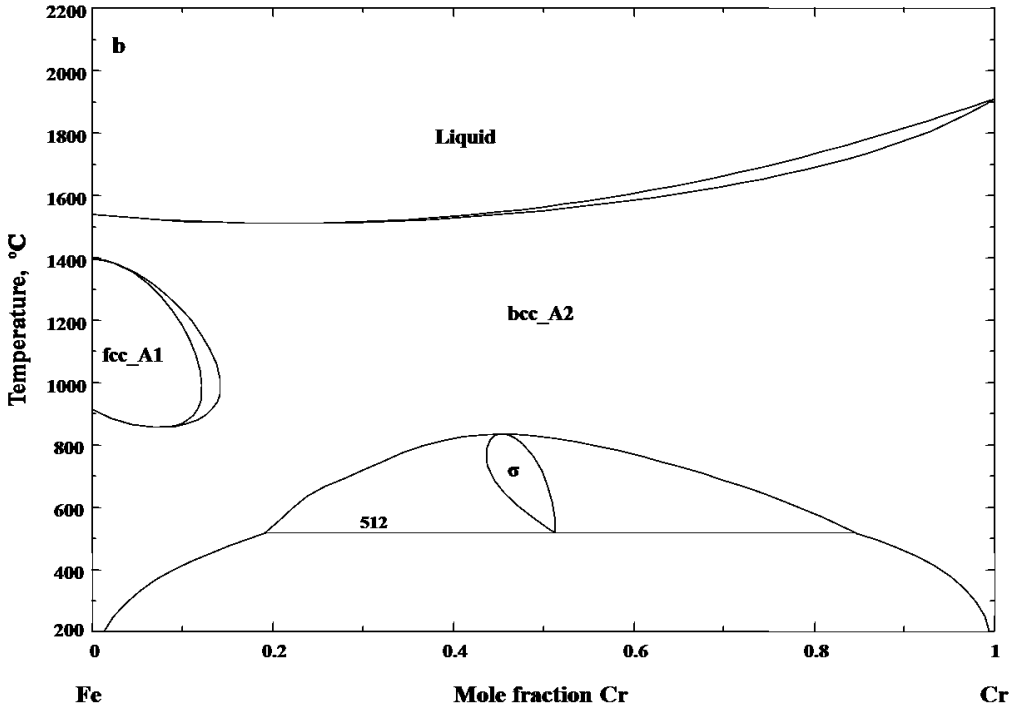
b
Liquid
bcc_A2
fcc_A1
σ
512
Temperature, °C
Fe
Mole fraction Cr
Cr

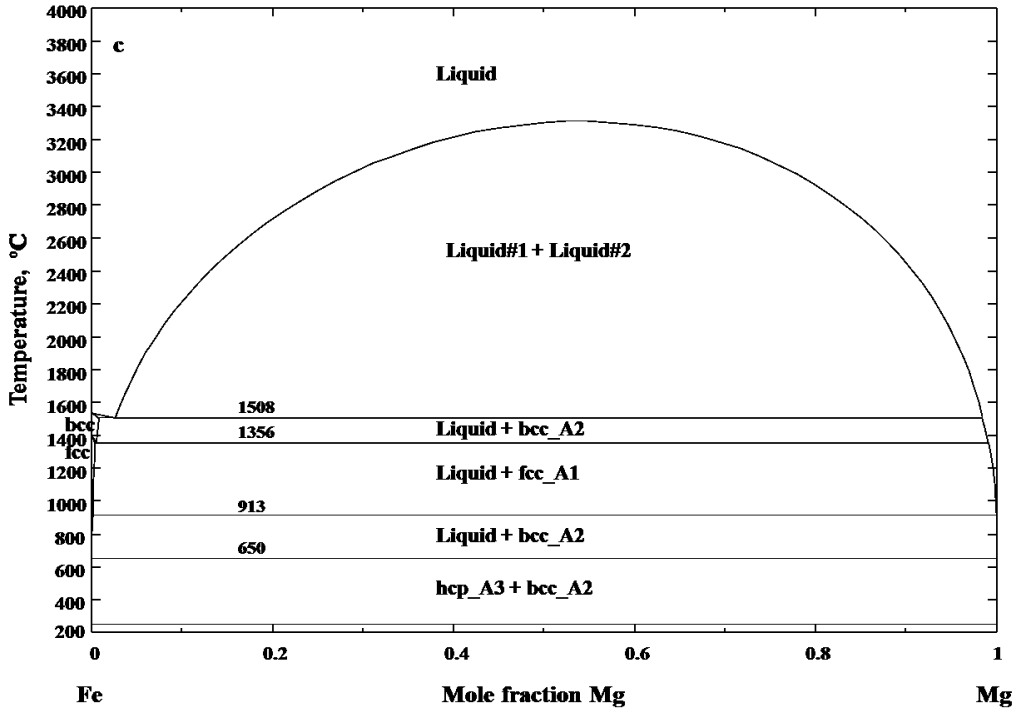
c
Liquid
Liquid#1 + Liquid#2
1508
bcc
1356
Liquid + bcc_A2
fcc
Liquid + fcc_A1
913
Liquid + bcc_A2
650
hcp_A3 + bcc_A2
Temperature, °C
4000
3800
3600
3400
3200
3000
2800
2600
2400
2200
2000
1800
1600
1400
1200
1000
800
600
400
200
0
0.2
0.4
0.6
0.8
1
Fe
Mole fraction Mg
Mg

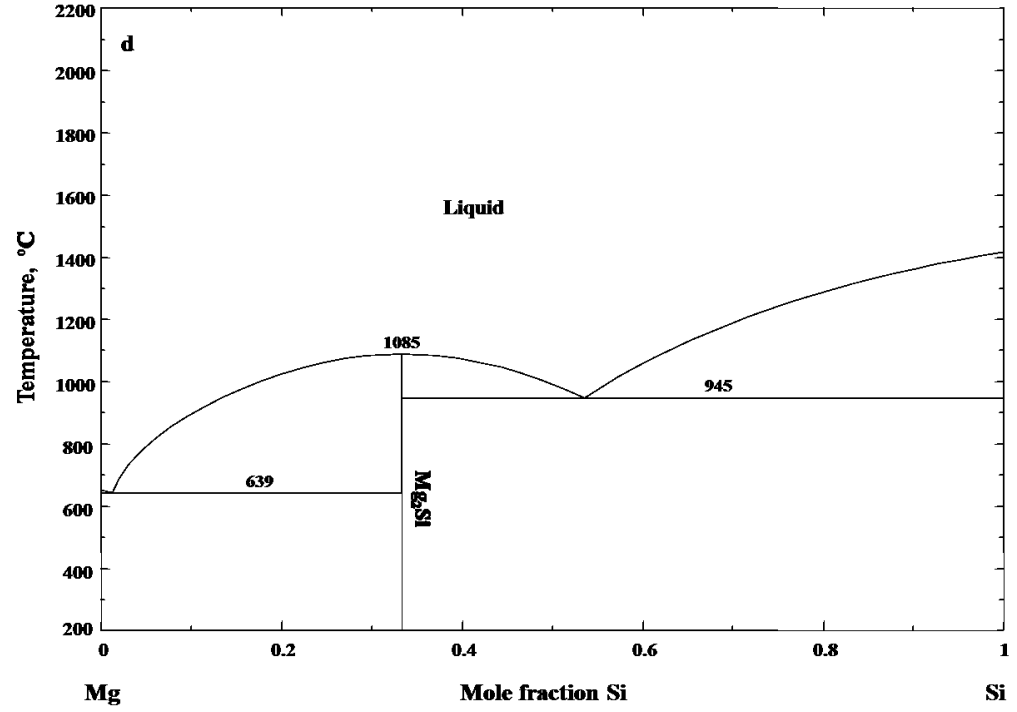
d
Liquid
1085
945
639
Mg2Si
Temperature, °C
2200
2000
1800
1600
1400
1200
1000
800
600
400
200
0
0.2
0.4
0.6
0.8
1
Mg
Mole fraction Si
Si

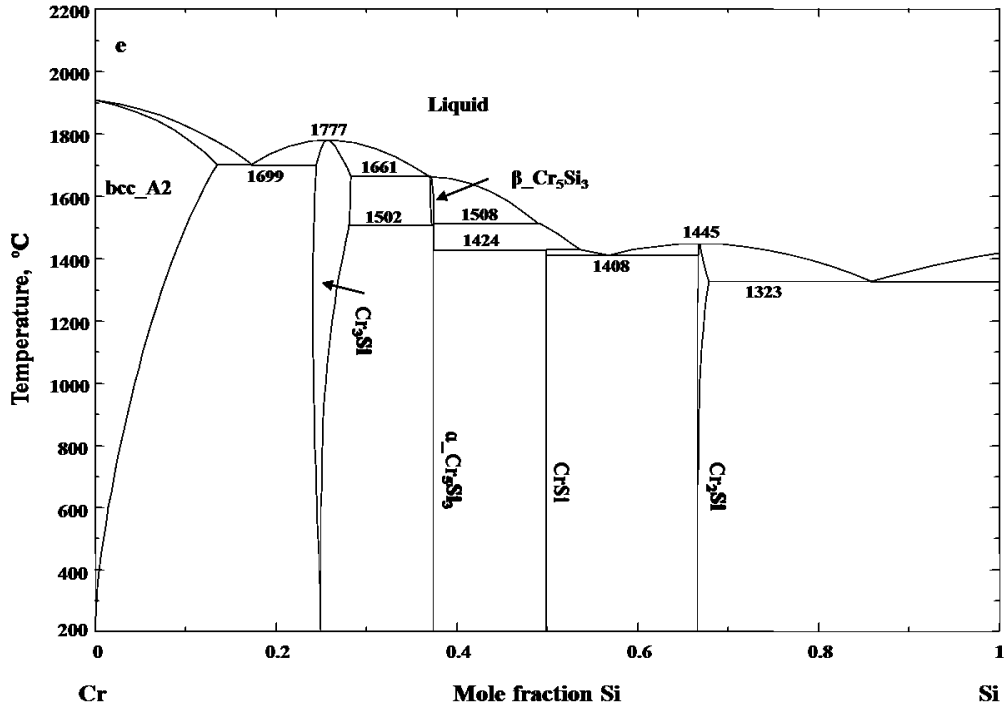

Fig. 11.1 Calculated phase diagram of (a) the Fe-Si system, (b) the Fe-Cr system, (c) the Fe-Mg system, (d) the Mg-Si system, and (e) the Cr-Si system.

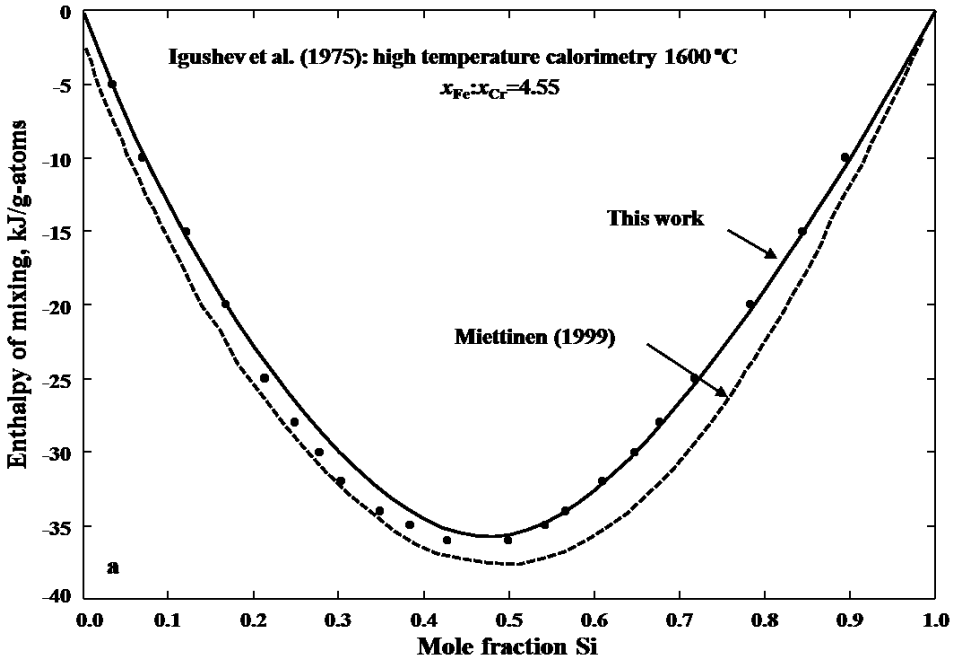
Igushev et al. (1975): high temperature calorimetry 1600 °C
x_{Fe}:x_{Cr}=4.55
This work
Miettinen (1999)
a
Enthalpy of mixing, kJ/g-atoms
Mole fraction Si
0
-5
-10
-15
-20
-25
-30
-35
-40
0.0
0.1
0.2
0.3
0.4
0.5
0.6
0.7
0.8
0.9
1.0

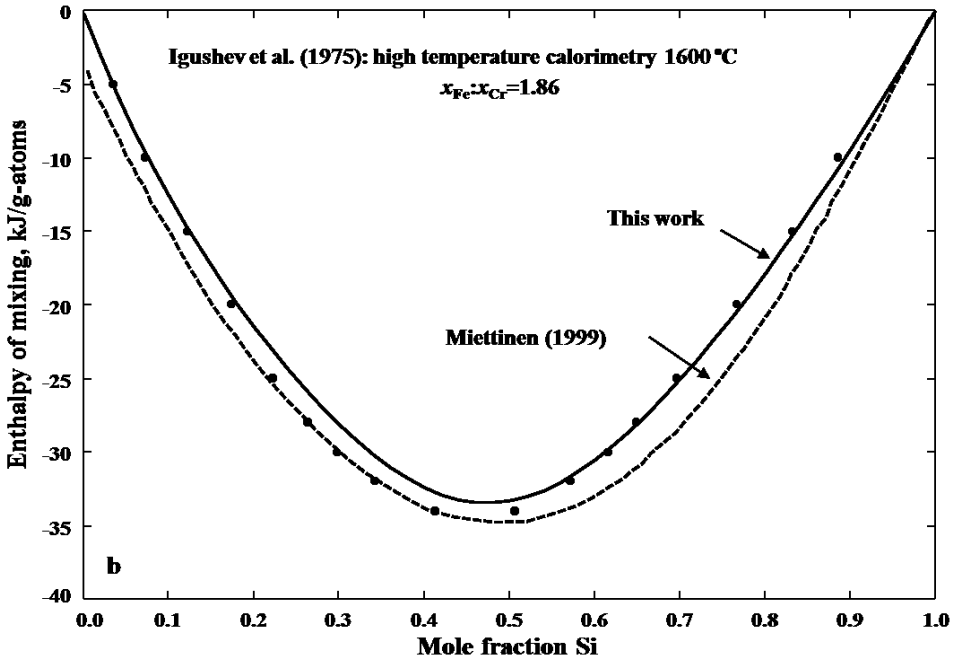
Igushev et al. (1975): high temperature calorimetry 1600 °C
x_{Fe}:x_{Cr}=1.86
This work
Miettinen (1999)
b
Enthalpy of mixing, kJ/g-atoms
Mole fraction Si
0
-5
-10
-15
-20
-25
-30
-35
-40
0.0
0.1
0.2
0.3
0.4
0.5
0.6
0.7
0.8
0.9
1.0

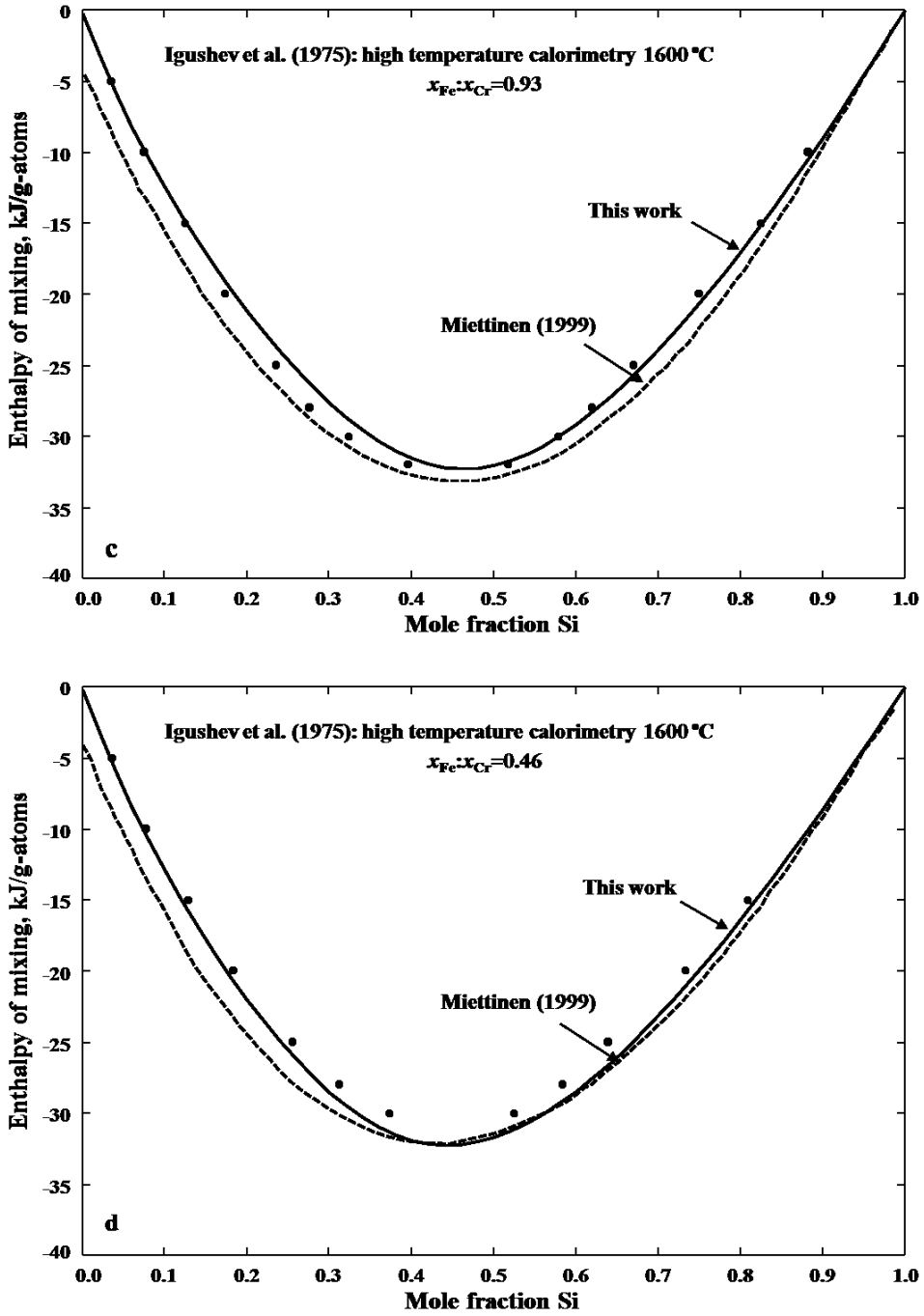

Fig. 11.2 The calculated enthalpy of mixing of the Fe-Si-Cr liquid phase from pure liquid Fe, Cr, and Si along with the experimental data. (a) Fe/Cr atomic ratio of 4.55, (b) Fe/Cr atomic ratio of 1.86, (c) Fe/Cr atomic ratio of 0.93, and (d) Fe/Cr atomic ratio of 0.46.

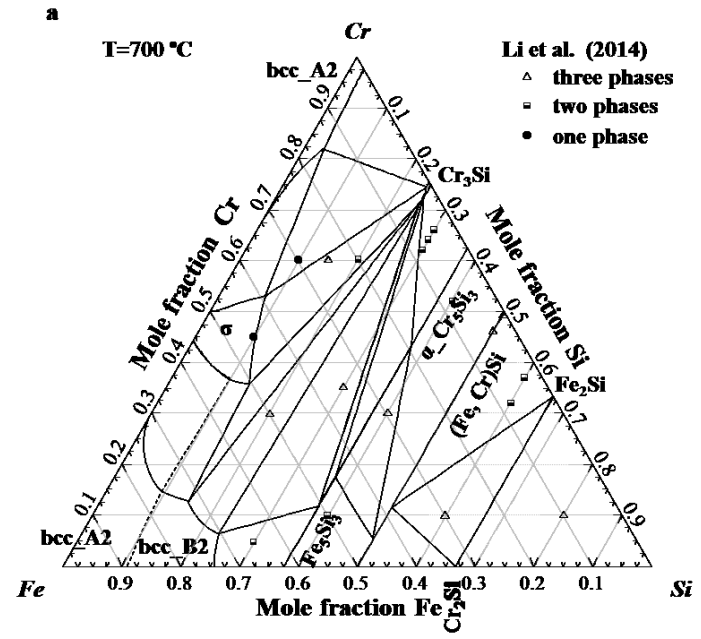
a
T=700 °C
Li et al. (2014)
three phases
two phases
one phase
Cr
Fe
Si
bcc_A2
bcc_B2
σ
Cr3Si
α_Cr5Si3
(Fe, Cr)Si
Fe2Si
Fe5Si3
Cr2Si
Mole fraction Cr
Mole fraction Si
Mole fraction Fe

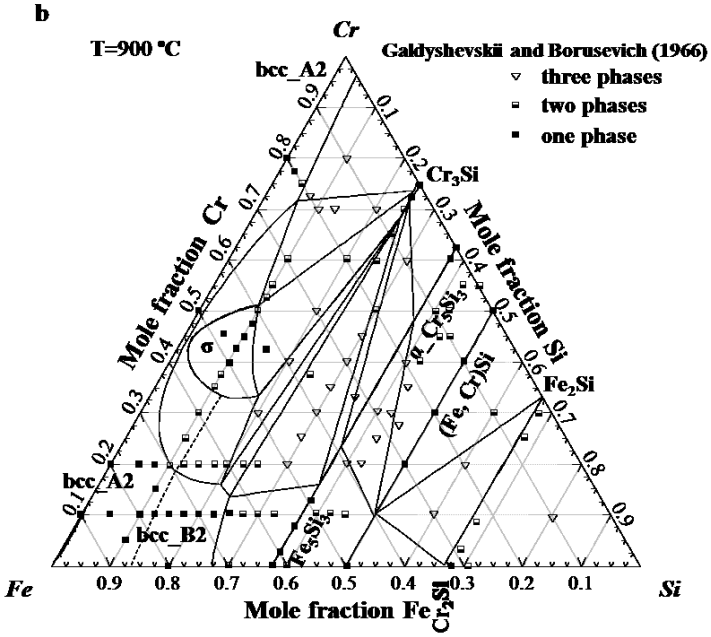
b
T=900 °C
Galdyshevskii and Borusevich (1966)
three phases
two phases
one phase
Cr
Fe
Si
bcc_A2
bcc_B2
σ
Cr3Si
α_Cr5Si3
(Fe, Cr)Si
Fe2Si
Fe5Si3
Cr2Si
Mole fraction Cr
Mole fraction Si
Mole fraction Fe

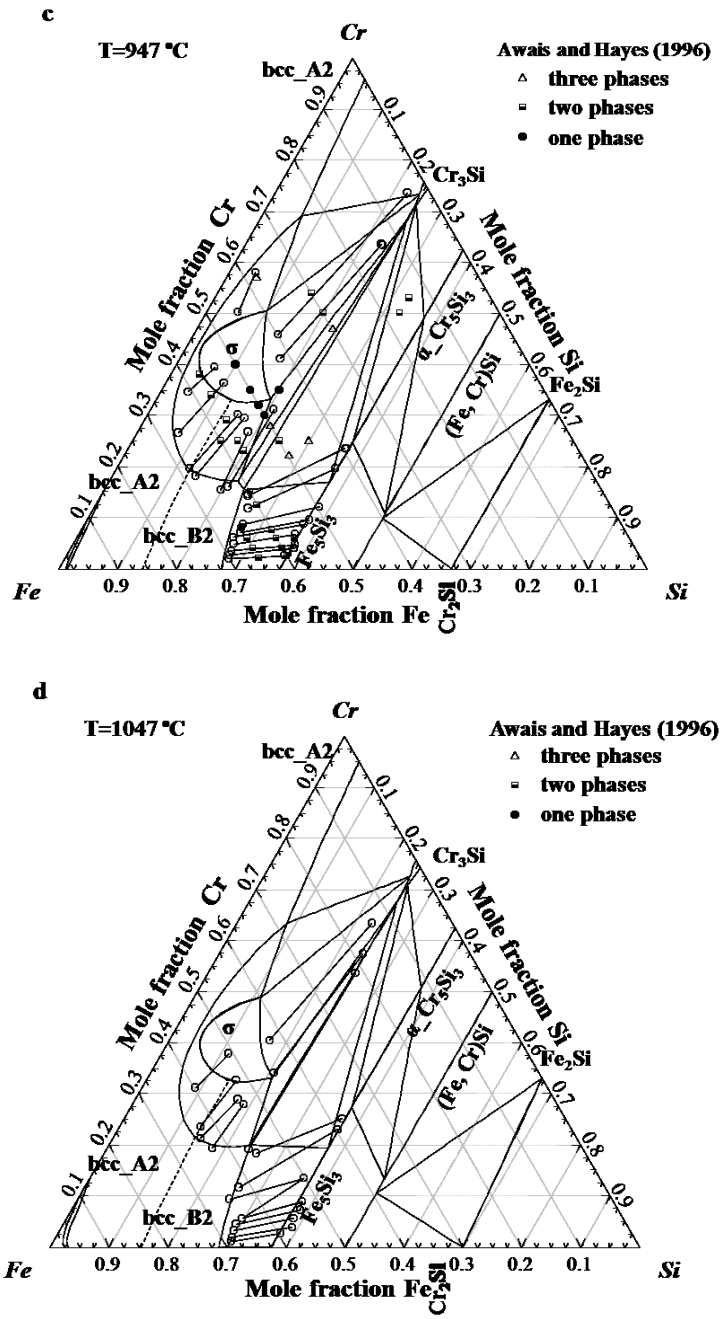

Fig. 11.3 The calculated isothermal sections of the Fe-Si-Cr system along with the experimental data at different temperatures. (a) 700 °C, (b) 900 °C, (c) 947 °C, and (d) 1047 °C.

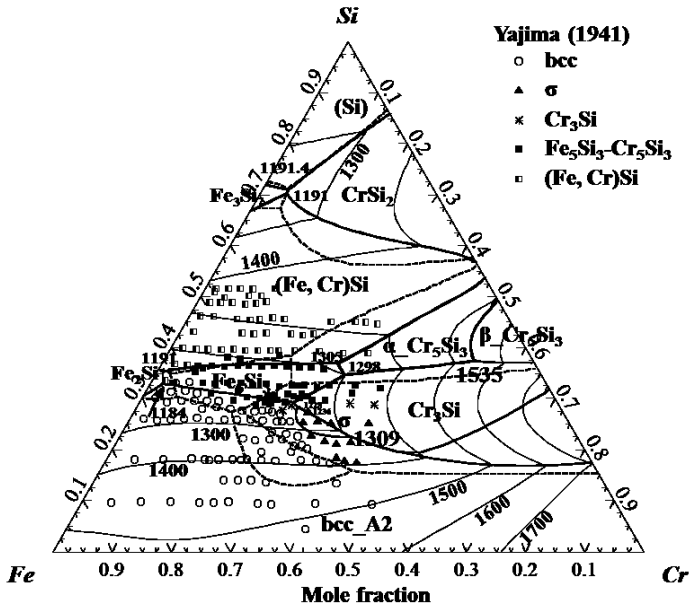

Fig. 11.4 The calculated liquidus projection of the Fe-Si-Cr system along with the experimental data.

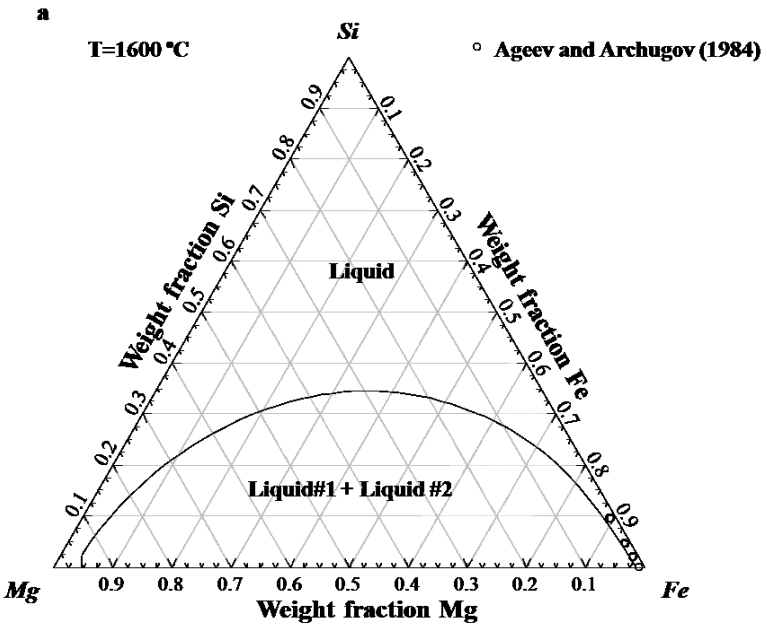
a
T=1600 °C
Si
Ageev and Archugov (1984)
Weight fraction Si
Weight fraction Fe
Liquid
Liquid#1 + Liquid #2
Mg
Fe
Weight fraction Mg

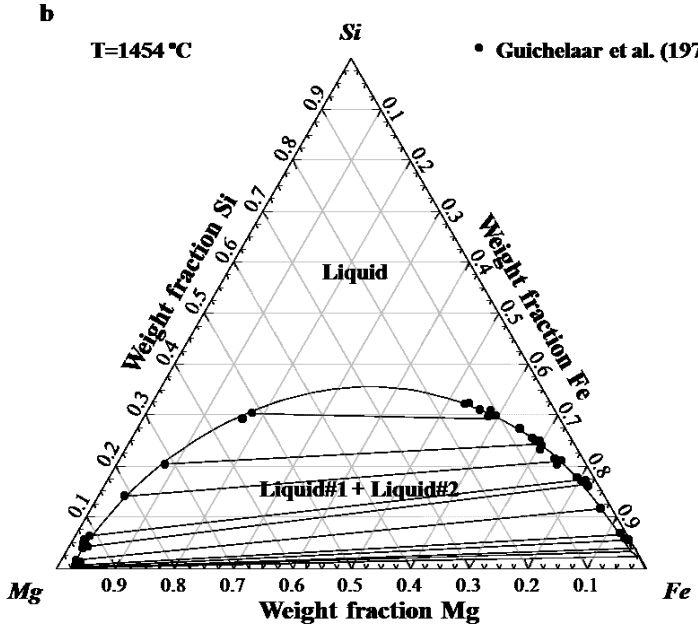
b
T=1454 °C
Si
Guichelaar et al. (1971)
Weight fraction Si
Weight fraction Fe
Liquid
Liquid#1 + Liquid#2
Mg
Fe
Weight fraction Mg

c

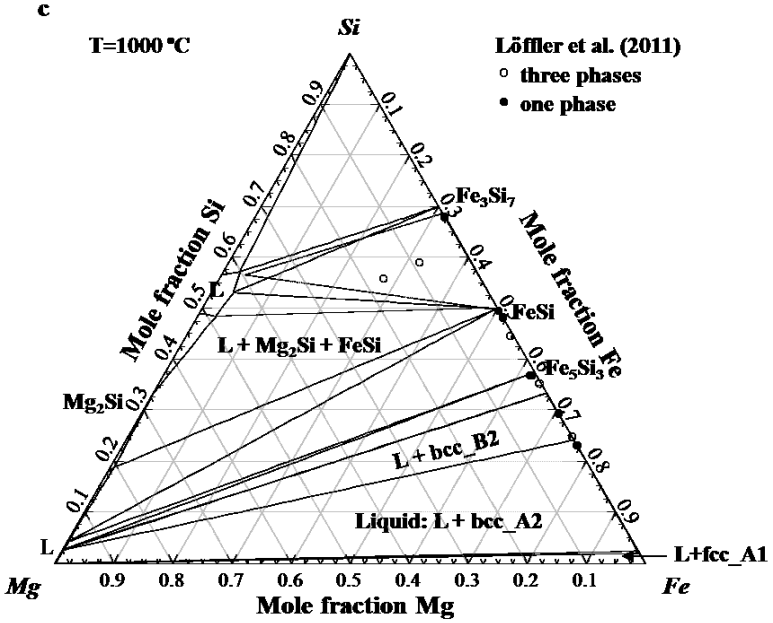
T=1000 °C
Si
Löffler et al. (2011)
three phases
one phase
Fe3Si7
Mole fraction Si
Mole fraction Fe
L
FeSi
L + Mg2Si + FeSi
Fe5Si3
Mg2Si
L + bcc_B2
Liquid: L + bcc_A2
L
L+fcc_A1
Mg
Fe
Mole fraction Mg

d

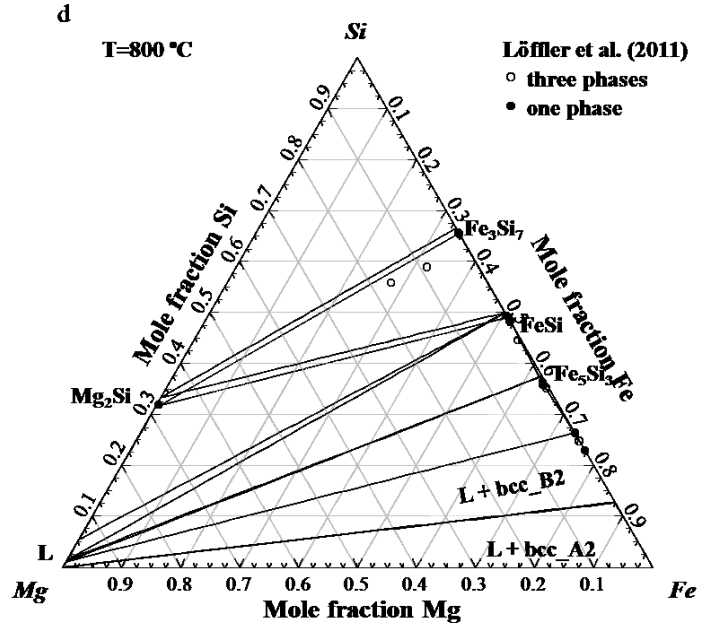
T=800 °C
Si
Löffler et al. (2011)
three phases
one phase
Fe3Si7
Mole fraction Si
Mole fraction Fe
FeSi
Fe5Si3
Mg2Si
L + bcc_B2
L + bcc_A2
L
Mg
Fe
Mole fraction Mg

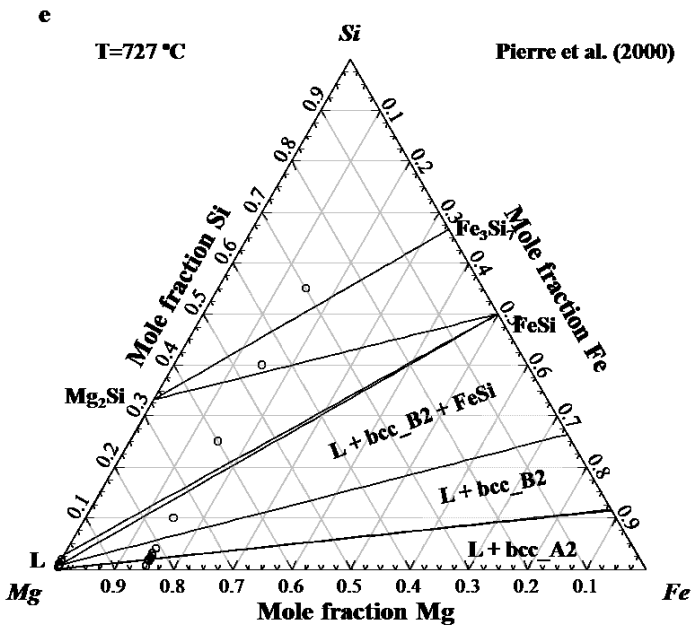

Fig. 11.5 The calculated isothermal sections of the Fe-Si-Mg system along with the experimental data at different temperatures. (a) 1600 °C, (b) 1454 °C, (c) 1000 °C, (d) 800 °C, and (e) 727 °C.

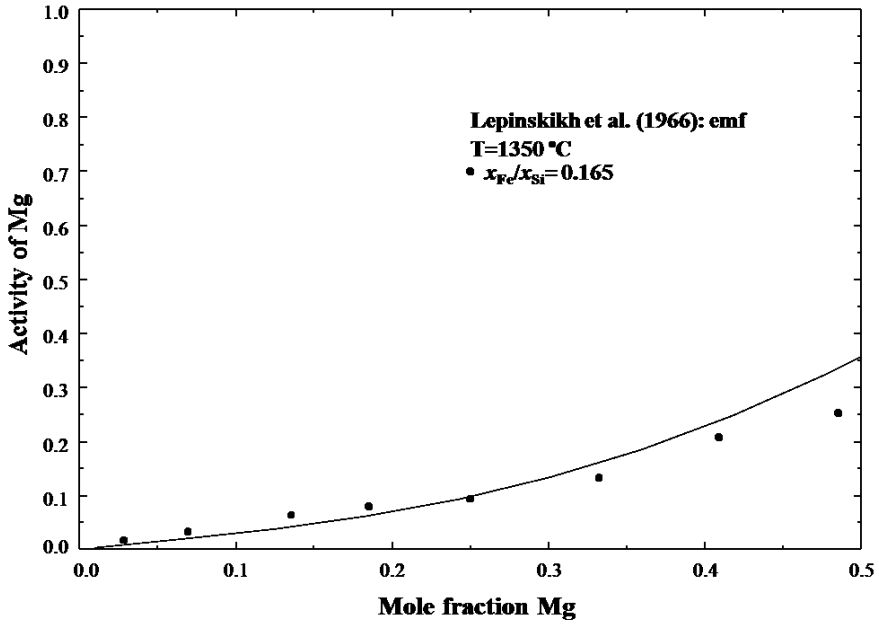

Fig. 11.6 The calculated activity of Mg with respect to the liquid Mg standard of the Mg/Fe ratio of 0.165 section at 1350 °C along with the experimental data.

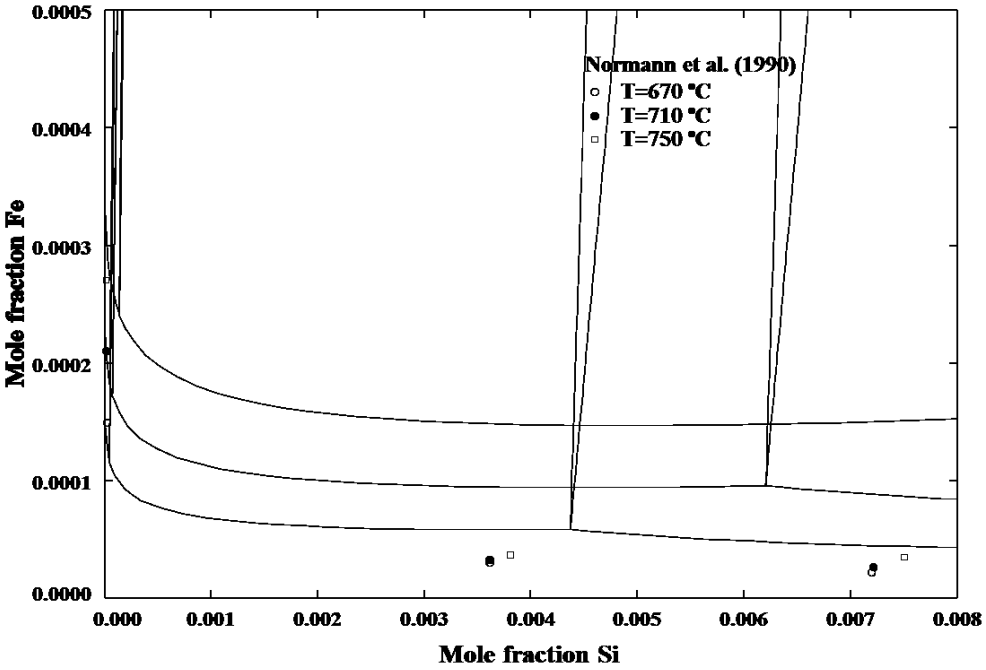

Fig. 11.7 The calculated solubilities of Fe and Si in liquid Mg at 670, 710, and 750 °C along with the experimental data.

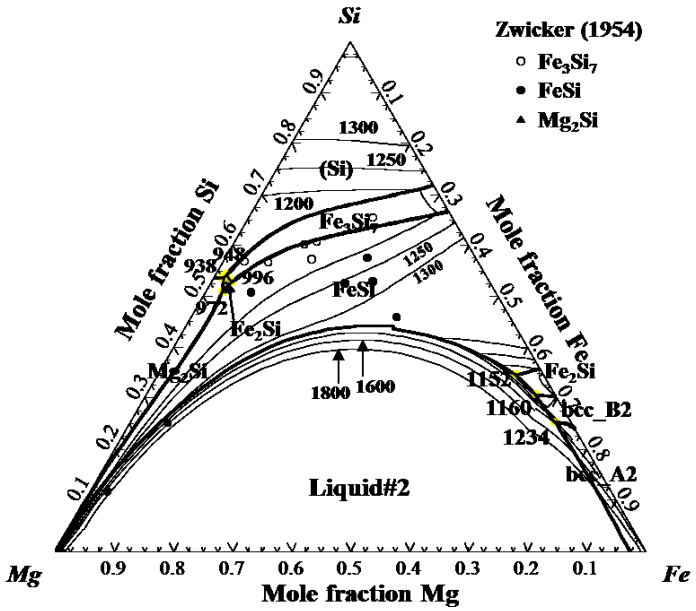

Fig. 11.8 The calculated liquidus projection of the Fe-Si-Mg system.

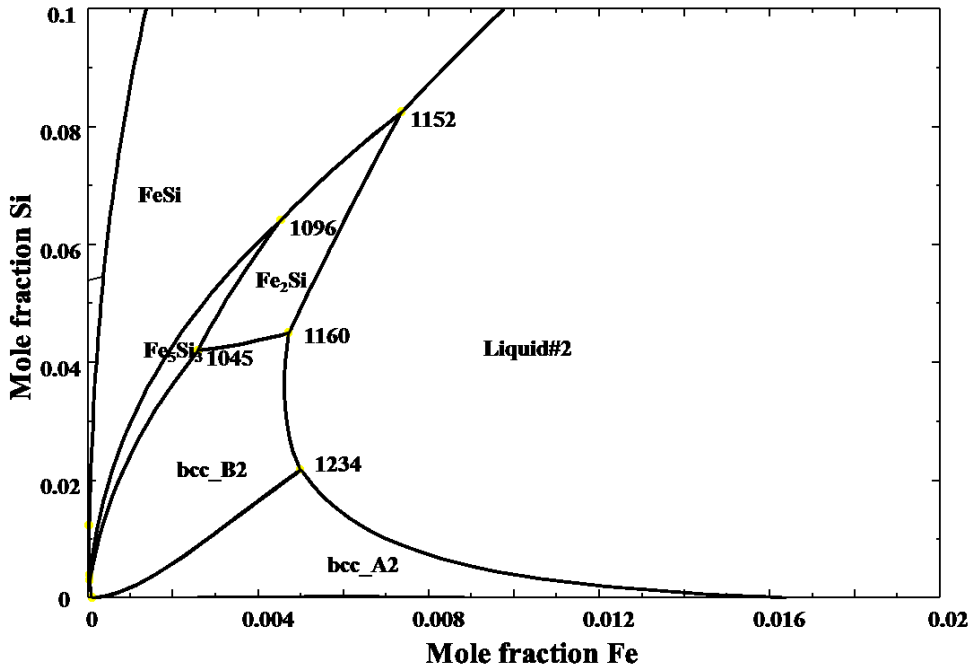

Fig. 11.9 Enlarged part of the liquidus projection of the Mg rich Fe-Si-Mg system.

Chapter 12 Applications of the developed thermodynamic database

Senlin Cui and In-Ho Jung

Department of Mining and Materials Engineering, McGill University, 3610 University Street, Montreal, Quebec, H3A 0C5, Canada

12.1 Recycling of aircraft Al alloys

Abstract

With the increasing demand of energy saving and environment protection, the recycling of the end-of-life aircraft Al alloys as a valuable source of secondary Al becomes an important issue. In the current study, the thermochemistry reactions related to the aircraft Al alloy recycling process are investigated using thermodynamic calculations with the CALPHAD-type database. The possible process of all the major alloying elements removal is discussed. Zn can be effectively removed from Al melt by vaporization in low pressure. The precipitation of α-$Al_{15}(Fe, Mn)_3Si_2$ (AlFeMnSi_alpha) followed by a sedimentation and filtering method can be used for Fe and Mn removal, which is highly depending on the silicon concentration in Al melt (effective only when Si content is between 2 wt.% and 20 wt.%). Similarly, Si can be removed by Ca addition to precipitate $CaAl_2Si_2$ when Si contents is higher than 6.43 wt.%. Ti and Zr can be removed by adding B contain agent to form $(Ti, Zr)B_2$. The addition of KF and NaF in the molten flux is effective in preventing the Al_2O_3 inclusion formation and controlling the total amount of MgO formation in Al melt. The current thermodynamic simulation indicates that the well sorted 7xxx and 2xxx aircraft Al alloys can be recycled to the mostly used Al 7075 and 2024 alloys, respectively. The unsorted aircraft Al alloys can also be recycled into Al 2024 alloy with more recycling steps.

Key words:

Aluminum alloy; Recycling; Thermodynamic calculation.

12.1.1 Introduction

Aluminum is the most widely used light metal for structural applications. The production of primary Al is energy intensive and significantly contributes to the greenhouse gas emission [1]. Recycling of Al from obsoleted Al products can effectively reduce the energy consumption and CO_2 emission. For more than 80 years, Al alloys have been used as the primary material for the structural parts of aircraft due to their high specific mechanical properties, light weight, and fatigue performance. Thousands of end-of-life aircrafts have been obsoleted in the so called “graveyard”. It is known that more than 70 wt.% of a commercial airplane are using Al alloys [2]. Thus, the obsoleted aircraft itself is an important source of secondary Al production.

Historically, 2xxx, 6xxx, 7xxx, and 8xxx series alloys were utilized in the manufacturing of airplane. 2xxx and 7xxx series alloys are the predominant aircraft alloys, while 6xxx and 8xxx series have only limited usage. To a large extent, therefore, aircraft alloys can be classified into 2xxx and 7xxx series alloys. Table 12.1.1 listed several typical Al alloys which are used in airplane. It can be seen from the table that Zn, Cu, Mg, Si, Fe, Mn, and Cr, are the major alloying elements in these Al alloys. The most promising recycling process for aircraft Al alloys is that they can be directly recycled into aerospace grade alloys. Since Al 2024 and 7075 are the mostly used Al alloys in aircraft [3], the current study aims to analyze the possibility of recycling aircraft alloys to Al 2024 and 7075 alloys via thermodynamic calculations.

12.1.2 Recycling process

In an ideal recycling process, the aircrafts can be systematically disassembled. All the Al components are collected separately from other parts and pre-sorted into 2xxx and 7xxx series alloys. Then the pre-sorted components will be well cleaned, shredded, and re-melted to provide metal in a most useful way. The 2xxx series alloys can go back to 2024 and 7xxx series alloys back to 7075 alloy. That is, the retired Al components from aircraft are recycled to the aircraft grade. The key determinants in this process are sorting, de-coating, and composition refinement. Sorting of alloys into 2xxx and 7xxx series is technically achievable, since the Cu and Zn contents

in 2xxx and 7xxx series are quite different. 2xxx series alloy has a high Cu content and 7xxx series alloy is rich in Zn. For instance, a portable spectrometer can be designed for this purpose. In real recycling process, 2xxx, 6xxx, and 7xxx series alloys in the best situation can be separated. However, it is hard to separate each series of alloy in details, for example 2024 and 2014. In the worst case, Al alloy components are only separated from other metallic components without further classification. The composition refinement process is to control the melt composition to a target alloy composition. The controlling of the amount of different alloy elements and removal of certain unfavorable alloy elements are the key part.

12.1.3 Aircraft Al recycling simulation

Three possible situations are considered in this study: (i) a mixture of 2xxx series, (ii) a mixture of 7xxx series, and (iii) a mixture of all the aircraft Al alloys. For simplification, the aircraft alloys considered in this study are 9 alloys as listed in Table 12.1.1. 7xxx series alloys include 7075, 7475, 7175, and 7050. 2xxx series alloys include 2024, 2014, 2026, and 2324. 6013 is taken as a representative of 6xxx series alloys.

In this study, the average composition of each alloy is used to prepare the alloy mixture. Since the amount of each alloy used in aircraft is unknown and varies with aircraft model, a random mixture of different alloys is prepared in this study. 50000 g of 7475, 40000 g of 7150, 30000 g of 7075, and 60000 g of 7050 are mixed for 7xxx series alloys (Called as “Mix 7xxx”), and 40000 g of 2024, 50000 g of 2014, 60000 g of 2026, and 30000 g of 2324 are mixed for 2xxx series alloys (Called as “Mix 2xxx”). 40000 g of 2024, 50000 g of 2014, 60000 g of 2026, 3000 g of 2324, 20000 g of 6013, 100000 g of 7050, 70000 g of 7075, 60000 g of 7150, and 50000 g of 7475 are mixed as the unseparated aircraft alloys (“Mix all”). These mixed alloy compositions are listed in Table 12.1.1. It can be seen that the “Mix 7xxx” and “Mix 2xxx” alloys can be easily refined to 7075 and 2024, respectively, if Zr can be effectively removed. All the other elements are within or lower than the nominal composition of 7075 and 2024. The composition of all the alloying elements less than the specification can be easily adjusted by adding a certain amount of pure elements. For the “Mix all” alloy, Mg, Zn, and Zr exceed the nominal composition range of 2024.

In the following section, the removal or refinement of each major alloying element will be first discussed based on thermodynamic calculation using the FactSage software [4]. For the thermodynamic calculations, FTlite, FTsalt, FToxid, and FactPS thermodynamic databases are used. The details of these databases are described elsewhere [5]. The recycling case of the "Mix all" alloy is more complex and a series of recycling stage will be discussed.

12.1.3.1 Composition control of Al melts: Thermodynamic analysis

Recent thermodynamic studies by Nakajima et al. [6] and Hiraki et al. [7] indicated that only Mg (Ca), Li (Na and K), and Zn in Al alloys can be removed by thermochemical reactions. All the recycling calculations in this study assume full equilibrium, which is typically not achieved in the industrial process.

12.1.3.1.1 Removal of Mg (Ca)

Mg can be removed by chlorination process, electrochemical process, vaporization, and oxidation process. Cl_2 gas or $AlCl_3$ can be used for the chlorination process. The disadvantage of using Cl_2 is that the possible air pollution and the possible formation of HCl gas and MgO inclusions when H_2O presents. On the other hand, the solid flux process using $AlCl_3$ and AlF_3 is very slow in reaction rate and a large amount of flux is needed. Electrochemical process is a considerably expensive way. Vaporization is also a slow process, and oxidation will inevitably introduce MgO inclusion in the Al melts. Chlorination is the most applicable way in industry. Ca (chemically more reactive than Mg) can be removed also by chlorination.

To elucidate the Mg removal using Cl_2 gas, 100 g of Al-5 wt.% Mg was reacted with Cl_2 gas under the protection of NaCl-KCl salt at 700 °C. In the calculation, the amount of NaCl-KCl salt (NaCl:KCl=1:1 in mole faction) was varied from 0 to 100 g. 100% yield of Cl_2 gas (full equilibrium) was assumed. In reality, the yield of Cl_2 gas can be varied largely depending on the injection technology. The simulated results are shown in Fig. 12.1.1. The main chemical reaction is $Mg + Cl_2\ (g) = MgCl_2\ (s, l)$.

As can be seen in Fig. 12.1.1(a), Mg can be effectively removed from Al melt to a level of 10^{-5} wt.% by the addition of Cl_2 gas at 700 °C. However, the addition of flux does not have apparent effect on Mg removal when the Cl_2 gas is less than 15 g. In details, the remaining Mg level is higher than that without any flux when the flux amount is less than 40 g, and lower when the flux amount is larger than 40 g. When the flux amount is less than 20 g noticeable amount of Al_2Cl_6 species is calculated in molten salt. As can be seen, the Cl_2 gas is used for the formation of $MgCl_2$, $AlCl_3$, and Al_2Cl_6. The activity of $MgCl_2$ (l) is calculated in Fig. 12.1.1(d). Figs. 12.1.1(b) and (c) show the calculated composition and actual amount of $MgCl_2$, $AlCl_3$, and Al_2Cl_6 in molten salt when Cl_2 (g) is 25 g.

In summary, Cl_2 gas is very effective in removal of Mg in Al alloy. Thermodynamically, molten salt flux is not necessary to remove Mg from liquid Al. Flux would be necessary to quickly remove $MgCl_2$ to the surface of Al melt by dissolving solid $MgCl_2$ into molten slat to prevent the suspension or re-entry of $MgCl_2$ in liquid Al. Therefore, proper selection of salt flux which can dissolve $MgCl_2$ instantly would be important in this chlorination Mg removal process. Removal of Ca in molten Al is similar to that of Mg.

12.1.3.1.2 Removal of Li (Na and K)

Li can be removed from the Al melt by chlorination using Cl_2 gas or chloride flux. During Li removal, the interaction between Mg and Li should be considered as the chlorination process also inevitably affects Mg.

The calculated composition profiles of Li and Mg without flux for Al-2 wt.% Mg-0.1 wt.% Li, Al-2 wt.% Mg-0.2 wt.% Li, and Al-2 wt.% Mg-0.5 wt.% Li alloys are calculated in Fig. 12.1.2(a) at 700 °C under varying Cl_2 amount. It can be seen from the diagram that Li concentration immediately drops with Cl_2 addition. When the Li concentration reaches about 0.01 to 0.001 wt.%, Mg starts to react with Cl_2 gas. About 7 g of Cl_2 gas can reduce the Mg and Li in 100 g of liquid alloys to a bottom level, further Cl_2 addition only decrease both Li and Mg, slightly. Chlorination using Cl_2 gas is not a suitable way to remove Li from Al in presence of Mg. The Li removal efficiency also depends on the initial Li content. The calculation results of the three alloys with

two different $AlCl_3$ containing fluxes are shown in Fig. 12.1.2(b). The simulated profiles are similar to those using Cl_2 gas as shown in Fig. 12.1.2(a). The fluxes are equimolar KCl and NaCl containing 10 and 20 percent of $AlCl_3$, respectively. Flux with 20 percent of $AlCl_3$ is more effective in removing Li and Mg. The calculated results for the fluxes where $AlCl_3$ is replaced by $MgCl_2$ are shown in Fig. 12.1.2(c). In this case, Mg can be preserved in the alloy melt while Li can be effectively removed. These results mean that Li can be removed by using $MgCl_2$ containing flux without changing Mg in Al alloy. However, a large amount of flux is required.

Al-Li based alloy is one of the aerospace Al alloys which is widely used, but not considered in this study. In order to check the removal of Li from the Al alloy mixture containing Al-Li alloys, thermodynamic calculation between 100 g of "Mix all" Al melts, 3 g of Li, and 299.5 g of flux (35.5 g NaCl, 46 g KCl, 18 g $AlCl_3$, and 200 g $MgCl_2$) was performed and the result is shown in Table 12.1.2. As can be seen, Li can be removed down to ppm level by reaction of $AlCl_3$ +3 Li = Al +3 LiCl. Even small increase in Mg content in Al alloy is calculated too.

12.1.3.1.3 Removal of Zn

Zn is easy to remove by vaporization because of its high vapor pressure. As Mg also has a relatively high vapor pressure, the vapor composition of three Al melts with different compositions as a function of both temperature and pressure are calculated in Fig. 12.1.3. The Zn can be more easily vaporized than Mg. For example, Zn can be already evaporated at above 10^{-4} atm, while Mg can be significantly vaporized below 10^{-3} atm at 650 °C. Relative vapor pressure of Zn to Mg can be decreased with increasing temperature as can be seen in Fig. 12.1.3(b). The change of Mg and Zn vapor pressures depending on the relative concentration of Mg and Zn in Al alloy is calculated in Fig. 12.1.3(c). In the calculation, Al alloy with 5 at.% (Mg + Zn) at 650 °C and 0.01 atm pressure. The optimum condition to remove Zn in Al alloy containing Mg, therefore, is low temperature and relative high pressure close to 1 atm. For example, argon bubbling under 0.01 to 1 atm pressure at 650 °C could be a reasonable process to reduce Zn.

12.1.3.1.4 Removal of Fe, Si, Mn, and Cr

According to Ashtari et al. [8] and de Moraes [9], the Fe and Mn can be removed from Al melt by changing the Fe/Mn ratio to form the α-$Al_{15}(Fe, Mn)_3Si_2$ (AlFeMnSi_alpha) phase followed by a sedimentation and filtering process. According to them, more than 60 % of Mn and Fe can be removed in this way. Fig. 12.1.4 is the currently calculated liquidus projections of the Al-Fe-Mn-Si system at 2 wt.% Si, 4 wt.% Si, and 6 wt.% Si. It can be seen from Fig. 12.1.4(a), α-$Al_{15}(Fe, Mn)_3Si_2$ is not able to form due to low silicon content. This is consistent with the experimental results from de Moraes et al. [9] where Fe cannot be removed by adding Mn in alloys E15F3M and E5F7M samples with a Si content of 0.25 wt.%. At 4 wt.% and 6 wt.% Si, the primary phase region of α-$Al_{15}(Fe, Mn)_3Si_2$ increases. The α-$Al_{15}(Fe, Mn)_3Si_2$ formation temperature is higher than that of primary Al, which ensures the subsequent filtering process applicable. Al alloy with Fe concentration within the α-$Al_{15}(Fe, Mn)_3Si_2$ primary phase region can be refined by adding Mn to form α-$Al_{15}(Fe, Mn)_3Si_2$ precipitates. This method is also applicable for the reduction of Mn in melt and works up to at least 20 wt.% Si. It should be noted that this method can only be practically applicable for Al alloys with high percentage of Si.

Si can be removed by adding Ca in the melt to form the $CaSi_2Al_2$ phase which is floated on the top layer of the melts [10]. Fig. 12.1.5 is the calculated liquidus projection of the Al-Ca-Si system in the Al rich corner. It can be seen that the Ca addition can promote the formation of $CaAl_2Si_2$ when the Si content in the melt is higher than 6.43 wt.%. It should be noted that composition limits will be changed to certain extent due to the multicomponent interactions in the melt. The amount of Cr added into Al is lower than 3 wt.% which is not an issue on alloy recycling. And no effective way to economically remove Cr from Al melt is found.

12.1.3.1.5 Removal of Ti and Zr

The solubility of Ti and Zr in Al is lower than 1 at.%. Ti is a common alloying element for both 7xxx and 2xxx series alloys, and Zr is added in certain special alloys. A review of the Ti and Zr containing phase diagrams indicates that Ti and Zr are very prone to form stable intermetallic phase with B. Fig. 12.1.6 presents the calculated isothermal sections of the Al-Zr-B and Al-Ti-B systems at 650 and 700 °C, respectively. Both TiB_2 and ZrB_2 are stable at 650 and 700 °C. At 700 °C, there is a stable phase region of Liquid + TiB_2 (ZrB_2) in the system. The addition of B

element in the Al melt will promote the formation of TiB_2 and ZrB_2 type stable precipitates. The solubility of B in Al is less than 20 ppm. Similar to the removal of Fe, the TiB_2 and ZrB_2 precipitates can be filtered after formation. The possible agent to be utilized for B can be BCl_3, B_2Cl_4, AlB_2, $Na_2B_4O_7$, etc.

12.1.3.1.6 Flux for refinement

The flux used in Al recycling can either be in solid state or liquid state depend on the detailed refining process. Basically, liquid flux with a lower density than the melt ensures a better metal-salt settling, a solid flux with a higher density than the melt can submerge in the melt much easily. The liquid flux used in Al refinement is normally equimolar of KCl and NaCl flux with the addition of certain amount of Na_3AlF_6, CaF_2, or $NaAlF_4$, because equal moles of KCl and NaCl gives a lowest melting point. Fig. 12.1.7 show the calculated isothermal sections of the $MgCl_2$-KCl-NaCl ternary system at 620, 650, 670, and 700 °C. The addition of the $MgCl_2$ phase can increase the stability range of the KCl-NaCl liquid flux. Besides, $MgCl_2$ can be used to control the direction of the main chemical reaction, for example, Li (in Al) + $MgCl_2$ (l) = 2 LiCl (l) + Mg (in Al) can happen with addition of $MgCl_2$ so that it prevents the consumption of Mg in the liquid Al. The same can happen with $AlCl_3$.

12.1.3.1.7 Removal of inclusions

The Al_2O_3 phase may form in the Al melts during the refining process due to the presence of H_2O and O_2 from air or argon gas during the de-zinc process. In industry, NaF and KF are added to the refining flux to remove the Al_2O_3 inclusion. Thermodynamic calculation was conducted to check the anti-oxidation ability of the “Mix all” alloy under the flux protection. The oxidation behaviors of 100 g “Mix all” alloy protected by three different fluxes, (1) 10 g NaCl and 10 g KCl, (2) 10 g NaCl, 10 g KCl, and 1 g KF, and (3) 10 g NaCl, 10 g KCl, and 1 g NaF, under O_2 atmosphere are calculated at 700 °C. The calculated amounts of MgO and Al_2O_3 formed as a function of O_2 amount are shown in Fig. 12.1.8. Al_2O_3 starts to form at 0.7, 3.8, and 5.2 g O_2 for flux without F, with KF, and NaF, respectively. MgO forms immediately after the O_2 gas addition. NaF shows more ability to reduce the total amount of MgO formation than KF. Al_2O_3 starts to

form only when the Mg content in the metallic melt deceases below a certain level. For example, 0.93148 wt.% Mg in the current calculation for the flux with NaF, which is substantially lower than the initial composition of 1.8365 wt.% Mg. The addition of KF and NaF can be very useful to reduce Al_2O_3 inclusions in the Al melts.

12.1.3.2 Refining the Al alloy melt: scenario 1

A preliminary thermodynamic calculation for the "Mix all" alloy indicates that the $AlZr_3$ phase can form in the melt at 660-630 °C and the fcc_A1 phase starts to form below 640 °C. As a first step, Zr was partially removed by keeping the melts at 650 °C and followed by filtering (assume a 100 % removal efficiency). The Zr content decreases to 0.05105 wt.% (see Table 12.1.3, De-Zr). And then, Zn can be removed from the remaining melt by way of evaporation. Certain inert gas which does not react with the Al melts will be the best choice. In the current work, Ar is selected. Ar bubbles can be introduced to the melts. Zn with a high vapor pressure can be taken away from the melt. In this way, Zn can be collected by simply cooling the gas and the gas can be reused until the Zn content reaches the required value. The vaporization temperature and pressure should be carefully selected. Fig. 12.1.9(a) shows the vapor composition as a function of temperature at 1 bar. As the temperature increases, Zn/Mg vapor ratio decreases. Fig. 12.1.9(b) is the vapor composition as a function of pressure at 650 °C. Zn/Mg vapor ratio keeps constant at the high pressure and decreases dramatically as the pressure decrease to 10^{-3} bar. Thus, a low temperature (650 °C) and high pressure (1 bar) is used. After 30000 g of Ar gas equilibrium with the liquid melt for 750 times, the Zn concentration decreases to 0.21958 wt.% (See Table 12.1.3, De-Zn).

Ti and Zr are removed by introducing B to form (Ti, Zr)B_2 precipitates. Here BCl_2 (B_2Cl_4) is used as B source. A KCl (500 g), NaCl (500 g), and $MgCl_2$ (1500 g) mixture is added to cover the melt to prevent the Mg consumption. The Zr content decreases to 150 ppm after adding 150 g BCl_2 for 8 times. Ti also apparently decreases. The current thermodynamic calculation indicates that the further addition of BCl_2 will dramatically decrease Zr, but the B content in the melt will increase. As a compromise, 150 ppm of Zr is kept in the melt. The liquid metal composition is shown in Table 12.1.3 as "De-TiZr". Finally, 5500 g Cu, 1300 g Si, and 650 g of Ti are added to

the melts to adjust the alloy composition. Fe is not added since it is always treated as impurity. The final alloy composition is presented in Table 12.1.3 as “new alloy”. All the alloying compositions except for Fe are very close to the nominal composition of 2024 alloy.

12.1.3.3 Refining the Al alloy melt contaminated by Fe: scenario 2

Fe contamination should be also considered during the aircraft recycling process. The Fe contamination can come from the sorting and shredding process. In case the Fe contamination is severe, the Fe content may exceed 0.7 wt.% in the alloy, the Al alloys is hard to recycling back to aerospace grade using solely thermodynamic refining without diluting. The formation of α-Al_{15}(Fe, Mn)$_3Si_2$ requires considerable amount of Mn and Si in the Al melts which is much higher than the nominal composition of aerospace grade Al alloys. In other word, the aircraft Al alloy can be reused as aircraft alloy only when the Fe contamination is not serious.

12.1.4 Summary

Thermodynamic calculations were carried out to study the recycling of aircraft Al alloys using FactSage thermodynamic databases. The removals of the major alloy elements were discussed. According to the current thermodynamic calculations, alloying elements like Mg (Ca) and Li (Na and K) can be removed from the Al melts by the chlorination process. Zn can be removed by the vaporization process. The interaction between Mg and Li, Mg and Zn should be always considered during Li and Zn removal for the Al alloy containing Mg. Improper flux composition selection or distillation condition will result in losing of Mg from the Al alloy. Alloying elements like Fe, Mn, and Si can be removed by a precipitation and filtering method. In detail, Fe and Mn can be removed by α-Al_{15}(Fe, Mn)$_3Si_2$ formation and Si in the form of $CaAl_2Si_2$ with Ca addition. However, the removal ability of Fe and Mn is strictly controlled by the amounts of Fe, Mn, and Si in the liquid Al, which is not related only to the Fe/Mn ratio. Ti and Zr have strong affinity with B. The addition of B will promote the formation of TiB_2 and ZrB_2 precipitates. But the amount of B addition should be carefully controlled since B has considerable solubility in Al alloys. The flux traditionally used in the Al recycling industry contains equal moles of KCl and NaCl. The current study indicates that the addition of $MgCl_2$ can substantially increase the stability

of liquid flux. Different flux can be used in each step of refinement. $MgCl_2$ and $AlCl_3$ can be added in the flux for specific purpose. NaF is found to have more effect than KF in reducing the Al_2O_3 inclusion and controlling the total amount of MgO formation during refinement.

The sorted 7xxx and 2xxx aircraft Al alloys can be recycled to the most used 7075 and 2024 alloys, respectively. The unsorted aircraft Al alloys can also be recycled into the 2024 alloy with more recycling steps.

Acknowledgement

The authors would like to thank the financial support from NSERC-Automotive Partnership Canada program in Canada. Senlin Cui would also like to thank the McGill Engineering Doctorate Award (MEDA) from McGill University for financial support.

References

1. Cullen, J.M. and J.M. Allwood, *Mapping the Global Flow of Aluminum: From Liquid Aluminum to End-Use Goods.* Environ. Sci. Technol., 2013. **47**(7): p. 3057-3064.
2. Starke, E.A., Jr. and J.T. Staley, *Application of modern aluminium alloys to aircraft.* Fundam. Alum. Metall., 2011: p. 747-783.
3. Dursun, T. and C. Soutis, *Recent developments in advanced aircraft aluminium alloys.* Mater. Des., 2014. **56**: p. 862-871.
4. http://www.factsage.com.
5. Jung, I.-H., S. Cui, J.-K. Lee, and S.-M. Park, *Thermodynamics of the Mg Recycling Process.* Jom, 2013. **65**(10): p. 1310-1316.
6. Nakajima, K., O. Takeda, T. Miki, K. Matsubae, S. Nakamura, and T. Nagasaka, *Thermodynamic analysis of contamination by alloying elements in aluminum recycling.* Environ. Sci. Technol., 2010. **44**(14): p. 5594-5600.
7. Hiraki, T., T. Miki, K. Nakajima, K. Matsubae, S. Nakamura, and T. Nagasaka, *Thermodynamic analysis for the refining ability of salt flux for aluminum recycling.* Materials, 2014. **7**(8): p. 5543-5553.

8. Ashtari, P., K. Tetley-Gerard, and K. Sadayappan, *Removal of iron from recycled aluminium alloys.* Can. Metall. Q., 2012. **51**(1): p. 75-80.
9. Lopes de Moraes, H., J.R. de Oliveira, D.C.R. Espinosa, and J.A.S. Tenorio, *Removal of iron from molten recycled aluminum through intermediate phase filtration.* Mater. Trans., 2006. **47**(7): p. 1731-1736.
10. Ashtari, P., B. Davis, and K. Sadayappan, *Removal of Si from recycled aluminium alloys.* Int. J. Cast Met. Res., 2012. **25**(2): p. 100-102.
11. Hunsicker, H.Y., *Development of Al-Zn-Mg-Cu Alloys for Aircraft.* Philos. Trans. A Math. Phys. Eng. Sci., 1976. **282**(1307): p. 359-376.
12. Starke, E.A. and J.T. Staleyt, *Applicaiton of modern aluminum alloys to aircraft.* Prog. Aerospace Sci., 1996. **32**: p. 131-172.

Table captions

Table 12.1.1 Nominal compositions of some 2xxx and 7xxx alloys [11, 12].

Table 12.1.2 Chemical reaction between 100 g of "Mix all" Al melts, with 3 g Li, and 299.5 g flux (35.5 g NaCl, 46 g KCl, 18 g $AlCl_3$, and 200 g $MgCl_2$) at 700 °C and 1 atm pressure.

Table 12.1.3 New alloy compositions compared with 2024 alloy.

Figure captions

Fig. 12.1.1 (a) The calculated Mg concentration profiles of an Al-5 wt.% Mg alloy reacting with Cl_2 gas under the protection of different amounts of slat. (b) The liquid salt composition profiles of an Al-5 wt.% Mg alloy reacting with 25 g Cl_2 as a function of the protective salt amount. (c) The total amount of $MgCl_2$, $AlCl_3$, and Al_2Cl_6 formed for an Al-5 wt.% Mg alloy reacting with 25 g Cl_2 as a function of the protective salt amount. And (d) calculated $MgCl_2$ activity profile of an Al-5 wt.% Mg alloy reacting with 25 g Cl_2 as a function of the protective slat amount.

Fig. 12.1.2 The calculated concentration profiles of Li and Mg in 100 g of Al-2 wt.% Mg-0.1 wt.% Li, Al-2 wt.% Mg-0.2 wt.% Li, and Al-2 wt.% Mg-0.5 wt.% Li alloys at 700 °C. (a) As a function of Cl_2 gas amount, (b) as a function of flux ($KCl:NaCl:AlCl_3$=4.5:4.5:1 and $KCl:NaCl:AlCl_3$=4:4:1) amount, and (c) as a function of flux ($KCl:NaCl:MgCl_2$=4.5:4.5:1 and $KCl:NaCl:AlCl_3$=4:4:1) amount.

Fig. 12.1.3 The calculated concentration profiles of Zn and Mg in the vapor. (a) As a function of pressure, (b) as a function of temperature, and (c) as a function of Zn concentration in Al melts.

Fig. 12.1.4 The calculated liquidus projection of the Al-Fe-Mn-Si system. (a) With 2 wt. % Si, (b) with 4 wt. % Si, and (c) with 6 wt. % Si.

Fig. 12.1.5 The calculated liquidus projection of the Al rich Al-Ca-Si system.

Fig. 12.1.6 The calculated isothermal sections of the Al-Zr-B and Al-Ti-B systems in the Al rich corner. (a) and (b) Isothermal sections of the Al-Zr-B system at 650 °C and 700 °C, respectively, (c) and (d) isothermal sections of the Al-Ti-B system at 650 °C and 700 °C, respectively.

Fig. 12.1.7 The calculated isothermal sections of the NaCl-KCl-$MgCl_2$ system at 620, 650, 670, and 700 °C.

Fig. 12.1.8 The calculated mass of the formed MgO and Al_2O_3 as a function of O_2 amount added to 100 g of the "Mix all" melt covered with 10 g NaCl + 10 g KCl flux, 10 g NaCl + 10 g KCl + 1 g KF, and 10 g NaCl + 10 g KCl + 1 g NaF at 700 °C. (FTPS, FT-oxide, FT-lite, FT-Salt).

Fig. 12.1.9 The calculated vapor fraction of Mg and Zn of the alloy melt before de-zinc process. (a) As a function of temperature and (b) as a function of pressure.

Table 12.1.1 Nominal compositions of some 2xxx and 7xxx alloys [11, 12].

Alloy	Cr	Cu	Fe	Mg	Mn	Si	Ti	Zn	Zr	other	Al
7075	0.18-0.28	1.2-2	0-0.5	2.1-2.9	0-0.3	0-0.4	0-0.2	5.1-6.1	0	0-0.15	Bal.
7475	0.18-0.25	1.2-1.9	0-0.12	1.9-2.6	0-0.06	0-0.1	0-0.06	5.2-6.2	0	0-0.15	Bal.
7175	0-0.04	1.9-2.5	0-0.15	2-2.7	0-0.1	0-0.12	0-0.06	5.7-6.7	0.08-0.15	0-0.15	Bal.
7050	0-0.04	2.0-2.6	0-0.15	1.9-2.6	0-0.1	0-0.12	0-0.06	5.7-6.7	0.08-0.15	0-0.15	Bal.
Mix 7xxx	0.10917	1.9528	0.1	2.3139	0.06111	0.080556	0.041667	6.0056	0.063889		
2024	0-0.1	3.8-4.9	0-0.5	1.2-1.8	0.3-0.9	0-0.5	0-0.15	0-0.24	0	0-0.15	Bal.
2014	0-0.1	3.9-5	0-0.7	0.2-0.8	0.4-1.2	0.5-1.2	0-0.15	0-0.25	0	0-0.15	Bal.
2026	0	3.6-4.3	0-0.07	1.0-1.6	0.3-0.8	0-0.05	0-0.06	0-0.1	0.05-0.25	0-0.15	Bal.
2324	0-0.1	3.8-4.4	0-0.12	1.2-1.8	0.3-0.9	0-0.1	0-0.15	0-0.25	0	0-0.15	Bal.
Mix 2xxx	0.033333	4.2028	0.17444	1.1556	0.63889	0.30833	0.06	0.13361	0.05		
6013	0-0.1	0.6-1.1	0-0.5	0.8-1.2	0.2-0.8	0.6-1	0-0.1	0-0.25	0	0-0.15	Bal.
Mix all	0.077188	2.7604	0.14354	1.8365	0.30208	0.20333	0.052292	3.5574	0.057083		

Table 12.1.2 Chemical reaction between 100 g of "Mix all" Al melts, with 3 g Li, and 299.5 g flux (35.5 g NaCl, 46 g KCl, 18 g $AlCl_3$, and 200 g $MgCl_2$) at 700 °C and 1 atm pressure.

100 g of "Mix all" Al melts + 3 g of Li + 299.5 g flux (35.5 g NaCl, 46 g KCl, 18 g $AlCl_3$, and 200 g $MgCl_2$) =		
298.53 gram Salt-liquid		
(6.1378	wt.% LiCl	FTsalt
+ 11.892	wt.% NaCl	FTsalt
+ 15.409	wt.% KCl	FTsalt
+ 66.561	wt.% $MgCl_2$	FTsalt
+ 9.7024E-18	wt.% $FeCl_2$	FTsalt
+ 1.3190E-28	wt.% $FeCl_3$	FTsalt
+ 9.5725E-10	wt.% $MnCl_2$	FTsalt
+ 2.9733E-07	wt.% $AlCl_3$_4coord	FTsalt
+ 2.4037E-16	wt.% Al_2Cl_6	FTsalt
+ 3.4463E-14	wt.% $AlCl_3$_5coord	FTsalt)
+ 103.97 gram Liquid		
(91.040	wt.% Al	FTlite
+ 5.2225E-17	wt.% Cl	FTlite
+ 7.4246E-02	wt.% Cr	FTlite
+ 2.6552	wt.% Cu	FTlite
+ 0.13807	wt.% Fe	FTlite
+ 1.7377E-09	wt.% K	FTlite
+ 5.3380E-05	wt.% Li	FTlite

+ 2.0847	wt.% Mg	FTlite
+ 0.29057	wt.% Mn	FTlite
+ 2.2819E-07	wt.% Na	FTlite
+ 0.19559	wt.% Si	FTlite
+ 5.0299E-02	wt.% Ti	FTlite
+ 3.4218	wt.% Zn	FTlite
+ 4.9099E-02	wt.% Zr	FTlite)

Table 12.1.3 New alloy compositions compared with 2024 alloy.

Alloy	Cr	Cu	Fe	Mg	Mn	Si	Ti	Zn	Zr	other	Al
2024	0-0.1	3.8-4.9	0-0.5	1.2-1.8	0.3-0.9	0-0.5	0-0.15	0-0.24	0	0-0.15	Bal.
Mix all	0.077188	2.7604	0.14354	1.8365	0.30208	0.20333	0.052292	3.5574	0.057083	0	91.010
De-Zr	0.077196	2.7607	0.14356	1.8367	0.30212	0.20336	0.052298	3.5578	0.051050	0	91.015
De-Zn	0.07999	2.8607	0.14875	1.7506	0.31305	0.21072	0.054191	0.21958	0.052898	0	94.310
De-TiZr	0.080133	2.8658	0.14902	1.6765	0.31361	0.21109	0.006048	0.21997	0.00015261	0	94.478
New alloy	0.0786	3.991	0.1467	1.6499	0.30864	0.48446	0.1443	0.21648	0.00015019	0	92.979
2024	0-0.1	3.8-4.9	0-0.5	1.2-1.8	0.3-0.9	0-0.5	0-0.15	0-0.24	0	0-0.15	Bal.

Figures

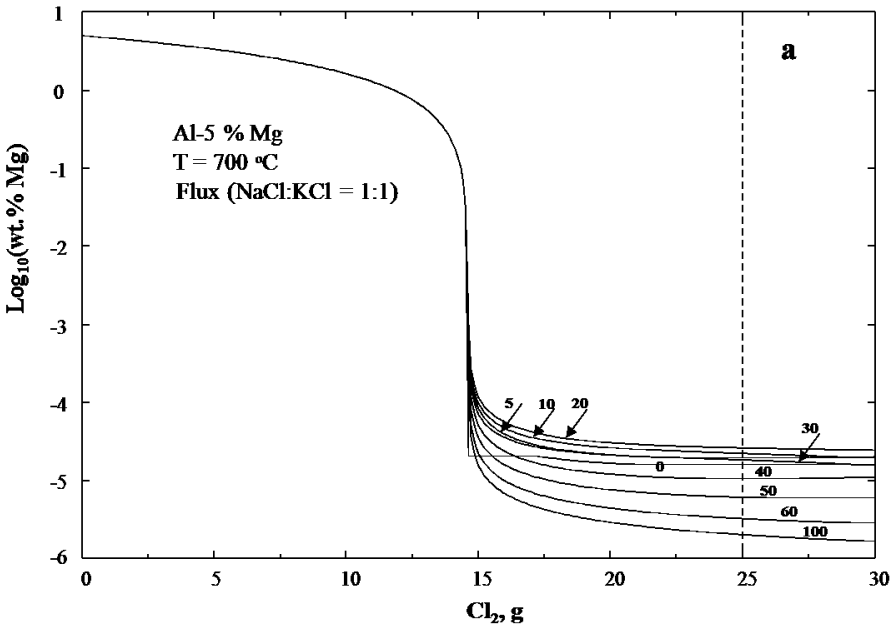
a
Al-5 % Mg
T = 700 °C
Flux (NaCl:KCl = 1:1)
Log10(wt.% Mg)
Cl2, g
5
10
20
30
0
40
50
60
100

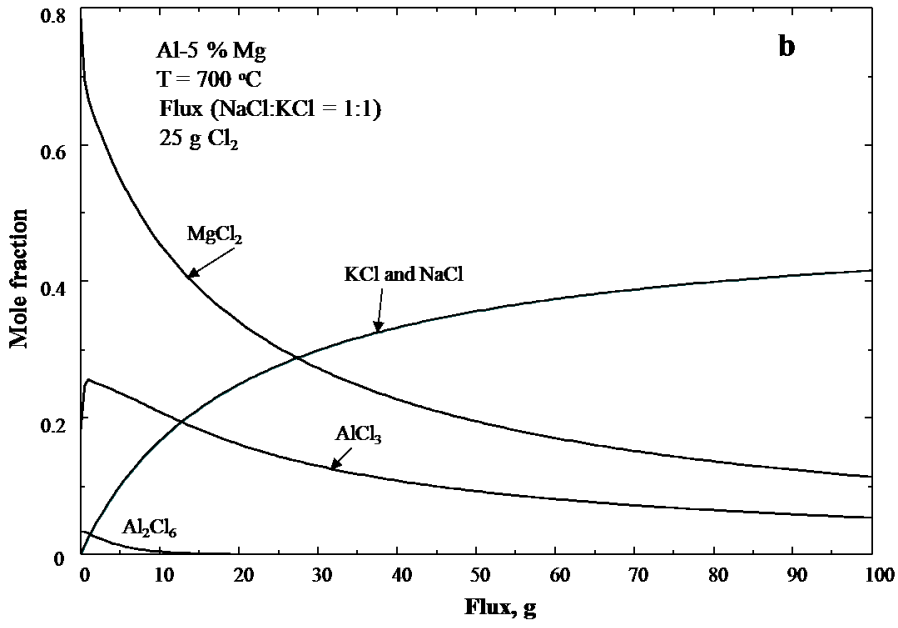
b
Al-5 % Mg
T = 700 °C
Flux (NaCl:KCl = 1:1)
25 g Cl2
Mole fraction
MgCl2
KCl and NaCl
AlCl3
Al2Cl6
Flux, g

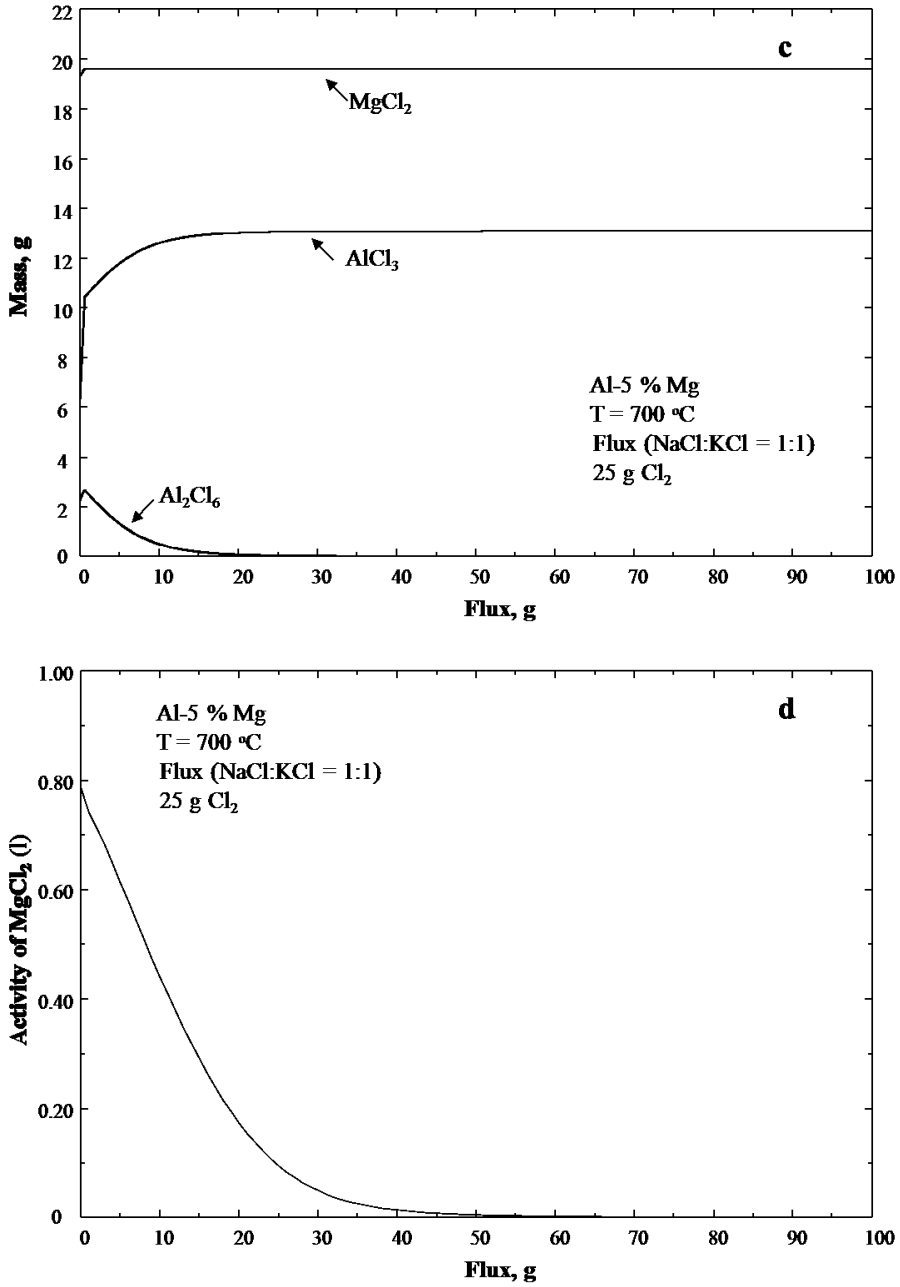

Fig. 12.1.1 (a) The calculated Mg concentration profiles of an Al-5 wt.% Mg alloy reacting with Cl_2 gas under the protection of different amounts of slat. (b) The liquid salt composition profiles of an Al-5 wt.% Mg alloy reacting with 25 g Cl_2 as a function of the protective salt amount. (c) The total amount of $MgCl_2$, $AlCl_3$, and Al_2Cl_6 formed for an Al-5 wt.% Mg alloy reacting with 25 g Cl_2 as a function of the protective salt amount. And (d) calculated $MgCl_2$ activity profile of an Al-5 wt.% Mg alloy reacting with 25 g Cl_2 as a function of the protective slat amount.

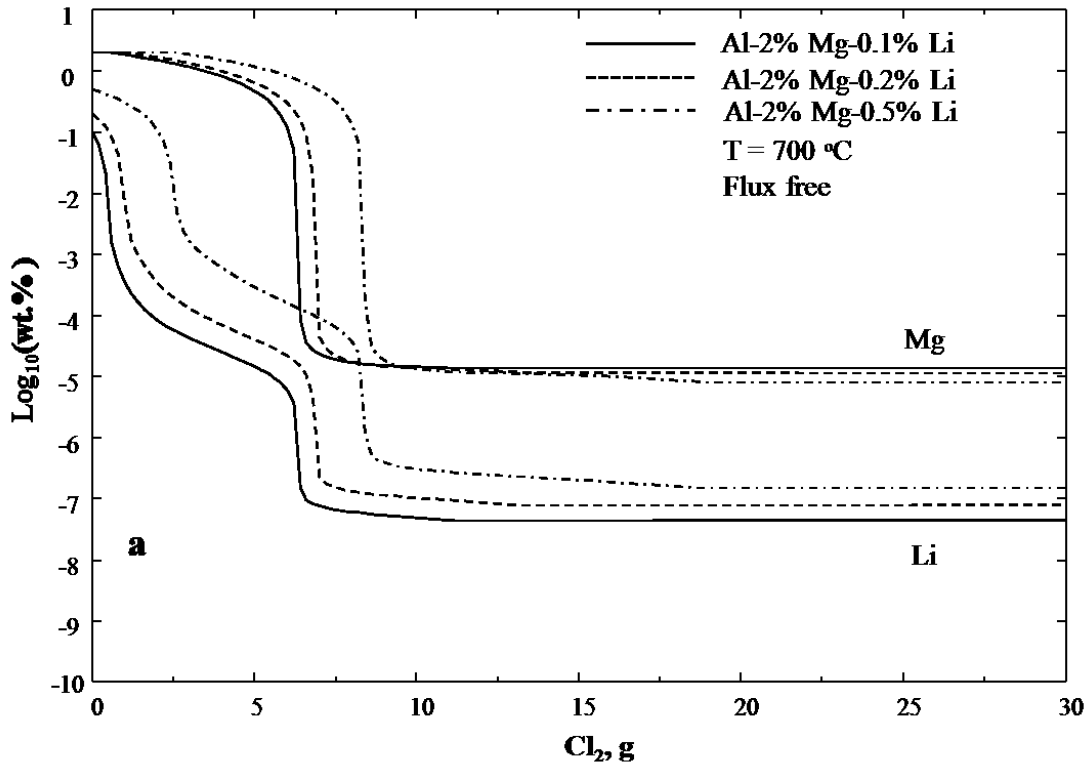
Al-2% Mg-0.1% Li
Al-2% Mg-0.2% Li
Al-2% Mg-0.5% Li
T = 700 °C
Flux free
Mg
Li
a
Log10(wt.%)
Cl2, g

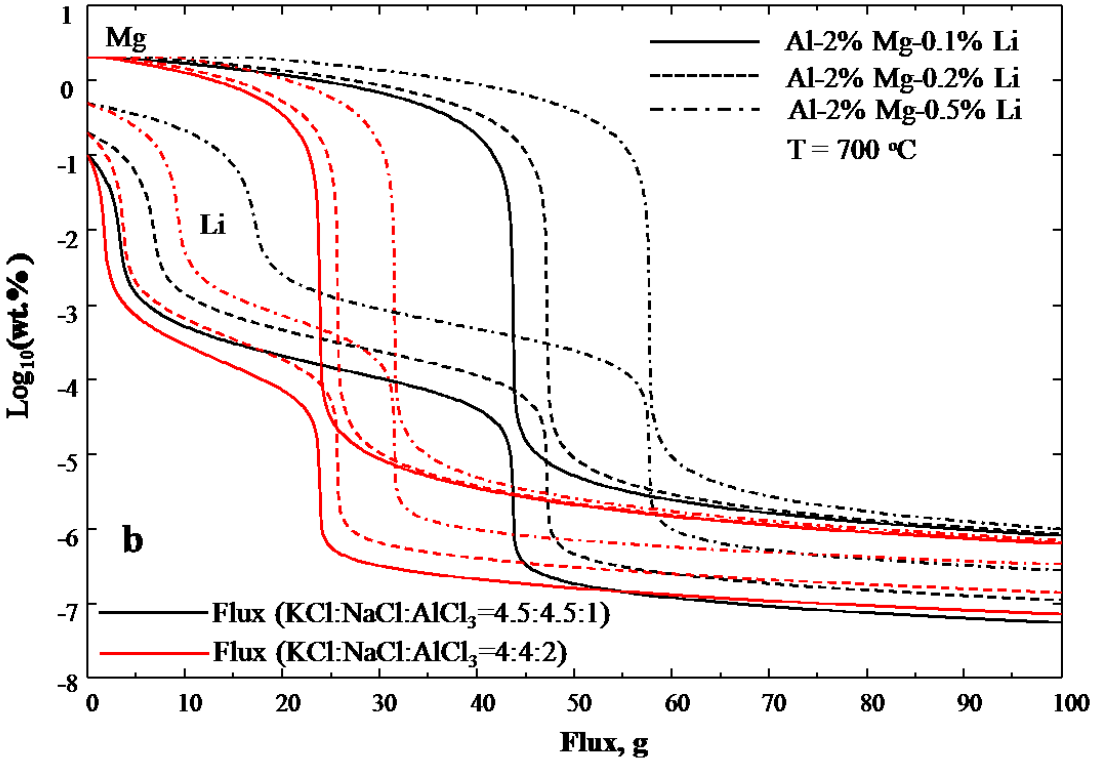
Mg
Li
Al-2% Mg-0.1% Li
Al-2% Mg-0.2% Li
Al-2% Mg-0.5% Li
T = 700 °C
b
Flux (KCl:NaCl:AlCl3=4.5:4.5:1)
Flux (KCl:NaCl:AlCl3=4:4:2)
Log10(wt.%)
Flux, g

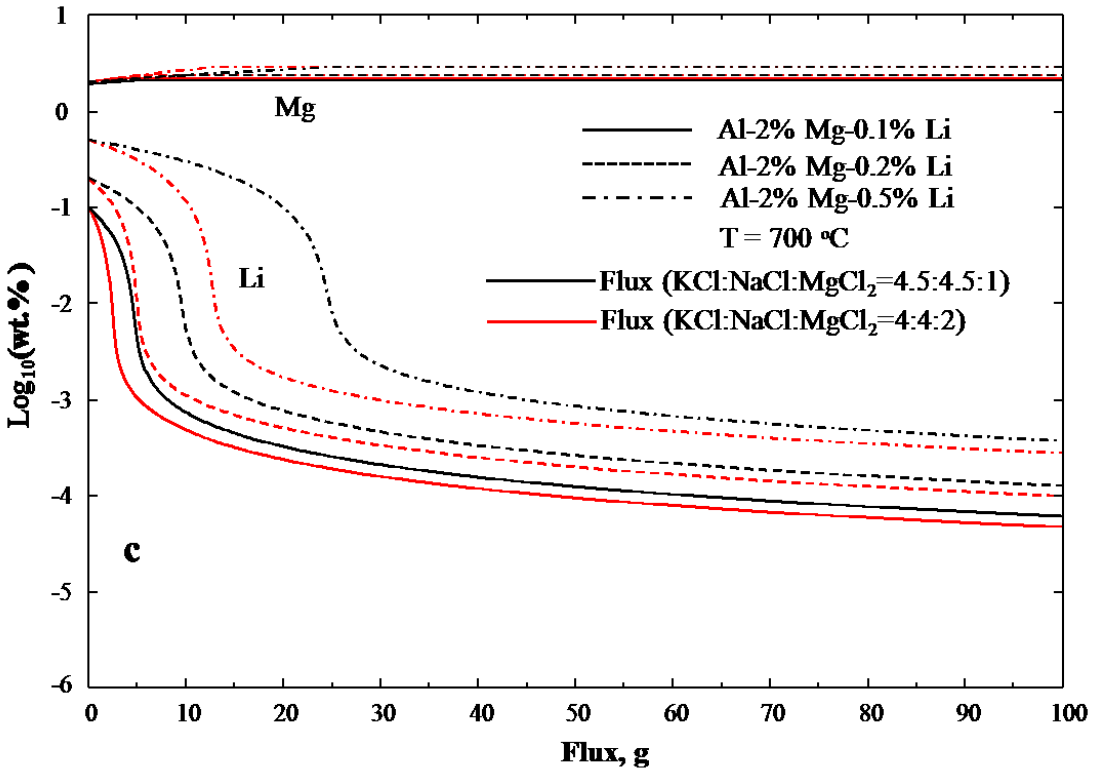

Fig. 12.1.2 The calculated concentration profiles of Li and Mg in 100 g of Al-2 wt.% Mg-0.1 wt.% Li, Al-2 wt.% Mg-0.2 wt.% Li, and Al-2 wt.% Mg-0.5 wt.% Li alloys at 700 °C. (a) As a function of Cl_2 gas amount, (b) as a function of flux (KCl:NaCl:$AlCl_3$=4.5:4.5:1 and KCl:NaCl:$AlCl_3$=4:4:1) amount, and (c) as a function of flux (KCl:NaCl:$MgCl_2$=4.5:4.5:1 and KCl:NaCl:$AlCl_3$=4:4:1) amount.

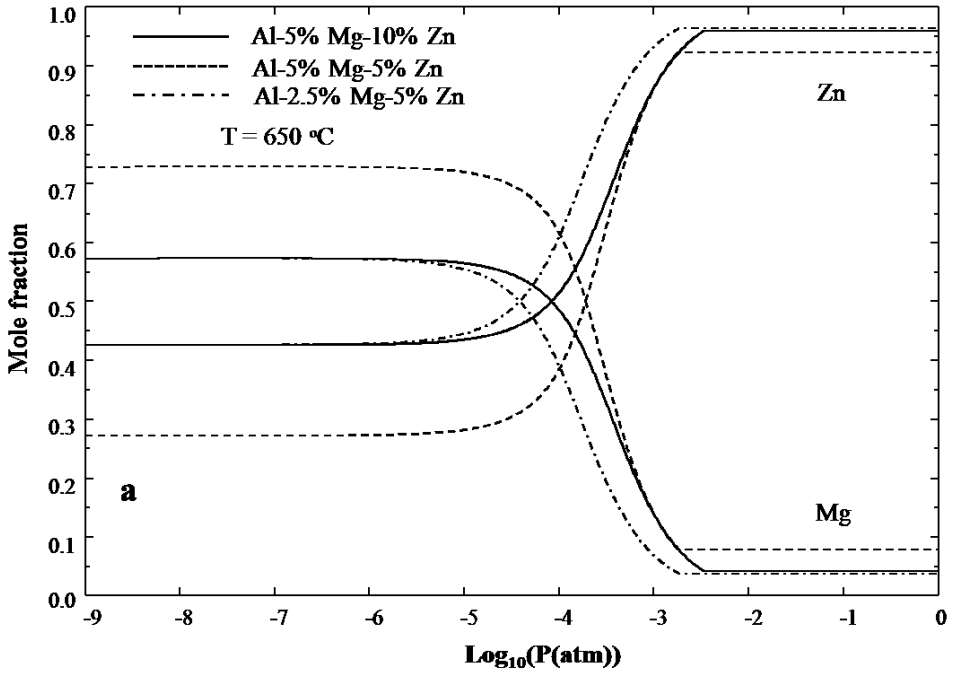
Al-5% Mg-10% Zn
Al-5% Mg-5% Zn
Al-2.5% Mg-5% Zn
T = 650 °C
Zn
Mg
a
Mole fraction
Log10(P(atm))

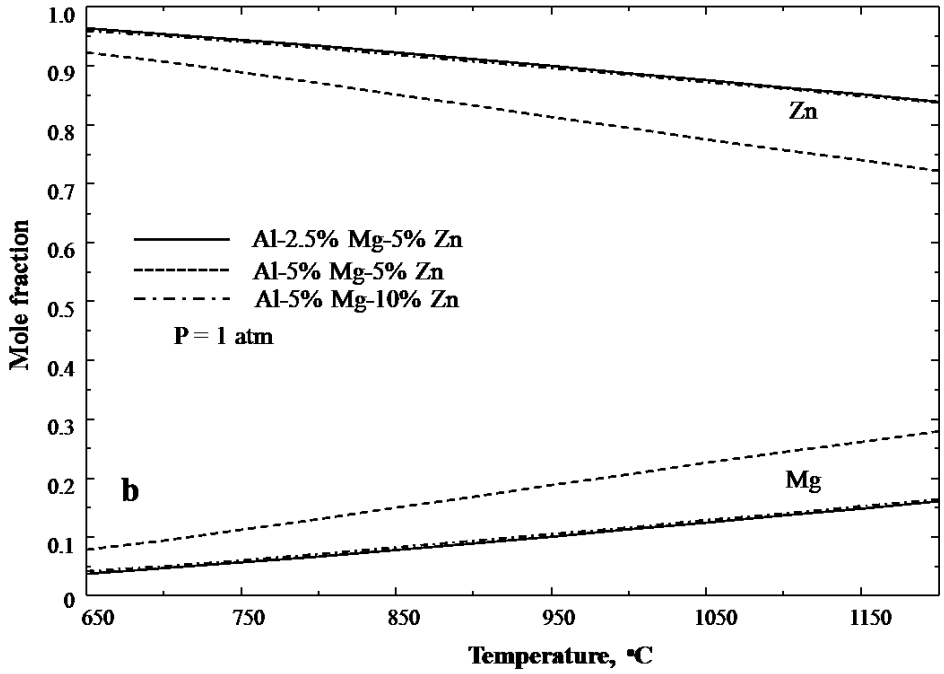
Zn
Al-2.5% Mg-5% Zn
Al-5% Mg-5% Zn
Al-5% Mg-10% Zn
P = 1 atm
Mg
b
Mole fraction
Temperature, °C

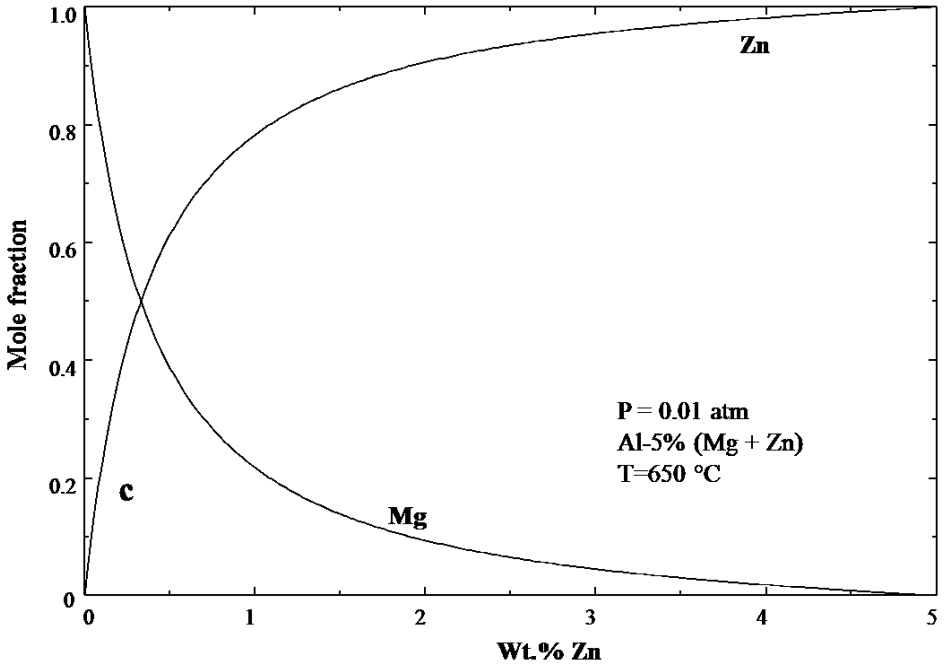

Fig. 12.1.3 The calculated concentration profiles of Zn and Mg in the vapor. (a) As a function of pressure, (b) as a function of temperature, and (c) as a function of Zn concentration in Al melts.

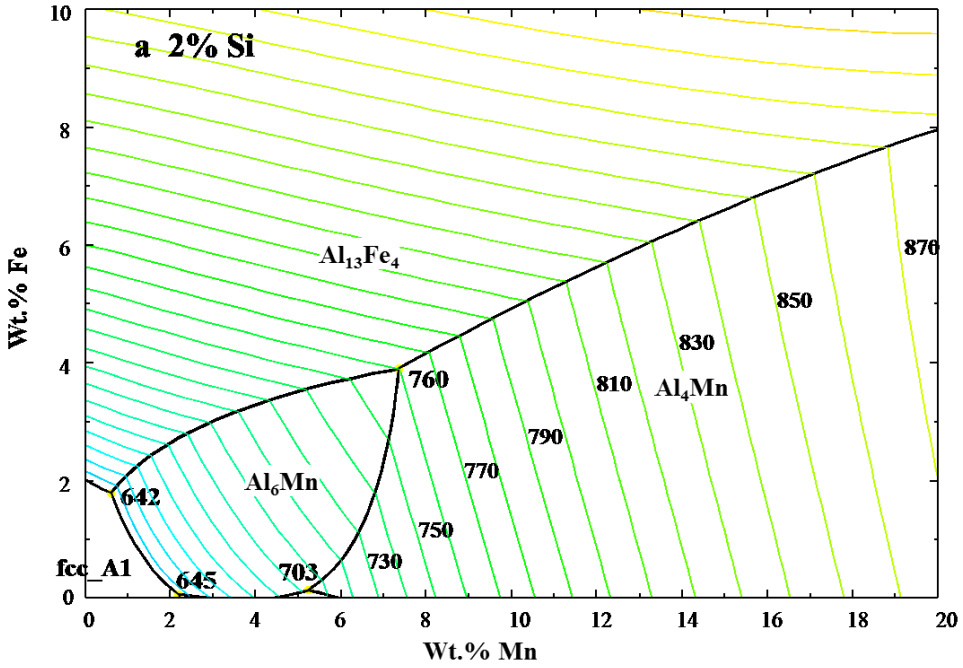
a 2% Si
Wt.% Fe
Wt.% Mn
Al13Fe4
Al6Mn
Al4Mn
fcc_A1
642
645
703
730
750
760
770
790
810
830
850
876

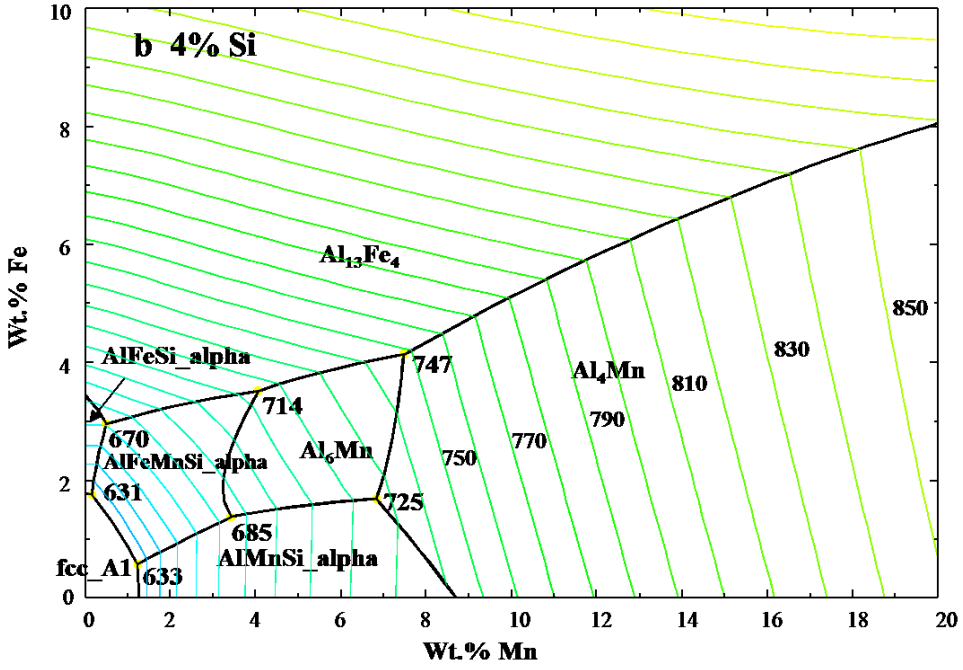
b 4% Si
Wt.% Fe
Wt.% Mn
Al13Fe4
AlFeSi_alpha
AlFeMnSi_alpha
AlMnSi_alpha
Al6Mn
Al4Mn
fcc_A1
670
631
633
685
714
725
747
750
770
790
810
830
850

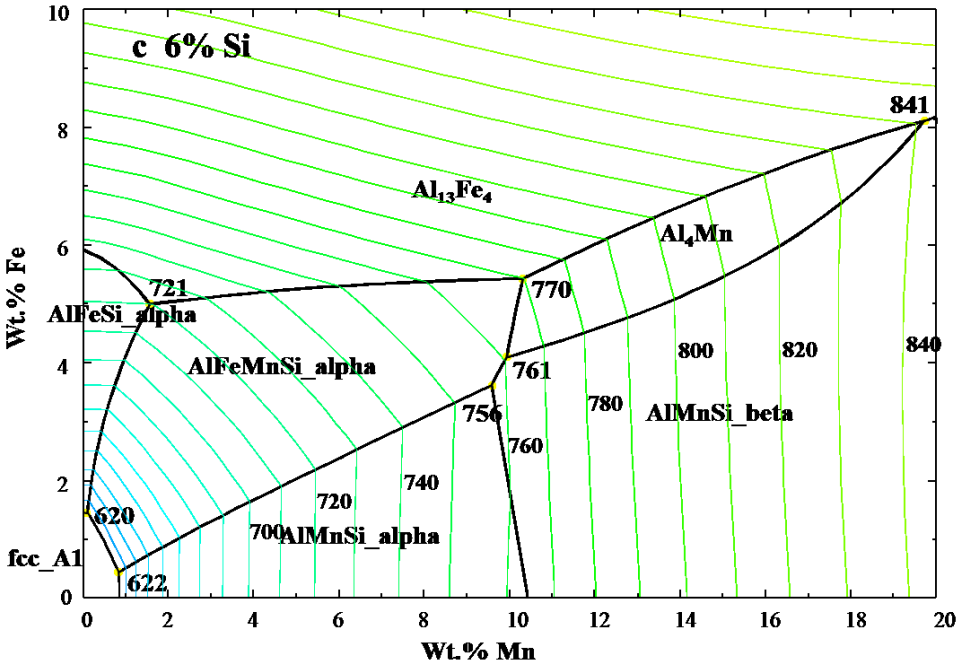

Fig. 12.1.4 The calculated liquidus projection of the Al-Fe-Mn-Si system. (a) With 2 wt. % Si, (b) with 4 wt. % Si, and (c) with 6 wt. % Si.

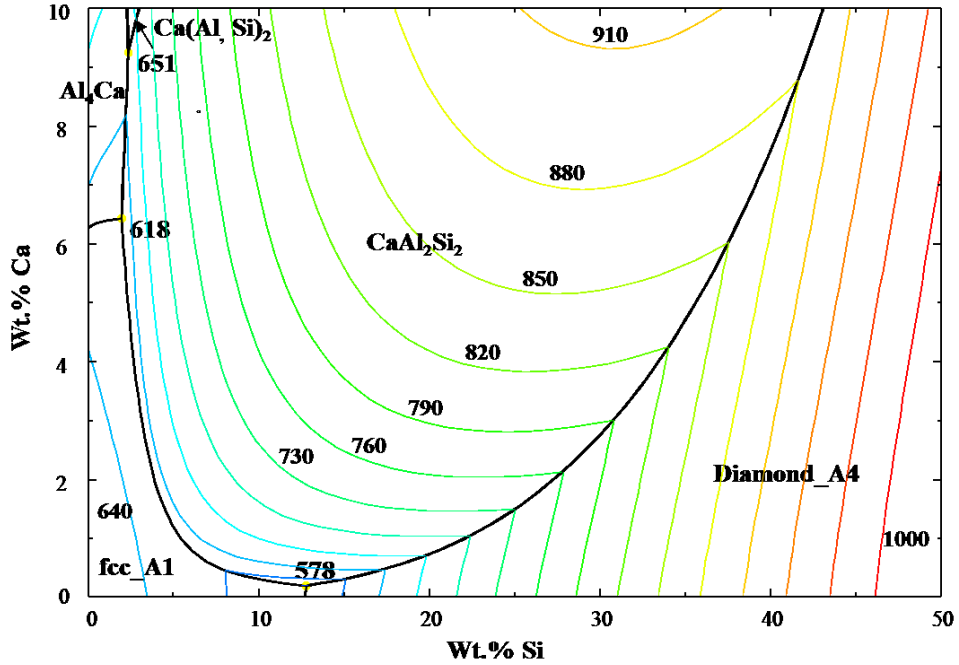

Fig. 12.1.5 The calculated liquidus projection of the Al rich Al-Ca-Si system.

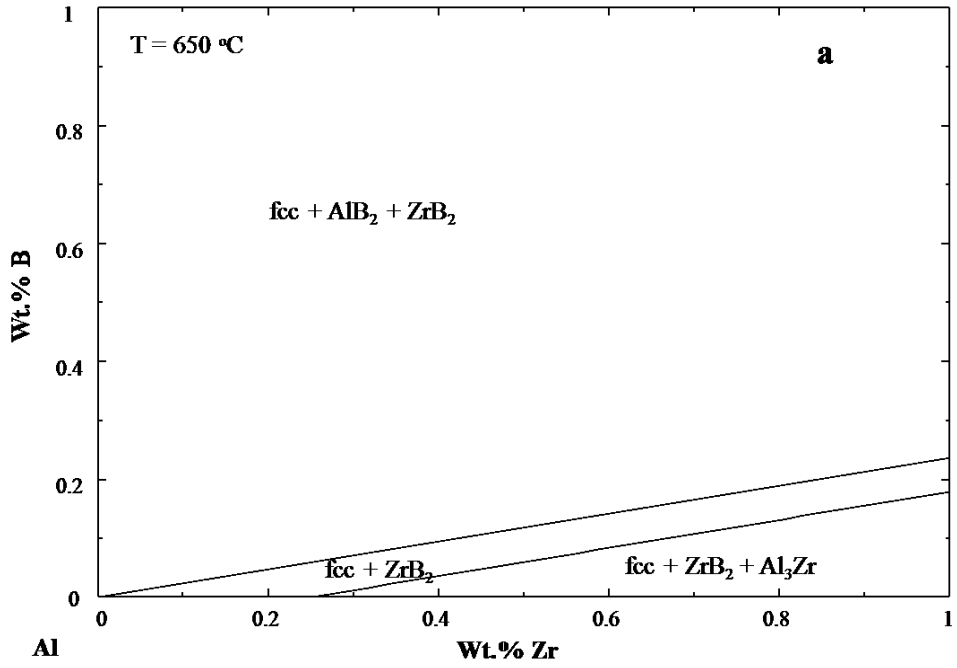
T = 650 °C
a
fcc + AlB2 + ZrB2
fcc + ZrB2
fcc + ZrB2 + Al3Zr
Wt.% B
Wt.% Zr
Al
0
0.2
0.4
0.6
0.8
1

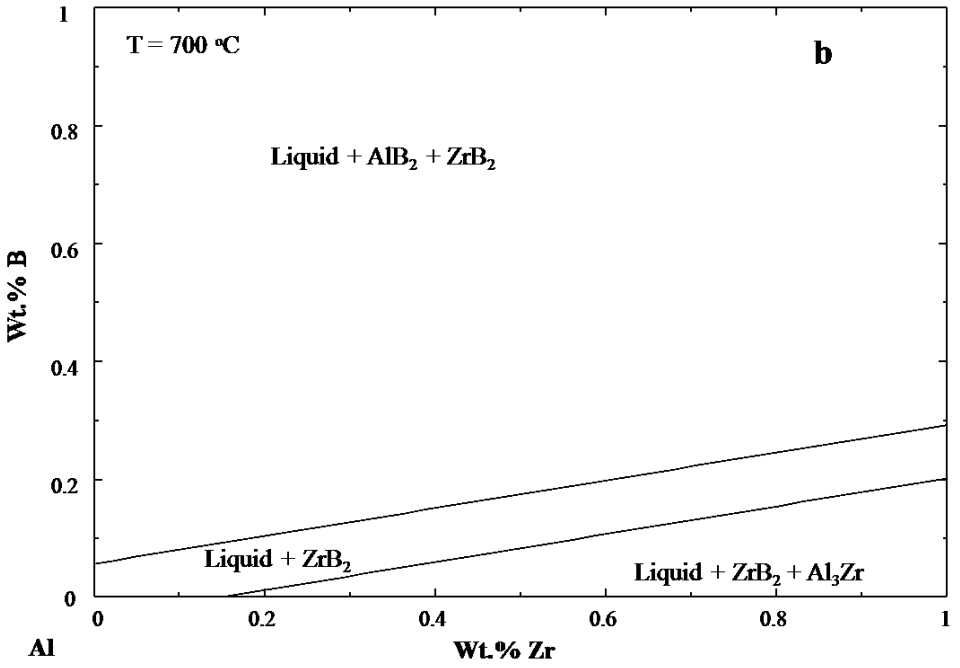
T = 700 °C
b
Liquid + AlB2 + ZrB2
Liquid + ZrB2
Liquid + ZrB2 + Al3Zr
Wt.% B
Wt.% Zr
Al
0
0.2
0.4
0.6
0.8
1

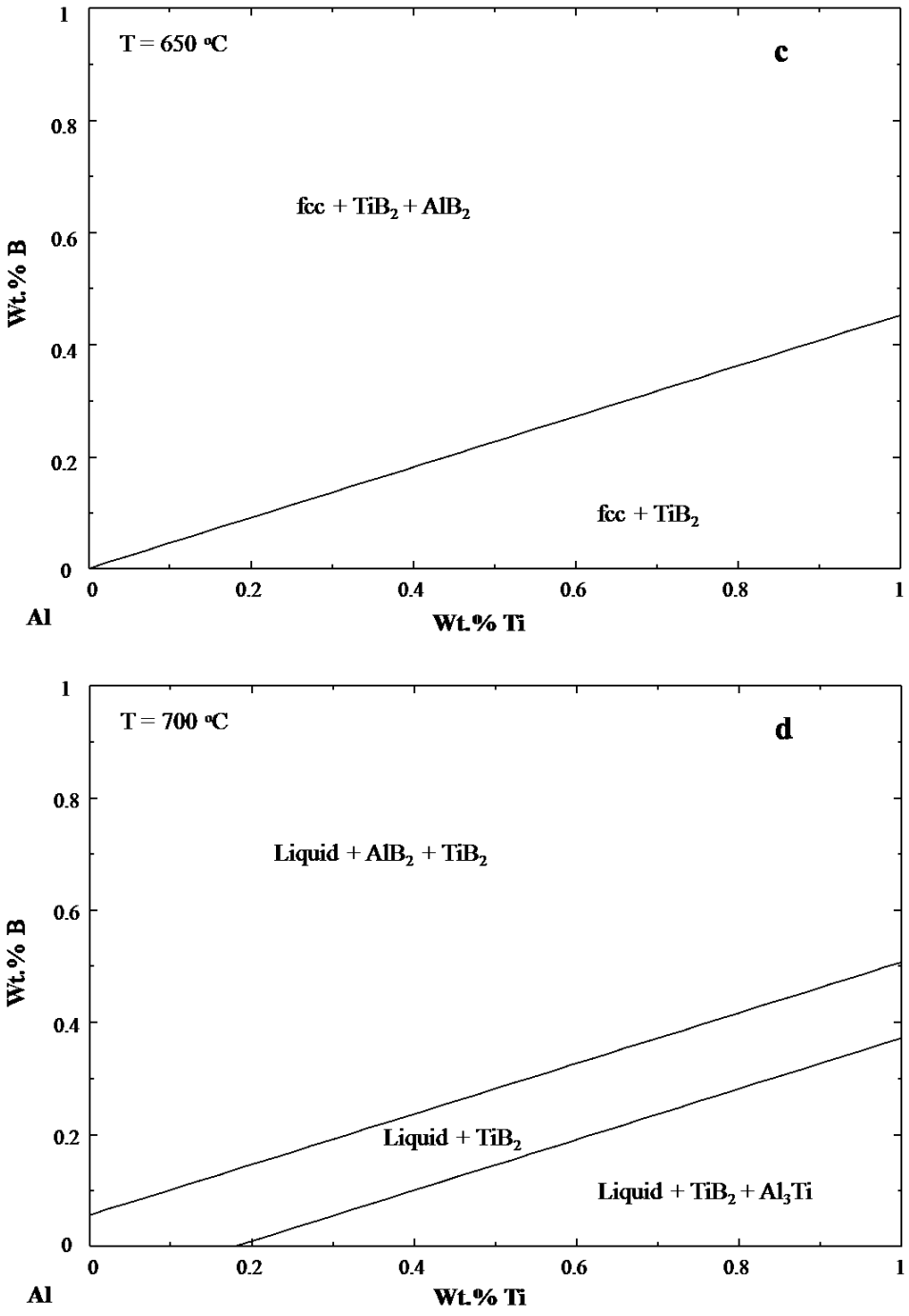

Fig. 12.1.6 The calculated isothermal sections of the Al-Zr-B and Al-Ti-B systems in the Al rich corner. (a) and (b) Isothermal sections of the Al-Zr-B system at 650 °C and 700 °C, respectively, (c) and (d) isothermal sections of the Al-Ti-B system at 650 °C and 700 °C, respectively.

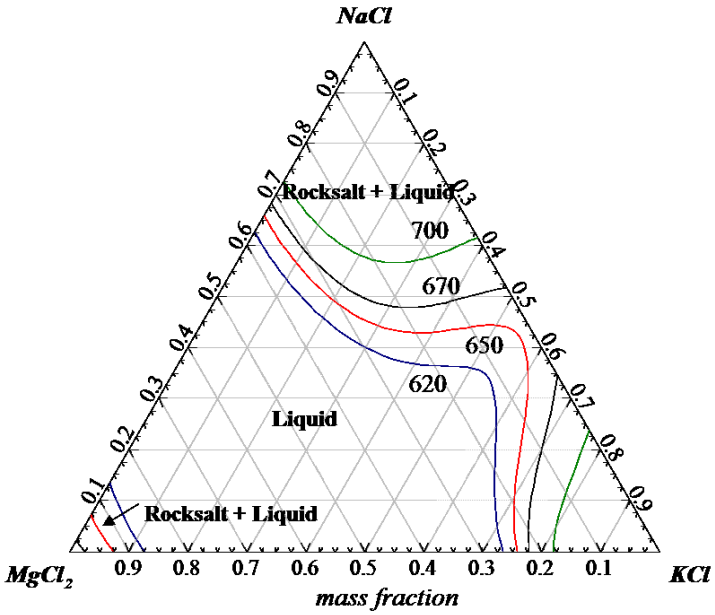

Fig. 12.1.7 The calculated isothermal sections of the NaCl-KCl-$MgCl_2$ system at 620, 650, 670, and 700 °C.

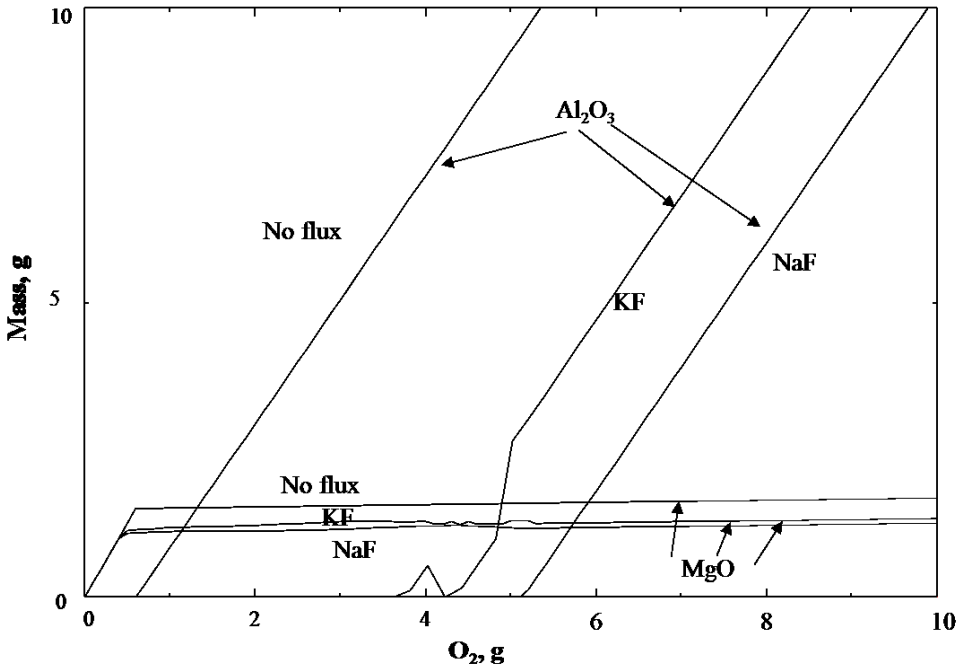

Fig. 12.1.8 The calculated mass of the formed MgO and Al_2O_3 as a function of O_2 amount added to 100 g of the "Mix all" melt covered with 10 g NaCl + 10 g KCl flux, 10 g NaCl + 10 g KCl + 1 g KF, and 10 g NaCl + 10 g KCl + 1 g NaF at 700 °C. (FTPS, FT-oxide, FT-lite, FT-Salt)

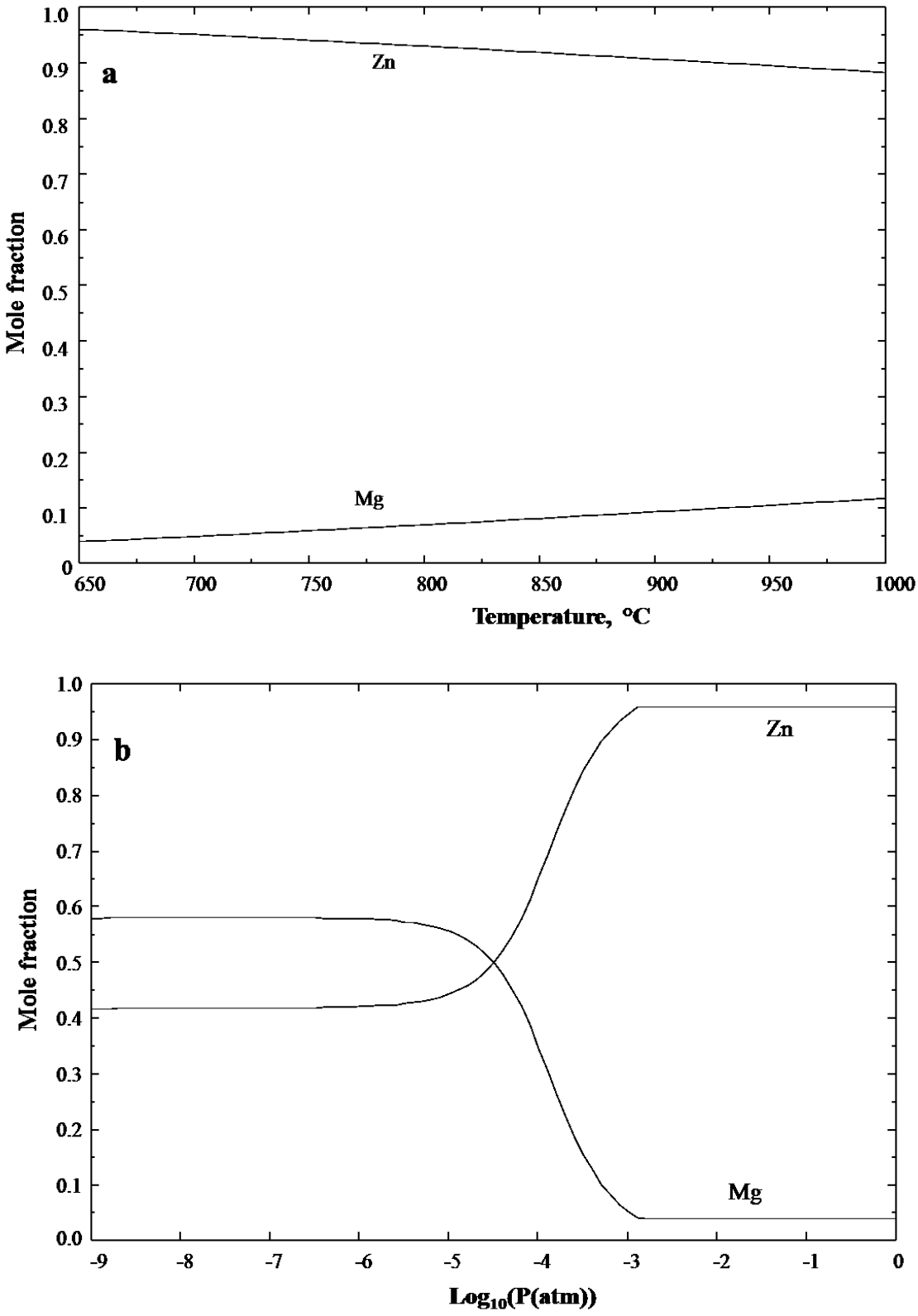

Fig. 12.1.9 The calculated vapor fraction of Mg and Zn of the alloy melt before de-zinc process. (a) As a function of temperature and (b) as a function of pressure.

12.2 Phase fraction diagram calculation for 6xxx series Al alloys

Abstract

Wrought Al alloy products are produced through a sequence of metallurgy and material process: casting, homogenization, extrusion or rolling, and final annealing. From thermodynamic calculation using the accurate and comprehensive thermodynamic database developed in the present study, the evolution of microstructure (especially Al matrix solid solution and various precipitates) can be analyzed depending on alloy composition and temperature. Such calculation results are useful for alloy design and process optimization. Phase fractions of all the possible precipitation phases can form in as-cast, homogenized, and annealed status of the Al-Mg-Si-Cu-Fe-Mn-Cr (6xxx series) alloys were calculated over the technically useful composition range. The solidification calculations for as cast microstructure were carried out using the Scheil-Gulliver calculation. The calculated phase fractions were validated by comparing with the as-cast microstructure of three Al alloy samples. The changes in secondary phase fractions depending on the alloying element in as-cast microstructure were analyzed by thermodynamic calculations. The phase fraction diagrams of all the possible equilibrium precipitation phases at 500 °C were mapped in the composition range of 0-1.1 wt.% Mg and 0-0.7 wt.% Si to investigate the microstructure at homogenization process. The influences of minor elements such as Cu, Fe, Mn, and Cr on the amount of each type of precipitates were also analyzed. In addition, the phase fraction diagram of the Mg_2Si phase at 177 °C was also mapped to understand the microstructure after final annealing process for 6xxx Al alloy. Based on the calculated diagrams, the possible Al alloy design strategy to produce highest strength is discussed.

Key words:

Aluminum alloy; Thermodynamic calculation; Solidification; Alloy design.

12.2.1 Introduction

Al alloys are widely used as the structural part in transportation sector due to their attractive properties, such as high strength, good corrosion resistance, formability, weldability, and low cost. Due to the continuous demands for weight reduction and improvement of fuel efficiency of automobiles, high strength Al extruded profiles of complex shape are needed in the transportation industry. 6xxx Al alloys, in particular 6063, are widely used for extrusion components in the automotive industry.

The as-cast billet of 6xxx series alloys cannot always satisfy the subsequent extrusion process. Due to the harmful precipitates formed during casting. For instance, the size and distribution of Mg_2Si critically determine the extrusion speed, and the grain boundary particles determine the surface finish [1]. Fe is the impurity element presented in 6xxx Al alloys, and Mg and Si are the major alloying elements. Fe impurity forms Fe-bearing intermetallic phases such as $Al_{13}Fe_4$, α_AlFeSi, β_AlFeSi, etc. Since the solubility of Fe in Al solid solution is very low. $Al_{13}Fe_4$ forms only in Al alloys with low Si content [2]. β_AlFeSi phase is highly faceted and poorly bonded to the matrix. This phase has brittleness and abrasive nature, and always forms at the grain boundaries and interdendritic regions during casting. β_AlFeSi is claimed to cause poor ductility and severely reduce the hot workability of Al alloys during extrusion process. The α_AlFeSi phase with compact Chinese script morphology and nonfaceted interface with Al matrix can improve the ductility and extrude-ability of Al alloys. The α_AlFeSi phase is also known to have no pickup defect during extrusion and can improve the properties and surface finish of the final products [3]. The unfavourable β_AlFeSi phase in the commercial 6063 alloys can transform into the less detrimental α_AlFeSi by prolonged heat treatment process [5]. However, the production cost will be increased.

Suitable amount of Cr and Mn has been used to modify the microstructure. Dispersoid phase like Al_7(Cr, Mn) can form during high temperature annealing (400-550 °C), and have strong effect on the recovery, recrystallization, and growth processes further induces a fine grain size. However, the introduction of Mn and Cr in Al alloys containing Si can also dramatically increase

the amount of coarse α_Al(Fe, Mn, Cr)Si phase which induces a rapid decrease of the alloy properties [4].

In the extrusion process, the microstructure of Al alloys is neither the cast microstructure nor the equilibrium microstructure, but a case in between. Recently, Sarafoglou and Haidemenopoulos [6] mapped the phase fractions of Mg_2Si and β_AlFeSi as a function of Mg and Si composition in the solidification microstructure via the CALPHAD (CALculaiton of PHAse Diagram) approach. They discussed only the effect of Mn content on the phase fraction, but the effect of other alloying elements, Fe, Cr, and Cu, on the solidification precipitates and equilibrium precipitates were not investigated. In the present study, systematic analysis for the effect of alloying elements such as Cu, Fe, Mn, and Cr, on both the solidification precipitates and equilibrium precipitates in Al 6xxx series alloys was carried out using the CALPHAD approach.

12.2.2 Methodology

12.2.2.1 Thermodynamic calculations

All the CALPHAD type thermodynamic calculations are carried out using the FactSage software [7]. The thermodynamic database of all the solution and stoichiometric phases related to the Al-Mg-Si-Cu-Fe-Mn-Cr system developed by the present authors is used for the thermodynamic calculations. In the database, all the 21 sub-binary systems were optimized. The thermodynamic descriptions of the Al-Mg system, Mg-Si system, Al-Si system, Cu-Si system, Al-Cu system, Cu-Fe system, Al-Fe system, Fe-Mg system, Fe-Mn system, Mn-Si system, and Mg-Mn system were taken from the previous work conducted by Chartrand [8], Harvey [9], Harvey [9], Kang and Jung [10], Saunders [11], Shubhank et al. [12], Phan et al. [13], Chartrand [14], Paek [15], Paek et al. [16], and Kang et al. [17], respectively. The thermodynamic descriptions of other binary sub-systems, the Al-Cr system [18], Al-Mn system [19], Cu-Cr system [20], Cu-Mg system [21], Cu-Mn system [20], Fe-Cr system [20], Cr-Mg system [18], Cr-Mn system [19], Cr-Si system [22], and Fe-Si system [23], assessed by the current authors were also utilized. The thermodynamic descriptions of the Al-Cu-Cr system [24], Al-Cu-Mg system [21], Al-Cu-Mn system [25], Al-Cu-Si system [21], Al-Cr-Mg system [18], Al-Cr-Mn system [19], Al-Cr-Si system [22], Cu-Fe-Cr

system [20], Cu-Mg-Si system [21], Cu-Fe-Mn system [20], Fe-Mg-Si system [26], Fe-Cr-Si system [26], and Al-Cu-Mg-Si system [21] assessed by the current authors were also integrated in the database. The Al-Fe-Si system assessed by Paek [27], Al-Fe-Mn system by Kim and Kang [28], Al-Mg-Si system by Harvey [9], Al-Mg-Mn system by Shukla and Pelton [29], Fe-Si-Mn system by Paek [30], and Al-Mn-Si system by Paek [31] were taken into account in the thermodynamic database. Other ternary and quaternary systems were treated as ideal systems. The major phases in 6xxx series Al alloys like the liquid phase, fcc_A1, $Al_{14}Fe_3$, α_AlFeSi, β_AlFeSi, α_AlMnSi, β_AlMnSi, Mg_2Si, Al_2Cu, Si, Q ($Al_3Cu_2Mg_9Si_7$), Al_7Cr, etc., are all available in the database.

The solidification calculations were carried out under the Scheil-Gulliver assumption. In this calculation, the diffusivities of alloying elements in the solid phases are assumed to be zero, and the diffusivities of alloying elements in the liquid phase are assumed to be infinite. This assumption has a certain rationality since the diffusivities of alloying elements in the liquid phase are several order larger than those in the solid state. Equilibrium phase fractions of precipitates were also calculated at 500 °C and 177 °C to represent the homogenization and final annealing stage, respectively.

12.2.2.2 Experimental procedure

Three Al alloys with their nominal compositions are listed in Table 12.2.1. The main difference from the original Al 6063 is the addition of Cr for Al_7Cr formation, change in Mg for Mg_2Si formation, and Cu for Al_2Cu formation. Billet casting (Sapa, Canada) was performed to prepare as cast billet. The diameter of the billet was 200 mm and the cooling rate was 20 K/s. The billet was cut perpendicular to the casting direction. Specimen with a size of one cubic centimeter was cut at the half distance from the surface to the center of the billet, grinded with SiC papers, and then polished with 3 μm and 1 μm diamond paste. All the intermetallic phases were characterized using scanning electron microscopy (SEM) and energy dispersive X-ray spectroscopy (EDS) analysis. The volume fractions of the precipitates were measured by using image analysis software ImageJ [32].

12.2.3 Results and discussions

12.2.3.1 Validation of the thermodynamic database

In order to validate the present thermodynamic database for the application to 6xxx series Al alloys, the calculated solidification phase fractions were compared with the experimentally measured data.

The calculated solidification path of the typical 6063 alloy is presented in Fig. 12.2.1(a). As can be seen from the diagram, the precipitation sequence is fcc_A1 → $Al_{14}Fe_3$ → α_AlFeSi → β_AlFeSi → Mg_2Si → $Al_8FeMg_3Si_6$ (π) → Si → Q. The solidification starts at 654 °C and ends at 512 °C. The mass of the precipitate phase as a function of the total mass percent of solid (that is, the degree of the completion of solidification) is shown in Fig. 12.2.1(b). The $Al_{14}Fe_3$ phase begins to form at 89.7 percent of solidification and reaches its maximum at 91.2 percent of solidification when α_AlFeSi phase begins to form. At 99.4 percent of solidification, β_AlFeSi starts to form. Following the formation of β_AlFeSi, the Mg_2Si, $Al_8FeMg_3Si_6$ phases, and Si form, and finish at the final eutectic reaction temperature 512 °C. The final eutectic reaction is L → fcc_A1 + Al_2Cu + Si + $Al_8FeMg_3Si_6$ + Q.

The calculated phase fractions in the as-cast microstructure are listed in Table 12.2.2. It is obvious that the precipitates cannot form if there is no segregation in the liquid phase during solidification. The calculated liquid composition as a function of solidification is shown in Fig. 12.2.1(c). The compositions of Mg, Si, and Fe show strong segregation in the liquid phase during the solidification process. It can be seen from the diagram that all the other precipitates except for the fcc_A1 phase only start to form when the solidification reaches almost 90 percent where the liquid phase is enriched with Mg, Si, and Fe.

Similar to the 6063 alloy, the simulated solidification paths of the three as-cast alloys are all presented in Fig. 12.2.2. The precipitation sequences of these three alloys are quite similar. The Cr containing alloys (Alloy 1 and 3) show Al_7Cr formation before the fcc_A1 matrix phase. As

shown in Table 12.2.2, the amounts of Q, Al_2Cu, and Mg_2Si in the three alloys are calculated apparently higher than those of 6063 alloy.

Fig. 12.2.3 shows the microstructure of the three cast alloys. Fig. 12.2.3(a) is the back scatter micrograph of alloy 1. The Chinese script shaped α_AlFeSi, very narrow needle like β_AlFeSi, and spherical shaped Q phase are detected. Similar microstructure can be seen in Fig. 12.2.3(b) and Fig. 12.2.3(c) for alloy 2 and 3, respectively. It worth note that the $Al_8FeMg_3Si_6$ particle with the same shape as Q phase was also observed in alloy 3. Other phases were not marked since the particles are very small. It worth note that the primary Al_7Cr phase was not clearly observed in the micrograph shown in Fig. 12.2.3. However, a lot of fine particles rich in Cr were detected in the Al matrix in the enlarged image of alloy 1 (Fig. 12.2.3(d)). The precipitates excerpt α_AlFeSi, β_AlFeSi, and Q were not detected under SEM in the present study. Most probably, the size of the precipitates is too fine to be detected. ImagJ software was utilized to analyze the area fraction of the precipitates in Figs. 12.2.3(a) to (c). A large area is considered during the image analysis to give a reasonable representation of the microstructure. Since it was difficult to separate the bright phases α_AlFeSi, β_AlFeSi, and Q, a total area of precipitates was measured. The volume fraction was calculated from the area fraction assuming particles are spherical. The measured total volume fraction of Q, $Al_8FeMg_3Si_6$, α_AlFeSi, and β_AlFeSi are listed in Table 12.2.3 compared with the Scheil simulation results. In the Scheil simulation results, only Q, $Al_8FeMg_3Si_6$, α_AlFeSi, and β_AlFeSi were computed for the comparison. Molar volume of all the phases were assumed to be the same. It can be seen from Table 12.2.3 that the experimental values are quite close to the simulation results.

12.2.3.2 Effect of alloying elements on the solidification microstructure

In order to investigate the effect of major alloying elements on the as-cast microstructure, Scheil calculation was performed to compute the amounts of each type of precipitate by changing the composition of each element from the baseline alloy composition of Al 6063. It is obvious that the current calculation cannot explore the whole composition matrix, but a general trend can be explored. This calculation results can give some guidance for Al alloy design.

All the computed results are shown in Fig. 12.2.4. It can be seen from Fig. 12.2.4(a) that Cr can effectively induce the formation of Al_7Cr as it reaches near 0.1 wt.%. Although there is slight increase in the weight fractions of α_AlFeSi, β_AlFeSi, Mg_2Si, Si, and $Al_8FeMg_3Si_6$, and slight decrease in the fraction of $Al_{14}Fe_3$, Al_2Cu, Al_4(Cr, Mn), $Al_{28}Cu_4Mn_7$, and Q, they are less significant. Fig. 12.2.4(b) shows the effect of Cu. The weight fraction of Cu bearing phase such as Al_2Cu, $Al_{28}Cu_4Mn_7$, and Q phases increases with the increasing Cu content. Since the formation of Q phase substantially consumes Si, the amounts of Mg_2Si and Si decrease with Cu content. Other phases like α_AlFeSi, β_AlFeSi, Al_4(Cr, Mn), $Al_8FeMg_3Si_6$, and $Al_{13}Fe_4$ show no significant difference. As can be seen in Fig. 12.2.4(c), β_AlFeSi is forming as soon as the Fe addition to the alloy system. When the amount of β_AlFeSi reaches 0.15 wt.%, α_AlFeSi begins to form. It is at 0.283 wt.% α_AlFeSi when the $Al_{13}Fe_4$ initiates to form because there is no Si available. The amounts of other phases show little difference with Fe content. The change in Mg content varies the precipitates in a more complex manner. According to the calculation in Fig. 12.2.4(d), the amount of α_AlFeSi first increases and then decreases till 0.9 wt.% of Mg. The amount of $Al_{14}Fe_3$ increases till Mg content increase to 0.9 wt.% and then starts to decrease. The amounts of β_AlFeSi, Al_4(Mn, Cr), and Si decrease as Mg content increases. On the other hand, the amounts of Al_2Cu, Mg_2Si, $Al_{28}Cu_4Mn_7$, and Q increase. The amount of $Al_8FeMg_3Si_6$ firstly decreases and then increases with increasing Mg content. According to the current calculation in Fig. 12.2.4(e), Mn has only slight influence on the amounts of different precipitates. With the increasing Si content, the amount of $Al_{14}Fe_3$ dramatically decreases due to the increased formations of α_AlFeSi, β_AlFeSi, Q, and $Al_8FeMg_3Si_6$. However, when the Si content reaches 0.45 wt.%, the α_AlFeSi amount starts to decrease because the composition of the alloy shifts to the β_AlFeSi phase region. The rest of phases show little changes with Si contents.

The calculation results are summarized in Table 12.2.4. In Table 12.2.4, increase of phase amount is indicated by “↑” and decrease is indicated by “↓”. As discussed above, the change of phase amount is not always straightforward due to the interplay of the alloying elements for the formation of different precipitates. With the help of Table 12.2.4, one can select the suitable alloy composition which can give the desired as-cast microstructure.

12.2.3.3 Equilibrium alloy phase fraction map

The equilibrium phase distribution of Al 6063 alloy is calculated in Fig. 12.2.5. Various precipitate phases are calculated. At high temperature, $Al_{13}Fe_4$, α_AlFeSi, and β_AlFeSi are formed first. Then, $Al_{13}Fe_4$ and α_AlFeSi are dissolved as temperature decrease, and $Al_8FeMg_3Si_6$ and Mg_2Si are forming. At low temperature, $Al_{12}Mn$, α_AlMnSi, and Al_2Cu are forming. This equilibrium phase distribution calculation can give an idea for the homogenization temperature. Unfortunately, there is no temperature region to completely dissolve precipitates in this case. Theoretically, in order to get rid of the harmful β_AlFeSi phase and minimize the precipitates, homogenization can be carried out at 590 to 610 °C. But this is too close to the melting temperature. Therefore, 460 to 500 °C can be taken as the homogenization temperature to reduce the amount of precipitates from as-cast microstructure. The amount of total precipitates of Al 6063 alloy is calculated to be about 0.87 wt.% as listed in Table 12.2.2. This can be reduced in the homogenization treatment.

The suitable extrusion temperature should be lower than the homogenization temperature, but it also requires relative low precipitate amount and high temperature for a fast diffusion for the alloying element. In this case it can be between 450 and 500 °C.

In the current work, equilibrium phase fractions of precipitate phases at 500 °C (the possible homogenization and extrusion temperature) were mapped in the composition range of 0-0.7 wt.% Si and 0-1.1 wt.% Mg. The effect of Cu, Fe, Mn, and Cr on the precipitate amounts was also investigated. Fig. 12.2.6(a) presents the calculated phase diagram of Al-Mg-Si alloy with 0.05 wt.% Cu, 0.15 wt.% Fe, and 0.03 wt.% Mn at 500 °C. The equilibrium phases at a given composition can be directly read from the diagram. The stable phase region of each equilibrium phase can be defined by its zero phase fraction lines. According to this concept, the phase diagram can be divided into 5 parts, as shown in Fig. 12.2.6(b). The red line to the up-right corner of the diagram named as region 1 is the Mg_2Si formation region. The green line to the top of the diagram named as region 2 where the $Al_8FeMg_3Si_6$ forms. Above the blue line is the β_AlFeSi phase formation region, named as region 3. The α_AlFeSi phase is only stable between the two orange lines (region 4), and the $Al_{14}Fe_3$ phase forms below the black line (named as region 5). In the

present study, the phase fraction of each precipitate was calculated according to the five phase areas.

Four series of phase fraction maps were calculated at 500 °C to show the effects of Cr, Cu, Fe, and Mn on the phase fraction of each precipitate phase. Fig. 12.2.7 shows the effect of Cr on the different precipitate phases. The Cr concentrations of 0.02 wt.% and 0.20 wt.% were used in the calculation, and the concentrations of Cu, Fe, and Mn were fixed to 0.05, 0.15, and 0.03 wt.%, respectively. The amount of $Al_{13}Fe_4$ decreases as Si content increases. The amount of $Al_8FeMg_3Si_6$ increases as the Si content increases. At the constant Si content, $Al_8FeMg_3Si_6$ shows the maximum amount at around 0.8 wt.% Mg. Mg_2Si increases when both the Mg and Si contents increase. The amount of α_AlFeSi firstly increases as Si content increases and then decreases with Si content. The amount of β_AlFeSi in region 3 increases with the increasing Si content, but when region 3 is overlapping with region 2, the amount of β_AlFeSi keeps decreasing due to the formation of $Al_8FeMg_3Si_6$. As shown in Fig. 12.2.7, Cr can effectively decrease the amount of $Al_{13}Fe_4$ and increase the amounts of Mg_2Si and $Al_8FeMg_3Si_6$. Besides, Cr can increase the amount of α_AlFeSi in the low Si region and decrease in the high Si region. The amount of β_AlFeSi will increase with Cr except for the part overlapped with region 2. Besides, the addition of Cr can induce the precipitation of Al_7Cr in the entire composition area as can be seen in Fig. 12.2.7(f). Fig. 12.2.8 shows the influence of Cu on the precipitates. Cu content was changed from 0.05 to 0.15 wt.%. As can be seen in the figure, Cu has nearly no influence to the precipitate amount. Fig. 12.2.9 shows the effect of Fe to the precipitates. The contents of $Al_{13}Fe_4$, α_AlFeSi, and β_AlFeSi can be substantially increased with the increased Fe content, while that of the $Al_8FeMg_3Si_6$ phase can be decreased. As shown in Fig. 12.2.9(c), the amount of Mg_2Si can be increased in the Si rich region and decreased in the Mg rich region. Fig. 12.2.10 compares the calculation results of 0.03 wt.% Mn with 0.1 wt.% Mn. The amounts of $Al_{13}Fe_4$, Mg_2Si, $Al_8FeMg_3Si_6$, α_AlFeSi, and β_AlFeSi change slightly but negligible with the variation of Mn. At 0.1 wt.% Mn, the $Al_{12}Mn$ phase becomes stable in the entire composition range investigated.

12.2.3.4 Discussion

From the above equilibrium and Scheil solidification calculations, the effect of major alloying elements on the as-cast and equilibrium microstructure can be understood. This information can be very helpful in new alloy design.

In the extrusion process, for example, the amount of β_AlFeSi is considered as a major constraint due to its brittle feature. In order to minimize the harmful effect of β_AlFeSi, we can choose suitable alloy composition to control the as-cast and equilibrium amount of β_AlFeSi, and employ the homogenization temperature to let the β_AlFeSi transform to α_AlFeSi. According to Table 12.2.4, increasing Mg contents and decreasing the contents of Si and Fe can effectively decrease the amount of β_AlFeSi in as-cast microstructure. On the other hand, the equilibrium amount of β_AlFeSi at 500 °C can be reduced by increasing Cu and decreasing Cr, Fe, Mn, and Si. An alternative way is to choose suitable homogenization procedure. For example, the β_AlFeSi phase can completely transform into α_AlFeSi, if the alloy is homogenized at 590 °C (much higher than the conventional homogenization temperature at about 500 °C) for a certain time as can be seen in Fig. 12.2.5. But this is impractical.

Another important issue considered in high strength 6xxx series alloy design is the formation of maximum amount of Mg_2Si at the precipitation temperature. The equilibrium amount of Mg_2Si can be the indication of the ability of precipitation hardening by metastable β' and β" phases which can be transformed to Mg_2Si by prolonged heat treatment. The Mg_2Si phase already formed before final heat treatment cannot be effective for precipitation hardening. Therefore, the difference of Mg_2Si amount between the heat treatment temperature and extrusion/homogenization temperature can be a useful indicator for the precipitation hardening ability. In the present study, 177 °C which is the typical annealing temperature of Al 6063 alloys was used for annealing calculation. The equilibrium amount of Mg_2Si of Al-Mg-Si alloys with constant 0.02Cr-0.05Cu-0.15Fe-0.03Mn content at 177 °C is calculated in Fig. 12.2.11. According the calculation results, the Mg_2Si phase has its maximum amounts along the Mg/Si ratio 1.731:1. Addition of Mg can not increase the amount of Mg_2Si, and the addition of Si can decrease the amount of Mg_2Si formation. The red line indicates the limit composition for the Mg_2Si formation at 500 °C, and the blue line indicates the zero phase fraction line of $Al_8FeMg_3Si_6$ at 500 °C where the β_AlFeSi phase fraction begins to decrease rapidly. The green colored rectangular indicates the alloy composition range of

commercial 6063 alloy which is close to the Mg/Si ratio of 1.731:1. Even though in the composition range there will be a certain amount of Mg_2Si (<0.47 wt.%) formation at the homogenization temperature, the ability of precipitation hardening is still not significantly decreased. If the Mg/Si ratio changes to 1:1 which indicates excess of Si, the ability of Mg_2Si formation shows a certain decrease compared to Mg/Si ratio of 1.731:1 at 177 °C. However, as there is no Mg_2Si formation along the 1:1 ratio line at 500 °C, Al alloy with Mg/Si ratio of 1:1 can still produce a large amount of β' and β" precipitation hardening phase as indicated by Gupta et al. [33].

Considering the minimization of the β_AlFeSi phase and reasonably low amount of the $Al_8FeMg_3Si_6$ phase at extrusion/homogenization temperature (500 °C), and maximum amount of precipitation hardening ability at 177 °C, the most optimum alloy composition range can be suggested as shown in the hatched area in Fig. 12.2.11. Of course, the annealing time for the maximum precipitation hardening should be optimized by experiment. In addition, the effect of solutes, Mg, Si, Cu, and Mn on the extrusion flow behavior and solid solution hardening should be further considered to narrow down the alloy composition. The addition of Cr should be beneficial for the reduction of grain growth during and after extrusion.

12.2.4 Summary

In the current work, a newly developed thermodynamic database for Al alloys has been used for the comprehensive thermodynamic analysis for Al 6xxx alloy development. Influence of various alloying elements such as Fe, Mn, Cu, and Cr on the precipitate formation in the Al-Mg-Si alloy was calculated using the Scheil cooling calculation for as-cast microstructure analysis and using equilibrium calculation for homogenization at 500 °C and final heat treatment at 177 °C. The iso-phase fraction contour maps for various precipitates were generated to show the summary of the effect of different alloying elements. Based on the thermodynamic analysis, the most optimum alloy composition for high strength Al 6xxx alloy is suggested for new alloy development.

Acknowledgement

The authors would like to thank the financial support from NSERC-Automotive Partnership Canada program in Canada. Senlin Cui would also like to thank the McGill Engineering Doctorate Award (MEDA) from McGill University for financial support.

References

1. Abdel-Aziz, A.E.-H.K., A.A. Vertman, and A.M. Samarin, *Thermochemistry of Fe and Ni melts.* Izv. Akad. Nauk SSSR, Met., 1966(3): p. 19-30.
2. Ji, S., W. Yang, F. Gao, D. Watson, and Z. Fan, *Effect of iron on the microstructure and mechanical property of Al-Mg-Si-Mn and Al-Mg-Si diecast alloys.* Mater. Sci. Eng., A, 2013. **564**: p. 130-139.
3. Couto, K.B.S., S.R. Claves, W.H. Van Geertruyden, W.Z. Misiolek, and M. Goncalves, *Effects of homogenisation treatment on microstructure and hot ductility of aluminium alloy 6063.* Mater. Sci. Technol., 2005. **21**(2): p. 263-268.
4. Han, Y., K. Ma, L. Li, W. Chen, and H. Nagaumi, *Study on microstructure and mechanical properties of Al-Mg-Si-Cu alloy with high manganese content.* Mater. Des., 2012. **39**: p. 418-424.
5. Onurlu, S. and A. Tekin, *Effect of heat treatment on the insoluble intermetallic phases present in an AA 6063 alloy.* J. Mater. Sci., 1994. **29**(6): p. 1652-5.
6. Sarafoglou, P.I. and G.N. Haidemenopoulos, *Phase fraction mapping in the as-cast microstructure of extrudable 6xxx aluminum alloys.* Int. J. Mater. Res., 2014. **105**(12): p. 1202-1209.
7. http://www.factsage.com.
8. Chartrand, P., *Thermodynamic assessment of the Al-Mg system*. unpublished work.
9. Harvey, J.-P., *M.A.Sc. thesis. Ecole Polytechnique*, 2006.
10. Kang, D.H. and I.-H. Jung, *Thermodynamic assessment of the Cu-Si system*. unpublished work.

11. Saunders, N., *the Al-Cu system.* Cost 507 - Thermochemical database for light metal alloys, 1991. **2**: p. 28-33.
12. Shubhank, K. and Y.-B. Kang, *Critical evaluation and thermodynamic optimization of Fe-Cu, Cu-C, Fe-C binary systems and Fe-Cu-C ternary system.* CALPHAD Comput. Coupling Phase Diagrams Thermochem., 2014. **45**: p. 127-137.
13. Phan, A.T., M.-K. Paek, and Y.-B. Kang, *Phase equilibria and thermodynamics of the Fe-Al-C system: Critical evaluation, experiment and thermodynamic optimization.* Acta Mater., 2014. **79**: p. 1-15.
14. Chartrand, P., *Thermodynamic assessment of the Fe-Mg system.* unpublished work.
15. Paek, M.-K., *Thermodynamic assessment of the Fe-Mn system.* unpublished work.
16. Paek, M.-K., J.-J. Pak, and Y.-B. Kang, *Phase equilibria and thermodynamics of Mn-C, Mn-Si, Si-C binary systems and Mn-Si-C ternary system by critical evaluation, combined with experiment and thermodynamic modeling.* CALPHAD Comput. Coupling Phase Diagrams Thermochem., 2014. **46**: p. 92-102.
17. Kang, Y.-B., A.D. Pelton, P. Chartrand, P. Spencer, and C.D. Fuerst, *Thermodynamic database development of the Mg-Ce-Mn-Y system for Mg alloy design.* Metall. Mater. Trans. A, 2007. **38A**(6): p. 1231-1243.
18. Cui, S., I.-H. Jung, J.K. Kim, and J. Xin, *A coupled experimental and thermodynamic study of the Al-Cr-Mg ternary system.* submited to J. Alloys Compd.
19. Cui, S. and I.-H. Jung, *Thermodynamic modeling of the Al-Cr-Mn ternary system.* submitted to Metall. Mater. Trans. A.
20. Cui, S. and I.-H. Jung, *Thermodynamic modeling of Cu-Fe-Cr and Cu-Fe-Mn systems.* to be submitted.
21. Cui, S. and I.-H. Jung, *Thermodynamic modeling of Al-Cu-Mg-Si quaternary system.* to be submitted.
22. Cui, S. and I.-H. Jung, *Thermodynamic modeling of the Cr-Si and Al-Cr-Si systems.* to be submitted.
23. Cui, S. and I.-H. Jung, *Critical reassessment of the Fe-Si system.* submitted to CALPHAD.
24. Cui, S., *Thermodynamic assessment of the Al-Cu-Cr system.* unpublished work.
25. Cui, S., *Thermodynamic revison of the Al-Cu-Mn system.* unpublished work.

26. Cui, S. and I.-H. Jung, *Thermodynamic modeling of the Fe-Si-Cr and Fe-Si-Mg systems.* to be submited.
27. Paek, M.-K., *Thermodynamic assessment of the Al-Fe-Si system.* unpublished work.
28. Kim, M.-S. and Y.-B. Kang, *Thermodynamic Modeling of the Fe-Mn-C and the Fe-Mn-Al Systems Using the Modified Quasichemical Model for Liquid Phase.* J. Phase Equilib. Diffus., 2015. **36**(5): p. 453-470.
29. Shukla, A. and A.D. Pelton, *Thermodynamic Assessment of the Al-Mn and Mg-Al-Mn Systems.* J. Phase Equilib. Diffus., 2009. **30**(1): p. 28-39.
30. Paek, M.-K., *Thermodynamic assessment of the Fe-Mn-Si system.* unpublished work.
31. Paek, M.-K., *Thermodynamic assessment of the Al-Mn-Si system.* unpublished work.
32. https://imagej.nih.gov/ij.
33. Gupta, A.K., D.J. Lloyd, and S.A. Court, *Precipitation hardening in Al-Mg-Si alloys with and without excess Si.* Mater. Sci. Eng., A, 2001. **A316**(1-2): p. 11-17.

Table captions

Table 12.2.1 Alloy compositions of as-cast billets.

Table 12.2.2 Calculated phase amounts from the Scheil cooling calculation (wt.%).

Table 12.2.3 Total volume fraction of the Q, $Al_8FeMg_3Si_6$, α_AlFeSi, and β_AlFeSi phases from experiments compared with the calculated results.

Table 12.2.4 Effect of alloying elements addition on the precipitation formation during solidification.

Figure captions

Fig. 12.2.1 (a) Calculated solidification path of 6063 alloy, (b) calculated phase fraction, and (c) calculated micro-segregation of alloying elements in the liquid phase.

Fig. 12.2.2 Simulated solidification paths of (a) alloy 1, (b) alloy 2, and (c) alloy 3.

Fig. 12.2.3 Backscatter micrographs of (a) alloy 1, (b) alloy 2, (c) alloy 3, and (d) enlarged part of alloy 1.

Fig. 12.2.4 Effect of alloying elements on the amounts of precipitates formed during the solidification process. (a) Cr, (b) Cu, (c) Fe, (d) Mg, (e) Mn, and (f) Si.

Fig. 12.2.5 Calculated equilibrium phase distribution of 6063 alloy as a function of temperature.

Fig. 12.2.6 (a) Calculated isothermal section of the Al-Mg-Si alloys with 0.05 wt.% Cu, 0.15 wt.% Fe, and 0.03 wt.% Mn at 500 °C, (b) the stability region of each equilibrium phase.

Fig. 12.2.7 Phase fraction maps of the (a) $Al_{13}Fe_4$, (b) $Al_8FeMg_3Si_6$, (c) Mg_2Si, (d) α_AlFeSi, (e) β_AlFeSi, and (f) Al_7Cr phases in Al-Mg-Si-0.05Cu-0.15Fe-0.03Mn with 0.02Cr or 0.20Cr at 500 °C.

Fig. 12.2.8 Phase fraction maps of the (a) $Al_{13}Fe_4$, (b) $Al_8FeMg_3Si_6$, (c) Mg_2Si, (d) α_AlFeSi, and (e) β_AlFeSi phases in Al-Mg-Si-0.02Cr-0.15Fe-0.03Mn with 0.05Cu or 0.15Cu at 500 °C.

Fig. 12.2.9 Phase fraction maps of the (a) $Al_{13}Fe_4$, (b) $Al_8FeMg_3Si_6$, (c) Mg_2Si, (d) α_AlFeSi, and (e) β_AlFeSi phases in Al-Mg-Si-0.02Cr-0.05Cu-0.03Mn with 0.15Fe or 0.20Fe at 500 °C.

Fig. 12.2.10 Phase fraction maps of the (a) $Al_{13}Fe_4$, (b) $Al_8FeMg_3Si_6$, (c) Mg_2Si, (d) α_AlFeSi, (e) β_AlFeSi, and (f) $Al_{12}Mn$ phases in Al-Mg-Si-0.02Cr-0.05Cu-0.15Fe with 0.03Mn or 0.10Mn at 500 °C.

Fig. 12.2.11 Phase fraction map of Mg_2Si in Al-Mg-Si-0.02Cr-0.05Cu-0.15Fe-0.03Mn alloy at 177 °C.

Table 12.2.1 Alloy compositions of as-cast billets.

Alloy	Al	Si	Mg	Cu	Fe	Cr	Mn
6063	Bal.	0.4	0.49	0.01	0.16	0.0	0.029
#1	Bal.	0.4807	0.4965	0.148	0.1951	0.182	0.0965
#2	Bal.	0.5639	0.9118	0.1351	0.2011	0.0	0.095
#3	Bal.	0.5921	0.9171	0.1437	0.1987	0.1974	0.0957

Table 12.2.2 Calculated phase amounts from Scheil cooling calculation (wt.%).

Phase	6063	Alloy 1	Alloy 2	Alloy 3
fcc_A1	99.138	98.024	98.527	97.583
Al_7Cr	0	0.77332	0	0.91285
α_AlFeSi	0.23934	0.30383	0.32405	0.34757
β_AlFeSi	0.15525	0.20186	0.20305	0.21898
Al_2Cu	0.00548	0.0984	0.0944	0.0991
$Al_{13}Fe_4$	0.0613	0.0588	0.0600	0.0231
$Al_4(Cr,Mn)$	0.00135	0.0175	0.0231	0.0141
Mg_2Si	0.22844	0.19796	0.48494	0.49531
Si	0.11812	0.13921	0.1136	0.12526
Q	0.00661	0.11858	0.11378	0.11946
$Al_8FeMg_3Si_6$	0.0460	0.0611	0.0507	0.0559
$Cu_4Mn_7Al_{28}$	0.000304	0.00546	0.00524	0.00550

Table 12.2.3 Total volume fraction of the Q, $Al_8FeMg_3Si_6$, α_AlFeSi, and β_AlFeSi phases from experiments compared with the calculated results.

Alloy	measured	calculated
#1	0.00506	0.00744
#2	0.00662	0.00752
#3	0.00686	0.00765

Table 12.2.4 Effect of alloying elements addition on the precipitation formation during solidification.

Phase	Mn	Cr	Fe	Cu	Mg	Si
α_AlFeSi			↑		↓	↑↓
β_AlFeSi			↑		↓	↑
$Al_{13}Fe_4$			↑		↑	↓
Al_2Cu				↑		
$Al_4(Cr,Mn)$						
Mg_2Si				↓	↑	
Si				↓	↓	
$Al_8FeMg_3Si_6$					↑↓	↑
Q				↑		
$Cu_4Mn_7Al_{28}$				↑		
Al_7Cr		↑				

Figures

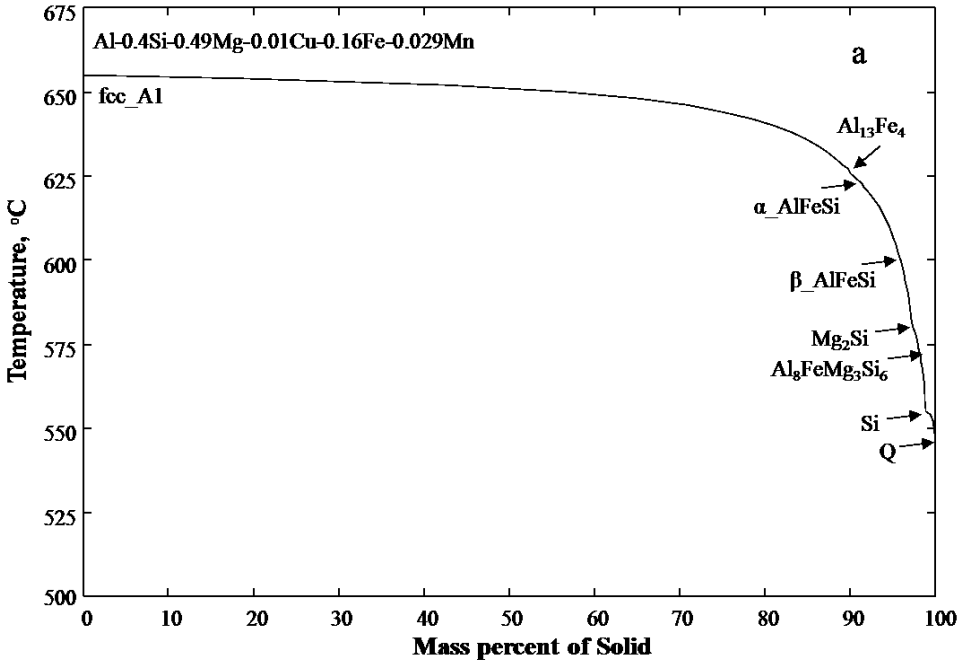
Al-0.4Si-0.49Mg-0.01Cu-0.16Fe-0.029Mn
a
fcc_Al
Al13Fe4
α_AlFeSi
β_AlFeSi
Mg2Si
Al8FeMg3Si6
Si
Q
Temperature, °C
Mass percent of Solid
675
650
625
600
575
550
525
500
0
10
20
30
40
50
60
70
80
90
100

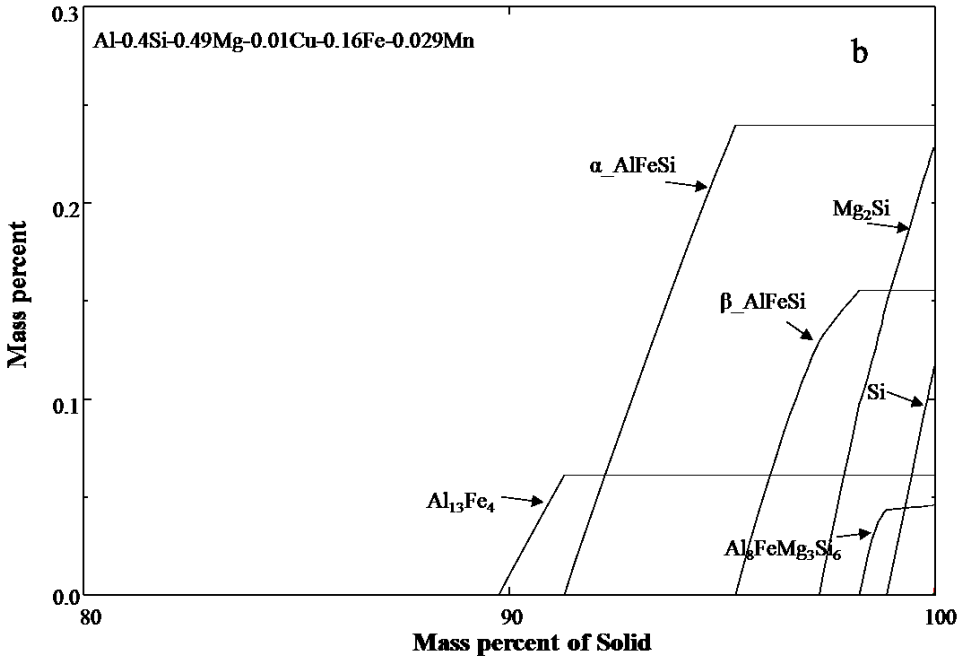
Al-0.4Si-0.49Mg-0.01Cu-0.16Fe-0.029Mn
b
α_AlFeSi
Mg2Si
β_AlFeSi
Si
Al13Fe4
Al8FeMg3Si6
Mass percent
Mass percent of Solid
0.3
0.2
0.1
0.0
80
90
100

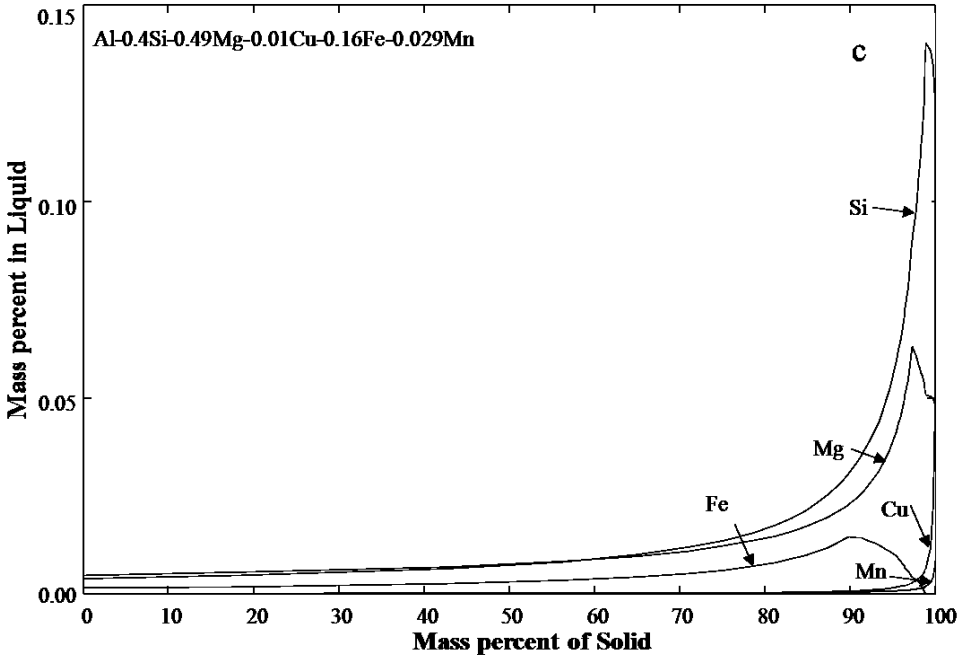

Fig. 12.2.1 (a) Calculated solidification path of 6063 alloy, (b) calculated phase fraction, and (c) calculated micro-segregation of alloying elements in the liquid phase.

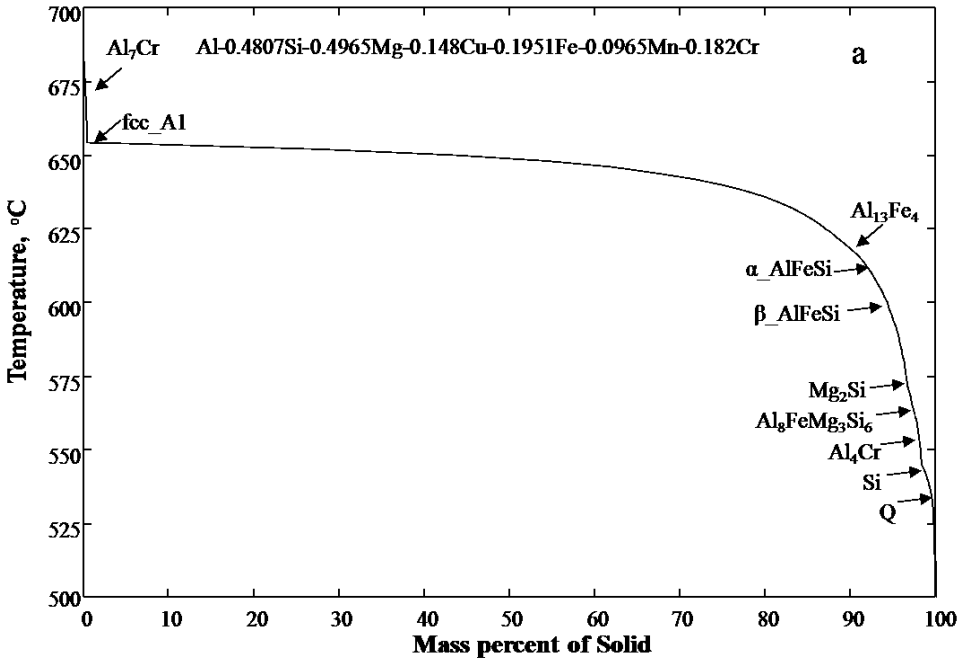
Al-0.4807Si-0.4965Mg-0.148Cu-0.1951Fe-0.0965Mn-0.182Cr
a
Al7Cr
fcc_A1
Al13Fe4
α_AlFeSi
β_AlFeSi
Mg2Si
Al8FeMg3Si6
Al4Cr
Si
Q
Temperature, °C
Mass percent of Solid
700
675
650
625
600
575
550
525
500
0
10
20
30
40
50
60
70
80
90
100

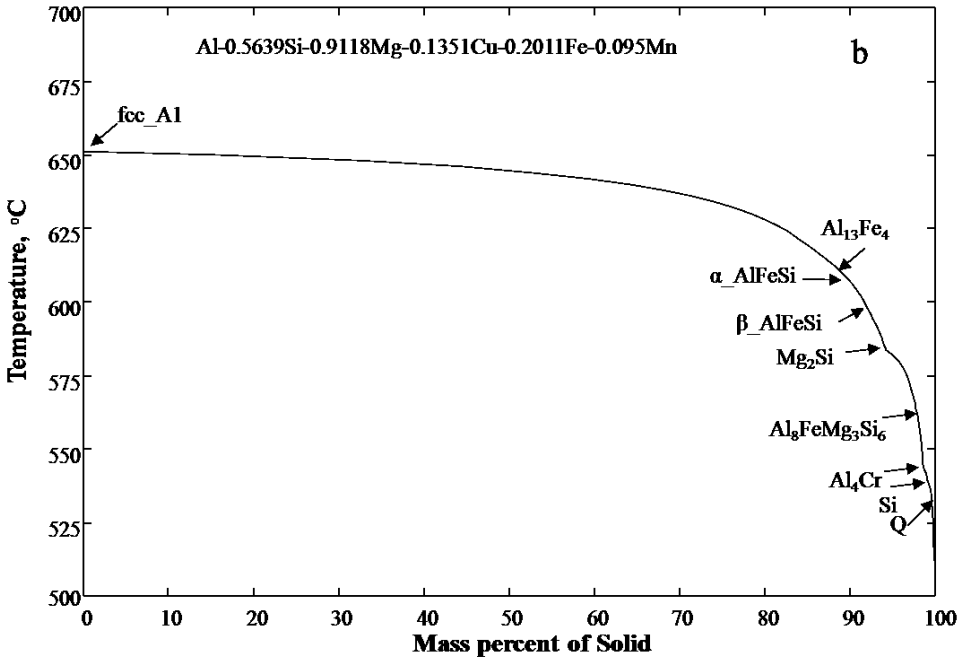
Al-0.5639Si-0.9118Mg-0.1351Cu-0.2011Fe-0.095Mn
b
fcc_A1
Al13Fe4
α_AlFeSi
β_AlFeSi
Mg2Si
Al8FeMg3Si6
Al4Cr
Si
Q
Temperature, °C
Mass percent of Solid
700
675
650
625
600
575
550
525
500
0
10
20
30
40
50
60
70
80
90
100

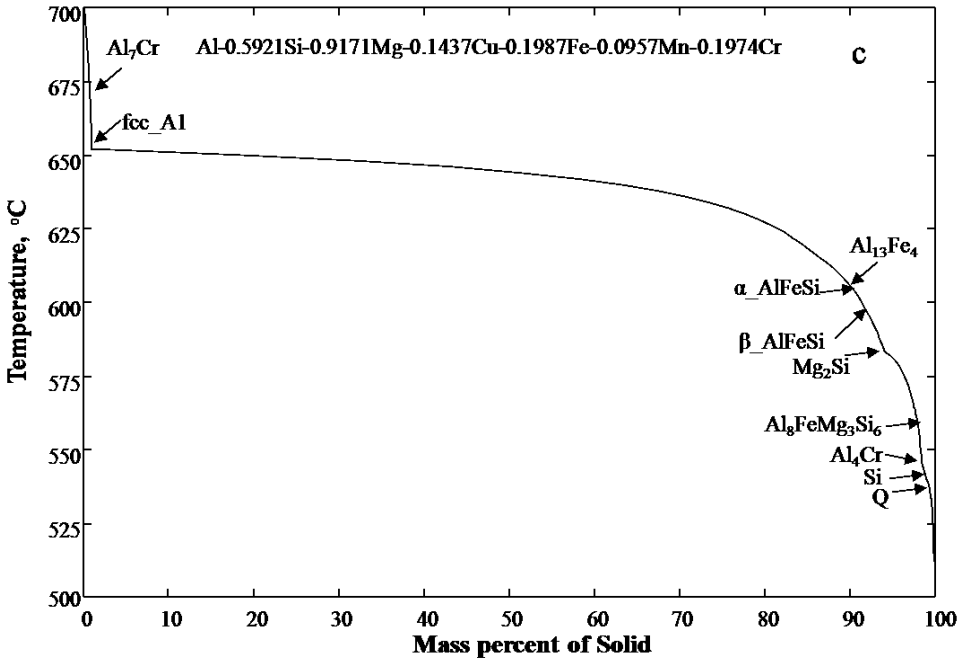

Fig. 12.2.2 Simulated solidification paths of (a) alloy 1, (b) alloy 2, and (c) alloy 3.

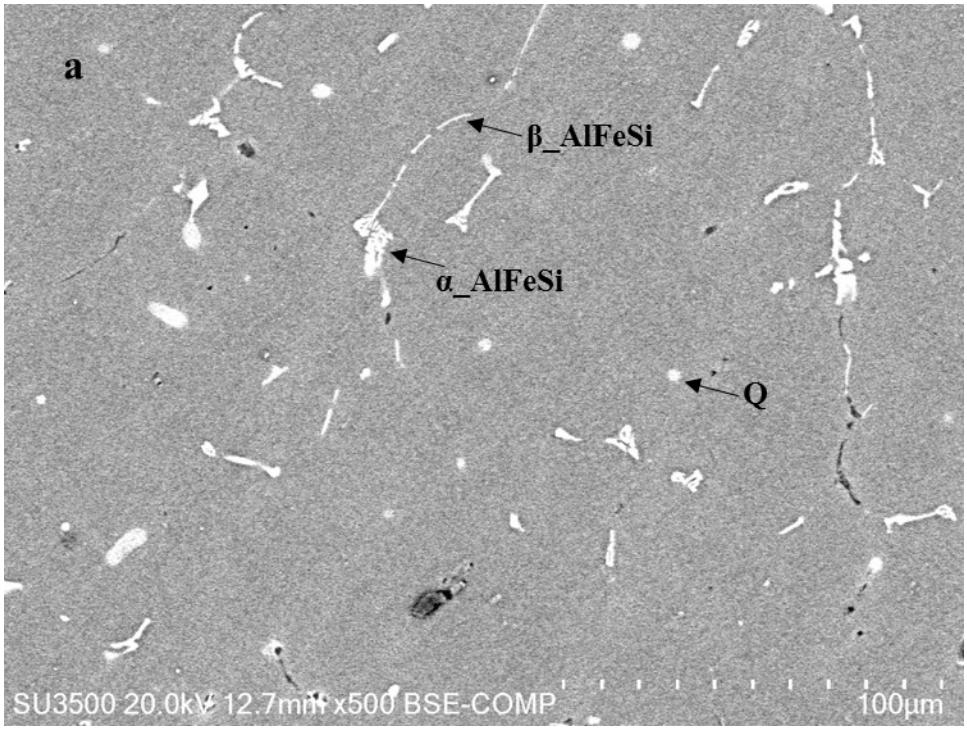
a
β_AlFeSi
α_AlFeSi
Q
SU3500 20.0kV 12.7mm x500 BSE-COMP
100μm

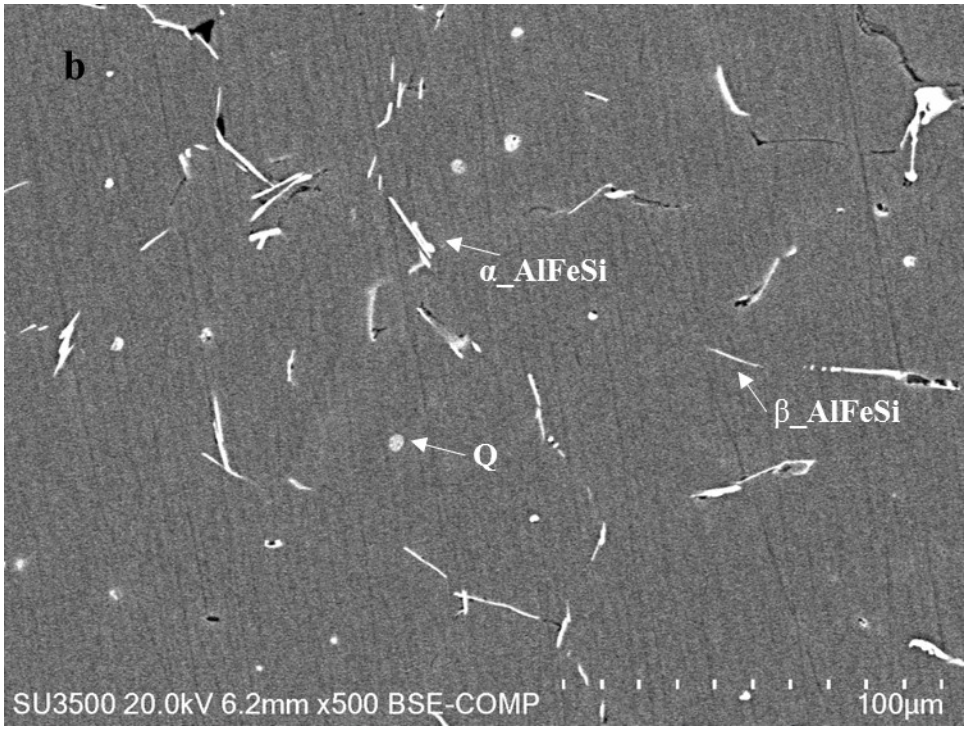
b
α_AlFeSi
β_AlFeSi
Q
SU3500 20.0kV 6.2mm x500 BSE-COMP
100μm

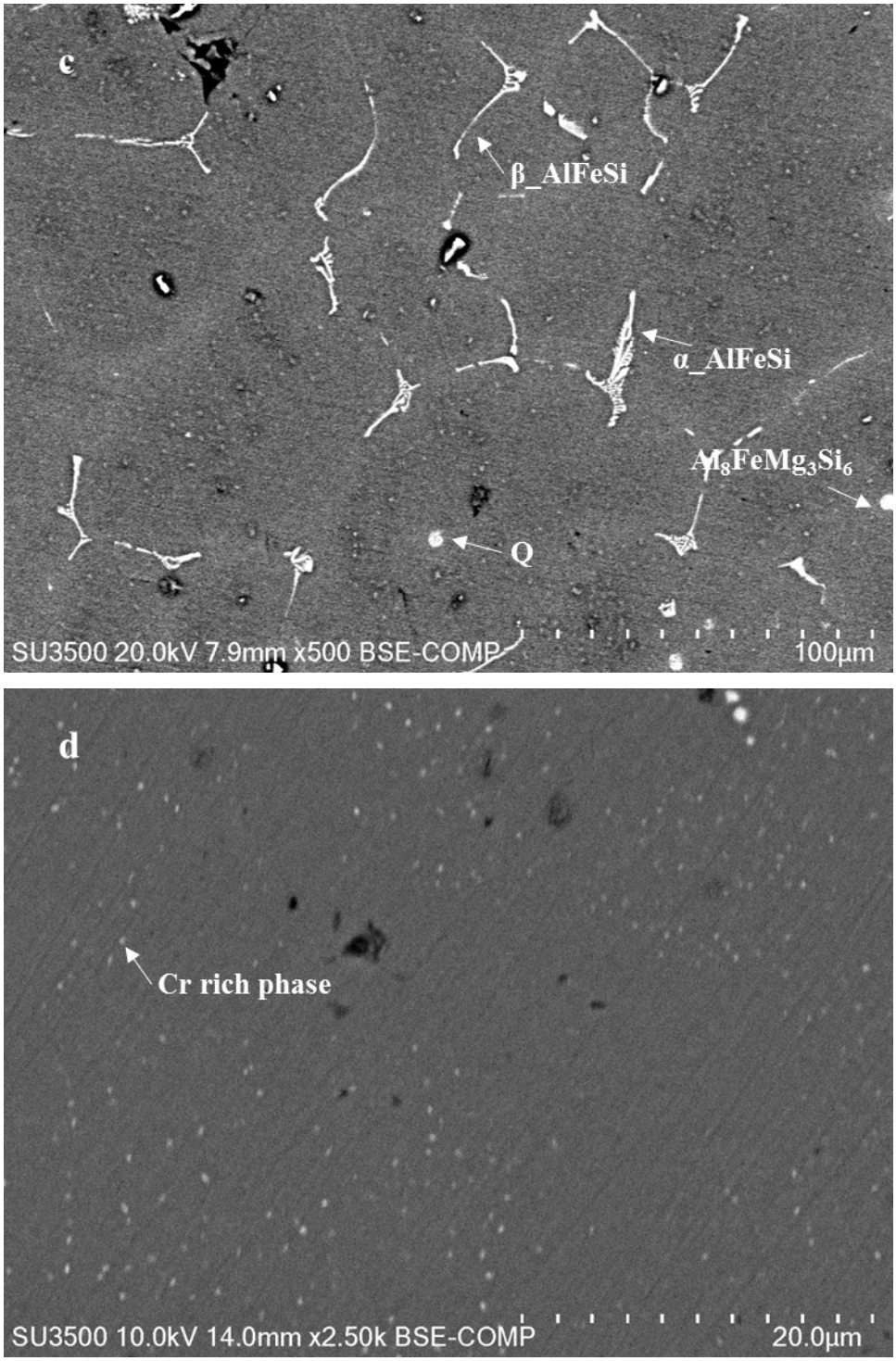

Fig. 12.2.3 Backscatter micrographs of (a) alloy 1, (b) alloy 2, (c) alloy 3, and (d) enlarged part of alloy 1.

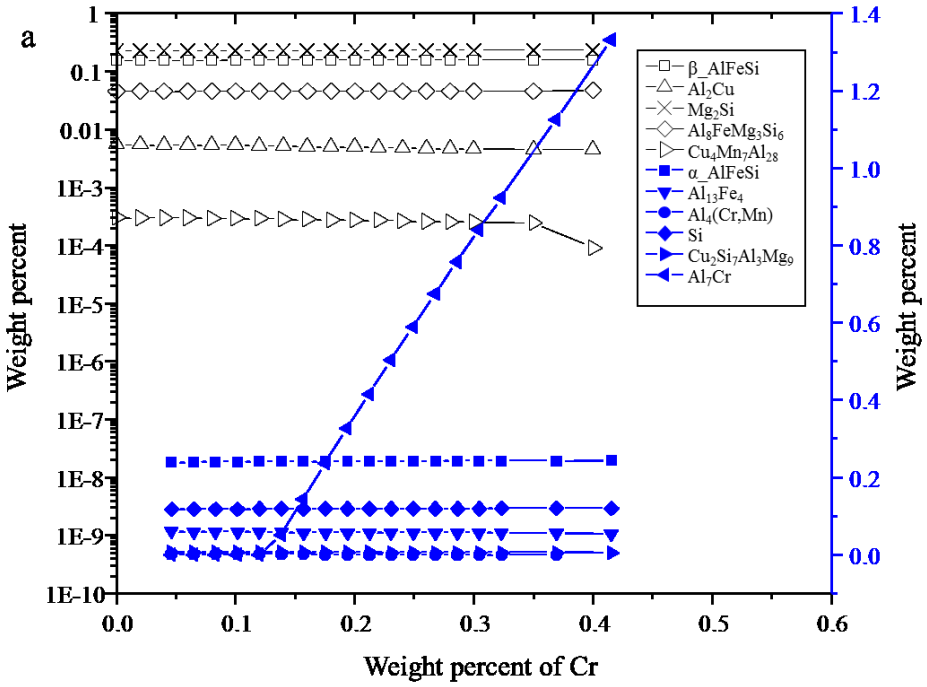
a
Weight percent
Weight percent
Weight percent of Cr
β_AlFeSi
Al2Cu
Mg2Si
Al8FeMg3Si6
Cu4Mn7Al28
α_AlFeSi
Al13Fe4
Al4(Cr,Mn)
Si
Cu2Si7Al3Mg9
Al7Cr

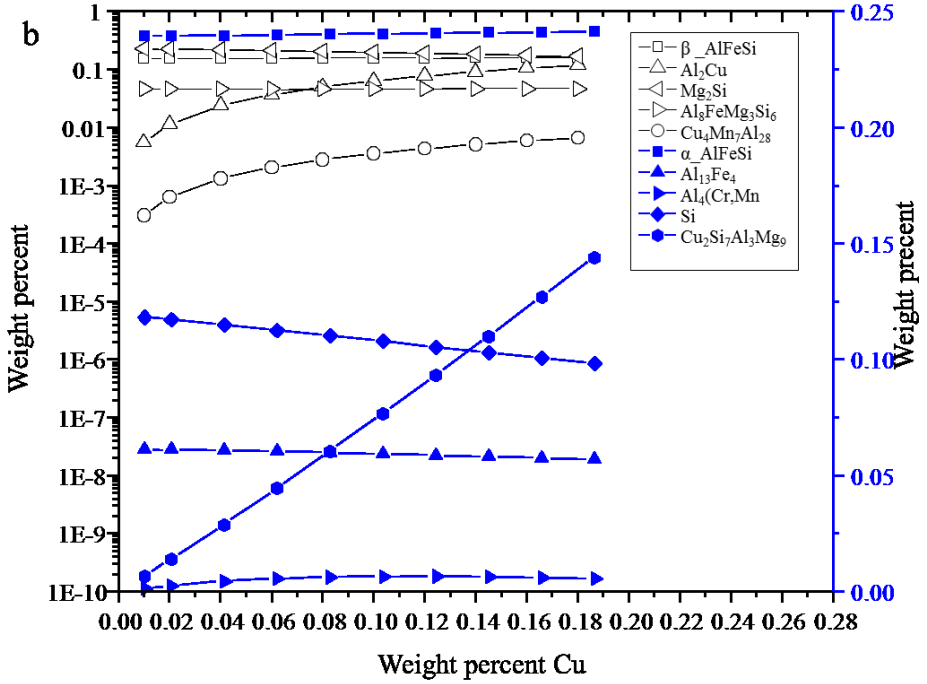
b
Weight percent
Weight precent
Weight percent Cu
β_AlFeSi
Al2Cu
Mg2Si
Al8FeMg3Si6
Cu4Mn7Al28
α_AlFeSi
Al13Fe4
Al4(Cr,Mn
Si
Cu2Si7Al3Mg9

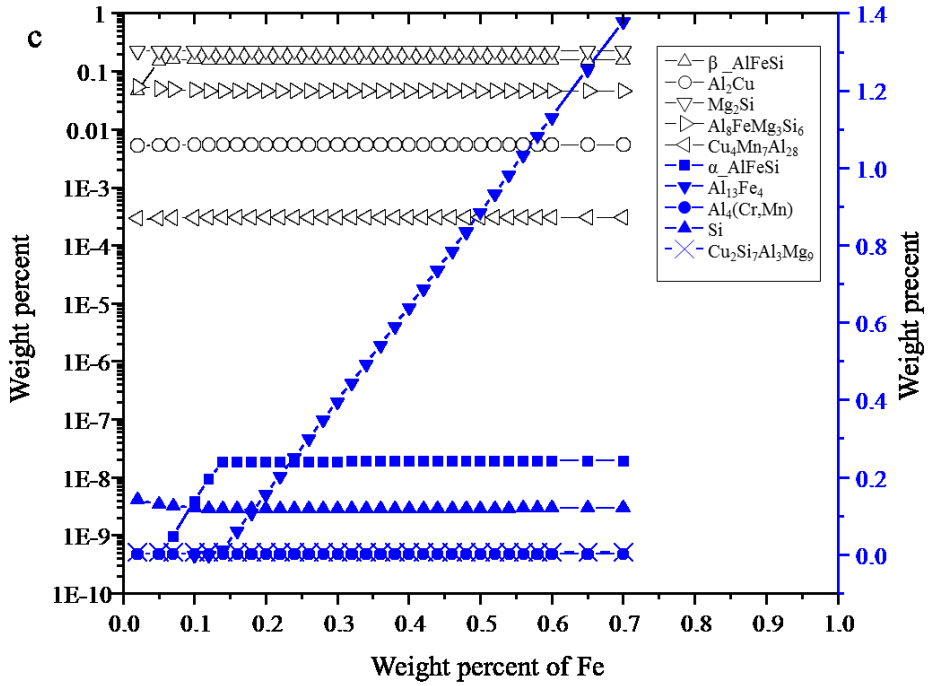
c
Weight percent
Weight precent
Weight percent of Fe
β_AlFeSi
Al2Cu
Mg2Si
Al8FeMg3Si6
Cu4Mn7Al28
α_AlFeSi
Al13Fe4
Al4(Cr,Mn)
Si
Cu2Si7Al3Mg9

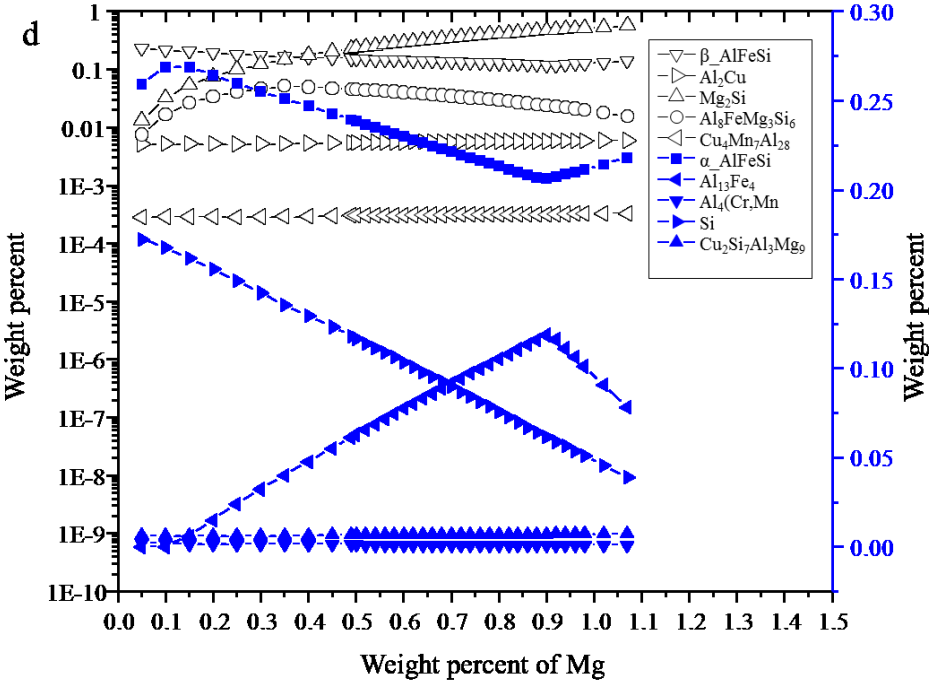
d
Weight percent
Weight percent
Weight percent of Mg
β_AlFeSi
Al2Cu
Mg2Si
Al8FeMg3Si6
Cu4Mn7Al28
α_AlFeSi
Al13Fe4
Al4(Cr,Mn
Si
Cu2Si7Al3Mg9

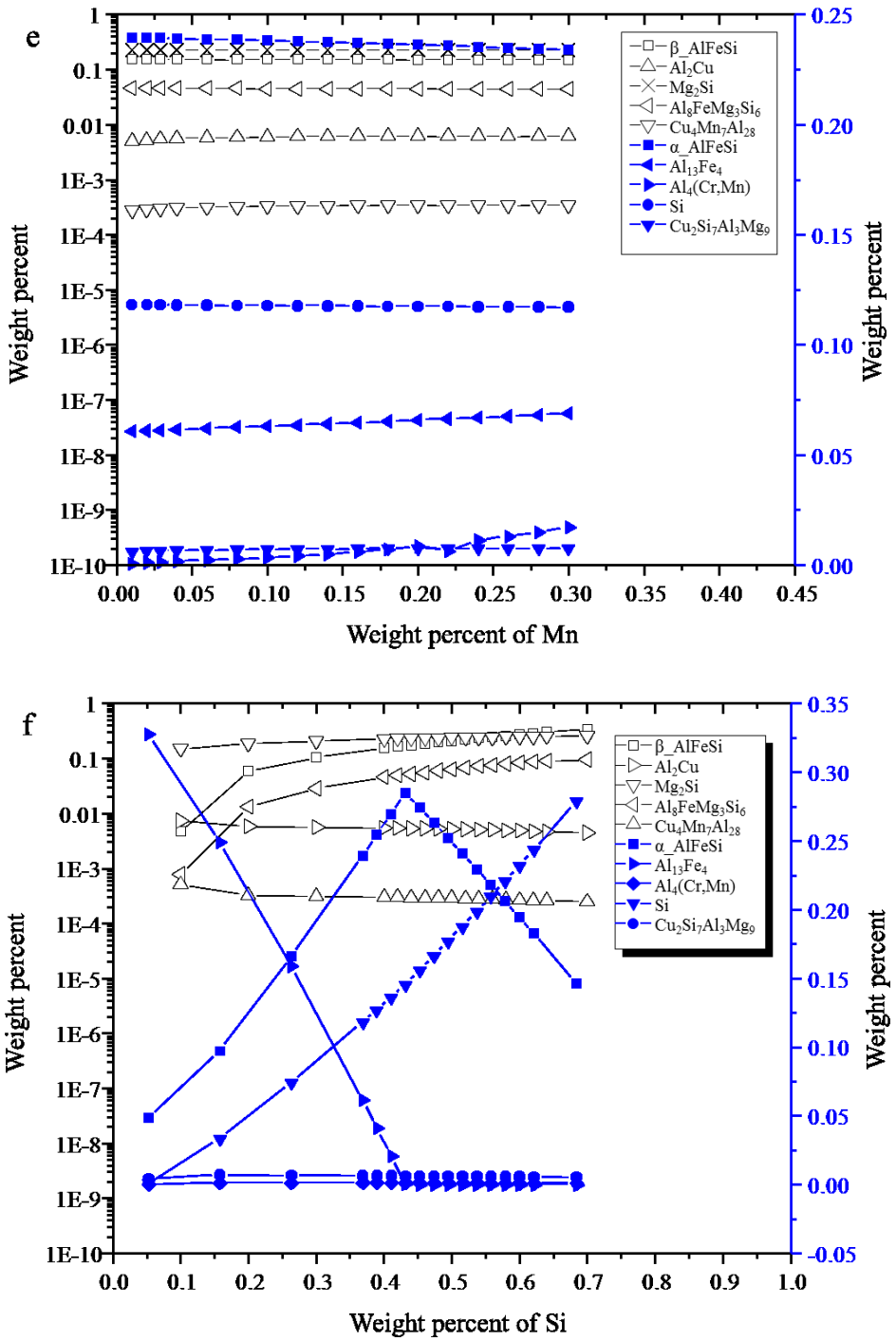

Fig. 12.2.4 Effect of alloying elements on the amounts of precipitates formed during the solidification process. (a) Cr, (b) Cu, (c) Fe, (d) Mg, (e) Mn, and (f) Si.

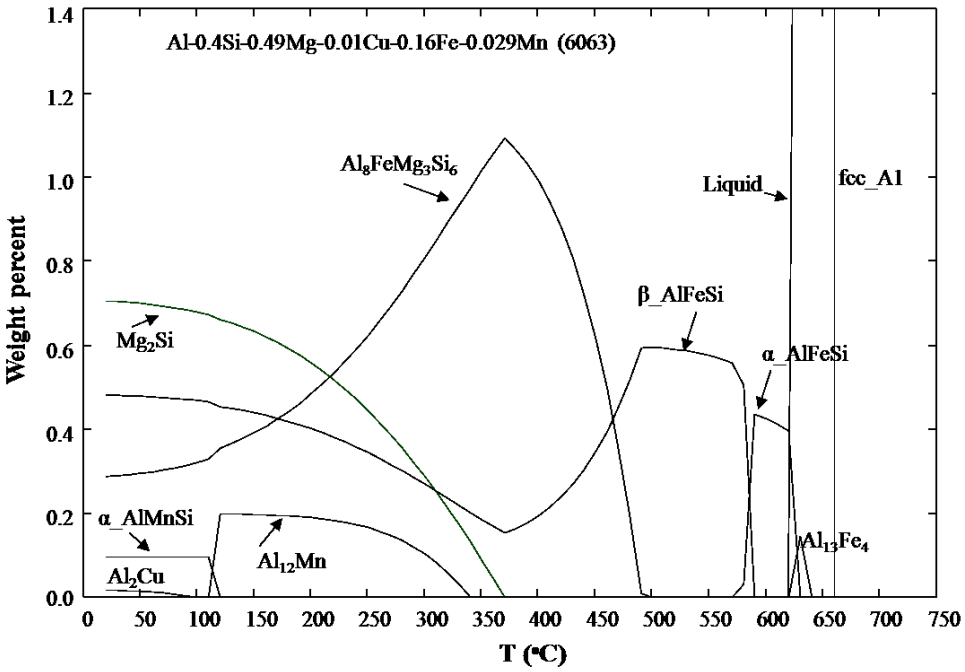

Fig. 12.2.5 Calculated equilibrium phase distribution of 6063 alloy as a function of temperature.

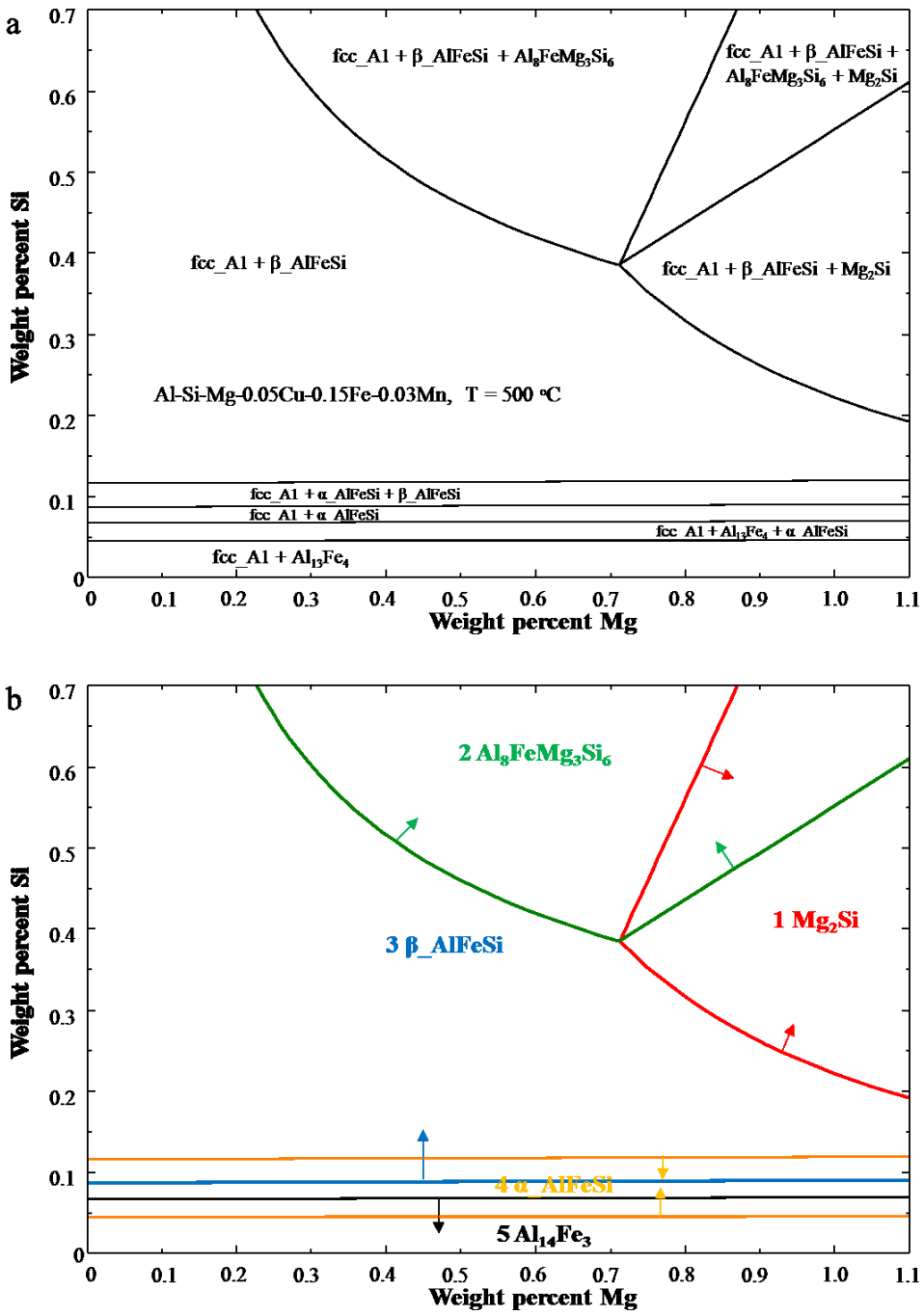

Fig. 12.2.6 (a) Calculated isothermal section of the Al-Mg-Si alloys with 0.05 wt.% Cu, 0.15 wt.% Fe, and 0.03 wt.% Mn at 500 °C. (b) the stability region of each equilibrium phase.

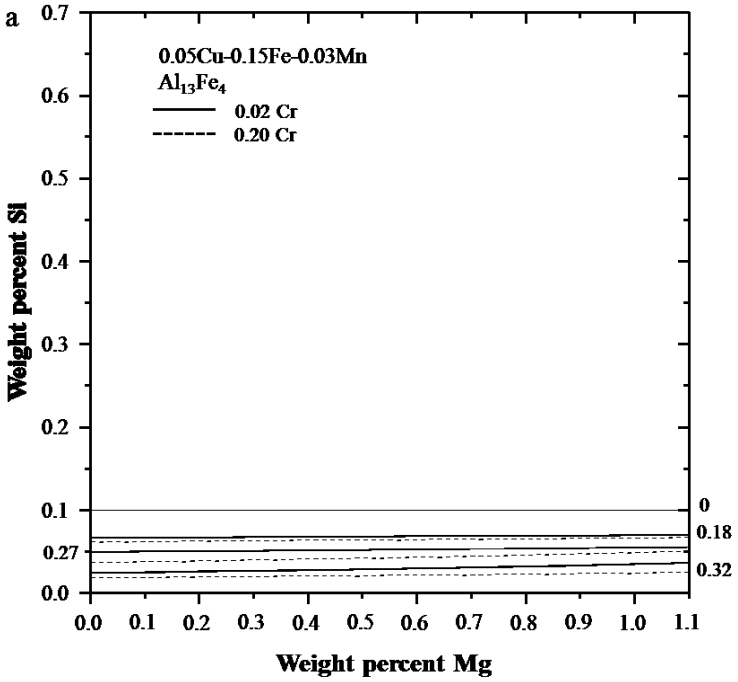
a
0.05Cu-0.15Fe-0.03Mn
$Al_{13}Fe_4$
0.02 Cr
0.20 Cr
Weight percent Si
Weight percent Mg
0
0.18
0.27
0.32

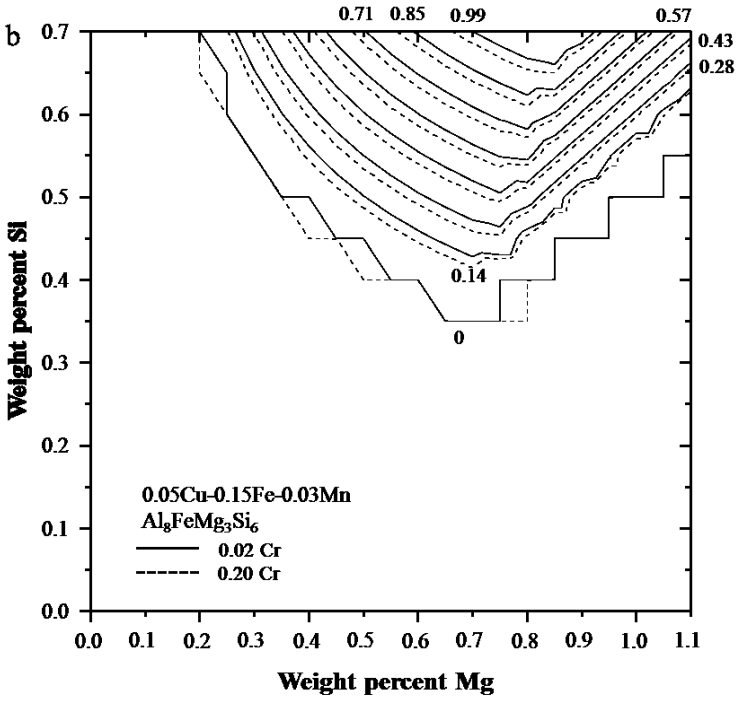
b
0.71
0.85
0.99
0.57
0.43
0.28
0.14
0
0.05Cu-0.15Fe-0.03Mn
$Al_8FeMg_3Si_6$
0.02 Cr
0.20 Cr
Weight percent Si
Weight percent Mg

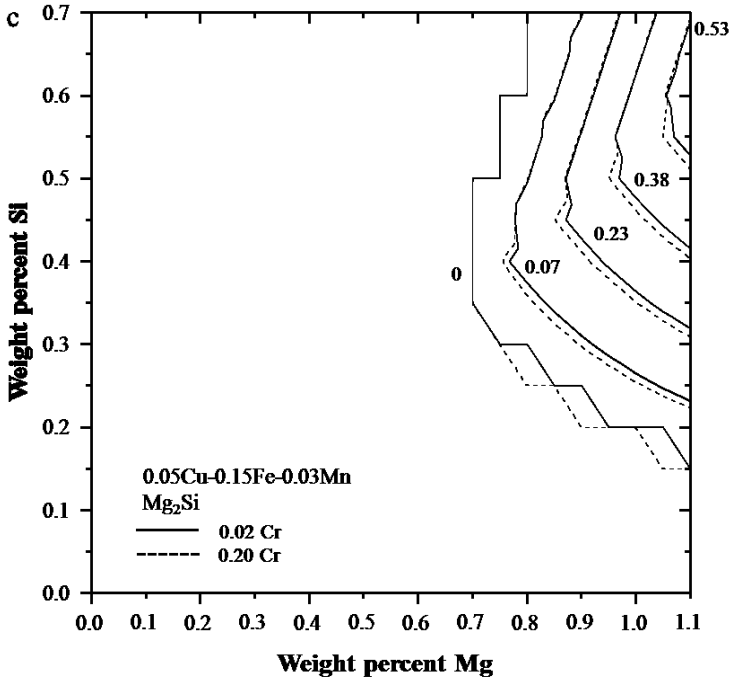
c
0.05Cu-0.15Fe-0.03Mn
Mg2Si
0.02 Cr
0.20 Cr
0
0.07
0.23
0.38
0.53
Weight percent Si
Weight percent Mg

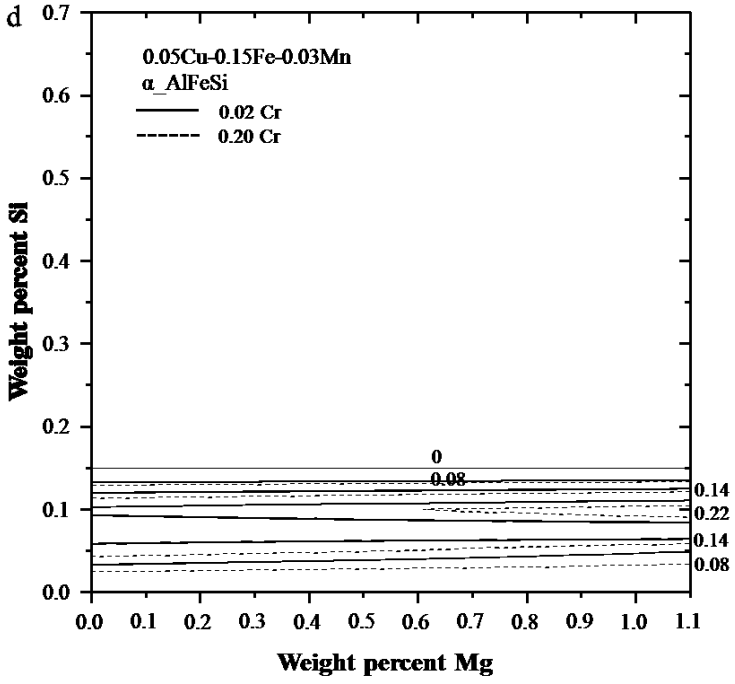
d
0.05Cu-0.15Fe-0.03Mn
α_AlFeSi
0.02 Cr
0.20 Cr
0
0.08
0.14
0.22
0.14
0.08
Weight percent Si
Weight percent Mg

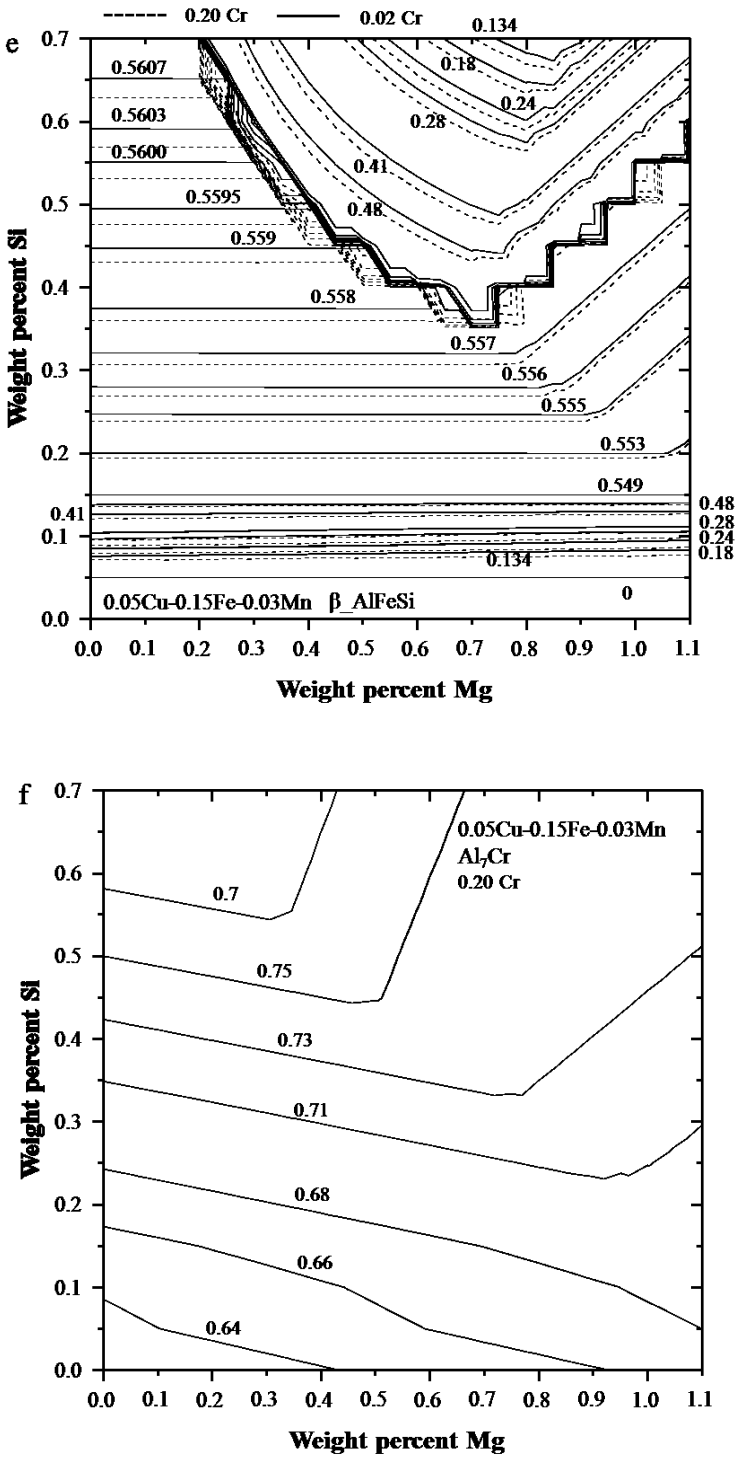

Fig. 12.2.7 Phase fraction maps of the (a) $Al_{13}Fe_4$, (b) $Al_8FeMg_3Si_6$, (c) Mg_2Si, (d) α_AlFeSi, (e) β_AlFeSi, and (f) Al_7Cr phases in Al-Mg-Si-0.05Cu-0.15Fe-0.03Mn with 0.02Cr or 0.20Cr at 500 °C.

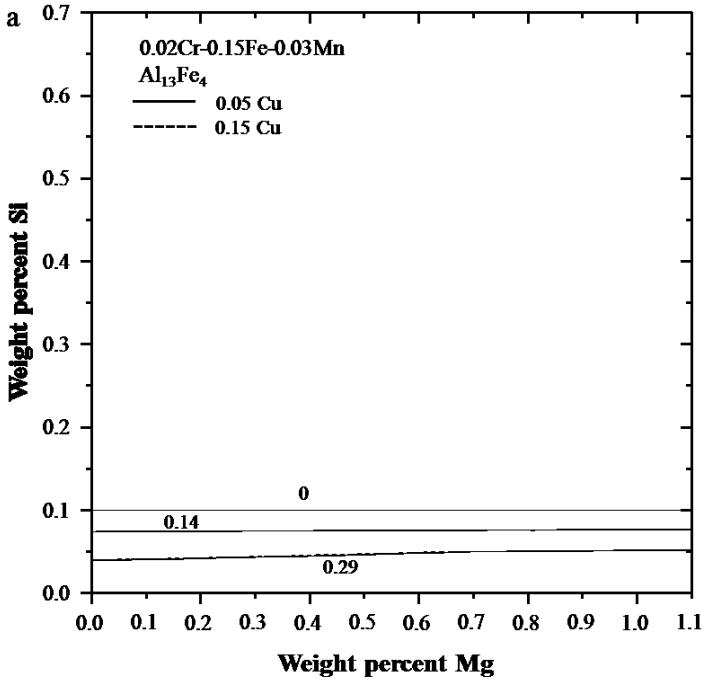
a
0.02Cr-0.15Fe-0.03Mn
$Al_{13}Fe_4$
0.05 Cu
0.15 Cu
0
0.14
0.29
Weight percent Si
Weight percent Mg

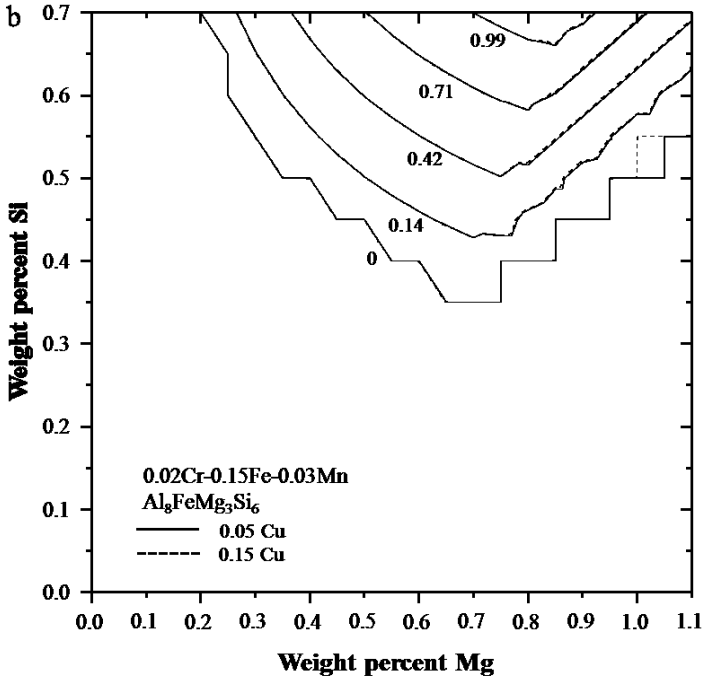
b
0.99
0.71
0.42
0.14
0
0.02Cr-0.15Fe-0.03Mn
$Al_8FeMg_3Si_6$
0.05 Cu
0.15 Cu
Weight percent Si
Weight percent Mg

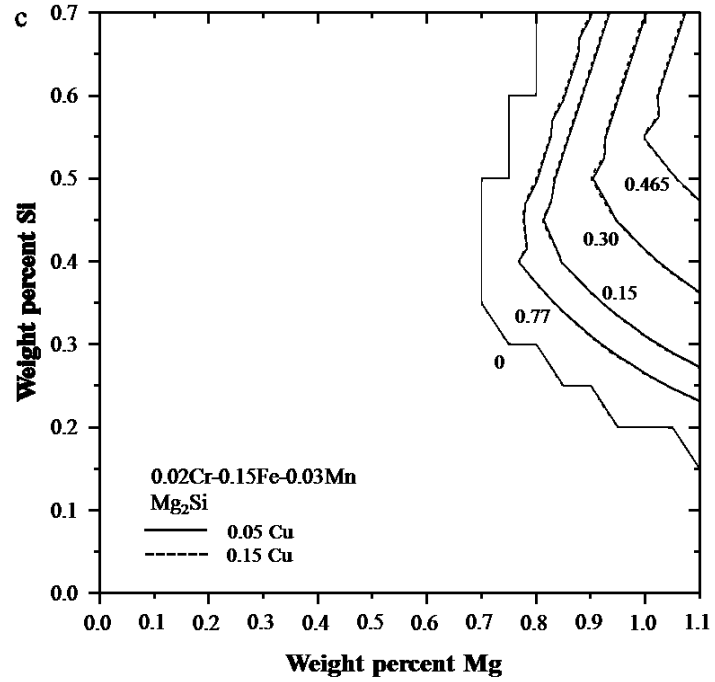
c
Weight percent Si
Weight percent Mg
0.465
0.30
0.15
0.77
0
0.02Cr-0.15Fe-0.03Mn
Mg2Si
0.05 Cu
0.15 Cu

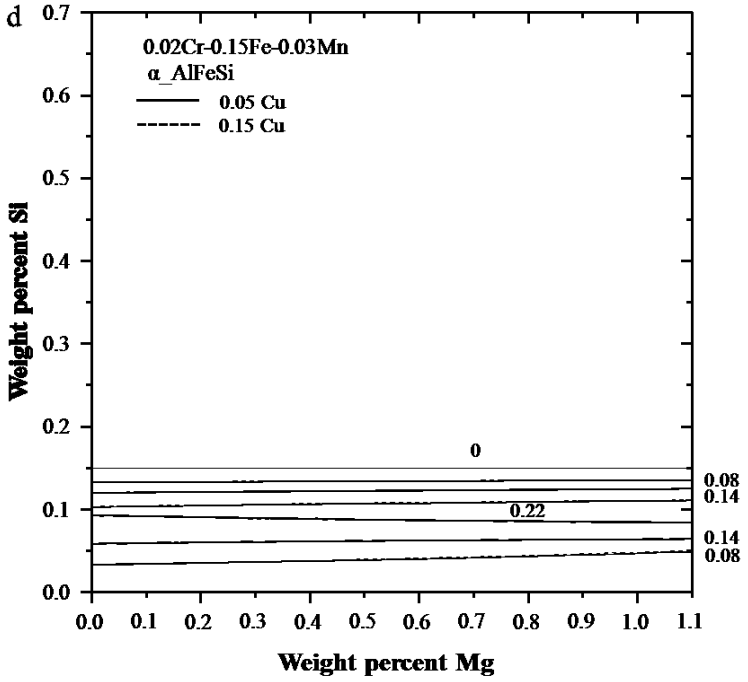
d
Weight percent Si
Weight percent Mg
0.02Cr-0.15Fe-0.03Mn
α_AlFeSi
0.05 Cu
0.15 Cu
0
0.08
0.14
0.22
0.14
0.08

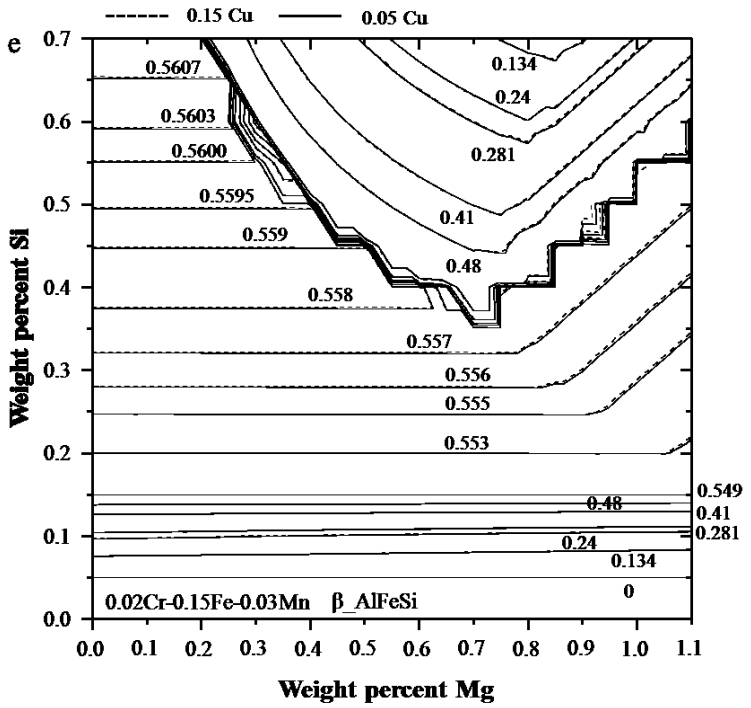

Fig. 12.2.8 Phase fraction maps of the (a) $Al_{13}Fe_4$, (b) $Al_8FeMg_3Si_6$, (c) Mg_2Si, (d) α_AlFeSi, and (e) β_AlFeSi phases in Al-Mg-Si-0.02Cr-0.15Fe-0.03Mn with 0.05Cu or 0.15Cu at 500 °C.

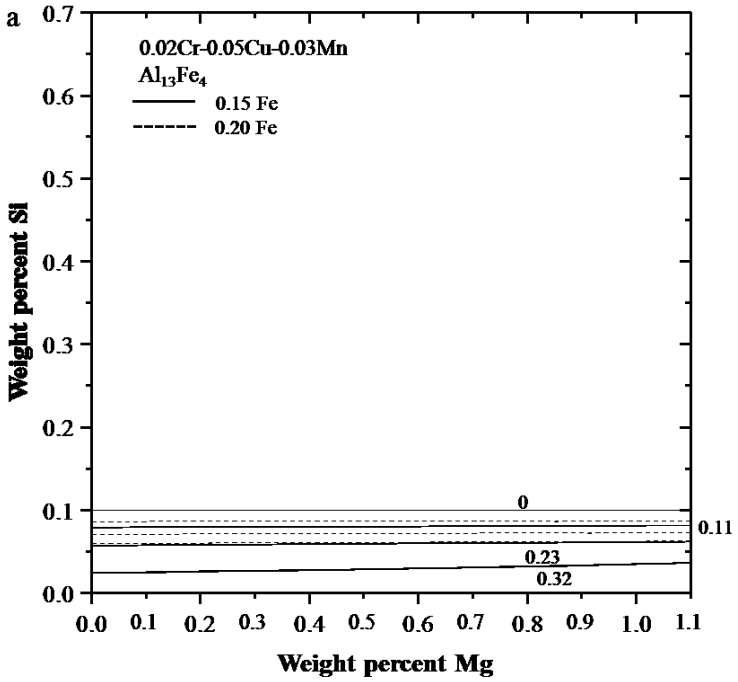
a
0.02Cr-0.05Cu-0.03Mn
$Al_{13}Fe_4$
0.15 Fe
0.20 Fe
Weight percent Si
Weight percent Mg
0
0.11
0.23
0.32

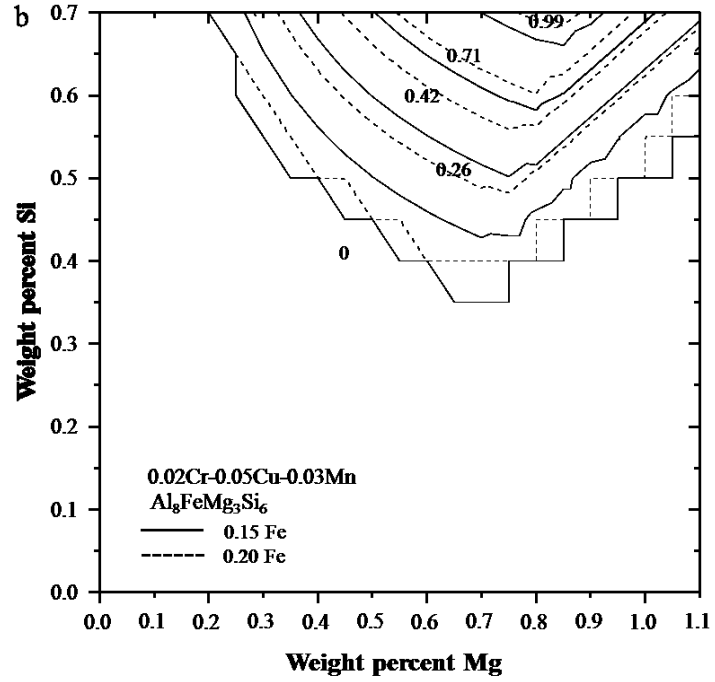
b
0.99
0.71
0.42
0.26
0
0.02Cr-0.05Cu-0.03Mn
$Al_8FeMg_3Si_6$
0.15 Fe
0.20 Fe
Weight percent Si
Weight percent Mg

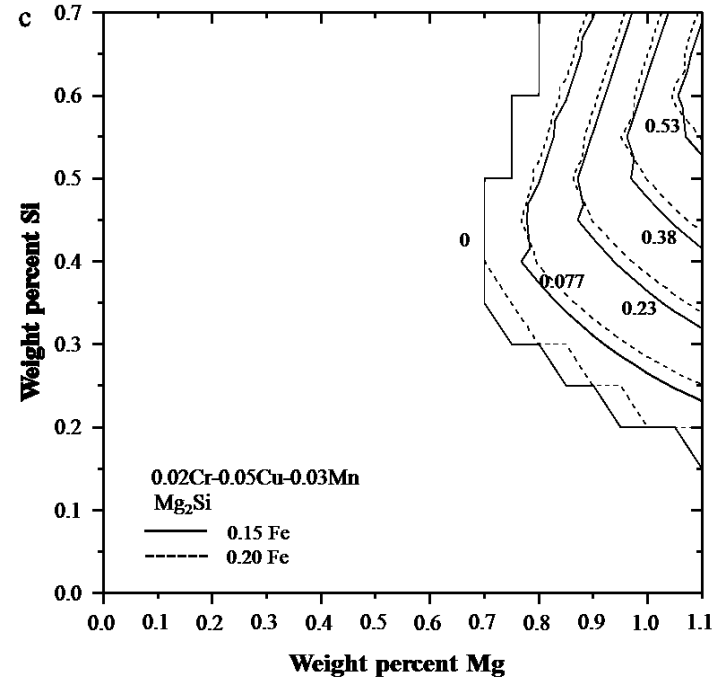
c
Weight percent Si
Weight percent Mg
0.02Cr-0.05Cu-0.03Mn
Mg2Si
0.15 Fe
0.20 Fe
0
0.077
0.23
0.38
0.53

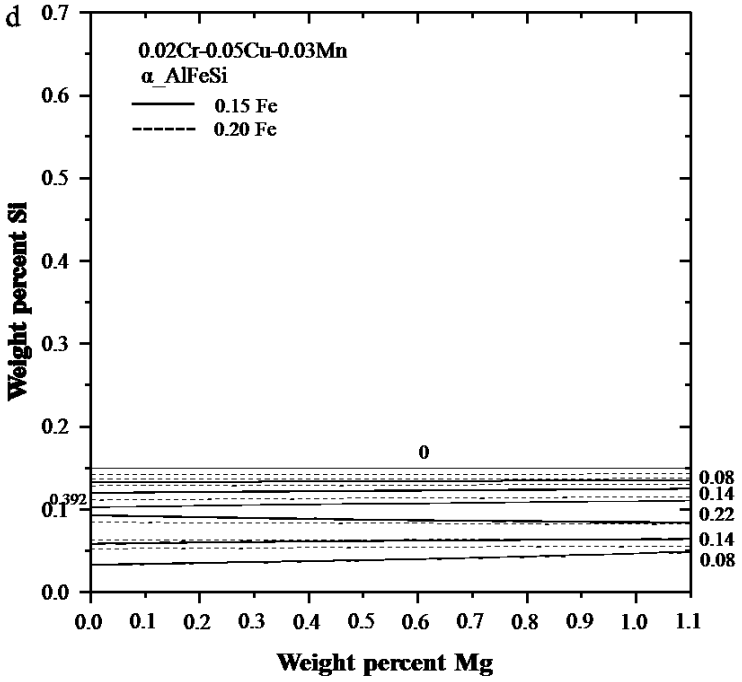
d
Weight percent Si
Weight percent Mg
0.02Cr-0.05Cu-0.03Mn
α_AlFeSi
0.15 Fe
0.20 Fe
0
0.392
0.08
0.14
0.22
0.14
0.08

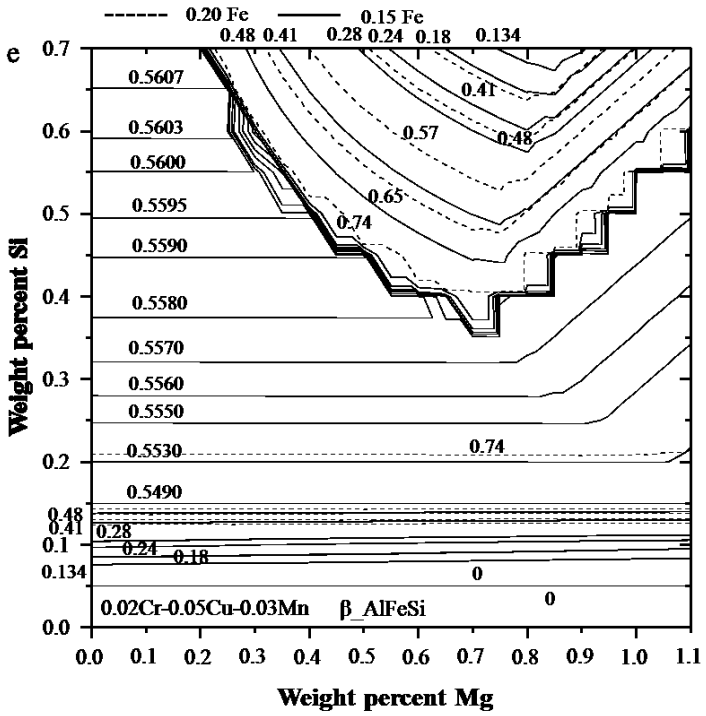

Fig. 12.2.9 Phase fraction maps of the (a) $Al_{13}Fe_4$, (b) $Al_8FeMg_3Si_6$, (c) Mg_2Si, (d) α_AlFeSi, and (e) β_AlFeSi phases in Al-Mg-Si-0.02Cr-0.05Cu-0.03Mn with 0.15Fe or 0.20Fe at 500 °C.

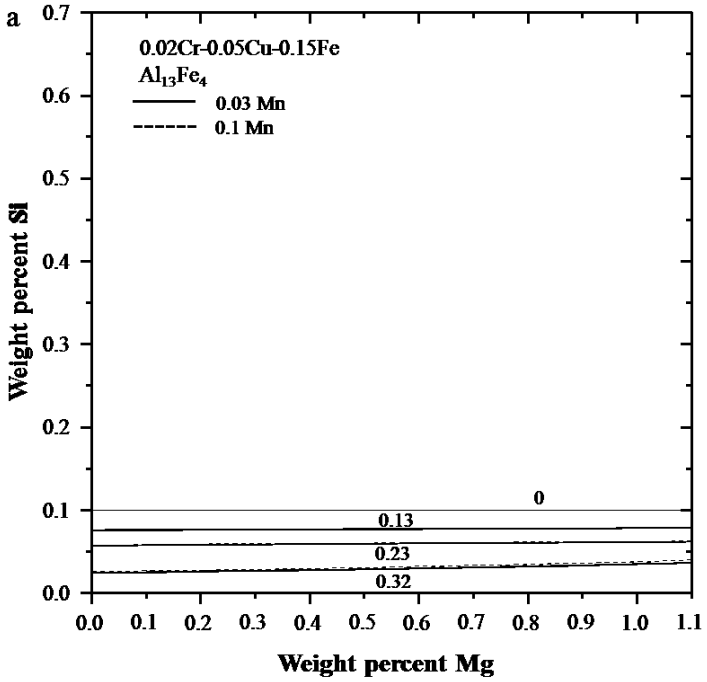
a
0.02Cr-0.05Cu-0.15Fe
$Al_{13}Fe_4$
0.03 Mn
0.1 Mn
0
0.13
0.23
0.32
Weight percent Si
Weight percent Mg

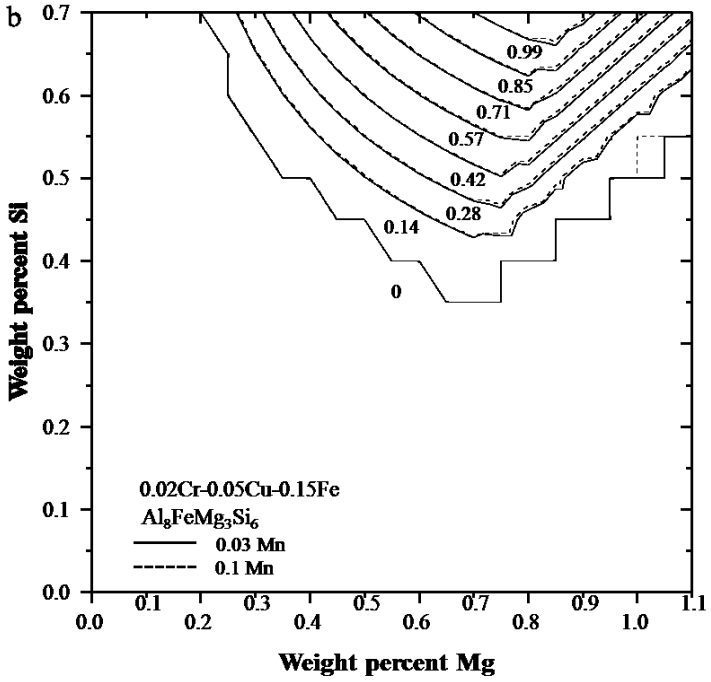
b
0.99
0.85
0.71
0.57
0.42
0.28
0.14
0
0.02Cr-0.05Cu-0.15Fe
$Al_8FeMg_3Si_6$
0.03 Mn
0.1 Mn
Weight percent Si
Weight percent Mg

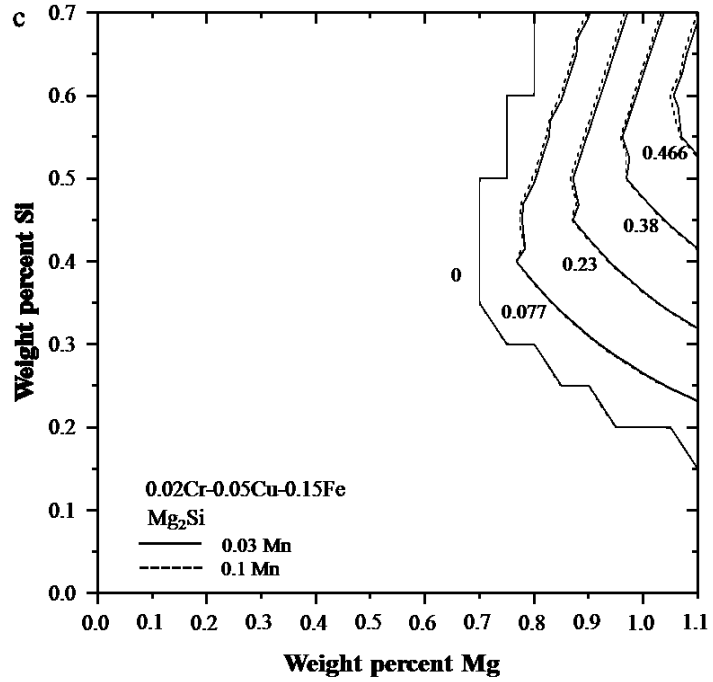
c
Weight percent Si
Weight percent Mg
0.02Cr-0.05Cu-0.15Fe
Mg2Si
0.03 Mn
0.1 Mn
0
0.077
0.23
0.38
0.466

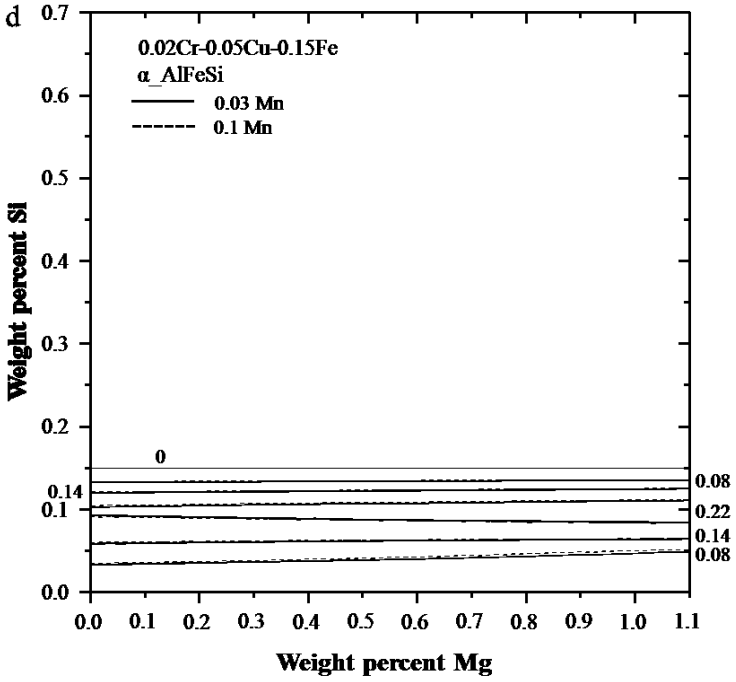
d
Weight percent Si
Weight percent Mg
0.02Cr-0.05Cu-0.15Fe
α_AlFeSi
0.03 Mn
0.1 Mn
0
0.14
0.08
0.22
0.14
0.08

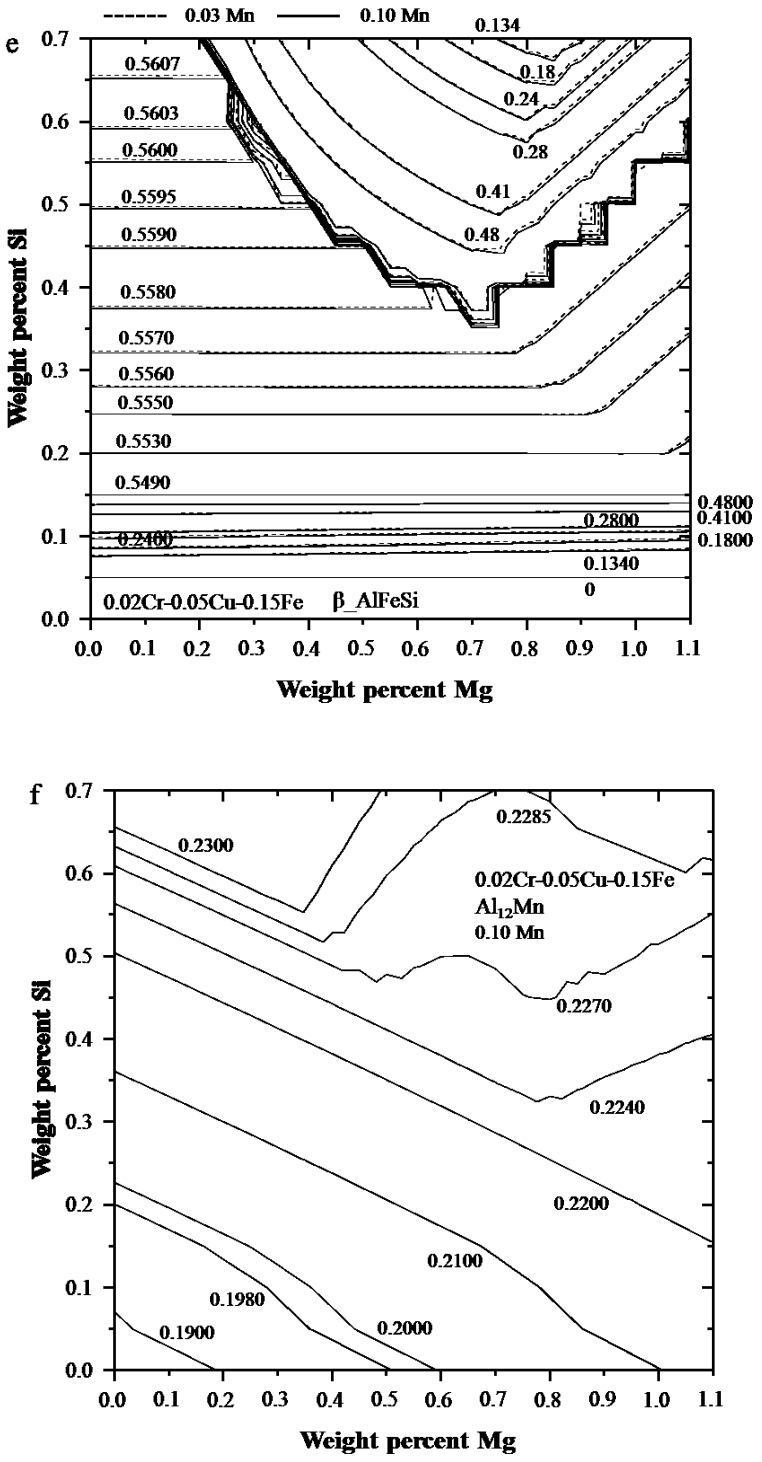

Fig. 12.2.10 Phase fraction maps of the (a) $Al_{13}Fe_4$, (b) $Al_8FeMg_3Si_6$, (c) Mg_2Si, (d) α_AlFeSi, (e) β_AlFeSi, and (f) $Al_{12}Mn$ phases in Al-Mg-Si-0.02Cr-0.05Cu-0.15Fe with 0.03Mn or 0.10Mn at 500 °C.

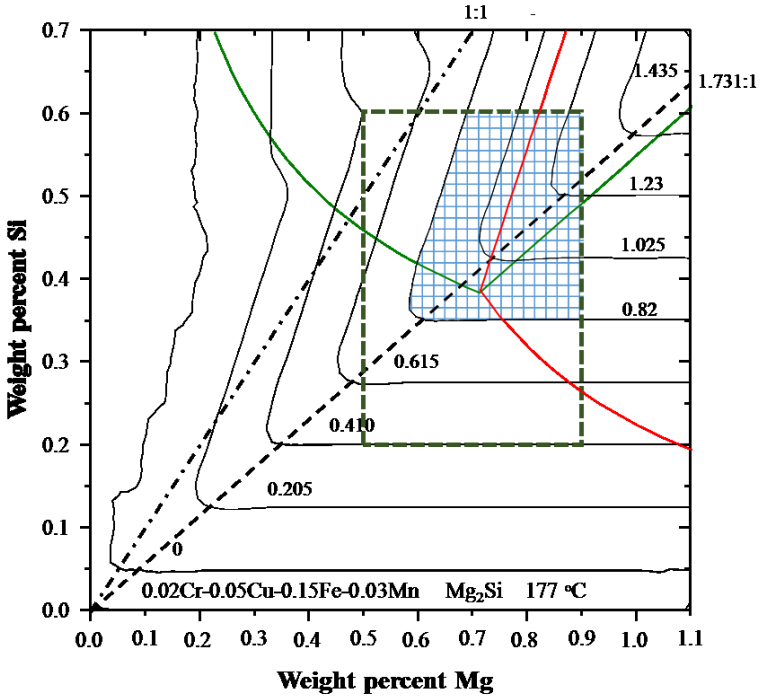

Fig. 12.2.11 Phase fraction map of Mg_2Si in Al-Mg-Si-0.02Cr-0.05Cu-0.15Fe-0.03Mn alloy at 177 °C.

Chapter 13 Summary and future work

13.1 Summary of the current thesis

The present research was carried out to develop a self-consistent thermodynamic database for the Al-Cr-Cu-Fe-Mg-Mn-Si system. Critical evaluation and thermodynamic modeling of the phase diagrams and thermodynamic properties of 10 binaries, 12 ternary systems, and multicomponent systems were performed. The discrepancies among the available data were resolved. The extrapolations were made in a thermodynamically reasonable way. The Gibbs energy of the liquid phase was modeled using the Modified Quasi-chemical Model (MQM) in pair approximation. The Gibbs energies of the solid phases, like fcc_A1, bcc_A2, cub_A13, cbcc_A12, diamond_A4, etc., were modeled using the Bragg-Williams random mixing model. All the other solid phases, like Q, γ_H_AlCr, γ_L_AlCr, Al_7Cr, etc., were modeled using the Compound Energy Formalism. The magnetic ordering was described using the Hillert-Jarl-Inden model, and the chemical ordering (A2/B2, B2/D03) was modeled using the split sub-lattice model. By combining the previously published thermodynamic descriptions in the literature, a thermodynamic database for the Al-Cr-Cu-Fe-Mg-Mn-Si system was constructed. Finally, the obtained thermodynamic database was applied to study the recycling of aircraft Al alloys and the alloy development for Al alloys. The summary of each chapter is presented below:

In Chapter 4, the phase relation in the Al rich corner of the Al-Cr-Mg system was re-investigated at 400, 450, and 500 °C via solid/solid diffusion couples, equilibrated alloys, and differential thermal analysis. The homogeneity range of the $Al_{18}Cr_2Mg_3$ phase was experimentally determined to be Al-(8.7±0.6) at.% Cr-(13.0±2) at.% Mg. The thermodynamic descriptions for the Al-Cr and Al-Cr-Mg system were obtained on the basis of the critically evaluated phase diagram and thermodynamic data in the literature and the new experimental data. Besides, the liquid phase of the Cr-Mg system was modified into MQM. The only compound $Al_{18}Cr_2Mg_3$ was modeled as a stoichiometric compound.

In Chapter 5, a revision of the Al-Mn system was conducted by adding the thermodynamic description of the γ_H (Al_8Mn_5) phase. The liquid Cr-Mn phase was remodeled using MQM on the basis of the previous assessment. Thermodynamic modeling for the Al-Cr-Mn ternary system was conducted on the basis of the critically evaluated phase diagram data in the whole composition and temperature range. The γ_L phase was modeled with a sub-lattice model, $(Al)_{12}(Cr, Mn)_5(Al, Cr, Mn)_9$. Similarly, $(Al, Cr, Mn)_2(Al, Cr, Mn)_3(Cr, Mn)_2(Al)_6$ was used for the γ_H phase. The $AlCr_2$ phase was modeled as $(Al, Cr, Mn)_1(Al, Cr, Mn)_2$. Al_4Cr and Al_4Mn form a continuous solid solution and was modeled with a sub-lattice model: $(Al, Va)_4(Cr, Mn)$. Similarly, $Al_{29}Mn_{10}$, $Al_{11}Cr_2$, $Al_{11}Cr_4$, Al_7Cr, $Al_{99}Mn_{23}$, Al_6Mn, and $Al_{12}Mn$ phases were modeled as $(Al, Cr, Mn)_{29}(Cr, Mn)_{10}$, $Al_{11}(Mn, Cr)_2$, $Al_{11}(Mn, Cr)_4$, $Al_7(Cr, Mn)$, $Al_{99}(Mn, Cr)_{23}$, $Al_6(Mn, Cr)$, and $Al_{12}(Mn, Cr)$, respectively.

In Chapter 6, thermodynamic modeling for the Cr-Si and Al-Cr-Si systems were conducted on the basis of the critically evaluated thermodynamic and phase diagram data. The heat capacities of several Cr-Si compounds were re-modeled. The ternary compounds τ1 ($Al_{13}Cr_4Si_4$), τ2 (Al_9Cr_3Si), τ3 ($(Al, Si)_{11}(Cr)_4$), and τ4 ($Al_{116}Cr_{63}Si_{21}$) were considered during the optimization process.

In Chapter 7, thermodynamic and phase diagram information available in the literature on the Cu-Cr system, Cu-Fe-Cr system, and Cu-Fe-Mn system were comprehensively evaluated. Then, thermodynamic modeling for the Cu-Fe-Cr and Cu-Fe-Mn systems were conducted. The thermodynamic descriptions of the liquid Fe-Cr and Cu-Mn systems were also optimized by MQM.

In Chapter 8, thermodynamic modeling for the ternary Al-Cu-Cr system was conducted on the basis of the critically evaluated phase diagram data. The ζ phase and the κ phase were modeled as $(Al, Cu)_{41}(Cr)_9$ and $(Al, Cu)_4(Cr)$, respectively. The β ($Al_{92}Cu_{67}Cr_{41}$), ψ ($Al_{65}Cu_{25}Cr_{10}$), and ϕ ($Al_{141}Cu_{36}Cr_{23}$) phases were modeled as stoichiometric compounds. The liquid phase of the Al-Cu-Mn system was revised into MQM.

Chapter 9 presented the thermodynamic modeling of the Cu-Mg, Al-Cu-Mg, Al-Cu-Si, and Cu-Mg-Si systems using the CALPHAD technique. A set of high quality and self-consistent

thermodynamic description for the Al-Cu-Mg-Si quaternary system was constructed. In the Cu-Mg system, all the thermodynamic and phase diagram data were very well reproduced. In the Al-Cu-Mg system, V ($Al_5Cu_6Mg_2$), S (Al_2CuMg), and U ($Al_7Cu_3Mg_6$) were modeled as ternary stoichiometric compounds. The T ($Mg_{32}(Al, Cu)_{49}$), Laves_C15, Laves_C14, and Laves_C36 phases were modeled as ternary solutions. In the Al-Cu-Si system, no ternary compound was modeled. The bcc_A2, hcp_A3, and γ_L phases were modeled with ternary extension. Two compounds E (Cu_3Mg_2Si) and D ($Cu_{16}Mg_6Si_7$) were treated. In the quaternary system, the Q ($Al_3Cu_2Mg_9Si_7$) phase was treated as a stoichiometric compound and the S (Al_2CuMg) phase was treated as a quaternary solution. All the thermodynamic and phase diagram information were very well reproduced.

In Chapter 10, thermodynamic and phase diagram data of the Fe-Si system available in the literature were critically evaluated and optimized. Two sets of improved thermodynamic descriptions for the Fe-Si system was obtained. In the first set of the descripiton, the liquid phase was modeled using MQM, and the other set of parameters employed the Bragg-Willimas random mixing model for the liquid phase. The A2/B2 and B2/D03 phase transitions were modeled using the split two and four sub-lattice models, respectively. The magnetic ordering was also well reproduced. Thermodynamic properties for the intermetallic compounds and solution phases were well reproduced.

In Chapter 11, the thermodynamic and phase diagram information available in the literature for the Fe-Si-Cr and Fe-Si-Mg systems were reviewed. Thermodynamic modeling for the Fe-Si-Cr and Fe-Si-Mg ternary systems were then conducted. The A2/B2 transition in the Fe-Si-Cr system were described. The phase equiliribria in subsolidus temperature and the primary crystalline phase region in the Fe-Si-Cr system were well reproduced. The high temperature miscibility gap in the Fe-Mg-Si system was also accurately described.

In Chapter 12, thermodynamic database was utilized to design the recycling strategy of aircraft Al alloys. The possibility of recycling aircraft Al alloys into useful aerospace grade Al alloy was investigated using thermodynamic calculations. The removal of major alloying elements was discussed. The current thermodynamic simulation indicates that the sorted 7xxx and 2xxx

aircraft Al alloys can be recycled to the most used 7075 and 2024 alloys, respectively. The unsorted aircraft Al alloys can also be recycled into the 2024 alloy with more recycling steps.

Subsequently, the developed thermodynamic database was used for the new front rail Al alloy design. The obtained thermodynamic database was firstly validated by comparing the amounts of precipitates formed in three casting alloys with those in the current Scheil simulation. Then the effect of variation of alloying elements on the precipitation behavior during solidification process was studied. Besides, the contour diagrams of the amount of different precipitates that can form in the equilibrium condition were calculated at extrusion temperature and ageing temperature. The effect of major alloying elements on the amount of precipitate can form was discussed, and the proper alloy composition to improve the extrusion ability of Al 6063 alloy was proposed.

13.2 Suggestion of future work

In the current work, only the important sub-systems in the Al-Cr-Cu-Fe-Mg-Mn-Si system were optimized. For the purpose of the development of an accurate thermodynamic database specific to only Al alloys, all the ternary and quaternary systems should be optimized. As a first suggestion, all the other ternary systems within the Al-Cr-Cu-Fe-Mg-Mn-Si system should be optimized. Key experiments (diffusion couple technique, equilibrated alloys, and differential thermal analysis) to determine the phase relation in the Al-Cr-Cu-Fe-Mg-Mn-Si system can be done to assist the thermodynamic database development. Considering there is a lack of enthalpy of mixing and enthalpy of formation for a lot of systems, a calorimeter can be developed to measure the enthalpy of formation and mixing of the target systems. In the commercial Al alloys especially aerospace alloys, Zn, Ti, B, and Zr are also among the most important alloying elements. It is necessary to include Zn, Ti, B, and Zr in the currently developed thermodynamic database also. As a second suggestion, the developed thermodynamic database should contain Zn, Ti, B, and Zr. In the future, binary systems, ternary systems, and quaternary systems included in the Al-Cr-Cu-Fe-Mg-Mn-Si-Zn-Ti-B-Zr system can be optimized to extending the current Al thermodynamic database to all the series of Al alloys.

Contributions to original knowledge

1 The thermodynamic descriptions of the Al-Cr, Cu-Cr, Cu-Mg, Cr-Si, Fe-Si, Cu-Mn, Fe-Cr, Cr-Mg, and Cr-Mn systems were optimized for the first time using the modified quasi-chemical model. The thermodynamic properties and phase diagram information for the Al-Cr, Cu-Cr, Cu-Mg, Cr-Si, and Fe-Si systems were accurately described for the first time. The thermodynamic description of the γ_H phase was incorporated in the Al-Mn ternary system for the first time.

2 The thermodynamic descriptions of the Al-Cu-Cr, Al-Cu-Mg, Al-Cu-Si, Al-Cr-Mg, Al-Cr-Mn, Al-Cr-Si, Al-Cu-Mn, Cu-Fe-Cr, Cu-Fe-Mn, Cu-Mg-Si, Cr-Fe-Si, Fe-Mg-Si, and Al-Cu-Mg-Si systems were assessed for the first time using the modified quasi-chemical model. The thermodynamic descriptions of the Al-Cu-Cr, Al-Cr-Mg, and Al-Cr-Mn systems were obtained for the first time. Gibbs energies for the liquid and solid phases were obtained on the basis of the CALPHAD technique which can give a good description of the thermodynamic properties and phase diagram.

3 The phase relations in the Al rich corner of the Al-Cr-Mg system were measured at 400, 450, and 500 °C via solid/solid diffusion couple, equilibrated alloys, and differential thermal analysis. The homogeneity range of the $Al_{18}Cr_2Mg_3$ phase was determined by using both EPMA and SEM analysis.

4 The obtained thermodynamic database was utilized to study the possibility of recycling aircraft Al alloys to aerospace grade Al alloys and to study the effect of major alloying elements on the amounts of precipitates can form under both the solidification condition and equilibrium condition. The aircraft Al alloy was verified to be able to be recycled into 7075 or/and 2024 alloys. The relation between the amount of precipitates and alloy composition of 6xxx series alloys was obtained.